Lecture Notes in Computer Science 4466

Commenced Publication in 1973
Founding and Former Series Editors:
Gerhard Goos, Juris Hartmanis, and Jan van Leeuwen

Editorial Board

Frank B. Sachse Gunnar Seemann (Eds.)

Functional Imaging and Modeling of the Heart

4th International Conference, FIMH 2007
Salt Lake City, UT, USA, June 7-9, 2007
Proceedings

Springer

Volume Editors

Frank B. Sachse
University of Utah
Nora Eccles Harrison Cardiovascular Research and Training Institute
95 South 2000 East, Salt Lake City, UT 84112-5000, USA
E-mail: fs@cvrti.utah.edu

Gunnar Seemann
Universität Karlsruhe (TH)
Institut für Biomedizinische Technik
Kaiserstr. 12, 76128 Karlsruhe , Germany
E-mail: Gunnar.Seemann@ibt.uni-karlsruhe.de

Library of Congress Control Number: 2007927991

CR Subject Classification (1998): I.4, J.3, I.6, I.2.10

LNCS Sublibrary: SL 6 – Image Processing, Computer Vision, Pattern Recognition, and Graphics

ISSN 0302-9743
ISBN-10 3-540-72906-2 Springer Berlin Heidelberg New York
ISBN-13 978-3-540-72906-8 Springer Berlin Heidelberg New York

Typesetting: Camera-ready by author, data conversion by Scientific Publishing Services, Chennai, India
Printed on acid-free paper SPIN: 12072910 06/3180 5 4 3 2 1 0

Preface

Functional imaging and modeling constitute important research approaches to gaining insights into the physiology and pathophysiology of the human heart. Applications of these approaches are promising to support clinical diagnosis and therapy of cardiac diseases, which are the most common cause of death in the western world and a major health problem in Asia.

The series of international conferences on "Functional Imaging and Modeling of the Heart" (FIMH) aims at integrating the research and development efforts in the field of cardiovascular imaging, image analysis and modeling. The main goal is to encourage collaboration between scientists in signal and image processing, imaging, applied mathematics, biophysics, biomedical engineering and computer science, and experts in cardiology, radiology, biology and physiology.

Previous FIMH conferences were held in Helsinki (2001), Lyon (2003), and Barcelona (2005). The 4th FIMH conference was the first outside Europe and took place at the University of Utah, Salt Lake City, USA, on June 7–9, 2007.

These proceedings present peer-reviewed contributions to the FIMH 2007 conference from Asian, European, North American and New Zealandian research groups. Their contributions cover topics of imaging and image analysis, electrophysiology, electro- and magnetocardiography, structure mechanics, and anatomical modeling. The contributions describe both experimental and computational studies. Several contributions are closely related to the clinical application of imaging and modeling approaches.

We would like to thank all authors for their excellent contributions to the FIMH proceedings, all members of the scientific committee for their invaluable efforts during the review process, and all members of FIMH steering committee for their outstanding scientific and organizational guidance.

June 2007

Frank B. Sachse
Gunnar Seemann

Organization

Conference Chairs

Frank B. Sachse, University of Utah, USA
Gunnar Seemann, Universität Karlsruhe, Germany
Alexey Zaitsev, University of Utah, USA

Organization Committee

Alejandro Frangi, Universitat Pompeu Fabra, Spain
Chris Johnson, University of Utah, USA
Rick Rabbit, University of Utah, USA
Ken Spitzer, University of Utah, USA

Scientific Committee

Amir Amini, Washington University St Louis, USA
Elsa Angelini, ENST, France
Theo Arts, Maastricht University, Netherlands
Leon Axel, New York University, USA
Nicholas Ayache, INRIA, France
Bart Bijnens, Katholieke Universiteit Leuven, Belgium
Peter Bovendeerd, Technical University Eindhoven, Netherlands
Juan Cebral, George Mason University, USA
Patrick Clarysse, CREATIS, Lyon, France
Piet Claus, Katholieke Universiteit Leuven, Belgium
Jean-Louis Coatrieux, LTSI, Rennes, France
Herve Delingette, INRIA, France
James Duncan, Yale University, USA
Riccardo Fenici, Catholic University of Rome, Italy
Alejandro Frangi, University Pompeu Fabra, Spain
Mireille Garreau, LTSI, Rennes, France
Alfredo Hernandez, LTSI, Rennes, France
Arun Holden, University of Leeds, UK
Gerhard Holzapfel, Royal Institute of Technology, Sweden
David Hose, University of Sheffield, UK
Edward Hsu, University of Utah, USA
Peter Hunter, Auckland University, New Zealand
Peter Kohl, University of Oxford, UK
Mike Kirby, University of Utah, USA
Andrew Laine, Columbia University, USA

Boudewijn Lelieveldt, Leiden University, Netherlands
Christian Lorenz, Philips Research Labs, Germany
Isabelle Magnin, CREATIS, Lyon, France
Andrew McCulloch, University of California, USA
Rob MacLeod, University of Utah, USA
Elliot McVeigh, NIH, USA
Dimitris Metaxas, Rutgers University, USA
Johan Montagnat, CREATIS, Lyon, France
Wiro Niessen, UMC, Netherlands
Alison Noble, Medical Vision Laboratory, Oxford, UK
Petia Radeva, Computer Vision Center, Spain
Hans Reiber, Leiden University Medical Center, Netherlands
Daniel Rueckert, Imperial College of Science and Technology, UK
Frank Sachse, University of Utah, USA
Gunnar Seemann, Universität Karlsruhe, Germany
Peter Sloot, University of Amsterdam, Netherlands
Bruno Taccardi, University of Utah, USA
Bernhard Tilg, University for Health Informatics and Technology, Austria
Max Viergever, UMC, Utrecht, Netherlands
Jeffrey Weiss, University of Utah, USA

Organization Team

Kraisorn Chaisaowong, RWTH Aachen University, Germany
Ted Dustman, University of Utah, USA
Matthias Reumann, Universität Karlsruhe, Germany
Shelley Smith, University of Utah, USA
Michael Tansella, Universität Karlsruhe, Germany
Denise Voisin, Westminster College, Utah, USA
Madeline Warren, Westminster College, Utah, USA
Daniel L. Weiss, Universität Karlsruhe, Germany

Acknowledgments

The FIMH 2007 was organized at the University of Utah, USA, with major involvement of the Nora Eccles Harrison Cardiovascular Research and Training Institute (CVRTI), the Scientific Computing and Imaging Institute (SCI), and the Bioengineering Department. Further credit is due for support from the Institute of Biomedical Engineering, Universität Karlsruhe (TH), Germany. The conference was co-sponsored by the IEEE Engineering in Medicine and Biology Society.

Table of Contents

Imaging and Image Analysis

Cardiac Electrophysiology

Electro- and Magetocardiography

Cardiac Mechanics and Clinical Application

Imaging and Anatomical Modeling

Local Wall-Motion Classification in Echocardiograms Using Shape Models and Orthomax Rotations

K.Y. Esther Leung and Johan G. Bosch

Biomedical Engineering, Thoraxcenter, Erasmus MC, Rotterdam, The Netherlands
k.leung@erasmusmc.nl
http://www.erasmusmc.nl/ThoraxcenterBME

Abstract. Automating the analysis of left ventricular (LV) wall motion can improve objective prediction of coronary artery disease. A new method for classifying LV wall motion using shape models with localized variations was developed for this purpose. These sparse shape models were built from four-chamber and two-chamber echocardiographic sequences using principal component analysis and orthomax rotations. The resulting shape parameters were then used to classify wall-motion abnormalities of LV segments. Compared with the shape model before rotation, higher classification correctness was achieved using significantly less shape parameters. The local variations exhibited by these shape parameters correlated reasonably with the location of the segments.

1 Introduction

Coronary artery diseases are a major cause of death in the western world. Detection of wall-motion abnormalities of the left ventricle (LV), widely accepted as predictors for these diseases, is therefore of great clinical importance. To improve the diagnostic quality of the detection, current visual analysis methods should be automated. The goal of this study is to evaluate a new automated classification approach to detect local wall-motion abnormalities, using point-distribution models with localized variations.

Point-distribution models, or shape models, are parametric representations of a set of shapes. First applied to face analysis, these models have since then been used in various medical image processing contexts, especially segmentation [1],[2]. Shape models are often built using Principal Component Analysis (PCA), which maximizes the variance of the input data. This results in models with global variations. In our previous work, PCA shape models of the LV endocardial borders were used to classify wall-motion abnormalities [3]. Clear correlations were found with respect to global clinical parameters (e.g. LV volume), as well as to local parameters (e.g. visual wall-motion scores). However, relatively many shape modes were needed to classify these *local* wall-motion scores, because *global* shape parameters were used. We therefore hypothesize that models with local variations should be able to predict local wall motion using less shape modes.

F.B. Sachse and G. Seemann (Eds.): FIMH 2007, LNCS 4466, pp. 1–11, 2007.

Several methods for building more localized shape models have been proposed, including independent component analysis [4] and various sparse PCA methods [5],[6]. Recently, Stegmann et al. [7] suggested a method using orthomax rotations, which is particularly attractive due to its computational feasibility in high-dimensional spaces. The applicability for localized classification was mentioned in that paper, but has not yet been investigated.

To determine whether localized shape models can improve classification of local wall-motion abnormalities of the left ventricle, shape models were constructed using PCA and rotated according to the orthomax criterion. Classification correctness, the number of shape modes needed, and cluster representation were studied, for different proportions of retained variance. The position of the local variations exhibited by the shape modes was compared with the location of the classified segment.

2 Methods

2.1 Shape Modeling

Shape models of the LV endocardial contours were constructed using full-cycle 2D+time (2D+T) echocardiograms. By modeling the complete cardiac cycle, typical motion patterns associated with certain pathologies were included. More details of the model can be found in our previous work [8].

Each 2D+T shape was represented as a vector $\mathbf{x}$, consisting of landmark coordinates in a number of cardiac phases. Shape models describing the main variations in a patient population were built using PCA:

$$\mathbf{x} = \bar{\mathbf{x}} + \mathbf{\Phi b} \ , \tag{1}$$

where $\bar{\mathbf{x}}$ denoted the average shape, $\mathbf{\Phi} = (\phi_1 | \ldots | \phi_p)$ the $n \times p$ matrix of orthogonal shape eigenvectors or modes, and $\mathbf{b}$ a vector of shape coefficients. Each shape could be seen as a point $\mathbf{b}$ in a p-dimensional parameter space spanned by the p orthogonal eigenvectors. Any new shape could be approximated in this PCA space using the pseudoinverse ($\mathbf{\Phi}^{-1}$) of the eigenvector matrix:

$$\mathbf{b} \approx \mathbf{\Phi}^{-1}(\mathbf{x} - \bar{\mathbf{x}}) \ . \tag{2}$$

To obtain a more compact model, k eigenvectors with the largest eigenvalues λ_i were kept, so that only a proportion f of the total variance $V = \sum_{i=1}^{p} \lambda_i$ was retained:

$$\sum_{i=1}^{k} \lambda_i \geq fV \ . \tag{3}$$

2.2 Orthomax Rotations

Orthomax rotations were applied to the PCA shape models to produce models with localized spatial variations [7],[9]. Orthomax rotations are reparameterizations of the PCA space so that the resulting Orthomax PCA (OPCA) space has

a simple basis. The orthonormal orthomax rotation matrix $\mathbf{R}$ is calculated by maximizing the criterion ξ:

$$\xi = \{\sum_{j=1}^{k}\sum_{i=1}^{n} G_{ij}^4 - \frac{\gamma}{n}\sum_{j=1}^{k}[\sum_{i=1}^{n} G_{ij}^2]^2\}/n \ , \tag{4}$$

where G_{ij} denotes the scalar element in the i^{th} row and j^{th} column in the rotated eigenvector matrix $\mathbf{G} = \mathbf{\Phi R}$, and γ is determined by the orthomax type. The shape coefficients after rotation $\mathbf{b}_R$ can be found with $\mathbf{b}_R = \mathbf{R}^{-1}\mathbf{b}$. Common orthomax types include varimax ($\gamma = 1$), quartimax ($\gamma = 0$), and parsimax ($\gamma = n(k-1)/(n+k-2)$) [9]. In this study, the varimax criterion [10] was investigated, although the other criteria gave similar sparse representations in our initial experiments.

Interestingly, the orthogonal orthomax criterion is equivalent to the Crawford-Ferguson criterion, which is a weighted sum of row and column complexity of the eigenvector matrix [11]. Therefore, orthomax rotations can be interpreted as a redistribution of the factor loadings of the eigenvector matrix so that each row or column has a minimum number of nonzero elements, i.e. columns or rows are as sparse as possible. When applied to a *shape* eigenvector matrix, the variation for a certain mode is emphasized in certain spatial regions of the shape, whereas the variation is suppressed in other regions (see Fig. 1).

An important property to consider is the number of modes k. PCA generates global modes which are ordered according to the variance of the input set. Therefore, PCA modes with low eigenvalues generally contain noise. Eliminating some of these modes may lead to more representative local variations in the OPCA shape model. However, if too many modes are removed, important information needed for classification may be lost. Also, a lower k generally results in less localized shape variations, because each mode must capture more variations (see Fig. 1).

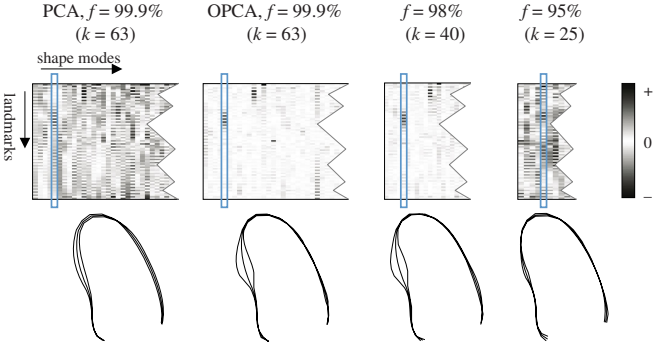

Fig. 1. Top row: eigenvector matrices of PCA and rotated PCA shape model of the four-chamber. Bottom row: end-diastolic shape variations of the fifth mode, showing more localization for higher proportions of retained variance in the shape model.

2.3 Data Description

The effect of orthomax rotations was demonstrated on dobutamine stress echo data from 129 unselected infarct patients participating in a clinical trial [3],[12]. Myocardial wall motion in these images was evaluated visually by consensus of two expert readers. The whole LV was subdivided into 13 segments (see Fig. 2), and all segments were given a motion score according to the four-point system (0 = normokinesia, 1 = hypokinesia, 2 = akinesia, 3 = dyskinesia) [12].

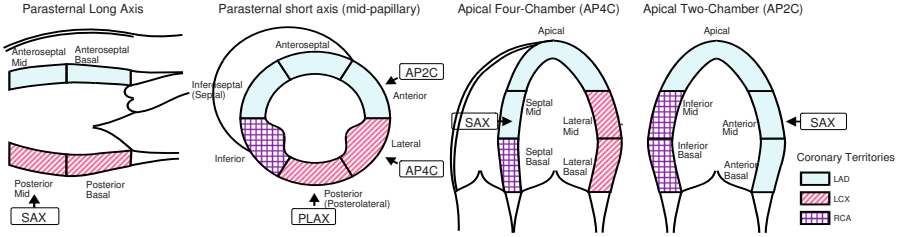

Fig. 2. Coronary territories (LAD = left anterior descending artery, LCX = left circumflex artery, RCA = right coronary artery) and LV wall segments

The transthoracic apical four-chamber and two-chamber sequences from the rest stage were available for shape modeling. Each time sequence was phase-normalized to 16 frames, where the first and last frame corresponded to end-diastole (ED) and the ninth frame to end-systole (ES). Endocardial borders were delineated using a semi-automated tracing program (ECHO-CMS system [13]), independent of the visual wall motion scoring. The contour in each frame was modeled by 37 landmark points.

The total data set was split randomly into a training set (TRN) of 65 patients and a testing set (TST) of 64 patients. Shape models of the four-chamber and two-chamber were built with the training set. Shape coefficients $\mathbf{b}$ and $\mathbf{b}_R$ were calculated for all data sets and used as the shape parameters in the classification. Different numbers of shape modes k were investigated (eq. 3): $f = 95\%$, 98%, 99% and 99.9% corresponding with $k = 27$, 40, 48, and 63 shape coefficients in the four-chamber model, and $k = 25$, 38, 46, and 62 shape coefficients in the two-chamber model.

2.4 Wall-Motion Classification

Linear discriminant analysis was performed to find an optimal classification of visual wall motion scores from a minimal number of shape parameters. According to our hypothesis, less shape parameters should be needed in the OPCA space than in the original PCA space.

Two classification experiments were performed, representing an 'ideal' situation and a 'worst-case' situation. In both cases, the shape model was trained on the TRN set. In the 'ideal' case, the classifier was trained on the TRN set using

a leave-one-out approach and tested on the TRN set only. In the 'worst-case' situation, the classifier was trained on the whole TRN set and then tested on all TST cases. This resembled classification in the real-world: both shape model and classifier were trained from a limited training set and tested on completely 'new' shapes. Wall-motion scores of each of the nine segments in the four-chamber and two-chamber views were grouped into two classes, representing normal (score = 0) and abnormal (score > 0) motion, before classification; this resulted in reasonably balanced classes in most cases.

To assess the classification in the PCA and OPCA space, cluster measurements were computed. The subset q of the k shape parameters used by the classifier was selected. Each shape could be seen as a point in this reduced q-dimensional classification space; ideally, points of a class should form a compact cluster, completely separated from the point-cluster of the other class. Measures of class compactness and class separation are the within-class scatter matrix $\mathbf{S}_W$ and the between-class scatter matrix $\mathbf{S}_B$ [14]. Since $\mathbf{S}_W$ and $\mathbf{S}_B$ are related to the variance of the point-cluster in each direction, a better measure of cluster quality is the ratio J of the trace of the two scatter matrices ([15], p. 311): $J = \frac{\mathrm{tr}(\mathbf{S}_B)}{\mathrm{tr}(\mathbf{S}_W)}$.

2.5 Categorizing Orthomax Shape Modes

Once the classifier had selected the subset of the OPCA shape modes for classifying each LV segment, we investigated whether these modes indeed exhibited the most prominent variation in that segment. Since this information did not directly result from the orthomax rotation, and manually categorizing all parameters would be a very time-consuming job, we applied an adapted version of the geometry-based sorting method proposed by Suinesiaputra et al. [14] (see Fig. 3).

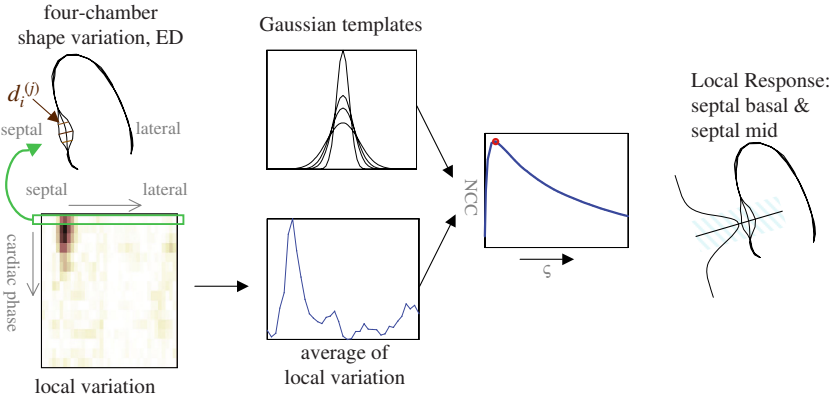

Fig. 3. Categorizing local variation into LV segments using Gaussian templates and normalized cross-correlation (NCC)

The goal of this method was to determine the position and spread of the most prominent local (spatial) variation, i.e. the *local response*, for each shape mode. The local variation $d_i^{(j)}$ of shape mode i was defined as the displacement perpendicular to the average contour caused by the shape variation $\mathbf{b}_i = \mathbf{e}_i$, where $\mathbf{e}_i$ was a vector with element $\sqrt{\lambda_i}$ at the i^{th} position and zero otherwise. For a slightly easier interpretation, the average $\bar{\mathbf{d}}_i$ of $d_i^{(j)}$ was calculated across the time dimension. Next, normalized cross-correlation (NCC) was performed between $\bar{\mathbf{d}}_i$ and Gaussian shape templates with different kernel sizes σ. The Gaussian template giving the maximum NCC for each shape mode represented the position and spread of the most prominent local variation. We attributed the shape mode to a wall segment if that segment fell within the full-width at half-maximum (FWHM $= 2\sqrt{2\ln 2}\sigma$) of the Gaussian template. This method could also detect noise modes with no prominent local variation, corresponding to a wide Gaussian template [14]. In that case, the shape mode was defined as having no local response.

In summary, the q shape modes used for classifying a certain LV segment were categorized and examined to see whether their local responses were related to the segment being classified. We checked whether the local responses were in the same or adjacent segment, and whether they were in the segments perfused by the same coronary artery, since correlations are expected between wall-motion scores in the same coronary territory (see Fig. 2).

3 Results

Varimax rotations were applied to four-chamber and two-chamber 2D+T shape models. The implementation in Matlab (v. 7.0.4 (R14), 2005), based on singular value decomposition, was used. Whereas PCA shape modes are ordered according to variance, thus exhibiting global variations in the first modes, OPCA modes show local variations in most modes (see Fig. 4).

Shape parameters were used to predict the presence of wall motion abnormalities per segment. Classification was performed using the Linear Discriminant Analysis option in statistical package SPSS (v. 11.0.1, 2001). Shape parameters were added using the 'stepwise' option. For shape models with $f = 99.9\%$ retained variance, varimax rotations reduced the number of parameters in segmental wall-motion classification, from 8.0 to 5.1 (see Table 1). Equal or better classification correctness was achieved with significantly less shape parameters for $f \geq 99\%$ (see Table 2). Cluster quality J (section 2.4) shows better cluster separation (larger J) in the OPCA space than the PCA space in most cases.

The local responses of the OCPA shape modes used in the classification were calculated (see section 2.5). The proportions of shape modes directly correlating with the classified segments are given in Table 3. For example, for $f = 99.9\%$, 63.0% of the modes used in classification gave a response in the same or adjacent segment, 28.3% of the modes gave a response in an other segment, and 8.7% of the modes were noise modes.

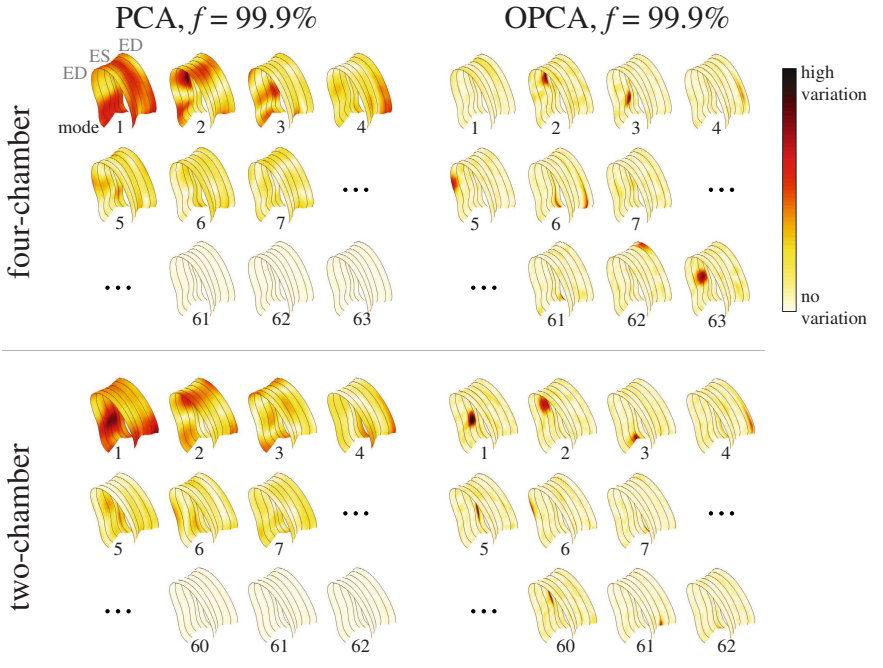

Fig. 4. PCA and varimax rotated modes. Absolute displacements of the landmarks due to ±3 SD model-variation are shown in color on the average 2D+T shape. PCA modes are ordered according to variance; OPCA modes are unordered.

Table 1. Classification correctness versus the number of PCA and OPCA shape parameters used, and the proportion of abnormal cases, for nine segments

		PCA $f = 99.9\%$			OPCA $f = 99.9\%$		
		Classification correctness		# parameters	Classification correctness		# parameters
View	Segment	TRN L-1-O	TST		TRN L-1-O	TST	
4C+2C	Apical	93.8%	81.3%	7	95.4%	85.9%	6
4C	Septal Basal	86.6%	70.3%	10	90.8%	64.1%	5
4C	Septal Mid	92.3%	73.4%	12	92.3%	73.4%	11
4C	Lateral Basal	86.2%	64.1%	8	90.8%	82.8%	2
4C	Lateral Mid	76.9%	69.8%	6	81.5%	71.4%	2
2C	Anterior Basal	95.4%	95.3%	3	96.9%	96.9%	2
2C	Anterior Mid	93.8%	74.6%	11	93.8%	76.2%	9
2C	Inferior Basal	84.6%	71.9%	5	90.8%	71.9%	5
2C	Inferior Mid	90.8%	65.6%	10	87.7%	65.6%	4
	mean	88.9%	74.0%	8.0	91.1%	76.5%	5.1
	SD	5.9%	9.4%	3.0	4.5%	10.5%	3.2

Table 2. Classification correctness versus the number of PCA and OPCA shape modes used (mean±SD), for different proportions of retained variance f in the shape models. * denotes significantly ($p < 0.05$, paired t-test) less shape parameters than PCA.

		Classification correctness		#parameters
	f	TRN L-1-O	TST	.
PCA	99.9%	$88.9 \pm 5.9\%$	74.0±9.4%	8.0 ± 3.0
OPCA	99.9%	$91.1 \pm 4.5\%$	76.5±10.5%	5.1 ± 3.2*
	99%	$88.9 \pm 5.9\%$	76.0±8.7%	5.7 ± 3.3*
	98%	$87.7 \pm 7.0\%$	75.8±9.5%	6.4 ± 3.5
	95%	$86.3 \pm 6.1\%$	76.3±9.0%	6.6 ± 3.7

Table 3. Categorizing shape parameters used in the classification according to their local responses

Retained variance f	99.9%	99%	98%	95%
same or adjacent segment	63.0%	60.8%	55.2%	66.1%
other segment	28.3%	31.4%	37.9%	25.4%
noise	8.7%	7.8 %	6.9%	8.5%
RCA territory (3 segments)	50.0%	41.2%	35.3%	42.1%
LAD territory (4 segments)	53.6%	53.3%	45.5%	63.6%
LCX territory (2 segments)	50.0%	50.0%	50.0%	42.9%
coronary territory, mean of 9 segments	52.2%	49.0%	43.1%	54.2%

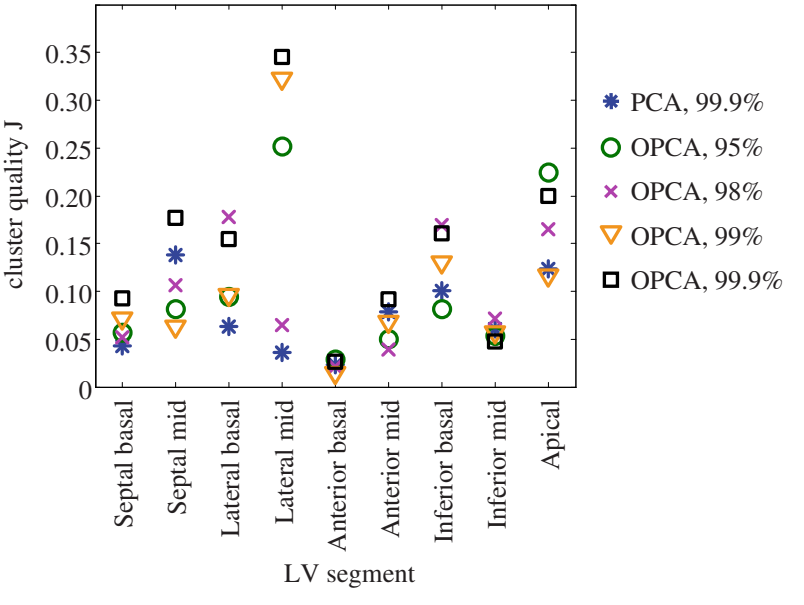

Fig. 5. Cluster quality J (section 2.4) for each wall segment and different number of modes

4 Discussion and Conclusions

In this study, we showed that localized shape models of the left ventricle can be generated with varimax rotations. Using these localized shape models, the number of parameters needed for classifying segmental wall motion abnormalities in 2D echocardiographic sequences was reduced significantly, without compromising classification correctness. The relatively large improvement in the lateral segment may be due to the combination of the varimax rotation and the variations in the TRN set, which by chance produced a sparser parameter representation for those segments.

Furthermore, the normal and abnormal wall motion classes were better separated in the OPCA parameter space than in the original PCA space. Although the data set is too small to determine a clear relationship between the improvement in classification correctness, the number of shape modes used, and cluster quality, classification is generally expected to be better in a well-defined parameter space. However, the cluster measurements revealed that there is still a reasonable amount of overlap of the classes, suggesting that better classification might be achieved with a nonlinear discriminant function. More advanced feature selection methods and nonlinear classifiers, such as support vector machines, might lead to a better class discrimination.

The local shape modes used in the classification correlated reasonably with the most prominent local variation, although other uncorrelated modes were used as well. The latter could partly be due to the categorization method, which only detected the location of the most prominent variation and not residual variations in other segments. Another reason may be the high variability of visual wall motion scoring. Regrettably, this variability could not be determined for this data set because the scoring was performed by consensus. In the future, we would like to use a more objective measure such as quantitative coronary angiography, to demonstrate the relationship between local shape variations and functional consequences of coronary lesions more precisely.

Although regional variation is important in analyzing wall motion, global shape changes may add valuable information, especially in the case of cardiac pathology. Therefore, classification using local variations, supplemented with a limited set of global variations, could lead to better results. In this context, the fact that the orthomax criterion also allows rotations of *subsets* of the shape model [16] is worth mentioning. This is a subject of further investigation.

Finally, since pathologies are typically spatially localized, we anticipate many medical applications where sparse representations are preferred to the conventional PCA approach. The orthomax criterion is shown to be suitable for building these sparse representations with relative ease. Although not explored in this study, sparse texture models can be constructed in a very similar manner [7]. The direct cardiac application would be to examine myocardial thickening, which might also be a predictor of coronary disease. In the future, we would like

to extend the method to coupled shape models of rest and stress stage cardiac contours, to investigate local differences in wall-motion.

Acknowledgments

Financial support from the Dutch Technology Foundation STW is gratefully acknowledged. We thank O. Kamp and F. Nijland for providing the patient data, G. van Burken for the data analysis support, and M. van Stralen, M. M. Voormolen, M. Sonka, and M. B. Stegmann for the useful discussions.

References

1. Cootes, T.F., Edwards, G.J., Taylor, C.J.: Active appearance models. IEEE Trans. Pattern Anal. Machine Intell. 23(6), 681–685 (2001)
2. Stegmann, M.B.: Generative interpretation of medical images. PhD thesis, Technical University of Denmark (2004)
3. Bosch, J.G., Nijland, F., Mitchell, S.C., Lelieveldt, B.P.F., Kamp, O., Reiber, J.H.C., Sonka, M.: Computer-aided diagnosis via model-based shape analysis: Automated classification of wall motion abnormalities in echocardiograms. Acad. Radiol. 12(3), 358–367 (2005)
4. Üzümcü, M., Frangi, A.F., Reiber, J.H.C., Lelieveldt, B.P.F.: Independent component analysis in statistical shape models. In: Proc. SPIE Med. Imag.: Image Processing, vol. 5032, pp. 375–383 (2003)
5. Zou, H., Hastie, T., Tibshirani, R.: Sparse principal component analysis. Tech. rep. Standford University (2004)
6. Sjöstrand, K., Stegmann, M.B., Larsen, R.: Sparse principal component analysis in medical shape modeling. SPIE Med. Imag.: Image Processing 6144, 61444X (2006)
7. Stegmann, M.B., Sjöstrand, K., Larsen, R.: Sparse modeling of landmark and texture variability using the orthomax criterion. SPIE Med. Imag.: Image Processing 6144, 61441G (2006)
8. Bosch, J.G., Mitchell, S.C., Lelieveldt, B.P.F., Nijland, F., Kamp, O., Sonka, M., Reiber, J.H.C.: Automatic segmentation of echocardiographic sequences by active appearance motion models. IEEE Trans. Med. Imag. 21(11), 1374–1383 (2002)
9. Browne, M.W.: An overview of analytic rotation in exploratory factor analysis. Multivar. Behav. Res. 36(1), 111–150 (2001)
10. Kaiser, H.F.: The varimax criterion for analytic rotation in factor analysis. Psychometrika 23(3), 187–200 (1958)
11. Crawford, C.B., Ferguson, G.A.: A general rotation criterion and its use in orthogonal rotation. Psychometrika 35(3), 321–332 (1970)
12. Nijland, F., Kamp, O., Verhorst, P.M.J., de Voogt, W.G., Bosch, H.G., Visser, C.A.: Myocardial viability: impact on left ventricular dilatation after acute myocardial infarction. Heart 87, 17–22 (2002)
13. Bosch, H.G., van Burken, G., Nijland, F., Reiber, J.H.C.: Overview of automated quantitation techniques in 2D echocardiography. In: Reiber, J.H.C., van der Wall, E.E. (eds.) What's New in Cardiovascular Imaging? Kluwer Academic Publishers, Boston (1998)

14. Suinesiaputra, A., Frangi, A.F., Üzümcü, M., Reiber, J.H.C., Lelieveldt, B.P.F.: Extraction of myocardial contractility patterns from short-axis MR images using independent component analysis. In: Sonka, M., Kakadiaris, I.A., Kybic, J. (eds.) Computer Vision and Mathematical Methods in Medical and Biomedical Image Analysis. LNCS, vol. 3117, pp. 75–86. Springer, Heidelberg (2004)
15. Webb, A.R.: Statistical Pattern Recognition, 2^{nd} edn. John Wiley & Sons Ltd, New York (2002)
16. Jolliffe, I.T.: Rotation of ill-defined principal component analysis. Appl. Statist. 38(1), 139–147 (1989)

A Fully 3D System for Cardiac Wall Deformation Analysis in MRI Data

F. Jamali Dinan[1], P. Mosayebi[1], H. Abrishami Moghadam[1], M. Giti[2], and S. Kermani[3]

[1] EE Dept. K.N.Toosi University of Technology, P.O.Box 16315-1355, Tehran, Iran
fjdinan2001@yahoo.com, parisa.mosayebi@gmail.com, moghadam@saba.kntu.ac.ir
[2] Tehran Univ. of Medical Science, Medical Imaging Center/Imam Hospital, Tehran, Iran
[3] Amirkabir University of Technology, Tehran, Iran

Abstract. This paper presents an enhanced version of our previous algorithm for point-wise tracking and analysis of cardiac motion based on 3D active mesh model. In the present software, a new 3D active surface model based on curve evolution techniques and level sets is used for automatizing the segmentation of endocardial boundary in the left ventricle in the first phase of cardiac cycle. Furthermore, cardiac muscle anisotropy is modeled and included in the tracking algorithm. Additionally, the tracking algorithm is improved in order to track the left ventriclular wall instead of left ventricular cavity in the previous version. Finally, a quantitative analysis of myocardial strain is performed using the motion estimation obtained by the tracking software. Experiments were performed on cardiac MRI images for tracking the left ventricle myocardium. The results of evaluation on a set of Gradient-Echo images reported in this paper clearly demonstrate the effectiveness of our algorithm for extracting motion parameters.

Keywords: deformable surface, three dimensional active mesh, strain mapping, cardiac MRI.

1 Introduction

Fundamental goal of many efforts in cardiac imaging is to assess the regional function of the left ventricle (LV) of the heart. The general consensus is that the analysis of heart wall dynamics (motion, thickening, strain, etc.) provides quantitative estimates of the location and extent of ischemic myocardial injury. However, imaging-based clinical analysis of regional LV function, usually from SPECT and echocardiography, often results in overestimation of the true myocardial infarction. More sophisticated quantitative analysis of myocardial dynamics may improve the accuracy in the estimation of myocardial injury [1].

Various models have been introduced previously to study heart wall dynamics. A 2.5 dimensional active contour model has been used for volume representation of the heart in a cardiac cycle in [2,7]. However, these models are not able to do point-wise tracking. Alternatively, mesh based algorithms were introduced to segment and track 3D structures in MRI cardiac images [1,3,8,14]. The mesh based tracking methods

F.B. Sachse and G. Seemann (Eds.): FIMH 2007, LNCS 4466, pp. 12–21, 2007.

previously introduced were presented in 2 or 2.5 dimensional space. However, heart is a non rigid moving object which deforms in 3D space. Hence, motion estimation using 2D image sequences do not measure the true movement of the heart. To solve these problems, we previously developed a fully 3D active mesh model based on a finite-element deformable volume to achieve efficient representation of global and local deformations of the left ventricle using cardiac MRI images [4]. Our model is advantagous with respect to 3D motion analysis of the cardiac muscle using tagged MRI [14] from other points of view. For example, our algorithm is able to track the motion in voxel resolution, while the resolution of tags in tagged MRI is considerably less than the image resolution.

For automatizing the developed tracking software, an accurate and efficient 3D segmentation algorithm was needed to automatically segment the left ventricle in the first phase of cardiac cycle. Primary works on automatic segmentation of cardiac images were based on simple techniques such as thresholding or region growing [5]. Some more elaborated approaches were probabilistic or statistical [6]. A disadvantage of probabilistic models is that they require a learning database to adapt themselves with the pathology. Therefore, this image database should be relatively large. A recent segmentation model is level set [7]. The level set model is problematic in including a priori information and also is computationally intensive for 3D+T cardiac data sets. Deformable models or active contours [8] and snake models rely on the edge-function, depending on the image gradient to stop the curve evolution. Chan and Vese proposed a different active contour model which was not based on the gradient of the image for the stopping process [9]. Their model could detect contours either with or without gradient. However, their model was presented in the two dimensional space [9]. In this paper, we have extended the model presented in [9] to three dimensions and used it for the segmentation of endocardial boundary in the left ventricle. By applying the segmentation algorithm to MRI cardiac images, the left ventricle was extracted and then filtered to eliminate noisy parts corresponding to papillary muscles. The extracted surface was used by the tracking algorithm.

For enhancing the tracking software, the cardiac muscle anisotropy was modeled and also the algorithm was adapted to track the left ventricular wall instead of endocardial wall motion in the left ventricle. Furthermore, since it has been shown that a comprehensive quantitative analysis of myocardial strain can more accurately identify ischemic injury than simple analysis of endocardial wall motion [1], we calculated the myocardial strain using the obtained motion estimation.

This paper is structured as follows. In section 2, we describe the 3D object segmentation model. In section 3, the enhanced tracking algorithm is introduced. In section 4, we formulate the strain calculation. Finally in section 5, the experimental results are presented and in section 6, conclusions are drawn.

2 Segmentation

Let I be a 3D image and B be an object located in I.We propose a 3D model for active contours to detect object B based on techniques of curve evolution. For this purpose, we consider the initial surface as a sphere which could be anywhere in I. The initial sphere starts deforming until it stops on the desired boundary.

Let Ω be a bounded open subset of R^3, with $\partial\Omega$ its boundary and u_0 be a given 3D image, $u_0 : \Omega \to R$ .Let us define the evolving Surface S in Ω, as the boundary of an open subset of ω (i.e. $S \subset \Omega$ and $S = \partial\omega$). In what follows, inside S denotes the region ω , and outside denotes the region $\Omega - \omega$ .Consider a simple case where the 3D image u_0 is formed by two regions of piecewise constant intensity.

Denote the intensity values by u_0^o and u_0^i .Furthermore, assume that the object to be detected has a region whose boundary is S_0 and its intensity is u_0^i . Then, consider the following "fitting" term:

$$F_1(S) + F_2(S) = \int_{inside(S)} |u_0(x,y,z) - c_1|^2 dxdydz + \int_{outside(S)} |u_0(x,y,z) - c_2|^2 dxdydz \tag{1}$$

The constants c_1 and c_2 are the averages of u_0 inside and outside S , respectively. If the surface S is outside the object, $F_1(S) \approx 0$ and $F_2(S) > 0$. In case that S is inside the object then, $F_1(S) > 0$ and $F_2(S) \approx 0$. If S is both inside and outside of the object then, $F_1(S) > 0$ and $F_2(S) > 0$. Finally, the fitting energy is minimized if $S = S_0$, i.e. if the surface S is the boundary of the object:

$$F_1(S) + F_2(S) = \int_{inside(S)} |u_0(x,y,z) - c_1|^2 dxdydz + \int_{outside(S)} |u_0(x,y,z) - c_2|^2 dxdydz \tag{2}$$

In our 3D active contour model, we will minimize the above fitting term and will add some regularizing terms to (1) to introduce the energy functional $F(c_1, c_2, S)$, defined by:

$$\begin{aligned} &F(c_1, c_2, S) = \\ &\mu \cdot Area(S) + \nu \cdot Volume(inside(S)) + \lambda_1 \int_{inside(S)} |u_0(x,y,z) - c_1|^2 dxdydz \\ &+ \lambda_2 \int_{outside(S)} |u_0(x,y,z) - c_2|^2 dxdydz \end{aligned} \tag{3}$$

Where $\lambda_1 > 0$, $\lambda_2 > 0$, $\nu \geq 0$ and $\mu \geq 0$ are fixed parameters.

Now we want to find the values of c_1 , c_2 and S so that $F(c_1, c_2, S)$ is minimized. This problem can be formulated using level sets as follows. The evolving surface S can be represented by the zero level set of the signed distance function (Lipschitz function) $\varphi : \Omega \to R^3$ as in (4).

$$\begin{cases} \varphi(x,y,z,t=0) = \pm d \\ S = \partial w = \{(x,y,z) \in \Omega, \varphi(x,y,z,) = 0\} \end{cases} \quad \begin{cases} \text{inside}(S) = w = \{(x,y,z) \in \Omega, \varphi(x,y,z,) > 0\} \\ \text{outside}(S) = w = \{(x,y,z) \in \Omega, \varphi(x,y,z,) < 0\} \end{cases} \tag{4}$$

In (4), d is the distance of (x, y, z) with boundary surface $\partial\omega$ in $t = 0$. Therefore, we replace the unknown variable S by φ . Now consider the Heaviside function H , and the Dirac measure δ :

$$H(z) = \begin{cases} 1, & z \geq 0 \\ 0, & z < 0 \end{cases}, \qquad \delta(z) = \frac{d}{dz} H(z) \tag{5}$$

We can rewrite the lateral surface $\varphi = 0$ and the inside regions $\varphi = 0$ with these functions. As H is positive inside the boundary surface and is zero in other regions, the volume of the inside regions will be the integral of $H(\varphi)$. The gradient of H defines the boundary surface. So summation of it on the assumed region defines the outside boundary surface, mathematically:

$$\begin{aligned} Volume\{\varphi > 0\} &= \int_{\Omega} H(\varphi(x,y,z))dxdydz \\ Area\{\varphi = 0\} &= \int_{\Omega} \nabla H(\varphi(x,y,z))dxdydz = \int_{\Omega} \delta_0(\varphi(x,y,z))|\nabla\varphi(x,y,z)|dxdydz, \end{aligned} \tag{6}$$

Similarly, we can rewrite the previous energy equations so that they are defined over the entire domain Ω rather than separated into inside (S): $\varphi \geq 0$ and outside (S) : $\varphi < 0$ Then, the energy $F(c_1, c_2, S)$ can be written as:

$$\begin{aligned} F(c_1, c_2, S) &= \mu \int_{\Omega} \delta(\varphi(x,y,z))|\nabla\varphi(x,y,z)|dxdydz + \nu \int_{\Omega} H(\varphi(x,y,z))dxdydz \\ &+ \lambda_1 \int_{\Omega} |u_0(x,y,z) - c_1|^2 H(\varphi(x,y,z))dxdydz + \lambda_2 \int_{\Omega} |u_0(x,y,z) - c_2|^2 (1 - H(\varphi(x,y,z)))dxdydz \end{aligned} \tag{7}$$

The constants c_1 and c_2 are the average of u_0 in $\varphi > 0$ and $\varphi < 0$, respectively. So they are easily computed as:

$$c_1(\varphi) = \frac{\int_{\Omega} u_0(x,y,z) H(\varphi(x,y,z))dxdydz}{\int_{\Omega} H(\varphi(x,y,z))dxdydz} \qquad c_2(\varphi) = \frac{\int_{\Omega} u_0(x,y,z)(1 - H(\varphi(x,y,z)))dxdydz}{\int_{\Omega} (1 - H(\varphi(x,y,z)))dxdydz} \tag{8}$$

Keeping c_1 and c_2 fixed, and minimizing F with respect to φ, we can deduce the Euler–Lagrange partial differential equation from (7). We parameterize the descent direction by $t > 0$, so the equation $\varphi_0(x, y, z)$ is:

$$\frac{\partial\varphi}{\partial t} = \delta(\varphi) \cdot \left[\mu \cdot div\left(\frac{\nabla\varphi}{|\nabla\varphi|}\right) - \nu - \lambda_1 (u_0 - c_1)^2 + \lambda_2 (u_0 - c_2)^2 \right] = 0, \tag{9}$$

For solving the above equation, $H(z), \delta(z)$ should be defined. Chan and Vese [9] propose:

$$H_\varepsilon(z) = \frac{1}{2} + \frac{1}{\pi}\arctan\left(\frac{z}{\varepsilon}\right), \delta_\varepsilon(z) = \frac{1}{\pi} \cdot \frac{\varepsilon}{\varepsilon^2 + z^2} \tag{10}$$

Chan and Vese [9] give the discretization and linearization of (9) as (11), where the forward differences of $\varphi^n_{h,j,k}$ are calculated according to (12).

$$\frac{\varphi^{n+1}_{i,j,k} - \varphi^n_{i,j,k}}{\Delta t} = \delta_\varepsilon\left(\varphi^n_{i,j,k}\right)\frac{\mu}{h^2}\Delta_x\left(\frac{{}^{x}_{\Delta+}\varphi^{n+1}_{i,j,k}}{\sqrt{\left({}^{x}_{\Delta+}\varphi^n_{i,j,k}\right)/(h^2) + \left(\varphi^n_{i,j+1,k} - \varphi^n_{i,j-1,k}\right)/(2h)^2 + \left(\varphi^n_{i,j,k+1} - \varphi^n_{i,j,k-1}\right)/(2h)^2}}\right) + \frac{\mu}{h^2}\Delta_y\left(\frac{{}^{y}_{\Delta+}\varphi^{n+1}_{i,j,k}}{\sqrt{\left(\varphi^n_{i+1,j,k} - \varphi^n_{i-1,j,k}\right)/(2h)^2 + \left({}^{y}_{\Delta+}\varphi^n_{i,j,k}\right)/(h^2) + \left(\varphi^n_{i,j,k+1} - \varphi^n_{i,j,k-1}\right)/(2h)^2}}\right) \tag{11}$$

$$\begin{aligned} {}^{x}_{\Delta-}\varphi_{i,j,k} &= \varphi_{i,j,k} - \varphi_{i-1,j,k}, {}^{x}_{\Delta+}\varphi_{i,j,k} = \varphi_{i+1,j,k} + \varphi_{i,j,k} \\ {}^{y}_{\Delta-}\varphi_{i,j,k} &= \varphi_{i,j,k} - \varphi_{i,j-1,k}, {}^{y}_{\Delta+}\varphi_{i,j,k} = \varphi_{i,j+1,k} + \varphi_{i,j,k} \\ {}^{z}_{\Delta-}\varphi_{i,j,k} &= \varphi_{i,j,k} - \varphi_{i,j,k-1}, {}^{z}_{\Delta+}\varphi_{i,j,k} = \varphi_{i,j,k+1} + \varphi_{i,j,k} \end{aligned} \tag{12}$$

The procedure of segmentation comprises the following steps:

1) In 3D image sequences the "Volume of Interest" is defined.
2) We define the initial surface φ^0 in φ_0 and also $n=0$ .Then $c_1(\varphi^n)$ and $c_2(\varphi^n)$ are obtained from (8) and φ^{n+1} is computed from (11).
3) If the result is acceptable, we go to the next step, else n=n+1 and we repeat step 2
4) Segmentation of the external cardiac wall is done manually by the operator.
5) The segmented image is filtered to eliminate noisy regions of the surface, for example the regions which correspond to papillary muscles
6) Linear interpolation is used to convert the voxels to cubic elements.
7) The segmentation result of the first frame is used for the active mesh software.

In Fig. 1-Left, we have shown the segmentation of the first phase of 4D gradient-echo images. In Fig. 1-Right, epicardial and endocardial contours of these images are shown.

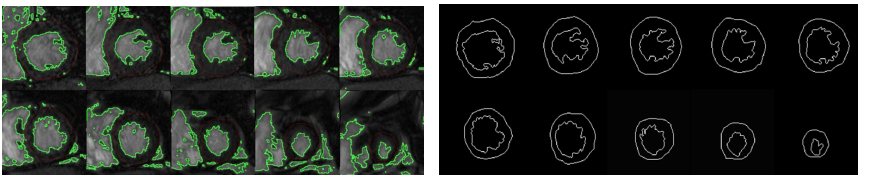

Fig. 1. Left: Segmentation of gradient-echo images Right: Epicardial and endocardial contours

3 Tracking

Let $I^t, t=1,2,...$ be a sequence of 3D images. For obtaining the deformations of the moving object, the boundary surface of the object is extracted from the first frame. We used the method introduced in section 2 for this purpose. Then the obtained face is approximated by a polyhedron. The vertices of the polyhedron are fed to a 3D Delaunay triangulation algorithm, which outputs a list of vertices and a list of tetrahedra. Let $T=\{V,F\}$ be a tetrahedral defined over the object region, where F is a set of tetrahedra and V is a set of tetrahedral vertices. To every vertex $P_i(x_i,y_i,z_i)\in V$ an elementary deformation vector $D_i=(dx_i,dy_i,dz_i)$ is assigned. For a point P in the tetrahedron $\Delta P_k P_l P_m P_n$, the deformation function $d(x,y,z)$ is calculated by linear interpolation from neighboring elementary deformation vectors using [4]:

$$d(x,y,z)=g_k(x,y,z)D_k+g_l(x,y,z)D_l+g_m(x,y,z)D_m+g_n(x,y,z)D_n \tag{13}$$

$$\begin{aligned} g_l(x,y,z)&=\frac{V(\Delta P_k P P_m P_n)}{V(\Delta P_k P_l P_m P_n)} & g_k(x,y,z)&=\frac{V(\Delta P P_l P_m P_n)}{V(\Delta P_k P_l P_m P_n)} \\ g_m(x,y,z)&=\frac{V(\Delta P_k P_l P P_n)}{V(\Delta P_k P_l P_m P_n)} & g_n(x,y,z)&=\frac{V(\Delta P_k P_l P_m P)}{V(\Delta P_k P_l P_m P_n)} \end{aligned} \tag{14}$$

$V(\cdot)$, is the volume calculation function. The 3D object is then modeled as a 3D elastic membrane (plate) which deforms with the virtual forces. From finite element theory [10], the strain energy associated with a thin plate is given by (15).

$$\varepsilon = \frac{1}{2} U^T K U \ , \ U = \left[..dx_i .. | .. dy_i .. | .. dz_i .. \right] , i = 1,2,...N \tag{15}$$

where U is a vector of elementary deformations, N is the number of vertices and K is the stiffness matrix. The stiffness matrix (similar to the stiffness constant of a spring) may be assembled from elementary stiffness matrices associated with each tetrahedral element [10]. The stiffness matrix is then given by:

$$K = \sum_{e \in f} Ke \ , \ K_e = V_e B^T D B \tag{16}$$

where F is the set of tetrahedral elements and K_e is the element stiffness matrix and V_e is the volume of the element and is a constant value. B is a 6×12 matrix with constant elements defined by the coordination of the vertices of tetrahedra. D is a 6×12 matrix defined by the material properties of the deforming body. The simplest model is the isotropic linear elastic model used widely in the image analysis literature. We have used his model for blood and the liquid inside:

$$D = \frac{E}{(1-v)(1-2v)} \begin{bmatrix} 1-v & v & v & 0 & 0 & 0 \\ v & 1-v & v & 0 & 0 & 0 \\ v & v & 1-v & 0 & 0 & 0 \\ 0 & 0 & 0 & 0.5-v & 0 & 0 \\ 0 & 0 & 0 & 0 & 0.5-v & 0 \\ 0 & 0 & 0 & 0 & 0 & 0.5-v \end{bmatrix} \tag{17}$$

In (17), E is Young modulus or shear modulus which controls the stiffness of the material, ν is Poisson's ratio and controls strain-stress properties of the material. In this paper the left ventricle is specifically modeled as a transversely elastic material to account for the preferential stiffness in the fiber direction. This is an extension of the isotropic linear elastic model which allows for one of the three material axes to have a different stiffness from the other two. The matrix D takes the form [11]:

$$D^{-1} = \begin{bmatrix} \frac{1}{E_p} & \frac{-v_p}{E_p} & \frac{-v_{fp}}{E_f} & 0 & 0 & 0 \\ \frac{-v_p}{E_p} & \frac{1}{E_p} & \frac{-v_{fp}}{E_f} & 0 & 0 & 0 \\ \frac{-v_{fp}E_f}{E_p} & \frac{-v_{fp}E_f}{E_p} & \frac{1}{E_f} & 0 & 0 & 0 \\ 0 & 0 & 0 & \frac{2(1+v_p)}{E_f} & 0 & 0 \\ 0 & 0 & 0 & 0 & \frac{1}{G_f} & 0 \\ 0 & 0 & 0 & 0 & 0 & \frac{1}{G_f} \end{bmatrix} \tag{18}$$

where E_f is fiber stiffness and E_p is cross fiber stiffness and v_p, v_{fp} are the corresponding Poisson's ratios of them and G_f is the shear modulus across fiber $\left(G_f \approx E_f / \left(2\left(1+v_{fp}\right)\right)\right)$. The fiber stiffness was set to be 3.5 times greater than cross

fiber stiffness. Poisson's ratio was set .4 for both. By choosing E_f =.05, E_p and G_f were calculated.

By estimation of the displacement of some points of the image in next frame using a similarity criterion, the elementary deformations U may be estimated using the least squares approach. $\delta_i = (\delta x_i, \delta y_i, \delta z_i)$ is the estimation of displacement of point $(\hat{x}_i, \hat{y}_i, \hat{z}_i)$.

$$\min_{D_i} \left\{ \sum_{i=1}^{M} \| d(\hat{x}_i, \hat{y}_i, \hat{z}_i) - \delta_i \|^2 + U^T K U \right\} \tag{19}$$

Using (13), the above minimization is seen to be equivalent to the minimization

$$\min_{U} \left\{ \| AU - B \|^2 + U^T K U \right\} \tag{20}$$

$$A = \begin{pmatrix} Q & 0 & 0 \\ 0 & Q & 0 \\ 0 & 0 & Q \end{pmatrix}_{3m \times 3n} \text{, } \mathrm{Q_{ij}} = \begin{cases} g_j(\hat{x}_i, \hat{y}_i, \hat{z}_i) \text{ , } & j = \{r,s,t,u\} \text{ if} \\ & (\hat{x}_i, \hat{y}_i, \hat{z}_i) \in \Delta P_r P_s P_t P_u \\ 0 \text{ , otherwise} \end{cases} \tag{21}$$

$$B = [\ldots \delta x_i \ldots | \ldots \delta y_i \ldots | \ldots \delta z_i \ldots]^{\mathrm{T}} \text{ , } \delta_i = (\delta x_i, \delta y_i, \delta z_i)$$

The solution to (19) is (22), which gives the displacement of all vertices of the mesh. By linear interpolation, the deformation vector (13) will be obtained for all pixels of the image.

$$\hat{U} = \left(A^T A + K \right)^{-1} A^T B \tag{22}$$

4 Strain Calculation

Abnormalities in the myocardial strain are detectable before first symptoms of a heart attack occur [12], so that measuring and visualizing the strain might represent a useful diagnosis tool. Generation of strain maps from the displacement is a fairly simple procedure. The Lagrangian strain tensor is defined as:

$$E_{ij} = \frac{1}{2} \left(\delta_{ab} \frac{\partial x_a}{\partial X_i} \frac{\partial x_b}{\partial X_j} - \delta_{ij} \right) \tag{23}$$

Using the less obscure matrix notation, $\mathrm{E_{ij}}$ can be written as:

$$E = \frac{1}{2}(C - I) \text{ and } \mathrm{C = FF^T} \tag{24}$$

where C is the Cauchy-Green deformation tensor and I is the identity matrix. The Cauchy-Green deformation tensor is defined as the inner product of the deformation gradient tensor F by itself, and thus becomes a symmetric tensor [13]. C being symmetric and I diagonal, it follows that E is a symmetric tensor as well. This can also be deducted directly from the definition in equation (23). Consequently, E can be expressed as:

$$E = \frac{1}{2} \left(FF^T - I \right) \tag{25}$$

where gradient tensor F is:

$$F = \frac{\partial x_i}{\partial X_j} = X_{i,j} \quad \text{i, j} = \{1,2,3\}, \qquad F = \begin{bmatrix} \frac{\partial x_1}{\partial X_1} & \frac{\partial x_1}{\partial X_2} & \frac{\partial x_1}{\partial X_3} \\ \frac{\partial x_2}{\partial X_1} & \frac{\partial x_2}{\partial X_2} & \frac{\partial x_2}{\partial X_3} \\ \frac{\partial x_3}{\partial X_1} & \frac{\partial x_3}{\partial X_2} & \frac{\partial x_3}{\partial X_3} \end{bmatrix} \tag{26}$$

5 Results

Experiments were performed on cardiac MRI images for tracking the left ventricle myocardium. The result of evaluation on one set of Gradient-Echo images is given in this section. MR imaging was performed on a Symphony Siemens 1.5 Tesla scanner. Short-axis images through the left ventricle were obtained with the gradient echo cine technique using the following parameters: TR = 43.44ms, TE = 1.59ms, flip angle = 53°, slice thickness = 4mm, field of view = 84.3750cm. The data set contained 6 frames per cardiac cycle, each frame containing 10 images with an in-plane resolution of 1.5mm×1.5mm for a 256×256 matrix and a resolution of 6mm perpendicular to the imaging plane. By interpolation, the image voxels were converted to cubic voxels of size 1.5mm×1.5mm×1.5mm. In Fig 2-Left, the MRI cardiac data is shown. In these images, the region containing the left ventricle is selected hence the size of image matrices is reduced to 128×128. In Fig. 2-Right, the result of segmentation of the left ventricle wall for the first phase of cardiac cycle is shown. In Fig. 3, the result of tracking the left ventricular wall by active mesh algorithm is shown. The results show

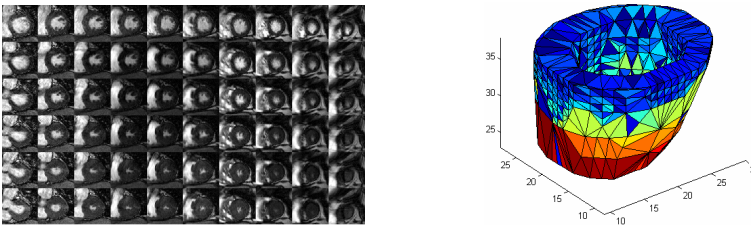

Fig. 2. Left: 4D Gradient-Echo MRI cardiac images, Right: The segmentation results of the left ventricle wall for the first phase of cardiac cycle

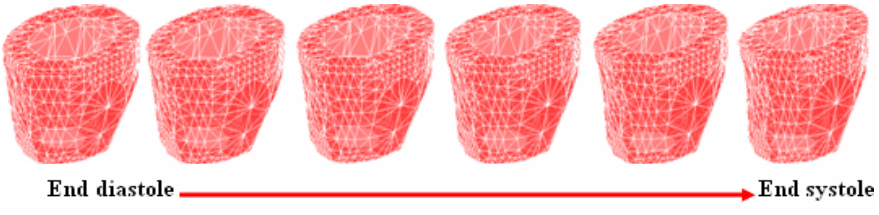

Fig. 3. The results of tracking the left ventricle wall in cardiac cycle by active mesh algorithm

that the algorithm can track the cardiac motion in all 3 dimensions with acceptable accuracy.

For quantitative evaluation of the algorithm performance in tracking the left ventricular wall, the tracked surfaces obtained by the algorithm and the surfaces extracted by segmentation software were compared. The comparison was done by finding the similarity index (SI) between the two surfaces and then the error was defined as 1-SI [4]. The obtained errors are indicated in Table 1. In Fig. 4 the radial, longitudinal and circumferential calculated strains are shown in End Systole.

Table 1. The tracking algorithm error

Frame	2	3	4	5	6	7
Error(%)	4.3	4.71	5.15	4.71	4.27	4.1

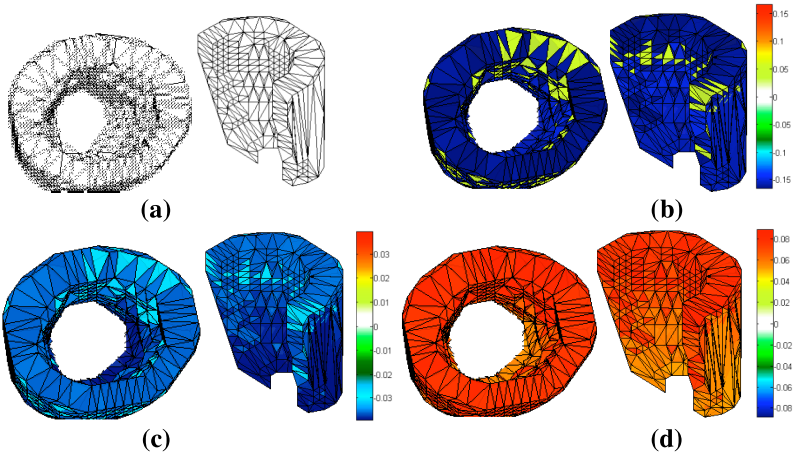

Fig. 4. The derived strains. a: End Diastole Strain. b: End Systole, circumferential strain. c: End Systole, longitudinal strain d: End Systole, radial strain.

6 Conclusion

We have enhanced and automatized our previously developed 3D active mesh model for motion tracking in a point-wise manner. Automatization was achieved by automatic segmentation of endocardial boundary in the first frame. For this purpose, we developed a novel 3D segmentation algorithm based on curve evolution technique and level set. Further enhancement to the tracking software was achieved by considering the cardiac muscle anisotropy. Moreover, we extended our model in order to track the left ventricular wall. Finally, we generated the strain maps from the displacements achieved by the tracking algorithm. Further improvements of the tracking software are foreseen. Some works are in progress to integrate cardiac muscle nonlinearity into our model. In addition, we plan to replace the present correlation-based search method with shape-based tracking method which seems to be

better choice for perpendicular and tangential motion estimation. Finally, a regularization term can be added to energy functional for reducing the computational cost as well as obtaining a more robust estimation of deformation fields.

References

1. Shi, P., Sinusas, A.J., Constable, R.T., Ritman, E., Duncan, J.S.: Point-Tracked Quantitative Analysis of Left Ventricular Surface Motion from 3-D Image Sequences. IEEE Trans. Med. Image 19, 36–50 (2000)
2. Abrishami Moghaddam, H., Lerallut, J.F.: Volume Visualization of the Heart Using MRI 4D Cardiac Images. Journal of computing and information technology 6, 215–228 (1998)
3. Pham, Q.C., Vincent, F., Clarysse, P., Croisille, P., Magnin, I.E.: A FEM-Based Deformable Model for the 3D Segmentation and Tracking of the Heart in Cardiac MRI. IEEE conf. on Image and Signal Processing and Analysis, pp. 250–254 (2001)
4. Mosayebi, P., Moghaddam, H.A., Giti, M.: A Fully 3D Active Mesh Model for motion Tracking in Cardiac MRI. MICCAI workshop, vol. 1, pp. 131–138 (2006)
5. Maes, L., Bijnens, B., Suetens, P., Werf, F.V.D.: Automated contour detection of the left ventricle in short axis view in 2d echocardiograms. Machine Vision and Appl. 6, 1–9 (1993)
6. Lorenzo-Valdes, M., Sanchez-Ortiz, G.I., Elkington, A.G., Mohiaddin, R.H., Rueckert, D.: Segmentation of 4D cardiac MR images using a probabilistic atlas and the EM algorithm. Med. Image Anal. 8(3), 255–265 (2004)
7. Paragios, N.: A level set approach for shape-driven segmentation and tracking of the left ventricle. IEEE Trans. Med. Imag. 22, 773–776 (2003)
8. McInerney, T., Terzopoulus, D.: A dynamic finite element surface model for segmentation and tracking in multidimensional medical images with application to cardiac 4d image analysis. Computerized Medical Imaging and Graphics 19(1), 69–83 (1995)

Automated Tag Tracking Using Gabor Filter Bank, Robust Point Matching, and Deformable Models

Ting Chen, Sohae Chung, and Leon Axel

Radiology Department, New York University, School of Medicine
650 First Ave, New York City, NY, 10016, USA
{ting.chen,sohae.chung,leon.axel}@med.nyu.edu

Abstract. Tagged Magnetic Resonance Imaging (tagged MRI or tMRI) provides a means of directly and noninvasively displaying the motion of the myocardium. Reconstruction of the motion field is needed for quantitative analysis of important clinical information, e.g., the myocardial strain. In this paper, we present a two-step method for this task. First, we use a Gabor filter bank to generate a corresponding phase map of tMRI images. Second, deformable models are initialized at the discontinuities in the wrapped phase map, and are deformed under the influence of the image gradient to track the motion of tags. Unlike previous approaches, a Robust Point Matching (RPM) module has been integrated into the model evolution to avoid false tracking results caused by 1) through-plane motion, and 2) small tag spacing. The method has been tested on a numeric phantom, as well as in vivo heart data. The experimental results show that the new method has a good performance on both synthetic and real data, and has the potential to be used in clinical applications.

Keywords: Tagged MRI, Gabor Filter, Motion Tracking, Deformable Model, Robust Point Matching.

1 Introduction

Magnetic Resonance Imaging (MRI) with magnetization tagging provides a means of directly and noninvasively displaying the motion of the myocardium, as the tagged regions are visible in MR images, and move exactly like the underlying (and otherwise featureless) tissue [1], [2]. Thus the deformation of tag lines reflects the deformation of the underlying heart wall. However, efficient means of analyzing the tagged images are needed for practical quantitative study of regional heart functions. While several methods have been proposed for tagged image analysis, currently the most popular automated method is the Harmonic Phase (HARP) analysis technique [3]. HARP is essentially phase analysis of a single side band demodulation of the tags, carried out in the Fourier domain.

Gabor filters [4] are sinusoidally modulated Gaussians that can be convolved with an image to extract the local periodic "stripe" content. They provide an alternative method for automated tag analysis that has some formal relationship

F.B. Sachse and G. Seemann (Eds.): FIMH 2007, LNCS 4466, pp. 22–31, 2007.

to, but is distinct from, HARP. The Gabor filter is a natural match to the tag pattern and can be used to optimally localize tags in both the image domain and the frequency domain. One potential advantage of Gabor filters against HARP is that the parameters of the Gabor filter can be adjusted corresponding to different tag spacing and orientation. Note that when heart is contracting, the local tag spacing and orientation are different from region to region, due to the deformation. Unlike HARP, which assumes there is no change in the tag spacing and orientation during the cardiac cycle, the Gabor filter can adjust to the local image configuration by changing its parameters, so that it can avoid some errors such as the false bifurcations of tags in the phase output that may be seen with HARP in large deformations. In [5] we introduce the use of the Gabor filter bank. At each myocardial pixel, the response to a group of filters with different tag spacing and orientation are calculated, and the local orientation and tag spacing are computed from the weighted summation of three filters with the largest responses. Using the result, we can compute the local phase information, and then derive the displacement and the strain. However, the error in the displacement calculated from the Gabor filter bank still increases as the deformation in the myocardium increases, possibly because the Gaussian kernel in the Gabor filter blurs local features during the computation. When the tag line has a high curvature, the phase calculated from the Gabor filter may not match the local deformation in magnitude.

Both HARP and Gabor filters are based on the use of frequency domain analysis. Other tag tracking methods, such as the active contours (snakes) [6] and spline models [7], work in the image domain. Usually, a parameterized model of the tag line (an active contour, or a B-spline) is deformed under the influence of the image gradient. However, one major shortcoming of the gradient-driven methods is that the model may converge to a false tag line or the myocardial surfaces instead of the tag it is supposed to converge to. Two reasons for such errors are 1) the through-plane motion may cause sudden appear and/or disappear of tags close to the myocardial surfaces; and 2), as the heart contracts, the tag spacing becomes smaller and the myocardium deformation increases, so that the deformation can be larger than the tag spacing in magnitude. This can cause the model to "jump" to a false tag.

Robust Point Matching (RPM) [8] is a computer vision technique for finding the correspondence between two sets of points. It has been widely implemented to solve rigid and nonrigid registration problems. By using a simulated annealing scheme [9], it can find the the correspondence between two point sets with different numbers of points.

In this paper, we introduce a novel tag tracking method integrating Gabor filters, the RPM, and deformable models. First, the phase map is generated by the Gabor filter bank. Then RPM is used to match landmark points in two images to be tracked. The matching result guides the gradient fitting so that there will be no mismatch between models and tags. The deformable model provides the RPM with a realistic underlying transformation function, so that there will be no mismatch between landmarks at two time phases in the cardiac cycle caused by over smoothness.

The rest of the paper is organized as follows. Section Two provides background information on the Gabor filter and the Gabor filter bank. In Section Three we introduce our new tag tracking method. We present experimental results on a numeric phantom as well as *in vivo* heart data in Section Four. Also in Section Four, we evaluate the method by comparing it against the "ground truth" and other tag tracking methods. We have a brief discussion and draw our conclusions in Section Five.

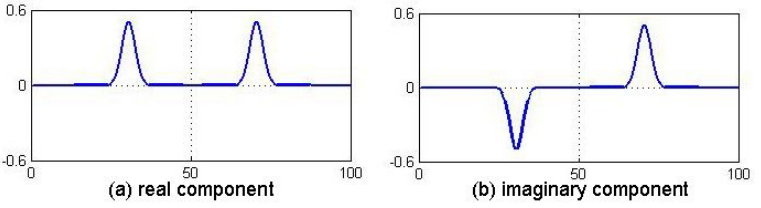

Fig. 1. The real and imaginary components of a Gabor filter in the Fourier domain

2 Gabor Filter and Gabor Filters Bank

A Gabor filter [2] is a sinusoidally modulated Gaussian that can be convolved with an image to extract the local periodic "stripe" content. It is simply expressed as a Gaussian multiplied by a complex sinusoid in the image domain, as shown below:

$$h(x, y) = g(x', y') \cdot \exp[-i2\pi(u_0 x + v_0 y)] \tag{1}$$

with center frequency (u_0, v_0) and the spatial coordinate $(x', y') = (x\cos(\theta) + y\sin(\theta), -x\sin(\theta) + y\cos(\theta))$ rotated by θ with respect to the x axis. $g(x', y') = \frac{1}{2\pi\sigma_{x'}\sigma_{y'}} \exp(-\frac{(\frac{x'}{\sigma_{x'}})^2 + (\frac{y'}{\sigma_{y'}})^2}{2})$ is a Gaussian filter with the spatial standard deviations $\sigma_{x'}$, $\sigma_{y'}$. This complex function $h(x, y)$ can be split into its real and imaginary components h_R and h_I (even and odd functions, respectively):

$$h_R(x, y) = g(x', y')\cos(-2\pi(u_0 x + v_0 y)) \tag{2}$$

$$h_I(x, y) = g(x', y')\sin(-2\pi(u_0 x + v_0 y)) \tag{3}$$

After the heart starts to contract, the local tag spacing and orientation may change. The response to a pair of Gabor filters with sine and cosine modulations can be used to find the local tag phase. The filtering operation can be efficiently carried out in the Fourier domain. The Fourier transform of the real (2) and imaginary (3) components of a Gabor filter as shown in Fig. 1, is given by:

$$H_R(u, v) = \frac{1}{2}(G(u - u_0, v - v_0) + G(u + u_0, v + v_0)) \tag{4}$$

$$H_I(u, v) = \frac{i}{2}(G(u - u_0, v - v_0) - G(u + u_0, v + v_0)) \tag{5}$$

where $G(u, v) = F(g(x, y))$ and $F(\cdot)$ denotes the Fourier transform. As we can see in (4) and (5), real and imaginary filters are the sum of two Gaussian functions in the Fourier domain centered at the frequencies (u_0, v_0) and $(-u_0, -v_0)$. The final form of a 2D Gabor filter in the Fourier domain is:

$$H(u, v) = H_R(u, v) + iH_I(u, v) \tag{6}$$

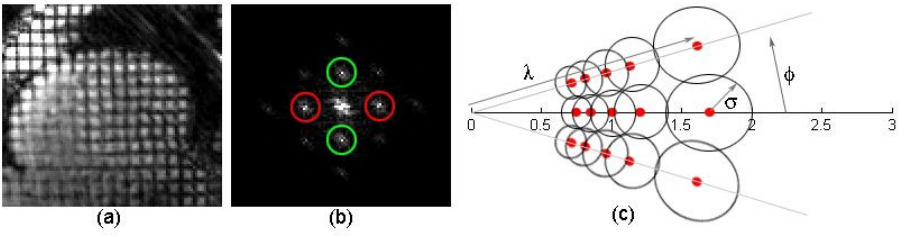

Fig. 2. (a) A cardiac MRI image with grid tags. (b) The magnitude of the Fourier transform of the tagged MR image. Peaks inside red circles correspond to vertical tags and green circles to horizontal tags. (c) A bank of Gabor filters in the Fourier domain with parameters ν, θ and σ. The red dots represent centers of Gabor filters in the Gabor filter bank. The value of the horizontal axis is $\frac{\nu}{\nu_{ini}}$ in the Fourier domain.

Our analysis is based on the Fourier transformation of tagged MRI images. Fig. 2 shows an end-diastolic grid-tagged short axis image of a normal volunteer Fig. 2(a) and its transform in the Fourier domain Fig. 2(b). There are 4 first harmonic peaks in Fig. 2(b). A pair of red peaks correspond to vertical tags and a pair of green peaks correspond to horizontal tags. From these peaks, we can find the initial frequencies (u_{ini}, v_{ini}) of vertical and horizontal tags. Here, let us focus on vertical tags first for easier explanation. A similar process can be derived for horizontal tags. For a 2D Gabor filter in the Fourier domain, we need to set up three parameters: frequency ν, orientation θ and the filter size σ.The tag spacing d_{tag} for vertical tags in the image domain is:

$$d_{tag} = \frac{1}{\nu} \tag{7}$$

Note that frequency ν is equivalent to the distance between (u_{ini}, v_{ini}) and the DC peak in the Fourier domain (see Fig. 2(b)). Equation (7) shows that when the tag spacing changes, the distance between the corresponding harmonic peak and the DC peak also changes reciprocally in the Fourier domain. That is, if d_{tag} is decreasing, then ν is increasing and vice versa. With the location of the DC peak stable, the harmonic peaks move as the tag spacing changes and so should the corresponding Gabor filter. Fig. 2(c) shows the corresponding locations of the centers of Gabor filters (red dots) in the Fourier domain when d_{tag} is changed by one pixel steps in the image domain. The orientation θ is determined

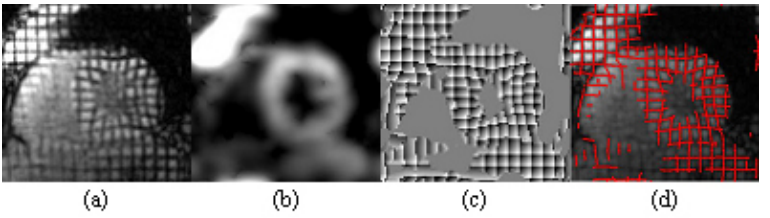

Fig. 3. (a) a deformed grid tag image, (b) the magnitude output of Gabor filters bank, (c) 2D phase map generated by Gabor filters bank, and (d) tag lines (red) automatically recovered from phase

by $\phi = \phi_{ini} + n \cdot \Delta\phi$, where $n = 0, \pm 1, \pm 2, \ldots$ and $\phi_{ini} = 0$ for vertical tags, $\pi/2$ for horizontal tags. The parameter σ determines the size of the Gaussian filter in the Fourier domain. It is chosen proportional to the frequency position, i.e., $\sigma = k \cdot \nu$, where $k > 0$ (See circles in Fig. 2(c)).

We calculate the response to a bank of Gabor filters with different spacing and orientation. Responses are different for different parameter-sets, and is maximal when the parameter-set is close to the local tag spacing and orientation in the image. To minimize the error, an interpolation of the parameters of the three top responding filters at a given location is used to estimate the local tag spacing and orientation, and the responses of these three filters are combined to compute the local phase information using (6). The phase corresponding to the local tag pattern is a material tissue property and calculated in the range $[-\pi, \pi)$ from the output of the Gabor filter bank (See Fig. 3(c)). We can generate the tag line locating at the corresponding discontinuities in the wrapped phase map. This is a completely automatic process (see Fig. 3(d)).

From the response to the filter bank, we can estimate the local position (phase) relative to the tag pattern, and acquire a Lagrangian description of the motion. However, the calculated displacement map may not fully capture large deformations in the myocardium, as shown in Fig. 4.

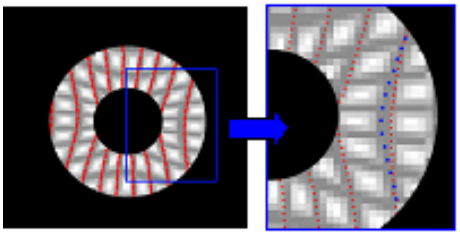

Fig. 4. Left: a grid tagged phantom image and the recovered tag locations (red) from the phase distribution. Right: a magnified image of blue area in the left image. Blue dots show the correct corresponding tag positions.

3 Tag Tracking Method

3.1 Robust Point Matching

Suppose we are tracking the motion of tags from the ith image (denote as I_i) to the $i+1$th image (denote as I_{i+1}) in one image sequence. We can discretize tags in each image into a group of 2D or 3D points (image pixels). Usually these two point-sets are closely correlated, but without a one-to-one correspondence because 1) a material point in the image plane at time t_i may move out of the image plane at t_{i+1} due to the through plane motion, and 2) we can only discretize tags into entities as small as image pixels. Therefore, during the cardiac cycle, more than one pixel in the ith image may map to one pixel in the $i+1$ image as the heart contracts (the partial volume effect). However, for some subsets of these two point-sets, e.g., the intersection points in grid tag images, the multi-to one correspondence can be neglected, and RPM can handle the through-plane motion by mapping points with no correspondence to an outlier. In our tracking method, for simplicity, we choose to match a subset of the intersection points of tags and the epicardial surface, denoted as $P = \{p_j, j = 1, 2, \ldots, M\}$ and $Q = \{q_k, k = 1, 2, \ldots, N\}$ for I_i and I_{i+1}, respectively.

Given a Gabor-filter-built phase map with no local ambiguities such as false bifurcations, the correspondence between P and Q is dense enough for us to match discontinuities in the two phase maps, as shown in Fig. 6. Assume that from I_i to I_{i+1}, the underlying motion field can be expressed as a non-rigid transformation function f. A point $p_j \in P$ in I_i is mapped to its new location $p'_j = f(p_j)$ in I_{i+1}. Thus the matching problem is equivalent to the minimization of the energy function $E_{Z,f}$:

$$\min_{Z,f} E(Z, f) = \min_{Z,f} \sum_{j=1}^{M} \sum_{k=1}^{N} z_{jk} \|q_k - f(p_j)\|^2 + \lambda \|\nabla \cdot (\nabla f)\|^2 - \zeta \sum_{j=1}^{M} \sum_{k=1}^{N} z_{jk} \quad (8)$$

where $Z = z_{jk}$ is the binary correspondence matrix, $z_{jk} \in 0, 1$ for $j = 1, 2, \ldots, M + 1$ and $k = 1, 2, \ldots, N + 1$. For points without a correspondent, we set the location of outliers for both point-sets to be the centroid of the segmented myocardium mask. The matrix is subject to the constraints $\sum_{j=1}^{M+1} z_{jk} = 1$ for $k = 1, 2, \ldots, N$ and $\sum_{k=1}^{N+1} z_{jk} = 1$ for $j = 1, 2, \ldots, M$. λ and ζ are both positive weights for terms in the energy function. The term $\lambda \|\nabla \cdot (\nabla f)\|^2$ is a smoothness constraint on the transformation function. $\zeta \sum_{j=1}^{M} \sum_{k=1}^{N} z_{jk}$ is used to minimize the existence of outliers in the final matching result.

To accommodate the nonrigid point matching in our tag tracking problem, we use the fuzzy correspondence matrix Y to replace Z in (8). Thus the energy function changes to:

$$E(Y, f) = \sum_{j=1}^{M} \sum_{k=1}^{N} y_{jk} \|q_k - f(p_j)\|^2 + \lambda \|f\|^2 + T \sum_{j=1}^{M} \sum_{k=1}^{N} y_{jk} \log y_{jk} - \zeta \sum_{j=1}^{M} \sum_{k=1}^{N} y_{jk} \quad (9)$$

where $y_{jk} = \frac{1}{T}\exp(\frac{-\|q_k - p'_j\|^2}{2T})$ still satisfies $\sum_{j=1}^{M+1} y_{jk} = 1$ for $k = 1, 2, \ldots, N$ and $\sum_{k=1}^{N+1} y_{jk} = 1$ for $j = 1, 2, \ldots, M$ with $y_{jk} \in [0, 1]$. Also, an entropy term $T\sum_{j=1}^{M}\sum_{k=1}^{N} y_{jk} \log y_{jk}$ is added to the energy function, according to deterministic annealing [9]. The temperature parameter T is higher at the start of the tracking process so that the energy function favors fuzzy correspondence to maintain its convexity, and gradually decreases to zero during the tracking for a global binary solution of Y.

The transformation function f is defined as a combination of the image gradient flow and the minimization of the square distance between point-sets. It seeks to minimize the following energy function:

$$E_{trans} = \lambda_1 \sum_{j=1}^{M} I(p'_j) + \lambda_2 \sum_{j=1}^{M}\sum_{k=1}^{N} \|p'_j - q_k\| y_{jk} \tag{10}$$

where λ_1 and λ_2 are weights for the image gradient and the point distance, respectively.

3.2 Deformable Model

After the point matching, we derive the correspondence between the discontinuities in two phase maps (produced by the Gabor filter bank). We then initialize a group of deformable contours at these discontinuities, each corresponding to one segment of tags in the tMRI image. The contours move under the influence of the external force f_{ext} and the phase constraint f_{phase}, following the Lagrangian equation:

$$\dot{d} + \mathbf{K}d = f_{ext} + f_{phase} \tag{11}$$

where $\mathbf{K}$ is the stiffness matrix that controls the smoothness of the deformable contour, d is the displacement, and $\dot{d}$ is the speed of the deformation.

The external force is derived from the tagged MRI image, in the form of gradient flow:

$$f_{ext} = -\nabla(g \cdot I)) \tag{12}$$

where g is the Gaussian operator, and I is the original image. The external force alone cannot guarantee an accurate convergence of the deformable contour and the corresponding tag because 1) the local noise and imaging artifacts may produce erroneous gradient information, and 2) a small tag spacing may cause the deformable contour to move to other edges in the image instead of converging to the corresponding tag. Therefore we design a supplementary phase force field, which is derived from the output of the Gabor filter bank, to constrain the movement of deformable contours. Given the wrapped phase output R of the Gabor filter bank, the phase constraint at pixel $x \in I_{i+1}$ has the following form:

$$f_{phase}(x) = -|U(R_i(x) - R_{i+1}(x))|^{-1} \cdot \nabla(\pi - |R(x)|) \tag{13}$$

where $U(\cdot)$ is an unwrapping operator. The magnitude of the phase constraint is inversely proportional to the local phase change so that the phase influence decreases when the local deformation increases, and vice versa.

4 Experiments

First we tested our method on a numerical phantom. An annulus overlaid with grid tags deforms following an underlying 2D displacement field, which is the "ground truth" in the validation of our method. We compared the displacement maps generated by our method against those generated using the HARP method. The results show that our method has a better performance (with smaller error magnitude, and more smooth distribution). We also quantitatively validated the method by calculating the root mean square (RMS) error between output of our method and the "ground truth" displacements. the result is shown in Tab. 1. Except for the first and last image in the sequence, where displacements in both directions are small, the error rate is underneath 5%. The result demonstrated the robustness of our motion tracking method.

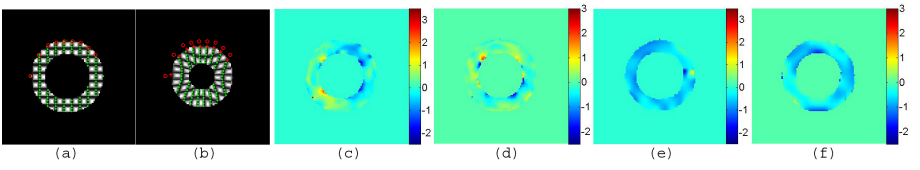

Fig. 5. (a) matching points (red "o") and tags ("green dots")in an undeformed image, (b) matching points (red "+")and tags in a deformed image, (c) and (d), the $x-$ and $y-$ displacement map generated by HARP, (e) and (f), the $x-$ and $y-$ displacement map generated using Gabor filters bank, RPM, and deformable models

We also tested the strength of our method on *in vivo* heart data. In Fig. 6 we present the tag tracking results for a healthy volunteer and a patient. In both cases, tags have been tracked accurately despite large deformations and the through-plane motion. The tag tracking results are used to generate the 2D Lagrangian displacement map. We used the method that has been proposed in [10] to generate dense displacement maps.

After generating the displacement map, we derived the in plane myocardial strain map for the healthy volunteer and the patient, respectively. The results are shown in Fig. 7. The overall process takes less than one minute for an image

Table 1. The comparison between the RMS error and the mean magnitude of displacements (in pixels)

phase	2	3	4	5	6	7	8	9	10
Mean x Disp.	.0973	.2049	.3337	.408	.4419	.404	.3297	.203	.1014
RMS error in x Disp.	.0058	.0088	.0103	.0111	.0112	.0104	.0094	.0079	.0076
Error ratio in x Disp. (%)	5.96	4.29	3.09	2.72	2.53	2.57	2.85	3.89	7.5
Mean y Disp.	.0968	.2059	.3361	.422	.4614	.4274	.3555	.2322	.1312
RMS error in y Disp.	.0068	.0085	.01	.0111	.0115	.011	.0107	.0105	.0109
Error ratio in y Disp. (%)	7.02	4.13	2.98	2.63	2.49	2.57	3.01	4.52	8.31

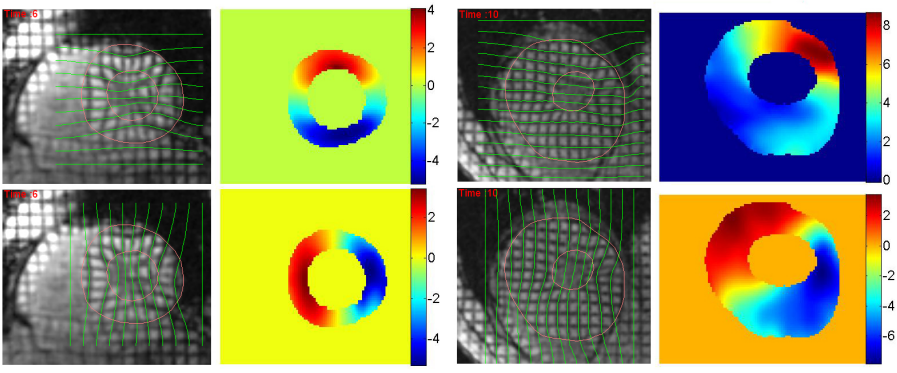

Fig. 6. Left: tag tracking in the myocardium of a healthy volunteer. Right: tag tracking in the myocardium of a patient with hypertrophic cardiomyopathy. In each group, the left upper image is the tracking of horizontal tags, left lower image is the tracking of vertical tags, right upper image is the distribution of the displacement component parallel to the y-axis, and right lower image is the displacement distribution for the x-axis component. Green lines are the tags, the epi- and endo- cardial surface have been segmented using a semi-automated segmentation tool.

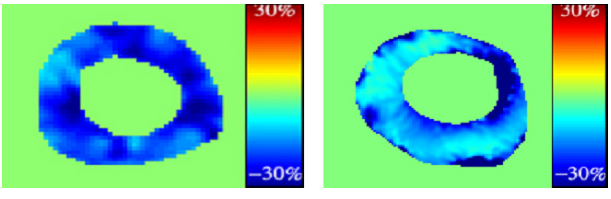

Fig. 7. Left: strain distribution in the healthy heart. Right: strain distribution in patient's heart. Notice that the magnitude of the principal strain in patient's heart is much less than that of the healthy volunteer.

sequence of size 100 by 100 pixels by 10 phases on a desktop PC with 2.66GHz Dual 2 Core CPU, and the reconstructed strain maps indicate differences between the healthy subject and the patient, which may be of clinical importance.

5 Discussions and Conclusions

In this paper, we have presented a novel tag tracking technique, which integrates the Gabor filters, the RPM, and the deformable models. The method has a robust performance on tagged numerical phantoms and *in vivo* tagged MRI images, especially in myocardial regions with large deformation. It has the following advantages: First, the phase map created by Gabor filters is used as the input for RPM. The underlying phase map provides a natural formulation for the transformation function in the RPM energy so that tags in two different images can be matched with each other rapidly and robustly. Second, the RPM provides

a smooth and relatively accurate initialization for the deformable models, so that we reduce the chance of false assignment in the tag tracking. And third, the phase map generated by the Gabor filters also acts as a natural constraint during the evolution of deformable models. These three methods are tightly integrated in order to achieve the best performance in tag tracking. Experimental results show a better tracking performance against an other tracking technique, HARP, and its timing performance is acceptable for clinical applications.

In the future, we can improve the method by extending it into a 3D method. More experiments and validation, especially for *in vivo* pathological data, are needed to fully evaluate the performance of the method, and to build potential clinical applications.

References

1. Axel, L., Dougherty, L.: MR imaging of motion with spatial modulation of magnetization. Radiology 171, 841–845 (1989)
2. Axel, L., Dougherty, L.: Improved method of spatial modulation of magnetization (SPAMM) for MRI of heart wall motion. Radiology 172, 349–350 (1989)
3. Osman, N.F., McVeigh, E.R., Prince, J.L.: Imaging heart motion using Harmonic Phase MRI. IEEE Trans. on Medical Imaging 19(3), 186–202 (2000)
4. Gabor, D.: Theory of communication. J. IEE 93(3), 429–457 (1946)
5. Chen, T., Axel, L.: Using Gabor filters bank and temporal-spatial constraints to compute 3D myocardium strain. In: Proceedings of EMBC (2006)
6. Metaxas, D.: Physics-based Deformable Models: Application to Computer Vision, Graphics and Medical Imaging. Springer, Heidelberg (1996)
7. Amini, A.A., Chen, Y., Elayyadi, M., Radeva, P.: Tag surface reconstruction and tracking of myocardial beads from SPAMM-MRI with parametric B-spline surfaces. IEEE Trans. on Medical Imaging 20(2), 94–103 (2001)
8. Chui, H., Rangarajan, A.: A New Point Matching Algorithm for Non-Rigid Registration. Computer Vision and Image Understanding 89(2–3), 114–141 (2003)
9. Gold, S., Rangarajan, A.: A graduated assignment algorithm for graph matching. Pattern Analysis and Machine Intelligence 18(4), 377–388 (1996)
10. Axel, L., Chen, T., Manglik, T.: Dense myocardium deformation estimation for 2D tagged MRI. In: Proceedings of FIMH, pp. 446–456 (2005)

Strain Measurement in the Left Ventricle During Systole with Deformable Image Registration

Nikhil S. Phatak, Steve A. Maas, Alexander I. Veress, Nathan A. Pack, Edward V.R. Di Bella, and Jeffrey A. Weiss

Department of Bioengineering and
Scientific Computing and Imaging Institute
University of Utah
Salt Lake City, UT
jeff.weiss@utah.edu

Abstract. The objective of this study was to validate a deformable image registration technique, termed Hyperelastic Warping, for left ventricular strain measurement during the systole using cine-gated nontagged MRI with strains measured from tagged MRI. Tagged and non-tagged cine images were obtained on a 1.5 T Siemens Avanto clinical scanner with a TrueFISP imaging sequence. The Hyperelastic Warping solution was evolved using a series of non-tagged images in 10 phases from end-diastole to end-systole. The solution may be considered as ten separate Warping problems with multiple Templates and Targets. At each stage, an active contraction was initially applied to the FE model, and then Warping penalty forces were utilized to generate the final registration. Warping results for circumferential strain were correlated (R^2 =0.59) with results obtain from tagged MR images analyzed with a HARP algorithm. Results for fiber stretch, LV twist, and transmural strain distribution were similar to values in the literature. Hyperelastic Warping represents a novel approach for quantifying 3-D regional strains within the myocardium with a high resolution.

1 Introduction

Left ventricular function is typically considered representative of overall cardiac performance, since the left ventricle (LV) controls systemic perfusion and corresponds to the oxygenation and nutrition supply of the entire body. The most commonly used global measure of left ventricular performance is ejection fraction. However, localized measures such as wall deformation, strain, or fiber stretch are actual measures of myocardial contractile function.

Invasive approaches for measuring cardiac deformation include the use of implanted markers and sonomicrometers. These studies have typically been carried out in animal models [1, 2], although strain measurements using surgically implanted markers in humans have also been reported [3]. Advances in medical imaging technology have made it possible to perform non-invasive measurement of strain in the heart. Non-invasive methods of measuring strain in the left ventricle include MR tagging [4], 2-D echocardiography [5], and radionuclide ventriculography [6].

F.B. Sachse and G. Seemann (Eds.): FIMH 2007, LNCS 4466, pp. 32–40, 2007.

Algorithms for deformable image registration [7-9] have become a viable option for myocardial strain measurement due to the availability of images with high spatial and temporal resolution with techniques such as cine-magnetic resonance imaging [10]. Deformable image registration is used to determine a deformation map that aligns the features of one image with the corresponding features in another image [8]. If these image pairs represent distinct states of deformation, it is possible to determine the strain in the tissue from the deformation map that aligns the image datasets. However, regularizing functions and *a priori* data are typically necessary to ensure physically-reasonable predictions. Our laboratory has developed and applied Hyperelastic Warping [7, 9, 11, 12], a specific algorithm for deformable image registration, to measure strain directly from medical image data. Hyperelastic Warping combines an image-based energy calculated from the intensity fields of the image pairs with a hyperelastic regularization of the underlying deformation field. An initial template image is chosen to represent the material in the reference configuration, while a target image is chosen to represent the same material after deformation. A spatially-varying body force is produced to deform the discretized template image into the target image by minimizing an energy functional.

Hyperelastic Warping has been previously validated during diastole using an initial cine-MR image dataset from a normal human subject and a forward FE model of diastolic filling. However, the use of deformable image registration to determine strain during systole is considerably more challenging since the forces acting on the myocardium are generated by myofiber contraction within the ventricular wall rather than the passive mechanics associated with diastolic filling, and MR image data does not typically provide image texture within the wall to guide registration transmurally. The purpose of this study was to develop a methodology for measuring left ventricular deformation during systole with Hyperelastic Warping using cine-MR images by combining deformable image registration with a realistic model of systolic contraction directly in the image regularization term.

2 Methods

Image Acquisition. A normal volunteer with no history of cardiac pathology (male, age 30) was imaged using cine-gated MRI images of the left ventricle, acquired with a TrueFISP sequence, during the entire systolic phase of the cardiac cycle. Images were obtained on a 1.5 T Siemens Avanto scanner with a prototype 32 channel cardiac coil from InVivo (Gainesville, FL). For non-tagged images, TR = 50.0 ms, TE = 1.19 ms, flip angle = 57 degrees, resolution = 1.7 mm x 1.7 mm, slice thickness = 4 mm. Before Hyperelastic Warping analysis, pixel size was halved in each direction and the images were cropped to focus on the left ventricle. The processed images were 120 pixels (100 mm) x 120 pixels (100 mm) x 46 slices (2 mm thickness). A short axis mid-ventricular slice is depicted at 10 intermediate phases of systole (Figure 1). Horizontal and vertical tagged images were also obtained in 9 short-axis slices of the LV during the same acquisition session for validation. The spacing between the tags was 6 mm and each slice was 4 mm thick. For the tagged imaging sequence, TR = 58ms, TE = 4.6ms, flip angle = 14 degrees, and resolution = 1.7 mm x 1.7 mm.

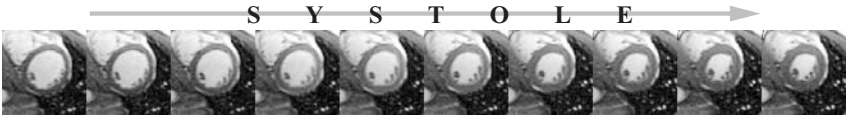

Fig. 1. Cardiac contraction depicted at a mid-ventricular short axis slice with 10 phases through systole used as multiple Templates/Targets for Hyperelastic Warping. The image at the first phase was used as initial Template at end-diastole and the image at final phase was used as a final Target at end-systole.

S*urface Reconstruction and FE Mesh Generation.* The epicardial and endocardial surfaces were manually segmented from the MR images at end-diastole. Cross-sectional contours of the left ventricle were extracted from the MRI dataset (SurfDriver, Kailua, HI) (Figure 2A). Both triangulated myocardial surfaces were imported into a FE preprocessing software (TrueGrid, XYZ Scientific, Livermore, CA) and a hexahedral FE mesh was created by projecting to the surfaces (Figure 2B) [13, 14]. The FE model consisted of 10,304 elements. Elements were 2-4 mm in size.

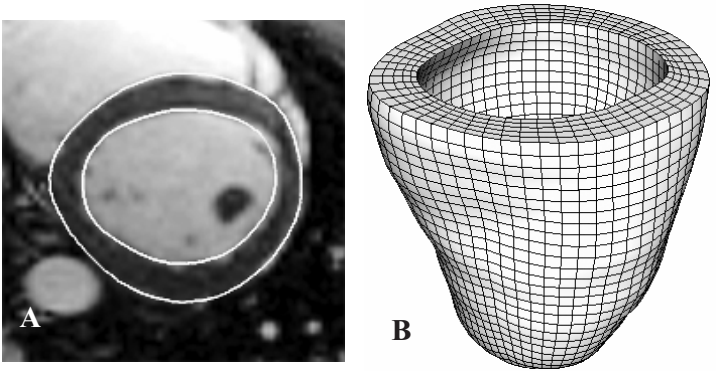

Fig. 2. (A) Epicardial and endocardial contours at sample basal slice. (B) Hexahedral finite element (FE) mesh used for Hyperelastic Warping analysis.

Constitutive Model. A transversely isotropic hyperelastic constitutive model was used to represent the myocardium, with the fiber direction varying from -90 degrees at the epicardial surface to +90 degrees at the endocardial surface for the basal level.[12] In addition, the inner and outer layers were varied in a helical pattern, such that the inner layer varied from +90 degrees to 0 degrees from the basal level to the apical level and the outer layer varied from + 90 degrees to 0 degrees from the basal level to the apical level.

The constitutive model represented fibers embedded in an isotropic matrix:

$$W = \mu(\tilde{I}_1 - 3) + F_2(\tilde{\lambda}) + \frac{K}{2}[\ln(J)]^2 . \quad (1)$$

Here, $\tilde{I}_1$ is the first deviatoric invariant of the right Cauchy-Green deformation tensor $\boldsymbol{C}$ [15], $\tilde{\lambda} = \sqrt{\boldsymbol{a}_0 \cdot \tilde{\boldsymbol{C}} \cdot \boldsymbol{a}_0}$ is the deviatoric fiber stretch along the local direction $\boldsymbol{a}_0$, μ is the shear modulus of the matrix, J is the Jacobian of the deformation, and K is the bulk modulus. The fiber stress-stretch behavior was represented as exponential, with no resistance to compressive load:

$$\begin{aligned} \tilde{\lambda}\frac{\partial F_2}{\partial \tilde{\lambda}} &= 0, && \tilde{\lambda} < 1, \\ \tilde{\lambda}\frac{\partial F_2}{\partial \tilde{\lambda}} &= C_3\left[\exp\left(C_4\left(\tilde{\lambda}-1\right)\right)-1\right], && \tilde{\lambda} \geq 1. \end{aligned} \tag{2}$$

Here, C_3 scales the stresses and C_4 defines the fiber uncrimping rate. A description of the constitutive model and its FE implementation can be found in Weiss *et al* [16]. Material coefficients were determined by a nonlinear least squares fit of the constitutive equation to published equibiaxial stress/strain curves [17] (μ = 2.50 KPa, C_3 = 0.27 KPa, and C_4 =21.0) [18]. A bulk modulus K = 210 KPa (two orders of magnitude higher than the shear modulus) was chosen to ensure near-incompressible material behavior.

Computational Solution. The Hyperelastic Warping algorithm has been integrated into the nonlinear FE code NIKE3D [19]. The formulation for the Warping solution is detailed in our previous publications [8, 12]. A series of 10 multiple templates/targets was used for Warping analysis of the left ventricle from end-diastole to end-systole. At each stage of registration, an active contraction was initially applied to the FE model, and then image-based Warping penalty forces were utilized to generate the decisive registration. The FE mesh was unconstrained in all six degrees-of–freedom during deformation.

A detailed description of the active contraction model and the material parameters for active contraction can be found in Guccione *et al.* [20, 21] and the description of its implementation may be found in Veress et al. [18]. The total Cauchy stress T in the fiber direction is defined as the sum of the active stress tensor and the passive stress tensor

$$T = T^{(p)} + T^{(a)}, \tag{3}$$

where $\boldsymbol{a}$ is the deformed fiber vector (unit length), defined by $\lambda \boldsymbol{a} = F \cdot \boldsymbol{a}_0$. The time-varying elastance model is a modification of the standard Hill equation that scales the standard equation by the variable C_t which governs the shape of the activation curve. The active fiber stress $T^{(a)}$ is defined as

$$T^{(a)} = T_{\max}\frac{Ca_0^2}{Ca_0^2 + ECa_{50}^2}C_t. \tag{4}$$

where $T_{\max}$ = 135.7 KPa is the isometric tension under maximal activation at the peak intracellular calcium concentration of $Ca_0 = 4.35$ μM. The length dependent calcium sensitivity is governed by the following equation:

$$ECa_{50} = \frac{(Ca_0)_{\max}}{\sqrt{\exp[B(l-l_0)]-1}}. \tag{5}$$

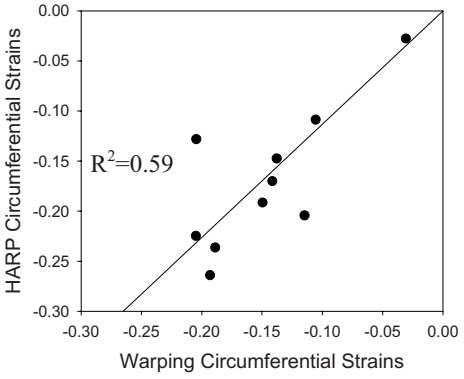

Fig. 3. Correlation plot for Warping circumferential strains vs. HARP circumferential strains. Results are comparisons of the average circumferential strain value at apical, mid-cavity, and basal slices from end-diastole through end-systole.

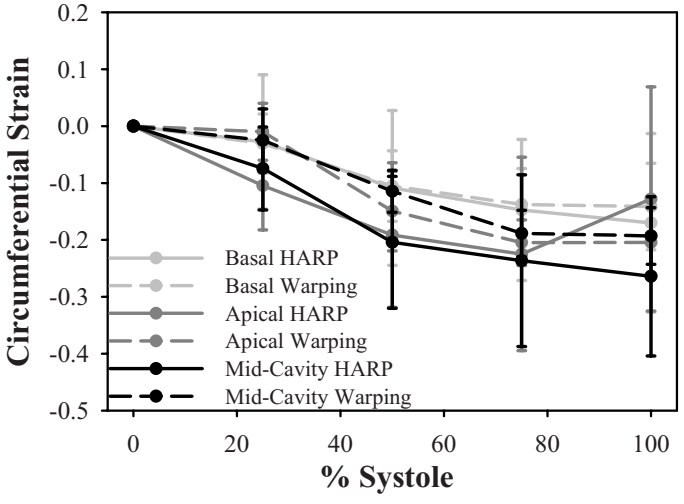

Fig. 4. Hyperelastic Warping circumferential strains (dashed lines) vs. HARP – measured strains (solid lines). Results are separated for apical slice (light gray), basal slice (dark gray), and mid-cavity slice (black). Error bars represent one standard deviation.

where $(Ca_0)_{\max} = 4.35$ μM is the maximum peak intracellular calcium concentration, $B =$ 4.75 μm^{-1} governs the shape of the peak isometric tension-sarcomere length, $l_0 = 1.58$ μm is the sarcomere length at which no active tension develops, and is the sarcomere length which is the product of the fiber stretch (deformed length/reference length) and the sarcomere unloaded length. In the FE implementation, the active contraction is governed by the product (an active

contraction stress) in (4) which was used to define a "load curve," specifying the degree of contraction and subsequent relaxation during the cardiac cycle.

Validation of the Hyperelastic Warping model was performed by comparing circumferential strain predictions developed through systole at basal, mid-cavity, and apical slices with those measured from tagged MR images. Tagged images were analyzed using a HARP (Harmonic Phase) algorithm implemented in Matlab, which parallels the technique introduced by Osman *et. al.*[22]

All values for fiber stretch, circumferential strain and radial strain are reported with the reference configuration defined at end-diastole. The Hyperelastic Warping analysis and HARP validation both progressed through end-systole. The tagged images had 5 phases through systole, while non-tagged images used for Hyperelastic Warping had 10 phases through systole. Circumferential strains from Hyperelastic Warping were compared directly with tagged MR strains measured with HARP analysis for apical, basal, and mid-cavity regions with 5 phases from end-diastole through end-systole.

3 Results

Computational Model. Hyperelastic Warping analysis of the left ventricle was performed on 4 processors of an SGI Origin 3800 (IP35 processors) and required approximately 40 minutes of wall clock time.

Validation of Circumferential Strains. The coefficient of determination for overall correlation between Hyperelastic Warping strains versus HARP tagging strains was R^2=0.59. (Fig.3). Results were plotted with circumferential strain developed from end-diastole to end-systole (Fig. 4) Fiber stretch is illustrated with the reference configuration at end-diastole (Fig. 5A) defined with a fiber stretch of 1.0, and stretches at mid-systole (Fig. 5B) and end-systole (Fig. 5C) shown for apical, mid-ventricular and basal slices. Fig. 6 shows strains for an apical slice sorted by wall position, from the endocardium to the epicardium.

4 Discussion

Values for left ventricular strain measures predicted by Hyperelastic Warping were in reasonable agreement with data from the literature. Mid-cavity LV fiber stretch during systole (0.88 ± 0.03, Fig. 5C) corresponds well with the values of mean systolic fiber stretch reported by Tseng *et al.* (0.88 ± 0.01). [23] Circumferential strains through the wall thickness (epicardial, -0.41±0.07; midwall, -0.18±0.11; endocardial, -0.15±0.08, Fig. 6C). were similar to Clark *et al.* who also reported a transmural gradient of circumferential shortening (epicardial, 44±6%; midwall, 30±6%, endocardial, 22±5%) [24]. Estimates of peak LV twist (9±3 degrees) measured from the deformation of the FE mesh grid-lines at end-systole (Fig. 5C) were similar to values reported by Takeuchi *et al* (7.7±3.5 degrees) [25].

The primary advantage of Hyperelastic Warping is the ability to measure 3-D strains throughout the myocardium with a high resolution. This may have significant clinical value, since the localization of myocardial strains is indicative of regional function. While the resolution of strain measurements from tagging is limited by the

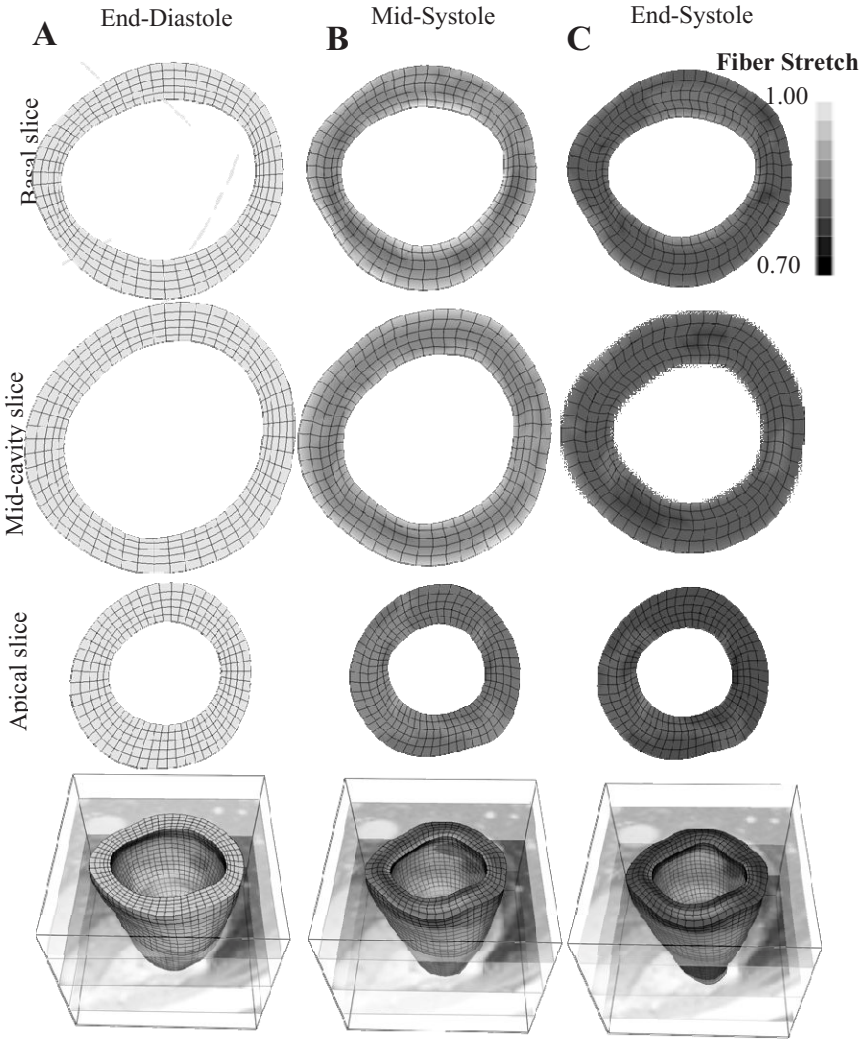

Fig. 5. LV fiber stretch during systole, with the development of the Hyperelastic Warping solution depicted at (A) End-diastole (B) Mid-systole and (C) End-systole. The deformed mesh is shown at apical, mid-cavity, and basal slices.

spacing of the applied tags, Hyperelastic Warping strains are limited by thickness of the pixel and the image content itself. A disadvantage of the Hyperelastic Warping technique is that, relative to MRI tagging analysis, it is computationally expensive. Future implementations of the technique will require automation of key steps of the procedure. In addition, mapping of detailed cardiac fiber orientation may be aided by diffusion tensor MRI. Advances in desktop processor speeds combined with high resolution cardiac imaging will make it feasible to measure cardiac strains with much greater accuracy, precision and speed.

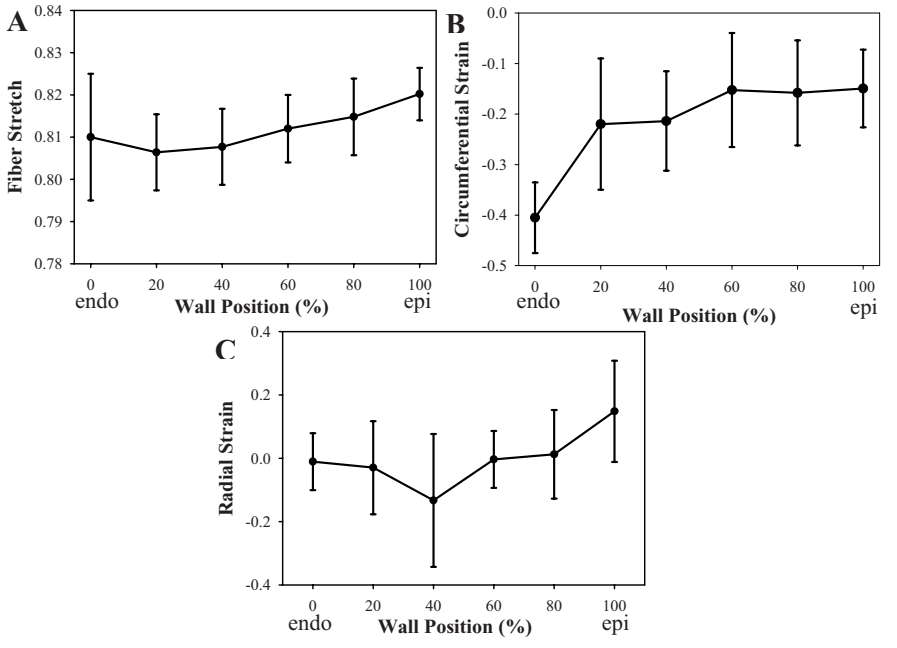

Fig. 6. Transmural strain results of Hyperelastic Warping analysis from end-diastole through end-systole for an apical slice location. (A) Fiber stretch (B) circumferential strain (C) radial strain plotted as a position of wall thickness with 0% as the endocardial wall 100% as the epicardial wall.

References

1. Papademetris, X., et al.: Estimation of 3-D left ventricular deformation from medical images using biomechanical models. IEEE Trans. Med. Imaging 21(7), 786–800 (2002)
2. Waldman, L.K., Fung, Y.-C., Covell, J.W.: Transmural myocardial deformation in the canine left ventricle: normal in vivo three-dimensional finite strains. Circulation Research 57, 152–163 (1985)
3. Ingels Jr., N.B., et al.: Evaluation of methods for quantitating left ventricular segmental wall motion in man using myocardial markers as a standard. Circulation 61(5), 966–972 (1980)
4. McVeigh, E.R., Zerhouni, E.A.: Noninvasive measurement of transmural gradients in myocardial strain with MR imaging. Radiology 180(3), 677–683 (1991)
5. Weidemann, F., et al.: Doppler myocardial imaging. A new tool to assess regional inhomogeneity in cardiac function. Basic Research in Cardiology 96(6), 595–605 (2001)
6. Lahiri, A., et al.: Effects of chronic treatment with calcium antagonists on left ventricular diastolic function in stable angina and heart failure. Circulation 81(suppl III), 130–138 (1990)
7. Veress, A.I., et al.: Strain measurement in coronary arteries using intravascular ultrasound and deformable images. J. Biomech. Eng. 124(6), 734–741 (2002)

8. Veress, A.I., Phatak, N., Weiss, J.A.: Deformable Image Registration with Hyperelastic Warping. In: Suri, Wilson, Laxminarayan (eds.) Handbook of Biomedical Image Analysis: Registration Models (Part A), vol. 3, Marcel Dekker, Inc, New York (2005)
9. Weiss, J.A, Rabbitt, R.D., Bowden, A.E.: Incorporation of medical image data in finite element models to track strain in soft tissues. SPIE 3254, 477–484 (1998)
10. Plein, S., et al.: Qualitative and quantitative analysis of regional left ventricular wall dynamics using real-time magnetic resonance imaging: comparison with conventional breath-hold gradient echo acquisition in volunteers and patients. Journal of Magnetic Resonance Imaging 14(1), 23–30 (2001)
11. Rabbitt, R.D., et al.: Mapping of hyperelastic deformable templates using the finite element method. SPIE 2573, 252–265 (1995)
12. Veress, A.I., Gullberg, G.T., Weiss, J.A.: Measurement of strain in the left ventricle during diastole with cine-MRI and deformable image registration. J. Biomech. Eng. 127(7), 1195–1207 (2005)
13. Ellis, B.J., et al.: Medial collateral ligament insertion site and contact forces in the ACL-deficient knee. J. Orthop. Res. 24(4), 800–810 (2006)
14. Gardiner, J.C., Weiss, J.A.: Subject-specific finite element analysis of the human medial collateral ligament during valgus knee loading. J. Orthop. Res. 21(6), 1098–1106 (2003)
15. Spencer, A.: Continuum Mechanics. Longman, New York (1980)
16. Weiss, J.A., Maker, B.N., Govindjee, S.: Finite element implementation of incompressible, transversely isotropic hyperelasticity. Computer Methods in Applied Mechanics and Engineering 135, 107–128 (1996)
17. Humphrey, J.D., Strumpf, R.K., Yin, F.C.: Determination of a constitutive relation for passive myocardium: II. Parameter estimation. Journal of Biomechanical Engineering 112(3), 340–346 (1990)
18. Veress, A.I., et al.: Normal and pathological NCAT image and phantom data based on physiologically realistic left ventricle finite-element models. IEEE Trans. Med. Imaging 25(12), 1604–1616 (2006)
19. Maker, B.N., Ferencz, R.M., Hallquist, J.O.: NIKE3D: A nonlinear, implicit, three-dimensional finite element code for solid and structural mechanics. Lawrence Livermore National Laboratory Technical Report, UCRL-MA #105268 (1990)
20. Guccione, J.M., McCulloch, A.D.: Mechanics of active contraction in cardiac muscle: Part I-constitutive relations for fiber stress that describe deactivation. Journal of Biomechanical Engineering 115, 72–81 (1993)
21. Guccione, J.M., McCulloch, A.D.: Mechanics of active contraction in cardiac muscle: Part II-constitutive relations for fiber stress that describe deactivation. Journal of Biomechanical Engineering 115, 82–90 (1993)
22. Osman, N.F., Prince, J.L.: Visualizing myocardial function using HARP MRI. Phys. Med. Biol. 45(6), 1665–1682 (2000)
23. Tseng, W.Y., et al.: Myocardial fiber shortening in humans: initial results of MR imaging. Radiology 216(1), 128–139 (2000)
24. Clark, N.R., et al.: Circumferential myocardial shortening in the normal human left ventricle. Assessment by magnetic resonance imaging using spatial modulation of magnetization. Circulation 84(1), 67–74 (1991)
25. Takeuchi, M., et al.: Age-related changes in left ventricular twist assessed by two-dimensional speckle-tracking imaging. J. Am. Soc. Echocardiogr. 19(9), 1077–1084 (2006)

Vessel Enhancement in 2D Angiographic Images

Sahla Bouattour and Dietrich Paulus

Institute of Computational Visualistics,
University of Koblenz-Landau, Germany
bouattour@uni-koblenz.de
http://www.uni-koblenz.de/agas

Abstract. In this paper we *extend* the Frangi filter[1] to recognize edges and do not enhance them. We give a theoretical framework for *optimal scale selection* and *choice of the free parameters*. We discuss *discretization* details concerning especially the discrete kernel used for building the scale-space and the choice of discrete scales. We present several experiments on phantom data to objectively and *quantitatively* compare and judge the filters. Experiments on real coronary angiograms enhance the improvement reached by the integration of the edge indicator.

Keywords: Vessel enhancement, multiscale analysis, phantom evaluation.

1 Introduction

In 2D coronary angiograms, vessels appear as curvilinear tubular structures having different widths. To recover the geometric structure, it is common to analyze the local partial derivatives of second order and build differential operators based on the sign and values of eigenvalues[1,2,3]. To recover the different widths, it is necessary to build operator answers at different levels of scales and to combine them[4]. The goal of vessel enhancement is to enhance *Just* the vessels and reduce noise especially in the background. It is important that the operations performed preserve the quantitative measures such as width of the vessel, and that the points with strongest response lie on the centerlines.

In this paper we extend the method proposed by Frangi et. al[1] to recognize edges and do not enhance them. Furthermore we perform a theoretical multiscale analysis to give theoretical values or bounds for the filter free parameters. Section 2 presents the new method. Section 3 discusses discretization details to get a proper realization. Section 4 presents experimental results, also on a phantom image. Finally Section 5 concludes this work.

2 Method

Given a continuous two-dimensional image $I(\bar{\boldsymbol{x}})$ ($\bar{\boldsymbol{x}} \in \mathrm{IR}^2$) that is observed at a scale $t \in \mathrm{IR}$, the Frangi et al. enhancement operator for bright vessels [1] is conceived as a filter with filter response:

$$r(\bar{\boldsymbol{x}}, t, \beta_1, \beta_2) = \begin{cases} 0 & \text{if } \lambda_2(\bar{\boldsymbol{x}}, t) > 0, \\ \exp(\frac{-\mathcal{R}_{\mathcal{B}}{}^2(\bar{\boldsymbol{x}},t)}{2\beta_1^2})(1 - \exp(-\frac{\mathcal{S}^2(\bar{\boldsymbol{x}},t)}{2\beta_2^2})), & \end{cases} \quad (1)$$

F.B. Sachse and G. Seemann (Eds.): FIMH 2007, LNCS 4466, pp. 41–49, 2007.

where $\lambda_1(\bar{\boldsymbol{x}},t)$ and $\lambda_2(\bar{\boldsymbol{x}},t)$ are the eigenvalues of the local Hessian computed at $\bar{\boldsymbol{x}}$ at scale t, such that $|\lambda_1(\bar{\boldsymbol{x}},t)| < |\lambda_2(\bar{\boldsymbol{x}},t)|$. The blobness measure $\mathcal{R}_{\mathcal{B}}(\bar{\boldsymbol{x}},t) = \frac{\lambda_1(\bar{\boldsymbol{x}},t)}{\lambda_2(\bar{\boldsymbol{x}},t)}$ measures the deviation from a blob by accounting for the eccentricity of the second order ellipse. $\mathcal{R}_{\mathcal{B}}(\bar{\boldsymbol{x}},t)$ cannot distinguish between a line and an edge. The structureness measure $\mathcal{S}(\bar{\boldsymbol{x}},t) = \sqrt{\lambda_1^2(\bar{\boldsymbol{x}},t) + \lambda_2^2(\bar{\boldsymbol{x}},t)}$ is the norm of the Hessian and is computed to distinguish between background and vessels. The parameters β_1 and β_2 tune the sensitivity of the filter to deviations in $\mathcal{R}_{\mathcal{B}}(\bar{\boldsymbol{x}},t)$ and $S(\bar{\boldsymbol{x}},t)$.

In order to distinguish between line and edge structures we propose to additionally integrate an edge indicator. Lorenz [3] proposed the following – here slightly modified – indicator:

$$E(\bar{\boldsymbol{x}},t) = \frac{|\nabla L(\bar{\boldsymbol{x}},t)|}{\sqrt{t}\lambda_2(\bar{\boldsymbol{x}},t)} \tag{2}$$

where $|\nabla L(\bar{\boldsymbol{x}},t)|$ is the local gradient magnitude at a point $\bar{\boldsymbol{x}}$ observed at scale t. At an edge both the gradient and λ_2 will be strong in magnitude. Within a vessel, just λ_2 will be big in magnitude. So it is expected that the value of E decreases within a vessel. We integrate the edge indicator within the Frangi filter as in eq. 3

$$r(\bar{\boldsymbol{x}},t,\beta_1,\beta_2) = \begin{cases} 0 & \text{if } \lambda_2 > 0, \\ \exp(\frac{-{\mathcal{R}_{\mathcal{B}}}^2(\bar{\boldsymbol{x}},t)}{2\beta_1^2})(1-\exp(-\frac{\mathcal{S}^2(\bar{\boldsymbol{x}},t)}{2\beta_2^2}))\exp(-|E(\bar{\boldsymbol{x}},t)|) \end{cases} \tag{3}$$

The continuous image observed at scale $t \neq 0$ is given by the convolution 4

$$L(\bar{\boldsymbol{x}},t) = I(\bar{\boldsymbol{x}}) * G(\bar{\boldsymbol{x}},t), \tag{4}$$

where $G(\bar{\boldsymbol{x}},t)$ is the Gaussian kernel with standard deviation $\sigma = \sqrt{t}$. Both the first order and the second order derivatives are computed by convolving the image $I(\bar{\boldsymbol{x}})$ with respectively the first and second derivatives of the Gaussian. The scale t is continuous and positive. $L(\bar{\boldsymbol{x}},t)$ is called the *scale-space* of the image $I(\bar{\boldsymbol{x}})$ [4].

As vessels appear in images with different widths, the application of filter 3 at different scales is necessary. Lindeberg proposed to use γ-parameterized normalized Gaussian derivatives: $\left(\frac{\partial G(\bar{\boldsymbol{x}},t)}{\partial \bar{\boldsymbol{x}}}\right)^{\gamma-\text{norm}} = t^{\frac{\gamma}{2}}\frac{\partial G(\bar{\boldsymbol{x}},t)}{\partial \bar{\boldsymbol{x}}}$, to get filter answers which are comparable for different scales. Using these operators, it can be easily shown that the normalization is directly transfused on the eigenvalues: $\lambda^{\gamma-\text{norm}}(\bar{\boldsymbol{x}},t) = t^{\frac{\gamma}{2}}\lambda(\bar{\boldsymbol{x}},t)$. Both the blobness measure $\mathcal{R}_{\mathcal{B}}{}^{\gamma-\text{norm}}(\bar{\boldsymbol{x}},t)$ and the edge indicator $E^{\gamma-\text{norm}}(\bar{\boldsymbol{x}},t)$ do not change. Just the structureness measure $\mathcal{S}^{\gamma-\text{norm}}(\bar{\boldsymbol{x}},t) = t^{\frac{\gamma}{2}}\mathcal{S}$ should be normalized. The normalized filter response is then given by eq. 5:

$$r^{\gamma-\text{norm}}(\bar{\boldsymbol{x}},t,\beta_1,\beta_2,\gamma) = \begin{cases} 0 & \text{if } \lambda_2 > 0, \\ \exp(\frac{-{\mathcal{R}_{\mathcal{B}}}^2(\bar{\boldsymbol{x}},t)}{2\beta_1^2})(1-\exp(-\frac{t^\gamma\mathcal{S}^2(\bar{\boldsymbol{x}},t)}{2\beta_2^2}))\exp(-|E(\bar{\boldsymbol{x}},t)|) \end{cases} \tag{5}$$

where $\mathcal{R}_{\mathcal{B}}(\bar{\boldsymbol{x}},t), \mathcal{S}(\bar{\boldsymbol{x}},t)$ and $E(\bar{\boldsymbol{x}},t)$ are computed based on the non-normalized Gaussian derivatives.

The multi-scale responses are combined by maximization:

$$R(\bar{\boldsymbol{x}},\beta_1,\beta_2,\gamma) = \max_t \left(r^{\gamma-\text{norm}}(\bar{\boldsymbol{x}},t,\beta_1,\beta_2,\gamma)\right) \tag{6}$$

Optimal Scale Selection and Choice of γ: In order to specify γ we assume a simple mathematical model for a 2D vessel with Gaussian profile, which is centered in the origin and parallel to the y-axis: $I_0(\bar{\boldsymbol{x}}) = G(\bar{\boldsymbol{x}}, t_0) = \frac{1}{\sqrt{2\pi t_0}} \exp\left(\frac{-x^2}{2t_0}\right) = G(x, t_0)$. The scale-space of $I_0(\bar{\boldsymbol{x}})$ is $L(\bar{\boldsymbol{x}}, t) = I_0(\bar{\boldsymbol{x}}) * G(\bar{\boldsymbol{x}}, t) = G(x, t_0 + t)$ for each value of y. The eigenvalues of the Hessian are $\lambda_1(\bar{\boldsymbol{x}}, t) = 0$ and $\lambda_2(\bar{\boldsymbol{x}}, t) = \frac{\partial^2 L(\bar{\boldsymbol{x}}, t)}{\partial x^2}$. Within the vessel we have $|x| < \sqrt{t_0}$, i.e λ_2 is negative. It follows $|\lambda_1(\bar{\boldsymbol{x}}, t)| < |\lambda_2(\bar{\boldsymbol{x}}, t)|$. The blobness measure $\mathcal{R}_{\mathcal{B}}(\bar{\boldsymbol{x}}, t) = 0$. The structureness measure $\mathcal{S}(\bar{\boldsymbol{x}}, t) = |\lambda_2(\bar{\boldsymbol{x}}, t)|$ and the edge indicator $E(\bar{\boldsymbol{x}}, t) = \frac{|-x|(t+t_0)}{\sqrt{t}(x^2-(t+t_0))}$.

The maximal filter response is expected in the middle of the vessel. At $x = 0$ we have $\mathcal{S}(\mathbf{0}, t) = -\frac{1}{\sqrt{2\pi}(t+t_0)^{\frac{3}{2}}}$ and $E(\mathbf{0}, t) = 0$. The normalized filter response becomes:

$$r^{\gamma-\mathrm{norm}}(\mathbf{0}, t, \beta_1, \beta_2, \gamma) = 1 - \exp\left(-\frac{t^\gamma}{4\pi\beta_2^2(t+t_0)^3}\right) \tag{7}$$

The scale for which this entity is maximal is given by:

$$\frac{\partial r^{\gamma-\mathrm{norm}}(\mathbf{0}, t_{\mathrm{opt}}, \beta_1, \beta_2, \gamma)}{\partial t} \stackrel{!}{=} 0 \longrightarrow t_{\mathrm{opt}} = \frac{\gamma}{3-\gamma} t_0 \tag{8}$$

If we want to have $t_{\mathrm{opt}} = t_0$ we choose $\gamma = \frac{3}{2}$.

It should be mentioned that a different ideal model could lead to another value of γ. The factor γ defines a proportionality between the optimal scale and the characteristic parameter of the assumed model. The later is here assumed to be the standard deviation. The real physical length of the corresponding vessel will be approximately six times greater. As real vessels are corrupted by noise, they will not perfectly overlap with the ideal model. So in the presence of noise the optimal scale is just a measure, where the structure of interest could have been best enhanced.

Choice of β_2: In general the value of β_2 depends on the strength of the noise and background structures in the image. It should be large in order to prevent enhancement of spurious low contrast data [5]. Based on the assumed ideal vessel model we will compute an upper bound for β_2 in the absence of noise. From eq. 5 it can be easily observed that the values of the filter answer $r^{\gamma-\mathrm{norm}}(\bar{\boldsymbol{x}}, t, \beta_1, \beta_2, \gamma)$ are bound within the interval $[0, 1]$. At $x = 0$, the filter answer of eq. 7 should be maximal for the optimal scale $t_{\mathrm{opt}} = t_0$ and $\gamma = \frac{3}{2}$; i.e the response $r^{\gamma-\mathrm{norm}}(\mathbf{0}, t_{\mathrm{opt}} = t_0, \beta_1, \beta_2, \frac{3}{2}) = 1 - \exp\left(-\frac{1}{8\pi\beta_2^2 t_0^{\frac{3}{2}}}\right) \stackrel{!}{=} 1$. We define a desired precision $\epsilon << 0$ for the exponential to be assumed equal to zero. We get therefore the upper bound for β_2

$$\beta_2 \leq \sqrt{-\frac{1}{8\pi \ln(\epsilon)}} \sqrt{t_0}^{\frac{3}{2}}. \tag{9}$$

This upper bound depends on the standard deviation of the assumed model $\sqrt{t_0}$. As a fixed value for β_2 is required for all considered scales, we get concrete values for β_2 by considering the maximal scale value. The bound given by eq 9 represents the part of β_2 which depends on the geometrical structure of the line model. It is to be understood as

an indication of the order of magnitude of β_2 in the ideal case. In real images β_2 should still be tuned heuristically, to count for the gray levels in the background at hand.

Choice of β_1: The value of β_1 should be small in order to distinguish between line-like and blob-like structures. If bifurcations or very tortuous vessels are not enhanced properly, increasing β_1 resolves that at the expense of also enhancing non-vessel background structures [5]. As $|\lambda_1(\bar{\boldsymbol{x}}, t)| < |\lambda_2(\bar{\boldsymbol{x}}, t)|$ and due to the symmetry of the exponential function we can compute the blobness based on the absolute values of the λ's. The values of $\mathcal{R}_{\mathcal{B}}{}^{\gamma-\mathrm{norm}}(\bar{\boldsymbol{x}}, t)$ are then bound between $[0, 1]$, It is one when the structure is a blob and it is near zero if the structure is a line or an edge. A value $\beta_1 = 0.33$ discards all blob similar structures. Greater values (≤ 1) are less discriminative, but more tolerant to deviations from the ideal model.

3 Discretization and Numerical Implementation

Two questions arise when we are given a discrete 2D image. First: How to get a discrete scale-space of the image? Second: How to discretize the scale parameter t?

Discrete Scale-Space: A straightforward discretization of eq 4 is accomplished by performing the *discrete convolution* of the image with the *discrete Gaussian kernel*, while keeping the scale parameter t continuous. The discretization of the Gaussian kernel can be performed in several ways. The most known are by directly computing the continuous Gaussian function at discrete locations (the *sampled Gaussian kernel*) or by integrating the continuous kernel over each pixel support region (the *integrated Gaussian kernel*). The sampled Gaussian kernel has the problem, that for small values of t the central coefficient of the sampled Gaussian can become very large and the sum of the corresponding filter coefficients will exceed one[4]. The integrated Gaussian kernel can be regarded as giving a more true approximation than the first method, especially at fine scales. The resulting approximation formula corresponds to discrete convolution with the kernel $g(n, t) = \int_{n-\frac{1}{2}}^{n+\frac{1}{2}} \frac{1}{\sqrt{2\pi t}} \exp^{-\frac{\xi^2}{2t}} d\xi$. This choice of filter coefficients is equivalent to the continuous formulation 4 if we let the continuous image be a piecewise constant function [4,6]. The kernel coefficients for the Gaussian, and its derivatives are computed as given in[6]. The mask sizes are computed automatically depending on the given σ such that the approximation error is set to a certain ϵ_g. At borders the gray values are mirrored.

Discrete Scales: In practice we need to choose a certain number of scales that best approximate the characteristic parameters in the image at hand. The maximum and minimum values of $\sigma = \sqrt{t}$ should be determined on the basis of the width range of the vessels of interest. In [2] the minimum number of scale was automatically determined based on certain response specific criteria. The set of discrete scales σ_i is computed according to $\sigma_i = \sigma_l s^i$ width $s > 1$ a scaling factor, $i = 0, 1, \cdots, n-1$ and n the number of scales such that $\sigma_l s^{n-2} < \sigma_h \leq \sigma_l s^{n-1}$. It follows that

$$n < \frac{\ln(\frac{\sigma_h}{\sigma_l})}{\ln(s)} + 2 \leq n + 1 \tag{10}$$

We took the smallest nearest integer value of eq. 10 for n. We get thus a logarithmic progressing of scales and an automatic determination of their number.

4 Experiments

4.1 Experiments on Phantom Data

We generated a phantom image ($420 \times 420 \times 8$) containing line structures having Gaussian profiles of different widths: A vertical line with $\sigma_0 = 1$, a horizontal line with $\sigma_0 = 5$ and a circular structure with $\sigma_0 = 3$ and radius $r = 100$. (see fig. 1). The vertical line crosses the circle along its middle axis. The horizontal line is shifted to the bottom by 30 pixels. The positioning of the lines aims to show the behavior of the filter on straight line, curvilinear structure as well as at crossings or bifurcations.

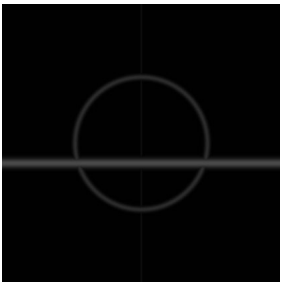

Fig. 1. Phantom image

By taking the ideal Gaussian profile $I_0(\vec{x})$ of sec. 2, lines with smaller width will be assigned brighter gray values. In real angiographic images the opposite behavior is rather observed. To simulate this phenomenon we inverted the proportionality with respect to σ. The underlying Gaussian profiles used for generating the phantom are $\frac{\sigma_0}{\sqrt{2\pi}}\exp\left(\frac{-x^2}{2\sigma_0^2}\right)$ for the straight lines and $\frac{\sigma_0}{\sqrt{2\pi}}\exp(-\frac{(r-\sqrt{x^2+y^2})^2}{2\sigma_0^2})$ for the circular profile. To be able to assess the enhancement effect we assigned a gray value of 15 to the maximum value of the line with the smallest width. Based on this, the gray level mapping function is linear. Background color was set to one. When two lines cross the maximal value in the overlapping area is taken.

We performed multiscale analysis with maximization of normalized responses. We used $\beta_1 = 0.33$, which is the most restrictive value. The maximal width in the image is $\sigma = 5$ and by choosing $\epsilon = 10^{-8}$ in eq. 9, we became a value of $\beta_2 = 0.52$. The normalization factor is $\gamma = 1.5$. We chose $\sigma_l = 1$, $\sigma_h = 5$. By setting the scaling factor of eq. 10 to $s = 1.5$ five scales were automatically computed $\sigma \in$

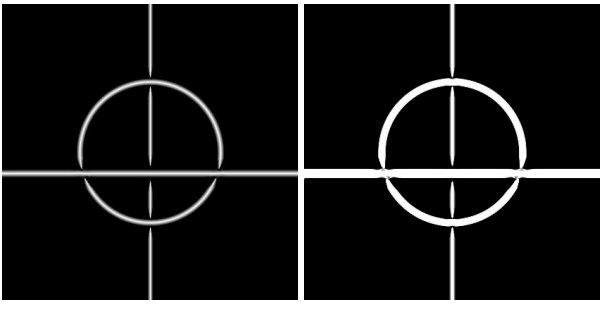

Fig. 2. Multiscale results with filter 5 (left) and filter 1 (right).$\beta_2 = 0.52$, $\beta_1 = 0.33$, $\gamma = 1.5$,$\sigma_l = 1$,$\sigma_h = 5$.

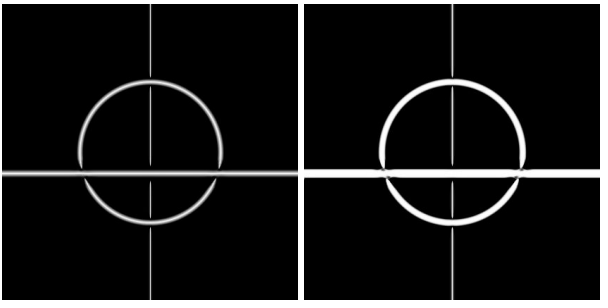

Fig. 3. Multiscale results with filter 5(left) and normalized Frangi filter 1(right). $\beta_2 = 2.0$.

$\{1, 1.5, 2.25, 3.375, 5.0625\}$. The results for filter 5 and normalized filter 1 are shown in figure 2. Tuning β_2 results in fig. 3.

The effect of both vessel enhancement filters can be quantitatively compared according to three factors: First which filter better increases the local contrast between vessel and background. Second which filter better preserves the original line width. And third which filter better enhances the centerlines of the vessels. Due to the symmetry of the phantom used we computed these values along one cross section for each of the three lines and excluded thus crossings since they do not have line properties. The local contrast was measured by the mean value of mean gray levels within the lines in the original and enhanced images. The width was computed by the mean value of the number of pixels whose gray levels are different from background. And the enhancement of the centerline was measured by computing the ratio of gray levels along the cross section of the lines and the gray value of the centerline. Tables 1 and 2 summarizes the quantitative results.

Table 1. Quantitative comparison between normalized Frangi filter 1 and extended filter 5: Comparison of local contrast and preservation of line width. Mean values over three line sizes are reported.

	image	**local contrast**	**width**
	original	21.025	15.66
$\beta_2 = 0.52$ Fig 2	normalized Frangi eq. 1	151.37	9.66
	extended filter eq. 5	77.467	9
$\beta_2 = 2.0$ Fig 3	normalized Frangi eq. 1	119.13	9
	extended filter eq. 5	69.321	8.66

By observing figures 2 and 3 both filters show very week responses in regions where two lines cross, i.e. where no line properties are present. This appears as a discontinuity. Normalization of the filters leads to comparable values along different scales. Especially great scales become higher responses. Both filters enhance the local contrast compared with the original one (table 1). The extended filter 5 results in lower local contrast since the additional edge indicator term in eq 3 is always within $[0, 1]$. The behavior of both filters is comparable with respect to preservation of the width of lines. It is basically reduced, especially for wide lines (see Also curves in table 2). This may be due to the

Table 2. Quantitative comparison between normalized Frangi filter 1 and extended filter 5: comparison of centerline enhancement. Top $\beta_2 = 0.52$; from left to right $\sigma = 1, 3, 5$ respectively. Bottom $\beta_2 = 2.0$; from left to right $\sigma = 1, 3, 5$ respectively. Original line: dot line, Frangi filter: dashed line, extended filter: continuous line. Cross section values are reported.

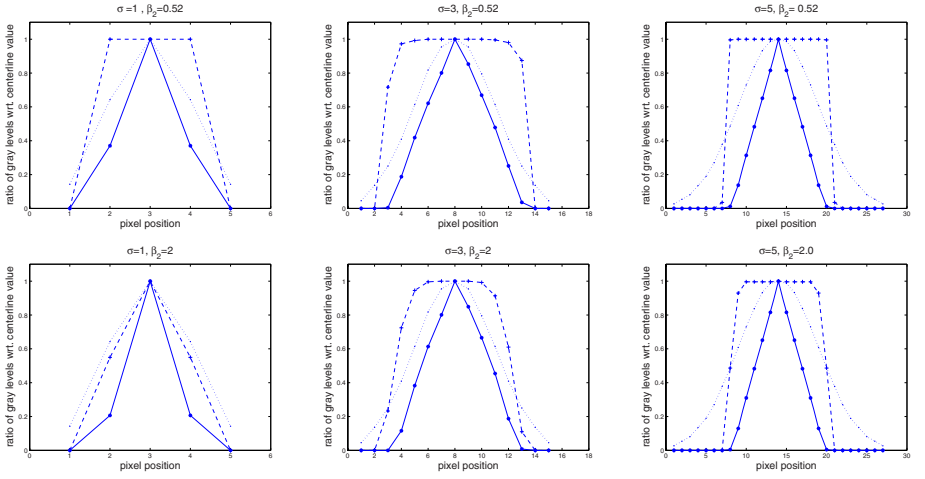

weak slope of wider lines. The gain from adding the edge indicator becomes clear by observing the curves of enhancement of the centerlines in table 2. The normalized filter 1 enhances the borders of the lines without particularly enhancing centerlines. The values accorded to the centerlines by filter 5 are more discriminative and facilitates further processing such as centerline extraction. Increasing β_2 increases the discriminative power –especially of the normalized Frangi filter–, decreases the local contrast and tends to reduce the resulting width of lines.

4.2 Experiments on Real Data

We apply vessel enhancement on real coronary angiograms ($512 \times 512 \times 8$) captured by a monoplane Siemens AXIOM Artis system (rotational angiography). The images

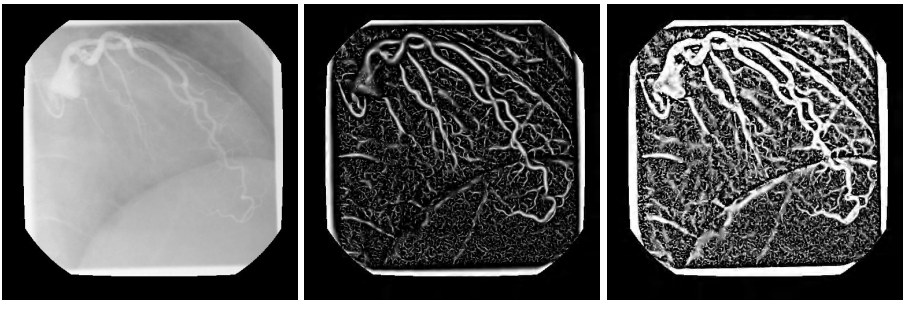

Fig. 4. From left to right: original image, filter 5, normalized filter 1 with same parameters

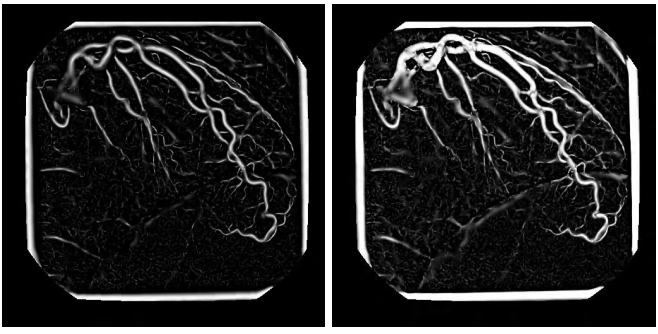

Fig. 5. Less Background noise. Left: filter 5 with $\beta_2 = 1.0$. Right: filter 1 with $\beta_2 = 1.0$.

have a black border, which is not considered in treatment. We set $\beta_1 = 0.5$, $\gamma = 1.5$ and $s = 1.5$. By choosing $\sigma_h = 4$ we become a value of $\beta_2 = 0.38$. For $\sigma_l = 1$ and $\sigma_h = 4$ five scales are automatically computed $\sigma \in \{1, 1.5, 2.25, 3.375, 5.0625\}$. Fig. 4 shows a typical image, its corresponding preprocessed images with both filters 5 and 1. Figure 5 shows two preprocessed images with variation of β_2 leading to less Background noise.

With the theoretical discussed values for the free parameters the filters 5 and 1 were able to enhance the interesting structure and also a lot of Background. Increasing β_2 eliminates background structures (fig. 5) and better reflects the real widths of vessels, as it was already observed in the phantom image. With real images we observe the poor discriminative performance of the responses of the Frangi filter 1 between centerlines and borders. Another consequence of non-distinction between edges and line structures

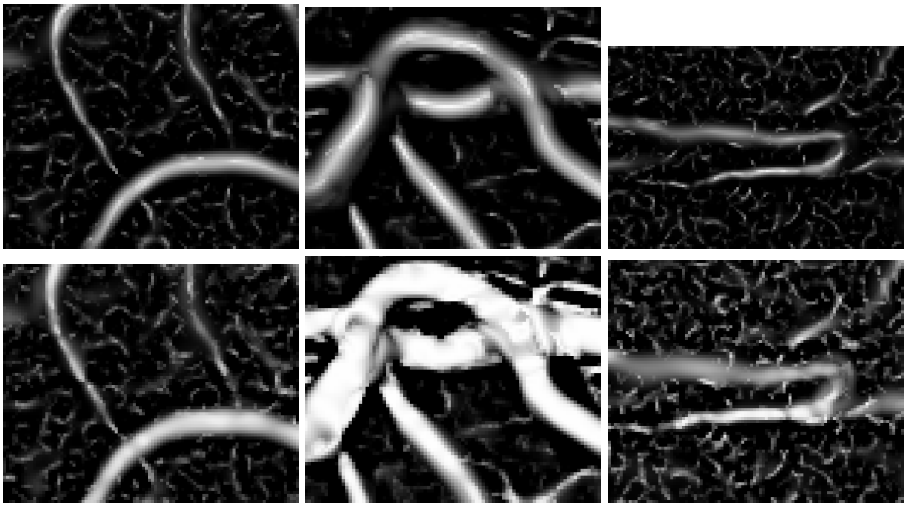

Fig. 6. Magnification of bifurcations, crossings and a tortuous vessel. Top: results of filter 5. Bottom: results of normalized filter 1.

is the enhancement of the diaphragm with the Frangi filter (fig. 4, right); as it is considered as an edge.

Both filters were able to recognize fine vessels and also fine ramifications, thanks to the multi-scale response. Problems arise with very tortuous vessels and at bifurcations or crossings, where the eigenvalues have comparable values and so no line properties can be detected (increasing β_1 does not ameliorate the result). Fig. 6 show magnified regions of different images where this effect is observed. At this magnified scale the improvement reached by integrating the edge indicator is again enhanced by the smooth responses and preservation of the vessel trajectory.

5 Conclusion

In this paper we extended the Frangi filter [1] for 2D-vessel enhancement to better differentiate between edges and line structures. We integrated the normalization of Gaussian derivatives in the filter response. We performed an optimal scale selection by assuming an ideal model and gave theoretical values or bounds for the filter free parameters. We presented experiments on phantom data to objectively and quantitatively compare and judge the filters in the ideal case. The performed extension lead mainly to stronger discrimination of the centerlines after enhancement. Experiments on real angiographic data showed this improvement under real conditions. This contribution is to be understood as preprocessing for further steps such as centerline extraction or temporal tracking of vessels for 3D heart motion recovery [7].

References

1. Frangi, A., Niessen, W.J., Hoogeveen, R.M., van Walsum, T., Viergever, M.A.: Model-based quantitation of 3-d magnetic resonance angiographic images. TMI 18(10), 946–956 (1999)
2. Sato, Y., Nakajima, S., Shiraga, N., Atsumi, H., Yoshida, S., Koller, T., Gerig, G., Kikinis, R.: 3d multi-scale line filter for segmentation and visialization of curvilinear structures in medical images. IEEE Medical Image Analysis 2(6), 143–168 (1998)
3. Lorenz, C., Carlsen, I.C., Buzug, T.M., Fassnacht, C., Weese, J.: A multi-scale line filter with automatic scale selection based on the hessian matrix for medical image segmentation. In: Proc. of the First Int. Conf. on Scale-Space Theory in Computer Vision, pp. 152–163 (1997)
4. Lindeberg, T.: Scale-space for discrete signals. IEEE Transactions of Pattern Analysis and Machine Intelligence 12(3), 234–254 (1990)
5. Schrijver, M., Slump, C.H.: Automatic segmentation of the coronary artery tree in angiographic projections. In: Proc. Program for Research on Integrated Systems and Circuits (PRORISC) (2000)
6. Steger, C.: An unbiased detector of curvilinear structures. PAMI 20(2), 113–125 (1998)
7. Bouattour, S., Arndt, R., Paulus, D.: 4d reconstruction of coronary arteries from monoplane angiograms. In: Gagalowicz, A., Philips, W. (eds.) CAIP 2005. LNCS, vol. 3691, Springer, Heidelberg (2005)

Effect of Noise and Slice Profile on Strain Quantifications of Strain Encoding (SENC) MRI

Tamer A. Yousef[1] and Nael F. Osman[1,2]

[1] Electrical and Computer Engineering Dept.
[2] Department of Radiology, Johns Hopkins University

Abstract. SENC is a new technique for imaging tissue deformation, such as the strain of cardiac tissue due to contraction. SENC strain quantifications are limited to one direction, the through-plane direction. However, this is sufficient to image circumferential and longitudinal strain in the long- and short-axis views, respectively. The factors that affect the accuracy of SENC strain mesurements are the slice profile and the signal-to-noise ratio (SNR). In this work, these factors are analyzed in order to optimize the SENC method for strain quantifications.

Introduction

MRI is an excellent modality for imaging the motion of moving tissues and tissue deformations including those of the heart. MRI is valuable in measuring cardiac wall motion. Methods such as tagging and phase contrast were able to noninvasively and accurately measure myocardial motion [1,2,3,4,5].Using such techniques, MR is considered the "gold standard" for assessment and measuring cardiac function [6].

Strain encoding (SENC) is a technique that has been developed to measure regional strain in a direct and straight forward way, *i.e.,* with no need for sophisticated postprocessing [7,8]. The measured strain component is limited, however, to the through-plane direction. This is not a serious limitation as the choice of the imaging planes determines the type of strain component, and, fortunately, the typical strain components (circumferential and longitudinal strain) can be viewed from conventional long- and short-axis views. SENC technique results were validated in comparison with other well established techniques like tagging and delayed enhancement [9]. While much work has been developed and published on the SENC technique, a thorough analysis of the accuracy of SENC, as well as its sensitivity to many crucial factors, has been lacking. For example, SENC relies on the slice profile of the excited slab to measure strain, which makes the computations of strain sensitive to the exact shape of the slice profile. Although the original work on SENC assumed a rectangular slice profile, it is important to understand the impact of changes in slice profile on the accuracy of the technique. Moreover, there has been no thorough analysis of the effect of noise on strain quantifications. In this work, we study those effects in order to optimize the selection of imaging parameters and minimize quantification error.

F.B. Sachse and G. Seemann (Eds.): FIMH 2007, LNCS 4466, pp. 50–59, 2007.

First, we will describe the basics of the SENC technique in section 1.1. Example for a typical SENC experiment with its results is given in section 1.2. In section 1.3, we analyze the relation between the computed and actual strain values for different slice profiles, assuming no noise. Then, in section 1.4, we describe how to design the SENC experiment parameters. Finally, the effect of noise is studied in Section 1.5. Numerical simulations and phantom experiments are preformed to validate the theoretical analysis.

1 Theory

1.1 The SENC Method

The SENC pulse sequence can be regarded as a variation of the 1-1 SPAMM tagging pulse sequence where the tagging gradient is along the slice-selection direction. First, the tagging pulses are applied, causing the tissue magnetization to be modulated by a sinusoidal pattern with tag surfaces parallel to the imaging plane. This sinusoidal pattern (tags) has a spatial frequency (ω_0). that is proportional to the $zero^{th}$ moment of the tagging gradient. After a short period of time, during which tissue deformation might occur, changes in the local tagging frequency of this sinusoidal pattern will occur. It has been demonstrated in [7] that the spatial frequency change is proportional to the local strain in the direction orthogonal to the imaging plane.

The acquired images are modified by adding a gradient moment in the slice-selection direction to cause demodulation with a specific spatial frequency, which is called the *tuning* frequency. As a result, the signal intensity of a pixel in the resulting images varies depending on two factors: the slice profile and the tuning frequency. Mathematically, an image acquired at a specific tuning frequency can be described by:

$$I\left(y;t;\omega_T\right) = \rho\left(y,t\right) S\left(\omega_T - \omega\left(y;t\right)\right), \tag{1}$$

where $I\left(y;t;\omega_T\right)$ refers to the signal intensity of a pixel located at a location y, with time t, $\rho\left(y,t\right)$ the proton density at that location, and $S(.)$ the Fourier transform of the slice profile—which is related to the envelope of the slice selection RF pulse [7]. The tuning frequency ω_T is, therefore, computed from the tuning gradient using:

$$\omega_T = \gamma \int G_T\left(t\right) dt \tag{2}$$

where γ is the gyromagnetic ratio. The spatial frequency $\omega\left(y;t\right)$ is a function of the local frequency of the tag pattern at that pixel, which, in turn, depends on local tissue deformation and strain.

In order to measure local strain, two images are acquired at two different tuning frequencies, a low-tuning image (I_L) with the tuning frequency ω_L, and a high tuning image (I_H) with the tuning frequency ω_H. Figure (1) illustrates the change of the low and high tuning image with different shifts in harmonic

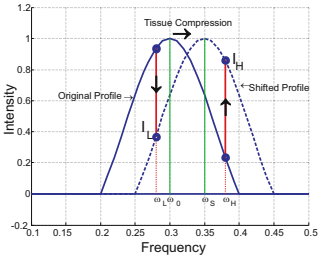

Fig. 1. Effect of Harmonic Shift on I_L and I_H. In case of negative strains (shortening of compression of tissue), the harmonic peak shifts toward a higher frequency. The signal at ω_L is decreasing while the signal at ω_H is increasing.

peaks due to changes in the local spatial frequency of tags caused by tissue deformation. It shows that I_L is directly proportional to local stretching while I_H is directly proportional to local contraction.

By acquiring these two images, the actual spatial frequency can be estimated at any given pixel using the center of mass method (as described in [7]):

$$\overline{\omega}\,(y;t) = \frac{\omega_L I\,(y;t;\omega_L) + \omega_H I\,(y;t;\omega_H)}{I\,(y;t;\omega_L) + I\,(y;t;\omega_H)}. \tag{3}$$

Then, the local strain at this pixel location can be estimated from this frequency shift using:

$$\overline{\varepsilon}\,(y;t) = \frac{\triangle\omega\,(y;t)}{\overline{\omega}\,(y;t)} = \left(\frac{\omega_0}{\overline{\omega}\,(y;t)} - 1\right). \tag{4}$$

These relations are valid as long as the the profile peak doesn't move outside the frequency range between ω_L and ω_H (i.e. the strain range should be within a specific range which is given apriori).

1.2 Example of Strain Measurement

Fig. 2 shows an example of SENC raw images (low and high tunings) and the resulting strain map. The images are for a four-chamber view of the heart of a normal subject imaged on a clinical 3T MR whole-body system(Gyroscan Intera, Philips Medical System, Best, The Netherlands). Images were acquired with FOV = 350*350mm, slice thickness = 8mm, matrix size 256*256. Acquisition was synchronized after the R-wave with temporal resolution = 22msec. Low and high tuning frequencies were adjusted so as to capture deformation strain ranges from 0% to -30% because it is a four -chamber view, the strain map shows the circumferential strain since it is the through plane strain components. Notice that difference in strain values between the endocardium and epicardium, as expected.

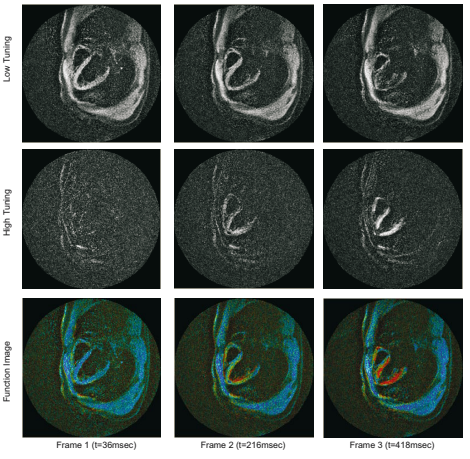

Fig. 2. Sample of SENC images. The vertical axis represents, from top to bottom, the low tuning, high tuning, and function images (strain maps registered on the anatomy images), the horizontal axis represents the time frames, from left to right, at 36, 216, and 418msec. The color map ranges from blue (for maximum stretching, 0%) to red (for maximum shortening, -30%). Through time, the myocardium starts to appear in the high tuning images while disappearing from the low tuning images.

1.3 Effect of Slice Profile on SENC Computations

The accuracy of the strain estimation depends on a number of factors in addition to the slice profile. In [10], it has been proved that the actual strain value (ε) and the estimated value ($\overline{\varepsilon}$), using equation (4), are exactly the same for the triangular and rectangular slice profiles. However, this is not necessarily true for all other profiles (see Fig. 3). Also, even for the triangular and rectangular profiles, the actual profile that is generated on the scanners is not perfect, either due RF pulses optimization (which may results in adding ripples to the profile) or due to the slightly field inhomogentiy that may occur.

Therefore, a mapping function is needed to correct measured strain due to inaccuracies in the slice profile. The correction in strain quantification from the estimated strain can be written as

$$\varepsilon = \mathcal{F}\left(\overline{\varepsilon}\right), \tag{5}$$

where $\mathcal{F}\left(.\right)$ can be determined for the exact slice profile in a *calibration* step prior to imaging. This calibration steps need not be frequently repeated. During this step, we aim to build the actual slice profile for a specific experiment then build the mapping function from this measured profile. More details is given in section 2.

1.4 SENC Parameters Design

It can be seen from (1.1) that the selection of ω_0, ω_L, and ω_H affects the dynamic strain range—*i.e.,* the strain range in which the strain can be accurately

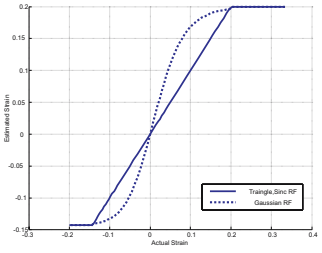

Fig. 3. Strain curves for different slice profiles. While triangle and sinc profiles show a simple first-order (linear) relation between the actual and estimated strain, the Gaussian slice profile results in a higher order relation. Note that the two curves are saturated at the same value for all the profiles, since saturation depends only on slice thickness and the assumed strain range but not on the profile.

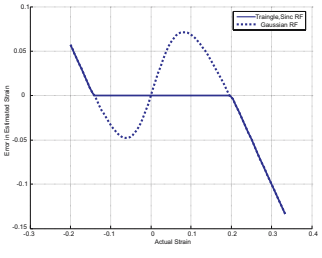

Fig. 4. Error in measured strain values for different slice profiles. Within a specific range of strain, triangular and sinc peaks have perfectly zero error, while the Gaussian peak has a strain-dependent error. However, the error becomes the same for all the profiles outside the required range, since the error becomes dependent on the slice thickness.

measured. It is important, then, to be able to design these parameters for a specific strain range, which is given apriori, bounded by maximum stretching ($\varepsilon_{max-stretching} \geq 0$) and maximum shortening ($\varepsilon_{max-shortening} \leq 0$). This is usually an accepted assumption in most of the strain quantification experiments like in cardiac application, which has nominal strain range from 0% to -30%, especially if the operator can adjust these bounds on-site if the actual range differs from the expected one (this will appear as a saturation in the strain quatifications as will be discussed in the next section).

Determining ω_L and ω_H. In case of stretching, the slice peak shifts to a lower frequency; however, in order to obtain signal from the high tuning, the right tail of the profile should not exceed ω_H. This means that the center of the peak should be greater than or equal to the difference of $\omega_H - B$, where B is the profile half-width. Since $\omega_H - B$ is the minimum frequency value that the peak can attain without the loss of the signal at ω_H, we can assign this value to

correspond to the maximum allowable stretching. Using Eq (4), we can derive the relation:

$$\varepsilon_{max-stretching} = \frac{\omega_0}{\omega_H - B} - 1, \tag{6}$$

or

$$\omega_H = \frac{\omega_0}{\varepsilon_{max-stretching} + 1} + B. \tag{7}$$

If the measured strain falls below the assumed $\varepsilon_{max-stretching}$, the peak right tail will be totally below ω_H and the measured signal at ω_H will go to zero. This forces the value of the estimated peak shift in (3) to be exactly equal to ω_L independant of what the real value is. Then the result strain will be saturated at the value of $\varepsilon_{max-stretching}$ (see the saturation effect in figure 3). Following the same line of reasoning, the relation between the maximium shortening and the low tuning frequency can written as:

$$\omega_L = \frac{\omega_0}{\varepsilon_{max-shortening} + 1} - B. \tag{8}$$

Thus, for a given ω_0, B, and the required strain range, the tuning frequencies can be computed. Notice that B depends on the slice thickness, and, in case of rectangular slices,

$$B = \frac{1}{SliceThickness}. \tag{9}$$

Hence, the only remaining parameter is ω_0.

Determining ω_0. The frequency ω_0 can be determined by considering a third constraint on the shifts of the slice profile. In order for Eq. (3) to be accurate, the lowest frequency (ω_L) should not be too low or it will detect signal from the untagged component of the tissue, *i.e.,* the DC component [11]. This means that ω_L should not pass the half-width of the slice profile, *i.e.,*

$$\omega_L \geq B. \tag{10}$$

Using Eqs. (8) and (10), we can determine a lower bound for the tagging frequency:

$$\omega_0 \geq 2B\left(1 + \varepsilon_{max-shortening}\right) \tag{11}$$

Because ω_0 should always be between ω_L and ω_H; therefore

$$\omega_0 \leq \omega_H, \tag{12}$$

which, when combined with (8) and (7) provides an upper limit for the tagging frequency of

$$\omega_0 \leq 2B\left(\frac{\left(1 + \varepsilon_{max-shortening}\right)\left(1 + \varepsilon_{max-stretching}\right)}{\varepsilon_{max-shortening} - \varepsilon_{max-stretching}}\right). \tag{13}$$

From (11) and (13), the exact choice of ω_0 will be a trade-off. The exact selection of $\omega_0$will address the strain sensitivity and noise immunity, which will be discussed in the next section.

1.5 Noise Effect on Strain Quantification

Assume that the white Gaussian noise components, n_L and n_H, are added to the signal components, I_L and I_H, respectively. Now, equation (3) can be re-written as

$$\overline{\omega}_n(y;t) = \frac{\omega_L(I_L + n_L) + \omega_H(I_H + n_H)}{(I_L + n_L + I_H + n_H)}$$

which can be re-arranged into:

$$\overline{\omega}_n(y;t) = \frac{\omega_L I_L + \omega_H I_H}{(I_L + I_H + n_L + n_H)} + \frac{\omega_L n_L + \omega_H n_H}{(I_L + I_H + n_L + n_H)}. \tag{14}$$

Then the expected value of the new shifted frequency $\overline{\omega}_n(y;t)$ can be given as:

$$E(\overline{\omega}_n(y;t)) = E\left(\frac{\omega_L I_L + \omega_H I_H}{I_L + I_H}\right) E\left(\frac{I_L + I_H}{I_L + I_H + n_L + n_H}\right) + E\left(\frac{\omega_L n_L}{I_L + I_H + n_L + n_H}\right) + E\left(\frac{\omega_H n_H}{I_L + I_H + n_L + n_H}\right). \tag{15}$$

To analyze equation (15) more, let's consider the different cases in which the ratio between the noise and signal components highly differs. In the high stretching strain values, the harmonic peak is shifted towards ω_L so the acquired intensity at ω_L has a very high SNR while the one acquired at ω_H has a lower SNR (i.e. $E(I_L) \gg E(n_L)$ and $E(I_H) \simeq E(n_L) \simeq E(n_H)$). The situation is very similar on the other side (for the high compression strain values). In the middle strain values between maximum stretching and maximum compression, the intenisties acquired at both ω_L and ω_H have relatively high SNR (i.e. $E(I_L) > E(n_L)$ and $E(I_H) > E(n_H)$). Noting also that the ω_L and ω_H are normally < 1 since the tag spacing is normally > 1 (a nominal values set for cardiac Imaging is $\omega_L = 0.25$, $\omega_0 = 0.26$ and $\omega_H = 0.38$ for 8mm slice thickness and to capture strain values from 5% to -30%) , so the third and forth terms of equation (14) can be neglected and equation (15) can be written as:

$$E(\overline{\omega}_n(y;t)) \simeq \Delta E(\overline{\omega}(y;t)), \tag{16}$$

where

$$\Delta = E\left(\frac{I_L + I_H}{I_L + I_H + n_L + n_H}\right).$$

Where, following the same reasoning in the SNR regions previous discussion, $\triangle$ is usually higher in the middle strain values region than the both the high compression and high stretching regions. By substituting Eq. (16) for (4), we obtain

$$\overline{\varepsilon_n} = \left(\frac{\omega_0}{\overline{\omega}.\Delta} - 1\right) = \frac{\overline{\varepsilon}}{\Delta} + \Delta', \tag{17}$$

where $\Delta' = (1 - \Delta)/\Delta$. Thus, the noise affects the strain curve (estimated vs. actual) in two ways: changing the slope to $\frac{1}{\triangle}$, and adding a bias $\triangle'$.

2 Experiments and Results

2.1 Generating the Strain Mapping Function

In order to build strain mapping function, needed in section 1.4, the actual slice profile along the k_z direction is required. A stationary phantom was imaged using the same protocol for the SENC technique with tagging frequency $\omega_0 = 0.3$ and slice thickness =10mm. However, instead of just imaging at only two tuning frequencies (ω_L and ω_H) as in SENC, the frequency values were spanned before and after the tagging frequency value where we expect the profile harmonic to appear (i.e. from $\omega = 0$ to $\omega = 0.7$ with a resolution $\triangle\omega = 0.01$). The ROI in the image is manually identified then the intensities values inside the ROI were averaged for each tuning image then normalized to build the profile. Then, for different strain values, the profile is shifted and the actual strain is calculated using the intensities at exactly the same tuning values that will be used in the actual SENC experiment. Then, the strain mapping function can be build from these corresponded values. The same methods can be used to generated the strain maps for any simulated silce profile.

2.2 Numerical Simulations

To simulate the noise effect, we assumed that the slice profile was rectangular (i.e. a sinc profile in the frequency domain along the k_z direction) and the strain inside a voxel ranges from maximum stretching strain to maximum shortening. So, sinc profile was simulated for a specific slice thickness. Then, white Gaussian noise was added to the profile and the magnitude values are calculated. SENC parameters (ω_0, ω_L and ω_H) were selected given the strain range and the slice thickness as in section 1.4. Then, the strain range values were spanned as follows: for each strain value, the shift in the harmonic peak is calculated and then the new profile values at ω_L and ω_H resulted from this shift are used to calculate the corresponding estimated strain using equations (3) and (4). This process was repeated for a large number of times then the average is calculated. Then, the whole process is repeated for different levels of the Gaussian noise corresponding to different levels of signal-to-noise (SNR) ratio.

3 Results

Figure (5) shows the ideal and the actual measured slice profile across K_z. Slight difference can be seen between the two curves. These differences may affect the strain computation. So, the strain mapping for such profiles is needed for accurate strain quantifications.

Figure (6) shows the effect of different levels of SNR on the slice profile in the frequency domain. Figure (7) shows the strain curve for different SNR values in the simulated data. As can be seen, as the SNR deteriorates, the slope of the strain curve decreases and the measurable strain range shrinks.

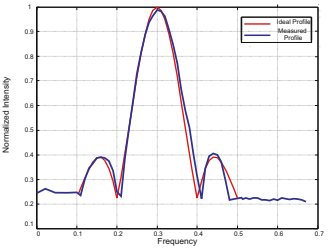

Fig. 5. Ideal and actual measured slice profile. Note the slight difference in the profile zero crossings which may result from slight field inhomogenity.

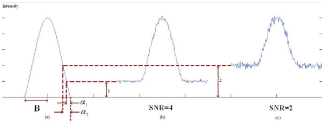

Fig. 6. Sinc peak for different SNR levels (a. SNR=∞, b. SNR = 4, c. SNR=2). As SNR decreases, the lower intensity values of the peak are hided with the noise components. α_1, α_2 represents the shrinkage of the available peak shift due to this noise effect.

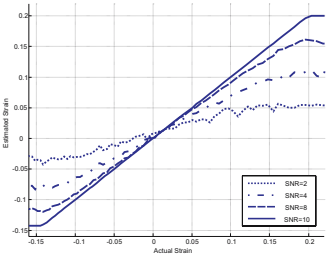

Fig. 7. Strain curves (estimated vs. actual) for different SNR (10, 8, 4 and 2). As SNR decreases, the slope of the strain curve decreases, which lowers the resolution of the measured strain. In addition, the curves start to saturate faster (at lower strain values). Note also that strain bias (at zero strain) increases as the SNR gets lower.

4 Discussion

The first effect of a low SNR appears in Figure (6), where the low intensity values (as in the profile sides) are more affected by noise than are higher intensity values. This creates a non-zero mean noise level that would hide low intensity values—which can hardly be distinguished. This results in shrinking the allowable range within which the peak can be shifted, and hence, shrinking the allowable strain range. The second effect, which is derived from Eq. (17), appears in Figure (7) in which the slope of the $\varepsilon - \overline{\varepsilon}$ curve decreases as the SNR gets lower. Besides,

a bias appears in the estimated strain values. While both the bias and slope can be solved (by a mapping table, for example), the resolution of the acquired strain values has already been lowered.

5 Conclusion

The effects of slice profile and signal-to-noise ratio (SNR)on the SENC technique quantifications are analyzed. The slice profile effect can be easily compensated for with non-rectagular profiles via a look-up table that can map the measured strain values into the actual one. The SNR level is shown to affect the strain measurments, by introducing a slope-change and a bias to the strain curve. These effects can be compensated for by a calibration scan to determine the SNR map, which can then be used to correct the strain quantifications.

References

1. Zerhouni, E.A., Parish, D.M., Rogers, W.J., Yang, A., Shapiro, E.P.: Human heart: tagging with MR imaging a method for noninvasive assessment of myocardial motion. Radiology 169, 59–63 (1988)
2. Axel, L., Dougherty, L.P.: Heart wall motion: improved method of spatial modulation of magnetization for MR imaging. Radiology 172, 349 (1989)
3. Pelc, N.J., Herfkens, R.J., Shimakawa, A., Enzmann, D.: Phase contrast cine magnetic resonance imaging. Magn Reson Q 7, 229–254 (1991)
4. Osman, N.F., Kerwin, W.S., McVeigh, E.R., Prince, J.L.: Cardiac motion tracking using CINE harmonic phase (HARP) magnetic resonance imaging. Magn Reson Med. 42, 1048–1060 (1999)
5. McVeigh, E.R.: Regional myocardial function. Cardiol Clin 16, 189–206 (1998)
6. Edvardsen, T., Gerber, B.L., Garot, J., Bluemke, D.A., Lima, J.A.C., Smiseth, O.A.: Quantitative Assesment of Intrinsic Regional Myocardial Deformation by Doppler Strain Rate Echocardiography in Humans. Circulation 106, 50 (2002)
7. Osman, N.F.: Imaging longitudinal cardiac strain on short-axis images using strain-encoded MRI, Magn. Resn. Med. vol. 46, pp. 324–10 (2001)
8. Pan, L., Stuber, M., Kraitchman, D.L., Fritzges, D.L., Gilson, W.D., Osman, N.F.: Real-time imaging of regional myocardial function using fast-SENC. Magn. Resn. Med. 55, 386–395 (2006)
9. Garot, J., et al.: Spatially Resolved Imaging of Myocardial Function with Strain-encoded MR: Comparison with Delayed Contrast-enhancement MR Imaging after Myocardial Infarction. Radiology 233(2), 596 (2004)
10. Osman, N.F.: Measuring Regional Cardiac Function Using Harmonic Phase Magnetic Resonance Imaging, Phd Thesis (2002)
11. Fischer, S.E., McKinnon, G.C., Maier, S.E., Boesiger, P.: Improved Myocardial Tagging Contrast. Magn. Resn. Med. 30, 191–200 (1993)

Reconstruction of Detailed Left Ventricle Motion from tMRI Using Deformable Models

Xiaoxu Wang[1], Joel Schaerer[2], Suejung Huh[1], Zhen Qian[1], Dimitis Metaxas[1], Ting Chen[3], and Leon Axel[3]

[1] Rutgers University, Piscataway NJ, 08854, USA
xiwang@cs.rutgers.edu
[2] CREATIS, CNRS UMR 5220, Inserm U630, INSA Lyon, 20, rue Albert Einstein 69621 Villeurbanne Cedex France
[3] New York University, 660 First Avenue, New York, NY, 10016, USA

Abstract. We present a system that reconstructs the 3D motion of the left ventricle (LV) for a full cardiac cycle using a deformable model built from tagged MR images. Two sets of cues are drawn from tagged MRI. The intersections of the three tagging planes, and the intersections of the LV boundary and the tagging planes, are interpolated onto the mesh vertices. We implement a deformable model to track the LV motion, utilizing Finite Element Methods (FEM) to keep the general shape and topology of the LV. This volumetric deformable model speeds up the FEM and facilitates the medical analysis. The LV motion reconstruction provides information for further analysis of cardiac mechanisms.

1 Introduction

Cardiac Tagged Magnetic Resonance Imaging (MRI) facilitates estimation of the detailed myocardial motion and the deformation of the left ventricle(LV) in vivo during the cardiac cycle. It provides information for the early diagnosis of cardiac disorders and quantitative analysis of cardiac diseases. Tagged MRI is an image with a set of parallel tagging planes orthogonal to the image plane, projecting onto the comparably brighter myocardium as a set of parallel dark lines. Reconstructing the 3D LV motion from tagged MRI can assist doctors to diagnose cardiac diseases earlier, and can be used for 3D strain analysis of the myocardium [1].

Finite Element Methods and quadric models have been widely used for the LV motion reconstruction. There has been a lot of work on 3D cardiac shape and motion analysis such as [2,3,4,5,6,7,8]. (Park 1995) [3] used parameter functions extended from [9] to estimate the 3D LV motion. The extended parametric deformable model is also used on the right ventricle(RV) for the diagnosis and analysis of the RV related cardiac diseases [4,5,6]. A Boundary Element Model(BEM) is used to extract local shape properties with high computational efficiency [7]. Deformable biomechanics models introduced in [8] considered the biomechanical material properties of cardiac muscles and yielded realistic strain fields. In this

F.B. Sachse and G. Seemann (Eds.): FIMH 2007, LNCS 4466, pp. 60–69, 2007.

paper, we introduce a 3D LV motion recovery system based on deformable models, which can achieve a faster convergence compared to methods using FEM only. FEM keeps the shape of an object by passing stress forces to neighboring vertices. In a detailed LV mesh with thousands of points, this procedure requires tremendous time before reaching the equilibrium. In our model, global deformations are intergraded seamlessly with local deformations to compute the real locations of mesh vertices. Global deformations can be quickly recovered for the whole objects, faster compared to local propagations. Local deformations are computed using FEM with linear elasticity, and the *Lamé* constants are computed for different anatomical regions. Finally we compute the strain and other deformation parameters on the total model displacements.

The rest of this paper is organized as follows. Section 2 introduces the procedure of reconstructing 3D motion of LV, and the methods in different steps. Section 3 presents the motion estimation results and analysis. Section 4 concludes this paper and proposes the future work.

2 Methods

This section describes the methods we used in reconstructing the 3D motion in several steps. First, LV boundaries and tagging line information are obtained from tagged MRI using Gabor Filters [10], Metamorphs [11] and spline models [12]. The intersections of the three tagging planes are calculated, as well as the intersections of the LV boundary and the tagging planes. These intersections can be used as material markers in LV motion tracking. Then we register a generic heart mesh to the image data by affine registration and non-rigid thin plate spline local fitting. The LV motion is reconstructed with a volumetric deformable model [3,9], which can recover the deformations like contractions and twists during systole.

2.1 Segmentation of the LV Boundaries

Since accurate contour segmentation is difficult to achieve without removing the tagging lines, a bank of Gabor filters are used to detect tagging lines in different orientations [10]. As a band-pass filter, the Gabor filter can eliminate the frequency of the tagging lines.

After removing tagging lines, the images are segmented by Metamorphs [11], a class of deformable models integrating both shape priors and interior texture. The model deformations are parameterized using the cubic B-spline based Free Form Deformation. Metamorphs can accurately segment both the epicardium and the endocardium of the LV.

The tagging lines are then tracked by active contour models, and are refined by spline models only using the tag information between the epicardium and the endocardium. The splines are separated to several portions to avoid the influence of the noise outside of the myocardium, which results in an accurate fitting [12]. With the above methods, the LV contours and the tagging lines can be automatically segmented and tracked.

2.2 Model Initialization and Registration

The generic model of the LV is built from MR images obtained from a healthy volunteer. The image information is obtained by manual segmentation with validation by an expert. The surface mesh was build by a Delaunay triangulation using geodesic distances, to preserve the topology of the object better [13]. This generic mesh provides an anatomically plausible model for the whole tracking procedure.

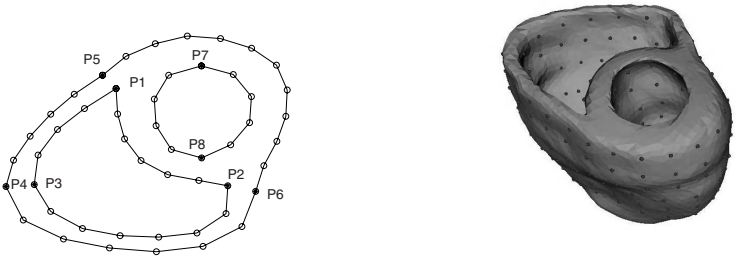

Fig. 1. (a) Landmarks on the contour (b) Registered model with landmarks on LV, RV endocardium and epicardium

To register the model with the image data, we use a set of landmarks, 50 landmarks per slice and 350 landmarks in total, on the contours defined by different curvatures [14]. The landmarks are calculated both on the image contours and on the corresponding slices of the model. We place the model on the image data location by an affine transformation including translation, rotation and isotropic scaling, and then use thin plate splines to fit the model locally.

2.3 Tag Line Incorporation

The intersections of the three tagging planes are material markers in the myocardium. A tagging surface can be reconstructed by tagging lines in MR images using thin plate splines. Because there is no analytic solution for calculating the intersections of three thin plate splines, and high complexity of the projection method proposed in [15], we turn the calculation of the intersections of three interpolated tagging planes into a simpler implementation with equivalent results. We calculate the intersections of horizontal and vertical tagging lines in SA images first. These intersection points are along the intersection lines of the two tagging planes which are orthogonal to the SA images. The intersection lines intersect with the third tagging plane, which is orthogonal to the LA image plane. This implementation avoids full interpolation of all three tagging surfaces, and simplifies the problem to that of calculating the intersections of lines and a surface.

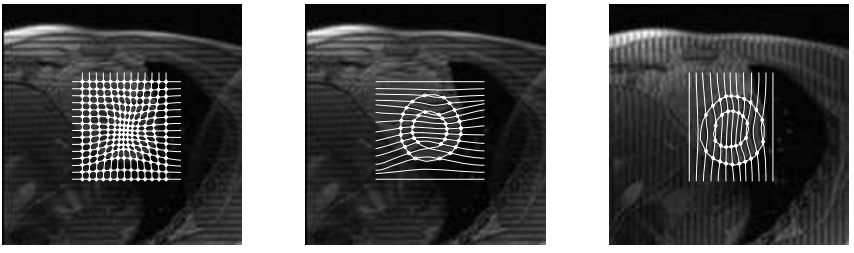

(a) (b) (c)

Fig. 2. (a) Intersections of tagging lines (b) Intersections of horizontal tagging lines and contours (c) Intersections of vertical tagging lines and contours

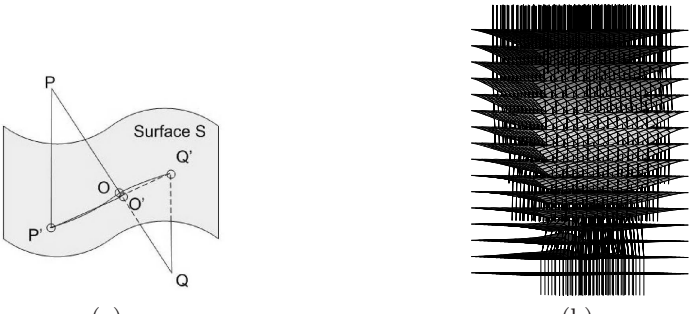

(a) (b)

Fig. 3. (a) Calculate the intersection of a curve and a surface (b) The intersection curves intersect with the tagging surfaces orthogonal to the LA images

Calculating the intersections of curves and surfaces can be viewed as calculating intersections of lines and planes in the small neighborhood of the intersections. The interpolated curve can be represented by a set of points and short lines connecting these points. We find the short line that intersects with the surface first. Then we project the two ends of the line P, Q to the surface as P', Q', as in Figure 3 (a). Since the curve is almost normal to the surface, the projection points are located very close to the intersection O. And a small area of the surface is close to a plane. Thus the intersection of PQ and $P'Q'$, denoted as O', is very close to the real intersection O. The location of O' is taken as the location of O in this paper.

We calculate the intersections of all tagging surfaces in the three orthogonal directions. Only the intersections in the myocardium are material points, and the other intersections in the blood or outside the LV are not valid for motion estimation.

2.4 Fast Motion Reconstruction Using Deformable Models

Using Lagrangian dynamics, we reconstruct the motion and deformation of the LV. We use the generated mesh to remove the intersections outside of the LV

(a) (b)

Fig. 4. Intersections within the myocardium (a) Viewed from the side (b) Viewed from base to apex

boundary. The intersections inside the LV boundary driving mid-systole are shown in Figure 4.

The positions of points on our deformable model relative to an inertial frame Φ of reference in space are given by a vector-valued, time-varying function $x(q,t) = (x_1(q,t), x_2(q,t), x_3(q,t))^T$. The transformation from the model-centered coordinate system to the world coordinate system is $x = c + Rp$, where c is the origin of the model-centered coordinate system ϕ in Φ and R is the rotation matrix describing the orientation of ϕ. p can be further decomposed to two parts $p = s + d$, to incorporate global and local deformation.

A deformable model can be controlled by a set of parameters defined as $q = (q_c^T, q_\theta^T, q_s^T, q_d^T)$, with $q_c = c$ and $q_\theta = \theta$, where θ is the rotation quaternion of the model. Our model is composed of multiple layers, and are defined in the same polar coordinates $s = (u, v)$, where $-\frac{\pi}{2} \leq u \leq \frac{\pi}{5}$ runs from apex to the base of the LV, $-\pi \leq v < \pi$ is horizontal, starts and ends at the place where the septum is located. The global deformation is determined by $q_s = (a_0, a_1, a_2, a_3, \tau)$, including scale a_0, radiuses in three directions a_1, a_2, a_3, and a twisting factor τ. The shape is defined as $s = T(e)$. For the k^{th} ellipsoid, $1 \leq k \leq w$, the geometric primitive e is defined as

$$e = a_0(k) \begin{pmatrix} a_1(k)cos(u)cos(v) \\ a_2(k)cos(u)sin(v) \\ a_3(k)sin(u) \end{pmatrix} \tag{1}$$

The shape represented by e is subject to the deformation T, which is the twist of the LV,

$$s = \begin{pmatrix} e_1 cos(\varphi) - e_2 sin(\varphi) \\ e_1 sin(\varphi) + e_2 cos(\varphi) \\ e_3 \end{pmatrix} \tag{2}$$

where $\varphi = \pi\tau sin(u)$.

The local displacements d can describe arbitrary deformations making the point deviate from s. We can express the displacements d as a linear combination of a set of basis function $d = \Sigma_i S_i q_{d_i}$, where the diagonal matrix S_i is formed

from the basis function and q_{d_i} are local degrees of freedom. In our approach, $q_d = (d_1, d_2, ..., d_n)$ since each vertex of the LV model has 3 degrees of freedom.

The velocity of a point on the model is given by

$$\dot{x} = \dot{c} + \dot{\mathbf{R}}p + \mathbf{R}\dot{p} \tag{3}$$

$$= \dot{c} + \mathbf{B}\dot{\theta} + \mathbf{R}\dot{s} + \mathbf{RS}\dot{q_d} \tag{4}$$

where $B = \partial(Rp)/\partial\theta_i$ and $\dot{s} = [\partial s/\partial q_s]\dot{q_s} = J\dot{q_s}$. J is the Jacobian of the reference shape with respect to the global deformation parameters. In the model expressed in equation 1 and 2, $\partial s/\partial q_s = (\partial s/\partial a, \partial s/\partial \tau) = ((\partial s/\partial e)(\partial e/\partial a), \partial s/\partial \tau)$, where $q_s = (a, \tau)$ and $a = (a_0, a_1, a_2, a_3)$.

$$\partial s/\partial e = \begin{pmatrix} cos(\varphi) & -sin(\varphi) & 0 \\ sin(\varphi) & cos(\varphi) & 0 \\ 0 & 0 & 1 \end{pmatrix}; \partial s/\partial \tau = \begin{pmatrix} \pi sin(u)(e_1(-sin(\varphi)) - e_2 cos(\varphi)) \\ \pi sin(u)(e_1 cos(\varphi) + e_2(-sin(\varphi))) \\ 0 \end{pmatrix} \tag{5}$$

$$\partial e/\partial a = \begin{pmatrix} a_1 cos(u)cos(v) & a_0 cos(u)cos(v) & 0 & 0 \\ a_2 cos(u)sin(v) & 0 & a_0 cos(u)sin(v) & 0 \\ a_3 sin(u) & 0 & 0 & a_0 sin(u) \end{pmatrix} \tag{6}$$

Equation 4 can be written as

$$\dot{x} = [\mathbf{I} \quad \mathbf{B} \quad \mathbf{RJ} \quad \mathbf{RS}]\dot{q} = \mathbf{L}\dot{q}, J = (J_1, ..., J_w), q_s = (q_{s_1}, ..., q_{s_w}). \tag{7}$$

We use lagrangian dynamics, coupling with Newton's second law and hooke's law of the string. The equation is

$$\mathbf{D}\dot{q} + \mathbf{K}q = F(t) \tag{8}$$

where q is the displacement of a structure and $\dot{q}$ is the velocity. $\mathbf{D}$ is the damping matrix, and in this paper it is diagonal and constant over time. $\mathbf{K}$ is the stiffness matrix. Equation 8 can be solved by

$$q_{t+1} = q_t + (F(t) - \mathbf{K}q_t)dt \tag{9}$$

To do dynamic analysis on a complex structure, Finite element analysis a standard tool to break the structure into parts. The stiffness matrix on $(q_c^T, q_\theta^T, q_s^T)$ is set to zero. The details of the stiffness matrix K_{dd} on local deformation are described in [16]. Except for the q_d, all other parameters derivatives need to be intergraded over the ellipsoid surfaces.

$$\dot{q} = f_q^T = (\int f^T[\mathbf{I} \quad \mathbf{B} \quad \mathbf{RJ}]du, f_d^T - \mathbf{K}_{dd}q_d^T) \tag{10}$$

We interpolate the image forces onto the vertices of the deformable model to avoid ill conditioning tetrahedra caused by irregular local forces. The motion reconstruction algorithm is described in the following,

Algorithm:

1. Given source markers S and target markers T:
2. Initialize current markers $C = S$;
3. Iterate until $distance(C, T) < Threshold$:
4. Calculate forces as vector field $T - C$;
5. Interpolate forces to the mesh vertices (V, f_V);
6. Calculate the $\dot{q}$ and update q;
7. Interpolate C from the new mesh.

Fig. 5. The algorithm to calculate meshes in different time slots

2.5 Strain Analysis Based on the LV Motion

We calculated the strain of the whole LV in the Cartesian coordinate system to provide further information. The strain field of each element with respect to their reference shapes are computed using the Lagrangian Green St. Venant, approach[17]. Within an element, a linear deformation is assumed. Given the reference shape and the deformed shape of an element, the deformation tensor T is computed as

$$TA = A', \tag{11}$$

where the reference shape tensor A and the deformed shape tensor A' are defined as

$$A = \left(x_{01}\ x_{02}\ x_{03} \right),\ x_{0i} = x_i - x_0 \tag{12}$$

$$\text{and } A' = \left(x'_{01}\ x'_{02}\ x'_{03} \right),\ x'_{0i} = x'_i - x'_0. \tag{13}$$

as shown in Figure 6

Note A is invertible as long as the reference shape is not degenerated. A^{-1} can be pre-computed and reused for each time frame. Given $T = A'A^{-1}$, the Green St. Venant strain tensor E is computed as

$$E = T^T T - I = \begin{pmatrix} \epsilon_{11}\ \epsilon_{12}\ \epsilon_{13} \\ \epsilon_{22}\ \epsilon_{23} \\ \epsilon_{33} \end{pmatrix} \tag{14}$$

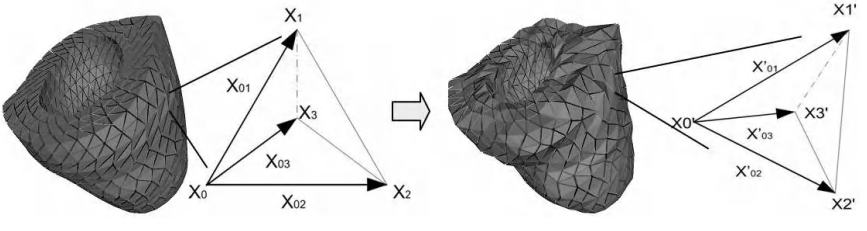

Fig. 6. An element on a reference frame and a deformed frame

The calculated strain is rotation invariant. Strains computed for a mid-LV slice is visualized in Figure 8.

3 Results on Motion Reconstruction and Strain Analysis

We construct the LV motion from the a set of MR images with seven SA slices and two LA slices. The registered generic LV model has 3076 vertices and 11328 tetrahedral elements. It takes about 3 minutes for the deformable model to converge on each frame on Intel Xeon 3.00GHz CPU, compared to 40 minutes taken by FEM. The results are shown in Figure 7. From the reconstructed LV motion sequence, we can identify the systole and the diastole. The myocardium twists clockwise while the LV contracts and counter-clockwise while the LV relax. The principle strains recovered by deformable models are shown in Figure 8. From 30 frames showing a full cardiac cycle, we analyze the first 20 frames. Figure 8 (a) shows that elongation strain on the septum is only 80% of that

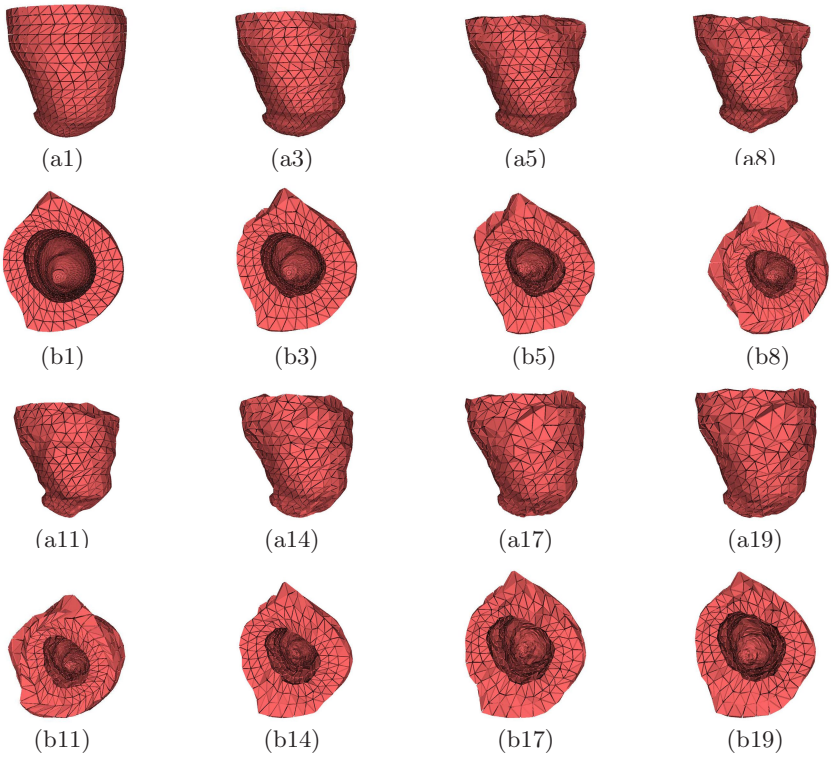

Fig. 7. From 30 time frames taken from a whole heart beating cycle, the selected few frames showing the motion are presented here. Row (a) images are viewed from side, and row (b) images are viewed from base, e.g.(a1) means frame 1 side view.

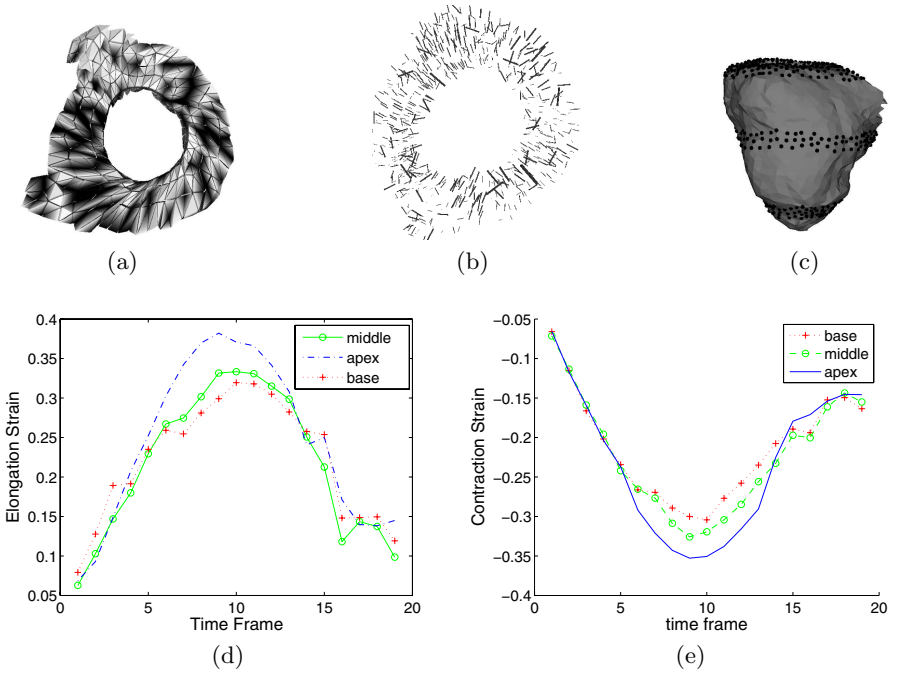

Fig. 8. Principle strains at the end systole (a) Magnitude of the elongation strain (minimum is black and maximum is white); (b) Elongation strain projected to the SA plane; (c) Three slices in (d) and (e); (d)Elongation strain over time (e)Contraction strain over time

on the free wall. Figure 8 (b) shows that most elongation strains are in radial direction. Figure 8 (d) and (e) shows how the strain changes through the cardiac cycle. Both elongation strain and contraction strain are larger in the apex than in the base.

4 Conclusions and Future Work

We describe a complete procedure of reconstructing 3D motion of the LV myocardium with tagged MR images. The motion is recovered by deformable models with high time efficiency, by integrating the motion trend of all vertices. In the mean time, deformable models achieve spacial accuracy by incorporating local deformations. The general shape of the generic model are maintained by FEM during the systole and the diastole. Strain computations are performed on each tetrahedron element of the LV to measure the deformation with respect to the initial frame. In the future, for computation of the detailed strain field with an element, a meshless approach may be able to be used.

Acknowledgments. We would like to thank Région Rhône-Alpes' EURODOC Programme.

References

1. Hu, Z., Metaxas, D.N., Axel, L.: Computational modeling and simulation of heart ventricular mechanics from Tagged MRI. In: FIMH 2005, pp. 369–383 (2005)
2. Young, A.A., Axel, L.: Three-dimensional motion and deformation of the heart wall. Radiology, p. 185 (1992)
3. Park, J., Metaxas, D.N., Axel, L.: Volumetric deformable models with parameter functions: A new approach to the 3D motion analysis of the LV from MRI-SPAMM. In: ICCV 1995, 700–705 (1995)
4. Park, K., Metaxas, D.N., Axel, L.: A finite element model for functional analysis of 4D cardiac-tagged MR images. In: MICCAI (1), pp. 491–498 (2003)
5. Park, K., Metaxas, D.N., Axel, L.: LV-RV shape modeling based on a blended parameterized model. In: MICCAI, pp. 753–761. Springer-Verlag, Heidelberg (2002)
6. Haber, E., Metaxas, D.N., Axel, L.: Motion analysis of the right ventricle from the mri images. In: Wells, W.M., Colchester, A.C.F., Delp, S.L. (eds.) MICCAI 1998. LNCS, vol. 1496, pp. 177–188. Springer, Heidelberg (1998)
7. Yan, P., Lin, N., Sinusas, A., Duncan, J.S.: A boundary element-based approach to analysis of lv deformation. MICCAI, pp. 778–785 (2005)
8. Sermesant, M., Forest, C., Pennec, X., Delingette, H., Ayache, N.: Deformable biomechanical models: Application to 4d cardiac image analysis. Medical Image Analysis, pp. 475–488 (2003)
9. Terzopoulos, D., Metaxas, D.N.: Dynamic 3D models with local and global deformations: Deformable superquadrics. IEEE Trans. Pattern Anal. Mach. Intell. 13(7), 703–714 (1991)
10. Qian, Z., Metaxas, D.N., Axel, L.: Extraction and tracking of MRI tagging sheets using a 3D gabor filter bank. In: Proceedings of Int'l Conf. of the Engineering in Medicine and Biology Society (2006)
11. Huang, X., Metaxas, D., Chen, T.: Metamorphs: Deformable shape and texture models, Computer Vision and Pattern Recognition (2004)
12. Axel, L., Chen, T., Manglik, T.: Dense myocardium deformation estimation for 2d Tagged MRI. In: FIMH, pp. 446–456 (2005)
13. Lötjönen, J., Reissman, P-J., Magnin, I.E., Nenonen, J., Katila, T.: A triangulation method of an arbitrary point set for biomagnetic problems. IEEE Transactions on Magnetics 34(4), 2228–2233 (1998)
14. Schaerer, J., Qian, Z., Clarysse, P., Metaxas, D., Axel, L., Magnin, I.E.: Fast and automated creation of patient-specific 3D heart model from Tagged MRI, MICCAI workshop (2006)
15. Kerwin, W., Prince, J.: Cardiac material markers from tagged MR images. Medical Image Analysis 2, 339–353 (1998)
16. Mäkelä, T., Pham, Q.C., Clarysse, P., Nenonen, J., Lötjönen, J., Sipilä, O., Hänninen, H., Lauerma, K., Knuuti, J., Katila, T., Magnin, I.E.: A 3-D model-based registration approach for the PET, MR and MCG cardiac data fusion. Medical Image Analysis 7, 377–389 (2003)
17. Fung, Y.C.: A first course in continuum mechanics. Prentice-Hall, Englewood Cliffs (1969)

Computer Aided Reconstruction and Motion Analysis of 3D Mitral Annulus

Zhu Lei[1], Yang Xin[1], Yao Liping[2], and Sun Kun[2]

[1] Institute of Image Processing and Pattern Recognition, Shanghai Jiao Tong University, Shanghai 200240, P.R. China
{july,yangxin}@sjtu.edu.cn
[2] Shanghai Children's Medical Center, Attached to Shanghai Jiao Tong University, Shanghai 200092, P.R. China
itaa2004@sina.com, sunkun@hotmail.com

Abstract. A computer aided reconstruction and motion analysis method of mitral annulus is presented in this paper. To begin with, the boundary points on mitral annulus are marked by doctors interactively. Since these points are not distributed uniformly and sequentially, secondly, it is necessary to re-arrange these points into a set of series points on a contour, the saddle-shaped mitral annulus. Thirdly, in order to analyze 3D mitral annulus motion, the mitral annulus is modeled by 3D non-uniform rational B-spline (NURBS). Fourthly, the dynamic parameters of the mitral annulus throughout the cardiac cycle are computed in a 3D Cartesian coordinate system. The experiments prove that the dynamic mitral annulus reconstruction and analysis program using computer aided method is provided a possible and convenient tool to diagnose and analyze the malfunction of mitral annulus.

Keywords: mitral annulus, reconstruction, analysis, dynamic model, echocardiography.

1 Introduction

Three-dimensional echocardiography offers a powerful tool for directly visualizing the spatial relation of cardiac structures. Although three-dimensional images easily demonstrate the configuration and dynamics of the entire mitral annulus during a cardiac cycle, it is difficult to recognize the non-planarity of the ring by original 3-dimensional imaging [1]. Therefore a 3D reconstruction system is required to extract and analyze mitral annulus from image data sets.

Extracting boundary points of mitral annulus in echocardiography images is a necessary first step to reconstruct mitral annulus. There are some extracting methods such as those based on snake model, geodesic active contour, the others based on prior knowledge [2, 3, 4]. Unfortunately, full-automated extracting the mitral annulus is a difficult task due to the poor spatial and contrast resolutions of 3D echo images [5]. In order to extract the mitral annulus reliably and correctly, interactive and computer aided method is adapted in our work.

F.B. Sachse and G. Seemann (Eds.): FIMH 2007, LNCS 4466, pp. 70–80, 2007.

Many researches presented the work on the dynamic behavior of mitral annulus. An early study performed by Ormiston et al. measured the cyclic changes in annular area and circumference throughout the cardiac cycle in eleven normal subjects [6]. Levine et al. addressed the three dimensional nature of mitral annulus structure and modeled as a hyperbolic, parabolic or saddle-shape [7]. In [8, 9], Powell et al reconstructed mitral annulus from 2D echocardiographic images and analyze the mitral valve. These studies provided the framework for three-dimensional analysis of annular geometry in clinical pathologies and the basis for understanding how annular geometry relates to normal physiological function. In [10-12], Kamp and Valocik defined three parameters to describe the size and motion of mitral annulus throughout the cardiac cycle, i.e. the distance between the highest and lowest points (distance D_{h-l}), the distance between two high points (distance D_{h-h}) and the distance between two low points (distance D_{l-l}) of saddle-shaped mitral annulus.

In this paper, a computer aided system which study the shape of the mitral annulus using 3D real time echocardiographic images is introduced. Three parameters suggested by Kamp and Valocik are measured in each frame during the cardiac cycle to examine the motion of mitral annulus.

2 Proposed Method

2.1 Extracting Mitral Annulus

In order to extract 3-dimensional curve of the mitral annulus, multiple long axis, cross-sectional views are shown sequentially and allow the doctor to mark the points interactively, denoted by P_i, on the mitral annulus. On the cross-sectional views, the boundary points of mitral annulus are easily recognized and traced for each frame (*See Figure 1*).

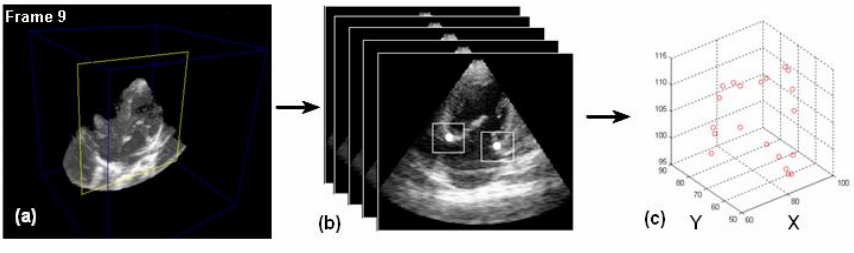

Fig. 1. Schematic diagram of extracted real time 3-dimensional reconstruction of the mitral annulus

In order to describe 3D mitral annulus, we establish a 3D Cartesian coordinate system, in which the XOY plane is superposed on level surface and Z axis is taken to direct for up. The points pointed by doctor are shown in this coordinate system in Figure 1(c).

In the process of extracting, the number of boundary points should be compromised to an appropriate value. Excessive points may increase the procedure complexity. On the contrary, few points could not describe shape of mitral annulus accurately. Therefore, 20 pointes on mitral annulus are marked for each frame in our work.

Although the point P_i on the annulus is obtained, these marked points are not distributed uniformly and sequentially to reconstruct close contour of mitral annulus. Therefore a sort step is needed to re-arrange these points as an ordered chain. Figure 2(a) illustrated the 20 ordered points on mitral annulus in the 3D Cartesian coordinate system.

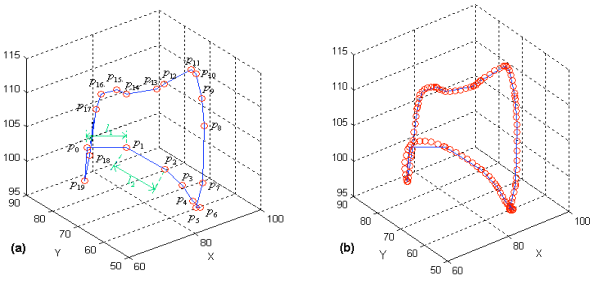

Fig. 2. Curve reconstruction using the Non-uniform rational B-spline algorithm

2.2 Curve Reconstruction

After the marked points are sorted as a sequential chain, a mathematical method for producing a closed three dimensional contour is needed to best represent 3D mitral annulus. As the non-uniform rational B-spline (NURBS) is flexible and smooth enough to depict a closed contour [13], we select it as our curve algorithm. Notice that each control point is very close to the neighboring points on the mitral annulus contour depicted by NURBS, we do not distinguish the control points and the points on the mitral annulus contour. The NURBS is defined as

$$C(u) = \frac{\sum_{i=0}^{N} w_i p_i n_{i,k}(u)}{\sum_{i=0}^{N} w_i n_{i,k}(u)} \tag{1}$$

where $p_i(x_i, y_i, z_i)$, $(i = 0,1,2,\ldots,N)$ is the control point, each of which is associated with a non-negative weight w_i (i.e., p_i has weight w_i >=0); N is number of control points, N=19 in Figure 2(a); $C(\mathrm{u})$ is the mitral annulus contour formed by NURBS, u is a parameter, and $n_{i,k}$ is basis functions of NURBS [13]. The basis functions $n_{i,k}$ for NURBS contour are polynomials of degree $(k-1)$, where parameter

k can be chosen to be any integer value in the range from 2 up to the number of control points, n+1. The functions $n_{i,k}$ are defined by the Cox recursion formulas [14]:

$$n_{i,1}(u) = \begin{cases} 1 & if\ u_i \le u \le u_{i+1} \\ 0 & otherwise \end{cases},$$
$$n_{i,k}(u) = \frac{u-u_i}{u_{i+k-1}-u_i} B_{i,k-1}(u) + \frac{u_{i+k}-u}{u_{i+k}-u_{i+1}} B_{i+1,k-1}(u) \quad u_k \le u \le u_{N+1} \tag{2}$$

where each basis function is defined over k subintervals of the total range of u. The selected set of subinterval endpoints u_i is referred to as a knot vector, and local control points for NURBS is achieved by defining the basis functions over subintervals of the total range of u. The parameter u is calculated by the Riesenfeld method while k is equal to 5 [15]:

$$u = \left\{u_0, u_1, \ldots u_m\right\} = \left\{ \underbrace{0,0,\ldots 0}_{k+1}, \underbrace{\frac{l_1+l_2+l_3}{L}, \frac{l_1+l_2+l_3+l_4}{L}, \ldots, \frac{\sum_{j=1}^{m-3} l_j}{L}}_{n-k}, \underbrace{1,1,\ldots,1}_{k+1} \right\} \tag{3}$$

where $l_i = \mid p_i - p_{i-1} \mid$, $m = n+k+2$, $L = \sum_{i=1}^{n} l_i, (i = 1,2,\ldots,N)$ (see *Figure 2*).

NURBS provides increased flexibility in controlling a curve shape. With unequally spaced intervals in the knot vector, we obtain different shape for the basis functions in different intervals, which can describe the deformation of the mitral annulus shapes.

2.3 Dynamics Parameters of Mitral Annulus

Kamp and Valocik [10, 11] investigated the geometric shape of the mitral annulus and the dynamic behavior of mitral annulus. They reported that the mitral annulus and leaflets are non-planar saddle-shaped structures which are similar to the so-called hyperbolic paraboloid (see *Figure3(a)*). There are two high points (peaks) lying anterior and posterior at the aortic insertion and posterior left ventricular wall and two low points (troughs) closest to the apex located medially and laterally (see *Figure 3(b)*).

In order to describe the non-planarity of the mitral annulus, some parameters can present motion of mitral annulus throughout the cardiac cycle, such as the distance between the highest and lowest points (distance D_{h-l}), the distance between two high points (distance D_{h-h}) and the distance between two low points (distance D_{l-l}) of the

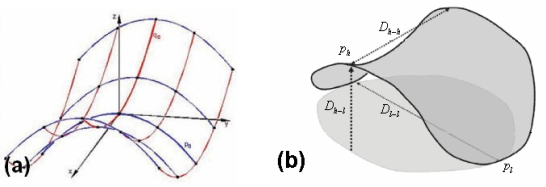

Fig. 3. Hyperbolic Parabolic, Schematic Representation of the Non-planar, Saddle-shaped Mitral Annulus and Its Characteristic Parameters [10]

saddle-shaped mitral annulus(see *Figure 3(b)*). If both the line passed through the two high points and the line passed through the two low points are vertical to the Z axis in 3D Cartesian coordinate system, the distance D_{h-l} can be computed as

$$D_{h-l} = | p_h - p_l | = Z_h - Z_l \tag{4}$$

where $p_h(x_h, y_h, z_h), z_h = \max(z_i)$, $p_l(x_l, y_l, z_l), z_l = \min(z_i)$; $(i = 0,1,2, \ldots, N)$.

2.4 Reference Plane

As the Z axis is not always vertical to the two lines, the distance D_{h-l} can not be obtained by the difference of Z value of the high point and the low point (see *Formula 4*). Therefore a new 3D Cartesian coordinate system has to be established in order to measure and analyze mitral annulus dynamics. Firstly, our solution is that a reference plane fit by least-squares to the reconstructed mitral annulus was derived. In the new 3D Cartesian coordinate system, the Z axis is corresponding to the normal vector of the reference plane, the Y axis corresponding to the posterior and anterior walls, and the X-axis corresponding to the septal and lateral walls. Appendix A gives the details of how to compute the reference plane using reconstructed mitral annulus in new 3D Cartesian coordinate system. Once we obtained the plane equation, we can compute the distances by calculating the perpendicular distance from each point to the reference plane.

2.5 Computation Parameters of Mitral Annulus

In order to obtain dynamics parameter D_{h-l}, firstly we compute the projection of the mitral annulus onto the reference plane. We draw beam which pass through those marked points on the mitral annulus and is vertical to the reference plane. The intersection points of the beam and the reference plane are projection of those points onto the reference plane, such as q_h is the projection of p_h, and q_l is the projection of p_l onto the reference plane. Fig. 4 below illustrates the geometry involved:

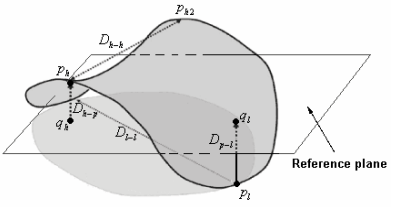

Fig. 4. Computation parameters of Mitral Annulus

The point which located at the front side of the reference plane and had the longest distance to the plane is the highest point p_h on the mitral annulus, and the distance between p_h and q_h is D_{h-p}. At the same time, the lowest point which located at the back side of the reference plane and had the longest distance to the reference plane is p_l, and its distance between p_l and q_l is D_{p-l}. Then we can get D_{h-l} with the following formula:

$$D_{h-l} = D_{h-p} + D_{p-l} \tag{5}$$

Through finding the distance from all of points to the reference plane, we can obtain the another high point p_{h2} and the other low point p_{l2} above and below the reference plane besides the above two points p_h and p_l respectively *(see Figure4).* Then the other two mitral annulus parameters can be obtained by the following formulas:

$$D_{h-h} = | p_h - p_{h2} | \tag{6}$$

$$D_{l-l} = | p_l - p_{l2} | . \tag{7}$$

3 Experiments and Results

3.1 Study Population

The study enrolled 15 normal healthy volunteers (Group N, 8 men, 7 women, mean age 1 year ± 5 months), and 12 patients with severe MR (Group S, 11 men, 1 women, mean age 1.5 year ± 3 months). All participants underwent real time three-dimensional echocardiography and gave informed consent to the study, which was approved by the Committee for the Protection of Human Subjects in Research at Shanghai Children's Medical Center.

3.2 Data Acquisition

The system consisted of a 2-MHz matrix array probe (Hewlett-Packard Co.) and an echocardiography imaging system (Hewlett-Packard SONOS 7500). These were

linked to a 3D reconstruction system with self-designed three-dimensional dynamics measure and analyses software and enable doctors to “en-face” visualize the mitral annulus’s movement throughout a cardiac cycle.

The 3D echocardiography images were recorded at 10 to 18 frames per cardiac cycle. Then the digital images were stored into the memory, and formatted into a cubic data set (208*160*144). Extracted 3D shapes of mitral annulus were obtained for all study normal children and patients. Acquisition time was within 5 minutes in one case. The time needed to reconstruct and analyze extracted 3D mitral valves was 15 minutes.

3.3 Dynamics of Mitral Annulus

The distance of D_{h-l}, D_{h-h} and D_{l-l} of mitral annulus throughout the cardiac cycle are measured. From Fig. 5, the distance of the highest point and the lowest point of mitral annulus is little smaller in the group of severe MR than the normal subject. However, the distance between two high points and the distance between two low points of mitral annulus in patients group are much greater than that in healthy children (*See Fig 6*).

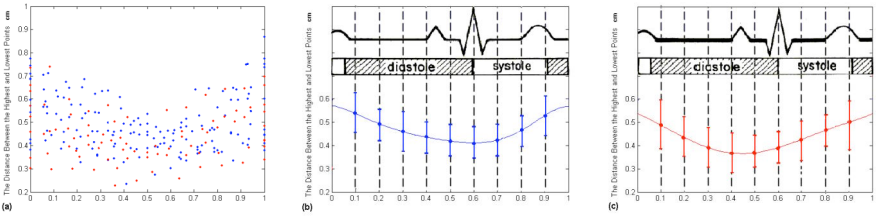

Fig. 5. The changes in the distance between the highest and lowest points on the mitral annulus during the cardiac cycle in 15 normal subjects (b) and 12 MR patients(c)

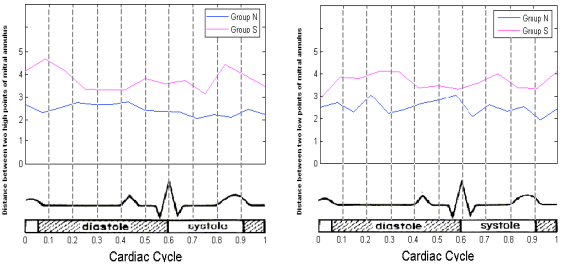

Fig. 6. Dynamic Distance between two high points and the distance between two low points of the Mitral Annuls throughout the Cardiac Cycle

4 Discussion

A computer- aided method of reconstructing and analyzing for mitral annulus using real time three-dimensional echocardiography has been presented. Using our self-designed

software system, we successfully demonstrated the shape of mitral annulus and quantified its deformation directly from the 3D data set. The results of dynamic motion of mitral annulus throughout the cardiac cycle are presented in Fig.7. By using extracted 3D data, we obtained similar configuration results of the mitral annulus, which have been previously reported [7,10,11].

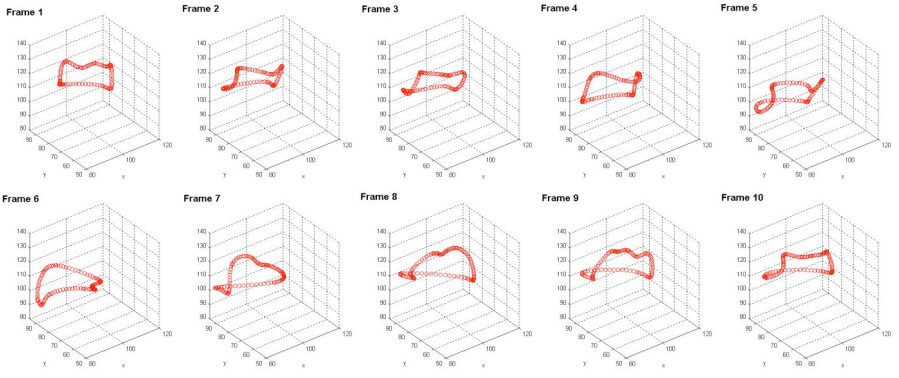

Fig. 7. Dynamics of the Mitral Annuls throughout the Cardiac Cycle

The presented technique is less time consuming compared with the previously reported method. Furthermore, extracted 3D images visualize the mitral annulus as though removed from whole image. The non-planarity of the annulus is verified by direct visualization of the annulus in three dimensional Cartesian coordinate system from different angels of view (*See Figure 8*).

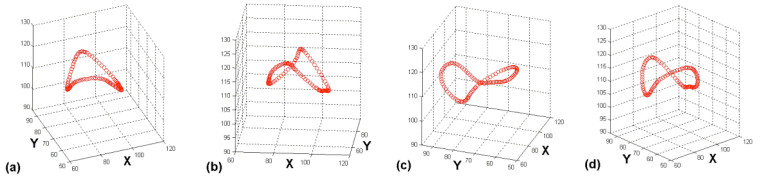

Fig. 8. Visualization of Mitral Annulus from Different Angles of View

Although the non-planarity shape observed in the group of severe MR was consistent with what is observed in normal children, there are some differences in motion parameters between two groups. The distance of the highest point and the lowest point of mitral annulus is smaller in the group of severe MR than the normal subject. Compared with the normal children, The distance of two highest points and the distance of two lowest points of the annulus are significantly larger in the severe MR group Therefore mitral annulus is dilated and flattened in the group of severe MR. 3D echocardiography is a promising technique that can provide precise 3-D geometry, which is difficult to understand by conventional 2-D echocardiography.

As the software system used in the presented study requires identification of mitral annulus for the manual tracing, further investigations using 3D extracting algorithm in 3D echocardiography image would be needed. he reference plane fit by least-squares algorithm provides a means for tracking annular non-planarity and computing motion parameters throughout a cardiac cycle. However better estimates of annular non-planarity can be achieved by fitting a hyperbolic parabolic to the surface of the leaflets which requires 3-D reconstruction of the leaflet surface which is proposed by Watanabe in [16]. An automated method for obtaining the outlines of the surface of the leaflets is currently under investigation.

5 Conclusions

This study demonstrates that extracted 3-dimensional data of mitral annulus by real time three-dimensional echocardiography providing a realistic visualization of the 3-dimensional annulus configuration. This technique is feasible in the evaluation of non-planarity and distance change between the highest and lowest points (D_{h-l}), the distance between two high points (D_{h-h}) and the distance between two low points (D_{l-l}) of mitral annulus in normal and patients with MR. The results show that computer aided reconstruction, measurement and analyze are feasible in the evaluation of configuration and dynamics of the mitral annulus.

Acknowledgements

This paper has been partially supported by China Natural Science Foundation (60572154) and National Basic Research Program of China (2003CB716104).

References

1. Jorapur, V., Voudouris, A., Lucariello, R.J.: Quantification of Annulus Dilatation and Papillary Muscle Separation in Mitral regurgitation: Role of Anterior Mitral Leaflet Length as Reference. Echocardiography-Journal Cardiovascular Ultrasound & Allied Techniques 22(6), 465–472 (2005)
2. Yamaura, Y., Yoshida, K., Hozumi, T., Akasaka, T., Morioka, S., Yoshikawa, J.: Evaluation of the mitral annulus by extracted three-dimensional images in patients with an annuloplasty annulus. The American journal of cardiology 82, 534–536 (1998)
3. Roelandt, J.R.T.C., Ten Cate, F.J., Vletter, W.B., Taams, M.A., Bekkeannulus, L., Glastra, H., Djoa, K.K., Weber, F.: Ultrasonic dynamic 3-dimensional visualization of the heart with a multi-plane transesophageal imaging transducer. J. Am. Soc. Echocardiogr. 7, 217–229 (1994)
4. Handschumacher, M.D., Sanfilippo, A.J., Weyman, A.E., Levine, R.A.: Dynamic 3D reconstruction of the normal human mitral valve from 2Dechocardiographic scans, Computers in Cardiology 1990. In: Proceeding, pp. 385–388 (23–26 September 1990)
5. Sheng, C., Xin, Y., Liping, Y., Kun, S.: Segmentation in Echocardiographic Sequences using Shape-based Snake Model Combined with Generalized Hough Transformation; vol. 22(1), pp. 33–45 (February 2006)

6. Ormiston, J.A., Shah, P.M., Tei, C., Wong, M.: Size and motion of the mitral annulus in man: I. A two-dimensional echocardiographic method and findings in normal subjects. Circulation, pp. 113–120 (1981)
7. Levine, R.A., Triulzi, M.O., Harrigan, P., Weyman, A.E.: The relationship of mitral annular shape to the diagnosis of mitral valve prolapse. Circulation 75, 756–767 (1987)
8. Powell, K.A., Rodrigruez, L., Patwari, P., et al.: 3-D Reconstruction of Mitral Annulus from 2-D Transesophageal Echocardiographic Images. Computers in Cardiology, p. 353–356 (25–28 September 1994)
9. Valocik, G., Kamp, O., Visser, C.A.: Three-dimensional echocardiography in mitral valve disease. Eur. J. Echocardiogr. 6(6), 443–454 (2005)
10. Levine, R.A., Robert, A., Marco, O., et al.: The relationship of mitral annular shape to the diagnosis of the mitral valve prolapse. Circulation, pp. 751–756 (1987)
11. Tsakiris, A.G., von Bernuth, G., Rastelli, G.C., Bourgeois, M.J., Titus, J.L., Wood, E.H.: Size and motion of the mitral annulus in anesthetized intact dogs. J. Appl. Physiol. pp. 611–618 (1971)
12. Levine, R.A., Handschumacher, M.D., Sanfilippo, A.J., Hagege, A.A., Harrigan, P., Marshall, J.E., Weyman, A.E.: Three-dimensional echocardiographic reconstruction of the mitral valve, with implications for the diagnosis of mitral valve prolapse. Circulation 80, 589–598 (1989)
13. Computer graphics, Sun JiaGuang, pp. 318–320. Tsinghua Press (1998)
14. Burger, P., Gillies, D.: Interactive computer graphics (1989)
15. Riesenfeld, R.F.: Non-unifrom B-spline curves, 2nd USA-JAPAN Conference proc. 1775, pp. 551–555
16. Nozomi, W., Yasuo, O., Yasuko, Y., Nozomi, W.: Mitral annulus flattens in ischemic mitral regurgitation: Geometric differences between inferior and anterior myocardial infarction: A real-time 3-dimensional echocardiographic study. Circulation 112, 458–462 (2005)

Appendix: Compute Reference Plane

Suppose the equation of the reference plane is:

$$f(x, y, z) = z - Ax - By - C = 0 . \tag{8}$$

The normal vector equation is

$$n = \begin{pmatrix} -A \\ -B \\ 1 \end{pmatrix}, \qquad \text{or } (x, y, z) \cdot n = C .$$

The distance d_i for characteristic point (x_i, y_i, z_i) on the annulus to the reference plan is

$$d_i = \frac{(z_i - Ax_i - By_i - C)}{\sqrt{A^2 + B^2 + 1}} \quad 0 \le i \le N \cdot \tag{9}$$

This distance is either positive or negative, depending on which side of the plane the point is located, front side or back side of the reference plane. If the point is on the plane, then $d_i = 0$. The least squares solution minimizes the expression

$$g(A,B,C) = \sum_{i=1}^{N} d_i = \frac{\sum_{i=1}^{N} (z_i - Ax_i - By_i - C)^2}{A^2 + B^2 + 1} \tag{10}$$

while $g(A,B,C)$ meet with

$$\begin{cases} \dfrac{\partial g(A,B,C)}{\partial A} = 0 \\ \dfrac{\partial g(A,B,C)}{\partial B} = 0 \\ \dfrac{\partial g(A,B,C)}{\partial C} = 0 \end{cases} \tag{11}$$

$$\Rightarrow \begin{cases} (A^2 + B^2 + 1)\sum (z_i - Ax_i - By_i - C)\cdot x_i = -A\sum (z_i - Ax_i - By_i - C)^2 \\ (A^2 + B^2 + 1)\sum (z_i - Ax_i - By_i - C)\cdot y_i = -B\sum (z_i - Ax_i - By_i - C)^2 \\ \sum (z_i - Ax_i - By_i - C) = 0 \end{cases}.$$

From the equation (8), it can be get the A, B, and C are

$$A = \frac{\left[\begin{array}{l} \sum y^2 (N\sum xz - \sum x\sum z) - (\sum y)^2 \sum xz - \\ N\sum xy\sum yz + \sum y(\sum xy\sum z + \sum x\sum yz) \end{array}\right]}{2\sum xy\sum x\sum y - N(\sum xy)^2 - (\sum x)^2\sum y^2 + \sum x^2 (N\sum y^2 + (\sum y)^2)}, \tag{12}$$

$$B = \frac{\left[N\sum yz - \sum y\sum z + A(\sum x\sum y - N\sum xy)\right]}{N\sum y^2 - (\sum y)^2}, \tag{13}$$

$$C = \frac{\left[\sum z - A\sum x - B\sum y\right]}{N}. \tag{14}$$

where N is the number of pointed points on the mitral annulus.

Volumetric Analysis of the Heart Using Echocardiography

Sándor M. Szilágyi[1], László Szilágyi[1,2], and Zoltán Benyó[2]

[1] Sapientia - Hungarian Science University of Transylvania,
Faculty of Technical and Human Science, Târgu-Mureş, Romania
szs@ms.sapientia.ro
[2] Budapest University of Technology and Economics,
Dept. of Control Engineering and Information Technology, Budapest, Hungary

Abstract. This paper presents a volumetric cardiac analysis and movement reconstruction algorithm from echocardiographic image sequences and electrocardiography (ECG) records. The method consists of two-dimensional (2-D) echocardiogram transformation, shape detection, heart wall movement identification, volumetric analysis and 4-D model construction. Although the semi-periodic behavior of the ECG and the breath caused heart rate variance disturbs spatial and temporal reconstruction, the presented algorithm is able to overcome these problems in most cases for normal and ventricular beats. The obtained model provides a tool to investigate volumetric variance of the heart and the phenomenon of normal and abnormal heart beating that makes possible to explore continuously the heart's inner structure.

Keywords: echocardiography, sequence analysis, QRS clustering, volumetric analysis, 3-D active appearance model.

1 Introduction

The most important health problem affecting large groups of people is related to the malfunction of the heart, usually manifested as heart attack, rhythm disturbances and pathological degenerations. One of the main goals of health study is to predict and avoid these kinds of tragic events, by identifying the most endangered patients and applying a preventing therapy.

Echocardiography is the fastest, least expensive and least invasive heart imaging method. Accordingly, it is one of the most commonly used techniques to quantify the ventricular systolic function in patients. The examination is based on visual analysis of myocardial wall motion and deformation by an experienced and trained physiologist. This investigation is subjective, experience dependent and the obtained results are only partially quantitative. The segmentation of the measured image sequences focuses on finding the exact boundaries of particular objects of interest, but it usually requires manual assistance.

F.B. Sachse and G. Seemann (Eds.): FIMH 2007, LNCS 4466, pp. 81–90, 2007.

Besides their several advantages, ultrasound images have the following drawbacks:

- They include not only the reflections from tissue transitions, but also several interference patterns (speckle noise). Consequently, tissues can hardly be distinguished by the intensity of their representing pixels.
- Image data highly depend on the position and angle of incidence of the ultrasound beam.
- A wide scale of imaging artifacts are frequently present, so still-frame images might contain only partial information.

In order to deal with these kinds of deficiencies, several automated segmentation techniques have been developed and reported. Geiser et al. [12] proposed arc filtering for boundary detection, while Brotherton et al. [6] gave a hierarchical fuzzy neural network solution. Dias and Leitão [9] introduced an iterative multigrid dynamic programming technique based on Rayleigh distributed random variables and a probabilistic model formulated within Bayesian framework. Belohlavek et al. [2] proposed the automated segmentation using a modified self-organizing map. Chalana et al. [7] traced the epi- and endocardial border using active contour models. In spite of their significant merits, these methods still neglect the following aspects:

- Sought boundaries are not always represented by the strongest edges.
- They use no a priori information concerning the allowable shapes and ranges of the segmented object.
- Segmented boundaries should be consistent with the cardiac cycle.

In the last decade, advances have been made in the content-based retrieval of medical images, such as extraction of boundaries of cardiac objects from echocardiography image sequences [10]. Montagnat et al. [20] used a two-simplex mesh-based cylindrical deformable surface to produce time-continuous segmentation of 3-D sequences. Angelini et al. [1] proposed a feature enhancement and noise suppression using a wavelet-like decomposition of the spatial frequency domain. A snake-based segmentation is carried out later on the denoised data.

Active appearance models (AAM), introduced by Cootes et al. [8], are promising image segmentation tools that may provide solutions to most pending problems of echocardiography, as they rely on both shape and appearance (intensity and/or texture) information. Bosch et al. proposed a robust and time-continuous delineation of 2-D endocardial contours along a full cardiac cycle, using an extended AAM, trained on phase-normalized four-chamber sequences.

To understand the physiology and patho-physiology of the heart, not only the electrical activity and spatial distribution of its structures is important, but also their movement during normal and abnormal cardiac cycles. The ECG signal is measured simultaneously with echocardiography sequence recording, in order to localize the investigated events. We developed an algorithm that reconstructs the heart wall boundaries and motion in order to determine the spatial and temporal cardiac activity.

Several papers in the literature have already reported the usage of spatial AAM [19,21]. The present work has the following contributions:

- Reported techniques classify ultrasound images only as belonging to systolic or diastolic interval. Our approach distinguishes normal and extra beats, and processes the corresponding images accordingly.
- ECG event classification makes possible the investigation of several pathological cases (e.g. volumetric effect of a given extra beat). Comparisons were made between normal and pathological cardiac cycles of the same patient.

2 Methods

Simultaneous echocardiography sequence recording and ECG signal measurement were carried out at the County Medical Clinic of Târgu-Mureş, using a 2-D echocardiograph that produces 30 frames per second, and a 12-lead ECG monitoring system that samples at 500 Hz frequency and 12-bit resolution. Each image frame received a time stamp, which served for synchronization with ECG events.

Two different series of measurements were recorded. The first series, which served for AAM training, consisted of 35 patients (12 of whom having extraventricular beats), 20 ultrasound sequences for each patient, of 10-15 seconds length each sequence, with previously established transducer placements. Based on these data, an a priori information database was created, which organized the ultrasound images grouped by corresponding ECG events.

The second series of measurements, which involved 4 patients, consisted of two stages. In the first stage, the same measurements were performed, as in the first series, in order to provide patient-specific training data for the AAM. In the second stage, several measurements were performed using different placements and positions of the transducer. In this order, image sequences were recorded at 17 parallel cross sections in horizontal and rotated (45° to the left and to the right) positions (see Fig. 1(a), (b), (c)), with a 1 cm inter-slice distance. We used 30 common axis planes that were placed at front, lateral and back side of the torso, as presented in Fig. 1(d), (e). For each patient a total number of $30 \times 17 \times 3 = 1530$, at least 2-3 second long image sequences were created.

The necessary minimal duration of the recorded image sequences was restricted by the semi-periodic behavior of the ECG signal. The spatial movement of the heart is constrained by the course of the depolarization-repolarization cycle [23]. For example, normal and ectopic beats imply different spatial heart movements. The studied ECG parameters, as presented in Fig. 2, were: shape of QRS beat, QT and RR distances. These parameters characterize the nature of a QRS complex, and were determined as presented in [22]. ECG event clustering was accomplished using Hermite functions and self-organizing maps [15,23]. Two main event clusters were created: normal and ventricular extra beats. This latter group, because of the patient specific manifestation of ventricular extras, had to be dealt with separately patient by patient. QRS beats not belonging to any of these clusters were excluded from further processing, together with their

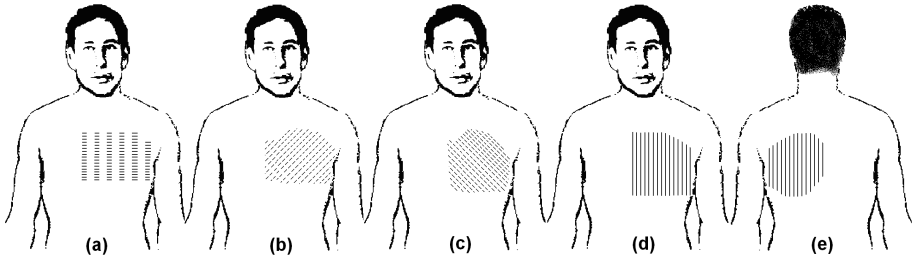

Fig. 1. Various positions of the parallel cross sections and the orientation of the transducer: (a) horizontal plane(s), (b) left rotated plane(s), (c) right rotated plane(s). Various positions of planes with common axis: (d) front view, (e) back view.

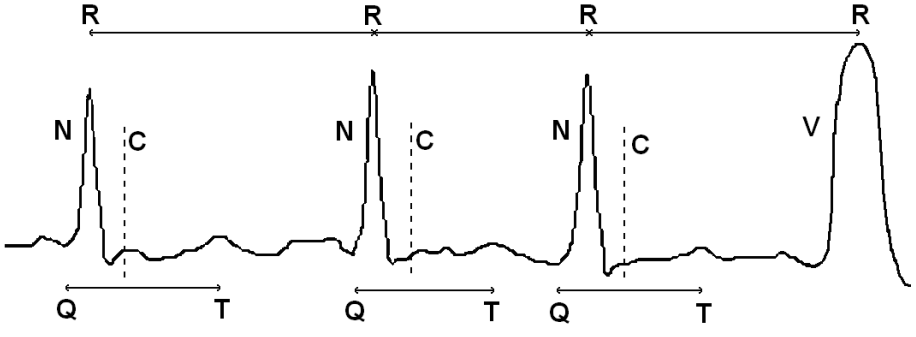

Fig. 2. Normal (N) QRS and extra ventricular QRS beat (V), with indicated RR and QT distances. Dotted lines denoted by C (maximal contraction) represent the minimal volume moment of heart during normal cardiac cycle.

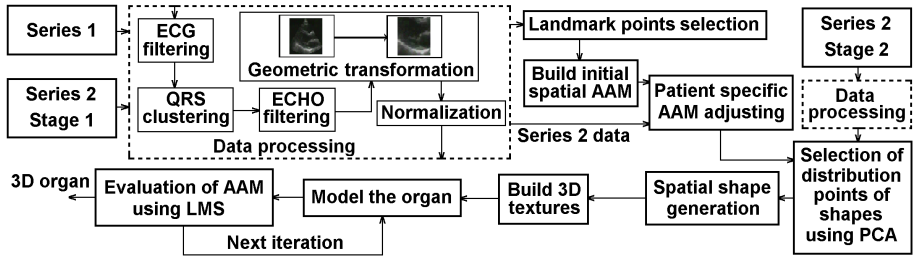

Fig. 3. Schematic representation of the data recording and analyzing procedure. All echocardiography and ECG data go through the same processing module. The AAM is constructed from the measurements of series 1, and fine tuned afterward using the patient specific data resulting from series 2 stage 1. Stage 2 data serve for the detailed cardiac volumetric analysis. Reconstructed 3-D objects are finally aligned using an iterative LMS-based algorithm.

corresponding ultrasound sub-sequences. A further condition for normal QRS complexes to be included was having RR distance between 700-800 ms and QT distance between 350-400 ms.

The time-varying evolution of the cardiac volume is determined by the interconnection of electrical and mechanical phenomena. In a whole cardiac cycle there are two extremity values. The maximal volume can be coupled with the starting moment of ventricular contraction. The depolarization wave normally starts from the sino-atrial node (SA) and propagates through the atrioventricular node (AV) and ventricles. The moment of minimal volume shortly precedes the termination of ventricular contraction, but is much more difficult to identify, due to the dead time of a normal cardiac cell. This delay is caused by the strange property of a regular cardiac cell, whose electric response is most directly caused by the depolarization wave (fast Na^+ channels), but the mechanical contraction is controlled by the much slower Ca^{2+} channels. The calcium channel opens at 10-20 ms after depolarization, and the maximal contraction follows in about 80 ms [24]. Figure 2 indicates the moment of minimal volume with a dotted line. The combination of the electrical and mechanical properties of the heart and the usage of knowledge-base allowed us to create a performance evaluation module that iteratively determines the most probable wall position, as shown in Fig. 3.

Figure 3 presents an overview of the image processing and volumetric reconstruction procedure. The first algorithmic step is noise elimination. Speckle noise represents a major difficulty to most ultrasound imaging applications [9]. In our case, the suppression of such phenomena was accomplished using the well-known motion-adaptive spatial technique presented in [11].

Due to the measuring technique of traditional echocardiography, the obtained images are distorted. In order to become suitable input for 3-D processing, they need to go through a normalization transform. Every recorded ultrasound slice is represented by a plane, whose spatial alignment depends on the position and rotational angle of the transducer. The normalization process also takes into consideration the distance of each image pixel from the transducer.

The training data of the AAM is constructed based on the spatial position of each echocardiography slice recorded in the first measurement series, and on the positions of the heart wall pieces that correspond to the contours manually recognized by an expert. By averaging these spatial distributions, a mean base 4-D heart shape model is obtained, which will be the starting point of the AAM [5,16]. Landmark points are determined using the technique proposed by Mitchell et al. [19]. The sparse character of the obtained spatial description model doesn't allow the landmark points have 3-D texture information. That is why we restricted the texture to 2-D.

Subjects have their own specific, time dependent inner structure, which cannot be approximated properly from a population of few dozens of individuals. In order to make further adjustments to the AAM, the base structure was adjusted to the patient using the measurements made in the second series, first stage.

The landmark points determined on the images recorded during the second stage of the second measurement series allow us to create a 3-D distribution point model, which was established according to [4,19]. Having the distribution points established, the AAM will be enabled to adjust itself to a diversity of biological factors like the phase of ECG and breathing. A detailed description of the manifestation of these phenomena and the model adaptation is given in [21]. Our algorithm acts similarly, but it treats the cardiac cycle differently: not only systolic and diastolic phases are distinguished, but also a QRS complex clustering is performed to give different treatment to normal and ventricular cardiac cycles.

Spatial texture maps are determined via averaging [21]. The visual aspect of heart and its environment, because of their mutual motion, is changing in time. AAM models only include information on the texture situated within the model.

The time dependent representation of the ultrasound slices obtained from the large stack of sequences enabled us to accurately determine the 4-D structure of the heart [19]. The iterative algorithm of the AAM demands the comparison of measured and expected shapes. The AAM was adjusted using a quadratic cost function, until the desired accuracy was obtained [18].

3 Results

Figure 4(a) presents two series of ultrasound slices indicating the contour of the left ventricle of the 2nd patient, detected during a ventricular contraction. The two rows of slices show two different angle views, having 60 ° angle difference. The four slices in each row represent subsequent images of the sequence, showing the approximately 100 ms duration of the ventricular contraction. Figure 4(b) shows two different reconstructed 3-D shapes of the left ventricle, which were obtained using 1527 distribution points.

The evolution in time of the heart volume during a normal and an ectopic (ventricular extra) RR period is presented by Fig. 5(a) and (b). As the depolarization wave in case of an ectopic beat starts from the ventricular area, the minimal volume is obtained earlier (the delay caused by the AV-node is skipped), and at a higher value compared to normal beats (the contraction of the heart is not optimally synchronized). The first moment of LV volumetric calculation ($t = 0$ ms) was considered at the moment of maximal positive deflection of the ECG signal.

Figure 6 presents a sensibility analysis of the QRS recognition algorithm. Figure 6(a) shows how the variation of the RR distances (shorter or longer than average) influences the recognition rate: the algorithm is more sensible for shorter RR periods. The effect of the variation of QT distances around the average value is shown in Fig. 6(b): the same absolute difference makes significantly more damage if it occurs in positive direction. Figure 6(c) reflects the relation between the shape of QRS complexes and recognition performance. The correlation coefficient of the QRS beat with the cluster averaged shape is directly proportional with the performance of the algorithm.

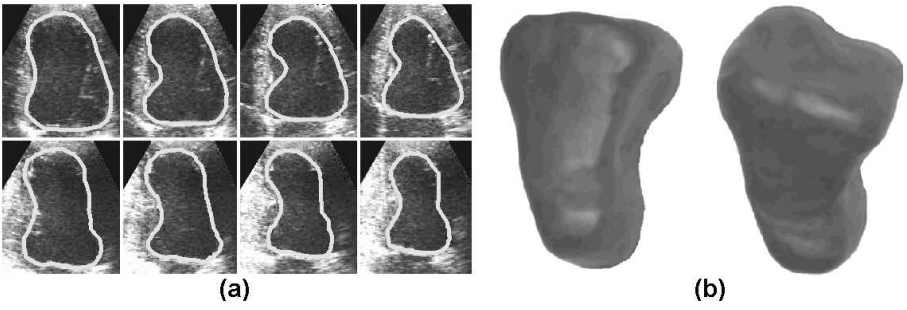

Fig. 4. Results of shape reconstruction: (a) time varying 2-D contour of the left ventricle (2nd patient), (b) reconstructed 3-D structure of the left ventricle

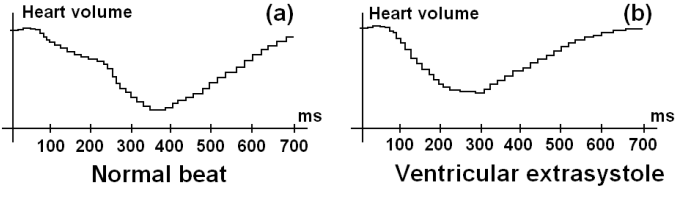

Fig. 5. Variation of heart volume during a normal cardiac cycle (a), and during a ventricular extra cycle (b)

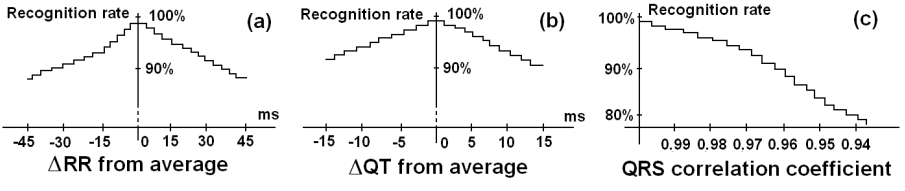

Fig. 6. Sensibility of QRS complex recognition algorithm to: (a) variations of RR distances, (b) variations of QT distances (both with respect to their average), (c) QRS shape correlation with average template

Table 1 presents the patient-dependent recognition rates for normal beats (average duration 707 ms) and ventricular beats (average duration 671 ms). The measurements were effectuated on four patients, and three of them produced ventricular extra-systolic beats.

The measurement circumstances were selected optimal (average QRS wave shape, average RR and QT distances) for performance values presented in Table 1. As this table reflects, the fourth patient did not produce any ventricular beats. We can observe a pronounced performance advantage of the algorithm for normal beats due its higher incidence.

Table 1. Patient-dependent recognition rate of various QRS beats in case of optimal circumstances (average QRS shape, average RR and QT distances)

Patient	Normal QRS beat	Ventricular extra-systole
1st patient	99.2 %	97.6 %
2nd patient	99.4 %	92.4 %
3rd patient	98.4 %	95.2 %
4th patient	98.6 %	No available data

4 Discussion

The recognition of the relation between echocardiography images and simultaneously recorded ECG signal is a key element in wall movement detection. Various events, such as aspiration and expiration influence the measured heart rate. During a whole cardiac cycle, the shape and volume of the left ventricle changes considerably.

It is difficult to determine the performance of the reconstruction method for the sporadically occurred ventricular extra-systolic beats. Even for patients that produce at least five extra beats with similar shapes in each minute, that are included in the same cluster, the reconstruction performance remains well below the normal QRS cluster's accuracy, due to the sparse distribution of the processable slices.

The visual aspect of the heart and its environment varies in time, due to their mutual motion. AAM models include information concerning inner texture only. It would be beneficial to build another AAM for the modeling of the environment, but the invisibility of the pericardium and lung tissues represents an enormous obstacle.

As we know, the left ventricular (LV) hypertrophy has been identified as a strong and independent predictor of various adverse cardiac events even in patients without associated cardiovascular disease [3]. This important clinical parameter has been subject to extensive scientific investigation [13]. The conventional 2-D echocardiography is the most commonly used imaging modality that supports LV wall mass determination. However, this method is based on geometric assumptions that do not include some possible abnormal ventricular shapes and variability in the distribution of LV mass, that hardens the development of an accurate, easily reproducible method for the quantification of ventricular mass.

Evaluation of intra-cardiac anatomy from two dimensional echocardiography image sequences requires a mental conceptualization process that is hardened by cardiac dynamics [17]. The dynamic modeling and visualization systems can help with the spatial interpretation of 3-D data of the heart, and make it possible to build the 3-D model of the heart [14].

This study is an attempt to evaluate, whether a virtual modeling and visualizing method is feasible for echocardiography, and if ultrasound images in a virtual reality can advance to a clinically useful tool in the technological process of the

future. Unfortunately the low number of patients and the long processing time reflect that the applicability and benefits of the presented volumetric analyzer and heart modeling method in clinical practice is still limited.

The spatial texture around voxels belonging to a dynamic organ suffers a deformation during contraction. Under such circumstances a compensation mechanism would be necessary, which is situated beyond the scope of the present paper.

5 Conclusions

The investigation of simultaneously recorded ECG and echocardiography images enables us to study the relations between the electrical and mechanical phenomena concerning the heart. The method presented in this paper performs correctly in case of normal and ventricular beats, that is, we can monitor the volumetric variance of the heart and its main components. This kind of approach of the problem may result in deeper understanding of several pathological cases like:

- effects of ectopic beats on the heart's pumping activity;
- risk of development of arrhythmias and fibrillation in case of pathological LV wall thickening;
- mechanical effects of Wolff - Parkinson - White syndrome.

Acknowledgements. This research was supported in part by the Sapientia Institute for Research Programmes, Domus Hungarica Scientiarium et Artium, and the Communitas Foundation.

References

1. Angelini, E.D., Laine, A.F., Takuma, S., Holmes, J.W., Homma, S.: LV volume quantification via spatiotemporal analysis of real-time 3-D echocardiography. IEEE Trans. Med. Imag. 20, 457–469 (2001)
2. Belohlavek, M., Manduca, A., Behrenbeck, T., Seward, J., Greenleaf, J.F.: Image analysis using modified self-organizing maps: automated delineation of the left ventricular cavity in serial echocardiograms. In: Proc. Visual. Biomed. Comp. Conf. pp. 247–252 (1996)
3. Benjamin, E.J., Levy, D.: Why is left ventricular hypertrophy so predictive of morbidity and mortality? Am. J. Med. Sci. 317, 168–175 (1999)
4. Besl, P.J., McKay, N.D.: A method for registration of 3-D shapes. IEEE Trans. Patt. Anal. Mach. Intell. 14, 239–256 (1992)
5. Bosch, J.G., Mitchell, S.C., Lelieveldt, B.P.F., Nijland, F., Kamp, O., Sonka, M., Reiber, J.H.C.: Automatic segmentation of echocardiographic sequences by active appearance motion models. IEEE Trans. Med. Imag. 21, 1374–1383 (2002)
6. Brotherton, T., Pollard, T., Simpson, P., DeMaria, A.: Echocardiogram structure and tissue classification using hierarchical fuzzy neural networks. In: Proc. IEEE Conf. Acoustics Speech Sign. Proc. 2, pp. 573–576 (1994)

7. Chalana, V., Linker, D.T., Haynor, D.R., Kim, Y.: A multiple active contour model for cardiac boundary detection on echocardiographic sequences. IEEE Trans. Med. Imag. 15, 290–298 (1996)
8. Cootes, T.F., Edwards, G.J., Taylor, C.J: Active appearance models. IEEE Trans. Patt. Anal. Mach. Intell 23, 681–685 (2001)
9. Dias, J.M.B., Leitão, J.M.N.: Wall position and thickness estimation from sequences of echocardiographic images. IEEE Trans. Med. Imag. 15, 25–38 (1996)
10. Duncan, J.S., Ayache, N.: Medical image analysis: progress over two decades and the challenges ahead. IEEE Trans. Patt. Anal. Mach. Intell. 22, 85–105 (2000)
11. Evans, A.N., Nixon, M.S.: Biased motion-adaptive temporal filtering for speckle reduction in echocardiography. IEEE Trans. Med. Imag. 15, 39–50 (1996)
12. Geiser, E.A., Wilson, D.C., Wang, D.X., Conetta, D.A., Murphy, J.D., Hutson, A.D: Autonomous epicardial and endocardial boundary detection in echocardiographic shor-axis images. J. Amer. Soc. Echocardiogr. 11, 338–348 (1998)
13. Haider, A.W., Larson, M.G., Benjamin, E.J., Levy, D.: Increased left ventricular mass and hypertrophy are associated with increased risk for sudden death. J. Am. Coll. Cardiol. 32, 1454–1459 (1998)
14. Issenberg, S.B., Gordon, M.S., Gordon, D.L., Safford, R.E., Hart, I.R.: Simulation and new learning technologies. Med. Teach 23, 16–23 (2001)
15. Lagerholm, M., Peterson, C., Braccini, G., Edenbrandt, L., Sörnmo, L.: Clustering ECG complexes using Hermite functions and self-organizing maps. IEEE Trans. Biomed. Eng. 47, 838–848 (2000)
16. Lelieveldt, B.P.F., van der Geest, R.J., Mitchell, S.C., Bosch, J.G., Sonka, M., Reiber, J.H.C.: 3-D active appearance models: fully automatic detection of endo- and epicardial contours in short-axis cardiac MR data. In: Proc. Int. Soc. Magn. Res. Med. (ISMRM) vol. 2 , p. 1668 (2002)
17. MacLeod, R.S., Brooks, D.H.: Recent progress in inverse problems in echocardiology. IEEE EMBS Mag. 17(5), 73–83 (1998)
18. Mitchell, S.C., Lelieveldt, B.P.F., Bosch, J.G., van der Geest, R.J., Reiber, J.H.C., Sonka, M.: Segmentation of cardiac MR volume data using 3D active appearance models. In: Proc. SPIE Med. Imag. pp. 433–443 (2002)
19. Mitchell, S.C., Bosch, J.G., Lelieveldt, B.P.F., van der Geest, R.J., Reiber, J.H.C., Sonka, M.: 3-D active appearance models: segmentation of cardiac MR and ultrasound images. IEEE Trans. Med. Imag. 21, 1167–1178 (2002)
20. Montagnat, J., Delingette, H., Malandain, G.: Cylindrical echocardiographic image segmentation based on 3-D deformable models. In: Taylor, C., Colchester, A. (eds.) Medical Image Computing and Computer-Assisted Intervention – MICCAI 1999. LNCS, vol. 1679, pp. 168–176. Springer, Heidelberg (1999)
21. Stegmann, M., Pedersen, D.: Bi-temporal 3D active appearance models with applications to unsupervised ejection fraction estimation, Progr. Biomed. Opt. Imag. Proc. SPIE 5746, pp. 336–350 (2005)
22. Szilágyi, S. M., Benyó, Z., Dávid, L.: Iterative ECG Filtering for Better Malfunction Recognition and Diagnosi. In: Proc. 5th Int. IFAC Symp. Modell. Contr. Biomed. Syst. pp. 295–300 (2003)
23. Szilágyi, S. M., Benyó, Z., Szilágyi, L.: Recognition of various events from 3-D heart model, 16th IFAC World Congr. Preprint, paper #4695, 1–6 (2005)
24. Winslow, R.L., Hinch, R., Greenstein, J.L.: Mechanisms and models of cardiac excitation-contraction coupling. In: Ganter, B., Mineau, G.W. (eds.) ICCS 2000. LNCS, vol. 1867, pp. 97–131. Springer, Heidelberg (2000)

Constrained Reconstruction of Sparse Cardiac MR DTI Data

Ganesh Adluru[1,3], Edward Hsu[2], and Edward V.R. Di Bella[2,3]

[1] Electrical and Computer Engineering department, 50 S. Central Campus Dr., MEB, University of Utah, Salt Lake City, UT, USA
gadluru@sci.utah.edu
[2] Department of Bioengineering, 50 S Central Campus Dr., University of Utah, Salt Lake City, UT, USA
edward.hsu@utah.edu
[3] UCAIR, Department of Radiology, 729 Arapeen Dr., University of Utah, Salt Lake City, UT, USA
ed@ucair.med.utah.edu

Abstract. Magnetic resonance diffusion tensor imaging (DTI) has emerged as a convenient and reliable alternative to conventional histology for characterizing the fiber structure of the myocardium. The acquisition of full data for different diffusion directions for a large number of slices often takes a long time and results in trade-offs in the number of slices and signal to noise ratios. We propose a constrained reconstruction technique based on a regularization framework to jointly reconstruct sparse sets of cardiac DTI data. Constraints on spatial variation and directional variation were used in the reconstruction. The method was tested on sparse data undersampled in both rectilinear and (simulated) radial fashions and compared to reconstructions from full data. The method provided reasonable reconstructions with half of the data for rectilinear undersampling and similar quality images with a quarter of the data if radial undersampling was used.

1 Introduction

The fiber structure of the myocardium plays a key role in determining the anisotropic mechanical and electrophysiological properties of the tissue. DTI has emerged as a convenient and reliable alternative to conventional histology for characterizing the fiber structure of the myocardium [1]. A limitation of current cardiac DTI is the long acquisition time, which often results in tradeoffs in the number of slices and signal to noise ratios. Methods [2, 3] have been proposed to reduce the acquisition time by acquiring sparse data in k-space for each orientation and reconstructing each image direction separately. The methods achieved accelerations up to a factor of two (R=2, using half of the data), but often require acquiring additional reference data. Also these methods do not exploit the correlations in the dimension of diffusion direction. Typically 6-12 or more diffusion directions are measured separately. We recently proposed a spatio-temporal constrained reconstruction framework to reconstruct sparse dynamic contrast enhanced MRI data. The method is based on regularizing the

F.B. Sachse and G. Seemann (Eds.): FIMH 2007, LNCS 4466, pp. 91–99, 2007.

data in both space and time dimensions and is applied to reconstructing dynamic cardiac perfusion images [4] from sparse data. A similar framework is proposed here to apply instead to space and diffusion dimensions to jointly reconstruct sparse cardiac DTI data for all directions at the same time with appropriate constraints.

2 Methods

2.1 Constrained Reconstruction

The most common technique to reconstruct cardiac MR DTI data is by applying an inverse 2D Fourier transform on fully acquired k-space data for each image. A separate image is acquired with gradients at different directions to give diffusion weighting at different orientations. At least six images, and a separate reference image without diffusion weighting, are obtained to determine the diffusion tensor and fiber orientations. When full data for each image direction are not acquired in k-space, reconstruction using the inverse Fourier transform leads to aliasing in the images. We have previously shown that the aliasing due to undersampling the data can be resolved using a regularization framework with different constraints [4, 5, 6]. For cardiac DTI, we chose two constraints, one in the dimension of diffusion weighting direction and the other, a spatial constraint. The constraint chosen in the dimension of diffusion direction is the total variation constraint. This constraint was chosen in order to preserve the sharp gradients in the diffusion-weighting direction dimension for each pixel in the image while resolving the artifacts due to undersampling. This constraint is mathematically represented in equation (1) below.

$$T = \sum_{i=1}^{N} \left\| \sqrt{\nabla_d \tilde{m}_i^2 + \beta^2} \right\|_1 \tag{1}$$

In the above equation, N is the total number of pixels in each image direction, ∇_d represents the rate of change in the diffusion weighting direction dimension, $\tilde{m}_i$ is the vector of complex pixel values in the diffusion weighting direction dimension of pixel i in the estimated image space data. β is a small positive constant and $\| \ \|_1$ represents the L1 norm.

The spatial constraint we chose is also a total variation constraint in order to preserve the spatial image gradients. The spatial constraint is shown below in equation (2).

$$S = \sum_{j=1}^{M} \left\| \sqrt{\nabla_x \tilde{m}_j^2 + \nabla_y \tilde{m}_j^2 + \beta^2} \right\|_1 \tag{2}$$

In the above equation, M represents total number of image directions in a given sequence for a single slice, ∇_x is the spatial gradient of the image in the x-direction, ∇_y is the spatial gradient in the y-direction and $\tilde{m}_j$ represents the complex image data for direction j in the given sequence.

Reconstruction from sparse data is performed using the constraints in equations (2) and (3) and preserving fidelity to the acquired sparse data. Reconstruction is performed by minimizing the cost function *C* given in equation (3) below.

$$\min_{\tilde{m}}(C) = \min_{\tilde{m}} \left[\begin{array}{l} \left\| WF\tilde{m} - \tilde{d} \right\|_2^2 + \alpha_1 \sum_{i=1}^{N} \left\| \sqrt{\nabla_d \tilde{m}_i^2 + \beta^2} \right\|_1 \\ + \alpha_2 \sum_{j=1}^{M} \left\| \sqrt{\nabla_x \tilde{m}_j^2 + \nabla_y \tilde{m}_j^2 + \beta^2} \right\|_1 \end{array} \right] \tag{3}$$

In the above equation (3), *W* represents the binary sparsifying pattern used to obtain sparse k-space data, $\tilde{d}$ which is from the full k-space data and $\| \ \|_2$ represents the L2 norm. α_1 and α_2 are the regularization parameters which are the weighting factors for the constraints. An iterative gradient descent technique with finite forward differences was used to minimize the above function. The complex image data was updated iteratively according to equation (4) shown below.

$$\tilde{m}^{n+1} = \tilde{m}^n - \lambda C'(\tilde{m}^n); \ n = 0, 1, 2... \tag{4}$$

In the above equation, *n* represents the iteration number, λ is the step size of the gradient descent method and $C'(\tilde{m})$ is the Euler-Lagrange derivative of the cost function, *C* in equation (3) with respect to $\tilde{m}$, which is given in equation (5) below.

$$C'(\tilde{m}) = \left\{ \begin{array}{l} 2 * (F^{-1}(WF\tilde{m}) - F^{-1}(\tilde{d})) - \alpha_1 \nabla_d \left(\dfrac{\nabla_d \tilde{m}}{\sqrt{\nabla_d \tilde{m}^2 + \beta^2}} \right) \\ -\alpha_2 \left(\begin{array}{l} \nabla_x \left(\dfrac{\nabla_x \tilde{m}}{\sqrt{\nabla_x \tilde{m}^2 + \nabla_y \tilde{m}^2 + \beta^2}} \right) \\ + \nabla_y \left(\dfrac{\nabla_y \tilde{m}}{\sqrt{\nabla_x \tilde{m}^2 + \nabla_y \tilde{m}^2 + \beta^2}} \right) \end{array} \right) \end{array} \right\} \tag{5}$$

2.2 Cardiac DTI Data

To test the above method, retrospective DTI experiments were simulated from datasets acquired in separate studies, including (a) diffusion-weighted spin-echo images (128 x 64 matrix size, 3.0 cm FOV, 2.0 mm thickness) encoded in 6 directions and 8 gradient levels per direction (48 images total) of excised dog heart right ventricular specimens at 7.1 T [2], and (b) diffusion-weighted images (256 x 256 matrix size, 10.0 cm FOV, 3.0 mm thickness) encoded in 12 directions of the left ventricle equatorial slice of intact sheep heart acquired at 2.0 T [3]. Two different undersampling schemes were used to generate sparse data from full k-space data. Fully acquired k-space data for each image direction was sparsified by removing phase encode lines in a variable density fashion in which 8 lines around the center of

k-space for each image direction were kept and the phase encodes away from the center were removed in a random fashion. Fig. 1a shows such an undersampling binary mask for a single image direction in the sequence. This sampling scheme was chosen as random undersampling can lead to less severe artifacts as compared to interleaved undersampling. The acceleration factor was defined as the ratio of the number of phase encodes acquired for full data to the number of phase encodes kept for the reconstruction. The second undersampling scheme was radial undersampling in which fully acquired rectilinear k-space data was first sampled on 256 radial lines to simulate radial data. Sparsification was done by removing the radial lines for each image direction. The set of radial spokes for each image direction were rotated by a random angle for different image directions in the sequence. Fig. 1b shows an example of a binary radial mask used to undersample full data in radial fashion. Acceleration factor was defined as the ratio of the number of radial lines in the full data (256) to the number of lines kept for reconstruction.

Fig. 1. (a) Image showing the binary mask for a single image direction to undersample full k-space data in variable density fashion by a factor of two. Six lines around the center of k-space are sampled and the lines outside are sampled in a random fashion. The white portion represents the region of k-space sampled. The phase encoding direction is horizontal. **(b)** Image showing the binary mask for a single image direction to undersample full data in radial fashion. White portion is the region of k-space sampled.

3 Results

3.1 Rectilinear Undersampling – Canine Heart Specimen

The results of the above approach for variable density undersampling by a factor of R=2 are shown in Fig. 2. Fig. 2a shows an image direction for a direction reconstructed from full k-space data using 2D inverse Fourier transform (IFT) with a line passing through it. Fig. 2b shows the corresponding image direction from sparse data using the constrained reconstruction method. Fig. 2c compares the corresponding signal intensity profiles for the images in Fig. 2a and Fig. 2b for the line shown in Fig. 2a.

Three sets of diffusion tensors were computed using (i) reconstructions from full data, (ii) reconstructions from sparse data using constrained approach and (iii) using

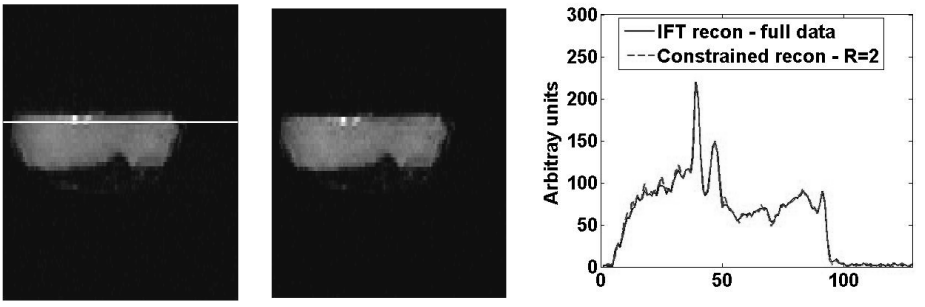

(a) (b) (c)

Fig. 2. (a) Image from the canine ex vivo heart specimen showing one diffusion encoded direction reconstructed from full data using IFT. A line passing through the image is also shown. **(b)** Corresponding image reconstructed from sparse data R=2 using the constrained reconstruction approach. **(c)** Comparison of the intensity profiles for the line shown in Fig. 2a for the images in Fig. 2a and Fig. 2b.

only half the number of image directions in the full dataset, for different datasets for different slices. The difference angles between the primary diffusion tensor eigenvectors (fiber orientations) were then computed. Fig. 3 shows the results on a single dataset, which shows the potential of the constrained approach. Fig. 3a shows the difference angle map between full data reconstructions and sparse data reconstructions. Fig. 3b shows the difference angle map between full data and using only half data. The mean deviation angle for the full-sparse is 8.84 ± 0.03 degrees while the value for full-half is 10.44 ± 0.03 degrees. This implies that the sparse data reconstruction using the constrained approach is better at capturing DTI fiber orientation.

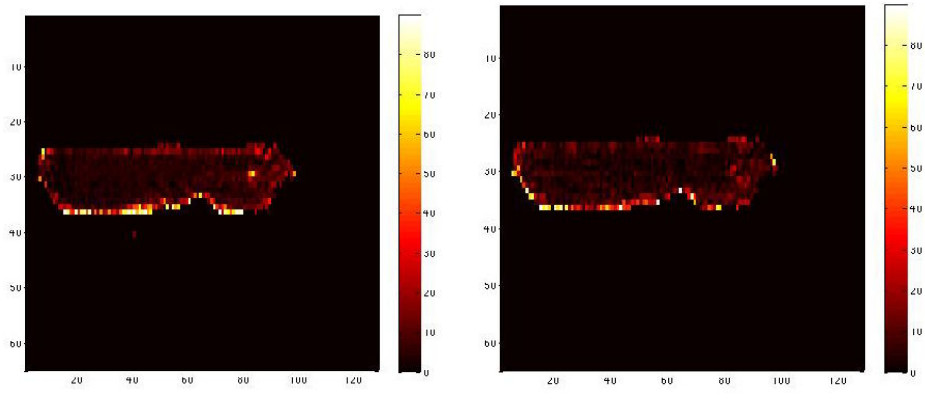

(a) (b)

Fig. 3. (a) Difference angle map between full data reconstructions using IFT and sparse data R=2 using the constrained reconstruction method. **(b)** Difference angle map between full data reconstructions using IFT and half the number of image directions reconstructed using IFT.

3.2 Radial Undersampling – Canine Heart Specimen

Results of the constrained reconstruction approach on radially undersampled data are shown in Fig. 4. Fig. 4a shows an image direction for a direction reconstructed from full k-space data with a line passing through it. Fig. 4b shows the corresponding image direction from sparse data, R=4 using the constrained reconstruction method. Fig. 4c compares the corresponding signal intensity profiles for the images in Fig. 4a and Fig. 4b for the line shown in Fig. 4a.

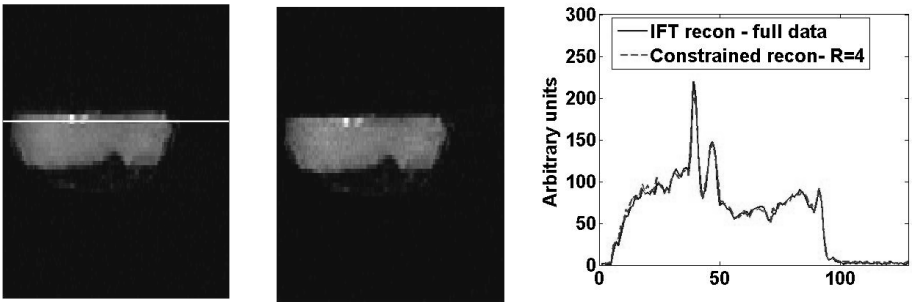

(a) (b) (c)

Fig. 4. (a) Image showing a diffusion weighted direction reconstructed from full k-space data. A line passing through the image is also shown. **(b)** Corresponding image reconstructed from sparse data R=4 using the constrained reconstruction approach. **(c)** Comparison of the intensity profiles for the line shown in Fig. 4a for the images in Fig. 4a and Fig. 4b.

3.3 Rectilinear Undersampling – Sheep Heart

The results of the constrained approach for R=2 data undersampled in variable density fashion for the sheep heart are presented in Fig. 5. Fig. 5a shows a single direction image reconstructed from full k-space data using IFT. Fig. 5b shows the corresponding image reconstructed from sparse data using the current method. The absolute difference image between Fig. 5a and Fig. 5b is shown in Fig. 5c. The peak intensity value in the Fig. 5c was about 15% of the peak intensity value in Fig. 5a.

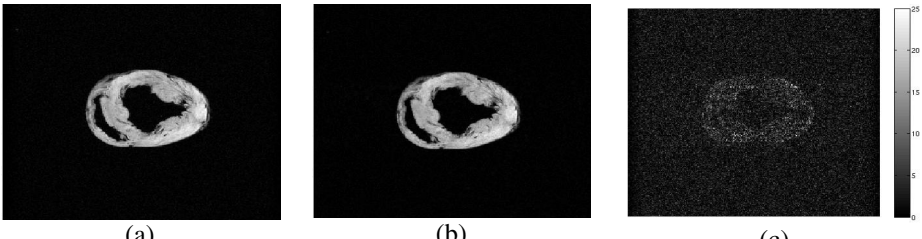

(a) (b) (c)

Fig. 5. (a) Image showing a diffusion weighted direction reconstructed from full k-space data for the sheep heart. **(b)** Corresponding image reconstructed from sparse data R=2 using the constrained reconstruction approach. **(c)** Absolute difference image between Fig. 5a and Fig. 5b.

4 Discussion

The parameters in the reconstruction method were empirically chosen based on the results for different datasets. The method was robust to small variation in the regularization parameters. We also note that formal methods, like the L-surface [7] technique can be used to determine the regularization parameters.

We found that the spatial and temporal constraints were almost equally helpful in reducing the artifacts from undersampling. Fig. 6 compares the effects of spatial and temporal constraints. Fig. 6a shows the absolute difference image between full data reconstruction using IFT and image reconstructed using IFT from R=2 data for a single image direction. Fig. 6b shows the absolute difference image between full data reconstruction using IFT and image reconstructed using only the temporal constraint, that is α_1 set to the empirical value and α_2 is set to zero in equation (3). Fig. 6c shows the absolute difference image between the image reconstructed from full data using IFT and the image reconstructed from R=2 data using spatial constraint only

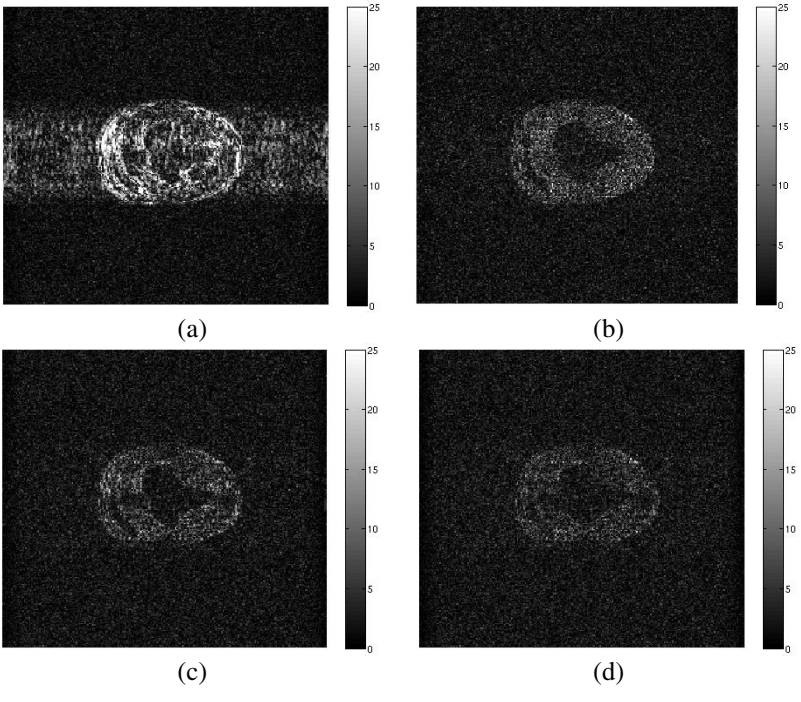

Fig. 6. (a) Image showing the absolute difference between full data reconstruction using IFT and R=2 data using IFT for a single image direction. **(b)** Image showing the absolute difference between full data reconstruction using IFT and R=2 data using only the temporal constraint. **(c)** Corresponding absolute difference image between full data reconstruction using IFT and R=2 data using spatial constraint only. **(d)** Corresponding absolute difference image between full data reconstruction using IFT and R=2 data using both spatial and temporal constraints.

that is α_1 is set to zero and α_2 is set to the empirical value in equation (3). Fig 6d shows the corresponding absolute difference between image reconstructed using full data using IFT and the image reconstructed using both spatial and temporal constraints. We can see that both the spatial and temporal constraints independently help reduce the artifacts but when combined together perform better in reducing the artifacts due to undersampling.

It is expected that the joint constrained reconstruction approach will perform better when more diffusion-weighted directions are measured. This is because neighboring directions are not independent, but have correlations. These correlations are implicitly used in the reconstruction to give "lossless" reconstructions from less data. Early results show the 12 direction sheep heart dataset performed better qualitatively than the 6 direction canine heart specimen dataset. Further work is needed to quantify these differences.

A limitation of the current study is that the results are from post-acquisition downsampling. Actually changing the DTI acquisition to acquire fewer phase encodes would be advantageous in terms of image artifacts, but could lead to either better or worse performance of the reconstruction method.

It was found that radial undersampling provided higher accelerations using the reconstruction method as compared to rectilinear undersampling. This could be due to the fact that radial undersampling leads to less severe artifacts as compared to rectilinear undersampling. Note that another limitation of the study is that the radial k-space data was generated from rectilinear k-space measurements, so do not reflect the actual measurements that would be made with a radial pulse sequence.

5 Conclusions

A constrained approach to reconstruct sparse cardiac DTI was proposed. The method has the potential to improve cardiac diffusion tensor imaging by acquiring less data in each diffusion weighted direction while reconstructing the entire set of diffusion-weighted images from multiple directions simultaneously. The method was tested on k-space data undersampled in both rectilinear and radial patterns. The results showed that the diffusion-weighted images could be reconstructed with little loss in the image quality.

References

[1] Hsu, E., Muzikant, A.L., Matulevicius, S.A., Penland, R.C., Henriquez, C.: Magnetic resonance myocardial fiber-orientation mapping with direct histological correlation. Am J Physiol, 274(5 Pt 2), H1627–1634 (1998)

[2] Hsu, E., Henriquez, C.: Myocardial fiber orientation mapping using reduced encoding diffusion tensor imaging. J. Cardiovasc. Magn. Reson. 3, 339–347 (2001)

[3] Jiang, Y., Hsu, E.: Accelerating MR diffusion tensor imaging via filtered reduced-encoding projection-reconstruction. Magn. Reson. Med. 53, 93–102 (2005)

[4] Adluru, G., Whitaker, R.T., DiBella, E.V.R.: Spatio-Temporal Constrained Reconstruction of sparse dynamic contrast enhanced radial MRI data. In: Proc. IEEE ISBI (To appear) (2007)
[5] Adluru, G., Awate, S.P., Tasdizen, T., Whitaker, R.T., DiBella, E.V.R.: Temporally Constrained Reconstruction of dynamic cardiac perfusion MRI. Magn. Reson. Med. (To appear) (2007)
[6] Portniaguine, O., Bonifasi, C., DiBella, E.V.R., Whitaker, R.T.: Inverse methods for reduced k-space acquisition. In: Proceedings of the ISMRM 11th Annual Meeting, Toronto, p. 481 (2003)
[7] Belge, M., Kilmer, M.E., Miller, E.L.: Efficient determination of Multiple Regularization Parameters in a Generalized L-curve Framework. Inverse Problems 18, 1161–1183 (2002)

An Experimental Framework to Validate 3D Models of Cardiac Electrophysiology Via Optical Imaging and MRI

Mihaela Pop[1], Maxime Sermesant[2,3], Desmond Chung[1], Garry Liu[1], Elliot R. McVeigh[4], Eugene Crystal[5], and Graham A. Wright[1]

[1] Department of Medical Biophysics, University of Toronto, Sunnybrook Health Sciences Centre, Toronto, Canada
mpop@swri.ca
[2] ASCLEPIOS project, INRIA Sophia Antipolis, France
[3] Division of Imaging Science, King's College, London, UK
[4] Laboratory of Cardiac Energetics, National Heart Lung and Blood Institute, National Institute of Health, Bethesda, Maryland, USA
[5] Arrhythmia Services, Sunnybrook Health Sciences Centre, Toronto, Canada

Abstract. Our aim is to develop a framework to validate 3-D computer models of cardiac electrophysiology using measurements of action potential obtained via optical imaging (based on voltage-sensitive fluorescence), and heart anatomy and fiber directions which are obtained from magnetic resonance imaging (MRI). In this paper we present preliminary results of this novel framework using a healthy porcine heart *ex vivo* model and the Aliev & Panfilov mathematical model. This experimental setup will facilitate the testing, validation and adjustment of computational models prior to their integration into clinical applications.

Keywords: computer modelling, electrophysiology, optical imaging, MRI.

1 Introduction

Computer modelling is a powerful tool used in electrophysiology to predict the electrical activity in normal and pathologic cases. In particular, it could help us understand and predict the arrhythmic events associated with myocardial infarction, a major cause of deaths [1]. Detailed ionic models, as well as macroscopic, phenomenological models have been proposed in computational electrophysiology to solve for the action potential (AP) propagation and its duration [2-5]. The mathematical approach is usually chosen by the investigators based on the available input and desired output parameters, as well as computational resources.

It is, however, very challenging to non-invasively obtain quantitative validation of these models from data close to *in vivo* geometry and physiology. To calculate the duration of the action potential, one needs the precise depolarization and repolarization times. Currently, monophasic action potentials (MAP) can be recorded *in vivo* via a catheter-electrode invasively inserted into the heart; however, this electrode records only one measurement (from the location where is positioned) [6]. To increase the number of simultaneous recordings, one can use an electrode-sock

F.B. Sachse and G. Seemann (Eds.): FIMH 2007, LNCS 4466, pp. 100–109, 2007.

(comprising 256 or more electrodes), but the sock records the extracellular potentials [7]. An alternative is given by the optical imaging technique, which has been shown to provide fast and accurate measurements of AP in explanted hearts prepared under physiological conditions close to those *in vivo* [8, 9]. The fluorescence dye is sensitive to the changes in transmembrane potential, therefore, the changes in the signal intensity can be recorded optically at submillimetric spatial resolution and high temporal resolution. To avoid erroneous estimations of the AP propagation and conduction velocity, a few methods have been proposed to reconstruct the 3D heart surface from 2D optical images [9-11].

Our aim is to build a validation framework for 3-D mathematical models of cardiac electrophysiology using measurements of action potential obtained from optical fluorescence images, as well as the anatomy and fiber directions obtained via MR imaging. The first task is to compare and adjust the predictions of the mathematical model with direct measurements of action potential in healthy hearts. A diagram of the validation framework is illustrated in Figure 1 below.

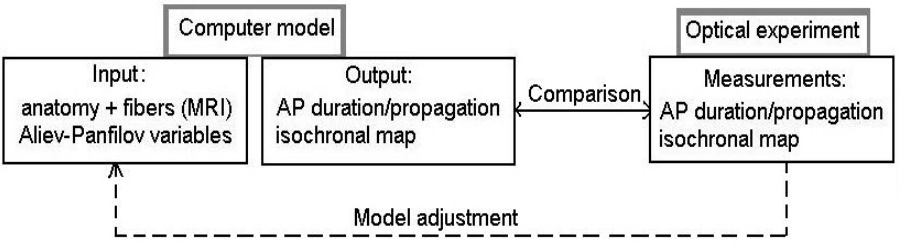

Fig. 1. Framework to construct the computer model from optical and MR images of the heart

In this paper we present preliminary results of this framework using explanted porcine healthy hearts and the Aliev & Panfilov monodomain model. The two-variable model developed by Aliev & Panfilov (based on reaction-diffusion equations) solves for the action potential without computing ionic currents [4].

2 Methodology

In this section we describe in detail the steps performed to build the validation framework proposed above. For simplicity, we describe these steps in the order they were accomplished. We first performed the optical experiment, and then used MR imaging to construct the computer model (i.e. the anatomy and fiber directions) of the same heart. The computational mesh was constructed from the anatomy scans and the simulations were performed with parameters that reproduced the experimental conditions (e.g. the position of pacing electrode, the duration of stimulus, etc). The initial input parameters of the model can be adjusted based on the measurements of action potential.

2.1 Optical Experiment

The animals were anesthetized, the chests opened and the hearts exposed (in accordance to the animal research protocol guidelines approved at Sunnybrook Health Centre, Toronto, Canada). The hearts were then immediately excised after euthanasia. The blood was flushed out and the aorta rapidly cannulated and attached to a Langendorff perfusion system. Throughout the experiments, the hearts were constantly perfused with oxygenated Tyrodes' solution (95%O2 & 5%CO2), maintained at a pH=7.0±0.3 and at a temperature of 37.0±0.5ºC. The hearts were paced at different constant frequencies between 1-2Hz via a bipolar stimulating Ag/AglCl2 electrode coated with gold at the tip to avoid polarization effects (GrassTelefactor, USA). The duration of the square stimulus was set to 10ms.

A 20ml bolus of fluorescence dye solution (0.2ml di4-ANEPPS, Biotium Inc) was injected into the heart via the perfusion line. To avoid motion artifacts, an electro-mechanical uncoupler (2,3-butanediome monoxime, Sigma Aldricht) was also injected in the perfusate solution, resulting in suppression of the heart motion. The dye was excited with green light (530±20nm) via 150W halogen lamps (MHF G150LR, Moritek Corp, Japan). To avoid photo-bleaching, the lamps were controlled by shutters (labeled 'S' in Figure 2 below). The emitted signals from the hearts were filtered through a high-pass filter (> 610nm) and captured by a high-speed dual-CCD system (MICAM02, BrainVision Inc. Japan).

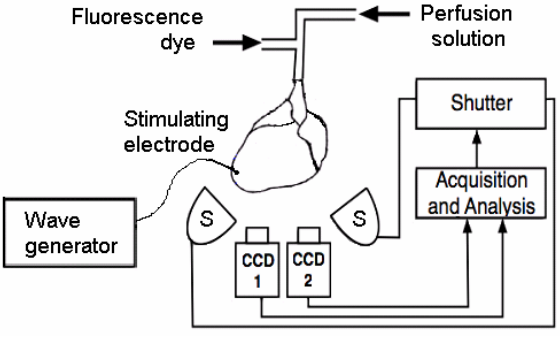

Fig. 2. Schematic of the optical experiment using a dual-camera system to record the action potential from the heart perfused ex vivo via a Langendorff system

The relative changes in the intensity of the fluorescence follow the changes in transmembrane potential. The recorded AP waves were denoised with a spatial-cubic filter and further analyzed with BV-Ana software (BrainVision, Japan).

The images recorded by the dual optical system were used to reconstruct the 3D surface of the heart. The details of the stereo reconstruction and calibration methods can be found elsewhere [11].

In the current work, 5-7 opaque markers were glued onto the epicardium to provide a way to register the optical images with the surface of the model from MR images. We estimate the rigid transformation between the markers' optical and MR 3D

coordinates by solving the least-squares difference using quaternions via a function implemented in the Visualization Toolkit (VTK, Kitware Inc.) libraries [12]. One marker was placed at the exact location of the stimulating electrode and this location was specified in the simulations.

2.2 Magnetic Resonance Imaging

At the completion of the optical experiment, the hearts were imaged using a 1.5Tesla Signa GE MR scanner for markers locations, anatomy, and fiber directions. For the markers locations we used a 3D fast spin echo (FSE) sequence using the following MR parameters: TE=60ms, TR=1000ms, slice thickness = 1.5 mm, a FOV and matrix yielding an in-plane interpolated resolution of 0.5x0.5mm. The diffusion-weighted imaging sequence was developed at the Laboratory of Cardiac Energetics (NIH/NHLBI, USA) [13] and implemented on our research scanner. We used the following MR parameters: TE=26ms, TR=800ms, NEX=1, *b*-value = 700, 7 directions for diffusion gradients, with the same FOV/matrix as for the 3D FSE series. The heart anatomy was extracted from the un-weighted images (i.e. b=0) and used to generate the volumetric mesh for the mathematical model.

2.3 Computer Model

We use the model of the heart described in [14] to perform our simulations. We briefly detail the Aliev and Panfilov model. In the system equations given in (1-2) we solve for *V*, the action potential, and *r,* the recovery variable contribution:

$$\frac{\partial V}{\partial t} = \nabla \cdot (D\nabla V) - kV(V-a)(V-1) - rV + I_{stim} \tag{1}$$

$$\frac{\partial r}{\partial t} = -(\varepsilon + \frac{\mu_1 r}{\mu_2 + V})(ku(u-a-1) + r) \tag{2}$$

The term *–kV(V-a)(V-1)* controls the fast processes (initiation and upstroke of action potential) via the threshold parameter *a*, while *r,* determines the dynamics of the repolarization phase. The term *Istim* represents the extra-stimuli (e.g. the pacing stimulus in the experiment). Most of the parameters (i.e. ε=0.01 a=0.1, k=8, μ_1=0.01 and μ_2=0.3) were set as in [2] to reproduce the shape, duration (i.e. 350ms) and restitution of AP obtained from experiments in canine cardiac tissue (the only available data in the literature, given in [15]). The model accounts for the heart anisotropy via the diffusion tensor, *D*, which depends on tissue diffusivity *d* (set to 1 for a normal/healthy conduction). The value in anisotropy ratio is set to 0.25 for an electrical wave propagating twice as fast along the fiber than in the transverse direction. The variables in the Aliev and Panfilov model are dimensionless, therefore they must be re-scaled to be related to physical values. For example, the normalized AP in the model varies between 0 and 1, which corresponds to real values of transmembrane potential between -90 and +20mV.

The heart surface mesh is created from the anatomy images using classical segmentation algorithms (thresholding, mathematical morphology, marching cubes)

and then the volumetric tetrahedral mesh is generated with the GHS3D package (INRIA, France).

We solve for the transmembrane potential using the Finite Element Method, with an explicit Euler time integration scheme. The code was written in C++ and uses OpenGL libraries to display the results. For the simulations presented in this study, we used a computational time step of $1x10^{-4}$s. The simulation time for one heart cycle (of 0.85s) on a mesh of approximately 41000 elements is about 10min on an Intel ® Pentium 4, 3.2GHz CPU, with 1Gb of RAM.

3 Results

The following section presents the results obtained in each step detailed in the methodology described above.

3.1 Optical Recordings of Action Potential

Figure 3.a shows a 2D image of the propagating AP acquired by one camera (with a 0.7mm spatial resolution and 3.7ms temporal resolution) at an instance in time marked by the dotted lines in the AP waveforms (obtained at a pacing frequency of 1.2 Hz at different pixel locations). Figure 3.b illustrates examples of AP waves recorded at other frequencies (i.e. 1.4, 1.6, 1.8 and 2Hz). The average duration of APD50 (the action potential measured at 50% repolarization) can be calculated for each frequency.

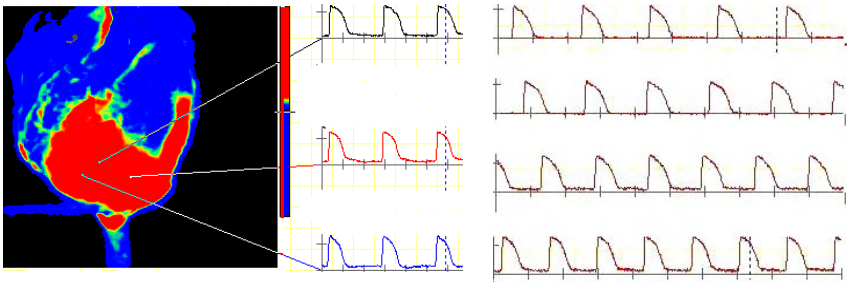

(a) (b)

Fig. 3. (a) The 2D optical image at one instance in time and the AP waves recorded at a pacing frequency of 1.2Hz, where the red color corresponds to the depolarized phase of AP, while the blue corresponds to the complete repolarized phase; (b) the normalized AP waves at other pacing frequencies

3.2 Three-Dimensional Stereo Reconstruction of Epicardial Surface

Results from the 3D stereo reconstruction are presented in Figure 4. Figure 4.a shows the surface reconstructed with the texture mapped and the markers visible in Figure 4.b. For the optical imaging configuration used to generate the results shown in this paper, the 3D reconstruction procedure was able to measure the depth of an image

point to within 2mm, and it's fronto-parallel position within 0.5mm. The action potential propagation, at one instance in time, was projected onto the 3D reconstructed surface and shown in Figure 4.c.

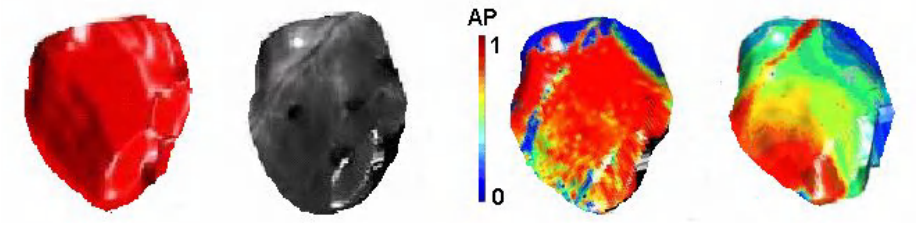

Fig. 4. Results from the 3D stereo reconstruction: surface rendering (a), texture mapping (b), propagation of normalized AP at one instance in time, for example the blue color indicates that the heart was completely repolarized (c) and isochronal map mapped onto the 3D surface (d)

The activation times can also be represented by isochrones (lines connecting pixels of equal activation time). Isochronal maps can be produced over one heart beat. An example is presented in Figure 4.d, where the isochrones were calculated with the BV-Ana software from the maximum and the minimum values of the transmembrane potential 50%(Vmax-Vmin), plotted with a 20ms interval, and mapped onto the 3D reconstructed surface. The 3D isochronal map can be used for comparisons with the output of the computer model. For this, the 3D optical surface and the 3D MR surfaces have to be registered via the markers (see **3.3**).

3.3 Registration of the 3D Optical Surface with 3D MR Surface

The stimulating electrode location (encircled) and the markers locations in the 2D optical images are shown in Figure 5.a and 5.b, respectively. Figure 5.c shows the markers visible in the MR volume-rendered image.

From the rigid transformation, the 3D positions (i.e. coordinates) of the markers were estimated by the optical stereo reconstruction to be within 1.2mm of their positions indicated in the volumetric MR scan.

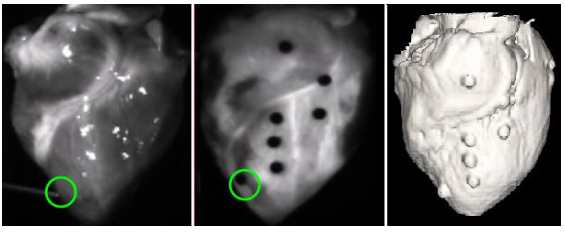

Fig. 5. The electrode position (a). The markers locations in fluorescence (b) and MR (c) images, respectively.

3.4 Fiber Directions

Figure 6 shows the fiber directions (in one of the hearts) obtained from diffusion-weighted MR images. The fiber directions can be visualized using MedINRIA[1] software (fig. 6.a.), which encodes the RGB colors for the three orthogonal directions. In the computational mesh, the fiber directions were specified at the baricenter of each tetrahedral element of the mesh (fig. 6.b).

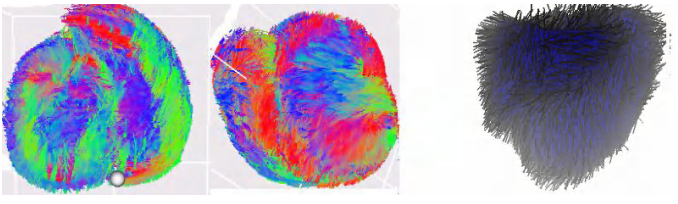

(a) (b)

Fig. 6. (a) Cross section and lateral view of one heart, with fibers reconstructed; (b) the fibers assigned in the computational mesh

3.5 Computer Simulation Results

Figure 7 displays simulation results produced with the threshold parameter *a* in the model initialized at *a*=0.1. The electrode location is depicted by the bright red dot in Figure7.a. Propagation of depolarization/repolarization wave on the heart at one instance in time is shown Figures 7.b and 7.c. An example of an isochronal map is given in Figure 7.d.

Figure 8.a shows an example of the changes in transmembrane potential (normalized values) predicted before the adjustment of Aliev-Panfilov model. These initial simulations produced an APD50 of 350ms at 1.2Hz. The value of threshold parameter *a* in the model was adjusted from a=0.1 to a=0.12, via a trial and error procedure, until the simulations produced an APD50=290ms at 1.2Hz (Figure 8.b) as measured in experiments.

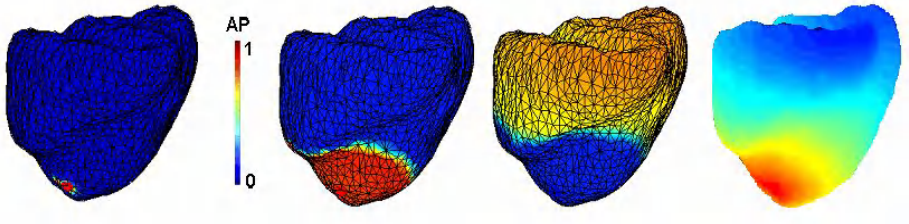

(a) (b) (c) (d)

Fig. 7. Simulations results of the mathematical model obtained with the canine data from [4]

[1] http://www-sop.inria.fr/asclepios/software/MedINRIA

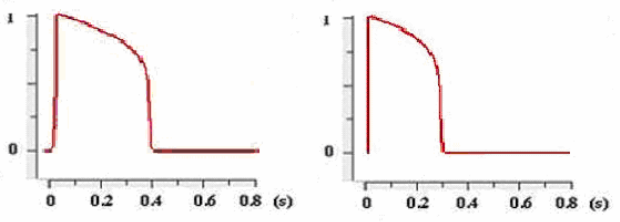

(a) (b)

Fig. 8. The changes in transmembrane potential over one heart cycle (at 1.2Hz) before (a) and after (b) the adjustment of the threshold parameter *a* in the model

4 Discussion and Future Work

The validation of computer models is an important step prior to their integration into clinical applications involving patients (i.e. diagnosis and therapy planning). Ionic models are accurate, but they are computationally expensive and need experimental validation at the same cellular scale. Alternatively, one can use the macroscopic model developed by Aliev and Panfilov. This model has been recently used to build maps of local apparent electrical conductivity by integrating information from measurements obtained via an epicardial sock in a dog heart model, *in vivo* [7, 16].

In the work presented here, we proposed a novel validation framework in an *ex vivo* model of healthy porcine hearts, and we have presented preliminary results. The AP duration and propagation is measured with high spatial (i.e. 0.7mm) and temporal resolution (i.e. 3.7ms) via optical imaging, which allowed us to observe the AP wave in detail. The computer model was then built from MR anatomy images of the same heart, and integrated with the structural anisotropy due to fiber directions. The main output of the model is the solution for transmembrane potential. This output can be adjusted to yield the same AP duration as in the optical recordings. However, only the adjustment of the threshold parameter is insufficient since it does not affect the shape of AP. It can be seen (by comparing Fig.3 and Fig.8) that the repolarization phase appears steeper in the calculated AP compared to the optical recordings. This could be due either to a limitation of the Aliev-Panfilov model or to our simplified fitting procedure. In this respect, the work will be extended to fit all of the model parameters from the restitution curve of AP (from the recordings at different frequencies, as in [4]). We do not expect significant differences between the model parameters obtained in [4] from the dog data, and our pig data.

To realistically compare the predictions with the measurements for the propagation of AP and the isochronal map, we proposed a 3D stereo reconstruction of the surface of the heart. The registration between the optical and MR surfaces performed very well (i.e. the markers' position in the optical and the MRI locations corresponded within 1.2mm). One of the markers gave the position of the pacing electrode enabling us to specify precisely the stimulus location in the simulations. The current image acquisition was limited to only one optical angle. A rotation of the heart in front of the cameras could enable the propagation of the electrical wave to be recorded from other angles as well, and to recover the entire surface of the heart.

However, the depth from which the optical signals originate makes the signal interpretation very complex, because the signals do not originate only from several millimeters beneath from the recording site. Instead, the epicardial optical signals contain a depth-weighted average of transmembrane potential signals generated by the fluorescent photons from a 3D volume beneath the surface. These findings were validated with other electrical models (i.e. bidomain and Luo-Rudy) [17-18]. It would be very interesting to compare the solution of the Aliev and Panfilov model with the calculated transmembrane potential generated by the flux of photons during the process of illumination and emission.

It was also shown that the morphology of optical AP changes with the change in the direction of the wave front propagation, because of the complex anisotropy of the myocardium [19]. However, in their study, the authors obtained the fiber orientations (on a 3D slab of tissue) via histology. In our model, the fiber directions are non-invasively obtained for the entire heart from MRI. Therefore, our framework allows one to investigate whether the Aliev and Panfilov model predicts such changes by varying the position of the pacing electrode (as this location is precisely identified via an opaque marker in the MR images).

Our ultimate goal is to predict the electrical propagation in pathologic cases. It is known that in structurally diseased hearts, the wave propagation is abnormal and vulnerable to reentry phenomena [1]. We plan to test the computer model by performing simulations to study the perturbations in the wave propagation, in the presence of anatomic blocks and areas of slow electrical conduction.

Acknowledgment

The authors would like to thank Dr. J. M. Rogers (University of Alabama, Birmingham, USA) for valuable discussions regarding the optical technique, Dr. Patrick Helm (University of Virginia, USA) for help with implementing the diffusion-weighted sequence on our scanner, Mr. A. Kim and Mr. K. Anderson for technical assistance with the optical set-up and to the veterinary technicians at Sunnybrook for help with the animal studies. This study was supported by funding from the Ontario Research and Development Challenge Fund, the Canadian Foundation for Innovation, and the Ontario Innovation Trust. Ms. Mihaela Pop is supported by a PhD scholarship from the Heart and Stroke Foundation of Canada.

References

1. Kebler, A., Rudy, Y.: Basic mechanisms of cardiac impulse propagation and associated arrhythmias. Physiological Review 84, 431–488 (2004)
2. Nash, M.P., Panfilov, A.V.: Electromechanical model of the excitable tissue to study reentrant cardiac arrhythmias. Progress in Biophys. Mol. Biol. 85, 501–510 (2004)
3. Clayton, R.H., Holden, A.V.: Dispersion of cardiac action potential duration and the initiation of re-entry: A computational study, Biomedical Eng. Online, pp. 4–11 (2005)
4. Aliev, R., Panfilov, A.V.: A simple two variables model of cardiac excitation. Chaos, Soliton and Fractals. 7(3), 293–301 (1996)

5. Aliev, R., Panfilov, A.V.: Modeling of heart excitation patterns caused by local inhomogeneity. Journal of Theoretical Biology 181, 33–40 (1996)
6. Kim, B.S., Kim, Y.H., Hwang, G.S., Pak, H.N., Lee, S.C., Shim, W.J., Oh, D.J., Ro, Y.M.: Action Potential duration restitution kinetics in human atrial fibrillation. Journal of the American College of Cardiology 39(8), 1329–1336 (2002)
7. Sermesant, M., Faris, O., Evans, F., McVeigh, E., Coudiere, Y., Delingette, H., Ayache, N.: Preliminary validation using in vivo measures of a macroscopic electrical model of the heart. In: Ayache, N., Delingette, H. (eds.) IS4TM 2003. LNCS, vol. 2673, pp. 230–243. Springer, Heidelberg (2003)
8. Efimov, I.R., Nikolski, V.P., Salama, G.: Optical imaging of the heart. Circulation Research. Jul. 9, 95(1), 21–33 (2004)
9. Kay, M.W., Amison, P.M., Rogers, J.M.: 3D surface reconstruction and panoramic optical mapping of large hearts. IEEE Trans. on Biomed. Eng. 51, 1219–1229 (2004)
10. Sung, D., Omens, J.H., McCulloch, A.D.: Model-based analysis of optically mapped epicardial patterns and conduction velocity. Ann. Biomed. Eng. 28, 1085–1092 (2000)
11. Chung, D., Pop, M., Sermesant, M., Wright, G.A.: Stereo reconstruction of the epicardium for optical fluorescence imaging. In: Esboll, BJ., Jorgensen, TM. (eds.) MICCAI Workshop on Biophotonics for diagnosis and treatment. IMM-Technical Report, pp. 33–40 (2006)
12. Horn, K.P.: Closed-form solution of absolute orientation using unit quaternions. Journal of the Optical Society of America A. 4, 629 (1987)
13. Helm, P., Tseng, H.J., Younes, L., McVeigh, E.R., Winslow, R.L.: Ex vivo 3D diffusion tensor imaging and quantification of cardiac laminar structure. Magnetic Resonance Medicine 54(4), 850–859 (2005)
14. Sermesant, M., Delingette, H., Ayache, N.: An Electromechanical model of the heart for image analysis and aimulation. IEEE Transactions on Medical Imaging 25(5), 612–625 (2006)
15. Elharrar, V., Surawicz, B.: Cycle length effect on restitution of action potential duration in dog cardiac fibers. Am. J. Physiology 244, H782–H792 (1983)
16. Moreau-Villeger, V., Delingette, H., Sermesant, M., Ashikaga, H., McVeigh, E.R., Ayache, N.: Building maps of local apparent conductivity of the epicardium with a 2-D electrophysiological model of the heart. IEEE Transactions on Biomedical Engineering 53(8), 1457–1466 (2006)
17. Bishop, M.J., Rodriguez, B., Eason, J., Whiteley, J.P., Trayanova, N., Gavaghan, D.J.: Synthesis of voltage-sensitive optical signals: Application to panoramic optical mapping. Biophysics J. 90, 2938–2945 (2006)
18. Hyatt, C.J., Mironov, S.F., Vetter, F.J., Zemlin, C.W., Pertsov, A.M.: Optical action potential upstroke morphology reveals near-surface transmural propagation direction. Circulation Research, 97, 277–284 (2005)
19. Vetter, F.J., Simons, S.B., Mironov, S., Hyatt, C.H., Pertsov, A.M.: Epicardial fiber organization in swine right ventricle and its impact on propagation. Circulation Research, 96, 244–251 (2005)

A Framework for Analyzing Confocal Images of Transversal Tubules in Cardiomyocytes

Eleonora Savio[1], Joshua I. Goldhaber[2], John H.B. Bridge[1], and Frank B. Sachse[1]

[1] Nora Eccles Harrison Cardiovascular Research and Training Institute, University of Utah, UT, USA
http://www.cvrti.utah.edu
[2] David Geffen School of Medicine, University of California, Los Angeles, CA, USA
http://www.cardiology.med.ucla.edu

Abstract. We introduce a framework to characterize and visualize the transverse tubular system of cardiac myocytes imaged with confocal microscopy. We imaged rabbit ventricular cells and cell segments with fluorescein linked to dextran. The image datasets were deconvolved with the Richardson-Lucy algorithm using the point spread function extracted from images of fluorescent beads. The transverse tubular system (t-system) was segmented with the methods of digital image processing. We reconstructed single transverse tubules and quantitatively described these in terms of length, cross-sectional area, ellipticity and orientation. These results should yield geometric markers for studies of protein distribution and provide insights into the function of the t-system.

1 Introduction

Three-dimensional images of living heart cells can now be obtained with scanning confocal microscopy. This technique is usually applied with fluorescent indicator dyes or antibodies tagged to a suitable fluophore. This permits specific labeling of compartments and proteins. After a raw image has been obtained, it is processed to correct, extract and quantify it.

The properties of confocal microscopic imaging systems can be characterized with the point spread function (PSF). PSFs describe the response of an imaging system to a point source of light. These PSFs can be obtained by imaging fluorescent beads. Precise knowledge of the imaging system's PSF is essential for accurate image restoration.

Recently, confocal microscopy and methods for digital image processing have been used to characterize the transverse tubular system (t-system) in rat ventricular cardiac myocytes [1]. The t-system supports fast propagation of electrical excitation into the cell interior. This system is composed of transversal tubules (t-tubules), which enter the myocyte primarily adjacent to Z disks [2]. In mammalian ventricular cells t-tubules occupy a large area of the sarcolemma, e.g. 42% in rabbit ventricular myocytes [3]. Morphological changes of the t-tubules have been associated with cardiac development, hypertrophy and heart failure [4,5].

F.B. Sachse and G. Seemann (Eds.): FIMH 2007, LNCS 4466, pp. 110–119, 2007.

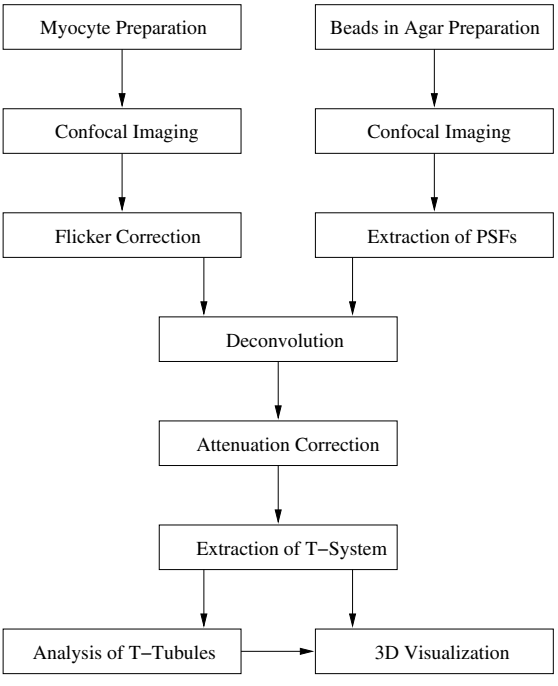

Fig. 1. Framework for processing confocal images of myocytes

Here, we present a framework for characterizing and visualizing the t-system of rabbit ventricular myocytes (Fig. 1). Whole cells and cell segments were imaged by confocal microscopy using fluorescein linked to dextran. The three-dimensional image datasets were deconvolved with the Richardson-Lucy algorithm using PSFs, which were extracted from images of fluorescent beads suspended in agar. The t-system was segmented and decomposed into its components. Single t-tubules were visualized and characterized with respect to length, cross-sectional area, ellipticity and orientation. These methods allow a quantitative description of t-tubule shape, which might provide landmarks for studies of protein distributions and co-localization. They may also provide insights into the function of the t-system.

2 Methods

2.1 Preparation of Cardiomyocytes

Ventricular myocytes were isolated from adult rabbit hearts by retrograde Langendorff perfusion with a recirculating enzyme solution containing collagenase ($1\ mg/ml$) and protease ($0.1\ mg/ml$). After the isolation, myocytes were stored at room temperature in a modified Tyrodes solution containing $0.1\ mM$ $CaCl_2$ and $12.5\ mM$ KCl until they were imaged.

2.2 Imaging of Cardiomyocytes

Images were usually obtained 4-8 h after cell isolation. Cells were superfused with membrane impermeant dextran (MW: 3,000-10,000) conjugated to fluorescein and then transferred to a coverslip.

We imaged cells with either a BioRad MRC-1024 laser-scanning confocal microscope (BioRad, Hercules, CA) and a 63x oil immersion objective lens (Nikon, Tokyo, Japan) or a Zeiss LSM 5 confocal microscope (Zeiss, Jena, Germany) together with a 60x oil immersion objective lens.

Three-dimensional image stacks with a spatial resolution of 133 x 133 x 133 nm and 100 x 100 x 100 nm, respectively, were obtained covering whole cells or large segments of them (Fig. 2). The dimension of the image stacks varied with cell size and their data volume ranged from 20 to 250 million voxels.

2.3 Flicker Correction

Several image stacks showed slice-wise discontinuous signal intensities, which might be artifacts produced by the imaging system or fluctuations of background illumination. Datasets with significant discontinuities were rejected. Minor discontinuities were corrected by slice-wise scaling of intensities. The scale factor was determined for each slice z by the ratio of expected and actual intensities. Expected intensities were obtained by averaging mean intensities in neighboring slices.

2.4 Deconvolution

The response g of an imaging system to given sources can be described by convolution of the source image f with the PSF h [6]:

$$g(\boldsymbol{x}) = (f \star h)(\boldsymbol{x}) = \iiint_{-\infty}^{\infty} f(\boldsymbol{x'})h(\boldsymbol{x} - \boldsymbol{x'})d\boldsymbol{x'} \tag{1}$$

Here, it is assumed that the response is linear and invariant with respect to translation.

Various methods for deconvolution of g exist including Fourier filtering, least-square regularization and Bayesian approaches [7]. In this work, we applied the iterative Richardson-Lucy algorithm to reconstruct the source image f [8]:

$$g_{n+1} = g_n \left(\frac{g_0}{g_n \star h} \otimes h \right) \tag{2}$$

with the cross-correlation operator $\otimes$ and $g_o \equiv g$.

We characterized the PSF h by imaging fluorescent beads in agar (Fig. 3). 10 images of single beads ($\varnothing$ 100 nm) were extracted, aligned and averaged. The PSF h was applied for deconvolution of imaging data (Fig. 4 a,b).

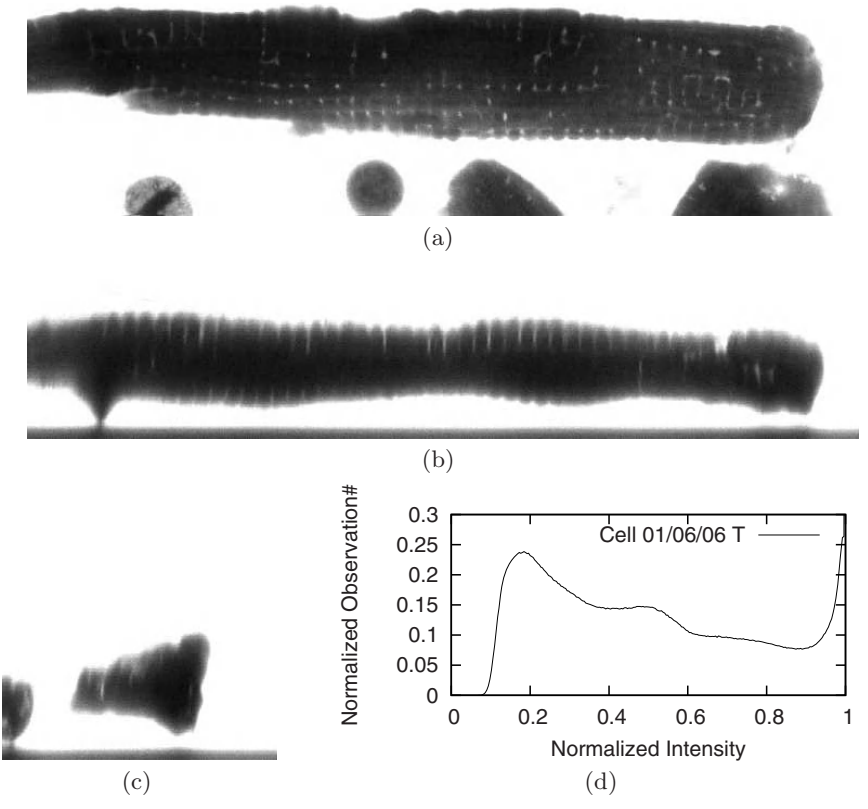

Fig. 2. Exemplary images of ventricular myocyte. The datasets describe a hexahedral region with a size of 102 μm x 34 μm x 20 μm by a lattice of 768 x 255 x 155 cubic voxels. Intensity distributions are shown in the central (a) XY (b) XZ and (c) YZ plane. (d) The histogram indicates overlapping ranges of intensities for extra- and intracellular spaces.

2.5 Attenuation Correction

Depth-dependent attenuation of signal intensity is an inherent property of optical imaging systems and can be described as a function of the attenuation coefficients for the exciting and emitted light, α_{exc} and α_{em}, respectively:

$$ln\frac{I(0)}{I(z)} = (\alpha_{exc} + \alpha_{em})z \tag{3}$$

with the depth z. Commonly, wavelengths of the exciting and emitted light differ. Typically, imaging systems provide an automated attenuation correction. However, analysis of our datasets showed that attenuation was still significant.

Our approach for attenuation correction was a-posteriori using information from each individual image stack: Average intensities were slice-wise calculated

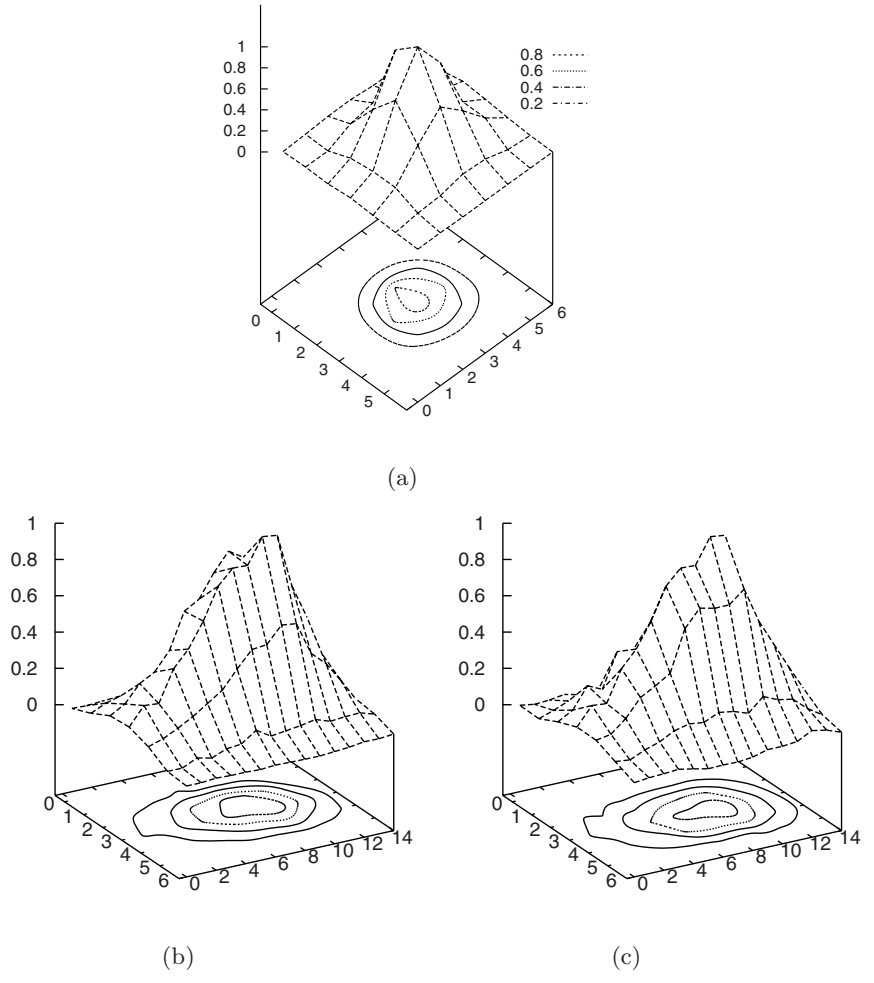

Fig. 3. Exemplary PSF for Zeiss LSM 5 with oil-immersion objective (63x, numerical aperture 1.4). Intensity distributions are shown in the central (a) XY (b) XZ and (c) YZ plane.

in regions filled only with dye. A 3rd order polynomial P was fitted to the averages by least squares. For each slice z a scaling factor s was determined by:

$$s = \frac{Max_{z \in [0,\ldots,N-1]} P(z)}{P(z)} \tag{4}$$

2.6 Segmentation of the T-System

The extracellular space was segmented with morphological operators and the region-growing technique in the median filtered deconvolved image data

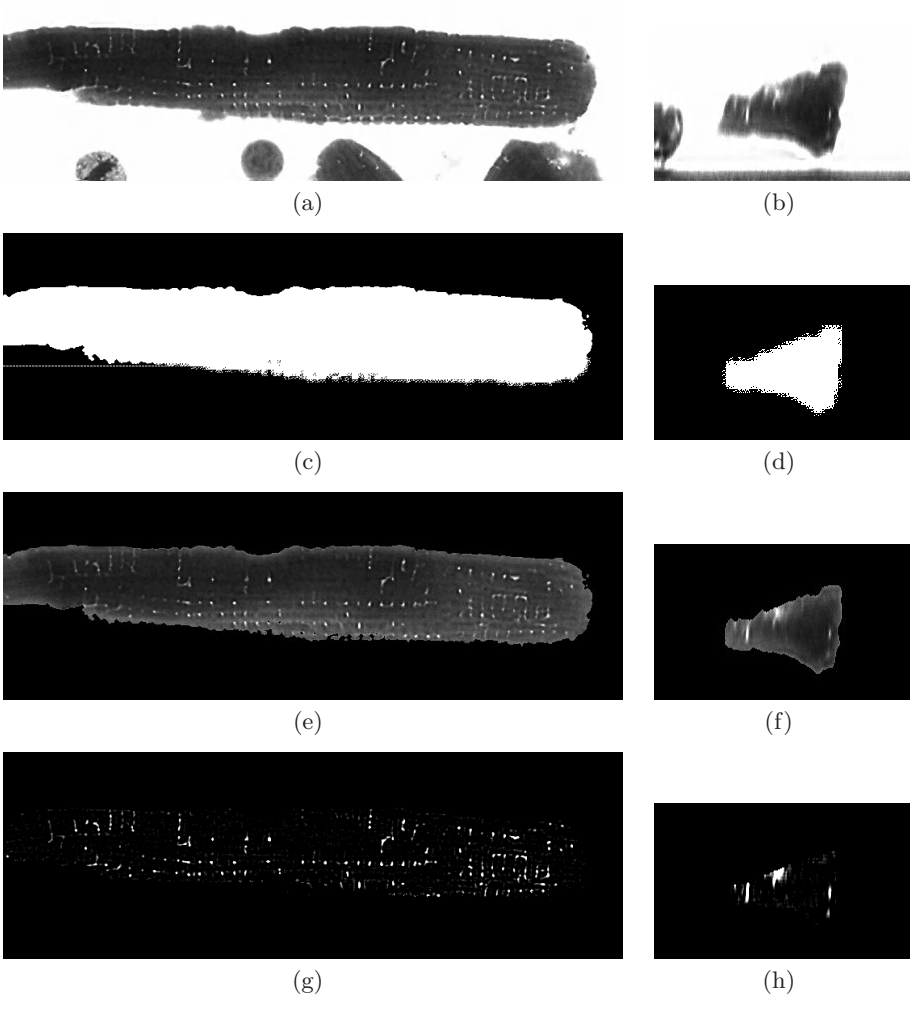

Fig. 4. Preprocessing of confocal images. The deconvolved images show increased image contrast of the t-system exemplified in a central (a) XY and (b) YZ plane. (c,d) The segmented images were created by region growing and morphological operators. The background segment (dark) served as a mask for various steps of further processing. (e,f) A segment containing intracellular space and the t-system was extracted applying the mask. (g,h) A high-pass filtered image was generated, which is used to extract seed points for region-growing of single t-tubules.

(Fig. 4 c,d) [9,10]. Subsequently, the extracellular segment was applied as a mask to extract a segment containing the myocyte together with the t-system (Fig. 4 e,f). All further processing was restricted to the latter segment.

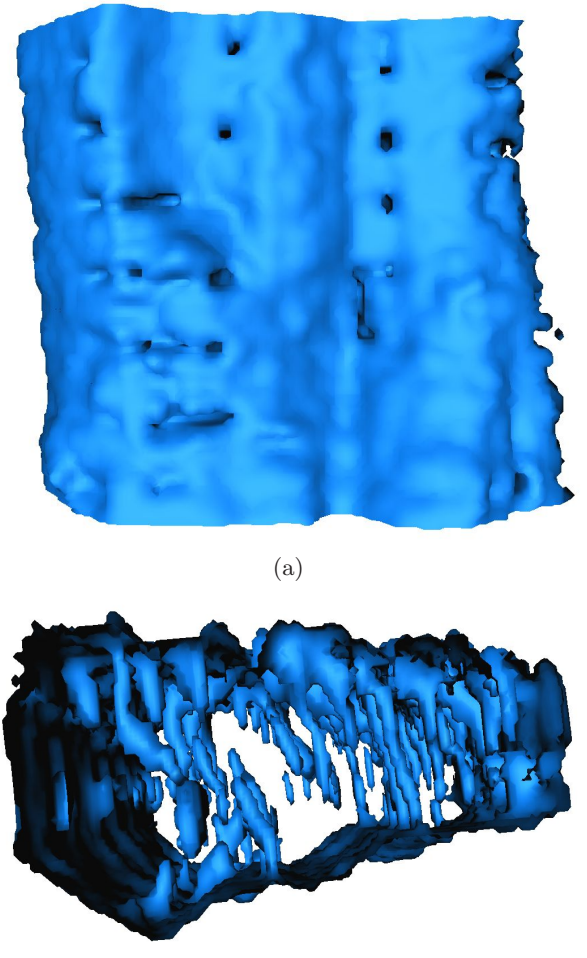

(a)

(b)

Fig. 5. Three-dimensional visualization of myocyte segment (a) from above with mouthes of t-tubules and (b) into inside with t-system. The myocyte's width is $\approx 20\mu m$.

2.7 Analysis of Transversal Tubules

Single t-tubules were segmented with the region-growing technique. Seed points for region-growing were determined by thresholding in a high-pass filtered image (Fig. 4 g,h).

A center line was fit for each t-tubule using the least square method. Cross-sectional intensities of the t-tubule segment and the adjacent background were projected onto the line. Background intensities were subtracted from the t-tubule

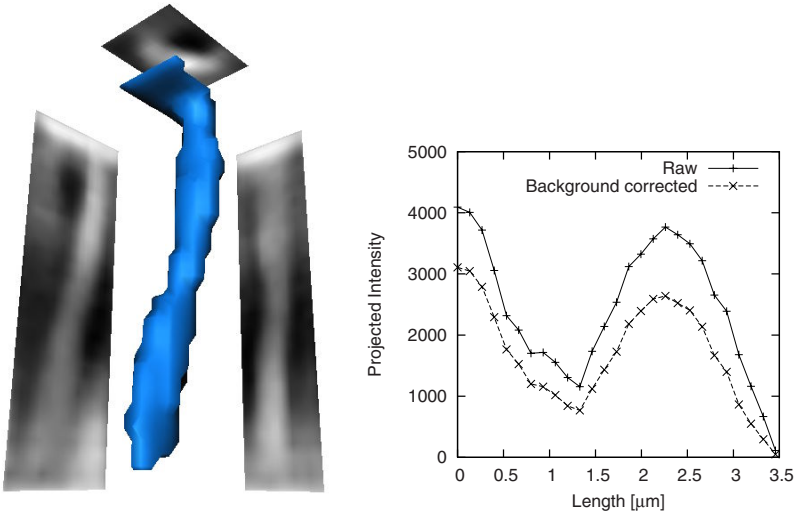

(a) (b)

Fig. 6. (a) Three-dimensional visualization of exemplary t-tubule together with averaged intensities projected on plane. (b) Raw and background-corrected intensity profiles.

intensities (Fig. 6b). Our analysis of the projected intensities revealed t-tubule length and the number of constrictions.

The t-tubule segment was sliced orthogonal to the center line. For each slice we performed a principal component analysis yielding cross-sectional eigenvectors $\boldsymbol{e}_1, \boldsymbol{e}_3$ and $\boldsymbol{e}_3$ and eigenvalues λ_1, λ_1 and λ_3 [9]. The eigenvalues and -vectors were applied to calculate cross-sectional eccentricity and orientation with respect to the long axis of the myocyte $\boldsymbol{c_l}$.

Eccentricity E of the cross-section was defined by:

$$E = \sqrt{1 - \lambda_3^2/\lambda_2^2} \tag{5}$$

The function is typically used to describe the eccentricity of an ellipse and its range is $[0, 1)$. The eccentricity of a circle is 0. In this work, a value of 0 indicates that the eigenvalues λ_2 and λ_3 in the cross-section are identical.

We calculated the orientation α from the cross-sectional minor eigenvector $\boldsymbol{e_3}$ assuming that the long axis $\boldsymbol{c_l}$ corresponds to the x-axis:

$$\alpha = atan(e_{3,y}/e_{3,x}) \tag{6}$$

A function value of 0^o indicates that the minor axis e_3 is parallel to $\boldsymbol{c_l}$. Values of $\pm 90^o$ indicate that the minor axis e_3 is orthogonal to $\boldsymbol{c_l}$.

3 Results

We applied the foregoing methods to process confocal microscopic datasets of more than 220 ventricular myocytes. A characterization of the cellular t-system was carried out for 10 datasets, which were selected by visual inspection and presented only minor artifacts and high image contrast.

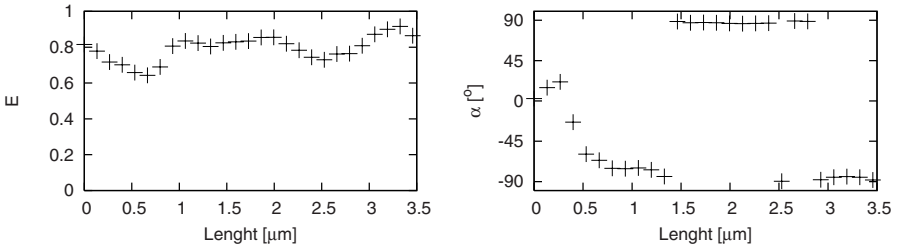

(a) (b)

Fig. 7. Analysis of single t-tubule. (a) Eccentricity E and (b) angle α between the minor eigenvector $\boldsymbol{e_3}$ and the long axis of the cell were determined for cross-sections.

The surface of a myocyte segment is shown in Figs. 5a,b. Mouths of t-tubules are visible in a regionally regular pattern (Fig. 5a) T-tubules mostly enter the myocyte from its upper and lower surface (Fig. 5b).

As an example we visualized a single t-tubule with a length of $\approx 3.5\mu m$ (Fig. 6a). Our analysis of t-tubules revealed constrictions, in which the cross-sectional area declines to $\approx 30\%$ (Fig. 6b). The eccentricity E ranged between 0.64 and 0.91 (Fig. 7a), which clearly demonstrates that a cross-section through the t-tubule is not circular. The orientation α of the t-tubular cross-section showed a rotation of $\approx 90^o$ from mouth to tip (Fig. 7b).

4 Discussion and Conclusions

We have presented a framework for processing confocal images of isolated cardiac myocytes together with a quantitative characterization of their t-system. The framework can be applied to characterize and compare the morphology of the t-system in various species. Furthermore, changes of the t-system can be quantitatively characterized, which have been associated with cardiac development and diseases.

The framework consists of several modules for deconvolution, reduction of artifacts, segmentation and visualization. The modules were implemented in C++, Perl and Matlab.

With this framework we restricted the application of image processing methods to those, which are mathematically well characterized transformations. In particular, we selected methods which preserve signal intensity. We analyzed single t-tubules using the deconvolved images and floating point arithmetic.

Acknowledgments

This work was supported by the Richard A. and Nora Eccles Harrison endowment, awards from the Nora Eccles Treadwell Foundation, and the National Institutes of Health Research grants No. HL62690 and No. HL70828.

References

1. Soeller, C., Cannell, M.B.: Examination of the transverse tubular system in living cardiac rat myocytes by 2-photon microscopy and digital image-processing techniques. Circ. Res. 84, 266–275 (1999)
2. Brette, F., Orchard, C.: T-tubule function in mammalian cardiac myocyte. Circ. Res. 92, 1182–1192 (2003)
3. Bers, D.M.: Excitation-Contraction Coupling and Cardiac Contractile Force. Kluwer Academic Publishers, Dordrecht, Netherlands (1991)
4. He, J., Conklin, M.W., Foell, J.D., Wolff, M.R., Haworth, R.A., Coronado, R., Kamp, T.J.: Reduction in density of transverse tubules and l-type ca(2+) channels in canine tachycardia-induced heart failure. Cardiovasc Res. 49, 298–307 (2001)
5. Wong, C., Soeller, C., Burton, L., Cannell, M.B.: Changes in transverse-tubular system architecture in myocytes from diseased human ventricles. In: Biophys. J (Annual Meeting Abstracts). (82), a588 (2002)
6. Hecht, E.: Optics, 2nd edn. Addison-Wesley, London (1987)
7. de Monvel, J.B., Le Calvez, S., Ulfendahl, M.: Image restoration for confocal microscopy: Improving the limits of deconvolution, with application to the visualization of the mammalian hearing organ. Biophys J. 80, 2455–2470 (2001)
8. Richardson, W.H.: Bayesian-based iterative method of image restoration. J. Opt. Soc. Am. 62, 55–59 (1972)
9. Gonzalez, R.C., Woods, R.E.: Digital Image Processing. Addison-Wesley, Reading, Massachusetts; Menlo Park, California (1992)
10. Sachse, F.B.: Computational Cardiology: Modeling of Anatomy, Electrophysiology, and Mechanics. LNCS, vol. 2966. Springer, Heidelberg (2004)

Computer Simulation of Altered Sodium Channel Gating in Rabbit and HumanVentricular Myocytes

Eleonora Grandi[1], Jose L. Puglisi[2], Stefano Severi[1], and Donald M. Bers[2]

[1] Department of Electronics Computer Science and Systems,
University of Bologna, Viale Risorgimento 2, 40136 Bologna, Italy
[2] Department of Physiology, Loyola University Chicago,
2160 South First Ave, 60153 Maywood, IL, USA
{egrandi,sseveri}@deis.unibo.it,
{jpuglis,dbers}@lumc.edu

Abstract. Mathematical models were used to explore sodium (Na) current alterations. Markovian representations were chosen to describe the Na current behavior under pathological conditions, such as genetic defects (Long QT and Brugada syndromes) or acquired diseases (heart failure). These Na current formulations were subsequently introduced in an integrated model of the ventricular myocyte to investigate their effects on the ventricular action potential. This "in silico" approach is a powerful tool, providing new insights into arrhythmia susceptibility due to inherited and/or acquired Na channelopathies.

Keywords: Na channelopathies, action potential, arrhythmias.

1 Introduction

The cardiac sodium (Na) channel controls cardiac excitability and the velocity of impulse propagation by initiating the action potential (AP). Different disorders in heart excitability have been related to derangements of the cardiac Na channel (Fig. 1) due to either genetic mutations or acquired diseases, such as heart failure (HF). These disorders are characterized by enhanced arrhythmia susceptibility [1].

A number of inherited diseases associated with mutations in *SCN5A*, the gene encoding the alpha subunit of the cardiac Na channel, have been discovered and linked to Long QT type 3 (LQT3) and Brugada (BrS) syndromes, conduction diseases and structural defects. Notably, mutations showing overlapping phenotypes have been characterized.

Amino acid 1795 site in the C-terminus of *SCN5A* is intriguing because one human mutation (Y1795C) causes a gain of function and LQT3, while a different human mutation at this same site (Y1795H) causes loss of function and Brugada syndrome [2]. A 9-state Markov model of the cardiac Na current was used to investigate these two Na channel mutations. The Y1795C mutation exhibited a significant sustained current when expressed in heterologous cell lines. A small maintained current was also observed in Y1795H. In addition, both mutations caused a significant shift of the inactivation process towards negative potentials.

F.B. Sachse and G. Seemann (Eds.): FIMH 2007, LNCS 4466, pp. 120–128, 2007.

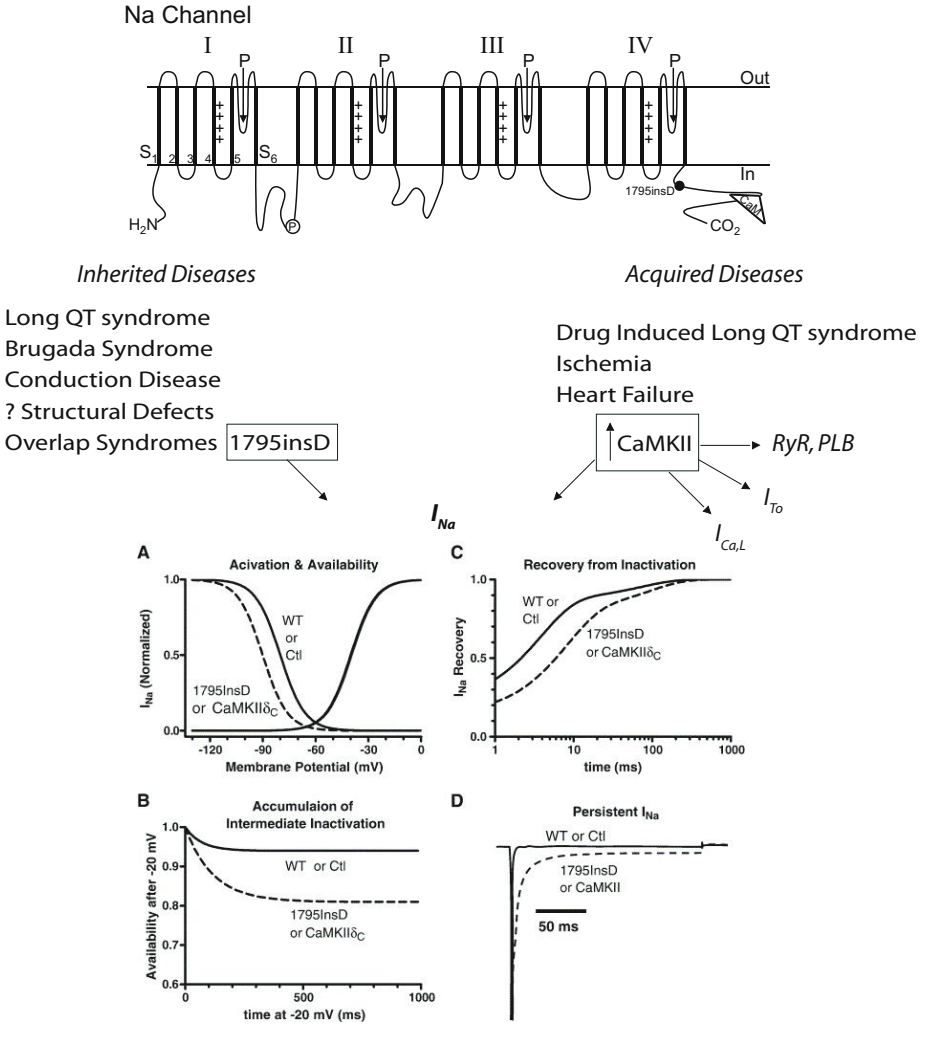

Fig. 1. Dysfunctions of the cardiac sodium channel associated to genetic mutations or acquired diseases have been linked to arrhythmia susceptibility. A Na channel human mutation (Asp insertion at 1795 in the C-terminus, 1795InsD), shows simultaneous Long QT 3-like and Brugada-like phenotypes in the same patients. Remarkably, 1795InsD mutant Na channels expressed in mammalian cells exhibit the same phenotype found for CaMKII-modified Na channel: leftward shift in the channel availability curve without changes in the activation curve (A), enhanced intermediate inactivation (B), slower recovery from inactivation (C) and presence of a persistent current upon prolonged depolarization (D).

Intriguingly, a single human mutation at this site (1795InsD) in *SCN5A* is linked to simultaneous LQT3 and BrS features. This 1795InsD mutation in humans has been studied in expressed Na channels [3]. It exhibits increased intermediate I_{Na} inactivation, slowed recovery from inactivation and availability is shifted to more

negative potentials (Fig 1A-C), all of which would reduce I_{Na} (loss of function) and could explain the Brugada-like symptoms of patients at higher heart rates. In addition this 1795InsD mutation causes persistent I_{Na} which fails to completely inactivate during long duration action potential (Fig 1D). This persistent I_{Na} would produce a gain of function, and that could contribute to action potential prolongation and LQT syndrome. This would be especially pronounced at low heart rates where I_{Na} recovery from inactivation may be more complete (even with the mutation) and where the longer intrinsic action potential duration would increase the impact of persistent I_{Na}. Clancy and Rudy [4] showed that a theoretical action potential model could simulate these behaviors, but they needed to extend the Markovian Na channel model that they used to include a bursting mode.

Emerging evidences now also link Na channel gating alterations to acquired diseases, e.g. drug-induced LQTS, cardiac ischemia and HF. In HF an enhanced persistent Na current contribute to a propensity to arrhythmias. Altered Na channel regulation may also occur in HF, causing a widespread form of acquired Na channel dysfunction. For example, Ca-Calmodulin dependent protein kinase II (CaMKII) is upregulated in HF and is more active [5]. Wagner et al. [6] recently showed that CaMKII regulates Na channel gating, and that upregulation of CaMKII in cardiac myocytes causes an extremely similar group of Na channel gating changes to those seen for the combined LQT/Brugada phenotype seen with 1795InsD (see Fig 1A-D). Again, one might expect then less Na channel availability at high heart rates, but more inward I_{Na} during long action potential at low heart rates.

However, the increased levels of CaMKII seen in HF may target several myocyte proteins [5]. CaMKII phosphorylates Ca transport proteins such as phospholamban, ryanodine receptors and L-type calcium channels (Fig. 1). In addition, novel data suggest that other ion channels, including sarcolemmal Na and K channels, may be regulated by this CaMKII.

To assess how CaMKII alters Na channel gating and how it may participate in arrhythmogenesis, we used a 13-state Markov model of the Na current to isolate the impact of altered Na channel gating on the action potential morphology and duration in HF.

2 Methods

2.1 Markov Models

The effects of Y1795C and Y1795H were simulated with a Markov model whose structure was proposed by Clancy and Rudy [4] for the wild type (WT) Na channel. It consists of 9 states: 5 inactivation states (2 close-, 1 fast- and 2 intermediate inactivation states), 3 closed states and 1 conducting open state (Fig. 2).

To simulate CaMKII-mediated alteration of the Na current, we adopted the 13-state model initially described by Clancy and Rudy [4] which contains two possible modes of gating, a background mode and a burst mode (Figure 3). The background mode reflects the normal sequence of activation and inactivation that most Na channels undergo after activation and is identical to the 9-state model previously used, whereas

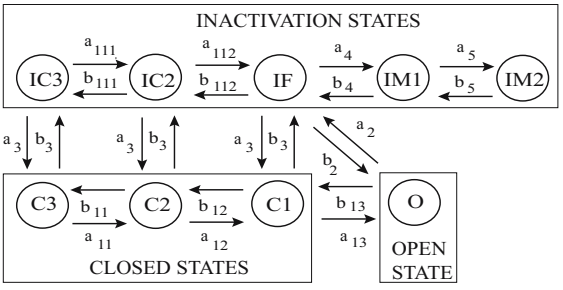

Fig. 2. Markov model of the cardiac Na channel used to simulate the LQT3 and BrS associated mutations. The channel model contains a 9-state background gating mode. Figure from [7].

the burst mode reflects a small population of channels that transiently fail to inactivate. The lower four states in Figure 3 (prefix "L") correspond to a burst mode of gating of channels that lack inactivation. Voltage independent transition rates between upper and lower states represent a probability of transition between the two modes of gating.

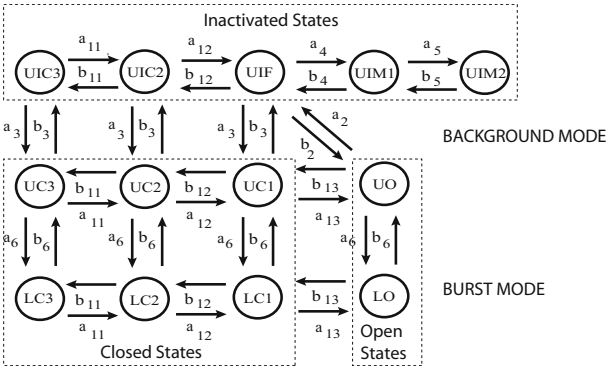

Fig. 3. Markov model of the cardiac Na channel used to simulate the effects of CaMKII overexpression. The channel model contains a 9-state background gating mode (upper states, prefix U) and a 4-state burst gating mode (lower states, prefix L). Redrawn from ref. [4].

In both models, the macroscopic current density is given by:

$$I_{Na} = G_{Na} \cdot P_o \cdot (V - E_{Na}) \quad where\ G_{Na} = \sigma \cdot g_{Na} \tag{1}$$

The variable P_O is the sum of all channel open probabilities, V is the membrane potential, and E_{Na} is the Na reversal potential. G_{Na} is the maximum membrane conductance: channel density (σ) times the unitary channel conductance (g_{Na}). The changes in channel state probabilities are described by first order differential

equations. Assuming N discrete channel states (N=9 and 13 in the present models), the probability of the channel residing in a particular state P_i at any time satisfies:

$$\frac{dP_i}{dt} = \sum_{j=1}^{N}\left[k_{ji} \cdot P_j(t,V)\right] - \sum_{j=1}^{N}\left[k_{ij} \cdot P_i(t,V)\right]$$
$$for\ i = 1,2,...,N-1;\ i \neq j\ and\ \sum_{j=1}^{N} P_i = 1 \tag{2}$$

The voltage-dependent rate constants k_{ij} describe the transition from state i to state j. Initial conditions are obtained by finding values for state probabilities from the steady-state equation:

$$\frac{dP_i}{dt} = 0 \tag{3}$$

A detailed description of model transition rates and parameter fitting procedure for the WT and mutant (Y1795C and Y1795H) Na current has been reported [7]. Similarly, we have begun to identify the parameters describing control and CaMKII-modulated Na currents to reproduce the results of the electrophysiological characterization reported by Wagner et al. [6]. The following voltage-clamp protocols were simulated to facilitate parameter identification: steady-state activation, steady-state inactivation, intermediate inactivation, recovery from inactivation, late current and fast and slow time constants of current decay. The parameters of the transition rates that maximally influence each voltage-clamp protocol were identified with an automatic procedure. The Nelder-Mead simplex direct algorithm was used to find the parameter values minimizing the sum of the least-square errors between model predictions and experimental data. The values proposed by Clancy and Rudy [4] were chosen as initial guesses in the minimization procedure to identify the transition rate parameters that allowed the best fitting of control data. The identified control set was subsequently used as initial guess to identify the CaMKIIδ_C channel parameters. Matlab 7 and Simulink (The MathWorks Inc.- Natick, Mass) were used for all the numerical computations.

2.2 Action Potential Models

We investigated in a previous study [7] the effects of the LQT3 and BrS mutations on the guinea pig ventricular AP by using the dynamic Luo and Rudy model (LRd). In the present work, the Markov models of the WT and mutant Na currents were incorporated into the ten Tusscher model of the human ventricular myocyte [8] implemented in Simulink 5 (The MathWorks. Inc- Natick, Mass; USA). Epi- (Epi), endocardial (Endo) and M cells were simulated.

As the experimental data of CaMKII overexpression were obtained in rabbit myocytes [6], LabHEART (implemented in Matlab 7, The MathWorks. Inc- Natick, Mass; USA) provided the initial basis for simulation in the rabbit ventricular AP [9].

The maximal conductance G_{Na} at 37°C was corrected with a Q_{10}=1.5 [10]. All the kinetic rates were normalized to 37°C with a Q_{10} of 2.1 [10]. Field stimulation of the computer cells was performed at different pacing rates and maintained until steady state AP was reached.

3 Results

3.1 Y1795C and Y1795H

Figure 4 shows the simulated human APs of Epi, M and Endo cells in WT and mutant conditions. AP duration but not morphology varied with changes in pacing frequency (40 up to 115 bpm).

The simulated Y1795C APs (Fig. 4, grey lines) were longer as compared with WT in the three cell layers, and showed remarkable increase of APD sensitivity to heart rate (Fig. 4). At low pacing rate (40-70 bpm, Fig.4 left and middle panels) AP prolongation occurred due to Na current gain of function leading to the presence of a persistent component during the plateau phase. At higher pacing rate (115 bpm, Fig.4 right panel) the effects of Y1795C on the APD were negligible.

The Y1795H mutant channel only slightly changed the AP morphology and duration with respect to the WT (Fig. 4, dashed lines). The reduced Na current availability (loss of function) of the Y1795H channel resulted in a mild reduction of the AP upstroke velocity as compared to the WT.

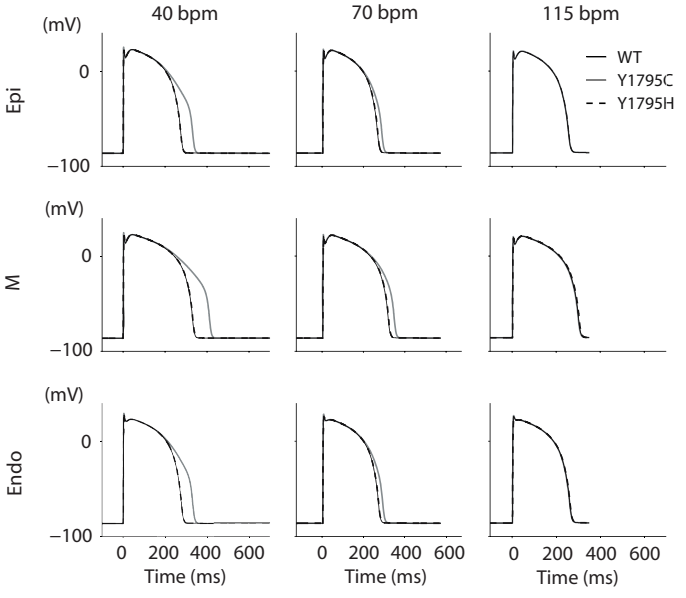

Fig. 4. Y1795C mutation (grey lines) affects AP of Epi, M and Endo cells in a rate dependent manner. The major effect is shown at the pacing frequency of 40 bpm where a significant AP prolongation occurs. The Y1795H mutation (dashed lines) has no effects on the AP of any cell types.

3.2 CaMKII Overexpression

The effects of the Na channel kinetic alterations due to CaMKII overexpession on the ventricular AP are shown in Figure 5 for three pacing rates: 180 (upper), 60 (middle), and 15 bpm (lower panel). The control AP (solid line) exhibits a characteristic spike-and-dome morphology and durations of 180, 310 and 500 ms respectively. In contrast, the CaMKII APs (dashed line) show distinctive rate-dependent duration effects. At fast rates (180 bpm), the CaMKII is indistinguishable from the control (Figure 5, upper panel, APD=180 ms). At slower rates (60 and 15 bpm [Figure 5, middle and lower panel]), APs exhibit a significant prolongation that is enhanced at slower pacing (APD=370 ms at 60 bpm and APD=670 ms at 180 bpm). At low frequencies, impaired fast inactivation and persistent I_{Na} outweigh the slowed recovery from inactivation because of long lasting diastolic intervals. This favors AP prolongation. However, at higher heart rates, shorter recovery interval prevents complete Na channel recovery resulting in a reduction of Na channel availability (loss of function). This reduces AP peak and abolishes sustained current without affecting AP duration.

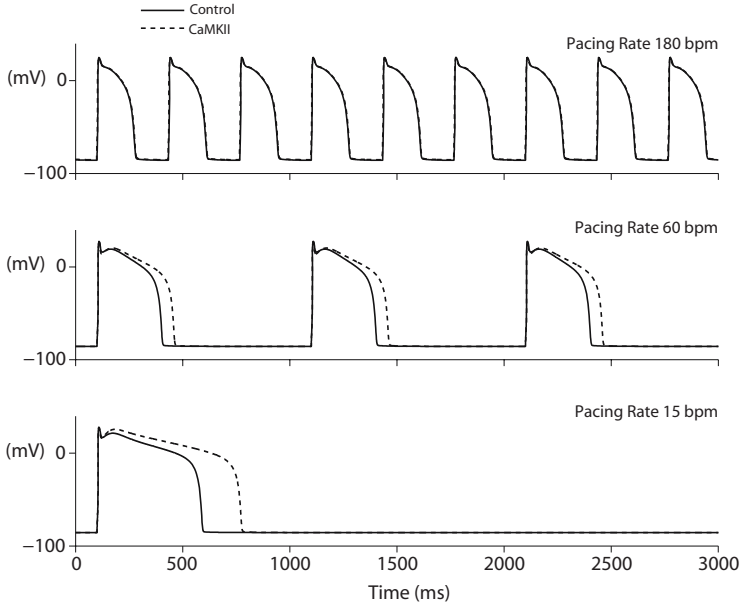

Fig. 5. CaMKII effects on Na channel gating affects AP in a rate-dependent manner. At lower heart rates, the enhanced late I_{Na} prolongs the AP (middle and lower panels); this effect is completely blunted at higher rates (upper panel).

4 Discussion

In this study we used two Markov models to analyze the effects of Na current alterations on cardiac excitability. The overall structures of these models were proposed by Clancy and Rudy and have been successfully used to simulate several Na current features both for WT and mutant channels [4,7].

This approach has been widely used to examine the potential arrhythmogenic role of genetic defects in the Na channel. Numerical simulation showed that in Y1795C mutation, associated with LQT3, bradycardia accentuates the APD prolongation as a consequence of an increased sustained I_{Na} at slower rates (Fig. 4). In addition, we showed that the effect of the late I_{Na} during bradycardia was more pronounced in M cell. These results are in agreement with the LQT3 phenotype and with the fact that life-threatening events occur during sleep. On the other hand, the Y1795H mutation induced only negligible changes on AP morphology, in accordance with the clinical findings that the Brugada Syndrome phenotype was concealed in the carriers of the mutation and only evident upon pharmacological challenge with Flecainide [2,7]. Interestingly, in our previous simulations [7] using the LRd ventricular AP model EAD occurred in Y1795C at low pacing rate. This discrepancy might be attributed to the differences in the current densities between different species (e.g. I_{Ks} and I_{Kr}) or in the kinetic properties of the L-type Ca current inactivation.

We expanded this strategy to a more common acquired disease, such as HF. As already discussed, CaMKII enhances intermediate inactivation and reduces Na channel availability, while at the same time impairing fast inactivation and enhancing persistent I_{Na}. These divergent alterations of the mutant Na channel (1795insD and CaMKII) cause a paradoxical phenotypic overlap of LQT3 and Brugada syndrome [3]. The "in silico" study performed by Clancy and Rudy [4] showed that this mutation disrupts fast inactivation, causing sustained Na current throughout the action potential plateau and prolonging cardiac repolarization at slow heart rates. At the same time, 1795insD augments slow inactivation, delaying recovery of Na channel availability between stimuli and reducing Na current at rapid heart rates. Similarly, the effects of CaMKII on the Na channel gating have a differential impact on the AP depending on the pacing rate. At low frequencies the simulations show a gain of function of the Na current, with the presence of a late current that prolongs the repolarization. This effect is much more pronounced at lower pacing rate (15 bpm), but it is still present at more physiological frequencies (60 bpm). The sustained current decreases with increasing pacing rate, where a loss of function (reduced peak current) is predicted. This loss of Na channel function due to the reduction in the channel availability would slow propagation and increase dispersion of repolarization. Therefore, it is conceivable that increased CaMKII activity in HF may alter Na channel gating thereby generating the substrate for life-threatening VT.

Of course HF and CaMKII can alter the behaviour of many ion channels, such that the effects on a single ion channel can be difficult to discern (compared to uncompensated single amino acid genetic mutations). Determining how multiple channel modifications individually contribute to altered electrophysiological substrate is an example of how such analyses with the mathematical approaches presented here are suitable to clarify the understanding arrhythmogenic mechanisms associated with mutation-dependent or acquired channelopathies.

5 Conclusions

The Markov model structures presented in this study, with different assignment of transition rates, are able to reproduce the main electrophysiological features characterizing cardiac Na current alterations due to genetic defects and more common

acquired diseases. The simulation of these models into an integrated description of the ventricular AP allows the assessment of the effects of Na channelopathies on the cardiac cell excitability. Since CaMKII affects several target proteins (Ca, Na and K transporters), the present analysis provides the starting point for a more comprehensive study involving the broader range of effects that characterize HF.

References

1. Tan, HL.: Sodium channel variants in heart disease: expanding horizons. J. Cardiovasc Electrophysiol 17(1), S151–S157 Review (2006)
2. Rivolta, I., Abriel, H., Tateyama, M., Liu, H., Memmi, M., Vardas, P., Napolitano, C., Priori, S.G., Kass, R.S.: Inherited Brugada and long QT-3 syndrome mutations of a single residue of the cardiac sodium channel confer distinct channel and clinical phenotypes. J. Biol Chem. 17;276(33), 30623–30630 (2001)
3. Veldkamp, M.W., Viswanathan, P.C., Bezzina, C., Baartscheer, A., Wilde, A.A.M., Balser, J.R.: Two distinct congenital arrhythmias evoked by a multidysfunctional Na+ channel. Circ. Res. 86, E91–E97 (2000)
4. Clancy, C.E., Rudy, Y.: Na+ Channel Mutation That Causes Both Brugada and Long-QT Syndrome Phenotypes. Circulation 105, 1208–1213 (2002)
5. Maier, L.S., Bers, D.M.: Role of Ca(2+)/calmodulin-dependent protein kinase (CaMK) in excitation-contraction coupling in the heart. Cardiovasc Res. (November 10, 2006)
6. Wagner, S., Dybkova, N., Rasenack, E.C., Jacobshagen, C., Fabritz, L., Kirchhof, P., Maier, S.K., Zhang, T., Hasenfuss, G., Brown, J.H., Bers, D.M., Maier, L.S.: Ca/calmodulin-dependent protein kinase II regulates cardiac Na channels. J. Clin Invest. 116(12), 3127–3138 (2006)
7. Vecchietti, S., Grandi, E., Severi, S., Rivolta, I., Napolitano, C., Priori, S.G., Cavalcanti, S.: In silico assessment of Y1795C and Y1795H SCN5A mutations. Implication for inherited arrhythmogenic syndromes. Am. J. Physiol Heart Circ Physiol 292, H56–H65 (2007)
8. ten Tusscher, K.H., Noble, D., Noble, P.J., Panfilov, A.V.: A model for human ventricular tissue. Am. J. Physiol Heart Circ Physiol. 286(4), H1573–1589 (2004)
9. Puglisi, J.L., Bers, D.M.: LabHEART: an interactive computer model of rabbit ventricular myocyte ion channels and Ca transport. Am. J. Physiol Cell Physiol. 281(6), C2049–C2060 (2001)
10. Maltsev, V.A., Undrovinas, A.I.: A multi-modal composition of the late Na+ current in human ventricular cardiomyocytes. Cardiovasc Res. 69(1), 116–127 (2006)

Scroll Waves in 3D Virtual Human Atria: A Computational Study

Sanjay Kharche[1], Gunnar Seemann[2], Joanna Leng[3], Arun V. Holden[4], Clifford J. Garratt[5], and Henggui Zhang[1]

[1] Biological Physics Group, School of Physics and Astronomy, University of Manchester, Manchester, M60 1QD, UK
[2] Institut für Biomedizinische Technik, Universität Karlsruhe (TH), Kaiserstr. 12, D 76218, Karlsruhe, Germany
[3] Directorate of Information Systems, University of Manchester, Manchester, M13 9PL, UK
[4] Institute of Membrane and Systems Biology, University of Leeds, Leeds, LS2 9JT, UK
[5] Manchester Heart Centre, Manchester Royal Infirmary, Oxford Road, M13 9WL, UK
Sanjay.Kharche@manchester.ac.uk

Abstract. Atrial fibrillation (AF) induced electrical remodelling of ionic channels shortens action potential duration and reduces atrial excitability. Experimental data of *AF-induced electrical remodelling* (AFER) from two previous studies on human atrial myocytes were incorporated into a human atrial cell computer model to simulate their effects on atrial electrical behaviour. The dynamical behaviors of excitation scroll waves in an anatomical 3D homogenous model of human atria were studied for control and AF conditions. Under control condition, scroll waves meandered in large area and became persistent when entrapped by anatomical obstacles. In this case, a mother rotor dominated atrial excitation. Action potentials from several sites behaved as if the atrium were paced rapidly. Under AF conditions, AFER increased the stability of re-entrant scroll waves by reducing meander. Scroll wave break up leads to wavelets underpinning sustained chronic AF. Our simulation results support the hypothesis that AF-induced electrical remodelling perpetuates and sustains AF.

Keywords: 3D model of human atria, atrial fibrillation, electrical remodelling.

1 Introduction

Atrial fibrillation (AF) affects a large section of the aged population and accounts for about 1% of the total National Health Service expenditure in the UK alone [1] and has an increasing prevalence. AF is the most common sustained arrhythmia which leads to loss in quality of life and further fatal cardiac complications. AF is characterized by an erratic ECG, which is possibly associated with ectopic foci or re-entrant electrical propagations in the atria. Paroxysmal AF induces electrical remodeling of membrane ionic channels in atrial cells [2, 3] and heterogeneous gap junctional remodelling of atrial tissue [4]. The mechanisms by which AF becomes persistent are poorly understood. Recently, *AF-induced electrical remodelling* (AFER) has been proposed

F.B. Sachse and G. Seemann (Eds.): FIMH 2007, LNCS 4466, pp. 129–138, 2007.

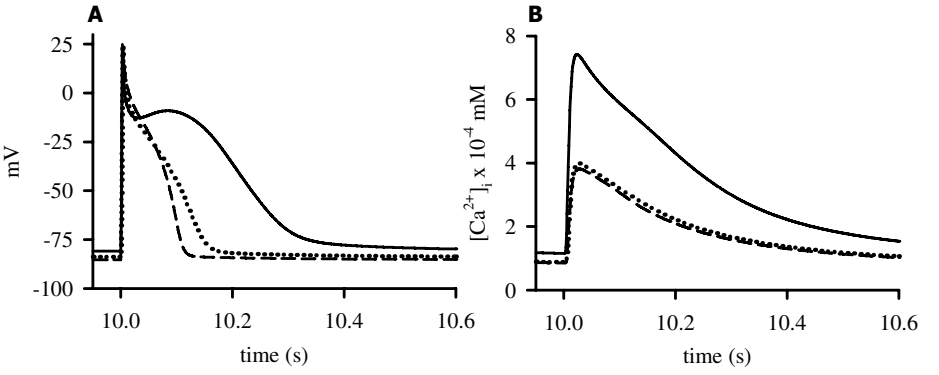

Fig. 1. Simulated human atrial cell AP (**A**) and intracellular $[Ca^{2+}]_i$ transient (**B**) under control (solid line), AF1 (long dash line) and AF2 (short dash line) conditions. The cell models were paced at a rate of 1 Hz and the 10^{th} AP and $[Ca^{2+}]_i$ transients were recorded.

as one of the mechanisms underlying the persistence of AF, which can cause APD shortening, reduction in atrial conduction velocity (CV), and therefore a possible increase in the stability of re-entrant scroll waves. In addition, anatomical obstacles due to the orifices of blood vessels (*e.g.* superior vena cava (SVC) and pulmonary veins) may provide a secondary mechanism to sustain AF. Atrial cells in the pulmonary vein regions can be auto rhythmic, which may trigger re-entry [5, 6, 7]. Paroxysmal AF is generally treated by suitable drug therapies [8, 9]; however persistent AF requires surgical intervention [10, 11, 12, 13].

The principle mechanism underlying AF is believed to be re-entrant atrial excitation. In this paper, we evaluated behavior of re-entrant scroll waves under control and AF conditions in an anatomically detailed 3D model of human atria. We incorporated data on AFER from two independent experimental studies [2, 3], into a biophysically detailed computer model of human atrial cell [14]. We characterized the effects of AFER on the electrical activities in atrial cells and spatially extended atrial tissue. Dynamical behavior of re-entrant scroll waves in the 3D homogenous anatomical model were characterized [15]. Our studies have shown that AFER alone has a major effect on atrial conduction and scroll wave dynamics, which helps to sustain AF. This study provides insights to understand how AF begets AF, in which paroxysmal AF changes to chronic AF due to AFER.

2 Methods

The computer model for human atrial electrical activity developed by Courtemanche *et al.* [14] was used in all simulations. The model was modified to incorporate the experimental data of AFER on human atrial myocytes by Bosch *et al.* [2] (AF1) and Workman *et al.* [3] (AF2) to simulate AF remodelling. In brief, the ionic channel remodelling in AF1 was modelled as a 235% increase of I_{K1}, 74% reduction of $I_{Ca,L}$, 85% reduction of I_{to}, a shift of -16 mV of the I_{to} steady-state activation, and a -1.6 mV shift of sodium current (I_{Na}) steady state activation. Fast inactivation kinetics of $I_{Ca,L}$ is

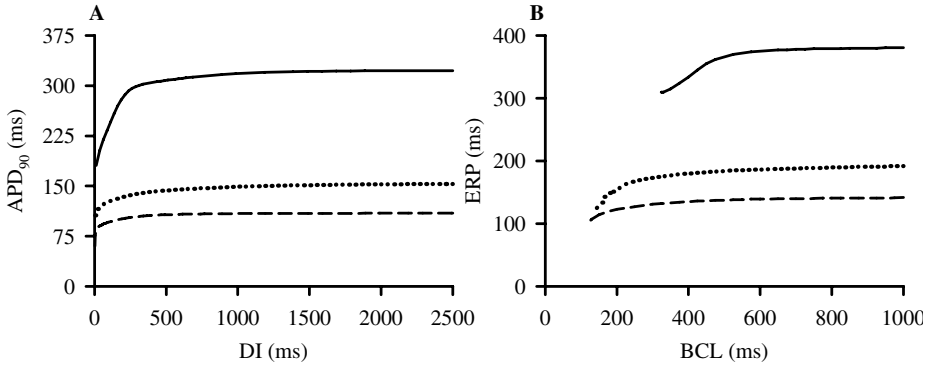

Fig. 2. Rate dependence of human atrial electrical activity under control (solid line), AF1 (long dashed) and AF2 (dotted line) conditions. **A:** APD restitution curve. The maximal slope for control was observed to be 0.91, while in AF1 and AF2 cases it was 4.63 and 1.55 respectively. **B:** ERP restitution curve. ERP at BCL = 1000 ms reduced from 381 ms in control, to 142 ms in AF1 and 192 ms in AF2 cases.

slowed down, and was implemented as a 62% increase of the time constant. The ionic channel remodelling in AF2 was simulated by a 90% increase of the inward rectifier potassium current (I_{K1}), 64% reduction of the L-type calcium current ($I_{Ca,L}$), 65% reduction of transient outward current (I_{to}), 12% increase of the sustained outward potassium current (I_{Ksus}), and a 12% reduction of the sodium potassium pump ($I_{Na,K}$).

Differences in APD and calcium ($[Ca^{2+}]_i$) transient among control, AF1 and AF2 were computed from the 10^{th} stimulus after pacing the model at a basic cycle length (BCL) of 1 s. Changes in APD and peak $[Ca^{2+}]_i$ transient were noted. AP restitution (APDr) was computed using a standard S1-S2 protocol where a premature stimulus (S2) was applied after 10 conditioning stimuli (S1) at a BCL of 1 s. Diastolic interval (DI) was defined as the time interval between 90% repolarization of the previous AP and the upstroke of current AP. A plot of APD against DI gave APDr. Maximal slopes of APDr curves were determined. Effective refractory period (ERP) was computed using the cell models and a modified S1-S2 protocol. ERP was defined as the minimum S1-S2 stimulus interval that produced an AP with peak potential over 80% of the last S1 AP peak potential [3]. ERP was determined for values of S1 from 100 ms to 1000 ms and ERP restitution curves were constructed by plotting ERP against S1-S2 interval. All stimuli were applied for 2 ms time duration with amplitude of 2 nA.

The cell models were incorporated into a parabolic partial differential equation formulation to construct mono-domain spatial models of electrical propagation of the form

$$C_m \partial v / \partial t = D \nabla^2 v - I_{ion} \tag{1}$$

where C_m is cell membrane capacitance, D is the diffusion coefficient that simulates the electrotonic interactions between cells via gap junctional coupling, v is the

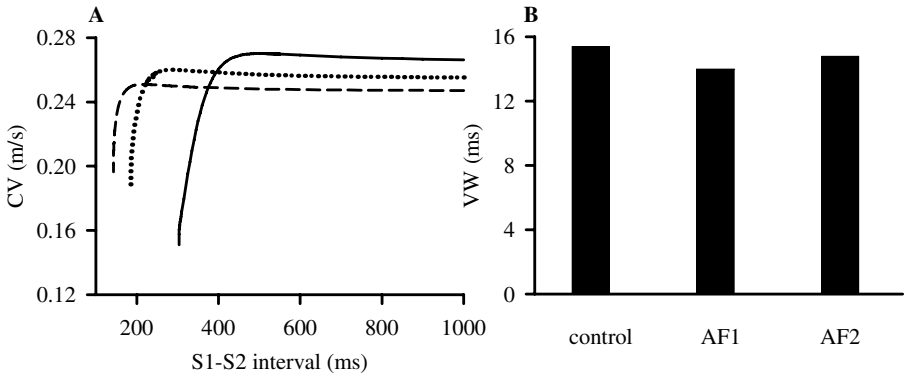

Fig. 3. A: Computed rate dependent intra-atrial conduction velocity for control (solid line), AF1 (dashed line) and AF2 (dotted line) conditions. Solitary wave conduction velocity was 0.27 m/s for control, while decreased to 0.25 m/s in AF1 and 0.26 m/s in AF2 conditions. **B:** computed VW in control and AF conditions.

membrane potential, and I_{ion} is the membrane current. The value of D was taken to be 0.03125 mm^2/ms to give a conduction velocity of 0.27 m/s for a solitary wave in control conditions [16]. The 1D model was taken to be 10 mm in length with a spatial resolution of 0.1 mm. The 3D anatomically detailed geometry of human female atria was obtained from [15]. It consists of left atrium, right atrium (RA), pectinate muscles, Bachmann bundles, and the pacemaker sinus node. Spatial resolution in the 3D anatomical model is 0.33 mm × 0.33 mm × 0.33 mm.

The 1D model was used to compute intra-atrial conduction velocity restitution (CVr) and temporal vulnerability window (VW). To compute CVr, a conditioning pulse stimulus was applied at one end of the strand, over a length of 0.3 mm with amplitude 2 nA and duration of 2 ms, after which a premature S2 stimulus was applied at the same location. The CV of resultant second propagation was computed as a function of the S1-S2 interval. To compute VW, the S2 was applied in the middle of the strand rather than at the conditioning stimulus end. The time window during which the S2 stimulus produced uni-directional retrograde propagation defined the tissue's VW. Wavelength of propagating APs was computed as the product of CV and APD.

Scroll wave re-entry in the 3D homogenous model was initiated in the largest contiguous surface of the right atrium using a cross-field protocol similar to that used in 2D idealized sheets of atrial tissue [16]. 3 s electrical activity was simulated in each case and APs at representative locations in the atria were registered for analysis.

Integration in time and space was carried out using an explicit Euler forward time step method while using central differences for spatial derivatives. The integration time step was taken to be 0.005 ms in the cell and 1D models. In the 3D simulations, a time step of 0.05 ms was seen to give solutions similar to the smaller time step of 0.005 ms as the space step was 0.33 mm.

Simulations were carried out on (i) Sun-Fire 880 UltraSPARC 24 CPUs shared memory system, and (ii) Bull Itanium2 208 CPUs distributed memory system with a single rail Quadrics QsNetII interconnect. The 3D simulations were carried out using

parallel OpenMP and MPI solvers developed in our laboratory. This allowed the simulations to be completed using both available resources. Due to run time limits, check-pointing was implemented in the MPI version where the state of the model was stored to allow continuation of the simulation after restart. This enabled optimal use of the Bull Itanium2 system. Visualization was carried out using AVS [17] and the local high performance visualization service in Manchester Visualization Centre.

3 Results

AFER [2, 3] produced a remarkable APD shortening and reduction in $[Ca^{2+}]_i$ transient amplitude. The APD was reduced by 65.3 % (108.5 ms) in AF1 and 52.8 % (147.6 ms) in AF2 cases, as compared to 313.0 ms in control case. Such APD reduction

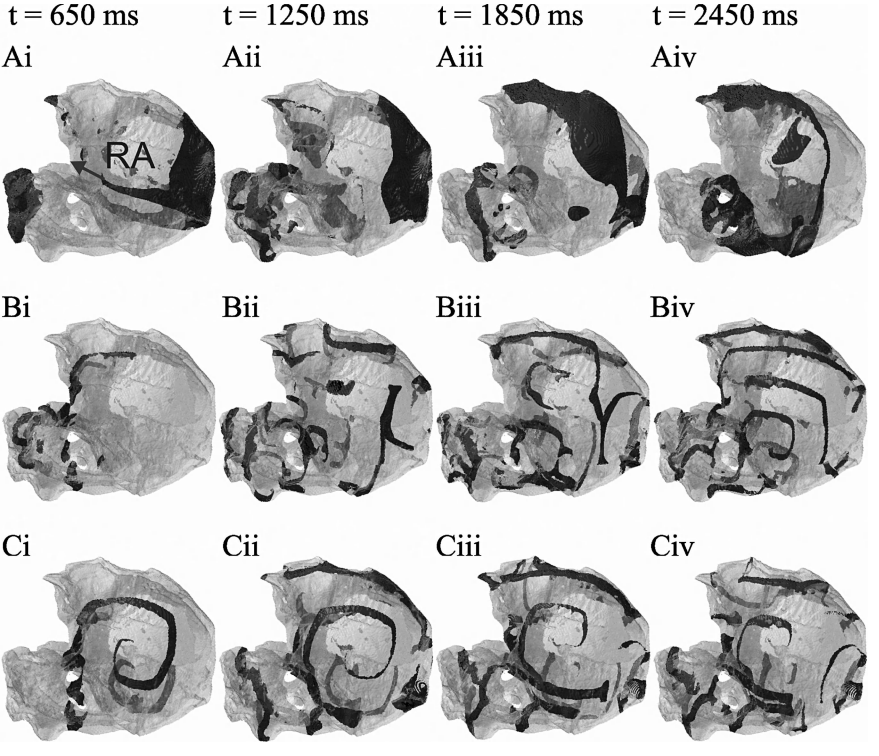

Fig. 4. Scroll waves in the 3D model where transparent grey shows anatomy and solid black denotes excitation. Panels **Ai, Aii, Aiii** and **Aiv** show frames from control simulation, **Bi, Bii, Biii** and **Biv** from AF1, and **Ci, Cii, Ciii** and **Civ** from AF2. Frames were taken at times as shown at the top of each column. The scroll wave in control meanders out of the right atrium and its initial meander direction is shown by an arrow in **Ai**. In AF1, the induced mother rotor breaks up into smaller persistent spiral wavelets. In AF2, the scroll wave is stable with small meander.

was consistent with experimental observation [2, 3]. AFER also hyper-polarized AP's resting membrane potential, which changed from -80.5 mV in the control to -85.2 mV in AF1 and -83.8 mV in AF2 cases. $[Ca^{2+}]_i$ transient amplitude was significantly reduced from 0.61 μM in control to 0.30 μM in AF1 and 0.31 μM in AF2 cases. Resting $[Ca^{2+}]_i$ was also reduced from 0.13 μM in control to 0.090 μM in AF1 and 0.094 μM in AF2. Simulated AP and $[Ca^{2+}]_i$ transient profiles are shown in Figure 1. APDr is shown in Figure 2**A**. APs were observed at much higher pacing rates than in the control case suggesting that AFER facilitates high frequency excitation as occurs during AF. At high pacing rates (i.e. small values of DI) APDr was investigated in detail such that it allowed an accurate estimation of the maximal slope of APDr. AF was seen to increase maximal slope from 0.91 in control to 4.63 in AF1 and 1.56 in AF2. AF reduced ERP at physiological rates of pacing (BCL of ~ 1 s) from 381.0 ms in control to 142.0 ms in AF1 and 192.0 ms in AF2. ERP is also reduced by AF as shown in Figure 2**B**.

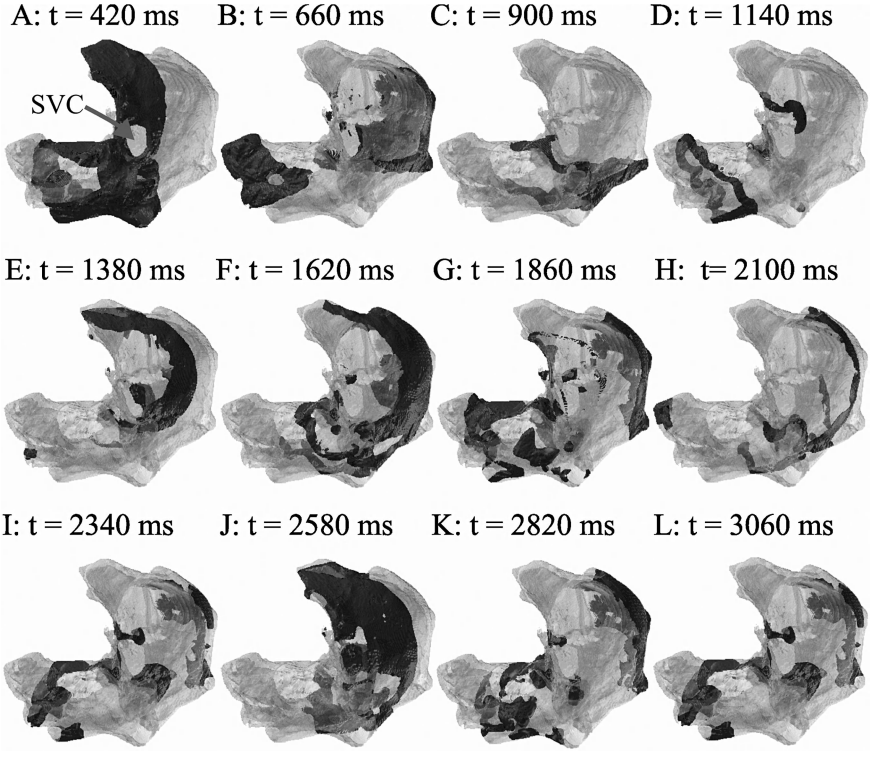

Fig. 5. Representative frames from the control simulation showing entrapment of scroll wave by SVC (**A**). After application of the re-entry inducing stimulus (**B**), the scroll wave quickly meanders away from the centre of the RA and is entrapped by the SVC (**C, D**). The scroll wave was entrapped to the SVC for the duration of simulated activity (3 s) (**E - L**).

CVr and VW were determined from the 1D model. Reduced excitability of atrial tissue due to AFER is reflected in the reduced CV of a solitary wave from 0.27 m/s in control, to 0.25 m/s in AF1 and 0.26 m/s in AF2. As shown in Figure 3**A** for CVr, atrial conduction is supported at much higher pacing rates under AF conditions as compared to control. When stimulus rate was 198 beats/min (S1-S2 interval < 303.5 ms) conduction in control tissue failed. However with AFER, atrial tissue supported propagation up to 421 beats/min (S1-S2 interval ~ 142.7 ms) for AF1 and 325 beats/min (S1-S2 interval ~ 184 ms) under AF2 conditions. AF reduced VW from

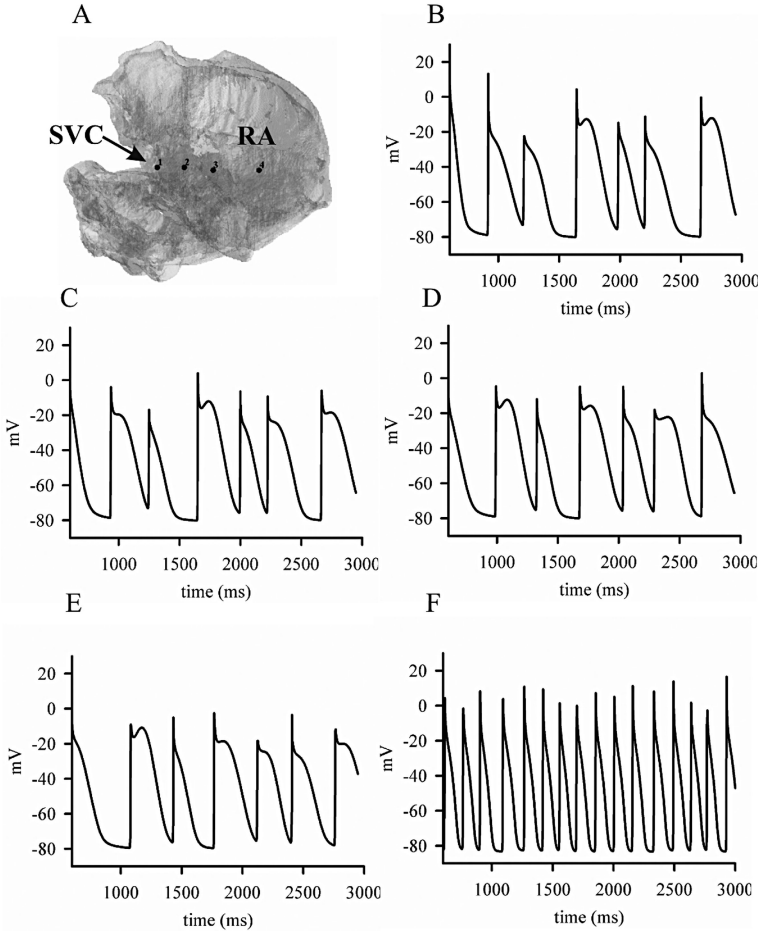

Fig. 6. A: Locations in the 3D atrial model where AP profiles were registered. AP profiles as registered from location 1, 2, 3, and 4 are shown in **B**, **C**, **D**, and **E** respectively. Panel **F** shows AP profile from the AF1 case from location 4. Such high frequency activity (as compared to control) is typical of the AF cases and persists throughout the simulated activity period of 3 s.

15.4 ms in control to 14.0 ms (10% reduction) in AF1 and 14.8 ms (4% reduction) in AF2 cases. The wavelength reduced from 84.50 mm in control, to 27.13 mm in AF1 and 38.38 mm in AF2.

In the 3D simulations, re-entrant scroll waves were initially induced on the largest contiguous surface of the RA. This offered the maximum possible space for the scroll waves to meander without anatomical interference. Figure 4 shows the evolution of scroll waves on the right atrial surface in the 3 cases. In the control case, the scroll wave quickly meanders away from the point of initiation (~ 350 ms after initiation). Quite often in cases when 2D and 3D idealized tissue models are used, the meandering scroll waves terminates when its filament reaches an edge. In the AF1 case, the scroll wave had a small wavelength, but the mother rotor degenerated into smaller wavelets. These wavelets continued to sustain erratic electrical activity throughout the homogenous model. A mother rotor was seen to emerge after about 2100 ms. In the AF2 case, the scroll wave was persistent and it meandered in a very small region leading to a sustained reentrant excitation driven by mother motor with lifespan more than the 3000 ms of simulation duration. In the control case, however, when trapped by an anatomical obstacle, the meandering scroll wave could also be stabilized with its filament rotating around the circumference of an anatomical obstacle. This is shown in Figure 5, where the scroll wave was trapped to the SVC orifice, became highly localized and persisted throughout the simulation. In this case, while the mother rotor was trapped by the SVC, the arm of this scroll wave continued to activate atrial tissue close to the SVC at a high rate. This gave rise to alternans type excitations, as shown by the AP profiles registered at various locations (Figure 6). Alternans were not observed in the AF1 or AF2 case, however the AP profiles indicate excitation at a much higher rate in the AF cases as compared to control.

4 Conclusion

Our simulation results have shown that AFER shortened atrial APD and increased the maximal slopes of APDR. It reduced atrial ERP and the intra-atrial conduction velocity, all of which facilitated high rate atrial excitation and conduction as one would observe during AF. This suggested the pro-arrhythmic effects of AFER. In the 3D simulations, scroll waves underwent a large meander in the control case. Such non-stationary scroll wave may self-terminate unless entrapped by anatomical obstacles formed by opening holes of valves. After being entrapped, the reentry sustained and acted as a mother motor to drive and pace atrial excitation. AFER stabilized reentry and reduced its meandering region. In this case, reentry became more stationary and persistent, though it broke up leading to multiple wavelets (in the AF1 case). When this occurred, atria had erratic electrical excitation activity with much higher rates resembling the disordered and irregular electrical activity as shown by ECG in AF patients. The simulated scroll waves have different dynamical behaviors under the AF1 and AF2 conditions, which may reflect the different stages of AF patients [2, 3, 20]. Further investigations are required to underpin such differences, though partial explanation can be related to the AFER-induced changes in the maximal slopes of APDr curves, which is larger in AF1 than in AF2. A large

APDr slop has been linked to unstable reentrant excitations [18, 19]. We concluded that AFER is pro-arrhythmic, helps to perpetuate and sustain re-entrant excitation in atria. This study provides first evidence in support of the hypothesis of AF begetting AF [2, 3].

Acknowledgments. This work was supported by British Heart Foundation (PG/03/140), BBSRC UK (BBS/B/1678X), the European Union BioSim Network of of Excellence (contract number LSHB-CT-2004-005137), and the Chinese NSFC (60571025) and 863 Program (2006AA01Z308).

References

1. Lip, G.Y.: Tello-Montoliu H. Management of atrial fibrillation. Heart. 92, 1177–1182 (2006)
2. Bosch, R.F., Zeng, X., Grammer, J.B., Popovic, C.M., Kuhlkamp, V.: Ionic mechanisms of electrical remodeling in human atrial fibrillation. Cardiovascular Res. 44, 121–131 (1999)
3. Workmanm, A.J., Kane, K.A., Rankin, A.C.: The contribution of ionic currents to changes in refractoriness of human atrial myocytes associated with chronic atrial fibrillation. Cardiovascular Res. 52, 226–235 (2001)
4. Jongsma, H.J., Wilders, R.: Gap junctions in cardiovascular disease. Circ. Res. 86, 1193–1197 (2000)
5. Rostock, T., O'Neill, M.D., Takahashi, Y., Sanders, P., Haissaguerre, M.: Interactions between two simultaneous tachycardias within electrically isolated pulmonary veins. J. Cardiovsac. Electrophysiol. 18, 441–445 (2007)
6. Huang, C.X., Hu, C.L., Li, Y.B.: Atrial fibrillation may be a vascular disease: The role of pulmonary veins. Med. Hypotheses 68(3), 629–634 (2007)
7. Kamanu, S., Tan, A.Y., Peter, C.T., Hwang, C., Chen, P.S.: Vein of Marshall activity during sustained atrial fibrillation. J. Cardiovasc. Electrophysiol. 17(8), 839–846 (2006)
8. Nattel, S., Carlsson, L.: Innovative approach to anti-arrhythmic drug therapy. Nat. Rev. Drug Discov. 5(12), 1034–1049 (2006)
9. Hersi, A., Wyse, D.G.: Medical management of atrial fibrillation. Curr. Cardiol. Rep. 8(5), 323–329 (2006)
10. Verdino, R.J.: The evolution of atrial fibrillation ablation from triggers to substrate. J. Electrocardiol. 39(4), S184–S187 (2006)
11. Purerfellner, H., Aichinger, J., Martinek, M., Nesser, H., Janssen, J.: Short- and long-term experience in pulmonary vein segmental ostial ablation for paroxysmal atrial fibrillation. Indian Pacing Electrophysiol. J. 6(1), 6–16 (2006)
12. Lazar, S., Dixit, S., Callans, D.J., Lin, D., Marchlinski, F.E., Gerstenfeld, E.P.: Effect of pulmonary vein isolation on the left-to-right atrial dominant frequency gradient in human atrial fibrillation. 3(8), 889–895 (2006)
13. Sulke, N., Sayers, F., Lip, G.Y.: Rhythm control and cardioversion. Heart 93(1), 29–34 (2007)
14. Courtemanche, M., Ramirez, R.J., Nattel, S.: Ionic mechanisms underlying human atrial action potential properties: insights from a mathematical model. Am. J. Physiol. 275, H301–H321 (1998)

15. Seemann, G., Hoper, C., Sachse, F.B., Dossel, O., Holden, A.V., Zhang, H.: Heterogeneous three-dimensional anatomical and electrophysiological model of human atria. Phil. Trans. A. 364, 1465–1481 (2006)
16. Biktasheva, I.V., Biktashev, V.N., Holden, A.V.: Self-termination of spiral waves in a model of human atrial tissue. In: Frangi, A.F., Radeva, P.I., Santos, A., Hernandez, M. (eds.) FIMH 2005. LNCS, vol. 3504, pp. 293–303. Springer, Heidelberg (2005)
17. Hanson, C., Jonson, Ch.: The visualization handbook. Elsevier, Butterworth-Heinemann (2005)
18. Byung-Soo, K., Young-Hoon, K., Gyo-Seung, H., Hui-Nam, P., Sang Chil, L., Wan Joo, S., Dong Joo, O., Young Moo, R.: Action potential duration restitution kinetics in human atrial fibrillation. J. Am. Col. Cardiol. 39(8), 1329–1336 (2002)
19. Xie, F., Qu, Z., Garfinkel, A., Weiss, J.: Electrical refractory period restitution and spiral wave reentry in simulated cardiac tissue. Am. J. Physiol. Heart Circ. Physiol. 283, 448–460 (2002)
20. Zhang, H., Garratt, C.J., Zhu, J., Holden, A.V.: Role of up-regulation of IK1 in action potential shortening associated with atrial fibrillation in humans. Cardiovasc Res. 66, 493–502 (2005)

Determining Recovery Times from Transmembrane Action Potentials and Unipolar Electrograms in Normal Heart Tissue

Piero Colli Franzone[1], Luca F. Pavarino[2], Simone Scacchi[1], and Bruno Taccardi[3]

[1] Dipartimento di Matematica, Universitá di Pavia and IMATI-CNR
Via Ferrata 1, 27100 Pavia, Italy
colli@imati.cnr.it
[2] Dipartimento di Matematica, Universitá di Milano,
Via Saldini 50, 20133 Milano, Italy
pavarino@mat.unimi.it
[3] Cardiovascular Research and Training Institute, University of Utah,
Salt Lake City, Utah
taccardi@cvrti.utah.edu

Abstract. In this study, we quantitatively analyze some frequently used markers of recovery time, derived from the transmembrane action potentials and from unipolar extracellular electrograms. To this end, we performed 3D numerical simulations by using the anisotropic bidomain model of normal cardiac tissue, coupled with the Luo-Rudy phase I membrane model. We show that the extracellular markers considered are very accurate estimates of (and very well correlated with) the transmembrane action potential markers of the repolarization phase, irrespective of T-wave polarity, repolarization sequence, and transmural distribution of intrinsic properties of the cell membrane.

1 Introduction

Determining activation and repolarization times on the cardiac surface and in the thickness of the ventricular walls is one of the main purposes of experimental and clinical cardiac electrophysiology. It has been well established that life-threatening cardiac arrhythmias are often associated with abnormal conduction and/or recovery times and high spatial gradients of recovery times and action potential durations. While methods for determining activation times from electrographic signals recorded directly from the heart have been firmly established during the past century, see e.g. [13,14] and recently refined [12], there are still uncertainties and controversies about the best method for determining recovery times.

The assessment of local repolarization is related to some time indexes associated to the downstroke of the transmembrane or monophasic [7] action potentials. Widely used markers are the time of the minimum derivative and the time where the potential reaches 90% of its resting value; these two markers are

F.B. Sachse and G. Seemann (Eds.): FIMH 2007, LNCS 4466, pp. 139–149, 2007.

generally considered to be the best standards for evaluating other markers that assess repolarization from extracellular unipolar recordings. In fact, transmembrane or monophasic action potentials can not be performed extensively in *in vivo* measurements and only the unipolar extracellular electrograms are practicable when studying the excitation and repolarization sequences on a large volume of a beating heart in *in vivo* experiments. Therefore, it is important to validate methods for assessing the local repolarization time from unipolar electrograms.

The most widely accepted method, based on the assumption that repolarization behaves as a plane traveling wave, consists of determining the time of occurrence of the *maximum time derivative* RT_{ue} during the T-wave in the unipolar electrogram [17,10]. Experimental measurements and computer simulations have confirmed that this marker is highly correlated with the minimum time derivative RT_v of the transmembrane potential. However, in 1991 Chen et al. [2] compared the recovery times yielded by the maximum derivative method with the time when a monophasic potential reaches 90% of the resting value during the downstroke phase and concluded that when the unipolar T-wave was positive, a better choice was the time of *minimum derivative* RT_{Chen} during the decreasing portion of the T-wave, see also [8,19]. Recent experimental work by Coronel et al. [6] reached opposite conclusions. On the other hand, Steinhaus [15], using a unidimensional model simulating a linear strand of heart muscle, showed that the method of the maximum derivative could produce significant errors in case of wave collisions and inhomogeneous membrane properties of the individual fibers in the model. We also considered the *minimum second time derivative* $\mathrm{RTd2}_{ue}$ during the T-wave as an estimate of the time $\mathrm{RT90}_v$ when the transmembrane potential reaches 90% of the resting value during the downstroke phase. The applicability of these markers to experimental noisy data will be investigated in future work.

To our knowledge, an extensive quantitative analysis of the discrepancies and limitations of these extracellular markers of repolarization time is not available in the literature. The goal of this work is to fully estimate the matching of transmembrane and extracellular potential markers by means of 3D simulations using the *bidomain* model coupled with the Luo-Rudy phase I system for the ionic membrane currents. We simulate the three-dimensional propagation of the activation and repolarization sequences taking into account: the rotating anisotropic structure of the fibers layers; different local stimulation sites in a slab with homogeneous properties of the cell membranes; transmural heterogeneity of the properties of the cell membranes resulting in different action potential duration (APD). Our results show that RT_{ue} and $\mathrm{RTd2}_{ue}$ are very accurate estimates of RT_v and $\mathrm{RT90}_v$, respectively, independently of T-wave polarity, repolarization sequence, and transmural intrinsic properties of the cell membrane.

2 Mathematical Models and Methods

Cardiac bidomain - LR1 model. In the bidomain model, the cardiac tissue is conceived as the superposition of two averaged continuous media, the intra and

the extracellular medium, whose anisotropy is characterized by the conductivity tensors $D_i(\mathbf{x})$ and $D_e(\mathbf{x})$. The intra and extracellular electric potentials u_i, u_e are described by a reaction-diffusion system, coupled with a system of ODEs for ionic gating variables $w \in R^Q$ and for the ions concentration $c \in R^p$; in this paper, we consider the phase I Luo-Rudy (LR1) model [9]. Denoting by $v = u_i - u_e$ the transmembrane potential then the bidomain model for an insulated cardiac domain Ω can be written as the following reaction-diffusion system:

$$\begin{cases} c_m \partial_t v - \operatorname{div}(D_i \nabla u_i) + i_{ion}(v,w) = i^i_{app} \\ -c_m \partial_t v - \operatorname{div}(D_e \nabla u_e) - i_{ion}(v,w) = -i^e_{app} \\ \partial_t w - R(v,w) = 0, \qquad\qquad w(\mathbf{x},0) = w_0(\mathbf{x}), \\ \partial_t c - S(v,w,c) = 0, \qquad\qquad c(\mathbf{x},0) = c_0(\mathbf{x}), \\ \mathbf{n}^T D_i \nabla u_i = 0, \quad \mathbf{n}^T D_e \nabla u_e = 0, \; v(\mathbf{x},0) = v_0(\mathbf{x}), \end{cases}$$

where $\partial_t = \partial/\partial t$, $c_m = \chi * C_m$, $i_{ion} = \chi * I_{ion}$, with χ the ratio of membrane area per tissue volume, C_m the surface capacitance and I_{ion} the ionic current of the membrane per unit area. The conductivity tensors are given by $D_{i,e} = \sigma_l^{i,e}\, \mathbf{a}_l \mathbf{a}_l^T + \sigma_t^{i,e}\, \mathbf{a}_t \mathbf{a}_t^T + \sigma_n^{i,e}\, \mathbf{a}_n \mathbf{a}_n^T$, where $\sigma_l^{i,e},\ \sigma_t^{i,e},\ \sigma_n^{i,e}$ are the conductivity coefficients measured along the corresponding directions $\mathbf{a}_l(\mathbf{x})$ (along fiber), $\mathbf{a}_t(\mathbf{x})$, $\mathbf{a}_n(\mathbf{x})$ (tangent and orthogonal to the radial laminae, respectively and both transversal to the fiber axis). We assume that the cardiac fibers rotate counterclockwise from epicardium to endocardium and have a laminar organization; see [3].

Repolarization time markers. In Table 1 are defined the activation time (AT), the repolarization time (RT), the activation-recovery interval (ARI) and the action potential duration (APD) markers related to both the extracellular waveforms u_e and the transmembrane potential v. The markers based on v are assumed to be the *reference times* of the cardiac cellular repolarization process.

Table 1. Definition of the AT, RT, ARI and APD markers

Transmembrane potential markers		Extracellular potential markers	
$\mathbf{AT}_v(x)$	$= \underset{t \in upstroke}{\operatorname{argmax}}\ \partial_t v(x,t)$	$\mathbf{AT}_{ue}(x)$	$= \underset{t \in QRScomplex}{\operatorname{argmin}}\ \partial_t u_e(x,t)$
$\mathbf{RT}_v(x)$	$= \underset{t \in downstroke}{\operatorname{argmin}}\ \partial_t v(x,t)$	$\mathbf{RT}_{ue}(x)$	$= \underset{t \in Twave}{\operatorname{argmax}}\ \partial_t u_e(x,t)$
$\mathbf{RT90}_v(x)$	$= t \in downstroke : v(x,t) = 0.9\, v_{rest}$	$\mathbf{RTd2}_{ue}(x)$	$= \underset{t \in Twave}{\operatorname{argmin}}\ \partial_{tt} u_e(x,t)$
$\mathbf{APD}(x)$	$= \mathbf{RT}_v(x) - \mathbf{AT}_v(x)$	$\mathbf{ARI}(x)$	$= \mathbf{RT}_{ue}(x) - \mathbf{AT}_{ue}(x)$
$\mathbf{APD90}(x)$	$= \mathbf{RT90}_v(x) - \mathbf{AT}_v(x)$	$\mathbf{ARId2}(x)$	$= \mathbf{RTd2}_{ue}(x) - \mathbf{AT}_{ue}(x)$

Numerical methods. The cardiac domain Ω considered is a cartesian slab of dimensions $2 \times 2 \times 0.5\ cm^3$ modeling a portion of the left ventricle. In all computations, a structured grid of $200 \cdot 200 \cdot 50$ hexahedral isoparametric Q_1 elements of size $h = 0.1\ mm$ was used in space in order to avoid numerical artifacts in the electrograms, see [5]. The time discretization is based on an Euler Imex method. We used the PETSc parallel library [1] in order to ensure

the parallelization and portability of our code, run on a Linux Cluster with 92 Xeon 2.4 GHz processors at the Math. Department of the University of Milan (www.ulisse.mat.unimi.it). Each simulation required about 21 - 24 h on 36 processors; further numerical details can be found in [3,4]. For our slab geometry, using the cartesian coordinate system $\{\mathbf{x}_1, \mathbf{x}_2, \mathbf{x}_3\}$, we choose $\mathbf{a}_t = \mathbf{e}_3$ and $\mathbf{a}_l(\mathbf{x}) = \mathbf{e}_1 \cos\alpha(x_3) + \mathbf{e}_2 \sin\alpha(x_3)$, $\mathbf{a}_n(\mathbf{x}) = -\mathbf{e}_1 \sin\alpha(x_3) + \mathbf{e}_2 \cos\alpha(x_3)$, where the angle $\alpha(x_3)$ prescribe the transmural fiber rotation, which is linear and counterclockwise from epicardium (-45^o) to endocardium (45^o), for a total amount of 90^o. The bidomain parameters are: $\chi = 10^3\ cm^{-1}, C_m = 10^{-3}\ mF/cm^2$, $\{\sigma_l^e, \sigma_l^i, \sigma_t^e, \sigma_t^i\} = \{2,\ 3,\ 1.35,\ 0.315\}\ m\Omega^{-1}cm^{-1}$ and $\sigma_n^e = \sigma_t^e/2,\ \ \sigma_n^i = \sigma_t^i/10$. These calibration parameters yields ideal plane wavefronts propagating along $\mathbf{a}_l(\mathbf{x}), \mathbf{a}_t(\mathbf{x}), \mathbf{a}_n(\mathbf{x})$ with velocities 60, 25, 10 $cm\ sec^{-1}$, respectively. The initial conditions are at the rest and we apply an appropriate stimulus on a small area (3 or 5 mesh points in each direction), set differently depending on the simulation. The reference potential is chosen to be the average extracellular potential on the slab volume, i.e. $\int_\Omega u_e(\mathbf{x}, t)dx = 0$. In each simulation, we saved the extracellular and transmembrane potential waveforms $u_e(x, t)$ and $v(x, t)$ at 36×11 nodes located in 6×6 points distributed on 11 intramural planes parallel to the endocardial surface. We postprocess the 36×11 waveforms for u_e and v, computing all the activation, repolarization, ARI and APD markers defined above. From this volume of data, we extract the following quantities for RT_{ue} ($\mathrm{RTd2}_{ue}$) vs RT_v ($\mathrm{RT90}_v$) and the related ARI vs APD: the average absolute difference *mean*, the associated standard deviation *std* and the correlation coefficients *corr* and $r2 = corr^2$.

3 Results and Discussion

We consider three different types of transmural distribution of the intrinsic APDs of the cells, one homogeneous (H-slab) and the other two heterogeneous (3-slab and W-slab). The transmural intrinsic heterogeneity is assumed to be the same along any transmural epi-endocardial straight line, i.e. in any plane parallel to the epicardium all cells have the same intrinsic APD. In the heterogeneous slabs, the intrinsic APD of the cells is obtained by multiplying the potassium current I_K in the LR1 model by a factor fact_{I_K}, as detailed in Table 2. This modulation factor is chosen in order to introduce a transmural APD profile with M-cell layers as in [16] (3-slab) or as in [18, Fig. 4], [11, Fig. 5] (W-slab), to mimic their experimental transmural APD profile; see [4] for more details.

H-slab. In case of H-slab we performed three simulations, with three different endocardial stimulation procedures: single central stimulus (H-slab_1), single left bottom vertex stimulus (H-slab_2) and two stimuli, one central and the other at the vertex (H-slab_3). Fig. 1 (a) reports the AT_v on the endocardial, midmyocardial and epicardial intramural sections (first row), the $\mathrm{RT90}_v$ on the same intramural sections (second row) and the AT_v and $\mathrm{RT90}_v$ on the diagonal transmural section parallel to the endocardial fiber direction, relative to the H-slab_3 simulation. Fig. 1 (b) shows the v and u_e waveforms in the 6 epicardial points

Table 2. Parameter calibration for modeling the transmural heterogeneities

slab type	H-slab	3-slab			W-slab			
number of layers	1	3			4			
		endo	mid	epi	endo	sub-endo	mid	epi
layer thickness (cm)	0.5	0.17	0.17	0.16	0.05	0.05	0.35	0.05
fact_I_K	1	2.62	1.95	2.88	2.71	1.95	2.47	2.88
APD (ms)	266	235	272	225	232	272	242	225

Table 3. H-slab: comparisons RT_v vs RT_{ue} and APD vs ARI over 396 exploring sites. mean:= average absolute difference $|RT_v\text{-}RT_{ue}|$ (|APD-ARI|), std:= standard deviation of the previous difference with respect to mean, max:= maximum of RT_v-RT_{ue} (APD-ARI), min:= minimum of RT_v-RT_{ue} (APD-ARI), corr:= correlation coefficient corr(RT_v,RT_{ue}) (corr(APD,ARI)) and r2:= $corr^2$.

simulation	comparison	mean	std	max	min	corr	r2
H-slab_1 central stim.	RT_v vs RT_{ue}	1.8585	1.1191	4.4178	-3.8153	0.9791	0.9586
	APD vs ARI	1.8736	1.1433	4.6678	-3.8153	0.3090	0.0955
	$RT90_v$ vs $RTd2_{ue}$	1.1181	0.7732	1.0040	-3.2129	0.9931	0.9863
	APD90 vs ARId2	1.1153	0.7684	1.1032	-3.2129	0.8582	0.7366
H-slab_2 vertex stim.	RT_v vs RT_{ue}	1.5982	1.3858	7.2259	-2.9846	0.9927	0.9854
	APD vs ARI	1.6002	1.3859	7.2259	-2.9846	0.6153	0.3785
	$RT90_v$ vs $RTd2_{ue}$	1.2285	0.8068	1.4137	-3.7700	0.9980	0.9961
	APD90 vs ARId2	1.2282	0.8067	1.4137	-3.7700	0.8833	0.7802
H-slab_3 2 stim.	RT_v vs RT_{ue}	2.2628	1.3029	6.8048	-3.9396	0.9509	0.9042
	APD vs ARI	2.2606	1.3044	6.8048	-3.9896	0.5287	0.2796
	$RT90_v$ vs $RTd2_{ue}$	1.3715	0.9408	2.3279	-3.9396	0.9768	0.9542
	APD90 vs ARId2	1.3700	0.9388	2.3279	-3.9396	0.8631	0.7450

Table 4. 3-slab and W-slab: comparisons RT_{ue} vs RT_v and ARI vs APD. Same format as in Table 3.

simulation	comparison	mean	std	max	min	corr	r2
3-slab	RT_v vs RT_{ue}	2.4708	1.5845	7.0832	-4.9774	0.9797	0.9599
	APD vs ARI	2.4704	1.5845	7.0832	-4.9774	0.9159	0.8389
	$RT90_v$ vs $RTd2_{ue}$	1.2332	0.9803	4.9774	-3.6373	0.9898	0.9798
	APD90 vs ARId2	1.2333	0.9799	4.9774	-3.6373	0.9702	0.9414
W-slab	RT_v vs RT_{ue}	2.2303	1.4418	6.8843	-4.4545	0.9785	0.9575
	APD vs ARI	2.2294	1.4427	6.8843	-4.4545	0.9207	0.8477
	$RT90_v$ vs $RTd2_{ue}$	0.9341	0.6329	2.6322	-2.4297	0.9941	0.9883
	APD90 vs ARId2	0.9342	0.6332	2.6322	-2.4297	0.9825	0.9654

indicated in Fig. 1 (a), showing typical performances of RT_{ue} for different T-wave polarity. Table 3 summarizes the comparison between the recovery markers in the three H-slab cases. The results show that, irrespective of the simulated repolarization sequence, the average discrepancy of RT_{ue} and RT_v ($RTd2_{ue}$ and

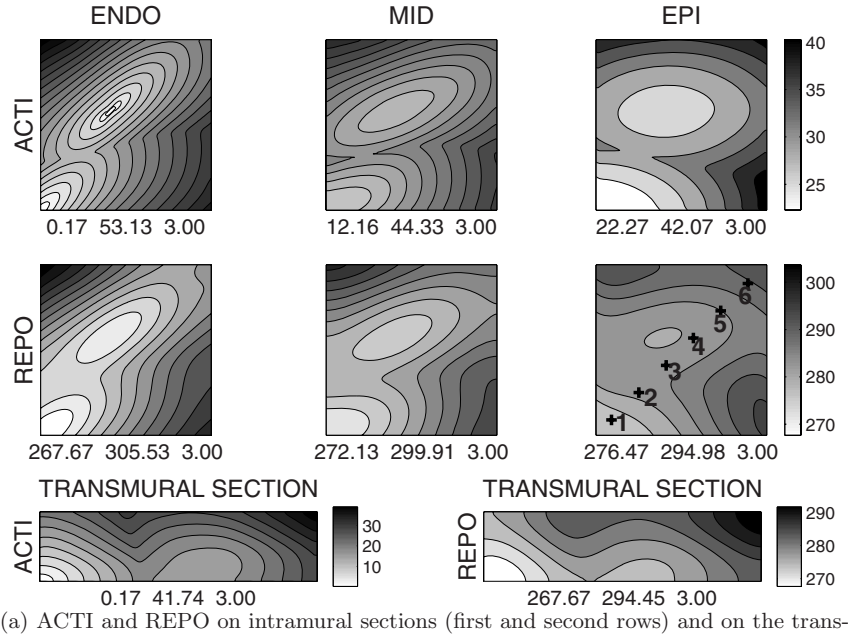

(a) ACTI and REPO on intramural sections (first and second rows) and on the transmural diagonal section perpendicular to the epicardium and passing through the sites indicated in the REPO-EPI panel (third row). Maximum, minimum and step of the displayed map are reported below each panel.

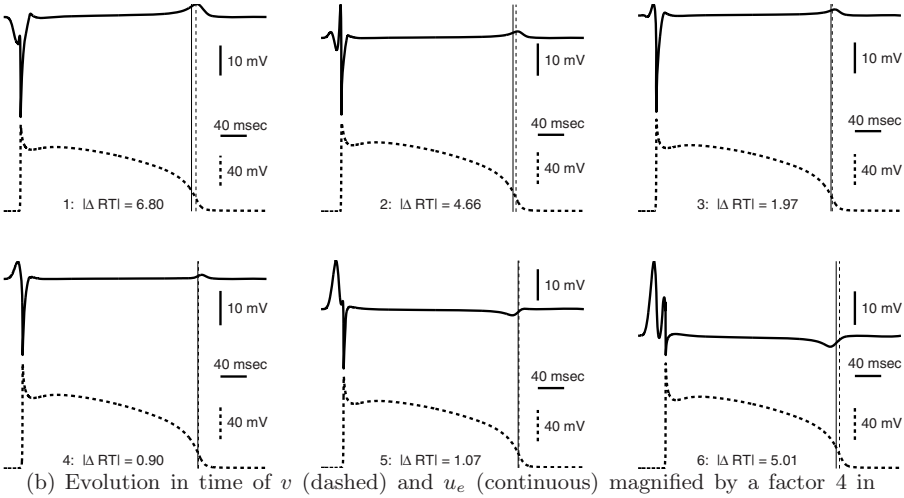

(b) Evolution in time of v (dashed) and u_e (continuous) magnified by a factor 4 in the 6 epicardial points on the secondary diagonal indicated above in (a), REPO - EPI panel. $|\Delta RT| = |RT_v - RT_{ue}|$.

Fig. 1. H-slab with 2 stimulation points

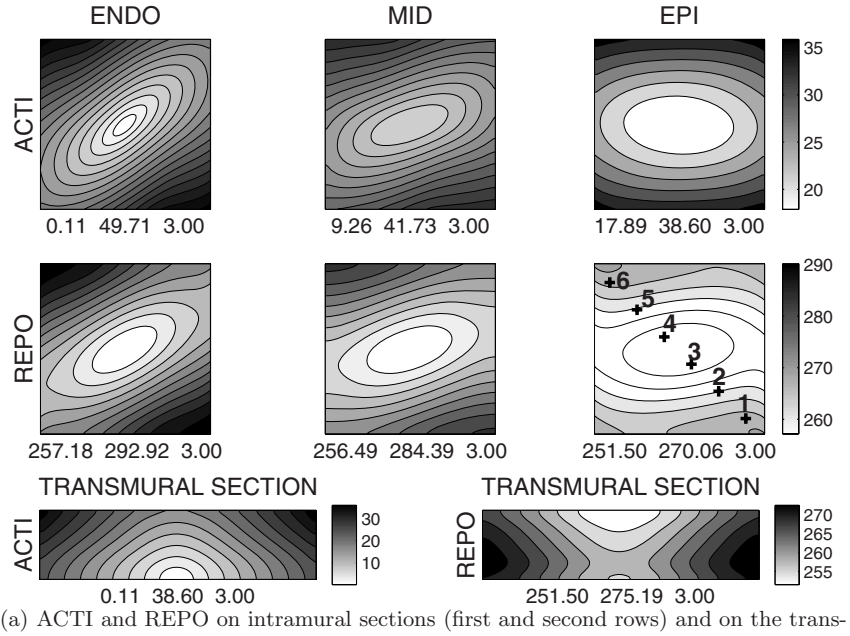

(a) ACTI and REPO on intramural sections (first and second rows) and on the transmural diagonal section perpendicular to the epicardium and passing through the sites indicated in the REPO-EPI panel (third row). Maximum, minimum and step of the displayed map are reported below each panel.

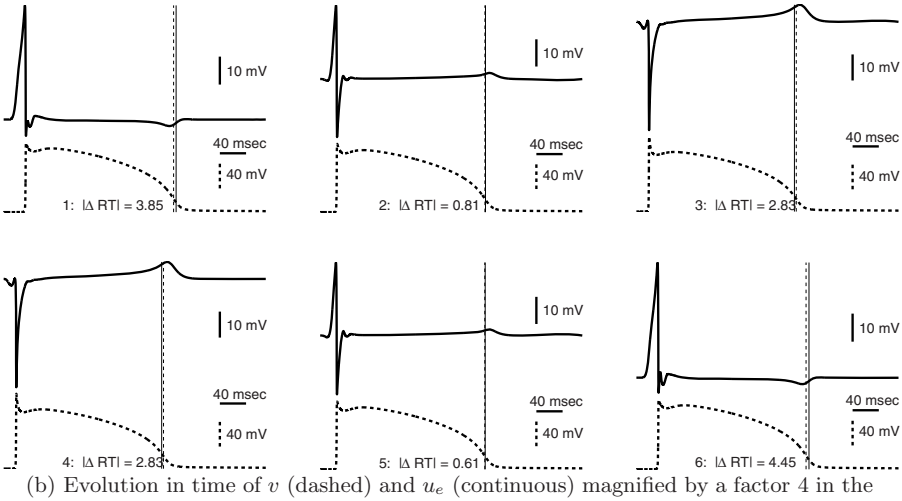

(b) Evolution in time of v (dashed) and u_e (continuous) magnified by a factor 4 in the 6 epicardial points on the main diagonal indicated above in (a), REPO - EPI panel. $|\Delta RT| = |RT_v - RT_{ue}|$.

Fig. 2. W-slab with central stimulation

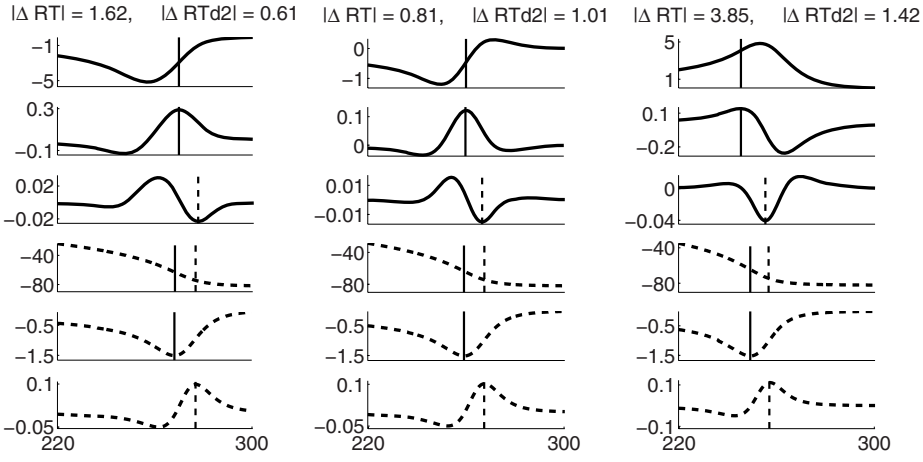

Fig. 3. T-wave zoom of u_e (first row), u_e time derivative (second row), u_e second time derivative (third row), v (fourth row), v time derivative (fifth row), v second time derivative (sixth row) in points 1,2,3 of Fig. 2 at distance 0.4 cm from the epicardium in W-slab. Point 1 (first column) has negative T-wave; point 2 (second column) has biphasic T-wave, point 3 (third column) has positive T-Wave.

$\mathrm{RT90}_v$) is less than 2.3 (1.4) ms, with a *std* less than 1.4 (0.98) ms. The same quantitative estimates apply to ARI and APD (ARId2 and APD90). Thus, the two extracellular markers RT_{ue} and $\mathrm{RTd2}_{ue}$ are accurate measures of RT_v and $\mathrm{RT90}_v$, respectively, and are highly reliable regardless of the polarity of the T-wave (positive monophasic, biphasic, negative monophasic). Analogously, ARI and ARId2 are accurate measures of APD and APD90, respectively, regardless of T-wave polarity. The maximal discrepancy of about 7.5 ms for RT_{ue} and of 2.5 ms for $\mathrm{RTd2}_{ue}$ occurs in an area near the stimulation site (the region repolarized first in H-slab) and in the front-boundary collision zones (the epicardial breakthrough areas). Similar localized errors had been found by Steinhaus [15] using a 1D model of propagation for estimating the influence of various factors affecting the performance of RT_{ue}. In spite of these localized discrepancies, our quantitative comparison validates the use of these extracellular markers to infer with satisfactory accuracy the associated transmembrane repolarization times.

3-slab and W-slab. In both these simulations, the stimulus was applied at the center of the endocardial surface. Table 4 contains the comparison between the markers for both the 3-slab and W-slab cases, using the same format of Table 3. With respect to the homogeneous H-slab, adding transmural heterogeneity yields a slight increase of both the average and maximum discrepancies for the RT_{ue} marker, while for the $\mathrm{RTd2}_{ue}$ marker only an increased maximum discrepancy amounting to 5 ms is observed. The location and origin of the maximum discrepancies are analogous to the H-slab. The markers accuracy does not seem to be correlated with the interaction between the fiber direction and the

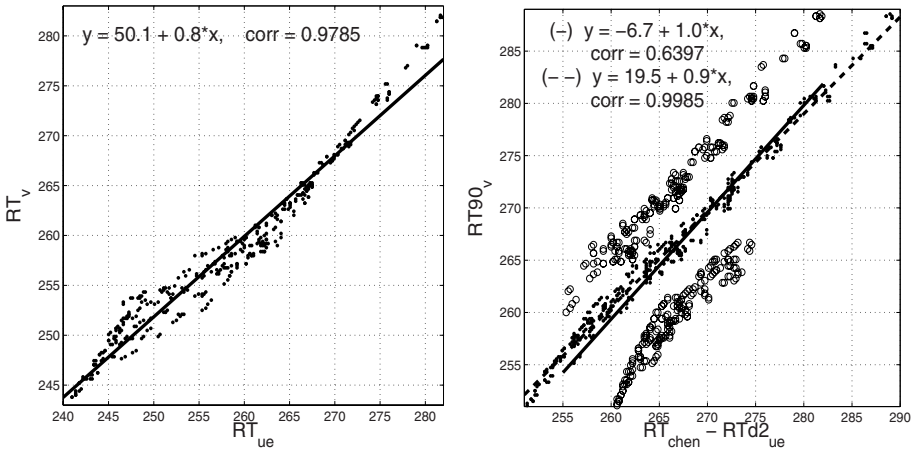

Fig. 4. W-slab: results of linear regression comparing RT_v vs RT_{ue} (left), $\mathrm{RT90}_v$ vs $\mathrm{RTd2}_{ue}$ (•) and $\mathrm{RT90}_v$ vs RT_{Chen} (o) (right)

local repolarization front. Fig. 2 (a) displays the activation and repolarization sequences and Fig. 2 (b) shows the v and u_e waveforms in the 6 epicardial points indicated in Fig. 2 (a). Fig. 3 reports T-wave zooms of u_e, v and their first and second time derivatives, showing the typical accuracy of our markers in three sites of W-slab with positive, negative and biphasic T-wave. In addition to the strict correlation between $\mathrm{RT90}_v$ and $\mathrm{RTd2}_{ue}$, this figure shows that the maximum second time derivative of v is also strictly correlated with the previous two markers. Fig 4 shows the linear regression fitting for RT_v vs. RT_{ue} (left), $\mathrm{RT90}_v$ vs $\mathrm{RTd2}_{ue}$ and $\mathrm{RT90}_v$ vs RT_{Chen} (right) for W-slab. Summarizing, the markers $\mathrm{RTd2}_{ue}$and RT_{ue} exhibit an average error, with respect to their best reference times, less than 2.5 and 1.3 ms respectively, with *std* less than 1.6 and 0.98 ms. Hence, $\mathrm{RTd2}_{ue}$ and RT_{ue} accurately signify $\mathrm{RT90}_v$ and RT_v, respectively, with a slightly better performance of the former. We also considered a variant RT_{Chen} of the RT_{ue} marker, proposed in Chen et al. [2], that uses the *time of minimum derivative* of u_e (instead of the maximum) when the T-wave is positive. This strategy yields two different estimates of $\mathrm{RT90}_v$ clearly visible in Fig. 4 (right panel), separated by the regression line (continuous), having a low global correlation coefficient. This marker produced worse estimates of $\mathrm{RT90}_v$ than our $\mathrm{RTd2}_{ue}$, with average discrepancy 6.26 ms and *std* 1.45 ms. Moreover, the $\mathrm{RTd2}_{ue}$ estimate of $\mathrm{RT90}_v$ exhibits a high correlation, confirmed by the regression line (dotted) also displayed in Fig. 4. The overall comparison shows that RT_{ue} and $\mathrm{RTd2}_{ue}$ are best estimates of RT_v and $\mathrm{RT90}_v$, respectively, regardless of T-wave polarity, repolarization sequence, and transmural intrinsic properties of the cell membrane.

In future work, we will address the performance of the extracellular markers in abnormal conditions associated to disease states, such as ischemic regions, the influence of more complex ionic models and of a surrounding bath.

References

1. Balay, S., et al.: PETSc Users Manual. ANL TR anl-95/11 - rev. 2.1.5, `http://www.mcs.anl.gov/petsc` (2002)
2. Chen, P.-S., et al.: Epicardial activation and repolarization patterns in patients with right ventricular hypertrophy. Circulation, 83, 104–118 (1991)
3. Colli Franzone, P., Pavarino, L.F.: A parallel solver for reaction-diffusion systems in computational electrocardiology. Math. Mod. Meth. Appl. Sci (M3AS) 14(6), 883–911 (2004)
4. Colli Franzone, P., Pavarino, L.F., Taccardi, B.: Effects of transmural electrical heterogeneities and electrotonic interactions on the dispersion of cardiac repolarization and action potential duration: A simulation study. Math. Biosci. 204(1), 132–165 (2006)
5. Colli Franzone, P., Pennacchio, M., Guerri, L.: Accurate computation of electrograms in the left ventricular wall. Math. Mod. Meth. Appl. Sci (M3AS) 10(4), 507–538 (2000)
6. Coronel, R., et al.: Monophasic action potentials and activation recovery intervals as measures of ventricular action potential duration: Experimental evidence to resolve some controversies. Heart Rhythm 3(9), 1043–1050 (2006)
7. Franz, M.R.: Monophasic Action Potentials: Bridging Cells to Bedside. Futura Publishing Company, Armonk NY (2000)
8. Gepstein, L., Hayam, G., Ben-Haim, S.A.: Activation-recovery coupling in the normal swine endocardium. Circulation 96(11), 4036–4043 (1997)
9. Luo, C., Rudy, Y.: A model of the ventricular cardiac action potential: depolarization, repolarization, and their interaction. Circ. Res. 68, 1501–1526 (1991)
10. Haws, C.W., Lux, R.L.: Correlation between in vivo transmembrane action potential durations and activation–recovery intervals from electrograms. Circulation 81, 281–288 (1990)
11. Poelzing, S., Rosenbaum, D.S.: Heterogeneous connexin43 expression produces electrophysiological heterogeneities across ventricular wall. Am. J. Physiol (Heart Circ. Physiol) 286, H2001–H2009 (2004)
12. Punske, B.B., et al.: Spatial methods of epicardial activation time determination in normal hearts. Ann. Biomed. Engrg. 31(7), 781–792 (2003)
13. Spach, M.S., et al.: Extracellular potentials related to intracellular action potentials in the dog Purkinje system. Circ. Res. 30, 505–519 (1972)
14. Spach, M.S., Dolber, P.C.: Relating extracellular potentials and their derivatives to anisotropic propagation at microscopic level in human cardiac muscle. Evidence for electrical uncoupling of side-to-side fiber connections with increasing age. Circ. Res. 58, 356–371 (1986)
15. Steinhaus, B.M.: Estimating cardiac transmembrane activation and recovery times from unipolar and bipolar extracellular electrograms: a simulation study. Circ. Res. 64(3), 449–462 (1989)
16. Viswanathan, P.C., et al.: Effects of I_{Kr} and I_{Ks} heterogeneity on action potential duration and its rate dependence. Circulation 99, 2466–2474 (1999)

17. Wyatt, R.P.: Comparison of estimates of activation and recovery times from bipolar and unipolar electrograms to in vivo transmembrane action potential durations. In: Proc. IEEE/Eng. Med. Biol. Soc. 2nd Ann. Conf. Washington, DC, pp. 22–25 (1980)
18. Yan, G.X., et al.: Characteristics and distribution of M cells in arterially perfused canine left ventricular wedge preparations. Circulation 98, 1921–1927 (1998)
19. Yue, A.M., et al.: Determination of human ventricular repolarization by noncontact mapping. Validation with monophasic action potential recordings. Circulation 110, 1343–1350 (2004)

Simulations of Cardiac Electrophysiological Activities Using a Heart-Torso Model

Heye Zhang[1], Linwei Wang[1], and Pengcheng Shi[1,2]

[1] Department of Electronic and Computer Engineering,
Hong Kong University of Science and Technology, Hong Kong
[2] School of Biomedical Engineering, Southern Medical University, Guangzhou, China

Abstract. Much attention has been drawn to adopt complicated and realistic physiological models for simulating cardiac electrophysiological activities with abundant computing resources for quite a long time. However, to incorporate these physiological meaningful models into the recovery/inverse framework for estimating patient-specific cardiac electrophysiological activities always needs to handle excessive computational loads caused by the complexities of models. Thus, a balance should be found between physiological meaningfulness and computational feasibility for the recovery/inverse framework. In this paper, a novel numerical scheme, combination of meshfree method and BEM (boundary element method), is proposed to simulate intracardiac and extracardiac electrophysiological activities, which is aimed to provide physiological meaningful simulations with feasible computation for our recovery/inverse approaches. In our simulations, intracardiac electrophysiological activities (transmembrane potentials, TMPs) are obtained by solving a modified Fitzhugh-Nagumo (FHN) model using the meshfree method, and then extracardiac electrophysiological activities (body surface potentials, BSPs) are calculated using BEM. Moreover, we demonstrate the ability of our meshfree-BEM framework through favorable results.

1 Introduction

Estimation of electrophysiological activities in the heart from potentials measured on the torso surface or medical images is a very ill-posed problem. But this inverse problem has attracted great interest in the electrophysiological community because of immediate clinical impact, and many efforts have been developed with fair results in the past [9,13,16,19]. Recently we proposed a model-based recovery framework to handle the electrophysiological inverse problem using BSPs and image sequences, and achieved promising outcomes [18,21]. In our multiframe recovery framework, the physiological meaningful and computational feasible model is a key issue, which should be carefully designed. In this paper, we describe the construction of an efficient physiological framework by taking advantages of the meshfree method and BEM to simulate TMPs and BSPs on the feasible computational power with respect to realistic representation of myocardial intrinsic structures, and torso geometry. In our work, a FHN-based

F.B. Sachse and G. Seemann (Eds.): FIMH 2007, LNCS 4466, pp. 150–159, 2007.

myocardial electrical propagation is solved upon the meshfree particle representation, whereafter the potentials on the torso surface are calculated using BEM upon the triangular mesh presentation of torso surface.

1.1 Physiological Models

In the past years, the most popular model for describing cardiac electrophysiological activities is the reaction-diffusion system [12,15], as well as Poisson equation for BSPs on torso surface [12]. With well-defined mathematical forms, the reaction-diffusion system of the excitable myocardium and Poisson equation of BSPs can more appropriately reproduce the electrical propagation phenomena [12,14,15] and BSPs patterns [12,15], and can properly be incorporated into the recovery/inverse framework. Though more sophisticated cellular models, closer to the biophysical properties of heart cells [8], are recently introduced, it is practically difficult to integrate these microscopic models into large-scale synchronous simulations of TMPs and BSPs due to the formidable computational loads [12], even nearly unfeasible in recovery/inverse framework currently. Thus, a physiological model, which preserves physiological meaningfulness along with feasible computation, will be a preference in the recovery/inverse framework. The modified FHN model, a simplified reaction-diffusion system, has been proved to be able to integrate the effects of the heart's geometrical complexity, nonuniform anisotropy, and material inhomogeneity [14,20]. Furthermore, computation can be reduced largely because of the polynomials used in the modified FHN model to approximate the cellular environment. Under the assumption of quasi-static electrical filed, Poisson equation is a proper model to describe the projections between TMPs and BSPs. [12,15].

1.2 Numerical Methods

Many numerical schemes have been applied to the reaction-diffusion system, including popular finite element methods (FEMs). Properly considering the geometrical complexity, the fiber structures and the material inhomogeneity, FEMs have produced fair results [11,14]. However, meshing for the heart is a very complicated and time-consuming task in the FEMs, with additional needs for taking care of the boundaries, material discontinuities and fiber structures. Further, for large-scale three-dimensional simulations, the computational costs of re-meshing for different patient-specific geometries often become prohibitively expensive. The emerging meshfree method, which has been heavily utilized in our previous works [18,21], represents an object by distributing sufficient sampling nodes within the space bounded by the object boundary surfaces, without the needs for mesh generation or complicated coordinate transformation. These properties are very attractive to the large-scale simulations of electrophysiological activities in different cardiac geometries, as well as the recovery/inverse approaches. Element-free Garlerkin method (EFGM) is recently introduced by T. Belytschko et al as an powerful numerical method [1,2,4]. A series of publications [2,3,7,17] have explored the numerical capabilities of EFGM, including

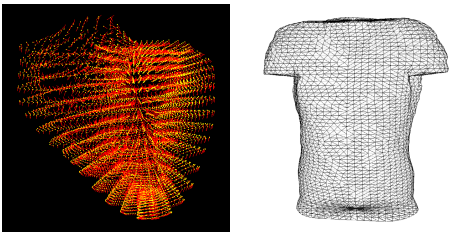

Fig. 1. From left to right: meshfree representation of the heart, triangular representation of torso surface

parallelization and comparison with FEMs. In this paper, EFGM is applied to solve the modified FHN model. Another advantage brought from EFGM is zero natural boundary condition can be handle by Galerkin weak form naturally. But to numerically solve Galerkin weak form with zero natural boundary condition by EFGM, sufficient sample nodes should be arranged in the boundaries. To solve the projections between TMPs and BSPs we choose BEM because of its superior performance in solving Poisson equation in the quasi-static electrical filed [12,15].

2 Methodology

2.1 Representation

In our meshfree-BEM framework, the heart is represented by a set of unstructured sample nodes, inside and in its boundaries, and torso surface is represented by triangular meshes (Fig.(1)). The density of the nodes distribution depends on the requirement of accuracy, and it can be easily refined through nodal addition or reduction.

2.2 Model of Intracardiac Electrophysiological Activities

Galerkin weak form of FHN model. The differential equations of a modified FHN model [14] are:

$$\begin{aligned} \frac{\partial u}{\partial t} &= f(u,v) + \bigtriangledown \cdot (D \bigtriangledown u) \\ \frac{\partial v}{\partial t} &= b(u - dv) \\ f(u,v) &= c_1 u(u-a)(1-u) - c_2 uv \end{aligned} \tag{1}$$

with natural boundary condition $\frac{\partial u}{\partial n} = 0$. Values of parameters are taken from [14], which are listed in Table 1. State variable u is the excitation variable which corresponds to the transmembrane voltage, v is the recovery current variable, n

Table 1. Parameters of FHN Model

Parameter	Value
a	0.13
b	0.013
$\mathbf{c}_1$	0.26
$\mathbf{c}_2$	0.1
d	1.0
diffuse term:	
$\mathbf{d}_f$	4.0
$\mathbf{d}_{cf}$	1.0

is the normal of the boundary, $f(u, v)$ is the excitation term, a, b, $c1$, $c2$ and d are parameters that define the shape of action potential. These parameters are constant over time but not necessary in space. The changes of state variables are determined by the excitation term $f(u, v)$ and diffusion term $\bigtriangledown \cdot (D \bigtriangledown u)$.

Galerkin weak form incorporates differential equations in integral form by using the weighted residual strategies so that they are satisfied over a domain in an integral sense rather than every point. Consider the integral form of equation (1), we have:

$$\int_\Omega \nu \frac{\partial u}{\partial t} d\Omega = \int_\Omega \nu \nabla \cdot (D \nabla u) d\Omega + \int_\Omega \nu f(u, v) d\Omega \tag{2}$$

$$\int_\Omega \nu \frac{\partial v}{\partial t} d\Omega = \int_\Omega \nu b(u - dv) d\Omega \tag{3}$$

Where ν is the trial function. The exact solution of equation (1) should always satisfy integral in equation (2) and (3). Evaluate integral in Equation (2) using Green's formulae:

$$\int_\Omega \nu \frac{\partial u}{\partial t} d\Omega = -\int_\Omega (\nabla \nu D \nabla u d\Omega) + D \oint_S \nu \tfrac{\partial u}{\partial n} dS + \int_\Omega \nu f(u, v) d\Omega \tag{4}$$

where S is the boundary of Ω and n is a vector normal to boundary. We can enforce natural boundary condition, $\frac{\partial u}{\partial n} = 0$, in equation (4) by eliminating $D \oint_S \nu \frac{\partial u}{\partial n} dS$, but sufficient meshfree sample nodes should be presented in the boundary S to guarantee the accuracy. In Galerkin procedure trial function could be placed by the shape function, Φ, of meshfree method here:

$$\int_\Omega \nu \frac{\partial u}{\partial t} d\Omega = -\int_\Omega (\nabla \nu D \nabla u d\Omega + \int_\Omega \nu f(u, v) d\Omega$$

$$\int_\Omega \nu \frac{\partial \Phi v}{\partial t} d\Omega = \int_\Omega \nu b(u - dv) d\Omega \tag{5}$$

Integral form in equation (5) is the Galerkin weak forms of equation (1). To solve the equation (5) we need to discrete them. Let U_I and V_I be the nodal value of

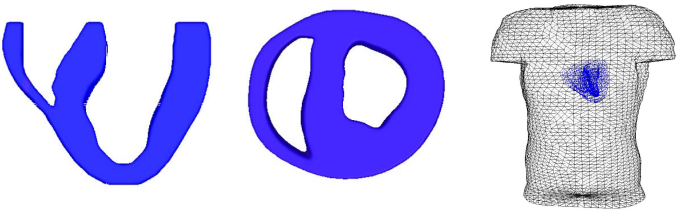

Fig. 2. From left to right: horizontal and longitudinal sections of cardiac geometry, position of the heart inside torso

field variables u and v at node set x_I, and let Φ be the shape function constructed from moving least square(MLS) approximation, which will be stated below. Then we have: $u \approx u^h = \Phi U_I$, $v \approx v^h = \Phi V_I$. if u, v and ν are replaced with ΦU_I, ΦV_I and Φ respectively, continuous forms of equation (5) can be written into discrete forms:

$$\begin{aligned} \frac{\partial U_I}{\partial t} \int_\Omega \Phi^T \Phi d\Omega &= -U_I \int_\Omega (\nabla \Phi^T D_{tran} \nabla \Phi) d\Omega + f(U_I, V_I) \int_\Omega \Phi^T \Phi d\Omega \\ \frac{\partial V_I}{\partial t} \int_\Omega \Phi^T \Phi d\Omega &= b(U_I - dV_I) \int_\Omega \Phi^T \Phi d\Omega \end{aligned} \tag{6}$$

where D_{tran} is the diffusion tensor transformed from local coordinate. Let D be the diffusion tensor of a point in local coordinate, which has such form:

$$D = \begin{bmatrix} d_f & 0 & 0 \\ 0 & d_{cf} & 0 \\ 0 & 0 & d_{cf} \end{bmatrix} \tag{7}$$

where d_f and d_{cf} are along fiber and cross fiber diffuse coefficients. Usually d_f is set to $4 \times d_{cf}$, which introduces anisotropic conductivities. Then we need to transfer D to the global coordinate. D_{tran} of one point, with α and β defining a rotation around the $z-$ and $y-$ axis of the global coordinate system according to the fiber orientation, can be defined:

$$D_{tran} = A^{-1} D A, \;\; A = R_{xz} R_{xy}$$

$$R_{xy} = \begin{bmatrix} \cos\alpha & \sin\alpha & 0 \\ -\sin\alpha & \cos\alpha & 0 \\ 0 & 0 & 1 \end{bmatrix}, \;\; R_{xz} = \begin{bmatrix} \cos\beta & 0 & \sin\beta \\ 0 & 1 & 0 \\ -\sin\beta & 0 & \cos\beta \end{bmatrix}$$

MLS approximation. In our approach, moving-least squares (MLS) [6] method is used to construct the shape functions, because of the the desired order of

consistency and smoothness throughout the entire domain provided by MLS approximation. In the MLS approximation, the approximation $u^h(\mathbf{x})$ becomes

$$u^h(\mathbf{x}) = \sum_{I=1}^{n}\sum_{j=1}^{m} p_j(x)(A^{-1}(\mathbf{x})B(\mathbf{x}))_{jI} \tag{8}$$

$$= \sum_{I=1}^{n} \phi_I(\mathbf{x})u_I \tag{9}$$

$$= \Phi(\mathbf{x})U_s \tag{10}$$

where

$$A(\mathbf{x}) = \sum_{I=1}^{n} w_I(x)p(x_I)P^T(x_I), w_I(x) \equiv w(x - x_I) \tag{11}$$

$$B(\mathbf{x}) = [w_1(x)p(x_1), w_2(x)p(x_2), ..., w_n(x)p(x_n)] \tag{12}$$

$$U_s^T = [u_1, u_2, ..., u_n] \tag{13}$$

In the above equations $w_I(x)$ is the cubic spline weight function, which is defined:

$$w(r) = \begin{cases} \frac{2}{3} - 4r^2 + 4r^3 \ \text{ for } \ r \le \frac{1}{2} \\ \frac{4}{3} - 4r + 4r^2 - \frac{4}{3}r^3 \ \text{ for } \ \frac{1}{2} < r \le 1 \\ 0 \ \text{ for } r > 1 \end{cases} \tag{14}$$

Let $r = \|x - xI\|/d_{mI}$, where d_{mI} is the radius of the influence domain of a node. Rewrite equation (6) with matrices:

$$\frac{\partial U_I}{\partial t} = M^{-1}KU_I + f(U_I, V_I) \tag{15}$$

$$\frac{\partial V_I}{\partial t} = b(U_I - dV_I) \tag{16}$$

$$f(U_I, V_I) = c_1U_I(1 - U_I)(U_I - a) - c_2U_IV_I \tag{17}$$

$$M_{i,j} = \int_\Omega \phi_i^T \phi_j d\Omega \tag{18}$$

$$K_{i,j} = \int_\Omega B_i^T D_{tran} B_j d\Omega \tag{19}$$

$$B_i = \begin{pmatrix} \phi_{i,x} \\ \phi_{i,y} \\ \phi_{i,z} \end{pmatrix} \tag{20}$$

Integration schemes. In EFGM a regular background mesh, which consists of non-overlapping regular cells is required in performing the integration of Galerkin weak form. Therefore, a background mesh of proper density needs to be designed to approximate solutions of desired accuracy and handle natural boundary conditions correctly. In the regular cell structures, there may exist cells that do not entirely belong to the problem domain. Thus, a simple visibility scheme that automatically separates the portion of the cell which lies outside of the physical domain is employed [1,2,4].

2.3 TMPs-BSPs Projection Model

The projection model describes the relation between TMPs and BSPs. In the quasi-static assumption, the problem is viewed in a passive volume conductor with the sources distributed only in the myocardium, and the governing Poisson equation:

$$\bigtriangledown \cdot(\sigma \bigtriangledown \psi) = - \bigtriangledown \cdot(\sigma_h \bigtriangledown u) \tag{21}$$

with given boundary conditions:

$$\psi(x) = h(x) \qquad x \in \Gamma_T \tag{22}$$

$$u(y) = g(y) \qquad y \in \Omega_H \tag{23}$$

$$\frac{\partial \psi(x)}{\partial n} = 0 \qquad x \in \Gamma_T \tag{24}$$

$$\frac{\partial u(y)}{\partial n} = 0 \qquad y \in \Gamma_H \tag{25}$$

where ψ is BSPs, u is transmembrane voltages, σ_h and σ are intracardiac and extracardiac conductivityies, Ω_H and Γ_H are the volume and surface of the heart, Γ_T is the torso surface. Applying BEM to equation (21) we get an equation with both surface and volume integral:

$$c(\varepsilon)\psi(\varepsilon) + \int_{\Gamma_T} \psi q^*(\varepsilon, x) d\Gamma_T - \int_{\Omega_H} (\bigtriangledown \cdot (\sigma_h \bigtriangledown u)) \psi^*(\varepsilon, x) d\sigma_h = \int_{\Gamma_T} q(x) \psi^*(\varepsilon, x) d\Gamma_T \tag{26}$$

where q^* and ψ^* are fundamental solutions with fixed forms. Commonly, the volume integral in equation (26) is approximated with simplified distributed dipoles [9,12]. Alternatively we attempt an innovative mesh free approximation of the volume integral whereby 1), the use of simplified models is avoided; 2), through integral by part, the boundary conditions in equation (22) within myocardium can be fulfilled. To ensure unique solutions, constrains defining potential references are added [12] and the linear transmembrane voltages-BSPs relationship is established with Minimal Norm (MN) method:

$$\Phi = (H_a^T H_a)^{-1} H_a^T B_a U = CU \tag{27}$$

where H_a,B_a are augmented forms of matrices H, B, where H results from the boundary integral with the BEM and B from volume integral with the mesh free method with details in [18].

3 Validations and Results

We test our framework in the authentic geometry, Auckland Heart Model[1] and Utah Torso Model [10], which are shown in Fig.(2). In order to assess the

[1] http://www.bioeng.auckland.ac.nz/cmiss/cmiss.php

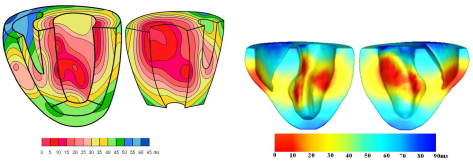

Fig. 3. Isochronic representation of ventricle activation. From left to right: published measurements, simulation of our meshfree framework.

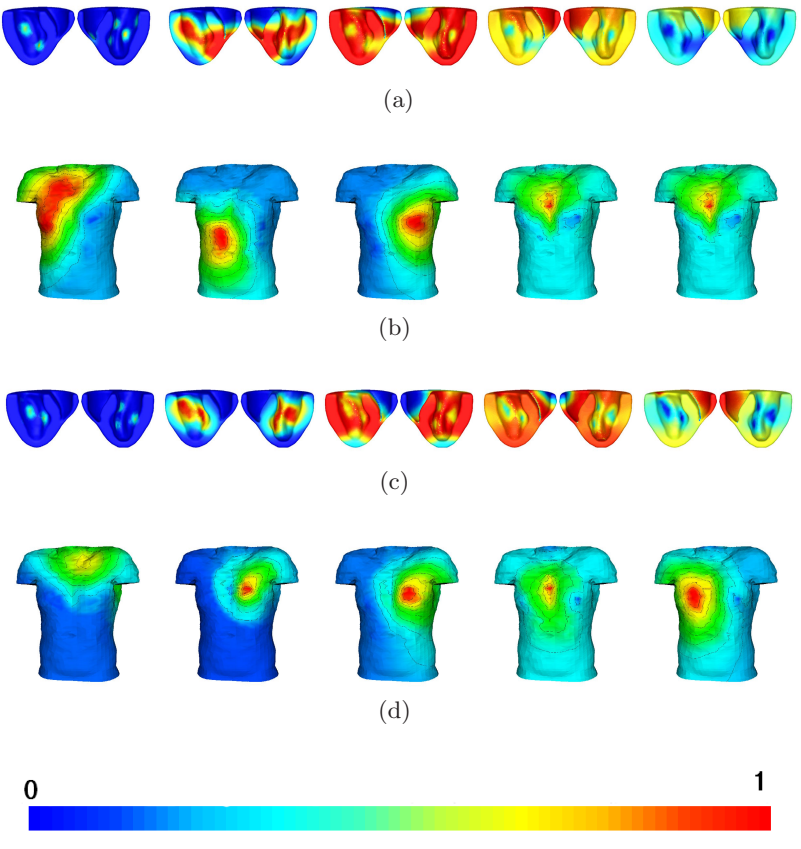

Fig. 4. Five samples of normal TMPs and BSPs during one cardiac cycle: (a) transmembrane potentials in the heart, (b) BSPs on the torso surface. Five samples of TMPs and BSPs during one cardiac cycle under the condition of RBBB: (c) transmembrane potentials in the heart, (d) BSPs on the torso surface. All the potentials are normalized between 0 and 1 and displayed according to color mapping bar.

accuracy and efficiency of our meshfree framework, propagation pattern of electrophysiological activities in Auckland Heart Model are solved with known diffusion tensors and purkinje network extremities. Since such measurements of purkinje network are not available yet, we have to define those extremities manually. From the figure (Fig.(3)[2]) generated from Durrer's measurements in the isolated human hearts, we can see that purkinje network extremities are located on the endocardium, and then we define similar locations of extremities in Auckland Heart Model by hand. The activation pattern in our simulation is qualitatively close to the published measurements as we can see in Fig.(3). Since it is reported that isolation of the heart leads to an increase in conduction velocity [5], and the duration of QRS waveform in healthy individuals varies from 70ms to 80ms, we can see the temporal length of our simulation is longer than Durrer's measurements, closer to the true duration of QRS waveform. We also simulate one case of heart disease, Right bundle branch block (RBBB) and its BSPs on the torso surface, which are compared to normal TMPs and BSPs in Fig.(4). In this comparison the differences between normal case and diseased case have shown the ability of our framework in reproducing different phenomena of cardiac electrophysiological activities.

4 Conclusion

We have presented a meshfree-BEM framework for simulating TMPs and BSPs in authentic geometries, which offers an effective alternative to the popular FEMs. Validations in heart and torso surface have demonstrated the ability of our meshfree-BEM framework in providing a physiological meaningful and computational feasible model for simulations and our recovery frameworks.

References

1. Belystchko, T., Krysl, P., Krongauz, Y.: A three-dimensional explicit element-free galerkin method. Int. J. Numer. Meth. Fluids 37, 229–256 (1997)
2. Belystchko, T., Lu, Y.Y., Gu, L.: Element-free galerkin methods. Int. J. Numer. Meth. Eng. 37, 229–256 (1994)
3. Dolbow, J., Belytschko, T.: Numerical integration of the galerkin weak form in meshfree methods. Comp. Mech. 23, 219–230 (1990)
4. Dolbow, J., Belytschko, T.: Numerical integration of galerkin weak form in meshfree methods. Comp. Mech. 23, 219–230 (1999)
5. Durrer, D., van Dam, R., Freud, G., Janse, M., Meijler, F., Arzbaecher, R.: Total excitation of the isolated human heart. Circulation 41(6), 899–912 (1970)
6. Lancaster, P., Salkauskas.: Surface generated by moving least squares methods. Math. Comp. 37(155), 141–158 (1982)
7. Liu, G.R.: Mesh free methods: moving beyond the finite element method. CRC Press, Boca Raton (2003)

[2] http://butler.cc.tut.fi/ malmivuo/bem/bembook/

8. Luo, C.H., Rudy, Y.: A dynamic model of the cardiac ventricular action potential - simulations of ionic currents and concentration changes. Circ. Res. 74, 1071–1097 (1994)
9. MacLeod, R.S., Brooks, D.H.: Recent progress in inverse problems in electrocardiology. IEEE EMBS Magazine 17(1), 73–83 (1998)
10. MacLeod, R.S., Johnson, C.R., Ershler, P.R.: Construction of an inhomogeneous model of the human torso for use in computational electrocardiography. In: EMBS, pp. 688–689 (1991)
11. Mulquiney, P.J., Smith, N.P., Clark, K., Hunter, P.J.: Mathematical modelling of the ischaemic heart. Nonlinear Analysis, 47, 235–244 (2001)
12. Pullan, A.J., Buist, M.L., Cheng, L.K.: Mathematically modelling the electrical activity of the heart: from cell to body surface and back again. World Science Publishing Co. Pte. Ltd, Singapore (2005)
13. Pullan, A.J., Cheng, L.K., Nash, M.P., Bradley, C.P., Paterson, D.J.: Non-invasive electrical imaging of the heart - theory and model development. In: Annals of Biomedical Eng. pp. 817–836 (2001)
14. Rogers, J.M., McCulloch, A.D.: A collation-galerkin finite element model of cardiac action potential propagation. IEEE Trans. BioMed. Eng. 41(8), 743–756 (1994)
15. Sachse, F.B.: Computational Cardiology: Modeling of Anatomy, Electrophysiology, and Mechanics. Springer, Heidelberg (2004)
16. Sanchez-Ortiz, G.I., Sermesant, M., Rhode, K.S., Chandrashekara, R., Razavi, R., Hill, D.L.G., Rueckert, D.: Localization of abnormal conduction pathways for tachyarrhythmia treatment using tagged MRI. In: MICCAI, pp. 425–433 (2005)
17. Singh, I.V.: Parallel implementation of the EFG method for heat transfer and fluid flow problems. Comp. Mech. 34, 453–463 (2004)
18. Wang, L.W., Zhang, H.Y., Shi, P.C., Liu, H.F.: Imaging of 3d cardiac electrical activity: A model-based recovery framework. In: Larsen, R., Nielsen, M., Sporring, J. (eds.) MICCAI 2006. LNCS, vol. 4190, Springer, Heidelberg (2006)
19. Wang, Y., Rudy, Y.: Application of the method of fundamental solutions to potential-based inverse electrocardiography. Ann. Biomed Eng. 34, 1272–1288 (2006)
20. Zhang, H.Y., Shi, P.C.: A meshfree method for solving cardiac electrical propagation. In: EMBS, pp. 349–352 (2005)
21. Zhang, H.Y., Wong, K.C.L., Shi, P.C.: Estimation of cardiac electrical propagation from medical image sequence. In: Larsen, R., Nielsen, M., Sporring, J. (eds.) MICCAI 2006. LNCS, vol. 4191, pp. 528–535. Springer, Heidelberg (2006)

An Anisotropic Multi-front Fast Marching Method for Real-Time Simulation of Cardiac Electrophysiology

Maxime Sermesant[1,2], Ender Konukoğlu[1], Hervé Delingette[1], Yves Coudière[4], Phani Chinchapatnam[3], Kawal S. Rhode[2], Reza Razavi[2], and Nicholas Ayache[1]

[1] INRIA Sophia Antipolis, Asclepios Team, France
[2] King's College London, Division of Imaging Sciences, UK
[3] University College London, Centre for Medical Image Computing, UK
[4] Nantes University, Jean Leray Mathematics Laboratory, France

Abstract. Cardiac arrhythmias can develop complex electrophysiological patterns which complexify the planning and control of therapies, especially in the context of radio-frequency ablation. The development of electrophysiology models aims at testing different therapy strategies. However, current models are computationally expensive and often too complex to be adjusted with limited clinical data. In this paper, we propose a real-time method to simulate cardiac electrophysiology on triangular meshes. This model is based on a multi-front integration of the Fast Marching Method. This efficient approach opens new possibilities, including the ability to directly integrate modelling in the interventional room.

1 Introduction

Treatment of cardiac arrhythmias has considerably changed in the last decades. Radio-frequency ablation techniques are becoming widely available as an alternative to drug therapy. These procedures can be highly effective with minimal side effects, but for some groups of patients have unsatisfactory success rates, may entail long procedures, and may involve high x-ray radiation dose to both patient and staff. Moreover, serious side effects can arise if the lesions extend beyond the target area. There is a need for substantial innovation in order to reliably achieve successful results in an acceptable time, with lower radiation dose and reduced risk of accidental damage to adjacent structures.

The aim of this research work is to design models of the cardiac electrophysiology that are suited for clinical use and to propose methods to combine these models with interventional data in order to better estimate the patient cardiac function and help in the guidance of procedures.

2 Electrophysiology Models

Modelling the cell electrophysiology is an active research area since the seminal work of Hodgkin and Huxley [4]. The precise modelling of the myocardium

F.B. Sachse and G. Seemann (Eds.): FIMH 2007, LNCS 4466, pp. 160–169, 2007.

involves a cell membrane model embedded into a set of partial differential equations (PDE) modelling a continuum. We can divide these models into three categories, from the more complex to the simpler (numerically):

- Biophysical models: semi-linear evolution Partial Differential Equation (PDE) with ionic models. Up to fifty equations for ion concentrations and channels [9,10]
- Phenomenological models: semi-linear evolution PDE with mathematical simplification of biophysical models. Reducing to two equations representing the intra- and extra-cellular potentials (bi-domain, mono-domain [2,11])
- Eikonal models: one static non-linear PDE for the depolarisation time derived from the previous models (Eikonal-Curvature [6], Eikonal-Diffusion [3])

Solutions of the evolution PDE are very computationally demanding, due to the space scale of the electrical propagation front being much smaller than the size of the ventricles. The motion of the front governed by the Eikonal equation is observed at a much larger scale, resulting in much faster computations.

For our interventional purpose, and as parameter adjustment often requires several simulations, we want to design a very fast model. Moreover, clinical data currently available is mainly on depolarisation times. For these reasons we chose to base the presented work on the Eikonal models. Even if these models are not able to precisely simulate the whole range of cardiac pathologies, they open up possibilities for fast estimation, filtering (smoothing), interpolation and extrapolation.

In [14], we presented an approach to simulate the Eikonal models with a Fast Marching Method (FMM), in order to obtain very fast computations. While this approach allowed us to take the front curvature influence into account, we could not integrate the repolarisation in this approach. However, the repolarisation is a very important phenomenon in many arrhythmias, for instance when the Action Potential Duration (APD) variation creates reentry waves. Moreover, it is often over several cycles that arrhythmias develop, and the FMM only solves for separate cycles. Finally, this approach could not cope with the anisotropy of the heart.

In this article we propose two important contributions in this fast model framework. First, we propose a FMM that takes into account the anisotropy of the medium in the computation of the propagation. Second, we introduce the repolarisation phenomenon in order to be able to simulate multi-front propagations.

3 The Anisotropic Fast Marching Method

3.1 The Fast Marching Method (FMM)

We first compare briefly the Eikonal approach to the PDE one. The classical FMM [16] can be used to solve the following isotropic Eikonal equation:

$$F\sqrt{\nabla T^t \nabla T} = 1$$

where T is the arrival time and F the speed function (D is the identity matrix in the isotropic case). In this method, points are separated in three sets: $UNKNOWN$, $TRIAL$, and $KNOWN$, and the $TRIAL$ set of points X is ordered along the increasing associated times $T(X)$. $\mathcal{N}(X)$ is the neighbourhood of X. In the initialisation step, all the points are put in $UNKNOWN$ with a time of $+\infty$, starting points are put in $KNOWN$ with a time of 0, and their neighbours are updated. The FMM algorithm is described briefly in Algorithms 1 and 2.

Algorithm 1. Fast Marching Method

while TRIAL list is not empty **do**
  $X \leftarrow \text{argmin}_{X \in TRIAL}\{T(X)\}$
  remove X from $TRIAL$ and add X to $KNOWN$
  for all $X_i \in \mathcal{N}(X)$ and $X_i \notin KNOWN$ **do**
    compute $T(X_i) = \text{UPDATE}(X_i, X)$
    if $X_i \notin TRIAL$ then add X_i to $TRIAL$
  end for
end while

Algorithm 2. Computation of $\overline{T}(X_i) = UPDATE(X_i, X)$ in a Triangulation

$\overline{T}(X_i) \leftarrow +\infty$
for all $\triangle(XX_iY) \in \triangle^X_{X_i} = \{\triangle(XX_iY) | Y \in \mathcal{N}(X_i)\}$ **do**
  if $Y \in KNOWN$ **then**
    $\overline{T}(X_i) \leftarrow \min\{\overline{T}(X_i), \min_{p\in[0,1]}(T(X)p + T(Y)(1-p) + [\mathbf{v}(p)^t D^{-1} \mathbf{v}(p)]^{1/2}/F)\}$
    where $\mathbf{v}(p) = \overrightarrow{XX_i}p + \overrightarrow{YX_i}(1-p)$
  else
    $\overline{T}(X_i) \leftarrow \min\{\overline{T}(X_i), T(X) + \overrightarrow{XX_i}^t D^{-1} \overrightarrow{XX_i}\}$
  end if
end for

This implementation of the FMM is different from the original one which uses an upwind discretisation of the gradient. We use here a closed-form solution of the minimisation in triangles, which seems to be less sensitive to obtuse angles than the original FMM (this has to be further studied.).

The Eikonal equation can be seen as an approximation for the computation of the propagating front from reaction-diffusion PDEs. To better understand the approximation, we present in Fig. 1 a comparison of the isochrones computed by the FMM and the Aliev and Panfilov reaction-diffusion system to simulate cardiac action potential [1]. The results from the different algorithms are presented on a triangulated square mesh with a center hole, composed of 13 000 nodes. The initialisation is in the bottom left corner. In this isotropic case, D is the identity matrix.

In this case, the isochrones of the FMM are close to what is produced by the PDE. One main difference is related to the boundary conditions. For the PDE,

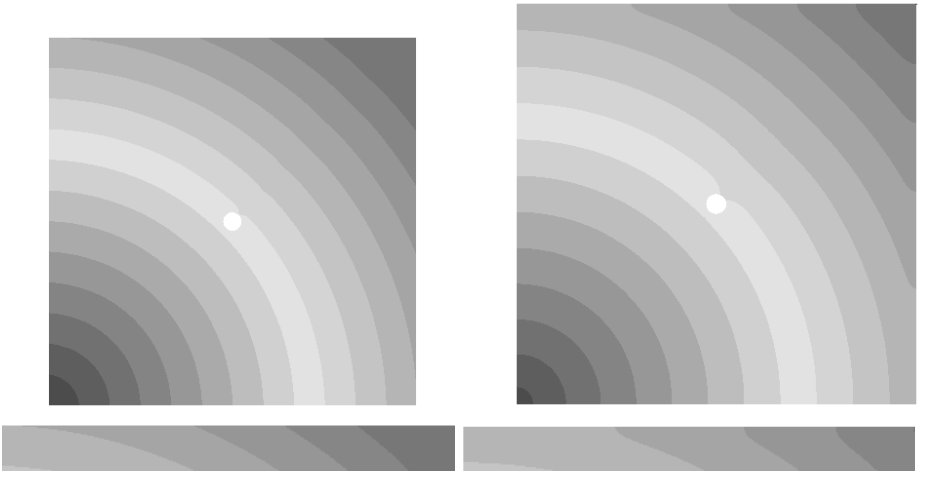

Fig. 1. (Left) Fast Marching on unstructured grid, (right) isochrones from the simulated PDE. Red corresponds to small times, blue to large times. (Bottom) close up on the top of the square to point out boundary condition differences effect.

these are Neumann boundary conditions, which impose the no-flux condition at the boundary, whereas the Eikonal equation has no such constraints. This is visible for instance at the top and right boundaries, where the PDE front is orthogonal to the edge and not the Eikonal one (see Fig. 1, bottom row, and around the central hole). There are ways to introduce this in the Eikonal approach, but this is still on going work on what are the proper boundary conditions for our case, and whether this will impact the simulation to a great extent.

Another difference can arise from the fact that the travelling wave solution of the PDE is only an asymptotic solution, whereas the Eikonal solution is directly in this stationnary state. This can be seen by varying the initialisation parameters of the PDE (shape of the front at the initial time).

The travelling wave solution to the PDE is an asymptotic state (as time tends to $+\infty$), whose isochrones are approximately solutions to the Eikonal equation (neglecting the effect of front curvature). Hence, part of the error between the PDE isochrones and the Eikonal solution arises from the transient propagation when the initial data for the PDE is chosen far from the asymptotic state.

The PDE system models a wide range of functional states (plane/spiral waves, relations between front curvature, local APD and speed, adaptive response to a periodic stimulation, etc), with the counterpart of complex parameter tuning and numerical stability/cost issues. Although accounting for simpler situations, the Eikonal model is clearly more adapted to our concern: fast computing compared to very sparse/local measurements.

A more precise and quantitative evaluation of both the modeling and the numerical approximation errors is on-going work.

3.2 The Anisotropic Fast Marching

The anisotropic Eikonal equation can be written in the form of:

$$F\sqrt{\nabla T^t D \nabla T} = 1$$

where D is the tensor creating anisotropy. Taking into account the anisotropy of the propagation is important in many cases of excitable media. But introducing this phenomenon in the FMM is not trivial. Indeed, the regular FMM uses the collinearity between the gradient and the characteristic direction to solve the equation very efficiently, but in the anisotropic case these directions do not match anymore.

There have been many different ways proposed to solve such anisotropic equations using single-pass [15,7] or iterative [5,12] methods. We use here a new fast algorithm for solving anisotropic Eikonal equation on general meshes without increasing the neighborhood and following the characteristic direction similar to single-pass methods [8]. The idea is to include a recursive correction scheme taking into account the fact that, due to anisotropy, the immediate neighborhood used for computation may not always contain the characteristic direction at the time it is computed. To achieve this, an additional $CHANGED$ list who is also empty at the beginning and who will be used for the recursive correction is introduced. This efficient algorithm, described in Algorithm 3, can cope with very important anisotropies and can be applied to more general forms of static convex Hamilton-Jacobi equations, and on Cartesian or unstructured grids. The anisotropic FMM algorithm is not significantly longer to compute than the classical algorithm, especially in the case of non-extreme anisotropies. For instance with a factor of three between longitudinal and transverse speeds, simulation on the 13 000 nodes took less than one second (see Fig. 2).

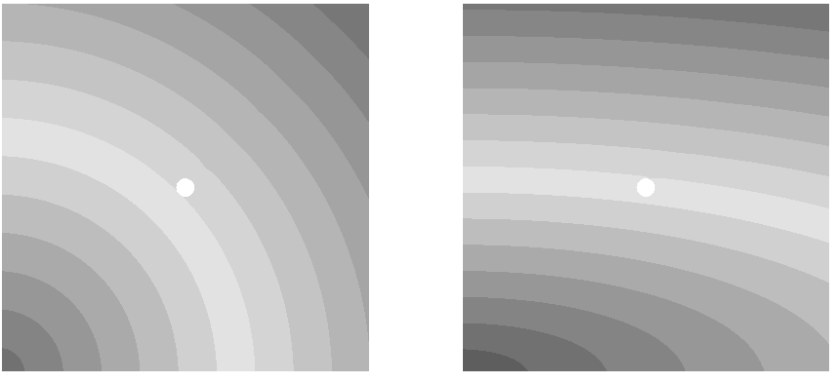

Fig. 2. (Left) Classical Fast Marching on unstructured grid, (right) Anisotropic Fast Marching (different colormap). The vertical speed is three times smaller than the horizontal speed.

Algorithm 3. Anisotropic Fast Marching

while $TRIAL$ or $CHANGED$ are not empty **do**
  if $CHANGED$ is not empty **then**
    $X \leftarrow \text{argmin}_{X \in CHANGED}\{T(X)\}$
    remove X from $CHANGED$
  else
    $X \leftarrow \text{argmin}_{X \in TRIAL}\{T(X)\}$
    remove X from $TRIAL$ and add X to $KNOWN$
  end if
  for all $X_i \in \mathcal{N}(X)$ and $X_i \in KNOWN$ **do**
    compute $\overline{T}(X_i) = \text{UPDATE}(X_i, X)$
    if $\overline{T}(X_i) < T(X_i)$ **then**
      $T(X_i) \leftarrow \overline{T}(X_i)$
      add X_i to $CHANGED$ list
    end if
  end for
  for all $Y_i \in \mathcal{N}(X)$ and $Y_i \in TRIAL \cup UNKNOWN$ **do**
    compute $\overline{T}(Y_i) = \text{UPDATE}(Y_i, X)$
    if $Y_i \in TRIAL$ and $\overline{T}(Y_i) < T(Y_i)$ **then**
      $T(Y_i) \leftarrow \overline{T}(Y_i)$
    else if $Y_i \in UNKNOWN$ **then**
      $T(Y_i) \leftarrow \overline{T}(Y_i)$
      remove Y_i from $UNKNOWN$ and add Y_i to $TRIAL$
    end if
  end for
end while

4 A Multi-front Fast Marching Approach

The FMM is a static method to solve for an evolving front, in the sense that the variable of the Eikonal equation is time. But in our simulation purpose, we can have several fronts evolving at the same time, because points can go back to a resting state, so they can be excited again before the first front disappeared.

The key idea is to introduce a time-stepping scheme while using the FMM to compute the propagation during each time step. Our application context is the Eikonal approximation of reaction-diffusion equations to simulate the propagation in excitable media. In this context, the state of each point may vary over time, for instance with a repolarisation state, when a point goes back to its equilibrium state.

In order to achieve this, we have to introduce a refractory state, between the excited and the equilibrium state, otherwise, any node going back to the equilibrium would immediately be excited again by his neighbours still excited. This is in agreement with natural phenomena, like nervous electrical action potential propagation, where cells have this refractory period. The Multi-Front FMM is described in algorithm 4.

Algorithm 4. Multi-Front Fast Marching Algorithm on a period T

```
integratedTime = 0.0
while integratedTime < T do
  elapsedTime = 0.0
  while TRIAL not empty and elapsedTime < timeStep do
    X ← argmin_{X∈TRIAL}{T(X)}
    remove X from TRIAL and add X to KNOWN
    for all X_i ∈ N(X) and X_i ∉ KNOWN do
      compute T(X_i) = UPDATE(X_i, X)
      if X_i ∉ TRIAL then add X_i to TRIAL
      elapsedTime = T(X_i) − integratedTime
    end for
    for all X ∈ KNOWN do
      if elapsedTime − T(X) > APD(X) then
        remove X from KNOWN and add X to REFRACTORY
        RepolarisationTime(X) ← T(X) + APD(X)
      end if
    end for
    for all X ∈ REFRACTORY do
      if elapsedTime − RepolarisationTime(X) > RefractoryPeriod(X) then
        remove X from REFRACTORY and add X to UNKNOWN
      end if
    end for
  end while
  integratedTime += timeStep
end while
```

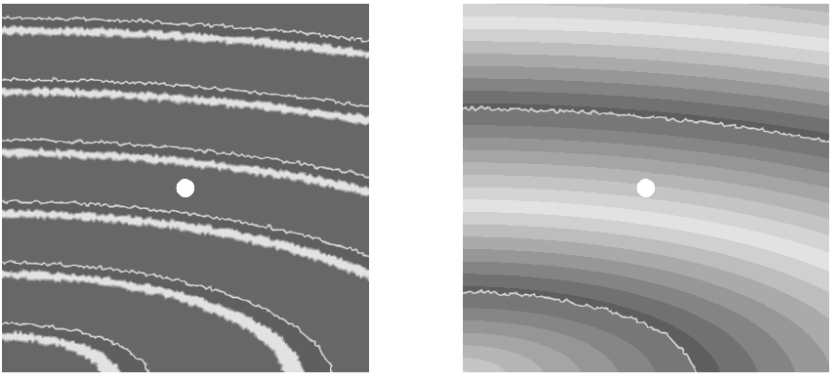

Fig. 3. (Left) Impulse train with the Multi-Front Fast Marching (anisotropic case). Excited vertices are in red and refractory vertices are in yellow. (Right) Corresponding isochrones with a reduced frequency to increase visibility.

This Multi-Front FMM is able to simulate an impulse train on a piece of excitable media (see Fig. 3, left). The visualised progressing front is not very

smooth, because it corresponds to an isochrone still being computed, but after the front, the resulting isochrones are smooth (see Fig. 3, right). Visualisation work still has to be made to improve this.

The computation speed can be adjusted by choosing the frequency at which the display must be updated (corresponding to the "time step" in this scheme). On recent computers and with smaller meshes (1000 nodes), such surface simulations could be done in "real-time": no synchronisation was done to ensure the timing of the simulation, but it was visually checked that with 30 frames per cycle, the computation time was below one second (one heart cycle is a bit less than a second).

5 Cardiac Electrophysiology Simulation

The presented algorithm was used to simulate transmembrane potential propagation in cardiac tissue. The idea is to compute the depolarization time using the Multi-Front Anisotropic FMM. Then, when a given vertex is depolarised, we use the time-stepping to know when the vertex goes into repolarisation and then refractory period, and when it is excitable again. We can thus show a pseudo transmembrane potential, which is at 10 mV when the vertex is depolarised (red), and -90 mV when it is excitable (blue).

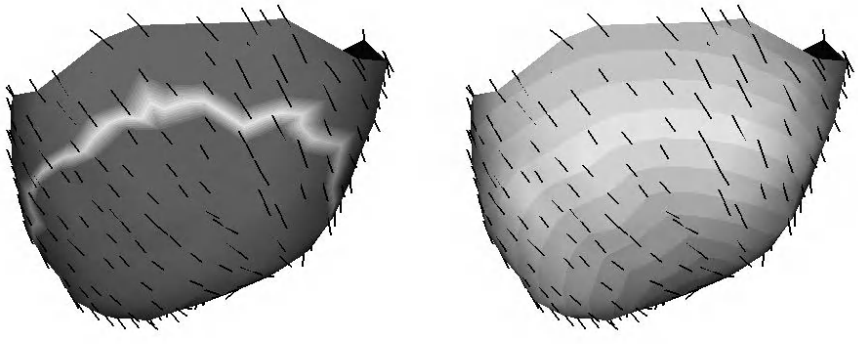

Fig. 4. Normal propagation on the epicardium, with an apical epicardial pacing. Black lines represent the fibre orientations. (Left) pseudo transmembrane potential. (Right) simulated isochrones.

We compute in a continuous way the propagation of different finite states. Compared to previous approaches in propagation simulation, it could be seen as a kind of "continuous cellular automaton": the states are discrete but the propagation is continuous.

We used this algorithm to simulate epicardial propagation of the Action Potential. As fibre orientation is tangential on the epicardium, and we simulate an epicardial pacing, this surface model can be seen as an approximation of the 3D

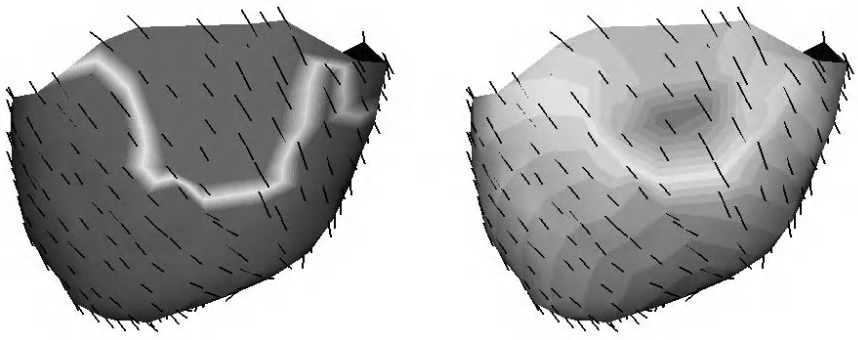

Fig. 5. Simulation of a scar with 10% of normal conductivity. Black lines represent the fibre orientations. (Left) pseudo transmembrane potential. (Right) simulated isochrones.

propagation (see Fig. 4). We integrate fibre orientations from DTI measurements. The depolarisation speed is 3 times faster along the fibre than transversally.

Low conductivity areas can also be added. For instance, a scarred area created with a conductivity of 10% of the normal conductivity was simulated, see Fig. 5.

These are just exemplar simulations, computed on a very crude mesh (248 points). The accurate simulation of arrhythmias needs to take into account the full 3D nature of the propagation and deal carefully with any discretisation approximation issues. We also need a thorough comparison between measured isochrones and simulated ones from a PDE or Fast Marching approach for pathological cases in order to fully validate the behaviour of these models.

6 Conclusion

We presented a new algorithm to achieve real-time simulations of cardiac electrophysiology. This model opens up possibilities for real-time filtering and interpolation of sparse and noisy catheter-based electrophysiology recordings, which could provide a better evaluation of pathology and planning of the therapy. An excellent example application is the planning of radio-frequency ablation. Such a real-time model could be embedded in an intervention simulator to test several ablation strategies.

Future work includes extension to volumetric propagation and reintroducing the influence of the curvature of the front on the propagation speed. The use of a restitution curve is quite straightforward in this framework, but having a relative refractory period will need a more precisely described action potential. Visualisation can be improved in order to have a smoother front by using already computed isochrones. Validation of this model should lead to the integration of simulated isochrones within XMR interventional data, that combine patient anatomy and electrophysiology mapping [13].

References

1. Aliev, R., Panfilov, A.: A simple two-variable model of cardiac excitation. Chaos, Solitons and Fractals 7(3), 293–301 (1996)
2. FitzHugh, R.: Impulses and physiological states in theoretical models of nerve membrane. Biophysical Journal 1, 445–466 (1961)
3. Colli Franzone, P., Guerri, L., Rovida, S.: Wavefront propagation in activation model of the anisotropic cardiac tissue: Asymptotic analysis and numerical simulations. J. Math. Biol. (1990)
4. Hodgkin, A., Huxley, A.: A quantitative description of membrane current and its application to conduction and excitation in nerve. Journal of Physiology 177, 500–544 (1952)
5. Kao, C., Osher, S., Tsai, Y.: Fast sweeping methods for static hamilton-jacobi equations. SIAM J. Numer. Anal. 42 (2005)
6. Keener, J., Sneyd, J.: Mathematical Physiology. Springer, Heidelberg (1998)
7. Kevorkian, J.: Partial differential equations: Analytical solution techniques. Springer, Heidelberg (2000)
8. Konukoğlu, E., Sermesant, M., Peyrat, J-M., Clatz, O., Delingette, H., Ayache, N.: A recursive anisotropic fast marching approach to reaction diffusion equation: Application to tumor growth modeling. In: Information Processing in Medical Imaging (IPMI'07). LNCS, Springer, Heidelberg, Accepted (2007)
9. Luo, C., Rudy, Y.: A model of the ventricular cardiac action potential: depolarization, repolarization, and their interaction. Circulation Research 68, 1501–1526 (1991)
10. Noble, D., Varghese, A., Kohl, P., Noble, P.: Improved guinea-pig ventricular cell model incorporating a diadic space, I_{Kr} and I_{Ks}, and length and tension dependent processes. Canadian Journal of Cardiology 14, 123–134 (1998)
11. Pollard, A., Hooke, N., Henriquez, C.: Cardiac propagation simulation. Critical Reviews in biomedical Engineering 20(3,4), 171–210 (1992)
12. Qian, J., Zhang, Y., Zhao, H.: A fast sweeping method for static convex hamilton-jacobi equations. UCLA Computational and Applied Mathematics Reports, 06-37 (2006)
13. Rhode, K., Sermesant, M., Brogan, D., Hegde, S., Hipwell, J., Lambiase, P., Rosenthal, E., Bucknall, C., Qureshi, S., Gill, J., Razavi, R., Hill, D.: A system for real-time XMR guided cardiovascular intervention. IEEE Transactions on Medical Imaging 24(11), 1428–1440 (2005)
14. Sermesant, M., Coudière, Y., Moreau-Villéger, V., Rhode, K.S., Hill, D.L.G, Ravazi, R.: A fast-marching approach to cardiac electrophysiology simulation for XMR interventional imaging. In: Duncan, J.S., Gerig, G. (eds.) MICCAI 2005. LNCS, vol. 3750, pp. 607–615. Springer, Heidelberg (2005)
15. Sethian, J., Vladimirsky, A.: Ordered upwind methods for static hamilton-jacobi equations: theory and algorithms. SIAM J. Numer. Anal. 41 (2003)
16. Sethian, J.A.: Level set methods and fast marching methods: Evolving interfaces in computational geometry, fluid mechanics, computer vision, and materials science. Cambridge University Press, Cambridge (1999)

Parallel Solution in Simulation of Cardiac Excitation Anisotropic Propagation

Yu Zhang[1], Ling Xia[1], Yinglan Gong[1], Ligang Chen[2], Guanghuan Hou[3], and Min Tang[4]

[1] Department of Biomedical Engineering, Zhejiang University, Hangzhou 310027, China
xialing@zju.edu.cn
[2] Center for Engineering and Scientific Computation
[3] Department of Mathematics, Zhejiang University, Hangzhou 310027, China
[4] Department of Arrhythmia, Cardiovascular Institute and Fuwai Hospital, Chinese Academy of Medical Science and Chinese Union Medical College, Beijing 100037, China

Abstract. Solution in simulation of cardiac excitation anisotropic propagation throughout the ventricular myocardium is computationally very expensive that demands the introduction of a high performance computing techniques. In this study, a canine ventricle model was constructed features a realistic anatomical structure, including intramural fiber rotation and a conduction system. By using operator-splitting scheme, adaptive time step and backward differentiation formulation techniques in a parallel implement, we solved mondomain equation successfully. The stimulation produced isochrone's map is close to the clinical record that obtained from the non-contact mapping system of Ensite 3000. The results show that the proposed methods can successfully be used to simulate heart excitation anisotropic propagation in three-dimensional anatomical large tissue size.

Keywords: Parallel computation, Cardiac excitation propagation, Simulation.

1 Introduction

Arrhythmias are electrical disorganized disturbances in the heart, which is life threatening in severe condition. The process of understanding these special rhythms must begin with a thorough comprehension of the normal spread of activation in the heart. Experimental techniques, including recordings with microelectrodes and extracellular electrodes, even non-contract mapping system can provide lots of useful information. However, each technique is associated with its own set of complications and limitations [1]. A ventricular model that can produce a correct normal activation sequence provides a desirable alternative tool for simulating pathological conditions, such as ischemia, infarction or ventricular arrhythmias [2]. Such a model must feature a realistic anatomical structure, including intramural fiber rotation and a conduction system. While it is not necessary that models completely replicate experiments, they must be sufficiently accurate and realistic such that, at most, their predictions can be used to adequately design subsequent experiments or procedures[1]. In this sense,

F.B. Sachse and G. Seemann (Eds.): FIMH 2007, LNCS 4466, pp. 170–179, 2007.

models are likely to become further integrated with experiments, providing a more efficient means for testing hypotheses and for investigating the impact of novel therapies [2].

Reaction-diffusion equations have been widely used to characterize myocardial physiological propagation and electrical behavior in several species including mouse [3], rabbit [4], canine [5] and human [6]. Because the bidomain equations are computationally very expensive, the complexity of the cardiac models demands the introduction of a high performance computing techniques [7]. In this study, we first give a brief introduction to the bidomain model, and how it may be reduced to the monodomain model. We then describe the numerical methods used in simulation of cardiac excitation propagation, and finally present simulation results and performance analysis.

2 Materials and Methods

2.1 Anatomy and Fiber/Tissue Properties

An intact canine heart was underwent diffusion tensor magnetic resonance imaging (DTMRI) in a 7.1 T MRI scanner at the Duke University Medical Center for In Vivo Microscopy to obtain both the geometry (see Fig. 1A, B) and fiber orientation (see Fig. 1G, H) [8]. At each pixel of the DTMRI an average fiber orientation was

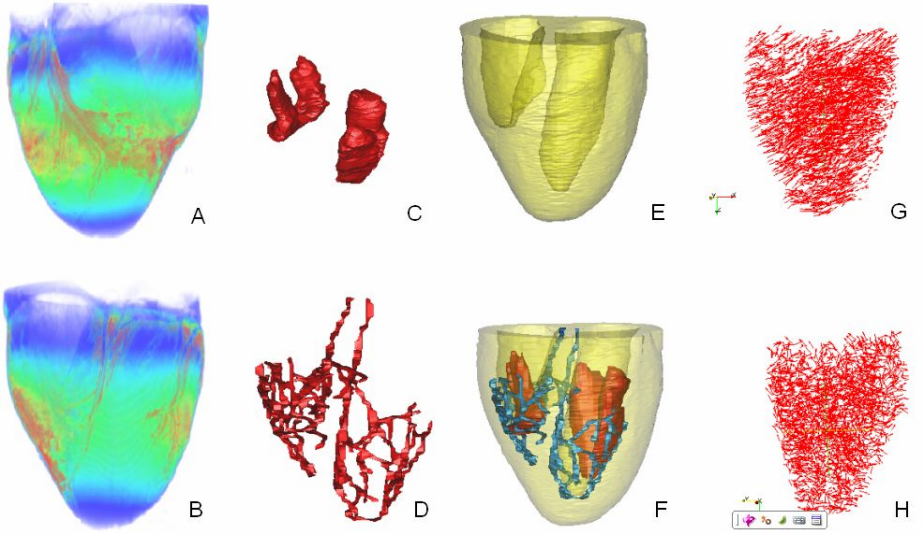

Fig. 1. Three-dimensional view of the dog ventricle anatomical model. The left panel (A, B) shows 3D view of the whole ventricle scanned from DTMIR at Duke University Center visualized by Volview® 2.0 and the next panel C displays view of the cardiac papillary tissue with manual segment, the panel D displays the initial activation points (Purkinje–myocardial junction sites) set according to the known anatomical structure of canine heart. Panel E, F show the selected cardiac tissue for final simulation. The right view G, H displays the fiber angles (G is front view, H is right view).

obtained. These data were segmented into a hexahedral mesh, consisting of cardiac tissue and cavities (see Fig. 1E). The spatial discrete matrix size of the original data is 256×128×128 corresponds to pixel size of 0.39 × 0.78 × 0.78mm. The data was manual segmented to functional modules according to the known anatomical structure of canine heart (see Fig. 1F) [9]. His bundle and initial activation points (Purkinje network–myocardial junction sites) are shown in Fig. 1D. Cardiac tissue was assumed to be anisotropic. Conductivities along (G_l=3.82ms/cm) and across (G_t=1.25ms/cm) cardiac muscle were chosen to reproduce normal canine conduction velocities, which were approximately 0.41m/s along fibers and 0.15m/s across fibers [10] physiologically.

2.2 Modeling Cardiac Electrophysiology

Basic ventricular cell model. In this study, the dynamic ionic model developed by Winslow et al. [11] is used. The model includes different ionic channel currents, described by the following differential equations:

$$\frac{dV_m}{dt} = -\frac{1}{C_m}\left(\sum I_x + I_{app}\right) \tag{1}$$

$$I_x = G_x \cdot (V_m - E_x), \tag{2}$$

where I_x is the current flow through the ion channel x, G_x is the conductance of the channel and Ex is the reversal potential for the channel.

Reaction-diffusion equations. Governing equations of bidomain model applied in heart is formed with the parabolic (3) and elliptic (4) equations:

$$\frac{\partial V_m}{\partial t}(x,t) = \frac{1}{C_m}\left[-\sum I_{ion}(x,t) - I_{app}(x,t) - \frac{1}{\beta}\nabla\cdot\left(D_e(x)\nabla\phi_e(x,t)\right)\right], \tag{3}$$

$$\nabla\cdot\left(\left(D_i(x) + D_e(x)\right)\nabla\phi_e(x,t)\right) = -\nabla\cdot\left(D_i(x,t)\nabla V_m(x,t)\right) \tag{4}$$

They can be simplified by the assumption of equal anisotropy (Eq.(5)), treating heart as homogeneous isotropic medium.

$$D_i(x) = \frac{1}{k}D_e(x) \tag{5}$$

$$\frac{\partial V_m}{\partial t}(x,t) = \frac{1}{C_m}\left[-\sum I_{ion}(x,t) - I_{app}(x,t) + \frac{1}{\beta}\left(\frac{k}{k+1}\right)\nabla\cdot\left(D_i(x)\nabla V_m(x,t)\right)\right] \tag{6}$$

The resulting parabolic equation is known as the monodomain equation (6), details about bidomain theory can be found in Ref. [12]. In order to solve the monodomain equations, an initial equation (7) as well as boundary conditions (8) is required:

$$V(x, t=0) = V(x) \tag{7}$$

$$n\cdot V(x, t=0) = 0\,. \tag{8}$$

2.3 Numerical Considerations

The equations of monodomain model were solved numerically using operator-splitting scheme technique in a parallel implement. Equations describing the state variables were updated with a fixed time step of 10μs by using backward differentiation formulation (BDF), which is a popular multi-step method for solving stiff ODEs. First, we introduce a temporal discretization of the time intervals. Let Δt be the global time step or the time interval between each integration process and *M* be an even number of fractional time steps. Define Δt'=Δt/M as the fractional diffusion time step. We set the discretization parameters as Δt =10μs, M=20, Dx=0.39mm and the tolerance for the ODE solver is set to 10^{-6}, other parameters were set as follows: k = 3, C_m = 1 F/cm^2, = 1000 cm^{-1}. The equations can be solved in the following steps:

1. Assume we know the value of x^n, y^n, and $V_m{}^n$ at t^n.
2. Compute $V_m{}^{n+1/2}$ in H by solving the parabolic equation (Eq.(6)) using a step size $\Delta t'$ repeated $M/2$ times. (Eq.(9) for monodomain)

$$V_m{}^{n+1/2} = V_m{}^n + \frac{\Delta t'}{C_m}\left[-\sum I_{ion}{}^n - I_{app}{}^n + \frac{1}{\beta}\left(\frac{k}{k+1}\right)\nabla\cdot\left(D_i \nabla V_m{}^n\right)\right] \tag{9}$$

3. Compute x^{n+1}, y^{n+1} by solving the ODEs of the cell model using backward differentiation formulation (BDF) based on an integration package called VODE (Variable coefficient ODE solver) [13], in which x^{n+1} represents gating variables, y^{n+1} represents I_{ion}.
4. Compute $V_m{}^{n+1}$ in H by solving the parabolic equation (Eq. (6)) (Same to step 2).

2.4 Parallelization Strategy

Computer Architectures. All the simulations are performed on a cluster of networked Dell Precision WorkStation 670 System (2R) which is a distributed share memory systems inter-connected by a 100 Mbit/s ethernet network. Each node consists of two 3.0GHz Xeon® processors and 4GB of shared memory as shown in Fig. 2A. The implementation achieves parallelism by utilizing message-passing protocol for communication among nodes in a MPICH domain built by Windows Server 2003 running MPICH2 Parallel Environment and Compaq Visual Fortran v6.6.c.

Domain Decomposition. The data parallelism paradigm is being employed where different processors perform the same function on different parts of the data. Be restricted by the memory and parallel technique, the spatial discrete geometrical matrix size had to be reduced from original 256×128×128 to 113×128×128 by sampling slice in long-axis (see Fig. 2C) along which the domain decomposition was performed (see Fig. 2D). The volume of the data matrix comprised 398,446 nodes (18.9% of the total number mesh points). Optimizing load balancing method was used to generate more efficient computational sub domain (see Fig. 2D).

Parallization using MPI. Solving the diffusion term or spatial current of each computational grid point requires the membrane potential from its nearest neighbor at every iterative beginning, which forms an 18-point stencil as shown in Fig. 2B. For

the grid points within a sub domain, this information is available in the node shared memory. For the grid points on the boundary of the sub domain, the information must be retrieved from adjacent sub domains before iteration (see Fig. 2E).

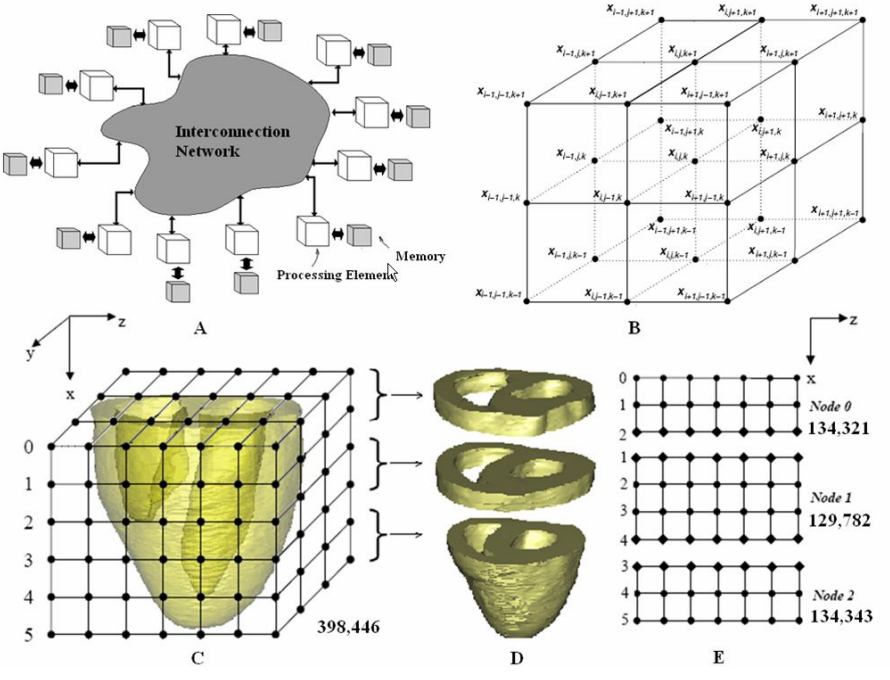

Fig. 2. Three-dimension view of the parallelization strategy. The panel A shows the distributed shared memory system consists of a set of nodes each with a main memory shared by the resident processors, and communication between nodes is accomplished via message-passing protocol. The next panel B displays view of the node points in three-dimensional, rectangular, equidistant mesh. The center of the sub-volume is node point $x_{i,j,k}$. The mesh is applied in conjunction with the finite differences method for discretization of bidomain equation. After that panel C displays the ventricle immersed in a finite difference grid, domain decomposition scheme partition the volume into sub domains (panel D) and distribute these blocks of short-axis sections to three SMP nodes for load balance (panel E).

3 Results

3.1 Simulations of Normal Activation of the Ventricles

Before the simulation work beginning, a clinical non-contact mapping of left ventricle in canine was prepared for validation. A deflectable catheter (Biosense Webster) was introduced into the chamber via the right femoral artery to sweep throughout the canine LV to establish three-dimensional endocardial geometry. After that, the normal sinus activation was recorded with isochronal maps (Fig. 3C). The activation of the left ventricle was analyzed using a filter setting of 8 Hz; A stimulus current with

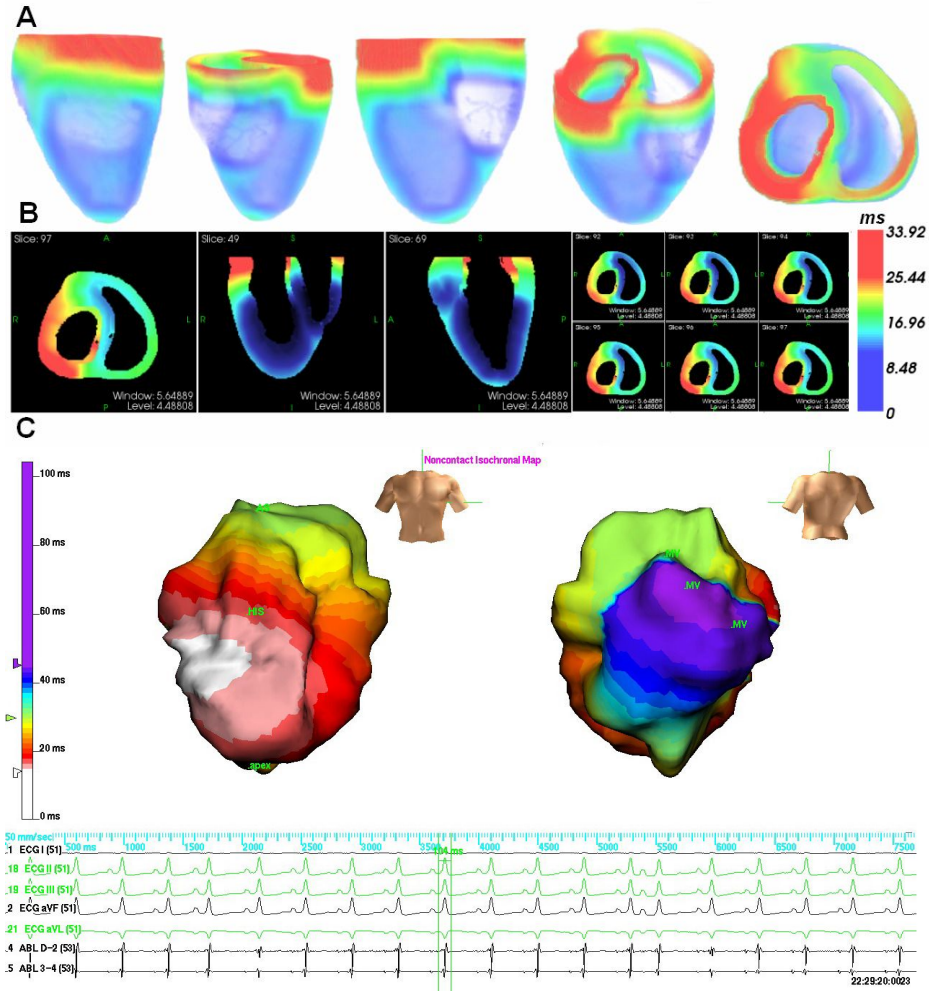

Fig. 3. Isochrones of simulated normal activation of the ventricles. The panel A shows 3D isochrones in different view of ventricle, and the panel B view displays the activation isochrones on slices of the tissue in the different direction. Panel C shows an isochronal map of left ventricle in single sinus activation mapping with EnSite 3000 System. The colors indicate the timing of activation, with white representing the earliest activation and purple representing the latest.

magnitude 100 μA/cm^2 was applied to the start of the His bundle located in the first layer perpendicular to the long axis of our heart model with duration of 0.5 ms to initiate propagation. Physiologically, these sites are cardiac cells that are first activated during the cardiac cycle. The Purkinje cells location was adjusted according to physiological conditions. This procedure was repeated until the stimulation produced isochrone's maps similar to clinical mapping. Our simulation results (Fig. 3A, B) shown the activation begin in mid-posterior septum and then propagated

to close area. The posterior wall, near the mitral valve (MV), is the latest activated area, which is closed to the mapping isochronal map of left ventricle in single sinus activation.

3.2 Performance of Parallelization Simulation

Generally, reducing the communications to the minimum and balancing the load among all processors is two of the most important aspects of a successful parallelization. The performance of this parallel computational model was tested by running 50 ms of simulation with WRJ cellular electrophysiological model.

Here, communication time (T_{comm}) is defined as time spent on exchanging short axis sections of data between nodes. Computation time (T_{comp}) accounted for all calculations involved in solving the monodomain equation. Efficiency and scaled speedup are defined as follows:

$$Q_{efficiency} = \frac{\sum_{i=Node(1)}^{Node(N)} T_{i,comp}}{\sum_{i=Node(1)}^{Node(N)} T_{i,comp} + \sum_{i=Node(1)}^{Node(N)} T_{i,comm}} \tag{10}$$

$$Q_{speedup} = \frac{\sum_{i=Node(1)}^{Node(2)} T_{i,comp} + \sum_{i=Node(1)}^{Node(2)} T_{i,comm}}{\sum_{i=Node(1)}^{Node(\mathrm{N})} T_{i,comp} + \sum_{i=Node(1)}^{Node(\mathrm{N})} T_{i,comm}} \tag{11}$$

Fig. 4 shows the efficiency and the scaled speedup of the parallel program as N numbers of computational nodes were used. Both the decrease in efficiency and the increase in speedup have a linear relationship with the number of nodes approximately. The system reaches a speedup of 9.37 and 60.1% of efficiency with 16 processors. Since the time cost of passing data between adjacent is fixed involved cost in top and bottom slices in each sub domain, it is independent with the number of the computational unit. Therefore, although the increased nodes will speedup computation time, the fixed cost time in communication possess a more proportion in total time. Thus result in a decreased efficiency which are coherent with the parallelization strategy employed. In this condition, the best way to hold the efficiency is to decrease the passing data and upgrade the bandwidth of the network inter-connected.

On the other hand, as shown in Table.1, although the total time cost in simulation implements speedup when we used more parallel computational unit, the max load imbalance rate got worse. Imbalance loading may result in inefficiency as processors with less work have to wait idly for the others at the synchronization point. If all of the myocardium points could be distributed among the SMP nodes equally, a high degree of load balance would be achieved and the efficiency can be improved. However, this is very difficult in simulation implement when using geometrical parallelization. Matrix parallelization and matrix preconditioned method is used well

in solving the full bidomain equations [7]. In this paper, we focus on solving mondomain equation to simulation the excitation sequence, in which we can avoid solving elliptic equation, and therefore, geometrical parallelization is implemented more easily.

Table 1. Efficiency and scaled speedup computed from computation, communication

N	Tcomm (s)	Tcomp (s)	Efficiency	Load Imbalance Rate
1	0	139492	100%	0
2	1988	69742	97.2%	0.9843%
4	5423	37873	88.5%	3.3209%
6	5631	21311	79.1%	5.2193%
8	5806	16698	75.7%	6.5355%
10	5845	13386	69.6%	6.7563%
12	5912	11590	66.2%	13.1072%
16	5945	8949	60.1%	14.2037%

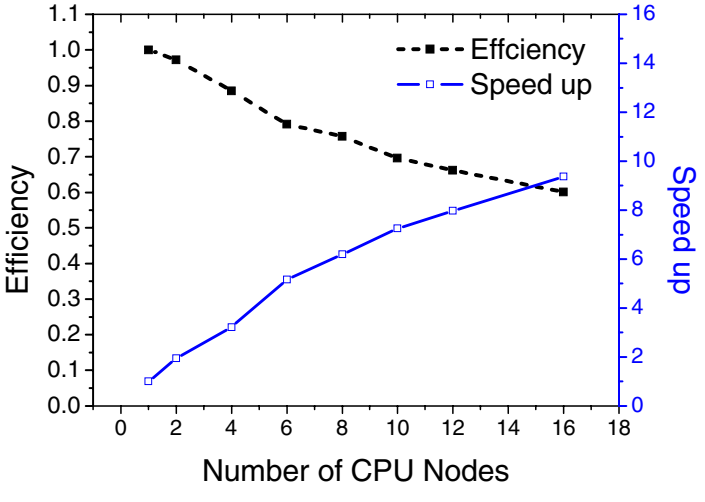

Fig. 4. Scaled speedup varies nearly linearly with increasing number of nodes

In this test, the load imbalance rate was calculated in each condition, results show that load imbalance rate increased to 6.7563% when 10 nodes were used in which the amount of 7.25 times speedup achieved. The load imbalance rate increases with the node number increases as shown in Table.1. Therefore, when using geometrical parallelization we must survey both the communications and load imbalance rate together to decide the best solution. In our case, the most economical selection of the processors unit should be kept no more 12. In addition, Table.1 for 2 nodes (Dual-Core CPU) condition shown the exchange of data among processors via shared

memory is faster than message passing. If the network condition could be improved or using multiprocessor shared memory system, the larger scale of parallelization is preferred.

4 Conclusion

This paper presented a complete parallel system implementation for the simulation of cardiac excitation anisotropic propagation on a three dimensional ventricular cardiac tissue with both the actual geometry and fiber orientation. The numerical kernel of the simulation process is combining the advantage of operator-splitting scheme, adaptive time step and backward differentiation formulation to give a better scheme for solving reaction-diffusion parabolic equations. The simulated heart excitation anisotropic propagation is validated and it suggests that such method may provide a good basis for heart simulation research in a more physiologically way. In this sense, the model is likely to become further integrated with experiments, providing a more efficient means for testing hypotheses and for investigating the impact of novel therapies.

Acknowledgments. This project is supported by the 973 National Key Basic Research & Development Program (2003CB716106), the 863 High-tech Researches & Development Program (2006AA02Z307), the National Natural Science Foundation of China (30570484) and the Program for New Century Excellent Talents in University (NCET-04-0550). The authors are also grateful to Dr. Edward Hsu and his colleagues from Medical Center for In Vivo Microscopy of Duke University for providing DTMRI data.

References

1. Trew, M.L., Caldwell, B.J., Sands, G.B., et al.: Cardiac electrophysiology and tissue structure: bridging the scale gap with a joint measurement and modelling paradigm. Exp. Physiol. 91(2), 355–370 (2006)
2. Noble, D.: Modeling the heart–from genes to cells to the whole organ. Science 295(5560), 1678–1682 (2002)
3. Tranquillo, J.V., Hlavacek, J., Henriquez, C.S.: An integrative model of mouse cardiac electrophysiology from cell to torso. Europace 7(2), 56–70 (2005)
4. Trayanova, N., Eason, J., Aguel, F.: Computer simulations of cardiac defibrillation: a look inside the heart. Comput Visual Sci. 4, 259–270 (2002)
5. Winslow, R.L., Scollan, D.F., Holmes, A., et al.: Electrophysiological modeling of cardiac ventricular function: from cell to organ. Annu Rev. Biomed Eng. 2, 119–155 (2000)
6. Potse, M., Dube, B., Richer, J., et al.: A comparison of monodomain and bidomain reaction-diffusion models for action potential propagation in the human heart. IEEE Trans Biomed Eng. 53(12 Pt 1), 2425–2435 (2006)
7. Lines, G.T., Buist, M.L., Grottum, P., et al.: Mathematical models and numerical methods for the forward problem in cardiac electrophysiology Computing and Visualization in Science, 5, 215–239 (2003)
8. Hsu, E.W., Muzikant, A.L., Matulevicius, S.A., et al.: Magnetic resonance myocardial fiber-orientation mapping with direct histological correlation. Am. J. Physiol. 274(5 Pt 2), H1627–1634 (1998)

9. Fishman, G.I.: Understanding conduction system development: a hop, skip and jump away? Circ Res. 96(8), 809–811 (2005)
10. Thomas, S.A., Schuessler, R.B., Berul, C.I., et al.: Disparate Effects of Deficient Expression of Connexin43 on Atrial and Ventricular Conduction: Evidence for Chamber-Specific Molecular Determinants of Conduction. Circulation 97(7), 686–691 (1998)
11. Winslow, R.L., Rice, J., Jafri, S., et al.: Mechanisms of altered excitation-contraction coupling in canine tachycardia-induced heart failure, II: model studies. Circ. Res. 84(5), 571–586 (1999)
12. Henriquez, C.S.: Simulating the electrical behavior of cardiac tissue using the bidomain model. Crit Rev. Biomed Eng. 21(1), 1–77 (1993)
13. Brown, P.N., Byrne, G.D., Hindmarsh, A.C.: VODE: A variable-coefficient ODE solver. SIAM J. Sci. Comput. 10, 1038–1051 (1989)

A Three Dimensional Ventricular E-Cell (3Dv E-Cell) with Stochastic Intracellular Ca^{2+} Handling

Pan Li, Matthew Lancaster, and Arun V. Holden

Institute of Membrane and Systems Biology and Cardiovascular Research Institute, University of Leeds, Leeds LS2 9JT, UK
bmbpli@leeds.ac.uk
http://www.cbiol.leeds.ac.uk

Abstract. To investigate the mechanisms underlying the initiation and propagation of intracellular Ca^{2+} waves, we developed a three-dimensional ventricular E-Cell (3Dv E-Cell), where cell membrane, nucleus, ryanodine receptor clusters, Z-disk, cytoplasm are modeled as spatially distributed structures. For the simulation of Ca^{2+} sparks and Ca^{2+} diffusion, a modified Fire-Diffuse-Fire model is used with stochastic rules for triggering Ca^{2+} release. The 3Dv E-Cell is used to illustrate how stochastic properties of Ca^{2+} sparks can lead to complex spatio-temporal intracellular wave processes and allows the incorporation of spatial data sets (protein distribution) into the geometry.

1 Introduction

Intracellular Ca^{2+} is responsible for regulating diverse cellular events, such as excitation-contraction coupling in muscle cells, gene expression, and secretion [1]. Changes in Ca^{2+} level can occur in microseconds (eg. ionic flow), milliseconds (eg. channel kinetics), seconds (eg. contractions) or hours (eg. remodelling), and can be microscoply localized, or propagate throughout cells and tissues [2]. Intracellular Ca^{2+} is supplied through Ca^{2+} channels from external cellular space, and also released from internal stores: sarcoplasmic reticulum (SR) in muscle cells or endoplasmic reticulum (ER) in other cells. In response to changes in membrane potential or stimulation, a variety of calcium systems are involved, such as L-type Calcium Channels (LCCs), Ryanodine Receptors (RyRs), Na/Ca exchange system (NCX), ATP-driven calcium pump, cytosolic calcium buffers, Inositol 1,4,5-trisphosphate (IP_3) signaling pathway. RyRs and IP_3s are are non-selective, high-conductance calcium release channels to SR or ER that contain very high concentrations of calcium. The spatially localized distribution of RyRs provides structural matrix for local control of calcium release units (CRUs) by LCCs, and is a strong determinant of Ca^{2+} wave initiation [3].

Ca^{2+} induced Ca^{2+} release (CICR) is a phenomenon where a small elevation in cytosolic Ca^{2+} leads to a larger release of Ca^{2+} from the internal stores, SR or ER. Ca^{2+} sparks, discovered by Cheng et al via confocal microfluorimetry

F.B. Sachse and G. Seemann (Eds.): FIMH 2007, LNCS 4466, pp. 180–189, 2007.

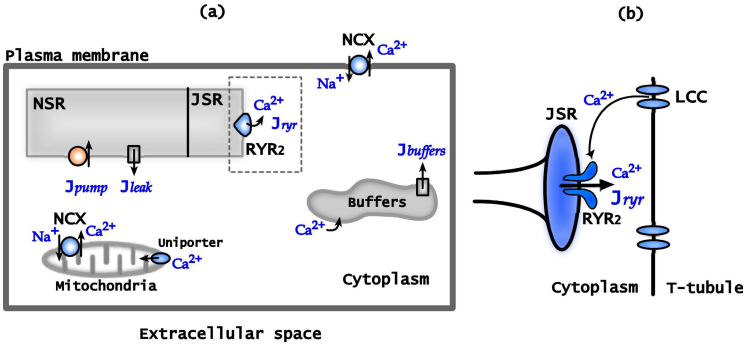

Fig. 1. Intracellular calcium dynamics and the mechanism of CICR. (a) During cell membrane depolarization, large amount of calcium is released from internal stores (Junctional SR, JSR) by J_{RyR}. The cytosolic calcium diffusion is retarded by calcium buffers and also mitochondrias. Released calcium from JSR will then be removed by pumping back to (Network SR, NSR) by J_{pump}, and also be removed out of the cell by NCX. (b) shows a more detailed illustration of CICR, where small amount of calcium release from LCCs activated RyR subtype 2 RyR_2 located at the surface of JSR, and leads to much large amount release of calcium, J_{RyR}.

[4], are the elementary Ca^{2+} release events from internal stores. They occur spontaneously and randomly from discrete, localized Ca^{2+} release sites, and summation of Ca^{2+} sparks give rise to the global Ca^{2+} transient, which activate the contractile myofilament. The spread of Ca^{2+} is greatly retarded by buffers, such as calmodulin and troponin C, therefore, CICR provides a way to amplify the microscopic initiation events into propagating Ca^{2+} signals to reach other initiation sites, such as neighboring RyRs. Ca^{2+} waves propagate throughout the cell, with conduction velocity of around 100 μm/s [6]. The relation between Ca^{2+} sparks and Ca^{2+} waves is complicated by cell structure, asymmetric spatial distribution of RyR clusters, anisotropic diffusion of Ca^{2+}, Ca^{2+} sensitivity of CRUs, Ca^{2+} buffers, and strength of Ca^{2+} current required to generate Ca^{2+} sparks.

Launched in 1996, E-Cell project is aiming to model and reconstruct biological phenomena in silico, and simulate cell behavior by numerically integrating the differential equations described implicitly in these reaction rules [7]. Most models of Ca^{2+} waves in cardiac muscles have CICR as the basic mechanism that is integrated with stochastic Ca^{2+} release of RyRs and anisotropy in diffusion. Simulation studies have been extended to two-dimensional (2D) space to reproduce spatio-temporal wave patterns [6] [8] , and also 3D spaces with details of subcellular structures [9]. However, we need to incorporate both 3D geometry and the stochastic nature of Ca^{2+} wave initiation and propagation. For example, in 2D models, calcium from SR will be released into a 2D region rather than a 3D subspace, and potentially lead to inaccurate estimates of release current strength [6]; besides, deterministic models use a fixed release threshold and so do not reproduce the stochastic aspect of calcium sparks (magnitude, duration)

[9]. In 2006, Izu et al. studied 3D interation between two neighboring z-disk of a sarcomere [3], here we extend the study and construct a three dimensional (3D) cardiac cell model that is coupled with stochastic intracellular Ca^{2+} dynamics.

We present a first generation 3D ventricular e-cell (3Dv E-Cell) with stochastic triggering of Ca^{2+} release to study spatio-temporal behaviors of Ca^{2+} sparks and intracellular Ca^{2+} waves, where the cell membrane, nucleus, cytoplasm, Ryanodine receptor clusters, Z-disk are modelled as spatially distributed structures. A modified Fire-Diffuse-Fire (FDF) model is used to mimic the biophysical properties of the cardiac ventricular cell.

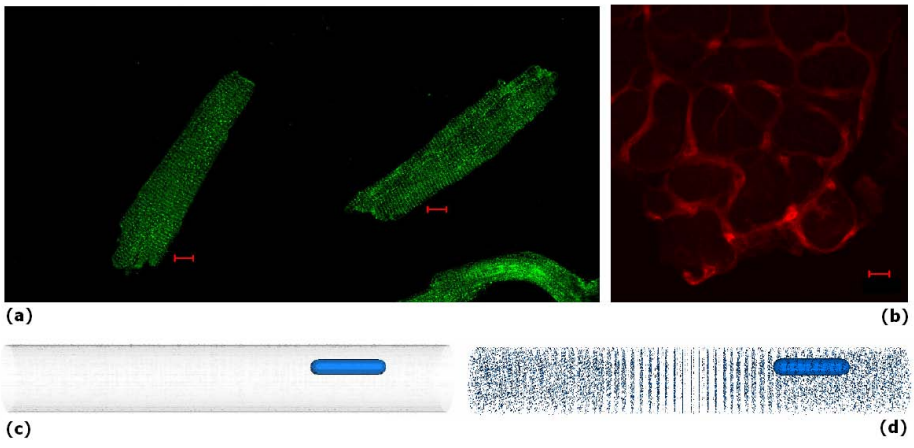

Fig. 2. (a) Confocal microscopic images of the rat ventricular cell with Ca^{2+} channel labeled by fluorescein isothiocyanate with the resolution of 0.5 μm, where the scale bar is 10 μm. (b) trasversal section of a piece of rat ventricular tissue. (c) we idealised the geometry of myocytes illustrated in (a) by a simple cylinder with semitransparent membrane and nucleus. (d) the visualization of 3D spatial distribution of RyR clusters.

2 Methods

2.1 Cell Geometry

The geometry of the 3Dv E-Cell is taken as a cylinder with diameter of 16 μm and length of 100 μm with the space step of 0.2 μm, which gives a 80 by 80 by 500 3D matrix with 3.2 million grid points. Following Ye Chen-Izu et al's measurements [10], the resting state spacing between neighboring Z-disks is 1.87$\pm$0.18 μm. RyR clusters are represented as individual grid points irregularly distributed on each Z-disk with the transverse spacing of 1.05$\pm$0.44 μm and the longitudinal spacing of 0.83$\pm$0.31 μm. The peripheral spacing of RyR clusters is 1.97$\pm$0.42 μm, in the 3Dv E-Cell we use the density of around 0.4/μm^2 for cell surface. This nucleus has a diameter of 5.0 μm and a length of 10.0 μm, and its center is located 20.0 μm from the end, and 5.0 μm from the surface of

the cell. The 3Dv E-Cell is segmented into cell membrane, cytoplasm, Z-disk, RyR clusters, nucleus, and each grid point is identified by a label acorrding to the segmentation. Grid points with the same label have same dynamics for simulation. Preliminary studies used a 2D model with width of 28.0 μm and height of 100.0 μm, which gives a 140 by 500 lattice with 70000 grid points, see Fig. 3-6.

2.2 Mathmatical Model of Ca^{2+} Sparks and Waves

We start with the FDF model of Smith et al [11], where a wave propagates by sequentially triggering Ca^{2+} sparks by diffusion. Once a RyR cluster fires, Ca^{2+} released diffuses to its nearest firing neighbors. A local wave may or may not be initiated dependent on the Ca^{2+} release strength and duration by Calcium Release Unit (CRU), diffusion coefficient, the cytosolic buffering system, calcium sensitivity, and spatial distribution of RyRs. After Ca^{2+} release the CRU enters refractory period. The mathematical description of Ca^{2+} sparks and calcium waves is a set of reaction-diffusion equations (1)-(8), based on Izu et al [6]. This simple model considers the exchange between the cytoplasm and the SR, and neglects Ca^{2+} flux through the cellular membrane. The diffusion coefficient D_c for free calcium is anisotropic, and we use 300 μm^2/s for long axis direction (along the cell) and 150 μm^2/s for other directions (x, y). Ca^{2+} release from SR is modeled as a point source, where i_{Ca} is the magnitude of a Ca^{2+} source that is sharply peaked at the origin [11]. In other words, the point source represents a calcium current i_{Ca} for a time τ, and total amount of calcium released equals to $\sigma_{RyR} \times \tau$. Both the strength of Ca^{2+} release and duration are important in the development of localised Ca^{2+} sparks or propagating waves. The standard Ca^{2+} release in this paper is equivalent to a 10 ms pulse (τ) with the strength of 2pA (i_{Ca}). Ca^{2+} buffers, internal stores are considered to be uniformly distributed over the geometry.

$$\frac{\partial \left[Ca^{2+}\right]}{\partial t} = \nabla \cdot \left(D_c \nabla \left[Ca^{2+}\right]\right) + J_{sum} \tag{1}$$

where

$$J_{sum} = J_{RyR} + J_{buffers} - J_{pump} + J_{leak} \tag{2}$$

$$J_{RyR} = \sigma_{RyR} \delta\left(\boldsymbol{r}\right), \sigma_{RyR} = \frac{i_{Ca}}{2F} \tag{3}$$

$$J_{buffers} = \sum_{n} J_n, \tag{4}$$

$$J_{pump} = \frac{v_{pump}\left[Ca^{2+}\right]^m}{K_{pump}^m + \left[Ca^{2+}\right]^m} \tag{5}$$

$$J_{leak} = J_{pump}\left(c_0\right) \tag{6}$$

with

$$\frac{\partial [CaB_n]}{\partial t} = -J_n \tag{7}$$

$$J_n = -k_n^+ \left[Ca^{2+}\right] \left([B_n]_T - [CaB_n]\right) + k_n^- [CaB_n] \tag{8}$$

n in Equation (4)(7)(8) is the index of buffers, see Table 1.

Table 1. Ca^{2+} buffers

	k_n^+ $\mu M^{-1}/s$	k_n^- s^{-1}	$[B_n]_T$ μM	K_n μM
Calmodulin	100	38	24	0.38
Troponin C	39	20	70	0.51

In our cell model, discrete RyR clusters are irregularly distributed at Z-disks, see Figure 2(d), and their probability to fire is governed by probability function P, based on Ca^{2+} concentration, and also the Ca^{2+} sensitivity factor K_{poss}. For any given Ca^{2+} sensitivity factor, higher Ca^{2+} concentration always indicates higher firing probability. For each timestep during simulation, a uniformly distributed random number u_{rand} between 0 and 1 is compared with result from probability function to decide either or not CRUs will fire. As described below, state function S for a CRU defines the state of resting or firing, and can only either be 0 or 1. Here, we use T_N^M to define the N_{th} sparks at site M.

$$S \in \{0, 1\} \tag{9}$$

$$P_{[Ca^{2+}]} = \frac{\left[Ca^{2+}\right]^n}{K_{poss}^n + \left[Ca^{2+}\right]^n} \tag{10}$$

$$S\left(P\right) = 1, if P_{[Ca^{2+}](\boldsymbol{r_N},t)} > u_{rand}, T_N^M > T_N^{M-1} + \tau_R \tag{11}$$

Table 2. Model parameters

Parameter	Standard Value	Definition
D_c	$300\mu m^2$/s z, $150\mu m^2$/s x,y	Ca^{2+} diffusion coefficient
τ	10 ms	Open time of calcium release unit
i_{Ca}	2pA	Amplitude of elemental Ca_{2+} release
F	96500 C/mol	Farady's constant
v_{pump}	200 $\mu M/s$	Maximum SR pump rate
K_{pump}	0.184 μM	SR pump Michaelis constant
m	4.0	Pump hill coefficient
n	1.6	Hill coefficient for $P_{Ca^{2+}}$
c_0	0.10 μM	Background calcium concentration

2.3 Numerical Methods

Unless indicated otherwise, for all the simulations, we used a finite difference method with the space step of 0.2 μm and time step of 10 μs. Zero-flux boundary conditions are implemented by setting the values of Ca^{2+} concentration for the gridpoints on the boundary equal to those for their immediate internal neighbors. Simulations are performed on SunBlade 2000 workstations. The initial conditions are set to be at rest, with calcium background concentration ($c_0 = 0.10\ \mu M$), see Table 2 for all the parameters.

3 Results

3.1 Normal Cell Excitaion

In ventricular tissue driven by the normal sinus rhythm, ventricular cells are excited by currents due to the propagating action potential wavefront. Membrane excitation triggers contraction via excitation-contraction coupling [2]. The 3D distribution of RyR clusters is the intracellular grid for Ca^{2+} signals, allowing coupling of localized and whole cell Ca^{2+} changes. A normal excitation of the cardiac cell produces the membrane depolarization of the action potential. Ca^{2+} influxes (Ca^{2+} current through channels) prodominantly in the T tubules activate most of the CRUs and incur SR releases, then free cytosolic calcium concentration arises uniformly throughout the cell. During the refractory stage, RyR clusters remain inactivate, Ca^{2+} is pumped out of the cell by NCX or back into the internal store SR by J_{pump}, restoring the resting state.

The magnitude of Ca^{2+} sparks depends on the strength and duration of Ca^{2+} release from internal stores, see Fig. 3(b)(c). Ca^{2+} sensitivity also plays a crucial role in formation of calcium sparks and wave. In Fig. 3(d), pseudo multi linescans of transverse section of the cell are recorded under different conditions, such as normal excitation following membrane depolarization, spontaneous travelling Ca^{2+} wave, resting cell with sparse, and localised Ca^{2+} sparks.

3.2 Planar Ca^{2+} Waves

Traveling waves are commonly observed in excitable media. Under centain conditions, Ca^{2+} waves can propagate throughout the cell. The spatial propagation of Ca^{2+} waves have been observed in a variety of cell types, and imaged by confocal microscopy with fluorescent calcium indicators [12] [13]. When a cell becomes overloaded with Ca^{2+}, a wavefront of intracellular Ca^{2+} may be evoked, or may develop spontaneously.

Spontaneous local Ca^{2+} release occurs in the 3Dv E-Cell when the Ca^{2+} sensitivity K_{poss} is high , i.e. RyR clusters have a high probability of opening, even when the Ca^{2+} concentration is low. If the calcium sensitivity is low, a spontaneous local calcium wave will only occur in the 3Dv E-Cell if calcium concentration is high (about 50 μM), or the magnitude of i_{Ca} is high, or release

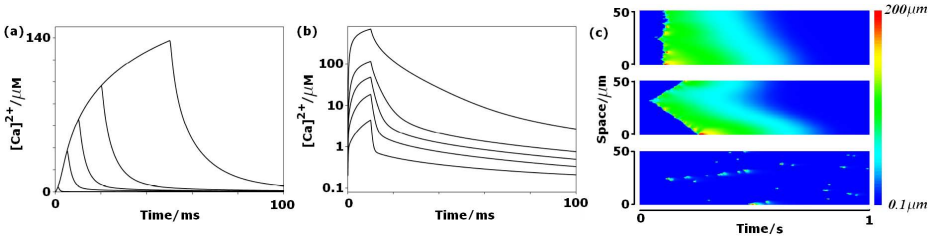

Fig. 3. (a) Ca^{2+} concentration curve at 0.6μm (from the point source) during calcium sparks with τ = 1ms, 2ms, 50ms, 10ms, 20ms, 50ms. Decay time is relatively fast compared to previous simulation studies, which could be due to the lack of calcium dye and different recruited buffers in this model. (b) Ca^{2+} concentration curve at 0.6μm during calcium sparks with i_{Ca} = 0.2pA, 0.5pA, 1pA, 2pA, 4pA, 10pA. (c) Pseudo line scans of Ca^{2+} concentration on 50μm space (with transverse spacing of RyRs) for 1 second, where (Top) i_{Ca} = 4.5pA, K_{poss} = 400μM, a uniformed calcium elevation is applied at t = 100ms, (middle) i_{Ca} = 4.5pA, K_{poss} = 200μM, once a CRU fires, most of the rest CRUs fires consequently and lead to a relative stable solitary wave, (bottom)i_{Ca} = 2pA, K_{poss} = 800μM, only sparse, localized calcium sparks can be observed.

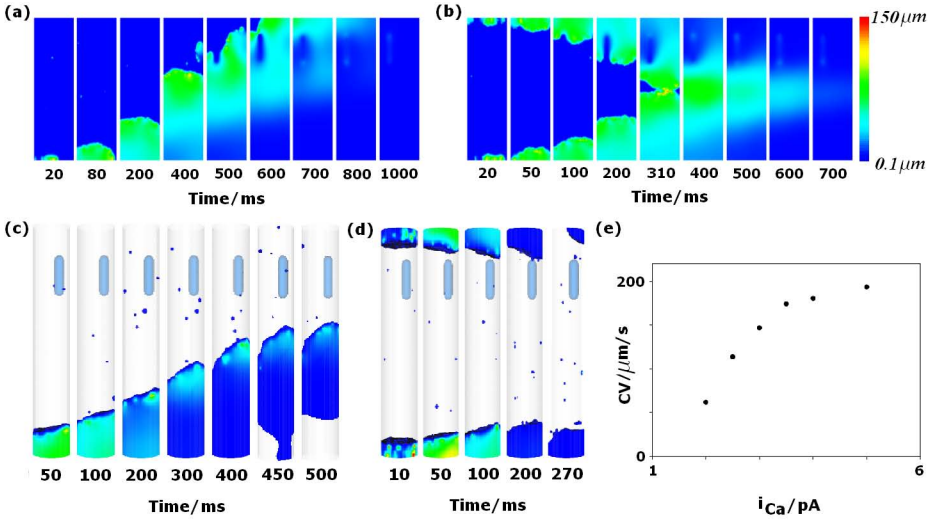

Fig. 4. Simulations of planar Ca^{2+} waves. (a) Solitary Ca^{2+} wave propagates throughout the cell,(b) Ca^{2+} waves initated at both ends of the cell, travel towards each other, and finally collide and annihilate, (c) 3D simulation of solitary wave initiated in one end with i_{Ca} = 8.0, K_{poss}= 1000μM. (d) Stimulus applied at both ends of the cell with i_{Ca} = 5.0, K_{poss}= 800μM, waves fail to propagate due to relatively small release current i_{Ca}. (e) Releationship between i_{Ca} and the Ca^{2+} planar wave conduction velocity (CV).

duration τ is long. To evoke calcium waves in the 3Dv E-Cell we use a low calcium sensitivity to avoid spontaneous initiation, and a high (8pA) i_{Ca}. The evoked calcium waves propagate without decrement, and annihilate on collision.

3.3 Microscopic Re-entrant Waves

Microscopic re-entrant Ca^{2+} waves have been observed inside cardiac cells [12]. Re-entrant spiral wave can be initiated in a 2D excitable medium model by a number of methods: S1-S2 protocol, wave cutting and propagation through heterogeneity or around obstacles. In our simulations, due to relative long refractory period and the geometry of the cell, although re-entrant Ca^{2+} waves can been initiated, the 2DVe-cell is not large enough to sustain a free spiral. However, nucleus does not actively participate in the CICR and has a lower diffusion coefficient compared to cytoplasm [8]. Such as obstacle allows the same wave to

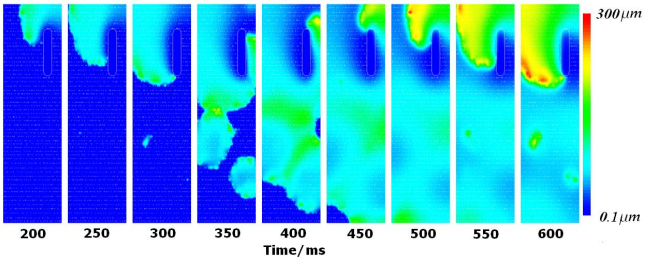

Fig. 5. Formation of microscopic spiral waves due to the nucleus. A Ca^{2+} wave is initiated close to the nucleus with i_{Ca} = 5.0pA, K_{poss} = 800μM, τ = 10ms, τ_R = 350ms. Ca^{2+} wave propagates along the nucleus due to the existance of the obstacle, and then lead to a microscopic spiral wave.

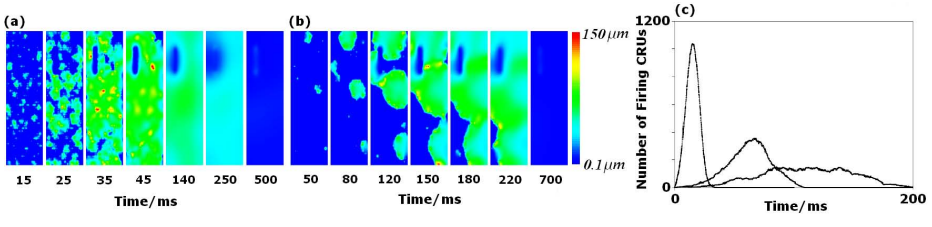

Fig. 6. Stochastic calcium release with different calcium sensitivity in 2D and 3D. (a) With high calcium sensitivity, where K_{poss} = 50μM, most of CRUs fire in less than 45ms, and enter the refractory period almost synchronously afterwards. The cell is back to resting status at around 500ms. (b) with medium calcium sensitivity, where K_{poss} = 400μM, at t = 50ms, there are three identified local caclium wave spontaneously initiated, and then evoke their neighbors to fire. Most of the CRUs enter the refractory period at around 220ms, and the cell returns to resting stage around 700ms. (c) Number of firing CRUs against time curve with K_{poss} = 25μM, 200μM, 400μM in the first 200ms.

return on other side of the nucleus, giving rise to an intracellular micro re-entry. In Fig. 5, microscopic spiral waves are illustrated when a local calcium wave initiated close to cell nuleus.

3.4 Calcium Sensitivity

The firing probability of the CRUs of the 3Dv E-Cell under the same free Ca^{2+} concentration increases with Ca^{2+} sensitivity K_{poss}. As K_{poss} is increased, spontaneous release becomes synchronised - see Fig. 6. This synchronisation can lead to auto-oscillatory activity. As K_{poss} is decreased in the 3Dv E-Cell, the global cell synchronisation breaks down into different intracellular domains. As K_{poss} is decreased, it is apparent that RyR clusters on the same Z-disk tend to synchronise more readiliy than between z disks, leading to a quasi-saltatory propagation of calcium waves along the cell.

At low K_{poss}, localised, discrete Ca^{2+} sparks occur intermittently, and occasionally lead to larger events - spatially restricted calcium waves that are confined to a small microdomain. These low K_{poss} pheneomena model the activity of the normal resting ventricular cell.

4 Conclusions

Here we introduce a 3D ventricular e-cell (3Dv E-Cell) implemented with stochastic triggering of Ca^{2+} release from SR, and studied Ca^{2+} sparks and the initiation of spatio temporal patterns of intracellular Ca^{2+} waves. When the cardiac cell has normal Ca^{2+} sensitivity, the stochastic model can produce localized Ca^{2+} sparks, but fail to produce local waves, even applied stimulus just above the normal threshold. With high Ca^{2+} sensitivity, the virtual cell can demonstrate calcium oscillations, and the RyR clusters fire in concert. The nucleus can act as an obstacle, and lead to intracellular re-entrant calcium waves.

The 3Dv E-Cell provides a platform within which local control models of Ca^{2+} release can be embedded, and more biophysicallly detailed representations of CRU stochasticity, and can be coupled with current generation cellular excitation models, eg. [14] [15].

In addition to allowing the dissection, in space and time, of the effects of different intracellular mechanisms, the 3Dv E-Cell can be developed to interact with experimental data from different individual cell. The constructed geometry - say the spatial distribution of RyR clusters - can readily be replaced by importing confocal imaging data stacks, to allow the 3Dv E-Cell to simulate data from individual single cell experiments, and to be modified for ventricular myocytes from different species.

Aknowledgement

P. Li is supported by ORSAS, Tetley and Lupton scholarship and CVCP IRS (International Research Scholarship). This work was supported by the European Union through the Network of Excellence BioSim, Contract No. LSHB-CT-2004-005137.

References

1. Berridge, M.J., Lipp, P., Bootman, M.D.: The versatility and universality of calcium signalling. Nature Reviews Molecular Cell Biology 1, 11–21 (2000)
2. Berridge, M.J, Bootman, M.D, Roderick, H.L: Calcium signalling: dynamics, homeostasis and remodelling. Nature Reviews Molecular Cell Biology 4, 517–529 (2003)
3. Izu, L., Means, S., Shadid, J., Izu, Y., Balke, C.: Interplay of ryanodine receptor distribution and calcium dynamics. Biophysical Journal 91, 95–112 (2006)
4. Cheng, H., Lederer, M., Cannell, M.: Calcium sparks: elementary events underlying excitation-contraction coupling in heart muscle. Science 262, 740–744 (1993)
5. Lopez, J., Jovanovic, A., Terzic, A.: Spontaneous calcium waves without contraction in cardiac myocytes. Biochem. Biophys. Res. Comm. 214, 781–787 (1995)
6. Izu, L., Wier, W., Balke, C.: Evolution of cardiac calcium waves from stochastic calcium sparks. Biophysical Journal 80, 103–120 (2001)
7. Tomita, M., Hashimoto, K., Takahashi, K., Shimizu, T., Matsuzaki, Y., Miyoshi, F., Saito, K., Tanida, S., Yugi, K., Venter, J., Hutchison, 3.: E-CELL: software environment for whole-cell simulation. Bioinformatics 15(1), 72–84 (1999)
8. Dupont, G., Pontes, J., Goldbeter, A.: Modeling spiral calcium waves in single cardiac cells role of the spiral heterogeneity created by the nucleus. Am. J. Physiol. Cell. Physiol. 271, C1390–C1399 (1996)
9. Okada, J., Sugiura, S., Nishimura, S., Hisada, T.: Three dimensional simulation of calcium waves and contraction in cardiomyocytes using the finite element method. Am. J. Physiol. Cell. Physiol. 288, C510–C522 (2005)
10. Izu, Y., McCulle, S., Ward, C., Soeller, C., Allen, B., Rabang, C., Cannell, M., Balke, C., Izu, L.: Three dimensional distribution of ryanodine receptor clusters in cardiac myocytes. Biophysical Journal 91, 1–13 (2006)
11. Smith, G., Keizer, J., Stern, M., Lederer, W., Cheng, H.: A simple numerical model of calcium spark formation and detection in cardiac myocytes. Biophysical Journal 75, 15–32 (1998)
12. Lipp, P., Niggli, E.: Microscopic spiral waves reveal positive feedback in subcellular calcium signaling. Biophysical Journal 65, 2272–2276 (1998)
13. Orchard, C., Mustafa, M., White, E.: Oscillations and waves of intracellular calcium in cardiac mucles cells. Chaos, Solitons and Fractals 5, 447–458 (1995)
14. Luo, C., Rudy, Y.: A Dynamic Model of the Cardiac Ventricular Action Potential - Simulations of Ionic Currents and Concentration Changes Circulation Research 74, 1071–1097 (1994)
15. TenTusscher, K., Noble, D., Noble, P., Panfilov, A.: A model for human ventricular tissue. American Journal of Physiology 286, H1573–H1589 (2004)

A Model for Simulation of Infant Cardiovascular Response to Orthostatic Stress

Yutaka Nobuaki[1], Akira Amano[1], Takao Shimayoshi[2], Jianyin Lu[3], Eun B. Shim[4], and Tetsuya Matsuda[1]

[1] Graduate School of Informatics, Kyoto University, Kyoto, Japan
{amano,nobuaki,tetsu}@i.kyoto-u.ac.jp
[2] ASTEM Research Institute of Kyoto, Kyoto, Japan
simayosi@astem.or.jp
[3] Cell/Biodynamics Simulation Project, Kyoto University, Kyoto, Japan
lu@biosim.med.kyoto-u.ac.jp
[4] Division of Mechanical & Biomedical Engineering, Kangwon National University, Korea
ebshim@kangwon.ac.kr

Abstract. We developed an infant circulation model which incorporates an accurate myocardial cell model including a beta adrenergic system. The beta adrenergic system is essential for the response reproduction of the baroreflex control system. The proposed model was constructed by modifying the parameters of a human adult circulation model with the aid of a guinea pig myocardial cell model, whose baseline heart rate is close to that of an infant. The presented model is in good agreement with results obtained in physiological experiments.

1 Introduction

To improve our knowledge on biological mechanisms, quantitative and integrative studies of each biological element are necessary. Despite the rapid advancement in the accumulation of quantitative data from biological elements, the integrated systems are still not well analyzed. The simulation of complex biological models is of great importance, due to its potency in the analysis of biological functions. Biosimulation models are also expected to develop into powerful tools for medical education.

As a consequence of their complex physiology obstetric patients, neonates, and children often require rapid therapeutic intervention in the acute phase. We believe that simulation models for these patients will be of significant use in medical training. Since the cardiovascular system is one of the most essential physiological systems, we focused on constructing a baseline cardiovascular simulation model for infants.

Goodwin et al. [1] presented an infant cardiovascular simulation model which consists of four heart chambers and 6 compartments. The model also integrates an autonomous nervous system, however, the heart chamber model is based on

F.B. Sachse and G. Seemann (Eds.): FIMH 2007, LNCS 4466, pp. 190–199, 2007.

a time varying elastance model, for which the evaluation of the effects on electrophysiological aspects of the myocardial cells is difficult. Since the myocardial cell models are becoming increasingly accurate[2], incorporation of the same into cardiovascular models is unquestionably desirable.

In this paper, we propose an infant cardiovascular model which incorporates such an accurate myocardial cell model.

2 Cardiovascular Model

Since our model considers an autonomous nervous system, we used a myocardial cell model which includes a beta adrenergic stimulus system. The model is constructed from elementary models decribed in this section(Table1).

Table 1. Elementary models of proposed infant cardiovascular model

Element	Model	Species	Reference
cardiac cell	Kyoto model	guinea pig	[3]
left ventricle	Laplace law		
circulation	Heldt model	adult human	[4]
control system	Heldt model	adult human	[4]

2.1 Myocardial Cell and Left Ventricle Model

The Kyoto model proposed by Noma et al was used for the myocardial cell model. The Kyoto model is an accurate cell model which incorporates most of the known ion channels and transporters, a mitochondria as well as a contraction model. In addition, it is the only model which incorporates a beta adrenergic system. The contractility of the model is modified by the isoproterenol (ISP) concentration (Fig.1). Note that the Kyoto model shows a decrease in maximum force and increase of minimum force when the heart rate increase (Fig.2).

For the left ventricle model the Laplace law was applied. Denoting the wall thickness with h, the radius with R, the LV pressure with P_{lv} and the myocardial cell force by F_{ext}, the Laplace law is represented as $2F_{ext}/R = P_{lv}/h$ [5]. Through this equation, LV pressure and volume are related to the cell contraction force.

2.2 Circulation Model

In clinical tests, the head up tilt (HUT) is commonly used for both, adults and infants, to verify the response of the baroreflex system. Likewise, in our study, HUT was used to test the baroreflex. Accordingly, the circulation model was considered to have several compartments, which account for posture change. The human adult circulation model proposed by Heldt et al. [4] is

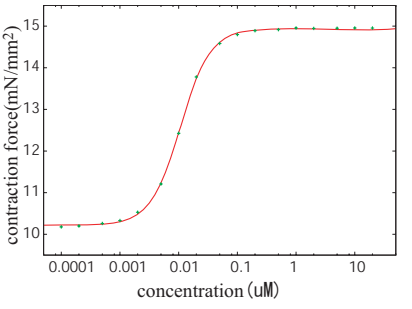

Fig. 1. Relation between ISP concentration and maximum contraction force

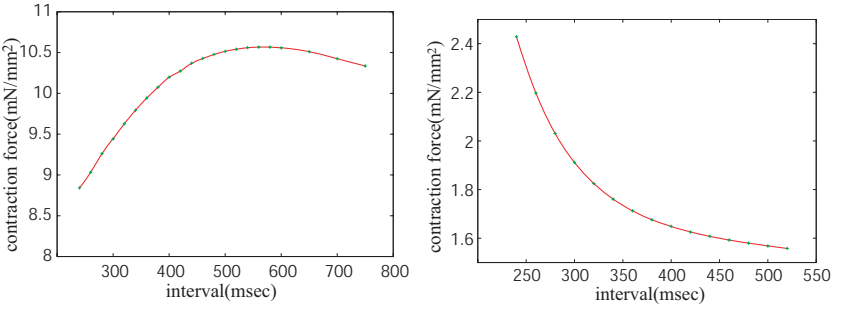

(a) Maximum force (b) Minimum force

Fig. 2. Relation between RR interval and force

mathematically formulated in terms of an electric analogous model with 12 compartments that can represent the posture change (Fig.3). 10 compartments representing the peripheral circulation show linear resistance (R) and capacitance (C). The legs, splanchnic and abdominal venous compartments exhibit nonlinear pressure-volume relations according to the following equation,

$$\Delta V = \frac{2 \cdot \Delta V_{max}}{\pi} \cdot \arctan\left(\frac{\pi \cdot C_0}{2 \cdot \Delta V_{max}} \cdot \Delta P_{trans}\right). \tag{1}$$

ΔV represents the compartment volume change due to change in transmural pressure ΔP_{trans}. ΔV_{max} represents the maximal change in compartment volume and C_0 the compartment compliance at baseline transmural pressure. An additional control system built into the model maintains the blood pressure which controls heart rate (HR), peripheral resistance (R), venous zero-pressure filling volume (V^0) and heart contractility (C_{sys}) [4].

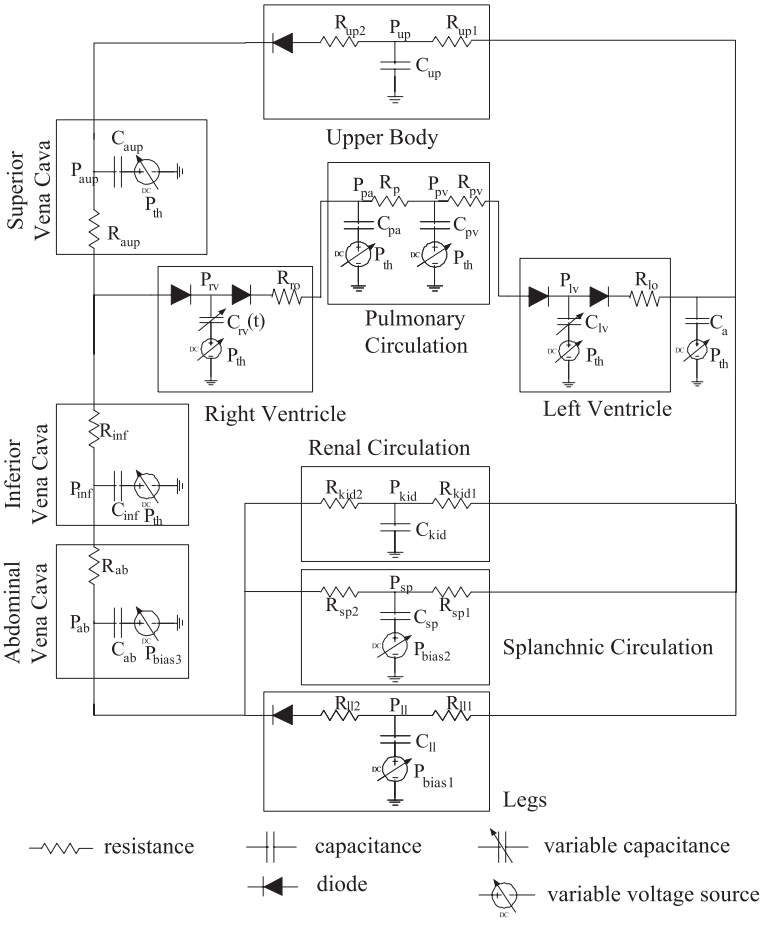

Fig. 3. Heldt circulation model. [4]

3 Construction of Infant Circulation Model

Since the species and the age of the subjects each model is based on is different from that of the human infant, we modified the parameters and the structure of each model.

3.1 Circulation Model Scaling

Since the baseline heart rate of infants is around 130–150(bpm), the myocardial model was constructed by means of the Kyoto model at a baseline heart rate of 150(bpm). The only modification to the model was multiplication of the cross-bridge sliding rate by 7.0, since the original value was determined for 25 degrees room temperature, while the temperature of an infant is around 37 degrees.

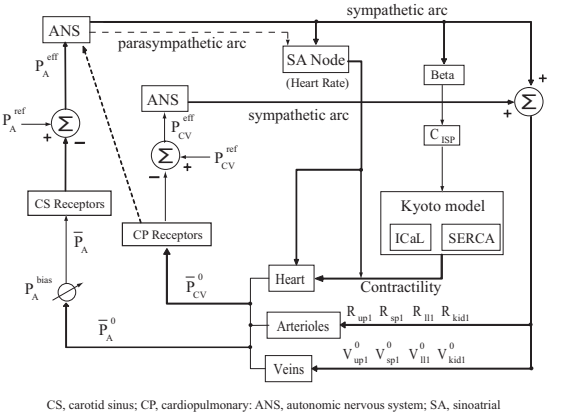

CS, carotid sinus; CP, cardiopulmonary: ANS, autonomic nervous system; SA, sinoatrial

Fig. 4. Block diagram of control system

For the circulation model, we modified the hemodynamic parameters of the Heldt model to fit the infant circulation parameters. Thereby, a scaling method proposed by Goodwin et al. [1] was employed. In their study, the adult human circulation model proposed by Beneken et al. [6] was adjusted to the circulation of a 6 month old infant. Each resistance parameter is multiplied by 2.0, the compliance parameter by 1/5.43 and zero-pressure filling volume by 0.13. The same scaling factors were adopted for our model.

We used the Heldt model initial compartment pressures as initial compartment pressures. From these pressure values, the initial compartment volumes can be calculated, leading to the initial total blood volume of 783.5ml which is slightly large compared to the physiological value of 640ml.

3.2 Control Model Modification

In the Heldt model, the heart function is controlled by its contractility and the given heart rate. We took over the same control system without any parameter modifications. However, in the Heldt model, heart contractility is controlled by the maximum elastance parameter of their time varying elastance model, while the contractility in our heart model is controlled by the ISP concentration. Thus, the control system was modified to influence the ISP concentration. Additionally, in the Heldt model, heart contractility is controlled independently from the heart rate, which is in opposition to the real myocardial cell as well as the myocardial cell model applied in our study. Consequently, deriving a transform function between original heart contractility control signal and ISP concentration was the first task.

An open loop control system was created using the original Heldt model and the pressure input to the baroreceptor varied.In this way, the relation between the heart contractility control signal and the mean blood pressure was determined. Subsequently an open loop control system using the Heldt model was

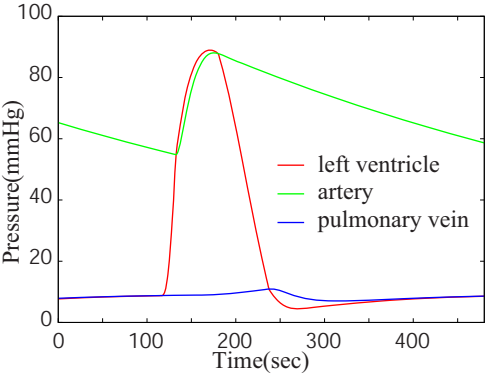

Fig. 5. Pressure at left ventricle, artery and pulmonary vein in resting situation in supine position

designed incorporating our Laplace heart model and the cell model. By changing the ISP concentration, the relation between the ISP concentration and mean blood pressure was deduced. By deleting the mean blood pressure parameter from these two functions, we obtained the desired transform function from heart contractility control signal to ISP concentration.

Subsequently, a compensation function for the heart contractility which is modified with the heart rate was derived. In the real cell, the relation between the cell force and heart rate changes nonlinearly according to the ISP concentration. However, in our model this relation is assumed to be independent of the ISP concentration. The block diagram of our control system is shown in Fig.4.

4 Experimental Results

4.1 Resting Hemodynamics

Figure 5 shows the resulting pressure at the left ventricle, artery and pulmonary vein in resting situation in supine position. Table 2 demonstrates that the hemodynamic parameters of the simulation results match the physiological values from [7][8][9].

4.2 HUT Test

Using the completed model a simulation experiment of the HUT test was conducted. To simulate the tilt effect, we applied following bias pressure to the lower three compartments in accordance with [4].

$$P_{bias} = \begin{cases} P_{max} \cdot \sin(\alpha(t)) & t_0 \leq t \leq t_0 + t_{tilt} \\ P_{max} \cdot \sin(\alpha_{max}) & t > t_0 + t_{tilt} \end{cases} \quad (2)$$

Table 2. Hemodynamic parameters in the supine position at rest

Variable	Target	Simulation results
Heart		
HR(bpm)	115-145	150
LVEDV(ml)	17	27.1
LVEDP(mmHg)	5	6.08
LVESV(ml)	5	13.4
LVESP(mmHg)	82	88.0
CO(L/min)	1.2-2.0	2.0
Circulation		
maxAP(mmHg)	70-110	87.1
minAP(mmHg)	50-65	54.3
CVP(mmHg)	3-12	1.8-3.2

HR: Heart rate, LVEDV: left ventricular end-diastolic volume, LVEDP: left ventricular end-diastolic pressure, LVESV: left ventricular end-systolic volume, LVESP: left ventricular end-systolic pressure, CO: cardiac output, maxAP: maximum arterial pressure, minAP: minimum arterial pressure, CVP: central venous pressure.

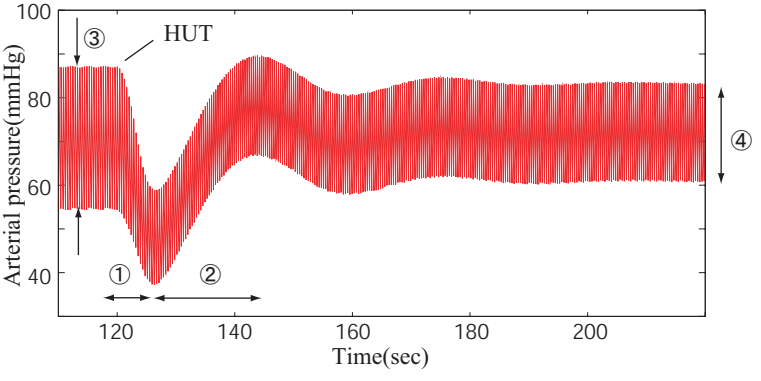

Fig. 6. Arterial pressure at HUT test

Here, t_0 and t_{tilt} denote starting and ending time of the tilt, α_{max} denotes the final angle of the tilt and P_{max} the maximum bias. We used 40.0, 7.0, 5.0 for the P_{max} of the renal, splanchnic and legs compartment, respectively.

In the physiological experiment with a human adult, the blood volume decreases by 600ml within 35 minutes [10]. This fact is modeled in the Heldt model as follows:

$$V_{total} = (5700ml - \Delta V) + \Delta V \cdot 0.9^{\frac{t-t_0}{60s}} \tag{3}$$

$$\Delta V = 600ml \cdot \sin(\alpha_{max}) \tag{4}$$

Table 3. Comparison of transient response to HUT test with experimental data

Variables	Unit	Simulation	experiments
(1)	s	6.3	2—9
(2)	s	17.6	4—30
(3)	mmHg	32.7	22
(4)	mmHg	23.2	17
(5)	beats/min	150	132
(6)	beats/min	169	150

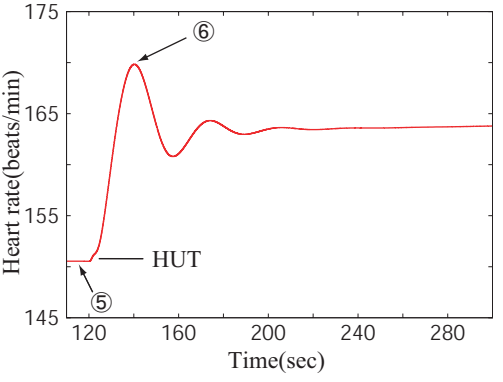

Fig. 7. Heart rate at HUT test

In our model, we modified the above equation to fit the total volume.

$$V_{total} = (783.9ml - \Delta V) + \Delta V \cdot 0.9^{\frac{t-t_0}{60s}} \quad (5)$$

$$\Delta V = 78ml \cdot \sin(\alpha_{max}) \quad (6)$$

In the simulation, the tilt angle was increased from 0 to 70 degree in 2 seconds. The tilt starting time was at 120 seconds. The resulting arterial pressure, heart rate are shown in Fig.6, Fig.7. The resulting features of the hemodynamics are shown in Table 3 in comparison with results gained in physiological experiments. The results are in good agreement with the experimental data.

5 Discussion

By means of the experimental results presented in section 4.1, we have verified that our simulation model is suitable to reproduce the physiological values of infant hemodynamics.

The simulation experiments explained in section 4.2, showed good agreement with experimental data published by Moss et al. [11](Fig.8). They reported that the pressure decreases within 2 to 9 seconds after the start of HUT, and recovers

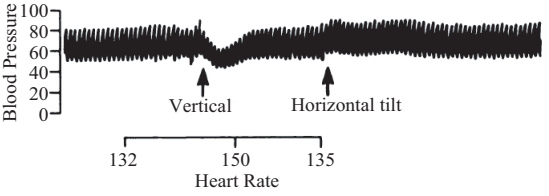

Fig. 8. Blood pressure of HUT test by Moss et al. [11]

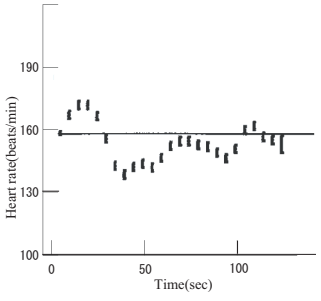

Fig. 9. Heart rate of HUT test by Edner et al. [12]

within 4 to 30 seconds. The pressure pulse width changes from 22 mmHg to 17 mmHg, which equals a 23% decrease. Further, they reported that the heart rate increases from 8 to 38 bpm which equals an 14% increase. Our simulation result showed 29% decrease of the pressure pulse width and 14% increase of heart rate, which is significantly close to the experimental data stated above.

Edner et al. reported the heart rate change when using a 45 degree HUT test [12](Fig.9). Their experimental results showed that the heart rate initially increases, but then decreases again and finally recovers. Also in this case, our simulation results were in good agreement with the experimental results.

From the above, we conclude that our circulation model and control model is capable to simulate the infant hemodynamics not only at resting position but also its response in a HUT test.

6 Conclusions

We developed an infant circulation model which incorporates an accurate myocardial cell model including a beta adrenergic system. The beta adrenergic system is essential in order to reproduce the response of the baroreflex control system. Our model showed good agreement with the physiological experiments. This model may be used to demonstrate the essential functions of the infant cardiovascular dynamics. Especially in clinical and medical training this could be a valuable tool.

Acknowledgement

The authors would like to express sincere thanks to Dr. Y. Shimizu, Kyoto Univ., for English proofreading. This work was supported by the Leading Project for Biosimulation, MEXT.

References

1. Goodwin, J.A., van Meurs, W.L., Sa Couto, C.D., Beneken, J.E.W., Graves, S.A.: A Model for Educational Simulation of Infant Cardiovascular Physiology. International Anesthesia Research Society 99, 1655 (2004)
2. Faber, G., Rudy, Y.: Action Potential and Contractility Changes in [Na+]i Overloaded Cardiac Myocytes: A Simulation Study. Biophys J. 78(5), 2392–2404 (2000)
3. Kuratomi, S., Ono, K., Matsuoka, S., Sarai, N., Noma, A.: Role of individual ionic current systems in ventricular cells hypothesized by a model study. Japanese Journal of Physiology 53, 105–123 (2003)
4. Heldt, T., Shim, E.B., Kamm, R.D., Mark, R.G.: Computational modeling of cardiovascular response to orthostatic stress. Journal of Applied Physiology 92, 1239–1254 (2002)
5. Regen, D.: Calculation of left ventricular wall stress. Circ. Res. 67, 245–252 (1990)
6. Jew, B., Dewit, B.: A physical approach to hemodynamic aspects of the human cardiovascular system. In: Reeve, EB., Guyton, AC. (eds.) Physical bases of circulatory transport: regulation and exchange. Philadelphia: Saunders, pp. 1–45 (1967)
7. Pruitt, AW., Gersony, WM.: The cardiovascular system. In: Behrman RE, (ed.) Nelson textook of pediatrics. 14th ed. Philadelphia: Saunders, pp. 1125–1227 (1992)
8. Gregory, GA.: Monitoring during surgery. In: Gregory, GA. (ed.) Pediatric anesthesia. New York: Churchill Livingstone, pp 261 – 279, (1994)
9. Graham Jr., TP., Jarmakani, MM.: Evaluation of ventricular function in infants and children. Pediatr. Clin. North Am. 18, 1109–1132 (1971)
10. Hagan, R., Diaz, F., Horvath, S.: Plasma volume changes with movement to the upright position. J. Appl. Physiol. 45, 415 (1978)
11. Moss, A.J., Emmanouilides, G.C., Monset-Couchard, M.: Vascular Responses to Postural Changes in Normal, Newborn Infants. Pediatrics 42, 250–254 (1968)
12. Edner, A., Katz-Salamon, M., Lagercrantz, H., Milerad, J.: Heart rate response profiles during head upright tilt test in infants with apparent life thereatening events. Archives of Disease in Childhood 76, 27–30 (1997)

Effects of Geometry and Architecture on Re-entrant Scroll Wave Dynamics in Human Virtual Ventricular Tissues

Alan P. Benson[1], Michael E. Ries[2], and Arun V. Holden[1]

[1] Computational Biology Laboratory, Institute of Membrane and Systems Biology & Cardiovascular Research Institute, Worsley Building, Faculty of Biological Sciences, University of Leeds, Leeds LS2 9JT, UK
alan@cbiol.leeds.ac.uk
http://www.cbiol.leeds.ac.uk
[2] School of Physics and Astronomy, University of Leeds, Leeds LS2 9JT, UK

Abstract. We examine the effects of cardiac geometry and architecture on re-entrant scroll wave dynamics by quantifying the scroll wave filament in two biophysically-detailed heterogeneous models of the human left ventricular free wall – a simple cuboid model and a wedge model constructed using DT-MRI data. For any given geometry, changing the architecture results in changes to the filament meander pattern, increases in filament length, changes to the filament curvature and local filament twist, and increases in the maximum twist along a single filament. Changes to the geometry also affect scroll wave dynamics, mainly due to the size of the tissue. We conclude that such differences in re-entrant scroll wave dynamics should be taken into account when interpreting results from simulations that use simple cardiac geometries and architectures.

Keywords: Cardiac arrhythmias, Re-entry, Cardiac structure, Diffusion tensor magnetic resonance imaging.

1 Introduction

Ventricular tachycardia (VT) and fibrillation (VF) are dangerous cardiac arrhythmias that are a major cause of morbidity and mortality in developed countries, yet they remain poorly understood [1]. One possible mechanism for the transition from VT to VF is when a single re-entrant wave of excitation (a scroll wave) that rotates around a phase singularity (a filament) with a high frequency breaks down into multiple wavelets [2]. Thus, understanding the dynamics of re-entrant scroll waves in the heart can help us to understand why, and under what conditions, the transition from VT to VF occurs.

Understanding the spatio-temporal pattern of propagation in the ventricles during arrhythmias requires direct visualisation of three-dimensional excitation propagation processes deep within the ventricular walls of a beating, in vivo heart. This is not yet technically feasible. Current in vitro optical mapping technologies can provide a panoramic view of ventricular surface activity [3] or of

F.B. Sachse and G. Seemann (Eds.): FIMH 2007, LNCS 4466, pp. 200–209, 2007.

concurrent activity on both the endocardial and epicardial surfaces [4], and 3D optical visualisation of intramural activity is still at the proof of concept stage of development [5]. Computational simulations using verified models of cardiac geometry, architecture and excitation therefore allow the study of propagation inside the ventricular wall [6,7,8], that cannot be achieved experimentally. Scroll wave dynamics are quantified from these simulations as measurements of, for example, filament number, length, location, curvature and twist [9].

Previous computational studies examining scroll wave dynamics have mostly been on simple cuboid geometries, using either qualitative or biophysical models for excitation – see references [1,2,9] for reviews. However, the geometry and architecture (i.e. fibre and sheet structure) of the heart is more complex than is assumed in these simple cuboid models [10]. As tissue fibre and sheet structure determines the diffusive spread of voltage throughout the heart, we are interested in the effects of realistic, complex tissue geometry and architecture on propagation.

At each point in the heart there are three principal orthogonal directions of diffusion – along the fibre axis, perpendicular to the fibre axis in the sheet plane, and normal to the sheet plane. These vectors can be determined experimentally using histological techniques [11], or using diffusion tensor magnetic resonance imaging (DT-MRI) [12]. This technique has recently been developed as a non-destructive, high-throughput method to determine the architecture of the heart: the primary [13,14,15] and secondary or tertiary [16] eigenvectors of the diffusion tensor have been validated as measures of fibre orientation and sheet structure, respectively. The diffusion tensor describing the spread of voltage can be constructed from these eigenvectors in order to reconstruct the geometry and the fibre and sheet architecture of the ventricles.

The aim of this study was to examine the effects of cardiac geometry and architecture on re-entrant scroll wave dynamics by quantifying the scroll wave filament in two biophysically-detailed heterogeneous models of the human left ventricular free wall – a simple cuboid model and a wedge model constructed using DT-MRI data.

2 Methods

Propagation of electrical excitation in cardiac tissue can be described by the non-linear cable equation

$$\partial V/\partial t = \nabla(\mathbf{D}\nabla V) - I_{\text{ion}} \ , \tag{1}$$

where V is membrane potential, t is time, ∇ is a spatial gradient operator, $\mathbf{D}$ is the diffusion tensor that characterises electrotonic spread of voltage through the tissue and I_{ion} is the total membrane ionic current density. For I_{ion} we use the ten Tusscher-Noble-Noble-Panfilov (TNNP) human ventricular model [17] that provides formulations for endocardial, midmyocardial and epicardial cells. We constructed two heterogeneous tissue models of the left ventricular free wall – a simple cuboid with a rule-based architecture and a wedge model

with architecture obtained from DT-MRI – with endocardial, midmyocardial and epicardial tissue occupying approximately equal fractions of the transmural distance in both cases. For each model, propagation of excitation was either isotropic, anisotropic or orthotropic.

2.1 Cuboid Model

A simple cuboid model of the ventricular wall with dimensions of $60 \times 60 \times 20$ mm was constructed. The fibre direction $\mathbf{f}$ always pointed parallel to the endocardial and epicardial surfaces and rotated 120° across the ventricular wall [10] at a rate of 6°/mm. The sheet direction $\mathbf{s}$ was always perpendicular to fibre direction and pointed in the transmural direction. By definition, the sheet normal direction $\mathbf{n}$ lay perpendicular to the plane spanned by $\mathbf{f}$ and $\mathbf{s}$. The diffusion tensor $\mathbf{D}$ was constructed as described by Eqns. (5-9) in Fenton & Karma [18], where the diffusion coefficient $D_{\parallel}$ is diffusion along the fibre axis, $D_{\perp 1}$ is diffusion in the sheet plane perpendicular to the fibre axis and $D_{\perp 2}$ is diffusion normal to the sheet plane (i.e. in the orthogonal directions $\mathbf{f}$, $\mathbf{s}$ and $\mathbf{n}$ respectively).

2.2 Wedge Model

The geometry and architecture of the wedge model was obtained from a DT-MRI dataset of the human ventricles (see Fig. 1 and Acknowledgments), which contains the scalar components of the three vectors $\mathbf{f}$, $\mathbf{s}$ and $\mathbf{n}$ with respect to a global Cartesian coordinate system. In a local coordinate system based on these orthogonal vectors, the diffusion tensor at a particular point in space is

$$\widetilde{\mathbf{D}} = \begin{pmatrix} D_{\parallel} & 0 & 0 \\ 0 & D_{\perp 1} & 0 \\ 0 & 0 & D_{\perp 2} \end{pmatrix} \quad . \tag{2}$$

As the three vectors $\mathbf{f}$, $\mathbf{s}$ and $\mathbf{n}$ are the eigenvectors of the diffusion tensor $\mathbf{D}$ with corresponding eigenvalues $D_{\parallel}$, $D_{\perp 1}$ and $D_{\perp 2}$, then the transformation matrix of $\widetilde{\mathbf{D}}$ to $\mathbf{D}$ is an orthogonal matrix $\mathbf{A} = (\mathbf{f}, \mathbf{s}, \mathbf{n})$. The diffusion tensor $\mathbf{D}$ is therefore given by $\mathbf{D} = \mathbf{A}\widetilde{\mathbf{D}}\mathbf{A}^{\mathrm{T}}$. Substitution then gives

$$\mathbf{D} = D_{\parallel}\mathbf{f}\mathbf{f}^{\mathrm{T}} + D_{\perp 1}\mathbf{s}\mathbf{s}^{\mathrm{T}} + D_{\perp 2}\mathbf{n}\mathbf{n}^{\mathrm{T}} \quad , \tag{3}$$

which can be used, along with the DT-MRI eigenvector files, to construct $\mathbf{D}$ at each node throughout the geometry and, therefore, to reconstruct fibre and sheet architecture in the tissue. The wedge dimensions are similar to those of the cuboid.

2.3 Isotropic, Anisotropic and Orthotropic Propagation

In all cases, we set the diffusion coefficient in the fibre direction $\mathbf{f}$ to $D_{\parallel} = 0.154$ $\mathrm{mm^2 ms^{-1}}$ to give a conduction velocity (CV) for a solitary plane wave of 0.7

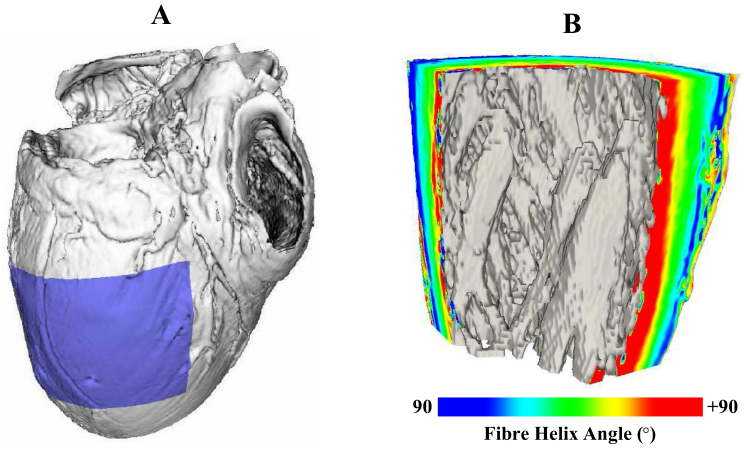

Fig. 1. (A) Visualisation of the human DT-MRI dataset geometry. The shaded area indicates the spatial extent of the wedge extracted from the left ventricular free wall. (B) View of the wedge geometry and fibre helix (inclination) angle from an endocardial aspect. Note the intricate structure of the endocardial surface, here shaded in grey. The helix angle, determined from the DT-MRI primary eigenvector [10] and visualised here on the cut surfaces of the wedge, shows a transmural rotation of approximately 120°.

$\mathrm{m\,s^{-1}}$ [17]. For isotropic propagation we set the diffusion coefficients in the three directions **f**, **s** and **n** the same, such that $D_{\parallel} = D_{\perp 1} = D_{\perp 2}$. To introduce fibre orientation we set the ratio $D_{\parallel}$:$D_{\perp 1}$ = 4:1 with $D_{\perp 1} = D_{\perp 2}$ such that CV is twice as fast along the fibre as across it, i.e. cylindrically anisotropic. To introduce sheet structure and orthotropic propagation, the diffusion coefficients were set with the ratio $D_{\parallel}$:$D_{\perp 1}$:$D_{\perp 2}$ = 36:9:1 after Colli Franzone et al. [19] to give a CV ratio of 6:3:1 in the three directions **f**, **s** and **n** respectively.

2.4 Filament Tracking and Quantification

The filament location can be defined as the intersection of the isosurfaces of activation and recovery variables. We chose the Na^+ current activation gate with a value of $m = 0.98$ as the the activation variable and the slow delayed rectifier K^+ current gate with a value of $xs = 0.02$ as the recovery variable, which gave a unique filament location for a single re-entrant scroll wave on the coarse DT-MRI geometry. The use of other variables such as V, $\mathrm{d}V/\mathrm{d}t$, or L-type Ca^{2+} current or Na^+ current inactivation gates (see reference [9] for a review) resulted in the filament tracking algorithm identifying numerous filaments for a single scroll wave.

The location of any filament is given by the position vector field **R** and the arclength along any filament is given by s. To calculate filament curvature we first calculated the unit vector field $\mathbf{T} = \mathrm{d}\mathbf{R}/\mathrm{d}s$ that lies locally tangent to the

filament. Then, from the Frenet-Serret equations, local filament curvature κ is given by the norm of the rate of change of this vector along the filament:

$$\kappa = \|\mathrm{d}\mathbf{T}/\mathrm{d}s\| \ . \tag{4}$$

To calculate filament twist, we used the method described by Fenton & Karma [18] by calculating the unit vector field $\mathbf{N}$ that points in the direction of the local voltage gradient and lies locally perpendicular to $\mathbf{T}$. Local twist w is then given by the triple product

$$w = \mathrm{d}\mathbf{N}/\mathrm{d}s \times \mathbf{T} \cdot \mathbf{N} \ . \tag{5}$$

For every point in $\mathbf{R}$ we then calculated the angle ϕ by calculating the integral of twist along the filament:

$$\phi = \int_0^s w \, \mathrm{d}s \ , \tag{6}$$

which gave the twist with respect to the epicardial end of the filament. The maximum change in this angle along any given filament, $\Delta\phi$, was used as a measure of maximum filament twist.

2.5 Integration

Equation (1) was integrated using a Forward Time Centred Space method, with an operator splitting and adaptive time step method [20] utilising a minimum time step of $\Delta t_{min} = 0.02$ ms and a maximum time step $\Delta T = 0.2$ ms. This method has previously been shown [20] to decrease computation time whilst maintaining accuracy of CV and action potential duration in one dimension (with values of ΔT up to 0.4 ms) and spiral wave cycle length in two dimensions (with values of ΔT up to 0.3 ms). We assume the maintenance of accuracy extends to three dimensions for $\Delta T = 0.2$ ms. Space steps in the cuboid model were $\Delta x = \Delta y = \Delta z = 0.33$ mm. In the wedge model, space steps were $\Delta x = \Delta y = 0.425$ mm and $\Delta z = 0.5$ mm as defined by the DT-MRI dataset, to give approximately $4{\times}10^5$ nodes inside the tissue. Neumann boundary conditions were imposed at the edges of each geometry by setting diffusion along the vector normal to the local tissue surface to zero. Initial conditions for all models were an untwisted scroll wave with a straight filament whose ends were located approximately centrally on the epicardial and endocardial surfaces. This scroll wave was obtained by stacking identical spiral waves obtained from two-dimensional simulations using the epicardial TNNP model with isotropic diffusion. Filaments were tracked and quantified using algorithms described in references [18,9]. The models were coded in C and parallelised under openMP. To further decrease computation time, voltage-dependent exponential functions were pre-calculated, with a resolution of 0.1 mV, and stored in an array for reference. Simulations were run locally on a Sun Fire 6800 shared memory machine utilising 24 Sun 750 MHz UltraSPARC III 64-bit processors.

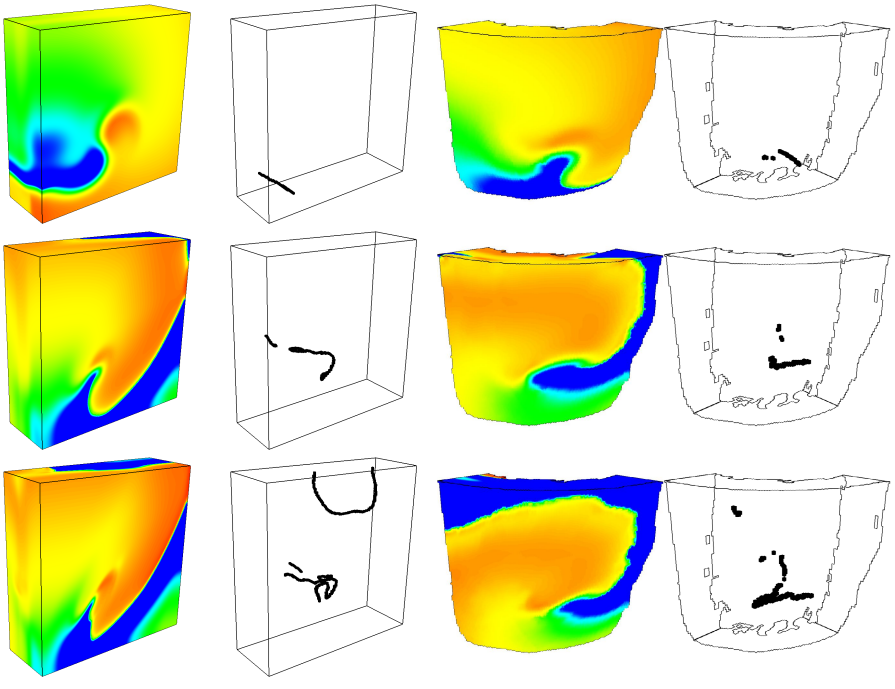

Fig. 2. Snapshots of membrane potential V and filament locations $\mathbf{R}$ after 2 seconds of simulation in isotropic (top), anisotropic (middle) and orthotropic (bottom) cuboid and wedge models. Membrane potential is colour-coded using the standard rainbow palette, from blue/dark (−70 mV) to red/light (30 mV). For both models the snapshots are from an epicardial aspect, with the scroll wave rotating clockwise.

3 Results

We integrated each model for 3 seconds, but for clarity only present data for 1 second of activity, between $t = 1$ and $t = 2$ s. Figure 2 shows snapshots at $t = 2$ s of membrane potential on the surface of the model geometries and corresponding filament locations, for both models under isotropic, anisotropic and orthotropic conditions. For the isotropic cuboid (Fig. 2, top left), the scroll wave dies out soon after as the filament reaches the boundary. The multiple filaments for the orthotropic cuboid (Fig. 2, bottom left) show the beginning of scroll wave breakup – numerous wavelets form soon after and the activation patterns in the tissue represent the complex patterns seen during VF. The analysis of this complex behaviour is left for future work. Note the numerous filaments present in the wedge model under all three conditions (Fig. 2, right). Rather than reflecting a complex state of activation as in VF, the multiple filaments here belong to a single filament that is broken by the intricate geometry of the endocardial

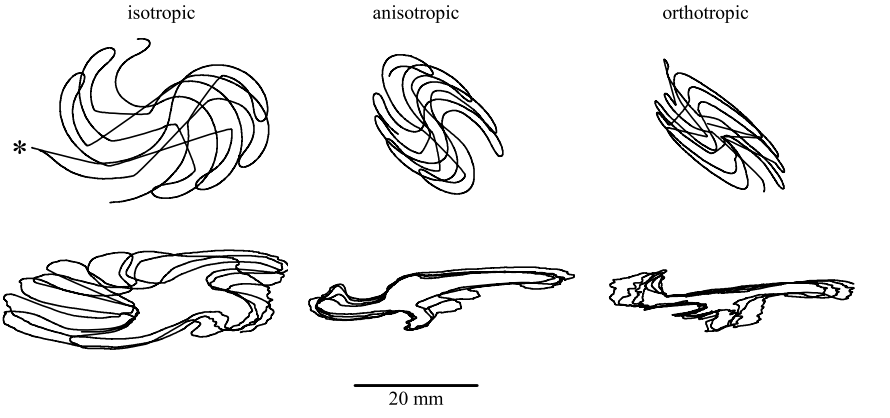

Fig. 3. Filament trajectories on the epicardial surface of the cuboid (top) or wedge (bottom) models during 1 second of simulation, under isotropic, anisotropic and orthotropic conditions. The asterisk on the isotropic cuboid trajectory indicates where the filament moved off the epicardial surface of the geometry.

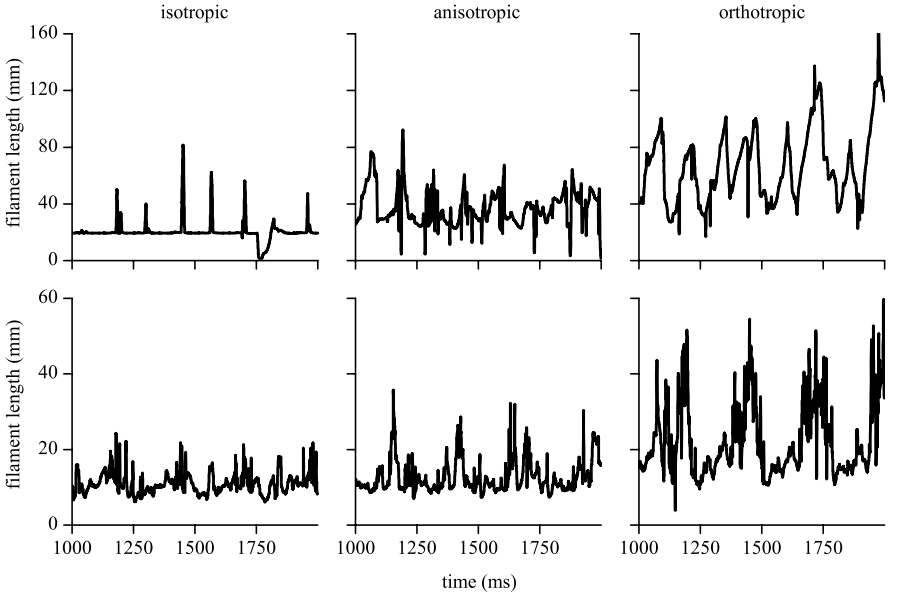

Fig. 4. Scroll wave filament length during 1 second of simulation in the cuboid model (top) and the wedge model (bottom), under isotropic, anisotropic and orthotropic conditions. Note the different scales on the ordinate for the cuboid and wedge models.

surface, e.g. papillary muscles. Thus, the number of filaments is not a useful measure to quantify scroll wave behaviour in the wedge model, and instead we calculate total filament length (see below).

Filament trajectories on the epicardial surfaces of the geometries are shown in Fig. 3. The asterisk on the isotropic cuboid trajectory indicates where the end of the filament moved off the epicardial surface of the geometry and onto the transmural surface – the filament then joined points on the endocardial and transmural surfaces for a short time, before the filament end returned to the epicardial surface in approximately the same location it had left. For the cuboid model (Fig. 3, top), changing from isotropy through anisotropy to orthotropy has the effect of rescaling the meander of the filament in the direction perpendicular to the fibre axis, which on the epicardial surface is the sheet normal direction. This is to be expected, as the diffusion coefficient in this direction is reduced for each of the conditions. Similar effects can be seen in the wedge model (Fig. 3, bottom) as one progresses from isotropy to orthotropy. Note also the qualitative differences between cuboid and wedge model trajectories.

Scroll wave filament length during 1 second of simulation is shown in Fig. 4. Note the different scales on the ordinate for the cuboid and wedge models (Fig. 4, top and bottom respectively). For all conditions, the filament length in the cuboid is longer than in the wedge, a result of tissue geometry (i.e. size) rather than architecture. Note also the reduction in filament length for the isotropic cuboid at approximately $t = 1750$ ms, which is due to the movement of the filament end onto the transmural surface and corresponds to the asterisk in Fig. 3. Oscillations of filament length are evident in all simulations, a consequence of filament twist which is due to the heterogeneous excitation kinetics in the models – see [8]. For both models, filament length increases as anisotropy and then orthotropy are introduced. This is due to the anisotropy or orthotropy being rotational, and so the principal direction of diffusion (i.e. the fibre axis) changes as a function of distance across the ventricular wall in the cuboid model. In

Table 1. Means ± standard deviations of κ (mm^{-1}) and the absolute values of w ($^\circ$/mm) and $\Delta\phi$ ($^\circ$) during 1 second of simulation in the cuboid and wedge models under isotropic, anisotropic and orthotropic conditions

		κ	$\lvert w\rvert$	$\lvert\Delta\phi\rvert$
cuboid:	isotropic	0.5 ± 0.7	1.0 ± 2.2	51.7 ± 40.3
	anisotropic	12.1 ± 59.8	3.4 ± 3.0	221.6 ± 111.1
	orthotropic	3.3 ± 7.3	5.8 ± 4.5	445.1 ± 151.5
wedge:	isotropic	0.8 ± 1.1	4.8 ± 3.9	64.0 ± 40.6
	anisotropic	2.8 ± 3.8	5.4 ± 4.5	96.2 ± 48.6
	orthotropic	3.8 ± 12.0	4.6 ± 3.8	161.4 ± 61.0

the wedge, this change is not only a function of transmural distance but also of base-apex distance. These rotational effects further increase the effects of the transmural excitation heterogeneity.

Curvature and twist in the filament is quantified in Table 1, as means and standard deviations for the 1 second period shown in Figs. 3 and 4. As twist can be positive or negative, we take the absolute values when calculating the means. Although curvature κ increases with anisotropy then orthotropy in the wedge model, the same pattern is not seen in the cuboid. Conversely, twist $|w|$ increases with anisotropy then orthotropy in the cuboid but not in the wedge. The maximum twist along a single filament, $|\Delta\phi|$, increases in both models as anisotropy and then orthotropy are introduced.

4 Conclusions

Using a biophysically-detailed model of cardiac excitation with spatially heterogeneous kinetics, we have shown that there are both qualitative and quantitative differences in the dynamics of re-entrant scroll waves between different cardiac geometries and architectures. We conclude that simple cuboid models with rule-based architecture do not accurately reproduce the complex geometry and architecture of the human ventricles. For any given geometry (i.e. cuboid or wedge), changing the architecture by introducing fibre structure to give anisotropic propagation and sheet structure to give orthotropic propagation results in changes to the filament meander pattern, increases in filament length, changes to the filament curvature and local filament twist, and increases in the maximum twist along a single filament. Changes to the geometry also affect scroll wave dynamics, mainly due to the size of the tissue, and the intricate structure of the endocardial surface in the wedge model means that filament tracking is not trivial. Thus, simulations of re-entry should take into account this complex geometry and architecture.

Acknowledgments. We thank Drs Patrick A. Helm and Raimond L. Winslow at the Center for Cardiovascular Bioinformatics and Modeling and Dr Elliot McVeigh at the National Institute of Health for provision of the human DT-MRI dataset. This work was supported by the European Union through the BioSim Network of Excellence (contract No. LSHB-CT-2004-005137). APB is supported by The Dr Hadwen Trust for Humane Research.

References

1. Jalife, J.: Ventricular fibrillation: mechanisms of initiation and maintenance. Ann. Rev. Physiol. 62, 25–50 (2000)
2. Clayton, R.H., Zhuchkova, E.A., Panfilov, A.V.: Phase singularities and filaments: simplifying complexity in computational models of ventricular fibrillation. Prog. Biophys. Mol. Biol. 90, 378–398 (2006)
3. Efimov, I.R., Nikolski, V.P., Salama, G.: Optical imaging of the heart. Circ. Res. 95, 21–33 (2004)

4. Evans, F.G, Gray, R.A.: Shock-induced epicardial and endocardial virtual electrodes leading to ventricular fibrillation via reentry, graded responses, and transmural activation. J. Cardiovasc. Electrophysiol. 15, 79–87 (2004)
5. Bernus, O., Wellner, M., Mironov, S.F., Pertsov, A.M.: Simulation of voltage-sensitive optical signals in three-dimensional slabs of cardiac tissue: application to transillumination and coaxial imaging methods. Phys. Med. Biol. 50, 215–229 (2005)
6. Benson, A.P., Halley, G., Li, P., Tong, W.C., Holden, A.V.: Virtual cell and tissue dynamics of ectopic activation of the ventricles. Chaos 17, 015105 (2007)
7. Benson, A.P., Aslanidi, O.V., Zhang, H., Holden, A.V.: The canine virtual ventricles: a platform for dissecting pharmacological effects on propagation and arrhythmogenesis. Prog. Biophys. Mol. Biol. (to appear)
8. Clayton, R.H., Holden, A.V.: Propagation of normal beats and re-entry in a computational model of ventricular cardiac tissue with regional differences in action potential shape and duration. Prog. Biophys. Mol. Biol. 85, 473–499 (2004)
9. Clayton, R.H., Holden, A.V.: A method to quantify the dynamics and complexity of re-entry in computational models of ventricular fibrillation. Phys. Med. Biol. 47, 225–238 (2002)
10. Gilbert, S.H., Benson, A.P., Li, P., Holden, A.V.: Regional localisation of left ventricular sheet structure: integration with current models of cardiac fibre, sheet and band structure. J. Cardio-thoracic Surgery (to appear)
11. LeGrice, I.J., Smaill, B.H., Chai, L.Z., Edgar, S.G., Gavin, J.B., Hunter, P.J.: Laminar structure of the heart: ventricular myocyte arrangement and connective tissue architecture in the dog. Am. J. Physiol. 269, H571–H582 (1995)
12. Basser, P.J., Mattiello, J., LeBihan, D.: MR diffusion tensor spectroscopy and imaging. Biophys. J. 66, 259–267 (1994)
13. Hsu, E.W., Muzikant, A.L., Matulevicius, S.A., Penland, R.C., Henriquez, C.S.: Magnetic resonance myocardial fiber-orientation mapping with direct histological correlation. Am. J. Physiol. 247, H1627–H1634 (1998)
14. Scollan, D.F., Holmes, A., Winslow, R.L., Forder, J.: Histological validation of myocardial microstructure obtained from diffusion tensor magnetic resonance imaging. Am. J. Physiol. 275, H2308–H2318 (1998)
15. Holmes, A.A., Scollan, D.F., Winslow, R.L.: Direct histological validation of diffusion tensor MRI in formaldehyde-fixed myocardium. Magn. Res. Med. 44, 157–161 (2000)
16. Helm, P.A., Tseng, H.-J., Younes, L., McVeigh, E.R., Winslow, R.L.: Ex vivo 3D diffusion tensor imaging and quantification of cardiac laminar structure. Magn. Reson. Med. 54, 850–859 (2005)
17. ten Tusscher, K.H.W.J., Noble, D., Noble, P.J., Panfilov, A.V.: A model for human ventricular tissue. Am. J. Physiol. 286, H1573–H1589 (2004)
18. Fenon, F., Karma, A.: Vortex dynamics in three-dimensional continuous myocardium with fiber rotation: filament instability and fibrillation. Chaos 8, 20–47 (1998)
19. Colli Franzone, P., Pavarino, L.F., Taccardi, B.: Simulating patterns of excitation, repolarization and action potential duration with cardiac bidomain and monodomain models. Math. Biosci. 197, 35–66 (2005)
20. Qu, Z., Garfinkel, A.: An advanced algorithm for solving partial differential equation in cardiac conduction. IEEE Trans. Biomed. Eng. 46, 1166–1168 (1999)

Can We Trust the Transgenic Mouse? Insights from Computer Simulations

Joseph Tranquillo and Adhira Sunkara

Bucknell University, Lewisburg PA 17837, USA
jvt002@bucknell.edu
http://www.facstaff.bucknell.edu/jvt002

Abstract. Over the past several decades, the mouse has gained prominence in the cardiac electrophysiology literature as the animal model of choice. Using computer models of the mouse and human ECG, this paper is a step toward understanding when the mouse succeeds and fails to mimic functional changes resulting from disease states and drug interactions.

1 Introduction

The transgenic mouse has enjoyed a large share of the spotlight in the cardiovascular literature over the past decade, primarily due to the relative ease of genetic manipulation [1,2,3,4,5,6,7], and miniaturization of recording techniques [8,9,10]. These advances have enabled models of human disease to be studied in mice at spatial scales ranging from protein channels to the whole heart. At first glance, the mouse appears to be a scaled version of the human heart. For example, the mouse heart rate is approximately 10 times faster than in the human, while the Action Potential Duration (APD) and left ventricular wall thickness are approximately 10 times smaller [7,11]. On the other hand, some measures are comparable. At the organ level, the human and mouse fiber organization and anisotropic conduction patterns are similar [12,13]. At the tissue level, the resting length constants and conduction velocities [1,14,15] are similar. At the protein level, most ion channels are conserved across species [11].

It is because some properties are similar while others are scaled that calls into question the use of the mouse as a model of human disease. For example, as the mouse and human length constants are similar but the ventricular wall thicknesses are an order of magnitude different, the mouse may not supporting the same transmural APD gradients as the human [16,17]. Furthermore, the dominate repolarization current in the mouse is I_{to} and I_{sus} while in the human I_{Ks} and I_{Kr} rectify the transmembrane potential [11,18,19].

An ideal animal model would be similar to the human at all scales and measurements. Although some animal models approach this ideal (e.g. Porcine), they are typically costly. The second ideal animal model would be one that is perfectly scaled compared to the human. Some computational models may achieve this [20], but no animal models are available. In the absence or difficulty of using these two ideal animal models, the next option is the one that has been adopted by the field; an animal that can be modified to mimic the human.

F.B. Sachse and G. Seemann (Eds.): FIMH 2007, LNCS 4466, pp. 210–219, 2007.

Accepting that it is impractical to perfectly scale the mouse to the human, it is important to understand the limitations of the mouse model. Although a systematic study is possible using experimental models, it is more efficient to explore the limitations in a computer model. This paper is a first step toward creating such models. The Electrocardiogram (ECG) has been targeted because: 1) genetic mutations at the protein level can have a an impact on the ECG. 2) simple simulations [21] may reproduce the impact of these mutations and 3) the mouse and human ECG have noticeably different morphologies [11,17,22,23].

2 Methods

2.1 Cellular Models

The ten Tusscher et al. [19] and Pandit et al. [18] ionic current models were used for human and mouse simulations respectively. Figure 1 is a comparison of epicardial action potentials and ionic currents for both models.

2.2 Cable Models

Ionically heterogeneous and spatially isotropic one dimensional monodomain ($dx = 0.01cm$, $\sigma = 1mS/cm$) cables were used to simulate the mouse and human left ventricular wall. The forward Euler ($dt = 2\mu s$) method was used for numerical integration. The profile of the human left ventricular wall was simulated by a $1.65cm$ cable divided into epicardial ($0-0.6cm$), M ($0.6-1.05cm$) and endocardial ($1.05-1.65cm$) regions [21]. The profile of the mouse left ventricular wall was simulated in a $0.2cm$ cable that was divided into epicardial ($0-0.1cm$) and endocardial ($0.1-0.2cm$) regions. Propagation in both cables was initiated by ten, supra-threshold current stimuli at the endocardial end of the cable. The pacing rate for the human was 1Hz while the mouse was 8Hz.

2.3 Computation of the Pseudo-electrocardiogram (pECG)

The pECG was computed as the extracellular potential (ϕ_e) generated by transmembrane currents (I_m) propagating down a cable surrounded by a large volume conductor ($\sigma_e = 6mS/cm$):

$$\phi_e = \frac{1}{4\pi\sigma_e} \int \frac{I_m}{r} dV$$

where r is the distance from the recording point to the current source I_m [24] and the reference electrode is at infinity. The current source is the sum of capacitive and ionic currents. In both mouse and human cables, the recording electrode was placed $1cm$ from the epicardium.

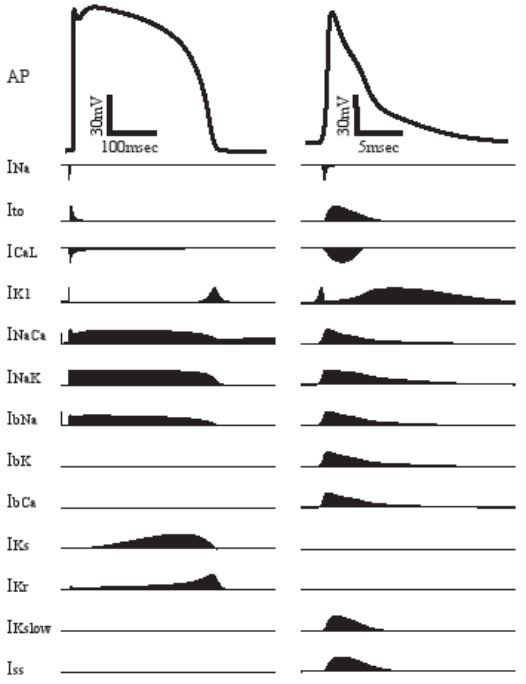

Fig. 1. Human (left) and Mouse (right) epicardial action potentials and currents

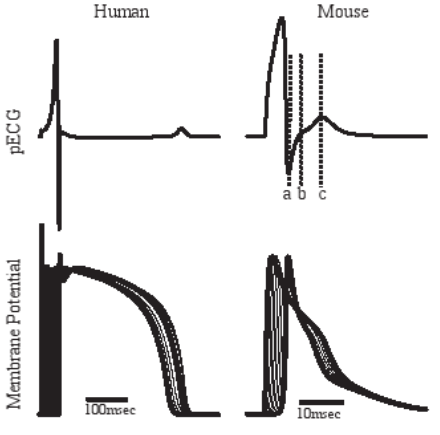

Fig. 2. Human pECG (left) and Mouse pECG (right). The mouse pECG was scored by: a) first deflection to minimum, b) minimum slope after a wave and before final deflection c) peak (or valley) of final deflection. For reference, bottom traces show the V_m time course of every $1mm$ and $200\mu m$ along the cable for the human and mouse respectively.

2.4 Simulation of Mutations

The maximum channel conductances were independently varied (both increased and decreased) for all currents shared by the two species (Figure 1). As I_{NaK} and I_{NaCa} do not play a large role in simple beat studies, we have ommitted these currents. Brugada Syndrome was simulated by a modification of I_{Na} activation and inactivation profiles [25]. The impact of adding a human I_{Ks} and I_{Kr} to the mouse model was also explored.

2.5 Analysis of Results

All results were analyzed for the tenth paced beat. The normal mouse epicardial and endocardial APDs were 13.5 and 26.1$msec$ respectively while the human epi, M and endo APDs were 270, 275 and 323$msec$ respectively (-60mV crossings). The mouse Conduction Velocity (CV) was 41cm/s while the human CV=40.5cm/s (delays in -60mV crossings). CVs do not significantly change unless noted. As scoring of the mouse ECG has not been standardized, we have adopted the a, b, c notion (Figure 2) proposed by Danik et al. [22].

3 Results

3.1 Comparisons of Normal Mouse and Human pECG

The simulated Normal Human pECG (Figure 2) shows a narrow QRS (corresponding to conduction of depolarization from endocardium to epicardium), slight J-wave elevation (corresponding to rapid repolarization) followed by a long isopotential (corresponding to the action potential plateau) and finally the T-wave (due to complex repolarization timing from epicardium to endocardium and finally the mid-wall). The simulated mouse ECG also shows a QRS-like complex (a-wave) that like the human corresponds to depolarization across the wall from endocardium to epicardium. As the epicardium depolarizes, the voltage gradient reverses briefly, giving rise to the b-wave. The origin of the b-wave therefore appears to be similar to the J-wave in the human, although it may be exaggerated. The epicardium rapidly repolarizes before the endocardium (as in the human), giving rise to a second voltage gradient reversal and the c-wave. The orgin of the b-wave therefore appears to be similar to the T-wave in the human.

3.2 Reduced I_{K1}

I_{K1} is a primary current in determining the resting membrane potential and underlies Andersen's syndrome. Blocking I_{K1}, raises the resting potential for both the mouse and the human (Figure 3A). In the human, the rise in resting potential partially inactivates Na^+ channels, leading to slower conduction and a broader QRS complex. Since all other currents are tuned to the original resting potential, a hyperpolarization follows repolarization that leads to a small non-zero

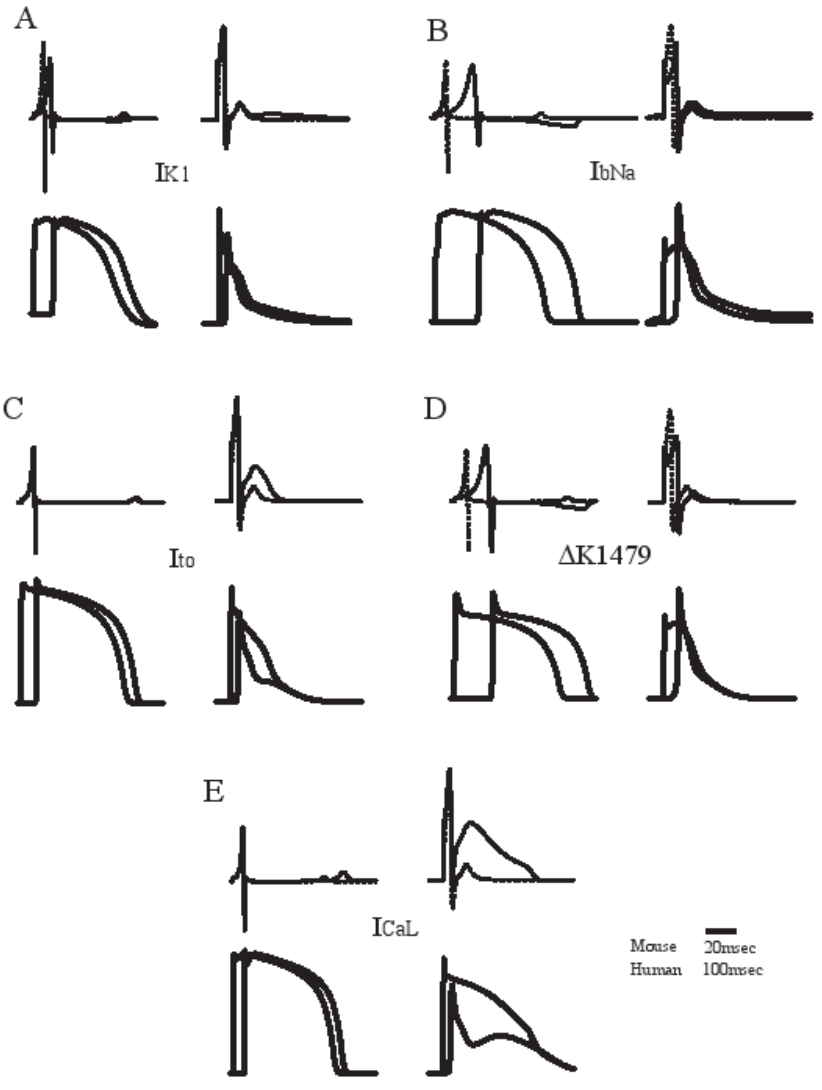

Fig. 3. A comparison of pECG (top) and action potentials (bottom) for human (left) and mouse (right) simulations. Data for each modification is shown in four panel groups. For reference, the dotted traces are the nominal pECG. Action potentials are the first and last in the cable. The time scales for mouse and human data are indicated in the lower right.

pECG after the T-wave. In the mouse the rise in resting potential has little impact on conduction velocity and the a and b waves are only slightly altered. The c-wave on the otherhand is significantly prolonged and broadened as a long-lasting gradient is established between epicardium and endocardium during repolarization.

3.3 Reduced I_{bNa} and I_{Na} Unmasking

I_{bna} is a long lasting inward current that when enhanced leads to a prolongation of the APD and QT interval. In the clinic, this condition is referred to as LQT3 and may be difficult to diagnose because the QT prolongation is relative. To unmask the condition, a Na^+ channel blocker (reduced I_{Na}) is given which widens the QRS in both normal and abnormal patients, but eliminates the isopotential and inverts the T-wave only in patients with LQT3. In our simulations, these behavior were reproduced in the human pECG (Figure 3B). In the mouse, however, the I_{Na} block did change the a wave but did not produce a morphological change in the b or c waves.

3.4 Reduced I_{to}

The transient outward current is present in both the mouse and human but the role played in repolarization is far more significant in the mouse. In the human, I_{to} is responsible for the action potential notch and has a relatively small impact on the APD or ECG (FIgure 3C). Blocking I_{to} in the human results in a slight increase in the J-wave and increase in the QT interval. The same simulated block in the mouse leaves early repolarization in epicardial cells unchanged while late repolarization shows a short and low voltage plateau. Endocardial cells, other the otherhand, remain at a considerably higher voltage level throughout repolarization. These findings have been observed experimentally by Guo et al. [26], Barry et al. [3] and Brunner et al. [2]. Both simulated and experimental studies show an increase in amplitude and width of the b and c waves.

3.5 ΔK1479 Mutation

A positive shift in activation or negative shift in inactivation kinetics of I_{Na} can lead to Brugada Syndrome [25]. Similar to LQT3, the disease is unmasked in the clinic by partially blocking I_{Na}. In simulations of the unblocked Brugada mutation, the pECG was similar to the nominal pECG for both the human and mouse (Figure 3D). A 70% I_{Na} block in the human mutation simulation, however, resulted in a "coved" T-wave similar to that observed in patients with Brugada Syndrome. A similar 70% I_{Na} block in the mouse mutation simulation did widen the a wave but did not change the morphology of the b or c waves. Further reduction of I_{Na} did not lead to morphological change until conduction was blocked.

3.6 Increased I_{CaL}

I_{CaL} is an inward current that counteracts repolarization. It is present in both the mouse and the human and has been implicated in a number of interesting phenomenon such as sustaining conduction when I_{Na} is reduced [27], modulating restitution properties and the stability of reentry [28], the genesis of early afterdepolarizations (EAD) [29] and the source of Timothy Syndrome (LQT8) [4]. In

the human model, a doubling of I_{CaL} resulted in a delayed T-wave (Figure 3E). The impact on the mouse was an increase in both epicardial and endocardial APD, the appearance of an EAD-like deflection in epicardial cells and a drastic amplitude increase and widening of the c-wave.

3.7 Overexpression of I_{Ks} and I_{Kr} in the Mouse

In the human, a partial block of I_{Ks} and I_{Kr} gave rise to an increased QT interval (not shown), a finding consistent with LQT1 and LQT2 respectively. Although I_{Kr} is present in the mouse, it plays little role in repolarization and is not included in the Pandit et al. model. The addition of the human I_{Ks} and I_{Kr} to the mouse ionic model had virtually no effect on the pECG. Both currents in the human have an impact because they have long time constants that act during the plateau. In the mouse, there is no defined plateau and the neither current has time to play a large role in repolarization. These findings mirror Babij et al. [30] where overexpression of I_{Kr} in the mouse did not generate arrhythmias or ECG abnormalities typically associated with LQT2. Likewise, use of a I_{Ks} blocker in the mouse only had an impact at slow heart rates [5].

4 Discussion

Over the past several decades, the mouse has gained prominence in the cardiac electrophysiology literature as the animal model of choice. The purpose of this paper was to compare normal and abnormal transmural conduction and repolarization in the genesis of the ECG for the mouse and human. The overall findings are: 1) It is possible for the mouse left ventricular wall to sustain gradients large enough to generate the c-wave deflection, 2) The human QRS complex is similar to the a-wave of the mouse and 3) The underlying ionic causes of the T-wave in the human and b and c waves of the mouse are different. These studies highlight the importance of carefully interpreting results from mouse models.

Although it is unclear how deflections in the mouse and human ECG are related, most mouse studies use the clinical PQRST notation. These simulation studies demonstrate that, like the human, the thin mouse ventricular wall is capable of sustaining the APD gradients that give rise to deflections corresponding to repolarization. However, the genesis of the b and c waves in the mouse are due to different ionic currents and APD gradients. These discrepancies have led to a wide variations in mouse ECG measurements in the literature [11,17,22]. To avoid future confusion, the authors suggest the development of a standardized mouse ECG scoring system that is distinct from the human scoring.

The transgenic mouse has helped to uncover some very significant biophysical mechanisms. For example, the impact of knocking out specific connexin isoforms (e.g. gap junctions) [6] have been directly linked to slowed conduction. A mouse model enabled the hypothesized depolarization associated with contact monophasic action potential recordings to be directly measured [9]. Perhaps the most important role for the mouse will be in systematically exploring reentry

initiation, maintenance and breakup [10,11,15]. Although, our simulation studies point out potential problems with studying repolarization diseases and therapies in the mouse, experimental repolarization studies may still yield very significant insights. Such studies can be used to unravel important molecular and cellular level dynamics that are more easily studied in the mouse. It is also possible that the normal mouse may be an ideal model to study human short QT syndrome. An interesting possibility would be to "design" a transgenic mouse in which I_{to}, I_{ss}, I_{Kslow}, I_{CaL} or some combination is modified to achieve a plateau in the mouse [2]. The appearance of this plateau may lead to an isopotential in the mouse ECG and a separation between the b wave and c wave. In this situation, the c-wave may more closely mimic the human T-wave. Therefore, the only caution of these simulations is that the value of functional results lies in the interpretation. The authors therefore propose that the results of mouse studies involving repolarization not be taken at face value, but rather are interpreted using computational or theoretical models.

Although both mouse and human pECG were morphologically similar to experimental ECG, the models presented were for isotropic one dimensional cables. This limitation could be lifted by including the impact of heterogeneous coupling through the wall or coupling via gap junctions [21]. As a further step toward increased realism, whole heart and torso models [31] could incorporate fiber architecture and anatomical features that would allow direct computation of a body surface ECG. It has been proposed [17] that the origin of the mouse c-wave is not a transmural gradient but rather an apex-base or left-right gradient. Furthermore, there is evidence to suggest that some regions of the mouse heart begin to repolarize before other regions have depolarized. A full model of the mouse heart and torso could explore these possibilities. On a cellular level, the impact of drugs and the modeling of diseases could be more accurately simulated using more complex models for I_{ion} [32,33] and non-uniform targeting of different cell types.

The authors anticipate that the mouse will continue to help reveal and validate important biophysical mechanisms and that computer models should and will be used to augment these findings.

Acknowledgments

The authors wish to thank the Bucknell University Research Program, REU program (Grant #PHY-0552790) and Pittsburgh Supercomputing center (Grant #IBN050003P).

References

1. Tamaddon, H.S., Vaidya, D., Simon, A.M., Paul, D.L., Morley, G.E.: High-resolution optical mapping of the right bundel branch in connexin40 knockout mice reveals slow conduction in the the specialized conduction system. Circ. Res. 87, 929–936 (2000)

2. Brunner, M., Guo, W., Mitchell, G.F., Buckett, P.D., Nerbonne, J.M., Koren, G.: Characterization of mice with combined suppression of I_{to} and $I_{K,slow}$. Am. J. Physiol Heart Circ. Physiol. 281, H1201–H1209 (2001)
3. Barry, D.M., Xu, H., Schuessler, R.B., Nerbonne, J.M.: Functional knockout of the transient outward current, Long-QT syndrome, and cardiac remodeling in mice. Circ. Res. 83, 560–567 (1998)
4. Salama, G., London, B.: Mouse models of long QT syndrome J Physiol. 578, 43–53 (2007)
5. Drici, M., Arrighi, I., Chouabe, C., Mann, J.R., Lazdunski, M., Romey, G., Barhanin, J.: Involvement of IsK-associated K^+ channel heart rate control of repolarization in a murine engineered model of Jervell and Lange-Nielsen syndrome. Circ. Res. 83, 95–102 (1998)
6. Morley, G.E., Vaidya, D., Samie, F.H., Lo, C., Delmar, M., Jalife, J.: Characterization of conduction in the ventricles of normal and heterozygous Cx43 knockout mice using optical mapping. J. Cardiovasc Electrophysiol. 10, 1361–1375 (1999)
7. Doevendans, P.A., Daemen, M.J., de Muinck, E.D., Smits, J.F.: Cardiovascular phenotyping in mice. Cardiovasc Res. 39, 34–49 (1998)
8. Berul, C.I.: Electrophysiological phenotyping in genetically engineered mice. Physiol Genomics 13, 207–216 (2003)
9. Knollmann, B.C., Tranquillo, J., Sirenko, S.G., Henriquez, C., Franz, M.R.: Microelectrode study of the genesis of the monophasic action potential by contact electrode technique. J. Cardiovasc Electrophysiol. 12, 1246–1252 (2002)
10. Vaidya, D., Morley, G.E., Samie, F.H., Jalife, J.: Reentry and fibrillation in the mouse heart: A challenge to the critical mass hypothesis. Circ. Res. 85, 174–181 (1999)
11. Nerbonne, J.M.: Studying cardiac arrhythmias in the mouse - a reasonable model for probing mechanisms? Trends Cardiovasc Med. 14, 83–93 (2004)
12. Jiang, Y., Pandya, K., Smithies, O., Hsu, E.W.: Three-dimensional diffusion tensor microscopy of fixed mouse hearts. Magn Reson Med. 53, 1133–1137 (2004)
13. Punske, B.B., Taccardi, B., Steadman, B., Ershler, P.R., England, A., Valencik, M.L., McDonald, J.A., Litwin, S.E.: Effect of fiber orientation on propagation: electrical mapping of genetically altered mouse hearts. J. Electrocardiol. 38(40-4), 40–44 (2005)
14. Nygren, A., Clark, R.B., Belke, D.D., Kondo, C., Giles, W.R., Witkowski, F.X.: Voltage-sensitive dye mapping of activation and conduction in adult mouse hearts. Annals of BME 28, 958–967 (2000)
15. Anumonwo, J.M.B., Tallini, Y.N., Vetter, F.J., Jalife, J.: Action potential characteristics and arrhythmogenic properties of the cardiac conduction system of the murine heart. Circ. Res. 89, 329–335 (2001)
16. Sampson, K.J., Henriquez, C.S.: Electrotonic influences on action potential duration dispersion in small hearts: a simulation study. Am. J. Physiol. Heart Circ. Physiol. 289, 350–360 (2005)
17. Liu, G., Iden, J.B., Kovithavongs, K., Gulamhusein, R., Duff, H.J., Kavanagh, K.M.: In vivo temporal and spatial distribution of depolarization and repolarization and the illusive murine T wave. J. Physiol. 555, 267–279 (2003)
18. Pandit, S.V., Clark, R.B., Giles, W.R., Demir, S.S.: A mathematical model of action potential heterogeneity in adult rat left ventricular myocytes. Biophys. J. 81, 3029–3051 (2001)
19. ten Tusscher, K.H.W.J., Nobel, D., Nobel, P.J., Panfilov, A.V.: A model for human ventricular tissue. Am. J. Physiol Heart Circ. Physiol. 286, H1573–H1589 (2004)

20. Harrild, D., Henriquez, C.: A computer model of normal conduction in the human atria. Circ. Res. 87, E25–36 (2000)
21. Gima, K., Rudy, Y.: Ionic current basis of electrocardiographic waveforms: A model study. Circ. Res. 90, 889–896 (2002)
22. Danik, S., Cabo, C., Chiello, C., Kang, S., Wit, A.L., Coromilas, J.: Correlation of repolarization of ventricular monophasic action potential with ECG in the murine heart. Am. J. Physiol. 283, H372–H381 (2002)
23. Agduhr, E., Stenstrom, N.: The appearance of the electrocardiogram in heart lesions produced by cod liver oil treatment. Acta Paediatr 33, 493–588 (1929)
24. Plonsey, R.: The active fiber in a volume conductor. IEEE Trans. Biomed Eng. 5, 371–381 (1974)
25. Zhang, Z.S., Tranquillo, J., Neplioueva, V., Bursac, N., Grant, A.O.: Sodium channel kinetic changes that produce Brugada syndrome or progressive cardiac conduction system disease. Am. J. Physiol Heart Circ. Physiol. 292, H399–H407 (2007)
26. Guo, W., Li, H., London, B., Nerbonne, J.M.: Functional Consequences of elimination of $I_{to,f}$ and $I_{to,s}$. Circ. Res. 87, 73–79 (2000)
27. Shaw, R.M., Rudy, Y.: Ionic mechanisms of propagation in cardiac tissue. Roles of the sodium and L-type calcium currents during reduced excitability and decreased gap junction coupling. Circ. Res. 81, 727–741 (1997)
28. Qu, Z., Weiss, J.N., Garfinkel, A.: Cardiac electrical restitution properties and stability of reentry spiral waves: a simulation study. Am. J. Physiol. 276, H269–283 (1999)
29. Viswanathan, P.C., Rudy, Y.: Pause induced early afterdepolarizations in the long QT syndrome: a simulation study. Cardiovasc Res. 42, 530–542 (1999)
30. Babij, P., Askew, R., Nieuwenhuijsen, B., Su, C., Bridal, T.R., Jow, B., Argentieri, T.M., Kulik, J., DeGennaro, L.J., Spinelli, W., Colatsky, T.J.: Inhibition of cardiac delayed rectifier K+ current by overexpression of the Long-QT syndrome HERG G628S mutation in transgenic mice. Circ. Res. 83, 668–678 (1998)
31. Tranquillo, J.V., Hlavacek, J., Henriquez, C.S.: An integrative model of mouse cardiac electrophysiology from cell to torso. Europace 2, 56–70 (2005)
32. Bondarenko, V.E., Szigeti, G.P., Bett, G.C.L., Kim, S., Rasmusson, R.L.: Computer model of action potential of mouse ventricular myocytes. Am. J. Physiol. Heart Circ. Physiol. 287, H1378–H1403 (2004)
33. Iyer, V., Mazhari, R., Winslow, R.: A computational model of the human left-ventricular epicardial myocyte. Biophys. J. 87, 1507–1523 (2004)

Relating Discontinuous Cardiac Electrical Activity to Mesoscale Tissue Structures: Detailed Image Based Modeling

Mark L. Trew[1], Bruce H. Smaill[1,2], and Andrew J. Pullan[1,3]

[1] Bioengineering Institute, The University of Auckland, Private Bag 92019, Auckland 1142, New Zealand
m.trew@auckland.ac.nz
[2] Department of Physiology
[3] Department of Engineering Science

Abstract. We relate aspects of discontinuous cardiac activation to the mesoscale myocardial structural feature of interlaminae clefts or cleavage planes. Specialized numerical and computational procedures have been developed for modeling cardiac activation which accounts for detailed myocardial geometric structures derived from specific tissue samples. This modeling allows both study and analysis of the effects of cleavage planes and other structural barriers to myocardial current flow. The results show that mesoscale discontinuities significantly affect the formation of virtual electrodes, and can result in discontinuous activation with midwall pacing.

1 Introduction

There is strong evidence that electrical activity in cardiac tissue is discontinuous and is influenced by the myocardial architecture [1,2,3]. It is accepted that defibrillating shocks would not produce cardioversion if the myocardium behaved as a continuum and structural discontinuities have also been proposed to explain the response of the myocardium to high voltage shocks [4,5,6]. However, an outstanding question remains: do the structural features of the myocardium responsible for discontinuous activation occur at the myocyte (microscale) level [1,2] or are larger mesoscale [5,7] or macroscale [8] structures responsible? Undoubtedly structural features at all scales contribute as a syncytium to what is ultimately observed as electrical behavior that cannot be explained by continuous theory. High-resolution fluorescence imaging studies [4] and theoretical modeling studies [9] suggest that the microscale contributions to discontinuous electrical activity may be less than those of other scales. We postulate that mesoscale structural features, in particular interlaminae clefts or cleavage planes, are among the more significant contributors to discontinuous electrical activity. This reflects the geometry, organization and spatial extent of these structures.

Studies in processed tissue have shown that cardiac ventricular myocytes are arranged in sheets 4-5 cells thick, separated by cleavage planes or collagenous

F.B. Sachse and G. Seemann (Eds.): FIMH 2007, LNCS 4466, pp. 220–229, 2007.

septae [10,11,12]. Data consistent with these observations has also been obtained from diffusion tensor MRI of fresh perfused hearts [13]. The laminar structure of myocardium has been convincingly related to mechanical function, especially ventricular wall thickening during systole [14]. The ability of myocyte layers to slide without significant shear stress is elucidated in support of this behavior. In contrast there have been limited studies into the impact of the same structures on electrical propagation [7,15,16,17].

The challenge to direct measurement of the influence of structures such as cleavage planes on electrical activation is the combination of the scale of the structure ($\sim$10-100 μm [9]) and the extent over which those measurements must be made ($\sim$1-10 mm). Consequently, even with high resolution transmural imaging studies [4,5], direct evidence of discontinuous activation linked to cleavage planes remains experimentally difficult to achieve at the time being. Computer modeling provides a means for addressing these limitations. This enables the consideration of electrical behavior at both the fine resolution necessary to capture the detailed structure and the gross tissue level. Developments over the last five years in tissue imaging, numerical techniques and computational resources have begun to enable the modeling of electrical activation using tissue-specific, discontinuous myocardial geometries [7,18,15,16]. Here we address two hypotheses using tissue-specific cardiac electrical modeling: (1) that realistic discontinuities in syncytial cellular coupling cause the wide-spread formation of virtual electrodes when an extracellular electric field is applied; and (2) that some realistic discontinuities in syncytial cellular coupling can give rise to significantly discontinuous activations from midwall pacing.

2 Methods

2.1 Detailed Tissue Structure Models

Detailed tissue samples have been obtained from rat LV free wall. The tissue samples were perfused with fixative and stain, embedded in resin and automatically milled and imaged using a confocal microscope imaging rig [11,12,16]. From the three-dimensional reconstructed images (Figs. 1(a) and 1(b)), cleavage planes and other myocardial discontinuities were segmented. We are currently working with two tissue samples (denoted A and B) and two segmentation methods: one manual (A) [7,15] and one automatic (B) [16]. The manual segmentation represents the most significant cleavage planes as finite element surfaces (Fig. 1(c)). The automatic segmentation is performed at a user-specified resolution (subsampled if necessary from the 3D image reconstruction) and non-myocardial features such as cleavage planes or blood vessels are identified and form a template to be used for modeling purposes (Fig. 1(d)).

2.2 Computer Modeling

Electrical behavior is represented by the bidomain model (1). The dependent variables are the transmembrane potential, V_m, and the extracellular potential, ϕ_e.

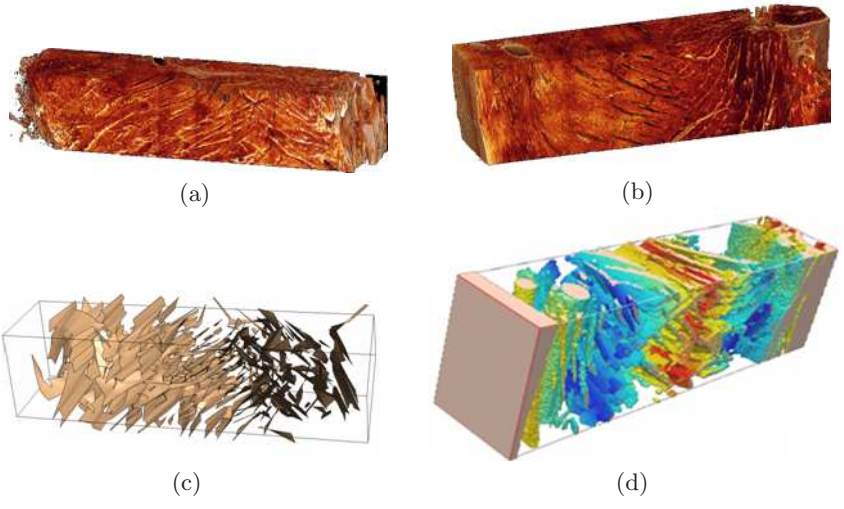

Fig. 1. Tissue imaging and processing. (a) Tissue A. Reconstruction of 3.6 by 0.8 by 0.8 mm confocal images. (b) Tissue B. Reconstruction of 4.36 by 1.15 by 0.9 mm confocal images. (c) Tissue A. Cleavage planes manually segmented into bilinear finite elements. (d) Tissue B. Automatic image segmentation into myocardium and non-myocardium regions.

$$\begin{aligned} A_m C_m \frac{\partial V_m}{\partial t} - \nabla \cdot (\boldsymbol{\sigma}_i \nabla V_m) &= \nabla \cdot (\boldsymbol{\sigma}_i \nabla \phi_e) - A_m I_{\text{ion}} \\ \nabla \cdot ((\boldsymbol{\sigma}_e + \boldsymbol{\sigma}_i) \nabla \phi_e) &= -\nabla \cdot (\boldsymbol{\sigma}_i \nabla V_m) - i_e \end{aligned} \tag{1}$$

Here A_m is the surface to volume ratio of the representative cell membrane between the domains, C_m is the specific capacitance of the membrane, $\boldsymbol{\sigma}_i$ and $\boldsymbol{\sigma}_e$ are the intra- and extra-cellular conductivity tensors, I_{ion} is the membrane ionic current and i_e is a current injection per unit volume into the extracellular space. The ionic current is determined using a simple cubic activation model [21] or a defibrillation modified Beeler-Reuter model [22]. Assuming isolated tissue, these equations are subject to the no-flux current boundary conditions given in Eqns. (2).

$$\begin{aligned} \nabla (V_m + \phi_e) \cdot (\boldsymbol{\sigma}_i \cdot \boldsymbol{n}) = 0 \quad \text{on} \quad \Gamma_O \cup \Gamma_C \\ \nabla \phi_e \cdot (\boldsymbol{\sigma}_e \cdot \boldsymbol{n}) = 0 \quad \text{on} \quad \Gamma_O \end{aligned} \tag{2}$$

Γ_O are the exterior boundaries and Γ_C are the internal boundaries in the intracellular domain, i.e. cleavage planes and other myocardial discontinuities.

For numerical modeling of the discontinuous myocardial structure with no-flux boundaries, methods based on the weak or integral forms of (1) are attractive, since this allows the natural enforcing of the no-flux boundary conditions given in Eqns. (2). An efficient finite volume based method [15] is used to discretize Eqns. (1) and (2).

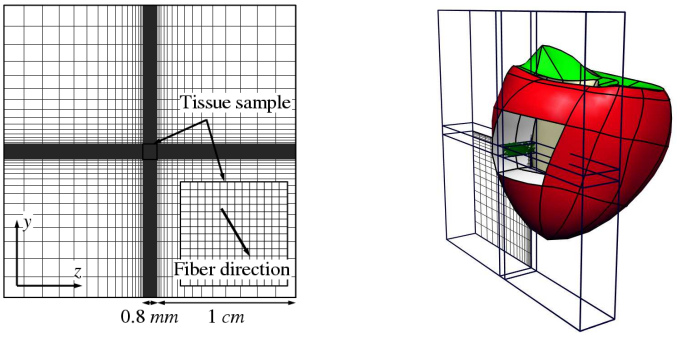

Fig. 2. Mesh padding about the tissue sample models A and B. The mesh is graded from the high-resolution region of interest to the lower interest exterior regions.

Studies have suggested that the conductivity of cardiac connective tissue is around 0.2-0.5 mS/mm [17,23]. This is similar to extracellular conductivities used by other researchers [20]. Here we use intracellular conductivities of 0.263 and 0.0263 mS/mm in the fiber and cross fiber directions. The extracellular conductivities are 0.263 and 0.1087 mS/mm. These give an intracellular anisotropy ratio of 10:1 and an extracellular ratio of 2.4:1, corresponding with those suggested by [24]. Orthotropy in the intracellular conductivity is obtained by explicit representations of cleavage planes.

The detailed geometry of tissue sample A is projected onto a finite volume mesh of a given spatial resolution. The minimum scale of myocardial discontinuity is then given by the resolution of the computational mesh. The image voxel segmentation of tissue sample B is subsampled directly to the desired resolution of the computational mesh.

As shown in Fig. 2 the computer model meshes of A and B are padded laterally to remove the near-field influence of the sample boundaries. The resulting tissue volume is similar to that of the rat ventricles. The mesh padding was graded to reduce the number of additional unknowns that were added to the modeling problem. In the mesh padding regions away from the detailed tissue sample either a low sheet-normal conductivity was used (for shock simulations) or a mesh of intracellular breaks (for unipolar or bipolar stimulations) was used to force the intracellular current flow to be approximately radial. The low sheet-normal conductivity was 0.008 mS/mm as suggested by [7].

3 Results and Discussion

3.1 Computational Aspects

Figure 3 highlights some of the numerical challenges inherent in detailed mesostructural modeling. For shock based modeling using tissue sample A (and the padding region) the virtual source distribution becomes independent of the

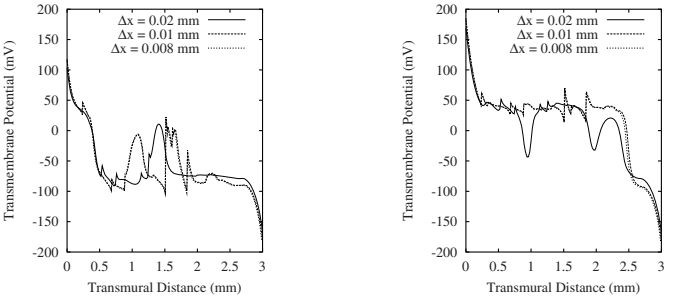

Fig. 3. Variation with mesh resolution of the computed transmembrane potential along the centerline of the structure model based on tissue sample A. A fixed 10 V/cm extracellular electric field is applied across the tissue sample. (a) 2 ms after stimulus application. (b) 4 ms after stimulus application.

mesh at a spatial resolution of approximately 10 μm. This translates into over 8.4 million degrees-of-freedom required to model sample A and 15.7 million degrees-of-freedom to model the larger sample B. It is important to note that although we are using a fine computational resolution, we are not attempting to model electrical behavior of cardiac tissue at a 10 μm resolution. This level of mesh resolution denotes the minimum dimension to which the geometry of the cleavage plane descriptions are resolved.

Problems are solved using a hyperthreaded 52 processor (Power 5, 1.9 GHz), 210 Gb shared memory IBM Regatta. For tissue sample A, simulations of length 10 ms require approximately 3-4 hours of elapsed wall time using 16 threads. The problems parallelize well. New multigrid-based solvers have been developed that account for discontinuous conductivities and the ill-conditioned or indefinate system arising from the discretization of the elliptic second equation of Eqn. (1) [25]. These developments have further enhanced solution times and problem capacity.

3.2 Virtual Electrodes and Cleavage Planes

The virtual source strengths due to conduction anisotropy and myocardial discontinuities were determined for simple two-dimensional problems. A bidomain model was used to predict the passive current density fields arising from bipolar extracellular stimulation of cardiac tissue. The intracellular current density field, $\boldsymbol{J}_i$, was used to determine the membrane current flows, i.e. $i_m = -\nabla \cdot \boldsymbol{J}_i$. Fig. 4 shows the variation in i_m in the vicinity of the electrodes and a myocardial discontinuity of varying length. These problems used the conductivity values given in Sec. 2.2 with the fiber direction oriented horizontally along the discontinuity. The positive membrane current flows are depolarizing and result in virtual cathodes. The current sources per unit volume along the discontinuities are approximately 75% of the cathodal current source, while the virtual

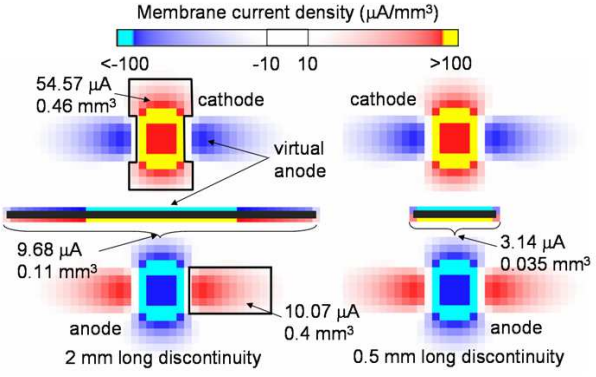

Fig. 4. Predicted virtual electrode strengths in two-dimensions arising from myocardial discontinuity and variable anisotropy ratios. The effects of different sizes of discontinuities are shown.

cathodes are 21%. However, the volume of tissue depolarised by the virtual source is important and for a given stimulus strength the larger dimension discontinuity will depolarise a larger volume of tissue over the activation threshold. In this context the definition of "larger" is related to both the shock strength and the set of conductivities. Note also that for smaller discontinuities the volume of tissue with a virtual cathode $> 100\ \mu\text{A/mm}^2$ is edge limited, but in the case of the 2 mm discontinuity it is not. The edge limitations cease at a discontinuity of length approximately 1 mm.

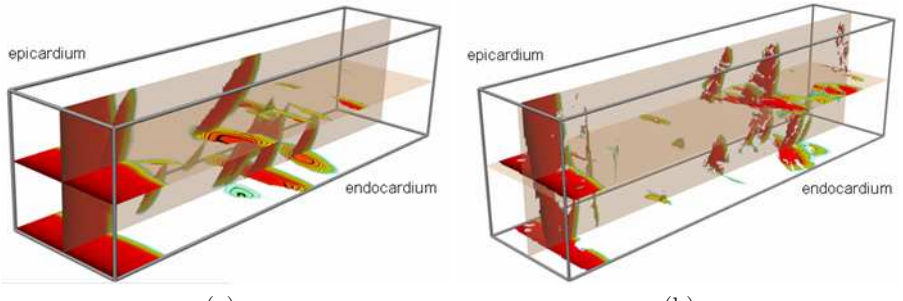

(a) (b)

Fig. 5. Distributions of transmembrane depolarizations from virtual electrodes in two tissue models 2 ms after the application of a rectangular 10 V/cm transmural shock. The cathode is located on the epicardium and the anode is located on the endocardium. (a) Tissue sample A. (b) Tissue sample B.

Simulations of extracellular shock stimulation in the three-dimensional detailed tissue models show intramural formation of virtual electrodes (Fig.5). In

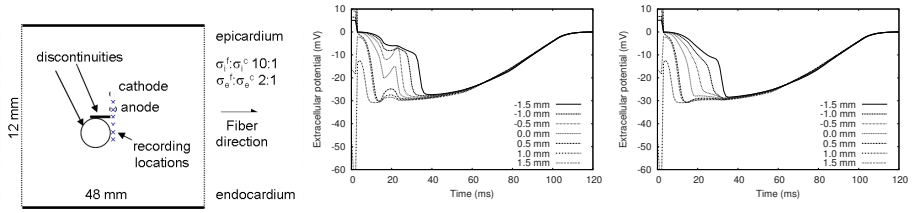

(a) (b) (c)

Fig. 6. The impact of structure geometry on extracellular potential traces. (a) A two-dimensional test problem. (b) Line discontinuity of length 2.0 mm. (c) Circle discontinuity of circumference 4.0 mm.

both models, the electrodes form on the anodal (in this case, endocardial) side of the larger intracellular discontinuities, with the early distributions being predominantly on the endocardial side of the midwall. These results refect previous experimental[4,5,6] and model[18,7] studies and support the hypothesis that under defibrillation strength shocks, myocardial discontinuities contribute to rapid transmural depolarization by seeding intramural virtual electrodes.

3.3 Non-uniform Activation and Cleavage Planes

When the stimulus strengths are near threshold, similar processes contribute to passive tissue depolarization and hyperpolarization across cleavage planes. However, the virtual electrodes are insufficiently strong to activate the tissue, although the potential gradient may be strong enough to diffuse sufficient extracellular current across the cleavage plane, that its consequent redistribution into the intracellular space facilitates subsequent activation [17]. In general for the case of near threshold stimulation it is predominantly the intracellular paths around the obstacles that dictate the spread of activation. This spread can be markedly discontinuous, especially from focal stimuli. Extracellular potential traces with multiple or fractionated deflections in the downstroke of the action complex have been observed following external stimulation in myocardium [26] and are usually taken to be indirect evidence of non-uniform or discontinuous activation. Figure 6 shows extracellular potential traces for a two-dimensional bidomain problem with both line and circle discontinuities. Only the line discontinuity (Fig. 6(b)) shows fractionated activation downstrokes in the vicinity of the discontinuity. Shorter line discontinuities showed progressively less downstroke fractionation. These results suggest that larger planar discontinuities (such as cleavage planes) may be largely responsible for fractionated downstrokes in electrograms.

Fig. 7 shows focal and plane stimuli activations in a detailed three-dimensional model of tissue A. The extracellular potential traces shown in Fig. 7(b) are similar to in-vivo observations with multiple activation downstrokes for focal activation but smoother deflections in sinus rhythm [27]. The geometric features of the relevant cleavage planes at four sample points are important in the analysis

of these extracellular potential traces. For a midwall stimulus, the sample points are equidistant from the stimulus point. However, 2 and 3 activate later than 1 and 4. In addition, 3 activates earlier than 2 and 1 activates earlier than 4. The geometric model shows the large cleavage planes nearest to the recording points impinging on the path from the stimulus site in two ways. (1) The path has a significant component parallel to the cleavage plane, i.e. minimal non-uniform activation, or the path has a significant component normal to the cleavage plane, i.e. most non-uniform activation (Fig. 7(c)). (2) The dimensions of the planes. The point with the most non-uniformity (2, Fig. 7(c)), lies adjacent to a large cleavage plane. In contrast, the point showing lesser non-uniformity (3, Fig. 7(c)) is adjacent to multiple smaller planes. These results unify previous observations that downstroke fractionation is dependent on the size of myocardial discontinuities [9] or the recording location relative to the local myofiber orientation [26].

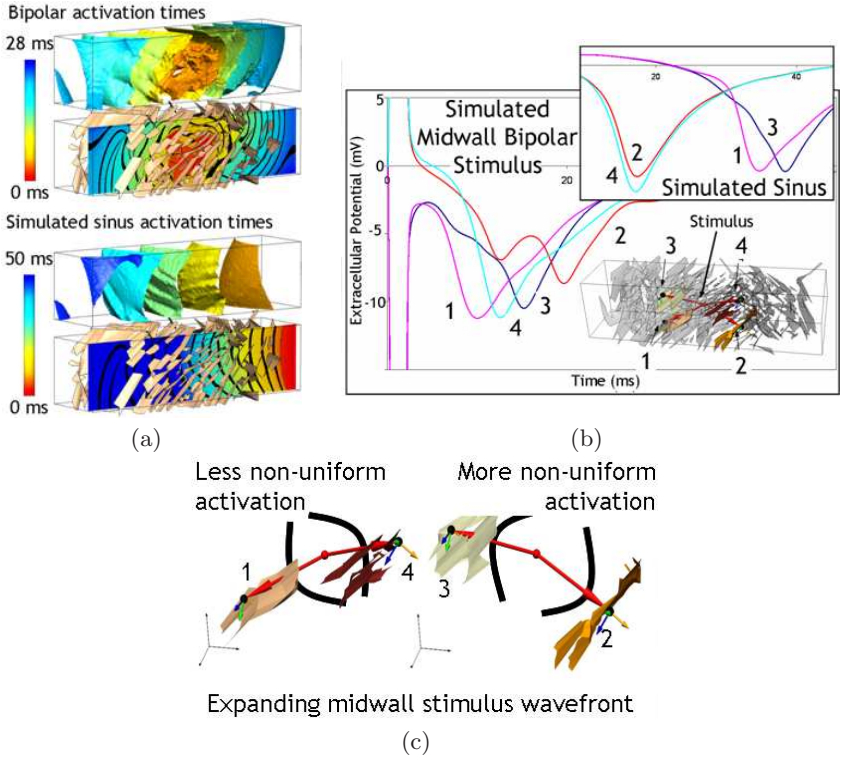

Fig. 7. The impact of cleavage plane structures on non-uniform activation. (a) Transmural activation for bipolar midwall and endocardial stimuli. (b) Extracellular potential traces at four intramural sample points. (c) Detail of key cleavage plane structures.

4 Conclusions

Direct modeling of myocardial cleavage planes provides new insights into the complexities of cardiac activation. It sheds light on the efficacy of defibrillation type shocks and assists in quantifying the impact of mesoscale structural geometry on experimental results. Understanding the response of detailed cardiac tissue models to stimuli may also be an important tool in the design of new pacing modalities for treating and preventing arrhythmias and heart failure.

Acknowledgements

Royal Society of New Zealand Marsden Fund; Health Research Council of New Zealand; and contributions from: Dr I.J. LeGrice (Figs. 1(a)-1(b)), Dr G.B. Sands (Fig. 1), Dr D.A. Hooks and Mr B.J. Caldwell.

References

1. Kléber, A.G., Rudy, Y.: Basic Mechanisms of Cardiac Impulse Propagation and Associated Arrhythmias. Physiol. Rev. 84, 431–488 (2004)
2. Spach, M.S., Heidlage, J.F., Barr, R.C., Dolber, P.C.: Cell Size and Communication: Role in Structural and Electrical Development and Remodeling of the Heart. Heart Rhythm. 4, 500–515 (2004)
3. Spach, M.S., Barr, R.C.: Effects of Cardiac Microstructure on Propagating Electrical Waveforms. Circ. Res. 86, e23–e28 (2000)
4. Sharifov, O.F., Fast, V.G.: Optical Mapping of Transmural Activation Induced by Electrical Shocks in Isolated Left Ventricular Wall Wedge Preparations. J. Cardiovasc Electr. 14(11), 1215–1222 (2003)
5. Fast, V.G., Rohr, S., Gillis, A.M., Kléber, A.G.: Activation of Cardiac Tissue by Extracellular Electrical Shocks: Formation of "Secondary Sources" at Intercellular Clefts in Monolayers of Cultured Myocytes. Circ. Res. 82, 375–385 (1998)
6. White, J.B., Walcott, G.P., Pollard, A.E., Ideker, R.E.: Myocardial Discontinuities. A Substrate for Producing Virtual Electrodes That Directly Excite the Myocardium by Shocks. Circulation 97, 1738–1745 (1998)
7. Hooks, D.A., Tomlinson, K.A., Marsden, S., LeGrice, I.J, Smaill, B.H., Pullan, A.J., Hunter, P.J.: Cardiac Microstructure: Implications for Electrical Propagation and Defibrillation in the Heart. Circ. Res. 91(4), 331–338 (2002)
8. Vetter, F.J., Simons, S.B., Mironov, S., Hyatt, C.J., Pertsov, A.M.: Epicardial Fiber Organization in Swine Right Ventricle and Its Impact on Propagation. Circ. Res. 96, 244–251 (2005)
9. Ellis, W.S., Auslander, D.M., Lesh, M.D.: Fractionated Electrograms From a Computer Model of Heterogeneously Uncoupled Anisotropic Ventricular Myocardium. Circulation 92, 1619–1626 (1995)
10. LeGrice, I.J., Smaill, B.H., Chai, L.Z., Edgar, S.G., Gavin, J.B., Hunter, P.J.: Laminar structure of the heart: ventricular myocyte arrangement and connective tissue architecture in the dog. Am. J. Physiol-Heart C. 269, H571–H582 (1995)
11. Young, A.A., LeGrice, I.J., Young, M.A., Smaill, B.H.: Extended confocal microscopy of myocardial laminae and collagen network. J. Microsc 192(2), 139–150 (1998)

12. Sands, G.B., Gerneke, D.A., Hooks, D.A, Green, C.R., Smaill, B.H., LeGrice, I.J.: Automated Imaging of Extended Tissue Volumes using Confocal Microscopy. Microsc. Res. Techniq. 67(5), 227–239 (2005)
13. Scollan, D.F., Holmes, A., Winslow, R.L., Forder, J.: Histological Validation of Myocardial Microstructure Obtained from Diffusion Tensor Magnetic Resonance Imaging. Am. J. Physiol-Heart C. 275, H2308–H2318 (1998)
14. Harrington, K.B., Rodriguez, F., Cheng, A., Langer, F., Ashikaga, H., Daughters, G.T., Criscione, J.C.,, I.N.B., Miller, D.C.: Direct Measurement of Transmural Laminar Architecture in the Anterolateral Wall of the Ovine Left Ventricle: New Implications for Wall Thickening Mechanics. Am. J. Physiol-Heart C. 288, H1324–H1330 (2005)
15. Trew, M.L., LeGrice, I.J, Smaill, B.H., Pullan, A.J.: A Finite Volume Method for Modeling Discontinuous Electrical Activation in Cardiac Tissue. Ann. Biomed Eng. 33(5), 591–600 (2005)
16. Sands, G.B., Trew, M.L., Hooks, D.A., LeGrice, I.J., Pullan, A.J., Smaill, B.H.: Constructing a Tissue-Specific Model of Ventricular Microstructure. In: Proc. 26th Ann. Int. Conf. IEEE EMBS, San Francisco, CA, pp. 3589–3592 (2004)
17. Street, A.M, Plonsey, R.: Propagation in Cardiac Tissue Adjacent to Connective Tissue: Two-Dimensional Modeling Studies. IEEE T. Bio.-med Eng. 46(1), 19–25 (1999)
18. Hooks, D.A., Trew, M.L., Smaill, B.H., Pullan, A.J.: Evidence that Intramural Virtual Electrodes Facilitate Successful Defibrillation. Model Based Analysis of Experimental Evidence. J. Cardiovasc Electr. 17(3), 305–311 (2006)
19. Sharifov, O.F., Fast, V.G.: Role of Intramural Virtual Electrodes in Shock-Induced Activation of Left Ventricle: Optical Measurements from the Intact Epicardial Surface. Heart Rhythm 3(9), 1063–1073 (2006)
20. Muzikant, A.L., Hsu, E.W., Wolf, P,D., Henriquez, C.S.: Region Specific Modeling of Cardiac Muscle: Comparison of Simulated and Experimental Potentials. Ann. Biomed Eng. 30, 867–883 (2002)
21. Hunter, P.J., McNaughton, P.A., Noble, D.: Analytical Models of Propagation in Excitable Cells. Prog. Biophys. Mol. Bio. 30(2/3), 99–144 (1975)
22. Skouibine, K.B., Trayanova, N.A., Moore, P.K.: A Numerically Efficient Model for Simulation of Defibrillation in an Active Bidomain Sheet of Myocardium. Math. Biosci. 166, 85–100 (2000)
23. Grill, W.M., Mortimer, J.T.: Electrical Properties of Implant Encapsulation Tissue. Ann. Biomed. Eng. 22, 23–33 (1994)
24. Roth, B.J.: Electrical Conductivity Values Used with the Bidomain Model of Cardiac Tissue. IEEE T. Bio.-med Eng. 44(4), 326–328 (1997)
25. Austin, T.M., Trew, M.L., Pullan, A.J.: Solving the Cardiac Bidomain Equations for Discontinuous Conductivities. IEEE T. Bio.-med Eng. 53(7), 1265–1272 (2006)
26. Punske, B.B., Ni, Q., Lux, R.L., MacLeod, R.S., Ersher, P.R., Dustman, T.J., Alison, M.J., Taccardi, B.: Spatial Methods of Epicardial Activation Time Determination in Normal Hearts. Ann. Biomed Eng. 31, 781–792 (2003)
27. Trew, M.L., Caldwell, B.J., Sands, G.B., Hooks, D.A., Tai, D.C.S, Austin, T.M., LeGrice, I.J., Pullan, A.J., Smaill, B.H.: Cardiac Electrophysiology and Tissue Structure: Bridging the Scale Gap with a Joint Measurement and Modelling Paradigm. Exp. Physiol. 91(2), 355–370 (2006)

Is There Any Place for Magnetocardiographic Imaging in the Era of Robotic Ablation of Cardiac Arrhythmias?*

Riccardo Fenici and Donatella Brisinda

Clinical Physiology - Biomagnetism Research Center, Catholic University of Sacred Heart, Largo A. Gemelli 8, 00168 Rome, Italy
feniciri@rm.unicatt.it

Abstract. This article reviews major problems and difficulties faced by the authors along more than twenty years of clinical application of magnetocardiography (MCG) as a tool to improve the diagnosis of arrhythmogenic mechanism(s), non-invasively. It is also emphasized that an exhaustive understanding of individual electrophysiology is mandatory before any intervention, which can modify the substrate and complicate the treatment of patients in the case of ablation failure. The reasons for scarce acceptance of MCG, compared with the success of recent methods for invasive three-dimensional electroanatomical imaging (3D-EAI), are discussed to provide suggestions for needed changes in R&D strategy. MCG might be a powerful method for non-invasive 3D-EAI, but appropriate tools for its clinical applicability are still lacking and need to be urgently developed, through serious investments and interdisciplinary cooperation.

Keywords: Magnetocardiography, Mapping, Ablation, Cardiac Arrhythmias.

1 Introduction

Invasive dynamic three-dimensional electroanatomical imaging (3D-EAI) is increasingly used in the catheterization laboratory for precise targeting and appropriate ablation of focal and/or reentry arrhythmogenic substrates [1]. Since 1995, new technologies have been also developed to visualize intracardiac mapping catheters without the need of fluoroscopy and to use them as a sort of intracardiac digitizer, which provides, sequentially or simultaneously, a drawing of endocardial geometry [2-5]. One of those systems, based on "magnetic" technology, is nowadays present in the majority of cardiac electrophysiology units and provides unrivalled support for interventional electrophysiology and new diagnostic capability to detect arrhythmogenic abnormalities in patients with cardiomyopathy [6]. Magnetic technology is also the base of robotic systems to navigate with high precision soft electrocatheters from a remote radiation-free location [7]. Alternatively, stereotactic navigation of amagnetic catheters under direct magnetic resonance imaging (MRI) control is under testing for dynamic display of the catheter position into the cardiac anatomy of the patient [8].

* Partially supported by grants Sigma-Tau research contract DS/2004/CR/#22 and by the National Science Foundation, SBIR phase II award #0349580.

F.B. Sachse and G. Seemann (Eds.): FIMH 2007, LNCS 4466, pp. 230–239, 2007.

Beside the progress of hardware technology, fast development of appropriate software tools for quick and accurate interactive reconstruction of cardiac chambers and dynamic imaging during interventional procedures have been the key factor facilitating widespread acceptance of such new methods at clinical level, in spite of high cost of the instrumentations and of the indispensable consumables (single use special catheters, electrode or coils patches, etc.).

Simultaneous progress of three-dimensional (3D) rendering of cardiac anatomy from multi-detector computer tomography (MDCT) or from MRI has provided the basis to reach a realistic electroanatomical imaging through multimodal integration of invasive electrophysiological information with the patient's true anatomy, preliminarily obtained with MDTC or MRI (Fig. 1).

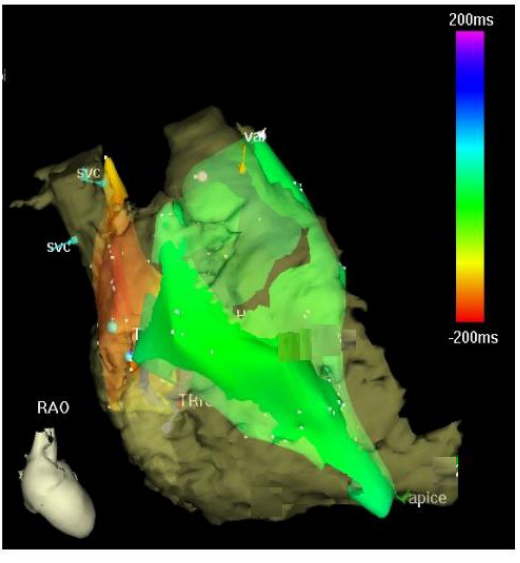

Fig. 1. Example of multimodal integration of three-dimensional electroanatomical imaging based on merging of CARTO® mapping and 3D rendering of right atrium and ventricle from multi-detector computer tomography

The availability of such high-tech tools and the improving results of catheter ablation are rapidly changing the guidelines for the treatment of cardiac arrhythmias favouring the interventional approach as more resolutive compared with chronic conservative drug therapy.

For an increasing number of arrhythmias catheter ablation is nowadays proposed to the patient as the first-line treatment. Also the "old" electrophysiologic study, which was carried out to investigate and understand the arrhythmogenic mechanism(s) underlying the individual clinical picture, is now often disregarded. In fact with the idea in mind that ablation will solve the problem, the exhaustive understanding of the electrogenic substrate is considered almost a useless time-consuming procedure.

During the intervention, cardiac mapping is carried out to get electro-anatomical landmarks, to match the patient's true 3D anatomical images (usually MDCT images) and to navigate the mapping/ablation catheter at the appropriate sites. Electrophysiological recordings are used to target the arrhythmogenic site(s) and to validate the efficacy of the ablation [2-5].

Now, if in the era of robotic electrophysiologic interventions the results of invasive methods are efficient and resolutive, why should we need non-invasive electrophysiologic imaging and in particular magnetocardiography (MCG)?

In this paper we will discuss some points of evidence, based on our clinical experience, which suggest that non-invasive preoperative evaluation of the patient is necessary to minimize the risks of ablation and/or to address pharmacological treatment in the case of failure. MCG might be the first choice method for non-invasive 3D-EAI, but urgent developments are required to transform MCG systems from research tools into user-friendly clinically acceptable devices.

2 Methods

As recently reported elsewhere [9], our most recent clinical experience on MCG use for the study of patients with cardiac arrhythmias is based on more that 550 recordings performed, from November 2002 to May 2006, with a 36-channel unshielded mapping system *(CardioMag Imaging Inc, Schenectady, NY)*, based on DC-SQUID sensors coupled to second-order axial gradiometers (pick-up coil 19 mm and 55-70 mm baselines), with an intrinsic sensitivity of 20 fT/√Hz in the frequency range of clinical interest [10].

Because the system is located in a catheterization laboratory, MCG is part of an exhaustive electrophysiologic investigation protocol, tailored to the diagnostic need of each arrhythmic patient. MCG is digitally recorded in the DC-100 Hz bandwidth (24 bits A/D conversion, with automatic electronic noise rejection, at 1 kHz sampling rate), together with the 12-lead ECG, oesophageal electrograms and, when indicated, with intracardiac signals *(CardioLab System*, *General Electric)*. Transesophageal and endocardial pacing are performed with a programmable cardiac stimulator *(MEDICO TECS II, Padua, IT)*. High-resolution Multiple Monophasic Action Potential (Multi-MAP) recording is performed with a single 6F amagnetic catheter, which can be localized by MCG, with a 3D accuracy of 2-7 mm, without the use of fluoroscopy [11]. MAP signals are differentially amplified, band pass filtered (DC-1 kHz) and digitized at the sampling frequency of 2 kHz.

To construct individualized 3D models of the patient's heart [12], two orthogonal fluoroscopic cardiac images are digitally recorded with a mobile digital fluoroscopy system *(Sias Spa, Bologna IT)*, after the MCG session. Magnetocardiographic signals are analyzed with the system software [10] and with the UNIX-based MCG software developed at the Helsinki University of Technology *(Neuromag, Finland)* [13]. When required, invasive 3D-EAI is performed with the CARTO® system (*Biosense Webster, USA)* in another catheterization laboratory of our university, where catheter ablation

is performed. 3D "rendering" of cardiac anatomy is obtained from MDCT or MRI *(General Electric)*.

3 Results and Discussion

The results of our investigation of specific groups of arrhythmic patients have been reported elsewhere [14-18]. Here we summarize some key-points of our experience using MCG as a non-invasive method for 3D-EAI, aiming to discuss which, in our opinion, are the pitfalls that have penalized MCG so far, and some suggestions for possible corrective interventions.

3.1 The Risk of Present Trend to Use Ablation as the First Line of Intervention

Along the last few years, the increasing success rate and the dramatic drop of interventional risk are convincing cardiologists that an aggressive policy is preferable to treat cardiac arrhythmias in a single-time cost-effective way.

On the other hand, clinical experience provides also evidence that failures of ablation are not rare and that in some patients, after multiple relapses of the arrhythmia, one has to give up and come back to traditional therapy. However, it is often more difficult to select the appropriate pharmacological treatment after that ablation has modified the original arrhythmogenic substrate in an unknown way.

For this simple reason we believe that the electrophysiologic mechanism(s) underlying cardiac arrhythmias should be well identified in the individual patient, before any ablation-induced modification of the substrate. In this view there is obviously still need and interest for any non-invasive diagnostic tools reliable for this purpose.

3.2 Reliability and Limitations of MCG-Based 3D-EAI

Two decades of research work have convinced us that MCG is an unrivalled non-invasive tool for contactless cardiac mapping, providing the possibility to restudy arrhythmic patients multiple times, to better understand the nature of the underlying arrhythmogenic mechanism(s).

Several preliminary studies have demonstrated that MCG is reliable to localize three-dimensionally different kinds of arrhythmogenic substrates. Beside localization of well-confined arrhythmogenic structures, such as a thin accessory Kent-type pathway [14] or focal tachycardias, MCG has been recently reported to provide also dynamic imaging of atrial reentry arrhythmias [19,20], which might be useful to classify and differentiate preoperatively patients with different types of atrial fibrillation. However, such results have been obtained with custom research tools, unavailable as commercial options and very far from the kind of imaging that are provided with systems for invasive cardiac mapping. This obviously might discourage the use of MCG in the "diagnostic cascade" of the arrhythmic patient candidate to ablation.

On the other hand it is absolutely evident that preoperative MCG 3D-EAI would be useful to define the reproducibility and stability of the arrhythmogenic substrate, to

differentiate patients with apparently similar ECG pictures but different electrophysiologic substrates and to plan the most appropriate interventional approach, prior to any invasivity.

3.3 Why MCG Has Failed Where Invasive 3D-EAI Has Been Rapidly Accepted?

The intuition that MCG could be used to guide aimed electrophysiology, myocardial biopsy and ablation of cardiac arrhythmias was originally patented already at the end of the eighties [21], and probably triggered the development of the later "magnetic" technology for invasive 3D-EAI and for the navigation of ablation catheters [22].

The invasive "magnetic" technology for 3D-EAI is nowadays widely accepted as an unrivalled support for interventional electrophysiology, whereas MCG is almost unknown and disregarded by clinical electrophysiologists, in spite of the capability to provide the same information non-invasively.

Thus the question is: what is missing that has impeded MCG, the oldest magnetic method, to have the same success and clinical acceptance obtained by its younger invasive brother?

In our opinion there are two major motivations: a) the lack of software development for appropriate imaging; b) the apparent lack of benefit for the industry in investing for such development.

a. Lack of Software Development

This point is self-explaining. In fact the development of appropriate software tools and user-friendly interface is mandatory. Without the appropriate software tools it is impossible to put MCG in the hands of the average cardiologist and pretend that they invest (or waste) their precious (and most often very limited or unavailable) time to reconstruct mentally and manually the 3D localization or the dynamic imaging of an arrhythmogenic substrate, which is automatic in the commercial systems for invasive 3D-EAI.

Which Should Be the Requirements for New Software Tools?

If the target is to develop tools to use the information obtainable with MCG for clinical use, it must be taken into account what comes out from years of experience using MCG to improve the understanding of individual electrophysiologic patterns of patients with cardiac arrhythmias.

First of all, MCG-based 3D-EAI is a complex time-consuming evaluation process, which requires multiple analytic iterations, frequently on a beat-to-beat basis, not only during spontaneous rhythm, but also during pacing or other dynamic tests. The diagnostic accuracy of MCG based 3D-EAI in fact can be enhanced by simultaneous electrophysiologic study with trans-esophageal atrial pacing [15] or pharmacologic tests, thus the number of situations to be analyzed might increase in individual cases.

At the moment the 3D presentation of the electrophysiological information provided by MCG is almost at a medieval level. For example, if one compares the software tools provided with systems for interventional electroanatomical imaging with those of commercially available MCG systems, is immediately evident that automatic protocols for multimodal integration of electrophysiological imaging and

3D "rendering" of cardiac anatomy from MDCT or MRI are standard options in the former and completely missing in the latter. Instead, automatization is needed to speed-up the MCG diagnostic procedure and to avoid bias due to presumptions.

The Design of New Software Is a Challenge that Deserves Interdisciplinary Work

Accomplishing this task will require the involvement of companies, clinicians, scientists and engineers. In fact it has to taken into account the nature of the specific clinical problem(s) to be solved, but also the way the cardiologists are used to work with their instrumentations.

For example, looking forward to using the 3D electroanatomical information preoperatively obtained with MCG to guide catheter ablation, software protocols for automatic or interactive imaging should follow the same rationale (i.e. use the same 3D anatomic images, acquires with the same reference landmarks in the different settings).

An appropriate understanding of the spatial relationship between MCG-based 3D-EAI of the target and fluoroscopic imaging of the mapping/ablation catheters is still lacking. In fact, from our clinical experience with MCG, we have found that, even using the same reference landmarks during data acquisition with MCG and fluoroscopic imaging, a lot of thought and experience was necessary in some cases, to understand and correct apparent disagreements in determining the position of the catheter successfully in order to ablate the substrate with appropriate MCG-based localization of the target (Fig. 2). The implementation of novel dynamic modelling of the beating heart and respiring lungs will be useful to improve accuracy [23].

Possible Sources of Matching Disagreement Between Fluoroscopy and MCG

Possible sources of matching disagreement can be inherent to the patient (e.g. respiration, "twisting" movement of the heart during contraction, skin displacement, torso rotations), or external (e.g. different geometry of the beds of the different imaging systems, slight tilt of fluoroscopy or of the MCG systems).

By using 3D rendering from MDCT (Fig. 2A) as the common anatomic structure between invasive (Fig. 2B) and MCG-based (Fig. 2C) and 3D-EAI, we were able to understand some other possible reasons for mismatch with fluoroscopy (Fig. 2D).

One of them is that fluoroscopic images during catheterization are taken in a random way, and the position of the distal terminal of the mapping catheter may fluctuate with respiration even several centimeters in respect of the external (chest surface) or internal (e.g. transesophageal) radiopaque markers used as reference points for image fusion with MCG, especially if the catheter is placed at the antero-lateral wall of the right ventricle. ECG-gated fluoroscopic imaging and comparison with MCG at the same respiratory phase might minimize the mismatch. The contribution of the electromechanical interval can also play a role in inducing a mismatch depending on the timing of the localization procedure during the cardiac interval.

On the other hand also the matching of non-invasive MCG-based 3D-EAI with that obtained with interventional mapping is not immediate at the moment, and there can be additional sources of error (i.e. if the patient moves in respect of the magnetic coils that are solid with the bed surface, during invasive cardiac mapping).

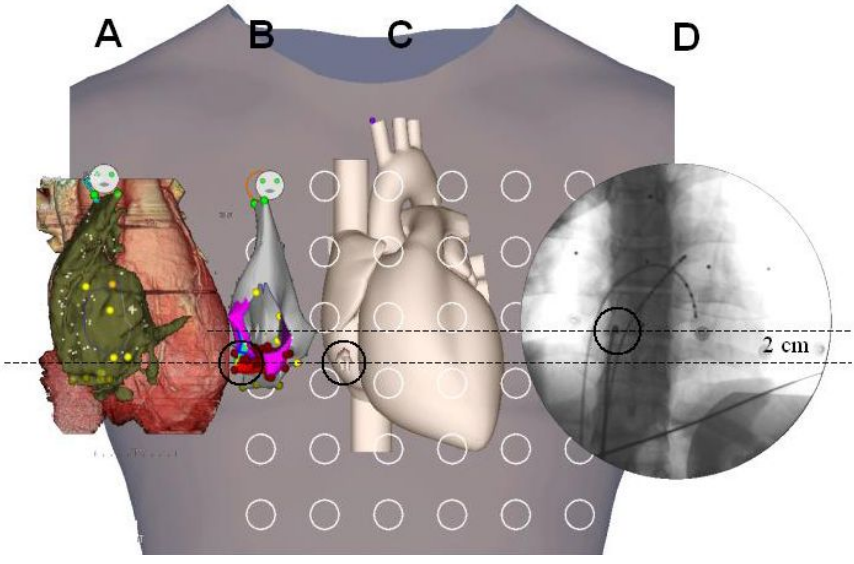

Fig. 2. Vertical mismatch (2 cm) between MCG localization (C) of a right anterior-inferior accessory pathway and fluoroscopic imaging (frontal view) of the catheter at the site of successful ablation (D). CARTO© 3D-EAI (B) and its integration with MDCT (A) confirm the accuracy of MCG-based imaging of the arrhythmogenic substrate (encircled).

b. Lack of Benefit for the Industry in Investing for Such Development

This point is crucial. Without investments and adequate manpower there is no possibility to transform MCG research tools into clinical devices. Companies who have constructed systems for invasive cardiac mapping, electroanatomical mapping and even most recent technology for robotic navigation of ablation catheters have obviously accepted to take the risk of big investments with a perspective of covering the costs in a medium or even long term. However, when the invasive systems have become ready for clinical testing and thereafter for commercialization, the simple use of such devices, independently whether the intervention was clinically successful or not, had the potential to provide an economical profit to the company, because the study of each patient implies the use of single-use consumables (catheters, patches electrodes, etc). Thus the cost of the instrumentation could be covered by a prevision of a certain number of investigated patients per year. This is not the case with MCG, which doesn't need electrodes, catheters or expensive consumables other than liquid helium not commercialized by the companies selling the instrumentation. Thus the high initial investment for the development of the MCG instrumentation cannot be damped even during the clinical testing phase with a "*pay per patient*" philosophy. On the other hand nowadays budget limitations often prevent universities and hospitals from buying high-cost research instrumentations or new technology, whenever their clinical utility has not been previously demonstrated. This lack of potential market discourages investment in R&D and the situation is frozen so far in a

"vicious circle", blocking the development of MCG technology at the step before that needed to demonstrate the clinical need and benefit of the method.

4 Future Applications

Beside short-term developments which are mandatory to provide MCG with the possibility to really enter in the diagnostic routine of arrhythmic patients, we believe that MCG has two additional interesting perspectives that deserve much attention to plan their medium-term development: a) Preoperative non-invasive programming of robotic systems to navigate ablation catheters, and b) Outline of cardiac anatomy based on current density imaging.

a. Preoperative Non-invasive Programming of Robotic Systems to Navigate Ablation Catheters

Nowadays magnetic technology has also been used to construct robotic systems to navigate with high precision electrocatheters from a remote radiation-free location [7]. Such robotic system has been integrated with an invasive 3D-EAI system and with MDTC anatomic imaging to guide ablation. Such integration program is also foreseen to develop automatized computer-driven ablative procedures. However this could be also a unique opportunity also for MCG. In fact MCG capability to provide 3D coordinates of an arrhythmogenic target and its automatic integration into 3D rendering of the patient's heart obtained from cardiac MDCT or MRI, might provide an individualized virtual model to plan and program non-invasively the ablation protocol of a robotic system and to test non-invasively its efficacy before the intervention.

b. Outline of Cardiac Anatomy Based on Current Density Imaging

Nakai et al have recently shown that, using a new space filter for visualizing the 3D electric current density from B_z magnetic fields, they were able to reconstruct from MCG, 3D outlines of patients'endocardial boundaries, corresponding to their cardiac MRI images [20,24]. Similarly Ogata et al [25] describe an advanced application of the current arrow method, aimed to provide 3D electroanatomical imaging of atrial and ventricular electrophysiological events, by projecting current arrow maps, reconstructed from frontal and posterior MCG, onto a 3D model of the heart. In spite of the use of a standard model as anatomical substrate, the imaging results are impressive and enhancing the MCG capability to provide 3D EAI without the need of other methods for anatomical imaging. Ogata et al have shown the interindividual reproducibility of current arrow patterns in visualizing both atrial and ventricular activation currents, with a reasonable spatial resolution. The next step needed is a combination of the Nakai and Ogata methods (i.e. a tailoring of the standard cardiac model to match the outline of the individual endocardial boundaries calculated with space filtering) and a more focused spatial separation of local electrophysiological, to detect local arrhythmogenic conduction and/or repolarization abnormalities.

5 Conclusions

MCG imaging of cardiac electrophysiology might be used as a non-invasive approach to localize the origin and the mechanisms of cardiac arrhythmias. Successful results have been obtained also with body surface potential mapping [26]. A comparative study to evaluate the relative merits of MCG and ECG methods, validated by comparison with invasive electroanatomical imaging in the same patients would be surely desirable, however such data are not available yet.

References

1. Blomstrom-Lundqvist, C., Scheinman, MM., Aliot, EM., Alpert, JS., Calkins, H., Camm, AJ., et al.: American College of Cardiology; ACC/AHA/ESC guidelines for the management of patients with supraventricular arrhythmias–executive summary. Circulation 108(15), 1871–1909 (2003)
2. Gepstein, L., Wolf, T., Hayam, G., Ben-Haim, SA.: Accurate linear radiofrequency lesions guided by a Nonfluoroscopic electroanatomical mapping method during atrial fibrillation. Pacing Clin Electrophysiol. 24(24), 1672–1678 (2001)
3. Wittkampf, FH., Wever, EF., Derksen, R., Ramanna, H., Hauer, RN., de Medina, EO.R.: LocaLisa: new technique for real-time 3-dimensional localization of regular intracardiac electrodes. Circulation 99(10), 1312–1317 (1999)
4. Gurevitz, OT., Glikson, M., Asirvatham, S., Kester, TA., Grice, SK., Munger, TM., et al.: Use of advanced mapping systems to guide ablation in complex cases: experience with noncontact mapping and electroanatomic mapping systems. Pacing Clin Electrophysiol. 28(4), 316–323 (2005)
5. Faddis, M.N., Chen, J., Osborn, J., Talcott, M., Cain, M.E., Lindsay, B.D.: Magnetic guidance system for cardiac electrophysiology: a prospective trial of safety and efficacy in humans. J. Am. Coll. Cardiol. 42(11), 1952–1958 (2003)
6. Corrado, D., Basso, C., Leoni, L., Tokajuk, B., Bauce, B., Frigo, G., et al.: Three-dimensional electroanatomic voltage mapping increases accuracy of diagnosing arrhythmogenic right ventricular cardiomyopathy/dysplasia. Circulation 14,111(23), 3042–3050 (2005)
7. Ernst, S., Ouyang, F., Linder, C., Hertting, K., Stahl, F., Chun, J. et al.: Initial experience with remote catheter ablation using a novel magnetic navigation system: magnetic remote catheter ablation. Circulation 109(12), 1472–1475 (2004)
8. Dickfeld, T., Calkins, H., Bradley, D., Solomon, S.: Stereotactic catheter navigation using magnetic resonance image integration in the human heart. Heart Rhythm. 2(4), 413–415 (2005)
9. Fenici, R., Brisinda, D.: Bridging non-invasive and interventional electroanatomical imaging: role of magnetocardiography. J. Electrocardiol. 40(Suppl 1), 47–52 (2007)
10. Fenici, R., Brisinda, D., Meloni, AM., Fenici, P.: First 36-channel System for Clinical Magnetocardiography in Unshielded Hospital Laboratory for Cardiac Electrophysiology. Int. J. of Bioelectromagnetism. 1, 80–83 (2003)
11. Fenici, R., Brisinda, D., Nenonen, J., Fenici, P.: Phantom validation of multichannel magnetocardiography source localization. Pacing Clin Electrophysiol. 26(1, Part II), 426–430 (2003)

12. Veisterä, H., Fenici, R., Lötjönen, J.: Online heart model creation for magnetocardiographic measurements. In: Halgren, E., Ahlfors, S., Hämäläinen, M., Cohen, D. (eds.) Proceedings of the 14th International Conference on Biomagnetism: vol. 415 (2004)
13. Nenonen, J.: Magnetocardiography. In: Clark, J., Braginski, A. (eds.) SQUID, Handbook, Berlin, Whiley-VCH, Chichester (2005)
14. Brisinda, D., Fenici, R.: Non-invasive Classification and Follow-up of WPW patients with unshielded Magnetocardiography and Transesophageal Atrial Pacing. Pacing and Clinical Electrophysiol. 30 (Suppl 1), S151–S155 (2007)
15. Fenici, R., Brisinda, D., Meloni, AM.: Non-invasive electrophysiologic study with amagnetic transesophageal pacing during unshielded multichannel magnetocardiographic mapping. Neurol Clin Neurophysiol. 30,14 (2004)
16. Fenici, R., Brisinda, D., Meloni, AM.: Clinical application of magnetocardiography. Expert Rev. Mol. Diagn. 5(3), 291–313 (2005)
17. Fenici, R., Brisinda, D.: Magnetocardiography provides non-invasive three-dimensional electroanatomical imaging of cardiac electrophysiology. Int. J. Cardiovasc Imaging. 22(3-4), 595–597 (2006)
18. Fenici, R., Melillo, G.: Magnetocardiography: ventricular arrhythmias. Eur. Heart J. 14(Suppl E), 53–60 (1993)
19. Yamada, S., Tsukada, K., Miyashita, T., Kuga, K., Yamaguchi, I.: Noninvasive, direct visualization of macro-reentrant circuits by using magnetocardiograms: initiation and persistence of atrial flutter. Europace. 5(4), 343–350 (2003)
20. Nakai, K., Kawazoe, K., Izumoto, H., Tsuboi, J., Oshima, Y., Oka, T. et al.: Construction of a three-dimensional outline of the heart and conduction pathway by means of a 64-channel magnetocardiogram in patients with atrial flutter and fibrillation. Int. J. Cardiovasc Imaging. 21(5), 555–561 (2005)
21. Fenici, R.R., CNR.: Biomagnetically localizable multipurpose catheter and method for magnetocardiographic guided intracardiac mapping, biopsy and ablation of cardiac arrhythmias. Unites States patent n.5056517, October 15, 1991 (filed July, 24, 1989)
22. Ben-Haim, S.A.: Apparatus and method for treating cardiac arrhythmias. United States Patent n.5, 391,199; February 21, 1995 (filed July 20 1993)
23. Haddad, R.: Un Model Numerique Anthropomorphique et Dynamique du Thorax Respirant et du Cœur Battant. Ph. D. These, CREATIS-CNRS UMR 5220, INSERM U630 – Lyon, France (2007)
24. Nakai, K., Izumoto, H., Kawazoe, K., Tsuboi, J., Fukuhiro, Y., Oka, T., et al.: Three-dimensional recovery time dispersion map by 64-channel magnetocardiography may demonstrate the location of a myocardial injury and heterogeneity of repolarization. Int. J. Cardiovasc Imaging 22(3-4), 573–580 (2006)
25. Ogata, K., Kandori, A., Miyashita, T., Tsukada, K., Nakatani, S., Shimizu, W. et al.: Visualization of three-dimensional cardiac electrical excitation using standard heart model and anterior and posterior magnetocardiogram. Int. J. Cardiovasc Imaging. 22(3-4), 581–593 (2006)
26. Berger, T., Fischer, G., Pfeifer, B., Modre, R., Hanser, F., Trieb, T. et al.: Single-beat noninvasive imaging of cardiac electrophysiology of ventricular pre-excitation. J. Am. Coll Cardiol. 48(10), 2045–2052 (2006)

Towards the Numerical Simulation of Electrocardiograms

Muriel Boulakia[2], Miguel A. Fernández[1], Jean-Frédéric Gerbeau[1], and Nejib Zemzemi[1]

[1] REO team, INRIA Rocquencourt, France
http://www-rocq.inria.fr/REO
[2] REO team, Laboratoire Jacques-Louis Lions, Université Paris 6, France

Abstract. We present preliminary results of the numerical simulation of electrocardiograms (ECG). We consider the bidomain equations to model the electrical activity of the heart and a Laplace equation for the torso. The ionic activity is modeled with a Mitchell-Schaeffer dynamics. We use adaptive semi-implicit BDF schemes for the time discretization and a Neumann-Robin domain decomposition algorithm for the space discretization. The obtained ECGs, although not completely satisfactory, are promising. They allow to discuss various modelling assumptions, for example the relevance of cells heterogeneity, the fiber orientation and the coupling conditions with the torso.

1 Introduction

We address the numerical simulation of electrocardiograms (ECG), namely the direct problem of cardiac electrophysiology. Our basic equations are the so-called bidomain model for the heart [4,16] coupled to a simple model for the torso.

The complexity of the electrical activity of the heart raise many modelling issues: strong nonlinearity due to the ionic currents, stiffness due to very different time scales, heterogeneity of cells, anisotropy due to the fibers, *etc.* Moreover, the modelling of many aspects of the problem is not yet well-established. In [20], more than 28 models of cardiac cells are reported, some of them including more than 50 parameters. The coupling conditions between the heart and the torso are also subject to controversy [11].

We have to face two opposite viewpoints: on the one hand, we would like to model as accurately as possible the physical phenomena described in the literature; on the other hand, we would like to keep as low as possible the complexity of the model, both in terms of computational effort and in terms of number of parameters. Our purpose is to obtain ECGs, and we propose to address, with the help of numerical simulations, what could be the "minimum requirements" of the model to reach this goal. For example, is a bidomain model necessary? what is the effect of the heart movement? how sensitive are the results to the anisotropy induced by fibers or the cells heterogeneity? is it really useful to strongly couple the heart with the torso? what should be the coupling conditions? how to handle the His bundle and the Purkinje fibers? *etc.* We do not address all these

F.B. Sachse and G. Seemann (Eds.): FIMH 2007, LNCS 4466, pp. 240–249, 2007.

questions in this paper. The point is mainly to present preliminary results and to draw some perspectives.

2 Modelling

We denote by $\Omega_{\rm H}$ the total domain occupied by the heart. In the microscopic scale, the cardiac tissue is assumed to be composed of two distinct media: the intracellular media, made of the cardiac cells, and the extracellular media, composed of the remainder of the heart. After an homogenization process, the intra- and extracellular domains are superimposed and occupy the whole domain $\Omega_{\rm H}$ [16,4]. We denote by $\boldsymbol{j}_{\rm i}$, $\boldsymbol{j}_{\rm e}$ and $u_{\rm i}$, $u_{\rm e}$ the intra- and extracellular densities of current and electric potentials respectively. The homogenized equation associated to the electrical charge conservation is:

$$\mathrm{div}(\boldsymbol{j}_{\rm i} + \boldsymbol{j}_{\rm e}) = 0, \quad \text{in} \quad \Omega_{\rm H}. \tag{2.1}$$

The homogenized equation governing the electrical activity of the cell membranes is given by

$$A_{\rm m}\left(C_{\rm m}\frac{\partial V_{\rm m}}{\partial t} + I_{\rm ion}(V_{\rm m}, w)\right) + \mathrm{div}(\boldsymbol{j}_{\rm i}) = A_{\rm m} I_{\rm app}, \quad \text{in} \quad \Omega_{\rm H}, \tag{2.2}$$

where $A_{\rm m}$ is a constant representing the average rate of membrane surface per unit of volume, the function $I_{\rm ion}$ represents the current due to the ionic exchanges, $I_{\rm app}$ is a given stimulation current, $C_{\rm m}$ is a capacity per unit of area of the membrane, $V_{\rm m}$ is the transmembrane potential defined by

$$V_{\rm m} = u_{\rm i} - u_{\rm e}, \tag{2.3}$$

and the vector function w is solution to a system of ordinary differential equations:

$$\frac{\partial w}{\partial t} + g(V_{\rm m}, w) = 0. \tag{2.4}$$

The precise definition of g and $I_{\rm ion}$ depends on the cell model. We can use a physiological ionic model (*e.g.* [13] or [6]) or a phenomenological one (*e.g.* [7] or [15]). In this paper, we consider the phenomenological model proposed by Mitchell and Schaeffer [15]:

$$I_{\rm ion}(V_{\rm m}, w) = -\frac{w}{\tau_{in}} V_{\rm m}^2 (1 - V_{\rm m}) + \frac{V_{\rm m}}{\tau_{out}}, \tag{2.5}$$

.

$$g(V_{\rm m}, w) = \begin{cases} \dfrac{w-1}{\tau_{open}} & \text{if } V_{\rm m} < V_{gate}, \\ \dfrac{w}{\tau_{close}} & \text{if } V_{\rm m} > V_{gate}, \end{cases} \tag{2.6}$$

where τ_{in}, τ_{out}, τ_{open}, τ_{close} and V_{gate} are given parameters. Note that this model is close to the model proposed in [24].

The current densities are linked to the electric potentials through the Ohm's law $\boldsymbol{j}_{\rm i} = -\boldsymbol{\sigma}_{\rm i}\boldsymbol{\nabla} u_{\rm i}$, $\boldsymbol{j}_{\rm e} = -\boldsymbol{\sigma}_{\rm e}\boldsymbol{\nabla} u_{\rm e}$, where $\boldsymbol{\sigma}_{\rm i}$ and $\boldsymbol{\sigma}_{\rm e}$ are the intra- and extracellular conductivity tensors. The system of equations within the heart therefore reads [12,17,18]:

$$\left\{\begin{array}{rl} A_{\rm m}\left(C_{\rm m}\dfrac{\partial V_{\rm m}}{\partial t} + I_{\rm ion}(V_{\rm m}, w)\right) - \operatorname{div}(\boldsymbol{\sigma}_{\rm i}\boldsymbol{\nabla} u_{\rm i}) = A_{\rm m} I_{\rm app}, & \text{in } \Omega_{\rm H}, \\ \operatorname{div}(\boldsymbol{\sigma}_{\rm e}\boldsymbol{\nabla} u_{\rm e}) = -\operatorname{div}(\boldsymbol{\sigma}_{\rm i}\boldsymbol{\nabla} u_{\rm i}), & \text{in } \Omega_{\rm H}, \\ \partial_t w + g(V_{\rm m}, w) = 0, & \text{in } \Omega_{\rm H}. \end{array}\right. \tag{2.7}$$

This model is often studied when the heart is isolated (*cf.* for example [2,3,4]). We are interested in coupling it with a simplified model of the electrical activity of the surrounding tissues (as done for example in [5,18] or [23]). The boundary $\partial\Omega_{\rm H}$ of the domain $\Omega_{\rm H}$, *i.e.* the interface between the heart and the extracardiac region is divided into two parts: the endocardium $\Gamma_{\rm endo}$ and the epicardium $\Gamma_{\rm epi}$. It is generally admitted (*cf.* [17,23]) that the intracellular current $\boldsymbol{j}_{\rm i}$ does not propagate outside the heart. Consequently, on the heart boundary $\Gamma_{\rm epi} \cup \Gamma_{\rm endo}$ we impose $\boldsymbol{\sigma}_{\rm i}\boldsymbol{\nabla} u_{\rm i} \cdot \boldsymbol{n} = 0$. The torso domain is denoted by $\Omega_{\rm T}$ and the potential in $\Omega_{\rm T}$ by u_T. The torso is seen as a passive conductor, thus u_T satisfies a Laplace equation:

$$\operatorname{div}(\boldsymbol{\sigma}_{\rm T}\boldsymbol{\nabla} u_T) = 0, \quad \text{in} \quad \Omega_{\rm T}, \tag{2.8}$$

where $\boldsymbol{\sigma}_{\rm T}$ represents the conductivity tensor of the torso. The boundary of the torso is divided into two parts: one internal $\Gamma_{\rm epi}$, in contact with the heart, and $\Gamma_{\rm ext}$ representing the external surface of the torso. The boundary $\Gamma_{\rm ext}$ is supposed to be insulated, thus we impose $\boldsymbol{\sigma}_{\rm T}\boldsymbol{\nabla} u_T \cdot \boldsymbol{n}_{\rm T} = 0$ where $\boldsymbol{n}_T$ is the outward unit normal on $\Gamma_{\rm ext}$.

On $\Gamma_{\rm epi}$, the following conditions are generally adopted in the literature:

$$\left\{\begin{array}{rll} u_{\rm e} = u_T, & \text{on} & \Gamma_{\rm epi}, \\ \boldsymbol{\sigma}_{\rm e}\boldsymbol{\nabla} u_{\rm e} \cdot \boldsymbol{n} = \boldsymbol{\sigma}_{\rm T}\boldsymbol{\nabla} u_T \cdot \boldsymbol{n}, & \text{on} & \Gamma_{\rm epi}. \end{array}\right. \tag{2.9}$$

They are formally obtained in [11] by an homogenization procedure. They correspond to a perfect electrical coupling between the heart and the torso. Nevertheless, the heart is separated from the torso by the pericardium which is a double-walled sac containing a serous fluid. Thus, it seems reasonable to assume the more general coupling conditions:

$$\left\{\begin{array}{rll} R_p\boldsymbol{\sigma}_{\rm e}\boldsymbol{\nabla} u_{\rm e} \cdot \boldsymbol{n} = R_p C_p \dfrac{\partial(u_{\rm T} - u_{\rm e})}{\partial t} + (u_{\rm T} - u_{\rm e}), & \text{on} & \Gamma_{\rm epi}, \\ \boldsymbol{\sigma}_{\rm e}\boldsymbol{\nabla} u_{\rm e} \cdot \boldsymbol{n} = \boldsymbol{\sigma}_{\rm T}\boldsymbol{\nabla} u_T \cdot \boldsymbol{n}, & \text{on} & \Gamma_{\rm epi}, \end{array}\right. \tag{2.10}$$

which takes into account a possible capacitive (C_p) and resistive (R_p) effect of the pericardium. To the best of our knowledge, this effect is not documented in the literature. The influence of R_p and C_p will be investigated through numerical simulations in a forthcoming work. Of course the classical relations (2.9) can be recovered from (2.10) by setting $R_p = 0$.

3 Numerical Methods

We define the open set Ω as the interior of $\overline{\Omega_{\rm H}} \cup \overline{\Omega_{\rm T}}$. Eliminating the unknown $u_{\rm i}$ in the previous system using (2.3), the above problem is equivalent to finding $u_{\rm e}$, $u_{\rm T}$, $V_{\rm m}$ and w such that $(2.10)_1$ and (2.4) are satisfied, and

$$A_m \int_{\Omega_{\rm H}} \left(C_{\rm m} \frac{\partial V_{\rm m}}{\partial t} + I_{\rm ion}(V_{\rm m}, w) \right) \phi + \int_{\Omega_{\rm H}} \boldsymbol{\sigma}_{\rm i} \boldsymbol{\nabla}(V_{\rm m} + u_{\rm e}) \cdot \boldsymbol{\nabla}\phi = \int_{\Omega_{\rm H}} I_{\rm app}\phi, \tag{3.11}$$

$$\int_{\Omega_{\rm H}} (\boldsymbol{\sigma}_{\rm i} + \boldsymbol{\sigma}_{\rm e}) \boldsymbol{\nabla} u_{\rm e} \cdot \boldsymbol{\nabla}\phi + \int_{\Omega_{\rm H}} \boldsymbol{\sigma}_{\rm i} \boldsymbol{\nabla} V_{\rm m} \cdot \boldsymbol{\nabla}\phi + \int_{\Omega_{\rm T}} \boldsymbol{\sigma}_{\rm T} \boldsymbol{\nabla} u_{\rm T} \cdot \boldsymbol{\nabla}\phi = 0, \tag{3.12}$$

for all $\phi \in H^1(\Omega)$. Note that this variational formulation takes into account very conveniently the coupling condition $(2.10)_2$. Under technical assumptions on the functions $I_{\rm ion}$ and g, and for $R_p = 0$, we have proved in [1] that this system admits a unique solution. This system is discretized in space using the Lagrangian P1 finite elements and in time using a semi-implicit scheme based on the BDF (*Backward Differentiation Formula*) methods. The heart and torso domains are solved iteratively with a Neumann/Robin domain decomposition method. We denote by Δt the time step and we assume that the solution is known until time t^n. Here is the procedure used to compute $(V_{\rm m}^{n+1}, u_{\rm e}^{n+1}, u_{\rm T}^{n+1}, w^{n+1})$.

The first step is to solve the ionic current, namely the equation (2.4) which is usually very stiff. We chose to use the `cvode` solver[1] which uses adaptivity, both in time and in order, and solves the implicit part of the equations with a Newton algorithm. For practical reason, it is convenient to uncouple this step from the solution of the bidomain equation. To this purpose, we extrapolate the unknown V_m. More precisely, w^{n+1} is obtained by $w^{n+1} = \sum_{j=0}^{p} a_{j,p} w^{n-j} - \Delta t b_{-1,p} g(\widetilde{V_{\rm m}}^{n+1}, w^{n+1})$, where $\widetilde{V_{\rm m}}^{n+1} = \sum_{j=0}^{q} \alpha_{j,q} V_{\rm m}^{n-j}$ is the extrapolation of order q of the previously computed $V_{\rm m}$, q being the order in time of the scheme used to compute $V_{\rm m}$ (see below), and $\alpha_{j,q}$, $a_{j,p}$ and $b_{-1,p}$ are the constants of the BDF methods [19].

The second step is to solve the bidomain-torso problem. We use a domain decomposition algorithm: assuming that $u_{\rm T}^{n+1,k}$ is given, we compute $V_{\rm m}^{n+1,k+1}$ and $u_{\rm e}^{n+1,k+1}$ solving a Neumann problem in $\Omega_{\rm H}$ with a q-order BDF time scheme: for all ϕ in the basis of the finite element space

$$\begin{cases} A_m \displaystyle\int_{\Omega_{\rm H}} C_{\rm m} V_{\rm m}^{n+1,k+1} \phi + \Delta t b_{-1,q} \int_{\Omega_{\rm H}} \boldsymbol{\sigma}_{\rm i} \boldsymbol{\nabla}(V_{\rm m}^{n+1,k+1} + u_{\rm e}^{n+1,k+1}) \cdot \boldsymbol{\nabla}\phi = \\ A_m \displaystyle\int_{\Omega_{\rm H}} \left(C_{\rm m} \sum_{j=0}^{q} a_{j,q} V_{\rm m}^{n-j} + \Delta t b_{-1,q} I_{\rm ion}(\widetilde{V_{\rm m}}^{n+1}, w^{n+1}) \right) \phi + \Delta t b_{-1,q} \displaystyle\int_{\Omega_{\rm H}} I_{\rm app}\phi, \\ \displaystyle\int_{\Omega_{\rm H}} (\boldsymbol{\sigma}_{\rm i} + \boldsymbol{\sigma}_{\rm e}) \boldsymbol{\nabla} u_{\rm e}^{n+1,k+1} \cdot \boldsymbol{\nabla}\phi \\ \quad + \displaystyle\int_{\Omega_{\rm H}} \boldsymbol{\sigma}_{\rm i} \boldsymbol{\nabla} V_{\rm m}^{n+1,k+1} \cdot \boldsymbol{\nabla}\phi = \int_{\Gamma_{\rm epi}} \boldsymbol{\sigma}_{\rm T} \boldsymbol{\nabla} u_{\rm T}^{n+1,k} \cdot \boldsymbol{n}_{\rm T} \phi. \end{cases} \tag{3.13}$$

[1] Sundials library, `http://www.llnl.gov/casc/sundials/`

Next, the potential $u_{\mathrm{e}}^{n+1,k+1}$ being known, we compute u_{T}^{n+1} solving the following problem in the torso Ω_{T}:

$$\begin{aligned} & b_{-1,q} \int_{\Omega_{\mathrm{T}}} \boldsymbol{\sigma}_{\mathrm{T}}^{n+1} \boldsymbol{\nabla} u_{\mathrm{T}}^{n+1,k+1} \cdot \boldsymbol{\nabla} \phi + \int_{\Gamma_{\mathrm{epi}}} \left(\frac{b_{-1,q}}{R_p} + \frac{C_p}{\Delta t} \right) u_{\mathrm{T}}^{n+1,k+1} \phi \\ = & \int_{\Gamma_{\mathrm{epi}}} \left(\frac{b_{-1,q}}{R_p} + \frac{C_p}{\Delta t} \right) u_{\mathrm{e}}^{n+1,k+1} \phi + \frac{C_p}{\Delta t} \int_{\Gamma_{\mathrm{epi}}} \sum_{j=0}^{q} a_{j,q} (u_{\mathrm{T}}^{n-j} - u_{\mathrm{e}}^{n-j}) \phi. \end{aligned} \tag{3.14}$$

To enforce a "strong coupling" (namely the transmission conditions (2.10)), we have to iterate in k between (3.13) and (3.14) until convergence, at each time step. We can also perform a "weak coupling" by performing only one iteration in k, or even by replacing condition $(2.9)_2$ by $\boldsymbol{\sigma}_{\mathrm{e}} \boldsymbol{\nabla} u_{\mathrm{e}} \cdot \boldsymbol{n} = 0$. This approximation will be considered in § 4.2.

4 Numerical Results

The torso geometry includes the lungs and the skeleton[2] (see Fig. 1). The heart geometry is simplified – based on intersecting ellipsoids – so that the fibers orientation can be given in terms of analytical functions (see Fig. 1). We refer to [22] for the details of the geometrical definition of the heart. Note that this simplified geometry only includes the ventricles. We therefore cannot simulate P-waves. The finite element meshes of the heart (61 512 tetrahedra) and the torso (311 117 tetrahedra) have been realized with `YAMS` [8] and `GHS3D`[9,10].

The conductivity tensors $\boldsymbol{\sigma}_{\mathrm{i}}$ and $\boldsymbol{\sigma}_{\mathrm{e}}$ are given by $\boldsymbol{\sigma}_{\mathrm{i},e}(x) = \sigma_{\mathrm{i},e}^{\mathrm{t}} I + (\sigma_{\mathrm{i},e}^{\mathrm{l}} - \sigma_{\mathrm{i},e}^{\mathrm{t}}) \boldsymbol{a}(x) \otimes \boldsymbol{a}(x)$, where $\boldsymbol{a}(x)$ is a unit vector parallel to the local fiber direction (Fig. 1, Left) and $\sigma_{\mathrm{i},e}^{\mathrm{l}}$ and $\sigma_{\mathrm{i},e}^{\mathrm{t}}$ are respectively the conductivity coefficients in the intra- and extra-cellular media measured along the fibers direction and in the transverse direction. Experiments show that $\sigma_{\mathrm{i},e}^{\mathrm{l}}$ and $\sigma_{\mathrm{i},e}^{\mathrm{t}}$ have different values, which means that intra- and extra-cellular media are anisotropic. We have taken into account this anisotropy. It is also established that they are spatially dependent. In particular, the conductivity is larger in the His bundle and the Purkinje fibers. Nevertheless, this space dependence is not considered in our simulations. The fact that the Purkinje fibers conducts very quickly the electrical signal is roughly modeled by taking an uniform initial stimulation on the endocardium. All the numerical experiments have been obtained with a very small value of R_p. This amounts to considering the standard transmission conditions (2.9). In the following section, the ECG are plotted according to the standard 12-leads ECG definition (see [14], for instance): $\mathrm{DI} = u_{\mathrm{T}}(L) - u_{\mathrm{T}}(R), \mathrm{DII} = u_{\mathrm{T}}(F) - u_{\mathrm{T}}(R), \mathrm{DIII} = u_{\mathrm{T}}(F) - u_{\mathrm{T}}(L)$, $\mathrm{aVR} = \frac{3}{2}(u_{\mathrm{T}}(R) - u_W), \mathrm{aVL} = \frac{3}{2}(u_{\mathrm{T}}(L) - u_W), \mathrm{aVF} = \frac{3}{2}(u_{\mathrm{T}}(F) - u_W)$, $\mathrm{V}_i = u_{\mathrm{T}}(V_i) - u_W$, for $i = 1, .., 6$, where the points L, R, F, $(V_i)_{i=1..6}$ are indicated in Fig. 1, and where $u_W = (u_{\mathrm{T}}(L) + u_{\mathrm{T}}(R) + u_{\mathrm{T}}(F))/3$.

[2] This geometry comes from Zygote Media Group, Inc. `http://www.zygote.com/`

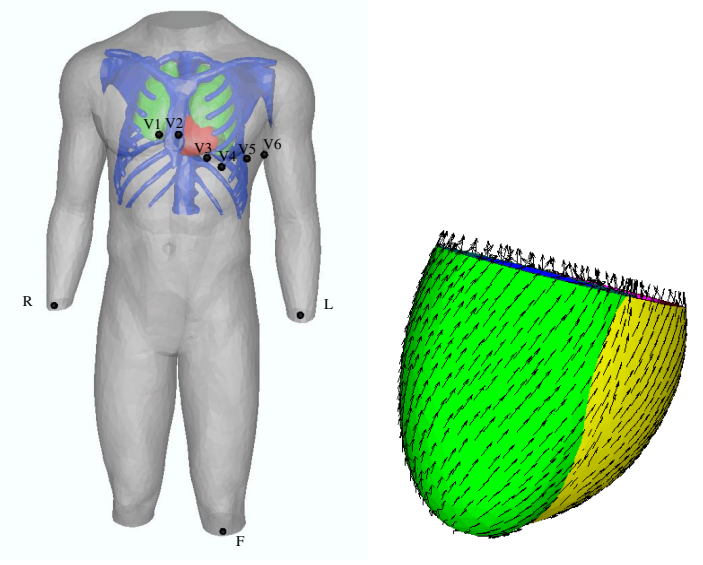

Fig. 1. Computational domains: torso and ECG leads (Left), heart with fibers (Right)

4.1 A Reference Simulation

We start from a "reference simulation", in which we take into account the anisotropy ($\sigma^{\mathrm{l}}_{\mathrm{i},e} \neq \sigma^{\mathrm{t}}_{\mathrm{i},e}$) and a cells heterogeneity across the wall of the left ventricule (see [21] for instance). This heterogeneity is achieved by taking a coefficient τ_{close} in (2.6) varying across the thickness direction. The initial stimulation is given by a volume current which acts on the whole endocardium (both left and right parts). The simulated ECG is reported in Fig. 2. Compared to a real ECG, we can notice that the waves have a correct orientation in each of the 12 leads. Some points have still to be improved, in particular the amplitude of the T-wave and the length of the QRS-complex. In the sequel, we play with various modelling assumptions and compare the results with this solution.

4.2 Weak Coupling with Torso

In order to reduce the computational cost of the heart-torso coupling, we can relax the coupling condition (2.9) to

$$u_{\mathrm{e}} = u_T, \qquad \text{and} \qquad \boldsymbol{\sigma}_{\mathrm{e}} \boldsymbol{\nabla} u_{\mathrm{e}} \cdot \boldsymbol{n} = 0, \qquad \text{on} \quad \Gamma_{\mathrm{epi}}. \tag{4.15}$$

The resulting system (2.7) and $(4.15)_2$ can be solved independently of the torso. Then, the ECG signals can be recovered in a second step by solving (2.8) with $(4.15)_1$. The results are reported in Fig. 3 (for the sake of conciseness we only report the DI, aVr, V1 and V4 leads). A comparison with Fig. 2 shows that the amplitude of the waves is slightly larger with the weak coupling. Nevertheless, the solutions are qualitatively similar. The following experiments will be done with (4.15).

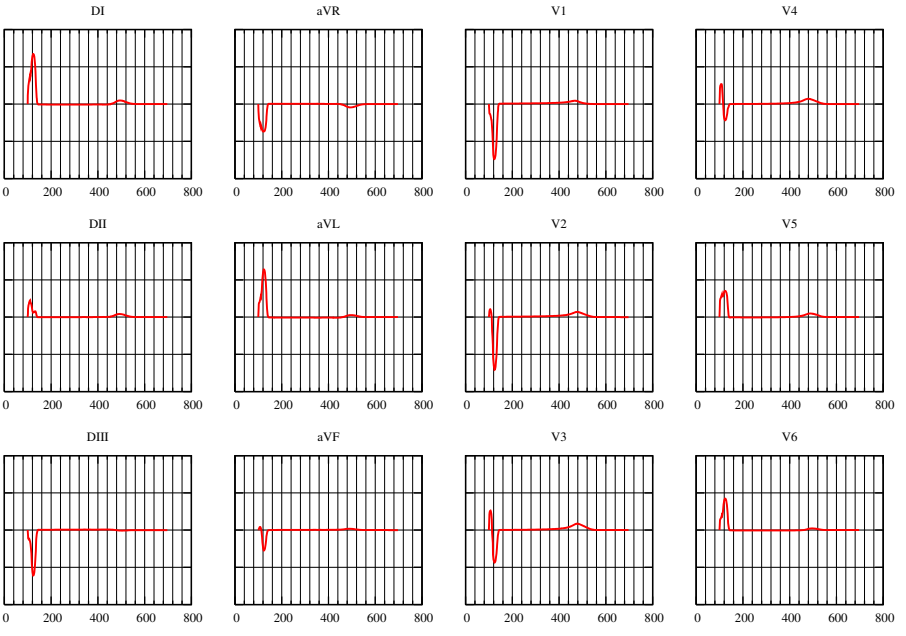

Fig. 2. Reference simulation: 12-leads ECG signals obtained by a strong coupling with the torso, including anisotropy and APD inhomogeneity. The units on the x-axis is milliseconds. The normalization on the y-axis is arbitrary, but the same on all the results of this paper.

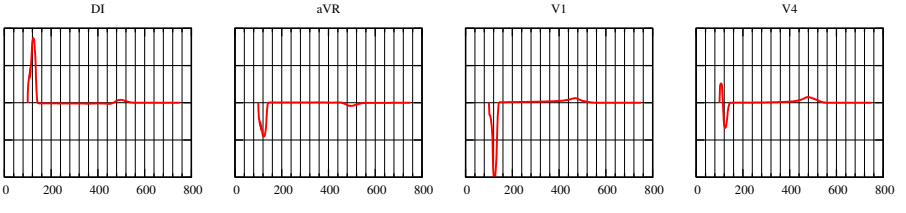

Fig. 3. Results obtained with a weak coupling with the torso (compare with Fig. 2)

4.3 Impact of Fibers

We now investigate the influence of the anisotropy of the conductivity tensors $\boldsymbol{\sigma}_{\mathrm{i}}, \boldsymbol{\sigma}_{\mathrm{e}}$ on the ECG signals.

We consider the numerical experiment described in §4.1 but now we consider isotropic conductivities by setting $\boldsymbol{\sigma}_{\mathrm{e}}^{\mathrm{l}} = \boldsymbol{\sigma}_{\mathrm{e}}^{\mathrm{t}}, \quad \boldsymbol{\sigma}_{\mathrm{i}}^{\mathrm{l}} = \boldsymbol{\sigma}_{\mathrm{i}}^{\mathrm{t}}$. Fig. 4 shows the corresponding ECG signals. We observe that the QRS-complex has a larger duration than in the anisotropic case (Fig. 2, Top). In addition, the T-wave is inverted in the the first Einthoven limb lead. The influence of anisotropy is much more

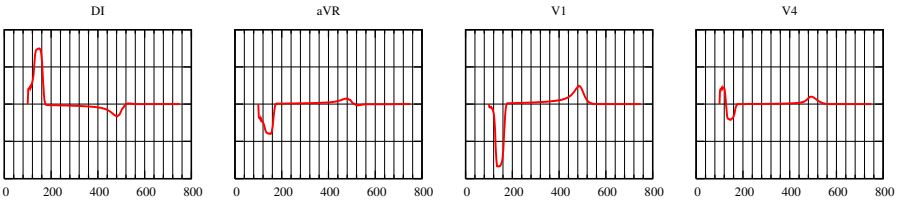

Fig. 4. ECG signals: isotropic conductivities

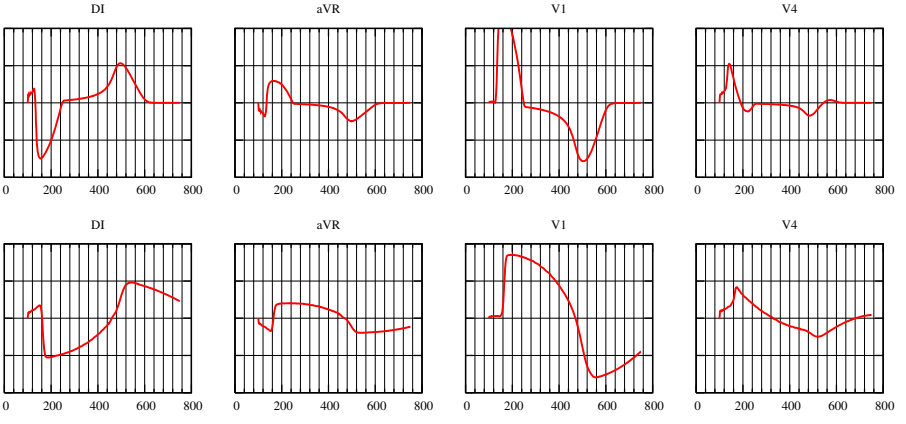

Fig. 5. Anisotropic (top) and isotropic (bottom) conductivities in a "pathological" case (right bundle-branch block). The sensitivity to the anisotropy is striking.

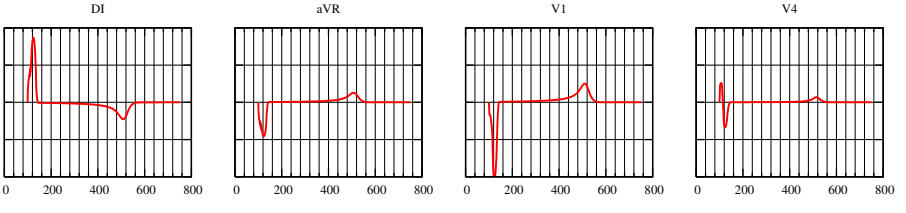

Fig. 6. ECG signals: with an homogeneous action potential duration the T-wave has the wrong sign on the first lead (compare with Figure 2)

striking when dealing with pathological stimulations. For instance, in Fig. 5 we have reported, the simulated ECG signals for a pathological stimulation (a right bundle-branch block) with anisotropic (top) and isotropic (bottom) conductivities. As expected, both results show a longer QRS complex compared to Fig. 2.

4.4 Impact of Cell Heterogeneity

We now investigate the role of the action potential duration (APD) heterogeneity on the ECG signals. For the sake of simplicity we restrict ourselves to a transmural heterogeneity, playing with the τ_{close} coefficient as mentioned in § 4.1.

In Fig. 6 we have depicted the ECG signals corresponding to an homogeneous APD (τ_{close} constant in (2.6)). In the first lead (Fig. 6, Left), we observe that the T-wave is inverted compared to the reference case (Fig. 2, Left-Top) and to what is usually observed in real ECGs.

5 Conclusion

We have presented a mathematical model for the electrical activity of the heart coupled to the torso. We started from a reference numerical simulation based on the Mitchell-Schaeffer dynamics, where we took into account the heart-torso coupling, the anisotropy due to the fibers, a simple heterogeneity along the left ventricle wall thickness. The resulting ECG is acceptable on the 12 standard leads. Then, we have shown that cell homogeneity yields inverted T-wave. We have also shown that a strong coupling with the torso has only a small influence on the ECG whereas anisotropy due to fibers orientation has to be taken into account in general. Further computations have to be carried out to confirm these results and to assess other points, like for example the relevance of the transmission conditions (2.10).

Acknowledgment. This work was partially supported by the CardioSense3D[3] project (INRIA). We would like to thank Michel Sorine for many fruitful discussions, in particular regarding the heart-torso transmission conditions. We also thank Elsie Phé for her work on the geometries and on the meshes generation.

References

1. Boulakia, M., Fernández, M.A., Gerbeau, J.-F., Zemzemi, N.: Mathematical analysis of a coupled bidomain-torso model in electrophysiology. Submitted
2. Colli Franzone, P., Pavarino, L.F.: A parallel solver for reaction-diffusion systems in computational electrocardiology. Math. Models Methods Appl. Sci. 6(14), 883–911 (2004)
3. Colli Franzone, P., Pavarino, L.F., Taccardi, B.: Simulating patterns of excitation, repolarization and action potential duration with cardiac bidomain and monodomain models. Math. Biosci. 1(197), 35–66 (2005)
4. Colli Franzone, P., Savaré, G.: Degenerate evolution systems modeling the cardiac electric field at micro- and macroscopic level. evolution equations, semigroups and functional analysis. Progr. Nonlin. Diff. Eq. Appl. 1(50), 49–78 (2002)
5. Coudière, Y., Pierre, C., Turpault, R.: Solving the fully coupled heart and torso problems of electrocardiology with a 3d discrete duality finite volume method. submitted (2006)

[3] http://www.inria.fr/CardioSense3D

6. Djabella, K., Sorine, M.: Differential model of the excitation-contraction coupling in a cardiac cell for multicycle simulations. In: EMBEC'05, vol. 11, pp. 4185–4190, Prague (2005)
7. Fitzhugh, R.: Impulses and physiological states in theoretical models of nerve membrane. Biophys. J. (1), 445–465 (1961)
8. Frey, P.: Yams: A fully automatic adaptive isotropic surface remeshing procedure. Technical report 0252, Inria, Rocquencourt, France (November 2001)
9. George, P.L.: Improvement on delaunay based 3d automatic mesh generator. Finite Elements in Analysis and Design 25(3-4), 297–317 (1997)
10. George, P.L., Borouchaki, H.: ultimate robustness in meshing an arbitrary polyhedron. Int. J. Numer. Meth. Engng. 58(7), 1061–1089 (2002)
11. Krassowska, W., Neu, J.C.: Effective boundary conditions for syncitial tissues. IEEE Trans. Biomed. Eng. 2(41), 137–199 (1994)
12. Lines, G.: Simulating the electrical activity in the heart. PhD thesis, Department of Informatics, University of Olso (1999)
13. Luo, C.H., Rudy, Y.: A model of the ventricular cardiac action ptentiel. depolarisation, repolarisation, and their interaction. Cir. Res. (68),1071–1096 (1994)
14. Malmivuo, J., Plonsey, R.: Bioelectromagnetism. principles and applications of bioelectric and biomagnetic fields. Oxford University Press, New York (1995)
15. Mitchell, C.C., Schaeffer, D.G.: A two-current model for the dynamics of cardiac membrane. Bulletin Math. Bio. (65),767–793 (2003)
16. Neu, J.C., Krassowska, W.: Homogenization of syncytial tissues. Crit. Rev. Biomed. Eng. 21(2), 137–199 (1993)
17. Page, E.: Cat heart muscle in vitro. part iii. the extracellular space. J. Gen. Physio. 1(46), 201–213 (1962)
18. Pierre, C.: Modélisation et simulation de l'activité électrique du cœur dans le thorax, analyse numérique et méthodes de volumes finis. PhD thesis, Laboratoire J. Leray, Université de Nantes (2005)
19. Quarteroni, A., Sacco, R., Saleri, F.: Numerical mathematics. In: Texts in Applied Mathematics, 2nd edn. vol. 37, Springer, Heidelberg (2007)
20. Sachse, F.B.: Computational Cardiology: Modeling of Anatomy, Electrophysiology, and Mechanics. Springer, Heidelberg (2004)
21. Sampson, K.J., Henriquez, C.S.: Electrotonic influences on action potential duration dispersion in small hearts: a simulation study. Am. J. Physiol. Heart Circ. Physiol. 289, 350–360 (2005)
22. Sermesant, M., Moireau, P., Camara, O., J., S.-M., Andriantsimiavona, R., Cimrman, R., Hill, D.L., Chapelle, D., Razavi, R.: Cardiac function estimation from mri using a heart model and data assimilation: advances and difficulties. Med. Image Anal. 10(4), 642–656 (2006)
23. Sundnes, J., Lines, G.T., Cai, X., Nielsen, B.F., Mardal, K.-A., Tveito, A.: Computing the electrical activity in the heart. Springer, Heidelberg (2006)
24. van Capelle, F.H., Durrer, D.: Computer simulation of arrhythmias in a network of coupled excitable elements. Circ. Res. 47, 453–466 (1980)

Experimental Measures of the Minimum Time Derivative of the Extracellular Potentials as an Index of Electrical Activity During Metabolic and Hypoxic Stress

Kwanghyun Sohn, David R. Sutherland, Qiansheng Liang, and Bonnie B. Punske

Nora Eccles Harrison Cardiovascular Research and Training Institute and Department of Bioengineering
University of Utah, Salt Lake City, UT 84112-5000, USA
punske@cvrti.utah.edu

Abstract. The time of the minimum time derivative of the extracellular potentials ($\Phi^{\wedge}$) is a marker for the instant of activation when the depolarizing sodium current reaches its maximum rate of increase. This study examined the normalized averaged value of $\Phi^{\wedge}$, $\Phi^{\wedge}_{na}$, as an index of electrical activity under metabolic and hypoxic stresses. Electrical mapping was performed using a 64-electrode cage array on Langendorff perfused isolated mouse hearts at three different glucose and insulin levels during hypoxia. The lower levels of glucose and/or insulin resulted in the largest decrease of $\Phi^{\wedge}_{na}$ during hypoxia. A significant decrease in $\Phi^{\wedge}_{na}$ was a predictor of increased total activation time and propagation pattern change, and irreversible damage was predicted by a 60% decrease of $\Phi^{\wedge}_{na}$. These results supported $\Phi^{\wedge}_{na}$ as an potentially useful index of electrical activity.

1 Introduction

The essence of the propagation of cardiac activation is the transmembrane current (I_m), which is the sum of ion currents (I_{ion}) and capacitive currents (I_c). I_m is governed by the cable equation for one-dimensional propagation along a uniform structure given in Eq. (1):

$$I_m = I_{ion} + I_c = \sum_i (V_m - E_i) G_i + C_m \frac{\partial V_m}{\partial t} \,, \tag{1}$$

where V_m is the transmembrane potential, E_i is the Nernst voltage, G_i is the membrane conductance, and C_m is the membrane capacity.

The cardiac action potential propagates by chain reaction between the ion and capacitive currents. Sodium ions rush into a myocyte driven by the potential and chemical concentration differences across the plasma membrane at the opening of sodium ion channels. This inward ion current depolarizes transmembrane voltage of the myocyte, and part of the ions redirect to downstream resting

F.B. Sachse and G. Seemann (Eds.): FIMH 2007, LNCS 4466, pp. 250–259, 2007.

myocytes, inducing capacitive transmembrane current. This outward capacitive current increases the transmembrane voltage of the resting myocytes over the activation threshold of the sodium ion channels, which, in turn, leads to ion currents. In addition, the total amount of the outward current at the leading edge of propagation is directly proportional to the propagation velocity [1].

The distribution of I_m over the plasma membrane gives rise to the extracellular potential (Φ), which, in a volume conductor of homogeneous extracellular conductivity σ_e, is given by Eq. (2):

$$\Phi(P,t) = \frac{1}{4\pi\sigma_e} \int_{Volume\ of\ Tissue} \frac{I_m}{r} dV \ , \tag{2}$$

where r is the distance from the observation point, P, to the transmembrane current source [1,2].

As shown in equation (2), the extracellular potential is influenced by the transmembrane current distribution with the weight of $1/r$, and in many cases Φ has a waveform with a biphasic deflection around the moment of activation. Φ increases slowly as the wave front of activation, with outward capacitive current, approaches, drops rapidly as the sodium ion channels immediately beneath the point P open, and returns to baseline values as the activation wave front moves down stream. The extracellular potentials have been used mostly to detect activation time for the propagation sequence, in virtue of the fact that the minimum time derivative, which occurs during the sodium ion influx, coincides in time with the maximum increase rate of G_{Na} and I_{Na}, as well as, the maximum slope of the transmembrane potential [3,4].

The peak-to-peak amplitude of the deflection of the Φ waveform at activation decreases as the position P moves away from the current source. Spach *et al.* [3] showed by computer simulations that the peak-to-peak amplitude of Φ decreases slower than the magnitude of the minimum derivative of Φ when r increases. Thus the magnitude of the minimum derivative of Φ, when compared to the peak-to-peak amplitude of Φ, is more influenced by local currents but less influenced by more distant currents. Based on the theory described above, we assumed that the magnitude of the minimum time derivative of Φ during the QRS is related to the maximum rate of change and hence total amount of transmembrane current at a given time during activation, therefore, we hypothesized that this parameter can be a useful qualitative measure of electrical activity.

Fatty acids are the major source for cardiac energy production in general, but glucose becomes the predominant fuel during anaerobic conditions due to its ability to produce ATP in the absence of oxygen via glycolysis [5]. Insulin, as well as anaerobic stimulation, enhances glucose transport through the membrane by translocation of glucose transporters to the cell membrane [6]. Morgan *et al.* [7] tested the effects of insulin on glucose transport and phosphorylation in the isolated and perfused heart of rats and showed that, in the absence of insulin, glucose transport is the rate limiting step for glucose uptake over phosphorylation in the physiological range of blood glucose concentration. Runnman *et al.* [8] also showed that removal of insulin causes a lower total glycolytic flux during hypoxia in the presence of 5 mM glucose. It is well known that under anaerobic

conditions, K_{ATP} channels on the sarcolemma open due to low ATP levels and this causes changes such as an increase in transmembrane voltage and a decrease in conduction velocity that affects the overall electrical activity.

The purpose of this experiment was to examine the normalized averaged value of $\Phi^{\wedge}$ ($\Phi^{\wedge}_{na}$) as an index of electrical activity by comparing it with other indices like propagation pattern and total activation time under metabolic and hypoxic stresses that varied glucose and insulin levels.

2 Methods

The Institutional Animal Care and Use Committee of the University of Utah reviewed and approved the experimental protocol for this study. C57BL/6 male mice (7-8 weeks) were injected with heparin and sodium pentobarbital in sequence at 10-minute intervals. After a deep plane of anesthesia was reached, the heart was rapidly excised and Langendorff perfused via the aorta with a modified Krebs solution. A custom made 64-electrode "cage" electrode array was slipped over the heart making contact with the ventricular free wall directly for some electrodes or via perfusate flowing between the heart and cage for other ones (Fig. 1). The heart then was positioned inside a custom-made heated chamber to maintain the surrounding temperature at 37°C, and was allowed to stabilize for 30 minutes prior to data acquisition. Extracellular potentials were measured during 30 minutes of oxygenation, 30 minutes of hypoxia, and 30 minutes of reoxygenation. The perfusate was bubbled with 95% O_2 and 5% CO_2 all the time except during hypoxia when it was bubbled with 95% N_2 and 5% CO_2.

The Krebs solution was composed of (in mM) NaCl 118, $NaHCO_3$ 25, KCl 4.1, $CaCl_2$ 2.5, $MgSO_4$ 1.2, EDTA 0.5, KH_2PO_4 1.2 and contained three different combinations of glucose and insulin for each heart. The first heart was perfused with 10 mM glucose and 2 units/ℓ insulin (g10i2), the second heart was perfused with 5 mM glucose and 2 units/ℓ insulin (g5i2), and the last heart was perfused with 5 mM glucose without insulin (g5i0). The perfusate was maintained at 37°C and a pH of 7.4. The aortic pressure was maintained between 60 and 75 mmHg and the flow rate remained between 1.5 and 2.5 mℓ/min.

The custom-made cylindrical electrode array was fabricated in our laboratory from 0.007 in. diameter silver wire. The cage was formed from a rectangular mesh and the wires were attached to the mesh. Five electrodes were arranged in each column with 1.29 mm interelectrode distance, and 13 columns were arranged circumferentially with 1.94 mm interelectrode spacing (Fig. 1). So the electrode array formed a cylinder 8.03 mm in diameter and 5.16 mm in length, which normally covered about 85% of lower part of the epicardial ventricular surface. Sixty-four unipolar electrograms were simultaneously recorded for 5 seconds from the electrode array, amplified and digitized at 4 kHz frequency and 12 bit resolution and stored on a Macintosh computer.

Recorded signals were calibrated and baselined between consecutive TP intervals. Activation time was computed as the time of the minimum time derivative during QRS intervals for each electrode [1,3]. The total activation time (TAT)

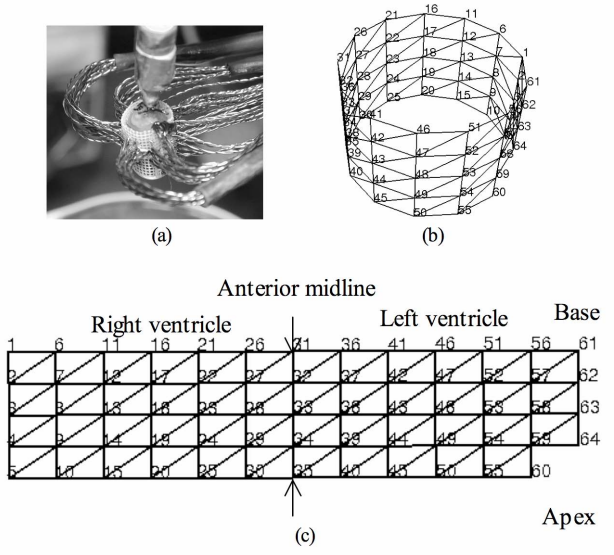

Fig. 1. The 64-electrode "cage" array. (a) Photo of the electrode array covering the heart. (b) The triangulated mesh geometry of the electrode array in three dimensions. (c) Two-dimensional triangulated mesh of the electrode array centered over the anterior midline of the heart with electrode numbers indicated.

over the measured area was computed as the time difference between the latest and the earliest activation. TAT values were normalized (TAT_n) by the TAT determined during baseline conditions, TAT_b. Changes in the propagation sequence during hypoxia were assessed by correlating all 64 activation times of a given beat with those obtained from a beat during baseline conditions (R_{act}).

As a surrogate measure of the relative magnitude of the transmembrane current during activation over the measured area during hypoxia and reoxygenation, the normalized minimum derivative of extracellular potential was introduced. The normalized averaged values of the minimum derivative were computed using Eq. (3),

$$\Phi^{\wedge}_{na}(t) = \frac{\Phi^{\wedge}_{a}(t)}{\Phi^{\wedge}_{a,b}} \,, \tag{3}$$

where $\Phi^{\wedge}(t)$ is the minimum time derivative of an extracellular potential of a beat measured at time t, $\Phi^{\wedge}_{a}(t)$ is $\Phi^{\wedge}(t)$ averaged over 64 electrodes and $\Phi^{\wedge}_{a,b}$ is $\Phi^{\wedge}_{a}$ averaged from values obtained during baseline conditions.

3 Results

Fig. 2 shows that for case g10i2, hearts were affected only slightly by hypoxia. The propagation pattern was conserved throughout hypoxia (panel a) and a slight increase in TAT was observed during hypoxia, but recovered during reoxygenation (panel b). $\Phi^{\wedge}_{na}$ was also constant except a small decrease at the beginning

of reoxygenation (panel c). In contrast to case g10i2, for case g5i0 hearts were severely influenced by hypoxic conditions. The propagation pattern was altered (panel a) and TAT increased three fold over control values immediately at the onset of hypoxia, and these changes did not recover during reoxygenation (panel b). $\Phi^{\wedge}_{na}$ dropped by 60% right at the onset of hypoxia and did not recover during reoxygenation (panel c). For the case of g5i2, hypoxia increased TAT two fold, but it finally recovered during reoxygenation (panel b). The propagation pattern remained relatively constant until changing after 17 minutes of hypoxia, but recovered immediately upon reoxygenation (panel a). $\Phi^{\wedge}_{na}$ decreased by 40% during hypoxia but recovered during reoxygenation (panel c).

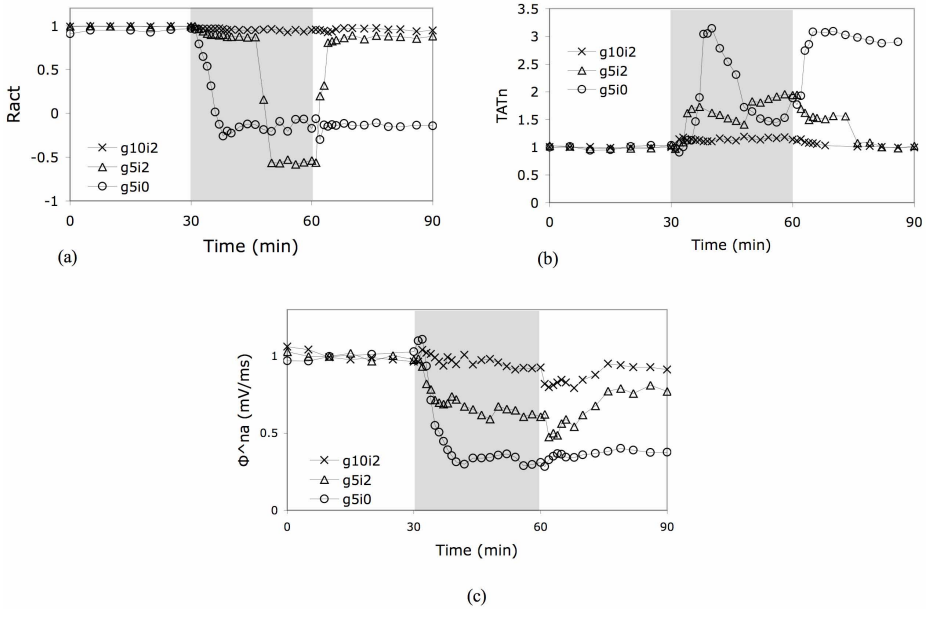

Fig. 2. a) Correlation coefficient, R_{act}, b) Normalized total activation time, $1/TAT_n$, and c) Normalized minimum time derivative, $\Phi^{\wedge}_{na}$, as a function of time for the three different combinations of glucose and insulin. Gray shaded region indicates hypoxia.

The changes in the activation sequence as quantified by the correlation coefficent R_{act} in Fig. 2a are demonstrated in Fig. 3 as series of isochronal maps during normal conditions, 10 and 30 minutes of hypoxia and after 30 minutes of reperfusion for each case of varied insulin and glucose. For the case of g10i2, (Fig. 3a) the maps show almost no changes in the activation sequence throughout the intervention. Fig. 3b, for the case of g5i2, shows the dramatic change in the activation sequence that has occurred at 30 minutes of hypoxia, reflected in the R_{act} value of -0.54. The greatest change in activation sequence occurs for the case of g5i0 (Fig. 3c). After only 10 minutes of hypoxia, the R_{act} value has decreased to -0.23, as reflected in the dramatic change in the sequence of activation.

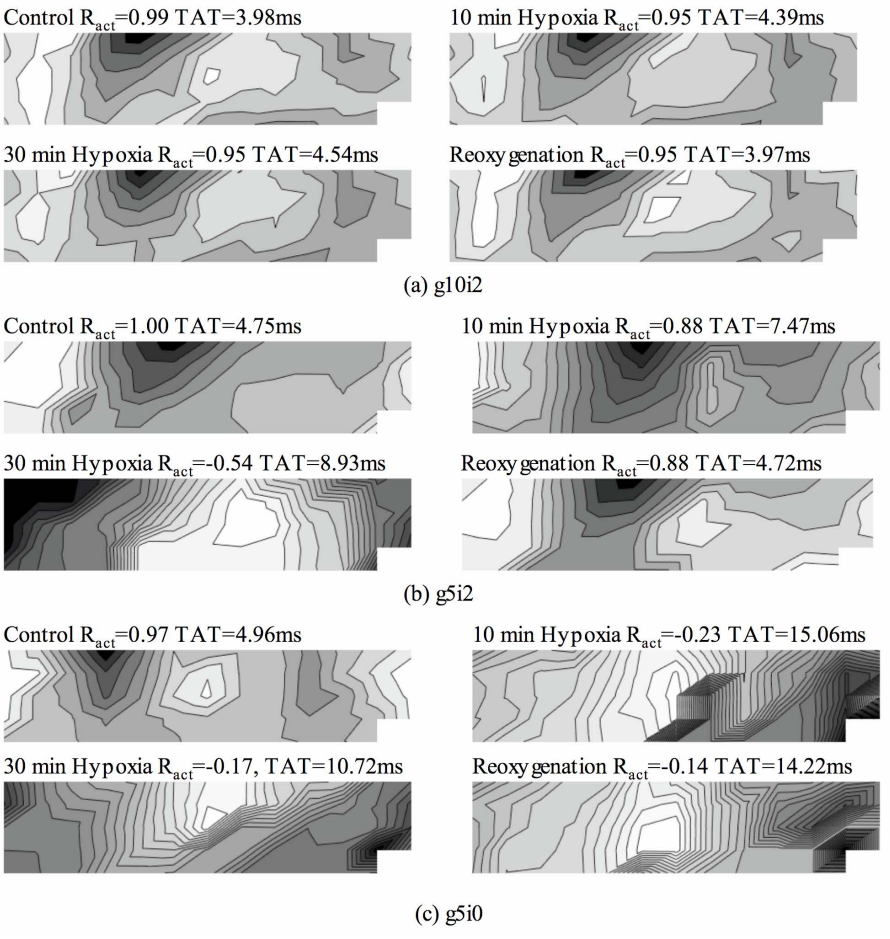

Fig. 3. Series of isochronal maps during control conditions, at 10 and 30 minutes of hypoxia, and after 30 minutes of reperfusion for a) 10 mM glucose and 2 units/ℓ insulin (g10i2), b) 5 mM glucose and 2 units/ℓ insulin (g5i2), and c) 5 mM glucose without insulin (g5i10). Activation propagates from white to black region.

Fig. 4 shows diverse responses of $\Phi^{\wedge}$ at different electrode locations. For example, in case g5i2 during hypoxia where the propagation pattern is altered, $\Phi^{\wedge}$ increased at electrode #2 and decreased at electrode #22 (panel a). In g5i0, $\Phi^{\wedge}$ at electrode #7 remained relatively constant while the majority of other electrode sites experienced a large decrease in $\Phi^{\wedge}$ at the onset of hypoxia (panel b).

Fig.5 displays the magnitude of $\Phi^{\wedge}$ from the second electrode in each electrode column at the conclusion of oxygenation, hypoxia and reoxygenation. For both cases, g5i2 (panel a) and g5i0 (panel b), $\Phi^{\wedge}$ values from the left ventricle (LV), electrodes 2–32, were normally larger than ones from the right ventricle (RV), electrodes 37–62, but decreased more during hypoxia. A summary of the changes in $\Phi^{\wedge}$ that occurred on the LV and RV are shown in Fig. 6. $\Phi^{\wedge}$ from electrodes

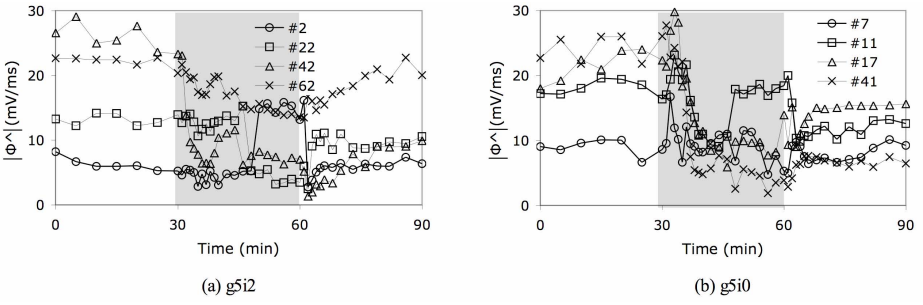

Fig. 4. The magnitude of $\Phi^{\wedge}$ as a function of time at various electrode sites indicated by electrode number in the legend for a) 5 mM glucose and 2 units/ℓ insulin (g5i2), and b) 5 mM glucose without insulin (g5i0). Gray shaded region indicates hypoxia.

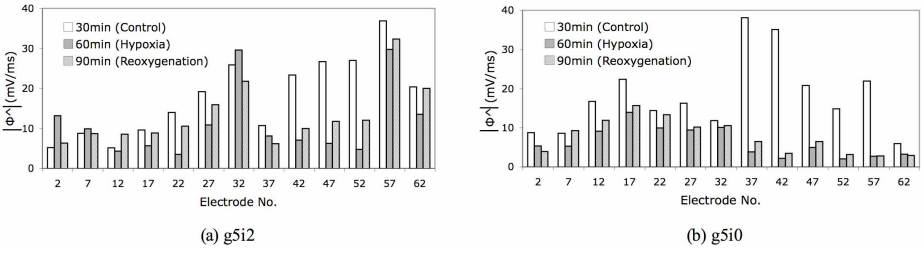

Fig. 5. $\Phi^{\wedge}$ as a function of individual electrode sites during control conditions, hypoxia and reperfusion for a) 5 mM glucose and 2 units/ℓ insulin (g5i2), and b) 5 mM glucose without insulin (g5i0). Electrodes 2–32 located on the left ventricle and 37–62 located on the right ventricle.

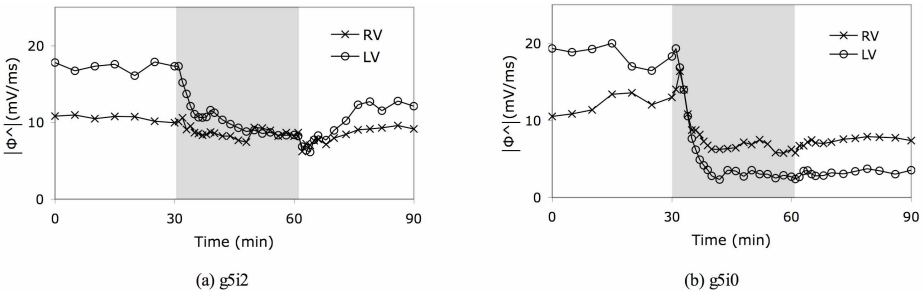

Fig. 6. Magnitude of $\Phi^{\wedge}$ averaged from electrodes 1–35 on the right and 36–64 on the left ventricles (RV and LV in legends) as a function of time for a) 5 mM glucose and 2 units/ℓ insulin (g5i2), and b) 5 mM glucose without insulin (g5i0). Gray shaded region indicates hypoxia.

1–35 covering the RV and 36–64 on the LV were averaged, and displayed as a function of time during the interventions. For case g5i2 (panel a), the LV showed a larger decrease and greater recovery of $\Phi^{\wedge}$ during hypoxia and reoxygenation. Case g5i0 also showed larger decrease of $\Phi^{\wedge}$ on the LV without recovery during reperfusion.

4 Discussion

Transmembrane current is the origin of the action potential, but directly measuring current with high resolution over the entire heart is not technically feasible. However, extracellular potentials, generated by transmembrane current, are easily measured. The inward flux of sodium ions initiates activation, and the time of the maximum increase rate of Na^+ current is coincident with the time of the minimum time derivative of Φ [3,4]. For this reason, extracellular potentials have been principally used for the detection of activation time. But there may be more potentially useful information available from these measures. It would be reasonable to assume that the magnitude of $\Phi^{\wedge}$ is closely related to the maximum increase rate of Na^+ current, because the two events are coincident. This experiment examined the potential usefulness of the normalized averaged value of $\Phi^{\wedge}$, as a qualitative measure of electrical activation which may be closely related to the transmembrane current at activation by comparing its values with those of other measures of propagation under hypoxic conditions.

Hearts suffer from a lack of readily available energy during hypoxia, and K_{ATP} channels open in response to decreased levels of ATP. This increases transmembrane voltage contributing to the inactivation of Na^+ channels [9]. The decrease in $\Phi^{\wedge}_{na}$ for cases g5i2 and g5i0 in Fig. 2c at the onset of hypoxia was likely a reflection of reduced Na^+ current by inactivation of a portion of the available Na^+ channels as a consequence of insufficient glucose transport. Clow *et al.* [10] showed glucose transport becomes the rate-limiting condition for glycolysis over phosphorylation during hypoxia, and Runnman *et al.* [8] showed that during hypoxia higher extracellular glucose levels were beneficial to cardiac function and removal of insulin was detrimental. According to their studies, case g5i0, with low glucose levels and without insulin, provides the worst conditions for glucose transport during hypoxia. Consistent with their findings, in our studies, case g5i0 resulted in the largest changes in R_{act}, TAT_n and $\Phi^{\wedge}_{na}$. The propagation speed decreased, which would be a consequence of reduced Na^+ current. Heterogeneous inactivation of Na+ channels may change the propagation pattern and more severe inactivation may even block conduction, consequences reflected in the R_{act} values and maps of activation sequence. Case g10i2, with high concentrations of glucose and insulin, provides the best opportunity for extracellular glucose utilization, and did not exhibit any significant changes in the parameters measured in this study during hypoxia. For the case of g5i2, we would expect less impact to the Na^+ current than g5i0 because of the insulin supply. Decrease of $\Phi^{\wedge}_{na}$ and an increase in TAT_n for case g5i2 were less than for case g5i0, and the propagation pattern did not change significantly until after 17 minutes. More importantly, propagation changes for

the case of g5i2 recovered during reoxygenation unlike g5i0, which implies that the conditions for the case g5i0 caused irreversible damage to the heart during hypoxia. Values of $\Phi^{\wedge}_{na}$ also tracked this irreversibility.

As explained above, the response of $\Phi^{\wedge}_{na}$ was similar to the physiologically expected response of Na^{+} transmembrane current to the metabolic stresses and demonstrated similar responses as the other measures of propagation. However, individual $\Phi^{\wedge}$ values from any one electrode frequently were poor indicators of the overall state of the heart, because extracellular potentials at different locations may show different responses to hypoxia. Extracellular potentials may be affected by the geometry of the heart, the activation pattern, and especially by the distance between the electrode and the cardiac surface. Higher $\Phi^{\wedge}$ values during oxygenation and a more sensitive response to hypoxia from the LV might be attributed to the thicker wall of the LV.

The long term goal of this research is to understand the relationship between electrical and metabolic changes in the heart during ischemic stress that leads to an increased cardiac risk, particularly in the setting of diabetes. There are specific challenges with the use of a mouse model to study electrical responses in the heart for understanding human disease, primarily the differences in cardiac ion currents and also the technical challenges with the extremely small size of the heart. However, these challenges are worth addressing in order to benefit from the availability of genetically altered mouse models that target specific physiologic aspects of diabetes and the metabolic syndrome.

In summary, this study showed that decreases in $\Phi^{\wedge}_{na}$ was a predictor of changes in other electrical markers such as total activation time, activation propagation pattern, and irreversible damage, and these results supported $\Phi^{\wedge}_{na}$ as an potentially useful index of electrical activity which might be closely related to the amount of available sodium current at the time of activation.

Acknowledgments

This research was supported by grants from the Nora Eccles Treadwell Foundation and the Richard A. and Nora Eccles Harrison Fund for Cardiovascular Research. The authors wish to acknowledge Mr. Bruce Steadman and Dr. Philip Ershler for the design and development of the data acquisition hardware and software and Mr. Ted Dustman for his efforts in designing our data processing software.

References

1. Spach, MS., Miller 3rd, WT., Miller-Jones, E., Warren, RB., Barr, RC.: Extracellular potential related to intracellular action potentials during impulse conduction in anisotropic canine cardiac muscle. Circ Res. 42, 188–204 (1979)
2. Plonsey, R.: Bioelectric phenomena, pp. 221–275. McGrawHill, New York (1969)
3. Spach, MS., Dolber, PC.: Relating extracellular potentials and their derivatives to anisotropic propagation at a microscopic level in human cardiac muscle. Evidence for electrical uncoupling of side-to-side fiber connections with increasing age. Circ. Res. 58, 356–371 (1986)

4. Spach, MS., Kootsey, JM.: Relating the sodium current and conductance to the shape of transmembrane and extracellular potentials by simulation: effects of propagation boundaries. IEEE Trans Biomed Eng. 32, 743–755 (1985)
5. Depre, C., Vanoverschelde, JL., Taegtmeyer, H.: Glucose for the heart. Circulation 99, 578–588 (1999)
6. Davey, KA., Garlick, PB., Warley, A., Southworth, R.: An immunogold labeling study of the distribution of GLUT 1 & GLUT 4 in cardiac tissue following stimulation by insulin or ischemia. Am. J. Physiol. Heart Circ. Physiol. Accepted on (December 11 2006)
7. Morgan, HE., Henderson, MJ., Regen, DM., Park, CR.: Regulation of glucose uptake in muscle. I. The effects of insulin and anoxia on glucose transport and phosphorylation in the isolated, perfused heart of normal rats. J Biol Chem. 236, 253–261 (1961)
8. Runnman, E.M., Lamp, S.T., Weiss, J.N.: Enhanced utilization of exogeneous glucose improves cardiac function in hypoxic rabbit ventricle without increasing total glycolytic flux. J. Clin. Invest. 86, 1222–1233 (1990)
9. Cascio, WE., Johnson, TA., Gettes, LS.: Electrophysiologic changes in ischemic ventricular myocardium: I. Influence of ionic, metabolic, and energetic changes. J. Cardiovasc Electrophysiol. 6, 1039–1062 (1995)
10. Clow, KA., Rodnick, KJ., MacCormack, TJ., Driedzic, WR.: The regulation and importance of glucose uptake in the isolated Atlantic cod heart: rate-limiting steps and effects of hypoxia. J. Exp. Biol. 207, 1865–1874 (2004)

Experimental Epicardial Potential Mapping in Mouse Ventricles: Effects of Fiber Architecture

David R. Sutherland, Qiansheng Liang, Kwanghyun Sohn, Bruno Taccardi, and Bonnie B. Punske

Nora Eccles Harrison Cardiovascular Research and Training Institute and Department of Bioengineering
University of Utah, Salt Lake City, UT 84112-5000, USA
punske@cvrti.utah.edu

Abstract. The purpose of this study is to introduce unique experimental measurements of extracellular potentials mapped from the epicardial surface of mouse hearts that reflect the same structural features seen in larger mammalian hearts. The measurements obtained in this study provide an important tool for studying the impacts of structural changes on propagation in genetically modified mouse models of cardiac disease. Unipolar electrograms were recorded using a high-resolution electrode array to map the epicardial surface of mouse hearts during atrial drive and at increasing transmural pacing depths. The extracellular potential maps revealed the underlying fiber structure of the mouse heart that is shown to be similar to those previously published from other species. This imaging technique, when integrated with computer models and diffusion tensor imaging can substantially contribute to our understanding of innovative genetic mouse models being used in the study of human cardiac disease.

1 Introduction

Normal cardiac function depends on the normal conduction of electrical impulses throughout the heart. Electrical propagation in the heart is affected by the structure of the heart muscle, including the Purkinje conduction system, anisotropy, cell-to-cell coupling systems, fiber rotation, and imbrication. Previous experimental studies showed that these structural features are reflected in larger mammalian hearts from the epicardial surface potentials as measured during ventricular pacing [1,2]. From the epicardial surface potentials we can obtain information about the local fiber orientation, the amount of transmural fiber rotation, and in which direction the wave front is traveling transmurally through the wall. The potential field as measured from the epicardium provides the unique ability to study the fundamental electrical activity and directly relate it to changes in the structure of the tissue volume.

Recent advancements in genetics and molecular biology have enabled the production of transgenic mice that exhibit highly specific modifications of the cardiac physiology. Recent work from our laboratory has studied different mouse

F.B. Sachse and G. Seemann (Eds.): FIMH 2007, LNCS 4466, pp. 260–268, 2007.

models with modifications that impact propagation through impairment of ionic transport and structural changes [3,4]. Interestingly, even changes in physiology that are seemingly not related to the known determinants of cardiac electric potentials have resulted in modified electrograms suggesting some type electrical impact [5]. Because the mouse heart is increasingly being used as a model for human cardiac disease, it is becoming imperative to characterize the structure and electrical activity of these hearts so meaningful inferences about human physiology and disease can be made.

In light of these needs, recent work has been done to describe the fiber structure of mouse hearts in three dimensions using magnetic resonance diffusion tensor imaging (DTI) [6]. These studies revealed that mouse hearts exhibit a linearly counterclockwise rotation of the myocardial fibers from the epicardium to the endocardium [6] similar to that reported for larger hearts [7]. By incorporating the three dimensional structure of the heart provided by DTI, a computer model describing propagation in a mouse heart has also been implemented [8]. This computer model integrates anatomic structure, tissue properties, and ionic activity to produce realistic maps of the spread of excitation. These types of computer simulations are indispensable in predicting outcomes and understanding the physiology of transgenic models.

The purpose of this study is to provide experimental measurements of extracellular potentials mapped from an electrode array closely surrounding the entire epicardial surface of mouse hearts. The techniques for making these measurements will provide an important tool for studying the impacts of structural changes on propagation in new genetically modified mouse models. In addition, the results can be compared with previously published results from other species to better understand the physiology and structure of the mouse heart. Finally, these results will provide measurements for verification and comparison with previously published computer simulations and results from DTI.

2 Methods

The University of Utah institutional animal care and use committee approved all experimental procedures performed in these studies. C57 Blk/6 male mice were administered heparin (3 Units/g) and anesthetized with sodium pentobarbital (100 mg/kg). A medial sternotomy was performed and the heart rapidly excised and perfused with Krebs-Henseleit solution (in mM: 118.5 NaCl, 25 $NaHCO_3$, 4.7 KCl, 1.2 $MgSO_4$, 0.5 EDTA, 1.2 KH_2PO_4, 2.5 $CaCl_2$, and 11 glucose) bubbled with 95% O_2 and 5% CO_2 in a modified Langendorff procedure. Perfusion temperature was maintained at 37°C. Perfusion pressure and flow rate were controlled by a gravity-fed system and maintained at 60 mmHg and greater than 1 mL/min respectively.

2.1 Electrode Array

The hearts were placed inside a 184-electrode "cage" array as shown in Fig. 1A [4]. The electrode array was fabricated by attaching 0.0762 mm diameter silver

wires to the intersections of a medical-grade mesh formed into the shape of a cylinder (see Fig. 1B). The mesh provided uniform 1 mm spacing with 23 columns and 8 rows of electrodes, measuring 7.32 mm in diameter and 7 mm in height. The exposed silver sites were chlorided to form Ag/AgCl electrodes. The array slipped tightly over the heart making contact with the ventricular freewalls directly and via perfusion fluid at the apex of the heart. Although this configuration allowed the heart to move within the array during contraction, the measurements of interest were obtained during excitation prior to contraction. A small acrylic chamber with an electrical heating element was closed around the isolated heart to maintain the temperature of the air surrounding the heart at 37°C.

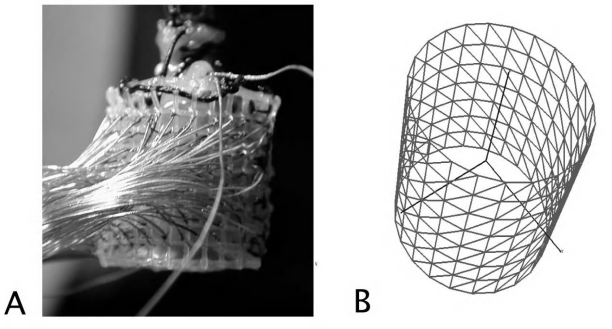

Fig. 1. (A) Photograph of the "cage" electrode array surrounding a mouse heart. (B) Triangulated mesh of the electrode 184 sites in 3 dimensions.

Two Ag/AgCl hooks made from 0.127 mm diameter wire were attached to the right atrium for bipolar pacing. A plunge needle electrode made from the tip of a 0.127 mm diameter stainless steel wire housed in 22-gauge (0.6438 mm diameter) needle was inserted into the heart via a micromanipulator. The tip of the electrode was advanced to increasing transmural depths for unipolar pacing with respect to another wire placed at the aortic root of the heart.

2.2 Data Acquisition and Processing

Unipolar electrograms were recorded from the ventricular surface during sinus rhythm and atrial and ventricular pacing via biphasic current injection at current levels just above the stimulation threshold and lasting 2 ms per phase. Recordings were referenced to a remote electrode placed at the aortic root. All 184 signals were simultaneously recorded at 8 kHz, digitized in 16-bit resolution and stored directly to a computer. Individual signals were calibrated and baselined using consecutive T-P intervals. Isopotential and isochronal maps were visualized in the form of linearly interpolated contour maps using Map3d software (http://www.sci.utah.edu/map3d) [9]. Activation time was determined as the time of the minimum value of the derivative during the downstroke of the

electrogram as measured from the earliest activation time. Isopotential maps are time-referenced to the time of the middle of the stimulus artifact.

3 Results

Fig. 2 shows an example of an activation time map recorded from an isolated mouse heart following atrial stimulation. The darker areas, indicating earlier activation breakthroughs, occur on both the right ventricle (RV) and the left ventricle (LV), with late areas of activation indicated by lighter shades occurring between the LV and RV breakthrough sites. Similar patterns of activation during atrial stimulation have been observed from multiple mouse hearts in our laboratory. The total epicardial activation time in the example shown in Fig. 2 is 2.64 ms. Similar measures from 4 additional hearts showed that the average

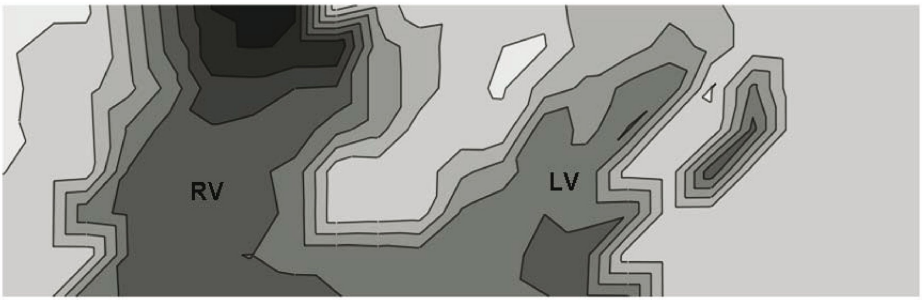

Fig. 2. An isochronal map of the normal ventricular sequence of activation in the mouse heart following atrial stimulation. Dark shades indicate early activation and lighter shades indicate late activation times. Each contour represents 0.364 ms.

ventricular activation time during normal sequences is 2.66 ± 0.5 ms. Maps of the normal sequence of activation give insight into the structure and influence of the specialized Purkinje conduction system.

Fig. 3 is an isopotential map recorded immediately following epicardial stimulation. This figure provides a classic example of the indication of the local underlying fiber direction revealed by ventricular point stimulation from a mouse heart. The elliptical shape of the dense band of negative (dark, dashed) isopotential lines shows the newly initiated wave front traveling faster along the direction of the myocardial fibers with the long axis of the ellipse aligned with the longitudinal fiber direction. At the basal end of the ellipse is a potential maximum that falls along the line drawn through the pacing site and along the long axis. This maximum, paired with a weak area of positivity found at the apical end of the elliptical wave front forms the classical linear quadrapole pattern of propagation previously described in other species [1,2].

Fig. 4 demonstrates the ability to capture the transmural rotation of the tissue fiber direction with the epicardial potential distribution. Fig. 4B shows

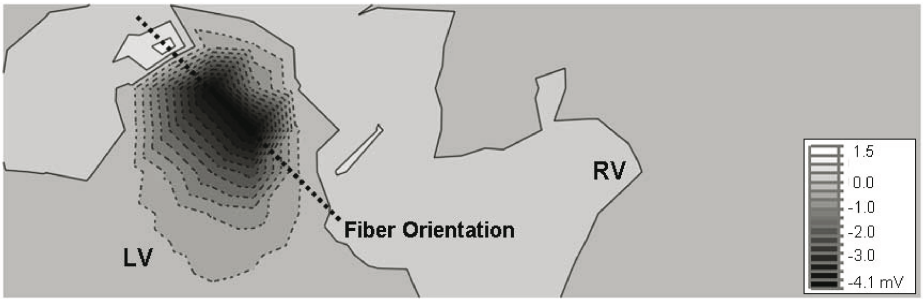

Fig. 3. Epicardial isopotential map immediately following epicardial point stimulation. The dark, dashed, dense band of isopotential lines indicates the presence of the activation wave front. Light solid lines indicate potential maxima aligned with the long axis of the elliptical wave front. The heavy dashed line along the main axis of the activation wave front ellipse represents the epicardial fiber direction.

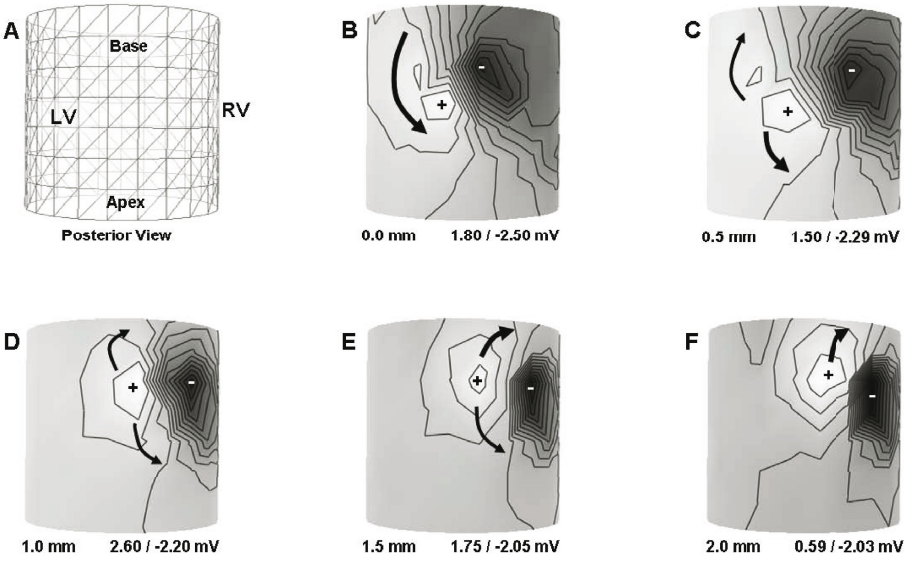

Fig. 4. The orientation of the heart (A) as shown in maps of epicardial potentials at 5.875 ms post pacing after advancing micromanipulator (B) 0.0mm, (C) 0.5mm, (D) 1.0mm, (E) 1.5mm, and (F) 2.0mm

an isopotential map recorded at 5.875 ms after the middle of the epicardial pacing artifact on the posterior LV. In this figure, the expansion of the potential maxima (shown by the arrows) is progressing in a counterclockwise direction as the wave front encounters counterclockwise fiber rotation as it propagates toward the endocardium. Figs. 4C–F show additional isopotential maps referenced to the same time after pacing at the same location but at increasing transmural

depths. Ventricular stimulation from the midmyocardial region of the freewall produces expansion and rotation of the potential maxima in both the clockwise and counterclockwise directions as the wave front encounters fiber rotation from the midwall to the endocardium and epicardium, respectively (see panels C–E). Similarly, endocardial stimulation (see Fig. 4F) produces clockwise rotation of the potential maxima as the wave front encounters only clockwise fiber rotation as it travels from the endocardium to the epicardium.

4 Discussion

The preliminary data presented here are highly consistent with previously reported potential distributions of fiber architecture in dog and rat [1,2]. From the presented examples, the isopotential lines immediately following pacing can give an indication of the local fiber direction and the elliptical shape of the isopotential lines can provide measures of the anisotropic ratio of conduction. In previous work the elliptical wave front is flanked on the long axis by two potential maxima. In our studies to date the apical maximum is much weaker than the basal maximum or in some cases hardly detectable. The work of Taccardi *et al.* [10] shows that the presence of a weaker maximum was attributed to the obliqueness of the fibers, the fact that the fibers are not parallel to the epicardial surface, but form a so-called "imbrication" angle with the surface. This tipping of the fibers will cause one maximum to be farther from the surface then the other contributing to the differences in amplitude. The example of these differences in the amplitudes of the potential maxima as shown in Fig. 3 may be related to this idea of obliqueness of the fibers, but is more likely attributed to the fact that as the curvature of the heart increases, from base to apex, the surface of the heart becomes farther from the electrodes measuring the potentials. This is a drawback in the cylindrical design of the array causing a decreased amplitude in some recordings closer to the apex. Other technical limitations of this imaging technique involve reducing the magnitude and duration of the stimulus artifact during pacing to eliminate overlap with the potentials of early activation, and improving the alignment of the array with the heart for reproducibility from study to study. In addition, our ability to accurately measure the true depth of the pacing needle is limited due to the compliance and resistance of the wall to the advancement of the micromanipulator. Resolving these technical issues is the focus of current studies in our laboratory.

The rotation and expansion of the potential maxima as seen in Fig. 4 are also very similar to those reported by other studies [1,2]. The potential maxima rotate with time in the counterclockwise direction following epicardial stimulation. As the wave front spreads in the transmural direction toward the endocardium and encounters the counterclockwise rotation of the fibers as described by Jiang *et al.* [6], the positive maxima will rotate to reflect the positivity along fibers ahead of the wave front at increasing depths. This rotation can be observed on the epicardial surface as an expansion and rotation of the positivity flanking the wave front.

Qualitative comparisons of our experimental results with the published work of Henriquez *et al.* [8] reveals that the experimental data are well represented by the model. The model data show the potential maxima flanking the excitation wave front that spreads from the point of stimulation on the epicardial surface along the direction of the underlying fibers [8]. In addition, the potential maps produced by the model also suggest an expansion and rotation of the potential maxima in the counterclockwise direction following epicardial stimulation.

The predominant method for experimental studies of propagation in small hearts, particularly mouse heart, is optical mapping [3,11]. This technique uses voltage sensitive dyes bound to the cell membranes of myocytes that upon excitation, emit light signals corresponding to the local membrane voltage in the form of action potentials. One advantage of using this technique is that it allows a large number of measurements with high spatial resolution without making contact with the surface of the heart. Results from optical mapping studies provide isochronal patterns of propagation, action potential duration and measures of conduction velocities. Some of these results have been compared qualitatively with results of computer simulations in mouse myocardium [8,12]. However, optical mapping does not provide a measure of the potential field like conventional electrical mapping does and therefore, cannot provide data that will reflect the three-dimensional anisotropy and transmural fiber architecture of the heart seen in diffusion tensor imaging [6] nor directly relate to the potential values generated by computer simulations [8].

Our studies can complement and extend the previous comparisons of computer simulation results with published optical mapping data. While optical mapping provides an important imaging modality for studying propagation in small hearts, our preliminary results stress the advantages of also performing conventional electrical imaging to enable the underlying structure to be revealed via the characteristics of the potential field. Innovative electrode fabrication offers the advantage of imaging electrical propagation in three dimensions, instead of two, giving a more complete three-dimensional surface representation of the spread of excitation covering both ventricles. Electrical imaging also eliminates the need for infusing toxic fluorescent dyes and more importantly eliminates the need to prevent contraction through the use of mechanical uncoupling drugs or applied pressure that can interfere directly with local propagation. For studies involving the effects of metabolic changes on electrical activity where normal contraction of the heart is essential, electrical imaging provides an appropriate method for studying propagation.

DTI results show that the fiber structure of the mouse heart is qualitativley similar to that seen in larger hearts although the measured degree of transmural fiber rotation in mouse was found to change approximately 150° from epicardium to endocardium [6]. While our preliminary electrical measurements reflect some degree of rotation, currently, our experimental technique has not been able to quantitatively reproduce this result. One possibility is that the potential maxima reflected on the epicardial surface following endocardial stimulation are not of sufficient magnitude in the mouse heart to measure reliably with the available

gain and signal-to-noise ratio. Another factor contributing to difficulties in determining the degree of rotation lies with the accurate determination of the pacing depth and location as previously mentioned. Thus, a reliable measure of the full rotation of the transmural fibers using the alignment of the potential maxima is the focus of current experiments.

In summary, this study provides high-resolution electrical images from mouse epicardium with detailed information of the propagation characteristics as well as of the local fiber architecture. This imaging technique, when integrated with computer models and diffusion tensor imaging, can substantially contribute to our understanding of innovative genetic mouse models of cardiac disease.

Acknowledgments

This work was supported by grants from the Nora Eccles Treadwell Foundation and the Richard A. and Nora Eccles Harrison Fund for Cardiovascular Research. The authors would like to gratefully acknowledge Mr. Bruce Steadman and Dr. Philip Ershler for the design and development of the data acquisition hardware and software, Mr. Ted Dustman for his efforts in designing "curly," our data processing software, and Ms. Alice England for her technical expertise in fabricating the electrode array.

References

1. Macchi, E., Cavalieri, M., Stilli, D., Musso, E., Baruffi, S., Olivetti, G., Ershler, P.R., Lux, R.L., Taccardi, B.: High-density epicardial mapping during current injection and ventricular activation in rat hearts. Am. J. Physiol. 275, 1886–1897 (1998)
2. Taccardi, B., Macchi, E., Lux, R.L., Ershler, P.R., Spaggiari, S., Baruffi, S., Vyhmeister, Y.: Effect of myocardial fiber direction on epicardial potentials. Circulation 90, 3076–3090 (1994)
3. Punske, B.B., Rossi, S., Ershler, P., Rasmussen, I., Abel, E.D.: Optical mapping of propagation changes induced by elevated extracellular potassium ion concentration in genetically altered mouse hearts. J. Electrocardiol 37 (Suppl), 128–134 (2004)
4. Punske, B.B., Taccardi, B., Steadman, B., Ershler, P.R., England, A., Valencik, M.L., McDonald, J.A., Litwin, S.E.: Effect of fiber orientation on propagation: electrical mapping of genetically altered mouse hearts. J. Electrocardiol. 38, 40–44 (2005)
5. Valencik, M.L., Zhang, D., Punske, B., Hu, P., McDonald, J.A., Litwin, S.E.: Integrin activation in the heart: a link between electrical and contractile dysfunction? Circ. Res. 99, 1403–1410 (2006)
6. Jiang, Y., Pandya, K., Smithies, O., Hsu, E.W.: Three-dimensional diffusion tensor microscopy of fixed mouse hearts. Magn. Reson Med. 52, 453–460 (2004)
7. Hsu, E.W., Henriquez, C.S.: Myocardial fiber orientation mapping using reduced encoding diffusion tensor imaging. J. Cardiovasc Magn Reson. 3, 339–347 (2001)
8. Henriquez, C.S., Tranquillo, J.V., Weinstein, D., Hsu, E.W., Johnson, C.R.: Three-dimensional Propagation in Mathematic Models: Integrative Model of the Mouse Heart. In: Zipes, D.P., Jalife, J. (eds.): Cardiac Electrophysiology From Cell to Bedside. Saunders, Philadelphia, pp. 273–281 (2004)

9. MacLeod, R., Johnson, C.R.: Map3d: Interactive scientific visualization for bioengineering data. In: IEEE Engineering in Medicine and Biology Society. 15th Annual International Conference, pp. 30–31. IEEE Press, Los Alamitos (1993)
10. Taccardi, B., Lux, R.L., Ershler, P.R., MacLeod, R., Dustman, T.J., Ingebrigtsen, N.: Anatomical architecture and electrical activity of the heart. Acta. Cardiol. 52, 91–105 (1997)
11. Nygren, A., Clark, R.B., Belke, D.D., Kondo, C., Giles, W.R., Witkowski, F.X.: Voltage-sensitive dye mapping of activation and conduction in adult mouse hearts. Ann. Biomed Eng. 28, 958–967 (2000)
12. Tranquillo, J.V., Hlavacek, J., Henriquez, C.S.: An integrative model of mouse cardiac electrophysiology from cell to torso. Europace 7 Suppl 2, 56–70 (2005)

Noninvasive Electroardiographic Imaging: Application of Hybrid Methods for Solving the Electrocardiography Inverse Problem

Mingfeng Jiang[1,2], Ling Xia[1], and Guofa Shou[1]

[1] Department of Biomedical Engineering, Zhejiang University, Hangzhou, 310027, P.R. China
xialing@zju.edu.cn
[2] The College of Electronics and Informatics, Zhejiang Sci-Tech University, Hangzhou, 310018, P.R. China

Abstract. Computing the epicardial potentials from the body surface potentials constitutes one form of the ill-posed inverse problem of electrocardiography (ECG). In this paper, we employ hybrid methods combining the least square QR (LSQR) with truncated singular-value decomposition (TSVD) to solve the inverse problem of ECG. Hybrid methods are based on the Lanczos process, which yields a sequence of small bidiagonal systems approximating the original ill-posed problem, and on another additional direct regularization (the truncated SVD method is used in the present investigation), which is used to stabilize the iteration. The results show that determining of regularization parameters based on the final projected problem rather than on the original discretization one has firmer justification and it takes much less computational cost. The computation time could be reduced by several tenfolds typically, while the performance of the hybrid method is maintained well compared with TSVD, LSQR and GMRes methods. In addition, comparing with LSQR method, the hybrid method can obtain the inverse solutions without facing the "semi-convergence" problem.

1 Introduction

To describe the ECG inverse problem mathematically, we can use the cardiac sources in terms of epicardial surface potentials, and solve a generalized Laplace's equation with Cauchy boundary conditions [1]:

$$\begin{cases} \nabla \cdot \delta \nabla \Phi = 0 \quad in \ \Omega \\ \delta \nabla \Phi \cdot n = 0 \quad on \ \Gamma_T \quad find \ \Phi_E \ on \ \Gamma_E \\ \Phi = \Phi_T \quad on \ \Gamma_T \end{cases} \tag{1}$$

where Φ are the electrostatic potentials, Φ_E and Φ_T is the potential on the epicardial surface and body surface respectively, δ is the conductivity tensor, Γ_T and Ω represent the surface and the volume of the thorax, and Γ_E is the surface of epicedium. Body surface potentials (Φ_T) are related to epicardial potentials (Φ_E) through the linear system of equations:

$$A\Phi_E = \Phi_T \tag{2}$$

F.B. Sachse and G. Seemann (Eds.): FIMH 2007, LNCS 4466, pp. 269–279, 2007.

where $\boldsymbol{A}$ is the geometry and conductivity transfer matrix reflecting the properties of the volume conductor between the epicardial surface and body surface, and the transfer matrix $\boldsymbol{A}$ can be obtained by the boundary element method (BEM)[2]. However, the matrix $\boldsymbol{A}$ is ill-posed in that small measurement errors in the surface potentials, or any geometry error in the volume conductor model used in the inversion procedure, lead to large perturbations in the epicardial distributions. The inverse problem of ECG is a linear least-square problem:

$$\boldsymbol{M}(\phi) = \min \left\| \boldsymbol{A}\Phi_E - \Phi_T \right\|_2 \tag{3}$$

where symbol $\| \ \|_2$ denotes the Euclidean norm of vector space. Techniques of regularization must be used when solving ill-posed problems to minimize the effects of the inevitable error by imposing constraints on the solution.

Some researchers have used the direct regularization techniques, such as Tikhonov regularization, Truncated Singular-value Decomposition (TSVD) [3]. Solving ill-posed problems can be impractical if the condition number n is large, but fortunately, regularization can be achieved through projecting $\boldsymbol{A}$ onto a k-dimensional subspace. The projection is often achieved through the use of iterative methods such as conjugate gradients (CG), GMRES, LSQR, and other Krylov subspace methods [4,5,6]. Krylov subspace algorithms tend to produce, at early iterations, solutions that resemble the reality more than later iterates which is the "semi-convergence" phenomenon of Krylov subspace. Therefore, the choice of the regularization parameter k, the stopping point for the iteration and the dimension of the subspace, is very important. Rudy et al used the GMRes method to reconstruct epicardial potentials without adding any constraints, and results showed that the accuracy of GMRes solutions was similar to that of Tikhonov regularization [7]. Another important family of regularization methods, termed hybrid methods [8], was introduced by O'Leary and Simmons [9]. These methods combine a projection method with a direct regularization method such as TSVD. Since the dimension k of the project problem is usually small relative to n, regularization of the restricted problem is much less expensive, but the end results can be very similar to those achieved by applying the same direct regularization technique to the original problem. In the inverse ECG problem, the regularization method based on the hybrid methods has been less touched on, and some researchers just use iteration regularization methods or direct regularization methods individually. In this paper, a hybrid method to solve the inverse ECG problem is introduced, and it's performance is compared with those of the direct method (TSVD) and iterative methods (LSQR and GMRes) afterwards.

2 Methods

2.1 Lanczos Bidiagonalization

In this section, an approach to regularize the projected problem of Krylov methods is introduced. Many Krylov methods have been proposed so far, here we focus on just one of them: the LSQR algorithm of Paige and Saunders [10].

For a rectangle $m \times n$ matrix A, the Lanczos bidiagonalization computes a sequence of Lanczos vectors $\mu_j \in IR^m$ and $v_j \in IR^n$ and scalars α_j and β_j, which meets $U^T AV = B_k$, B_k is the lower bidiagonal matrix:

$$B_k = \begin{pmatrix} \alpha_1 & & & \\ \beta_2 & \alpha_2 & & \\ & \beta_3 & \ddots & \\ & & \ddots & \alpha_k \\ & & & \beta_{k+1} \end{pmatrix} \tag{4}$$

In exact arithmetic, the Lanczos vectors are orthonormal such that

$$U_{k+1} = (u_1, u_2, ..., u_{k+1}) \in IR^{m \times (k+1)} \quad \text{and} \quad U_{k+1}^T U_{k+1} = I_{k+1}, \tag{5}$$

$$\mathbf{V}_k = (v_1, v_2, ..., v_k) \in \mathbf{IR}^{m \times k} \quad \text{and} \quad \mathbf{V}_k^T \mathbf{V}_k = \mathbf{I}_k, \tag{6}$$

The Lanczos bidiagonalization algorithm is given in Table 1.

Table 1. The Lanczos bidiagonalization algorithm

Choose a starting vector $\Phi_T \in IR^m$, and let

$\beta_1 = \|\Phi_T\|_2$, $\mu_1 = \Phi_T / \beta_1$, $v_0 = 0$

for $i = 1, 2, ..., k$ do

$r_i = A^T u_i - \beta_i v_{i-1}$;

$\alpha_i = \|r_i\|_2$;

$v_i = r_i / \alpha_i$;

$p_i = A v_i - \alpha_i u_i$;

$\beta_{i+1} = \|p_i\|_2$;

$u_{i+1} = p_i / \beta_{i+1}$;

end

After k iterations, it has effectively computed three matrices: a lower-bidiagonal matrix B_k and two matrices U_{k+1} and V_k, related by

$$\Phi_T = \beta_1 u_1 = \beta_1 U_{k+1} e_1 \tag{7}$$

$$AV_k = U_{k+1} B_k \tag{8}$$

$$A^T U_{k+1} = V_k B_k^T + \alpha_{k+1} v_{k+1} e_{k+1}^T \tag{9}$$

where e_i denotes the ith unit vector.

The quantities generated from $\boldsymbol{A}$ and $\boldsymbol{\Phi}_T$ by Lanczos bidiagonalization can now be used to solve the least -squares problem:

$$\min_{\Phi_E \in S} \left\| \Phi_T - A\Phi_E \right\|_2 \tag{10}$$

where S denotes the k-dimensional subspace spanned by the first k vectors v_i.

The solution we seek is of the form:

$$\Phi_E^{(k)} = v_k y^{(k)} \tag{11}$$

where $y^{(k)}$ is the vector with length k. And define $r^{(k)} = \Phi_T - A\Phi_E^{(k)}$ to be the corresponding residual and observe that

$$r^{(k)} = \beta_1 u_1 - AV_k y^{(k)} = U_{k+1}(\beta_1 e_1 - B_k y^{(k)}) \tag{12}$$

Here, we define $t_{k+1} = \beta_1 e_1 - B_k y^{(k)}$. Since U_{k+1} has, in exact arithmetic, orthonormal columns, this immediately suggests choosing $y^{(k)}$ to minimize $\left\| t_{k+1} \right\|$. Hence we are led naturally to the least-squares problem

$$\min \left\| \beta_1 e_1 - B_k y^{(k)} \right\|_2 \tag{13}$$

which forms the basis for LSQR. Computationally, it is advantageous to solve (13) using the standard QR factorization of B_k. Solving this minimization problem is mathematically equivalent to solve the normal equations involving the bidiagonal matrix:

$$\boldsymbol{B}_k^* \boldsymbol{B}_k \boldsymbol{y}^{(k)} = \boldsymbol{B}_k^* \beta_1 \boldsymbol{e}_1 \tag{14}$$

The matrix B_k may be ill-conditioned because some of its singular values approximate some of the small singular values of A. Therefore, solving the projected problem might not yield a good solution $y^{(k)}$, but we can use any of the direct regularization methods to regularize this projected problem. In this paper, TSVD is used to solve the projected problem.

2.2 Truncated Singular Value Decomposition (TSVD)

Let USV^T denote the singular value decomposition (SVD) of A, where the columns of U and V are the singular vectors, and the singular values are ordered as $\sigma_1 \geq \sigma_2 \geq \ldots \geq \sigma_n$. Then the solution (3) is given by

$$\phi_E = \sum_{i=1}^{n} \frac{\boldsymbol{u}_i^T \phi_b}{\sigma_i} \boldsymbol{v}_i \tag{15}$$

In practice, due to noise (i.e., measurement noise in Φ_B, geometry error in determining the matrix $\boldsymbol{A}$, as well as numerical discretization errors in the computations), independent components of Φ_E fewer than n can be estimated reliably. Accordingly, to ensure solution stability in the presence of noise, the dimensionality of the solution space is further restricted to $k < n$ and the smaller singular values from

σ_{k+1} to σ_n are also assumed to be zero. The solution is then given by Eq. (16) again, but with the matrices U, V and S truncated after the first k. Truncated SVD essentially involves a judicious choice of the regularization parameter k so as to result in a stable, low-residual solution.

$$\phi_{E_{TSVD}} = \sum_{i=1}^{k} \frac{\boldsymbol{u}_i^T \phi_b}{\sigma_i} \boldsymbol{v}_i \tag{16}$$

There exist different ways of choosing the regularization parameter. Here we employ the generalized cross-validation (GCV) technique [11], in which the regularization parameter is chosen as the index k that minimizes the GCV function:

$$\boldsymbol{GCV}(\boldsymbol{k}) = \frac{\left\| \boldsymbol{A}\phi_{Ek} - \phi_B \right\|_2^2}{(\boldsymbol{tr}(\boldsymbol{I} - \boldsymbol{A}\boldsymbol{A}_k^{\dagger}))^2} \qquad \boldsymbol{k} = 1, 2, ..., \tag{17}$$

where ϕ_{Ek} is a TSVD solution, $A_k^{\dagger}$ is the pseudo inverse of the closest rank-k approximation of $\boldsymbol{A}$, and tr ($\boldsymbol{A}$)denotes the trace of $\boldsymbol{A}$. The choice has the advantage that no *priori* information on the noise level is required, and it works well in practice.

2.3 Simulation Protocol

The simulation protocol was based on the realistic heart-torso model, as has been described in the references [12-14]. Fig.1 (A) shows the lung, epicardial and torso geometries. The epicardial geometry, however, was not the whole heart surface, just

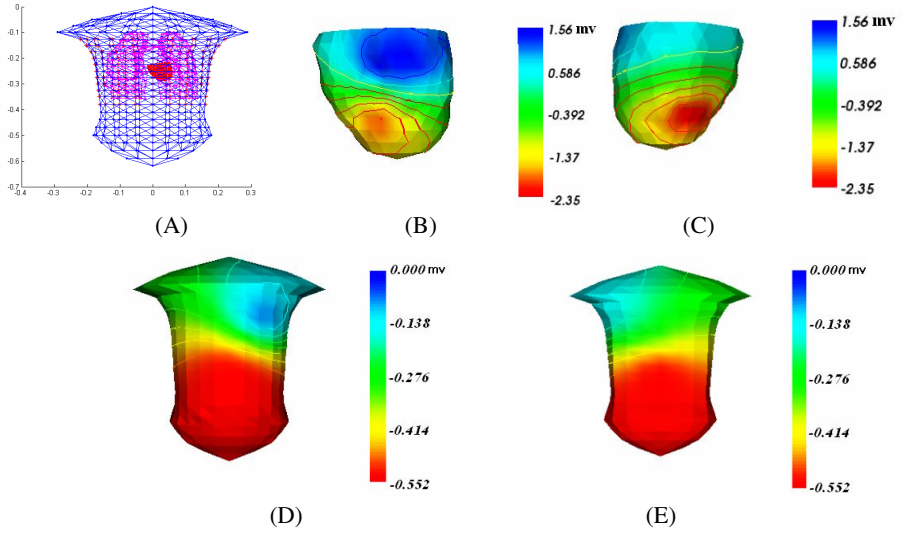

Fig. 1. The realistic heart and torso geometry model and the epicardial and torso potential distribution with a radial dipole in heart. (A) the realistic heart and torso geometry model, (B) the anterior view of the epicardial potentials distribution, (C) the posterior view of the epicardial potentials distribution, (D) the anterior view of the computed torso potentials distribution, (E) the posterior view of the computed torso potentials distribution.

included the ventricular part, which comprised 279 nodes and 531 triangles. The lungs comprised 297 nodes and 586 triangles. The torso model was made up of 412 nodes and 820 triangles. One radial current dipole located in the epicardial geometry and infinite-medium potential equations were used to approximate the epicardial potential distribution at the 279 epicardial node points, as shown in Fig.1 (B) (C). Torso potentials at its 412 surface node were computed from these 279 epicardial potentials using 412×279 matrix, determined by the boundary element method, as shown in Fig.1 (D) (E). In the inverse direction, potentials were only sought at 154 uniformly distributed epicardial points, to be computed from 220 torso sites distributed in the nearby of heart, as shown in Fig.1 (A), where * represent the electrode sites used in the clinical body surface mapping. Thus a 220×154 matrix was recomputed for the inverse solutions. This reduced 220×154 matrix was obtained by first computing a 412×154 matrix and then extracting rows corresponding to electrode position on the body surface, and the condition number is 1.3004e+011. Guassian measurement noises, with signal noise ratio (SNR) =50 dB, were added to the 220 torso potentials to mimic the real measurement. In addition, some geometry noises were added by offsetting the heart 1cm in each of two diametrically opposite directions, one inward toward the torso center and the other outward toward the anterior torso surface [15].

Since the epicaridal potentials are known in advance by forward calculation, the accuracy of inverse-recovered epicardial potentials can be evaluated by either the relative error (RE),

$$RE(\lambda) = \frac{\left\| \Phi_C - \Phi_E \right\|}{\left\| \Phi_E \right\|} \tag{18}$$

or the correlation coefficient (CC), given by

$$CC(\lambda) = \frac{\sum_{i=1}^{n} [(\Phi_C)_i - \bar{\Phi}_C][(\Phi_E)_i - \bar{\Phi}_E]}{\left\| \Phi_C - \bar{\Phi}_C \right\| \left\| \Phi_E - \bar{\Phi}_E \right\|} \tag{19}$$

where Φ_E denotes the known epicardial distribution, and Φ_C the computed one. The quantities $\bar{\Phi}_E$ and $\bar{\Phi}_C$ are, respectively, the mean values of Φ_E and Φ_C, over the n epicardial sites.

3 Results

Table 2 shows that after 55 iterations or more iterations projection we can get the relative error and correlation coefficient approximate to that of the original problem by using the TSVD regularization methods, but with less computation expense. The computation cost of TSVD methods and GCV parameter determination method are $O(mn^2)$ and $O(m)$ respectively. Now, we compute an approximate solution by projecting the discrete problem (m n) onto an even smaller dimensional space((k+1) k), via

iterative methods based on Krylov subspaces. So, the computation cost decreases from $O(mn^2) + O(m)$ to $O((k+1)k^2) + O(k)$[4]. In this simulation, the computation cost lessen from $O(220*150^2) + O(220)$ to $O(56*55^2) + O(55)$ after 55 iterations, that is, the computation cost of the project problem is 30 times less than that of the original problem.

Table 2. Comparison of RE and CC for TSVD regularization method on the original problem with 60 iterations project problem. The regularization parameters are selected by GCV method.

Problem	Regularization parameter	RE	CC
original problem	23	0.3289	0.9439
60 iterations project problem	56	0.3316	0.9433

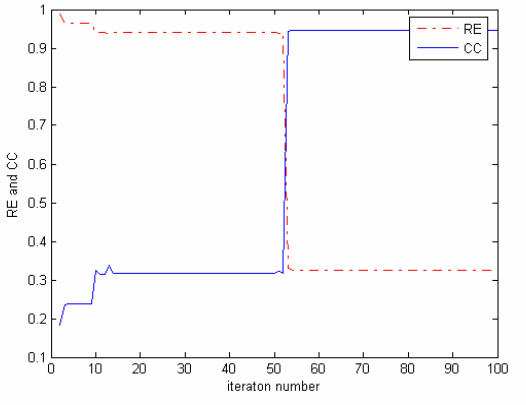

Fig. 2. RE and CC of the solution obtained by the hybrid method and GCV parameter selection with the iteration number

The RE and CC of the solution obtained by the hybrid method and GCV parameter selection method is consistent with that of the original problem by using the TSVD regularization methods after 57 iterations, as shown in Fig. 2. So, we just need 57 iterations or more to solve the ill-posed problem, and then use the direct regularization method to solve the project problem. The computation expensiveness can lessen to the least in such a way.

Fig.3 shows the epicardial potential distribution recovered inversely from the body surface potentials. TSVD, LSQR method (see in [6] for details), GMRes method (see in [7] for details) and hybrid methods were employed for comparison. The noises are supposed to be Gaussian white noise with signal noise ratio (SNR) =50 dB. The results show that approximate solutions were obtained by those four kind methods.

Fig.4 compares the RE and CC of the hybrid schemes with those of the corresponding LSQR iteration. As shown in Fig.4, the optimal solutions of hybrid method are similar to those of the LSQR method, while the LSQR get the optimal

solutions with less iteration. As expected, the hybrid scheme "regularizes" the ill-posed project problem maintaining the error at the optimal level when the LSQR iteration starts to diverge.

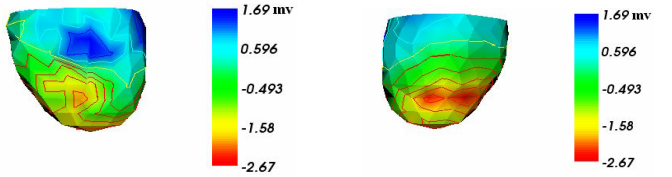

(A) RE: 0.3289 CC: 0.9439

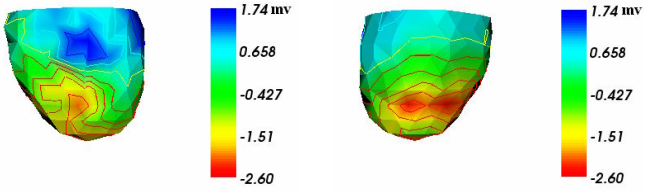

(B) RE: 0.3206 CC: 0.9458

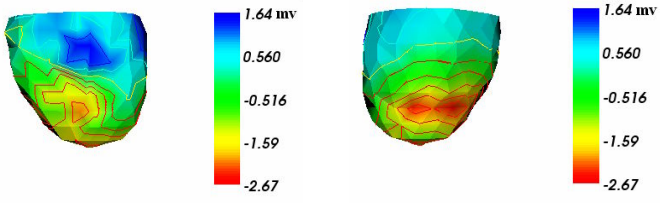

(C) RE: 0.3265 CC: 0.9442

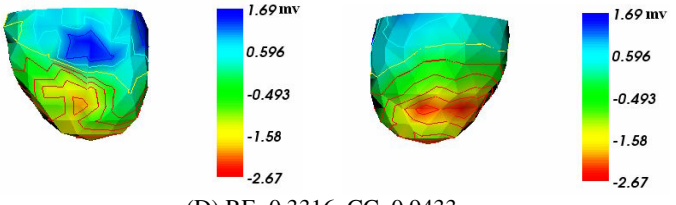

(D) RE: 0.3316 CC: 0.9433

Fig. 3. Epicardial potential distributions reconstructed from body surface potentials with the measurement noise of SNR=50dB. The left panel is the anterior view, and the right is the posterior view. (A) The inverse solutions by the TSVD method. (B) The inverse solutions by LSQR method. (C) The inverse solutions by GMRes method. (D) The inverse solutions by hybrid method. The CC and RE of each method is indicated at the below of each figure.

The performances of three regularization methods are summarized in Table3. In addition to the 50dB Gaussian measurement noise added to the torso potentials, two kind of geometry noise was also considered, the first with heart offset 1cm inwards, and the second with the heart offset 1cm outwards toward the anterior torso surface. As shown in Table 3, the hybrid method always leads to similar RE and CC compared with those of TSVD, LSQR and GMRes methods in different geometry noise levels.

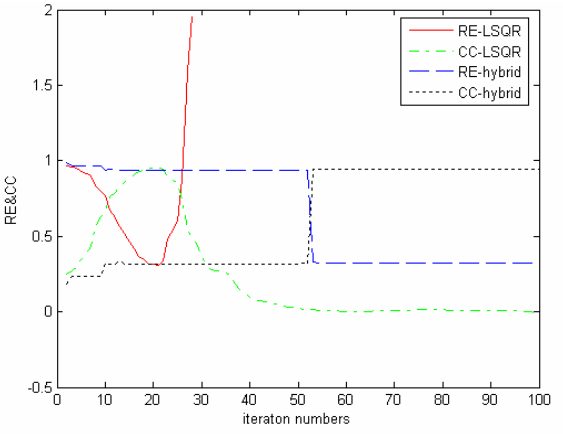

Fig. 4. Comparing the RE and CC of the hybrid schemes with those of the LSQR by using the same iterations

Table 3. Performance comparison of TSVD regularization , LSQR method and hybrid method in solving the ECG inverse problem (SNR=50 dB)

Heart offset	Regularization method	RE	CC
Without heart offset	TSVD	0.3289	0.9439
	LSQR	0.3206	0.9458
	GMRes	0.3265	0.9442
	hybrid	0.3316	0.9433
heart offset 1cm outward	TSVD	0.6521	0.7741
	LSQR	0.6320	0.7914
	GMRes	0.6325	0.7835
	hybrid	0.6558	0.7726
heart offset 1cm inward	TSVD	0.7495	0.8488
	LSQR	0.7350	0.8563
	GMRes	0.7424	0.8532
	hybrid	0.7512	0.8426

4 Discussions and Conclusion

Regularization is the key step in solving inverse problems. The common direct regularization techniques, such as Tikhonov method and TSVD method, try various ways to lessen the contribution of noises. Solving ill-posed problems can be impractical if the condition number n is large by using direct regularization methods. Due to the "semi-convergence" of iterative methods, the choice of iteration number has significant effect on the performances. The selection of stopping parameter, however, is not an easy task.

We apply the hybrid methods, which are based on the Lanczos process and TSVD regularization in terms of projection methods, to solve the ill-posed inverse problem

of ECG. The results show that the regularized solution obtained by project problem plus TSVD is almost similar to those of TSVD, LSQR and GMRes methods for the original problem. The computation cost of the proposed method, however, is much less than that of the direct methods, the computation time could be reduced by several tenfolds typically. In addition, by comparing the hybrid methods with LSQR method, the result shows that the hybrid methods can provide more stable solutions than LSQR method with iterations increasing. After some iteration number, the solutions of hybrid method keep optimal, so the determination of iteration number is not so critical. This research suggests that the proposed hybrid method may provide a useful tool for ECG inverse problem studies.

Acknowledgements. This project is supported by the 973 National Key Basic Research & Development Program (2003CB716106), the 863 High-tech Research & Development Program (2006AA02Z307), the National Natural Science Foundation of China (30570484) and the Program for New Century Excellent Talents in University (NCET-04-0550).

References

1. Rudy, Y., Messinger-Rapport,: The inverse problem in electrocardiography: Solutions in terms of epicardial potentials. CRC Crit. Rev. Biomed. Eng. 16, 215–268 (1988)
2. Seger, M., Fischer, G., Modre, R., Messnarz, B., Hanser, F., Tilg, B.: Lead field computation for the electrocardiographic inverse problem-finite elements versus boundary elements. Computer Methods and Programs in Biomedicine 77, 241–252 (2005)
3. Kilmer, M.E., O'Leary, D.P.: Choosing Regularization Parameters in Iterative Methods for Ill-posed Problems. SIAM J. Matrix Anal. Appl. 22, 1204–1221 (2001)
4. Hanke, M.: On Lanczos Based Methods for the Regularization of Discrete Ill-posed Problems. BIT 41, 1008–1018 (2001)
5. Brianzi, P., Favati, P., Menchi, O., Romani, F.: A framework for studying the regularizing properties of Krylov subspace methods. Inverse Problems 22, 1007–10216 (2006)
6. Jiang, M., Xia, L., Shou, G., Tang, M.: Combination of the LSQR method and a genetic algorithm for solving the electrocardiography inverse problem. Phys. Med. Biol. 52, 1277–1294 (2007)
7. Ramanathan, C., Jia, P., Ghamen, R., Calvetti, D., Rudy, Y.: Noninvasive Electrocardiographic Imaging (ECGI): Application of the Generalized Minimal Residual (GMRes) Method. Annals of Biomed. Eng. 31, 981–994 (2003)
8. Hansen, P.C.: Rank-Deficient and Discrete Ill-Posed Problems. Numerical Aspects of Linear Inversion, SIAM Monogr. Math. Model Comput. SIAM, Philadelphia (1998)
9. O'Leary, D.P., Simmons, J.A.: A bidiagonalization-regularization procedure for large scale discretization of ill-posed problems. SIAM J.Sci. Statist. Comput. 2, 474–489 (1981)
10. Paige, C.C., Saunders, M.A.: LSQR: An algorithm for sparse linear equations and sparse least squares. ACM Trans. Math. Software 8, 43–71 (1982)
11. Golub, G.H., von Matt, U.: Generalized cross-validation for large-scale problems. J. Comput. Graph. Statist. 6, 1–34 (1997)
12. Xia, L., Huo, M., Wei, Q., Liu, F., Crozier, S.: Analysis of cardiac ventricular wall motion based on a three-dimensional electromechanical biventricular model. Phys. Med. Biol. 50, 1901–1917 (2005)

13. Xia, L., Huo, M., Wei, Q., Liu, F., Crozier, S.: Electrodynamic Heart Model Construction and ECG Simulation. Methods of Information in Medicine 45, 564–573 (2006)
14. Xia, L., Zhang, Y., Zhang, H., Wei, Q., Liu, F., Crozier, S.: Simulation of Brugada syndrome using cellular and three-dimensional whole-heart modeling approaches. Phsiological Measurement 27, 1125–1142 (2006)
15. Johnston, P.R., Gulrajani, R.M.: A New Method for Regularization Parameter Determination in the Inverse Problem of Electrocardiography. IEEE Tran. Biomed. Eng. 44, 19–39 (1997)

Towards Noninvasive 3D Imaging of Cardiac Arrhythmias

Linwei Wang[1], Heye Zhang[1], and Pengcheng Shi[1,2]

[1] Medical Image Computing Group,
Hong Kong University of Science and Technology, Hong Kong
[2] School of Biomedical Engineering, Southern Medical University, Guangzhou, China
maomwlw@ust.hk

Abstract. In the efforts towards noninvasive imaging of cardiac electrophysiology from body surface potential recordings, it is of particular clinical interests to identify *patient specific* arrhythmogenesis and arrhythmic patterns. Since cardiac arrhythmias always involve intramural focal activities or transmural propagations, 3D cardiac transmembrane potential (TMP) mapping exhibits considerable potential utility. We have developed a general model-constrained Bayesian framework for noninvasive 3D TMP imaging from body surface potential maps (BSPMs). In this paper, it is adapted to imaging various cardiac arrhythmias, with proper specifications in accordance to different arrhythmogenic mechanisms under study. Representative phantom experiments are studied, with a focus on 1), demonstrating the benefits of 3D TMP imaging in cardiac arrhythmias; and 2), exploring the capability of the BSPM-based and general-model-constrained paradigm in complicate pathological conditions. In-depth post-analysis not only demonstrates the applicability of the framework in imaging cardiac arrhythmias and localizing intramural ectopic foci, but also indicate its merits and limitations for further improvements.

Keywords: noninvasive 3D imaging of cardiac electrophysiology, cardiac arrhythmias, Bayesian framework, data assimilation.

1 Introduction

Cardiac arrhythmias account for one-half of the deaths in patients with heart failures. With various arrhythmogenic mechanisms, its severity ranges from entirely benign to immediately life-threatening. Knowledge about individual patients, including the arrhythmogenesis location and the arrhythmic patterns, is thus critical for the preventative diagnosis, intervention and treatment of related heart diseases. In clinical practices, body surface recordings, such as body surface potential maps (BSPMs) and electrocardiograms (ECGs), are primary noninvasive diagnostic tools based on pattern-recognition/-matching and database localization [1]. As *remote* and *integrative* measurements of the entire cardiac electrical activity, however, ECGs/BSPMs lack the volumetric cardiac

F.B. Sachse and G. Seemann (Eds.): FIMH 2007, LNCS 4466, pp. 280–289, 2007.

information for accurate arrhythmogenesis location or regional arrhythmic activities. Alternative invasive cardiac mappings, though capable of providing such in-depth information, involve challenges such as complicate clinical procedures, myocardial irritation and susceptibility to electrical/motion artifacts [2].

Noninvasive imaging of cardiac electrophysiology from ECG/BSPMs, while still in its infancy, has taken on increasing clinical significance [3,4,5,6,7,8]. For decades, most relevant efforts are confined to reconstructions of equivalent physical sources [3,4] or transmembrane potentials (TMPs) on heart surfaces [5,6], failing to account for the anisotropic, inhomogeneous structure of the 3D myocardium. However, cardiac arrhythmias always involve intramural focal activities or transmural propagations. While these efforts could provide characterization of 3D cardiac pathophysiology, expert interpretation is required to deduce the arrhythmogenic mechanisms, arrhythmic patterns and arrhythmogenesis locations [9].

When the interests comes to noninvasive 3D cardiac electrophysiological imaging, the *a priori* physiological knowledge has been recognized as essential and recent efforts revolve around the physiological-model-based approaches to fully utilize such knowledge [7,8]. In practice, both the *a priori* physiological models and *patient specific* data are indispensable but imperfectly reliable. To address this issue, we have developed a model-constrained Bayesian framework to image the spatiotemporal evolution of 3D TMPs from BSPMs, given patient heart and torso structures from tomographic medical images [8].

Aiming towards noninvasive 3D imaging of cardiac arrhythmias, our current work adapts the general framework in accordance to specific arrhythmogenic mechanisms of interests. As initial efforts, this paper focuses on pathologies exhibiting volumetric abnormality, such as the transmural conduction disorders or intramural focal events. Post analysis on recovered arrhythmic activities, including the localization of the ectopic foci, not only indicates applicable framework setups in different arrhythmias, but also provides in-depth insights into the strengthes and limitations of the framework.

2 Methodology

2.1 3D Imaging of Cardiac Electrophysiology: The General Model-Constrained Bayesian Framework

The ultimate rationale of this model-constrained Bayesian framework is that the combination of *a priori* physiological knowledge and *patient specific* observations, with allowance for their respective uncertainties, is a necessary paradigm for the inverse electrocardiography (IECG) [8]. For an integral understanding, the essential architecture of this framework is outlined in Fig. 1 and briefly reviewed in the following.

Stochastic Cardiac Electrophysiological System. The cardiac electrophysiology is modeled as a stochastic nonlinear dynamic system in order to 1), incorporate *a priori* physiological knowledge to constrain the inverse solution, and

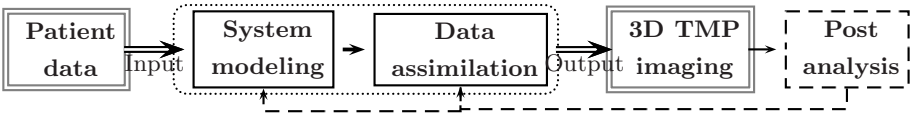

Fig. 1. The general framework for noninvasive imaging of 3D cardiac electrical pathophysiology (primary architecture is contained within the dotted frame): solid line indicates previous efforts, while dashed line represents developments in current work

establish physical-based TMP-BSP relationship; and 2), explicitly accounts for complicate model and data uncertainties in practice.

The constraining cardiac electrophysiological system, customized to patient heart-torso model derived from tomographic images, consists of the 3D TMP evolution model (1) for system dynamics, and the TMP-BSP projection model (2) for system observation:

$$\begin{cases} \frac{\partial \mathbf{U}}{\partial t} = -\mathbf{M}^{-1}\mathbf{K}\mathbf{U} + f_1(\mathbf{U}, \mathbf{V}) \\ \frac{\partial \mathbf{V}}{\partial t} = f_2(\mathbf{U}, \mathbf{V}) \end{cases} \tag{1}$$

$$\mathbf{\Phi} = \mathbf{H}\mathbf{U} \tag{2}$$

where (1) represents Fitzhugh-Nagumo-like (FHN) reaction-diffusion equations [10,11] and (2) is derived following the quasi-static electromagnetism. $\mathbf{U}$, $\mathbf{V}$ and $\mathbf{\Phi}$ are vectors of TMPs, repolarization variables and BSPs. $\mathbf{M}$ and $\mathbf{K}$, constructed based on the meshfree method, account for the intercellular coupling of electrical propagation, while $\mathbf{H}$ is obtained via a boundary element integral with embedded meshfree approximation [8]. The structures of patient heart and torso, including myocardial inhomogeneity and anisotropy, are encoded in these matrices. $f_1(\mathbf{U}, \mathbf{V})$ and $f_2(\mathbf{U}, \mathbf{V})$, general descriptors of cellular TMP dynamics, are to be specified in accordance to different applications.

Concerned with *model deficiencies* and *observation errors* in practice, a stochastic state space representation of (1,2) is formulated:

$$\mathbf{X}_k = \tilde{F}(\mathbf{X}_{k-1}) + \omega_k \tag{3}$$

$$\mathbf{Y}_k = \tilde{\mathbf{H}}\mathbf{X}_k + \nu_k \tag{4}$$

where the state vector $\mathbf{X}_k$ consists of unknown variables under study and varies in different applications. In pure TMP estimation, for instance, $\mathbf{X}_k = [\mathbf{U}_k^T \mathbf{V}_k^T]^T$. The observation vector $\mathbf{Y}_k = \mathbf{\Phi}_k$. $\tilde{F}(\cdot)$ and $\tilde{\mathbf{H}}$ are transformed from (1) and (2) respectively[1]. ω_k, ν_k correspond to independent, additive random errors (Gaussian) with zero means and covariances $\mathbf{Q}_{\omega_k}$, $\mathbf{R}_{\nu_k}$.

[1] The fourth-order Runge-Kutta solver is embedded in the inversion to implicitly discretize the dynamic model (1), so $\tilde{F}(\cdot)$ does not possess an explicit form.

Sequential Data Assimilation. Given patient specific BSPMs, sequential data assimilation is then performed on the constraining system to map patient specific TMPs from BSPMs. In brief, the prediction of the nonlinear TMP dynamics, following the TMP dynamic model (1), is firstly carried out by the unscented transform (UT) [12]. With the arrival of new BSPM data, the prior TMP predictions are subsequently corrected according to the TMP-BSP projection model (2), via the standard KF update. With common physiological knowledge, this sequential *prediction-correction* algorithm is initialized with the prior probabilistic distribution of $\mathbf{X}_0$ and iterates to convergence [2].

2.2 Noninvasive 3D Imaging of Cardiac Arrhythmias

The model-constrained Bayesian framework provides a rather general paradigm for the 3D imaging of cardiac electrophysiology. Towards the 3D imaging of cardiac arrhythmias, such general framework should be adapted in accordance to specific arrhythmogenic mechanisms under study.

Framework Specification. The foremost step during the specification involves the selection of appropriate TMP evolution models (1), primarily determined by the characteristic pathophysiological phenomena of interests and the preference of efficiency versus accuracy in practice. Then, the degree of model uncertainties is imposed in accordance to inevitable model-data mismatch. When necessary, higher degrees of uncertainties are introduced to reduce over-constraining and enhance patient specificity. Currently this is achieved by using *free* parameters which controls primary electrical properties. As such, we could focus on electrical behaviors rather than physiological changes in tissues, and ensure the tractability and feasibility of the inverse process. Based on these specifications, suitable data assimilation techniques, such as pure state estimation or joint/dual state-parameter estimation, could be chosen. Expert examinations on BSPMs/ECGs provide reliable guidance for this specification process, and exemplary framework setups in different cardiac arrhythmias will be given in section 3.

Nevertheless, note that the constraining models will not involve any *a priori* knowledge about the pathology under study, and the data assimilation is initialized with normal physiological knowledge. It gives a *rigorous* test on the performance of normal constraining models in pathological conditions.

Post-analysis. After obtaining estimated TMP dynamics, its difference from normal TMP dynamics is measured on each material point (particles in mesh-free representation of the heart model), through the correlation coefficient (CC) and the relative mean squared error (RMSE). Such simple local TMPs analysis provides a brief pathophysiology assessment.

For arrhythmogenesis localization, two different post-processings are employed. From the most negative 5-point derivative of individual TMP waveforms, the electrical activation time is generated to reflect possible intramural focal activities.

[2] Mathematical details are omitted due to the limited space.

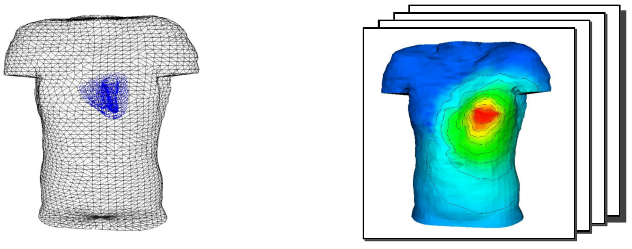

Fig. 2. Left: specific heart-torso model used in current study. The isotropic and homogeneous torso model is represented by triangular elements. The anisotropic and inhomogeneous heart model is composed of meshfree particles and embedded into the torso via a coarse registration according to the proper position, size and orientation of the heart. Right: representative input BSPM sequences.

In simultaneous state-parameter recovery, mixture-model-based clustering [13] is carried out on estimated parameters. Firstly, the parameter set is modeled by a finite normal mixture distribution, wherein each probability distribution corresponds to a group of parameters in the same pathophysiological conditions. The well-known EM algorithm is then performed to classify different groups of parameters and accordingly identify the arrhythmogenesis with abnormal-valued electrical properties.

The post-analysis can provide feedback to the framework for refined estimation (Fig. 1). Besides, it provides valuable insights into the strengthes and limitations of current framework, indicating applicable setups for different arrhythmias and directions for future improvements.

3 Results and Discussions

In the following, physically meaningful phantom experiments are carried out on a specific heart-torso model with geometry provided by [14] and [15] (Fig. 2 (left)). In order to demonstrate the benefits of 3D rather than heart-surface-based TMP imaging, current studies focus on typical cardiac arrhythmias with volumetric abnormality. Simulated BSPMs and TMP reference data for different pathological patterns are used as the *ground truth*, which can hardly be known for specific patients. Noise-corrupted BSPMs are used as framework inputs (Fig. 2 (right)). These initial computational experiments can give straightforward assessment of the applicability of this novel framework.

Brunch Bundle Blocks (BBB). BBB is a relatively frequent occurrence in a variety of medical conditions and usually have different clinical significance requiring different medical measures. Manifested as transmural conduction disorders, this type of pathology would be more closely understood by 3D rather than heart-surface-based TMP imaging. Since responsible mechanisms for BBBs are relatively straightforward, no particular requirements are imposed on the specification of the general Bayesian framework. In current studies, the normally

Table 1. RMSE, CC and maximum local errors of the estimates against ground truth for BBB conditions, in terms of mean ± deviance at the presence of 20dB WGN. The TMP values are normalized between 0 and 1.

Error Metric	RBBB	LBBB	posterior hemiblock	anterior hemiblock
RMSE	0.0179±0.0071	0.0493±0.0216	0.0615±0.0217	0.0645±0.0272
CC	0.9998±1.4e-004	0.9986±0.0012	0.9980±0.0015	0.9977±0.0023
Max.error	0.0408±0.0268	0.1085±0.0775	0.1269±0.1048	0.1428±0.1326

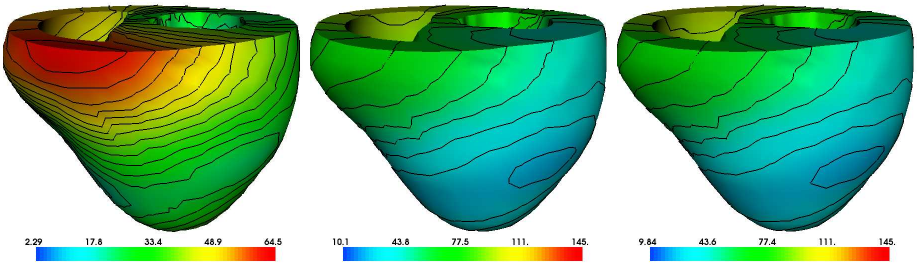

Fig. 3. 3D ventricular activation ischrones. Left to right: normal pattern, *true* RBBB pattern and estimated pattern computed from 3D TMP recovery in current framework. The color bar encodes the values of activation time. The black contour indicates the activation time ischrones.

parameterized FHN-type model [11] and pure state estimation is used to carry out a series of tests on different BBB conditions, including blockages in right brunch bundle (RBBB), left brunch bundle (LBBB) and left anterior / posterior fascicle (hemiblock). Table 1 summarizes the recovery errors at the presence of 20dB white Gaussian noises (WGN) in BSPMs, indicating the consistent accuracy of the results. For reference, the true 3D myocardial activation ischrone of RBBB is illustrated in Fig. 3 with its normal counterpart. Instead of normal simultaneous propagation in both ventricles, RBBB shows obvious abnormal sequential electrical propagation from the left to the right ventricle. The activation duration (encoded by the color bar) is also distinctly prolonged. Current framework closely recover the abnormality (Fig. 3), except for the initial period of the cardiac cycle due to the false *a priori* knowledge. These observations demonstrates the strength of the Bayesian framework in dealing with pathologies with BBB-type mechanisms.

Intramural Focal-Arrhythmia. Focal-arrhythmias, depending on the nature of the ectopic foci, might manifest either as occasional premature beats or serious ventricular tachycardia (VT) even ventricular fibrillation (VF). Due to the common existence of *intramural* focal activities, the potential of 3D TMP imaging for accurate localization of arrhythmogenesis is of considerable clinical utility, especially for guiding nonpharmacological clinical approaches (*e.g.* ablation).

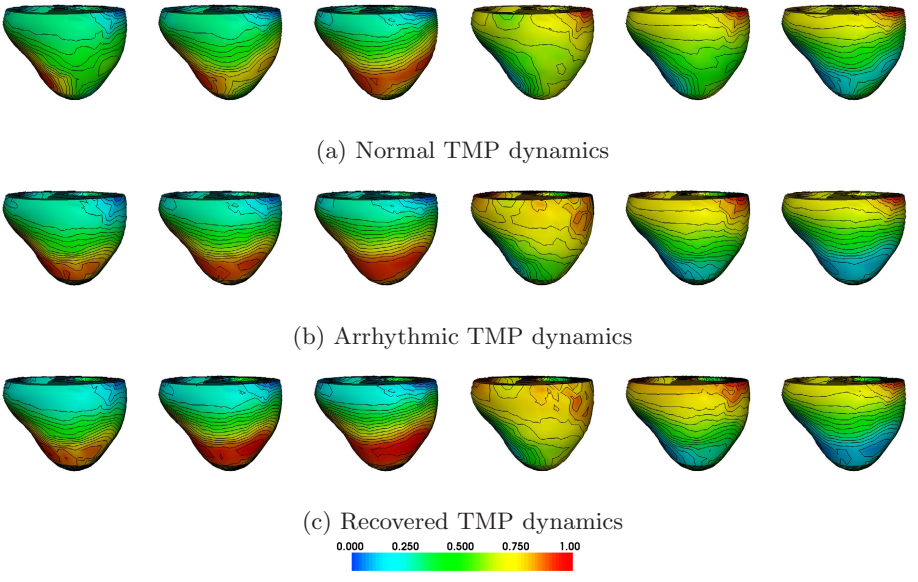

Fig. 4. Anterior view of 3D ventricular TMPs in focal-arrhythmia caused by premature excitations. Left to right: depolarization at 28, 31, 35ms; repolarization at 270, 273, 231ms. The color bar encodes the normalized TMP values, while the black contour indicates the isochrones.

Case descriptions. A specific region on the endo-/subendo-cardium is picked as the ectopic foci. Case I involves intramural premature excitation, which is induced by partially suppressing normal sinus rhythm and stimulating the ectopic foci at around $7ms$ after electrical pulses arrive at ventricles. This premature excitation takes control of ventricular excitation and replaces ordinary activation sequence (Fig. 4 (a)(b)). Case II represent VT caused by fast pacemakers or ventricular pacing, where the same foci is set with automatic rhythm faster than SA node. As a result, an abnormal second depolarization takes place within a cardiac cycle (Fig. 5 (a)).

Framework specification. To allow the influence of the refractoriness on the development of focal-arrhythmias, and capture the pathophysiological character without involving ambiguous physiological conditions underlying ectopic foci, the FHN-type model:

$$\begin{cases} \frac{\partial \mathbf{u}}{\partial t} = u(u-a)(1-u) - v \\ \frac{\partial \mathbf{v}}{\partial t} = b(u - dv) \end{cases} \tag{5}$$

with *excitability* controlled by a [10] is utilized. b, d, parameters controlling other electrical properties, are normal-valued in current study.

In case I, a involves time-variant even transient errors, thus pure state estimation is employed. In case II, the abnormal automaticity is related to physical

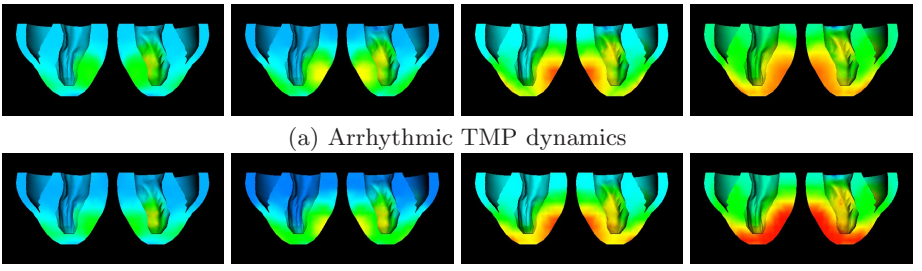

(a) Arrhythmic TMP dynamics

(b) Recovered TMP dynamics

Fig. 5. Volumetric TMP evolutions in focal-arrhythmia induced by fast pacemakers or ventricular pacing, showing the second depolarization sequence within a cardiac cycle (normally, TMPs are at resting values during this period). Left to right: abnormal depolarization at 296, 303, 310, 317ms. The same color bar as Fig. 4 is used.

conditions of the underlying tissues and gives persistent errors in a, hence both state estimation and dual state-parameter estimation are studied to enable the comparison between different framework setups.

Experiment results and discussions. The following studies are made on results from 20dB-WGN-corrupted BSPMs. In Case I, quality of the recovery generally falls into 2 groups. For premature excitations, consistent recovery is achieved with CC = 0.97 ± 0.0053 and RMSE = 0.19 ± 0.0707 in regions surrounding the ectopic foci, while the timely and accurate capture of the ectopic foci is not ensured. For delayed excitations, the framework fails near the assumed earliest excited tissues while farther away, it again provides satisfactory recovery with CC = 0.97 ± 0.0070 and RMSE = 0.16 ± 0.0813. The recovered 3D arrhythmic TMP maps are presented in Fig. 4 (c) and representative local TMP waveforms in Fig. 6. The electrical activation map is then generated on the results to detect the foci with descending likelihood, showing a 66.7% accuracy in capturing the true foci among the most likely suspects.

In Case II, by state estimation only, the abnormal second activation sequence is mostly captured with relatively correct temporal location except failures in assumed earliest excited tissues. Similarly, the farther away from those tissues the better is the result (CC = 0.98 ± 3e-004, RMSE = 0.07 ± 0.0245), while the nearer, the more it tends to be only of qualitative consistency (Fig. 6). Recovered second activation sequence is shown in Fig. 5 (b). Alternatively, dual estimation without prior knowledge on the foci (a on all material points are uniformly initialized with normal value 0.1) results in TMP estimates in similar quality, but the parameter clustering accurately identify the foci with abnormal values (a = -0.433 ± 0.0245) out of other normal tissues (a = 0.096 ± 0.0234).

Some interesting conclusions can be made from these experiments. For abnormality occurring near the beginning of the cardiac cycle, the performance in different regions heavily depends on their distances to the assumed earliest excited

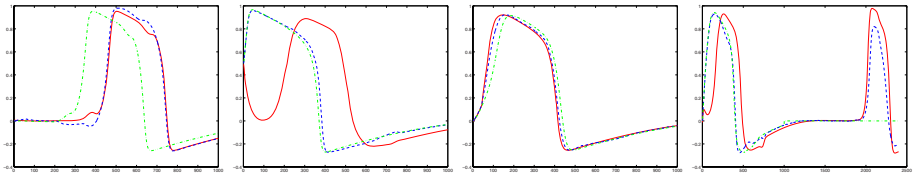

Fig. 6. TMP waveforms representative of different pathophysiological phenomena (x-axis: filtering steps, y-axis: TMP values). Left to right: delayed excitation farther from (first) and around (second) assumed earliest excited tissues, premature excitation (third) and faster excitation near prior earliest excited tissues (fourth). Comparisons are among the true arrhythmia (red), estimates (blue) and normal dynamics (green).

tissues. It can be naturally explained: at initial steps far away from algorithm convergence, the estimates are more inclined to the false prior information than patient data. For abnormality occurring later in the cardiac cycle, therefore, the accuracy improves along with the convergence of the algorithm.

As illustrated, the strength of the framework in consistently recovering abnormal excitations provides the possibility of approximate foci localization. For cases involving premature excitations, state estimation with electrical activation mapping is able to approximately locate the arrhythmogenesis. For those related to fast pacemakers, dual estimation can provide more accurate localization. These results are expected to be fed back to the framework to further improve recovery quality.

4 Conclusions

In this paper, we further develop the general Bayesian framework [8] and adapt it to specific cardiac arrhythmias with *volumetric* abnormality, so as to demonstrate the benefits and clinical significance of *3D* TMP imaging. At current stage, the framework can not provide as accurate arrhythmogenesis localizations as the state-of-art electrophysiological study (EPS), nor is it able to produce highly realistic description of cardiac arrythmic dynamics. However, its ability to extract volumetric and patient specific information in a noninvasive manner, including approximate location of intramural focal activity, is encouraging for its potential clinical/research significance.

As shown in this study, the lose of volumetric information in BSPMs largely impedes the 3D TMP imaging. While model-constrained paradigm appears as a solution, its performance in pathological conditions is degraded by the regional and time-variant model deficiencies. The incorporation of complementary, volumetric cardiac information into the BSPM-based recovery framework, we believe, would be necessary. Tomographic medical image sequences, which contain temporally sparse but spatially dense cardiac information, become ideal data sources to compensate these limitations. Therefore, we are seeking to improve the Bayesian framework to integrate the functional (BSPMs) and structural

images (tomographic image sequences) for 3D TMP mapping, wherein tomographic image sequences not only provide patient geometry but also dynamically complement BSPMs by offering volumetric and dynamic cardiac electrophysiological information.

References

1. Nash, M.P., Pullan, A.J.: Challenges facing validation of noninvasive electrical imaging of the heart. A N E (1) pp. 73–82 (2005)
2. Malkin, R.A. et al.: Advances in electrical and mechanical cardiac mapping. Physiol Meas 26, 1–14 (2005)
3. Oster, H.S., Taccardi, B., Lux, R.L., Ershler, P.R., Rudy, Y.: Noninvasive electrocardiographic imaging: reconstruction of epicardial potentials, electrograms, and isochrones and localization of single and multiple electrocardiac events. Circ. 96, 1012–1024 (1997)
4. Huiskamp, G., Greensite, F.: A new method for myocardial activation imaging. IEEE Trans. Bio. Med. Eng. 44(6), 446 (1997)
5. Pullan, A.J., Cheng, L.K., Nash, M.P., Bradley, C.P., Paterson, D.J.: Noninvasive electrical imaging of the heart: theory and model development. ABME pp. 817–836 (2001)
6. Messnarz, B., Modre, B.T.R., Fischer, G., Hanser, F.: A new spatiotemporal regularization approach for reconstruction of cardiac transmembrane potential patterns. IEEE Trans. Biomed. Eng. 51(2), 273–281 (2004)
7. He, B., Li, G., Zhang, X.: Noninvasive imaging of cardiac transmembrane potentials within three-dimensional myocardium by means of a realistic geometry aniostropic heart model. IEEE Trans.Biomed.Eng. 50, 1190–1202 (2003)
8. Wang, L., Zhang, H., Liu, H., Shi, P.: Imaging of 3d cardiac electrical activity: A model-based recovery framework. In: MICCAI. vol. I, pp. 792–799 (2006)
9. Oster, H.S., Taccardi, B., Lux, R.L., Ershler, P.R., Rudy, Y.: Electrocardiographic imaging: noninvasive characterization of intramural myocardial activation from inverse-reconstructed epicardial potentials and electrograms. Circ. 97, 1496–1507 (1998)
10. Rabinovitch, A., Aviram, I., Gulko, N., Ovsyshcher, E.: A model for the propagation of action potentials in non-uniformly excitable media. J. theor Biol. 196, 141–154 (1999)
11. Rogers, J.M., McCulloch, A.D.: A collocation-galerkin finite element model of cardiac action potential propagation. IEEE Trans Biomed Eng. 41(8), 743–757 (1994)
12. Julier, S., Uhlmann, J.: A new extension of the kalman filter to nonlinear systems. In: AeroSense. pp. 182–193 (1997)
13. Mclachlan, G.J., Basford, K.E.: Mixture models: inference and applications to clustering, N.Y (1988)
14. MacLeod, R., Johnson, C., Ershler, P.: Construction of an inhomogeneous model of the human torso for use in computational electrocardiography. In: IEEE EMBS. (1991) 688–689
15. Nash, M.: Mechanics and Material Properties of the Heart using an Anatomically Accurate Mathematical Model. PhD thesis, Univ. of Auckland, New Zealand (1998)

Forward and Inverse Solutions of Electrocardiography Problem Using an Adaptive BEM Method

Guofa Shou[1], Ling Xia[1], Mingfeng Jiang[1,2], Feng Liu[3], and Stuart Crozier[3]

[1] Department of Biomedical Engineering, Zhejiang University, Hangzhou, P.R. China, 310027
xialing@zju.edu.cn
[2] The College of Electronics and Informatics, Zhejiang Sci-Tech University, Hangzhou, P.R. China, 310018
[3] The School of Information Technology and Electrical Engineering, The University of Queensland, St. Lucia, Brisbane, Queensland 4072, Australia

Abstract. The construction of geometry models of heart-torso is critical for solving the forward and inverse problems of magneto- and electro-cardiography (MCG/ECG). Boundary element method (BEM) is a commonly used numerical approach for the solution of these problems and it requires the modeling of interfaces between various tissue regions. In this study, a new BEM (h-adaptive type) has been applied to the ECG forward/inverse problems. Compared with those traditional BEMs, the adaptive BEM can self-adjust the number and size of the boundary element (BE) meshes according to an error indicator, and thus can save a lot of computational time and also improve the accuracy of the forward and inverse solutions. In this paper, the procedure of the adaptive triangular mesh generation is detailed and the algorithm is tested using a concentric sphere model and a realistic heart-torso model. For the realistic torso model, to improve the numerical accuracy, a number of new nodes are added on the basis of initial torso BE meshes, and the corresponding node coordinates are determined using an approach called Parametric Fourier Representation (PFR) of closed polygons. The simulation results show that the adaptive BEM is more accurate and efficient than traditional BEMs and therefore it is a very promising numerical scheme for ECG forward/inverse problems.

Keywords: h-adaptive BEM, ECG, Forward Problem, Inverse problem.

1 Introduction

The main task of Electrocardiography (ECG) is to interpret the electrical activities of the heart from the recorded body surface potentials (BSPs), which involves the so-called "forward" and "inverse" problems [1]. The former deals with the modeling of the potential distribution on the body surface from equivalent cardiac sources or epicardial potentials (EPs), and the latter estimates the cardiac equivalent sources or reconstructs the EP distribution, myocardial activation sequences, etc.[1,2]. Similar to the electromagnetic imaging simulation study for electro- and magneto-encephalography (EEG/MEG) [3], the ECG forward/inverse problems require the construction of geometry models including torso, heart, and lung, etc. Once the geometry models are available, a numerical approach is required to solve the involved

F.B. Sachse and G. Seemann (Eds.): FIMH 2007, LNCS 4466, pp. 290–299, 2007.

field problem. The widely used numerical methods for electromagnetic problem can be classified into two categories [4]:

1. Volume approach, it is based on differential equations techniques, and typical algorithms include finite element method (FEM) [5, 6], finite difference method (FDM) [7] and finite volume method (FVM) [8].
2. Surface approach, it is based on integral function technique and the typical algorithm is the boundary element method (BEM) [5, 9, 10, 11].

For the surface approach, the interfaces of different conductivity regions are merely required for modeling. Therefore this approach can significantly reduce the number of unknown variables, however, it is very difficult to handle anisotropic regions; while the volume approach is very suitable to model the inhomogeneous volume conductor problems but it will lead to a large amount of unknown variables. These two approaches have their own advantages and can be applied to different problems. Seger [4] and Martin [12] even integrated these two methods for ECG field calculation.

In the BEM, the BE mesh is critical and directly influences the solution accuracy. In the field of computational bio-electromagnetic field, previous research on BEM can be summarized into two classes: construction of the realistic BE mesh model using a number of elements [13, 14], or sparse mesh model using higher-order elements [9, 11]. For ECG problem, to our knowledge, the adaptive method has only been used in FEM modeling of cardiac field [6]. In this study, we employ the adaptive BEM for this problem and attempt to find an accurate and efficient numerical scheme for forward/inverse solution.

Since the introduction of the adaptive BEM in the 1980s, it has been applied in various fields [15, 16]. In this paper, we used the h-adaptive BEM, in which the number of element increases by adding new nodes and the order of interpolation function is unchanged during refinement. In the h-adaptive BEM, it is important to determine the coordinates of those new added nodes. For regular model such as sphere, it is very easy to find the coordinates. For realistic torso model, it will be obtained indirectly, for example, through medical image reconstruction methods [17, 18]. In this study, the Parametric Fourier Representations (PFR) [18] of closed polygon is applied to estimate both the in-slices and inter-slices nodes.

In this paper, we firstly describe the modeling process of h-adaptive BEM for ECG problem, and then test the proposed algorithm with a concentric sphere model and a realistic human model. The inverse solutions using initial BE meshes and adaptive BE meshes are also compared.

2 Adaptive BEM Analysis for ECG Forward Problem

2.1 The Forward Problem

In terms of the EPs, the ECG forward problem can be formulated as Laplace's equation with Cauchy boundary conditions [1]:

$$\nabla \cdot \sigma \nabla \Phi = 0 \qquad \text{in } \Omega \tag{1}$$

$$\Phi = \Phi_0 \quad \text{on } \sum \subseteq \Gamma_T \quad \text{and } \sigma \nabla \Phi \cdot n = 0 \quad \text{on } \Gamma_T \tag{2}$$

where Φ is the quasi-electrostatic potentials, σ is the conductivity tensor, Γ_T and Ω represent the surface and volume of the thorax, respectively.

2.2 Boundary Integral Equation

Using the Green second identity

$$\int_S (A\nabla B - B\nabla A)\cdot \vec{n} dS = \int_V (A\nabla^2 B - B\nabla^2 A) d\Omega \tag{3}$$

and taking the fundamental solution u which satisfies

$$\nabla^2 u^* + \delta = 0 \tag{4}$$

where δ denotes Dirac's delta function, we have

$$c(p)\Phi(p) - \int_S (u^* \nabla\Phi - \Phi q^*)\cdot dS = 0 \tag{5}$$

where p is an arbitrary field point, q denotes $\nabla\frac{1}{r}$, while r is the distance between the source point and field point p, and $c(p)$ depends on the location of p: $c(p)=4\pi$ when p is inside Ω; $c(p)=0$ when p is outside Ω; $c(p)=2\pi$ when p is on the smooth boundary.

2.3 Discretization Error and Residual

After the discretization of the boundary S with M triangles and defining q as the charge and displace ▽Φ in Eq. (5), we have

$$c(p_i)\Phi(p_i) - \sum_{m=1}^{M} \int_{S_m} (u^* q - \Phi q^*)\cdot d\Gamma = 0 \tag{6}$$

The potential and flux charge values on the jth element are approximated by a linear combination of their nodal values and the interpolation functions are as follows.

$$\Phi(p_j) = \sum_i N_i(p_j)\cdot \Phi_i \quad \text{and} \quad q(p_j) = \sum_i N_i(p_j)\cdot q_i \tag{7}$$

The approximated solutions of Φ and q are $\hat{\Phi}$ and $\hat{q}$, respectively, and the errors of potential and charge, e_Φ and e_q, are

$$e_\Phi = \Phi - \hat{\Phi}, \quad e_q = q - \hat{q} \tag{8}$$

In Eq. (6), if we substitute $\hat{\Phi}$ and $\hat{q}$ for Φ and q, Eq. (6) is not satisfied perfectly and therefore, the residual R is

$$R(p_j) = c(p_j)\hat{\Phi}(p_j) - \sum_{m=1}^{M} \int_{S_m} (u^* \hat{q} - \hat{\Phi} q^*) \cdot d\Gamma \tag{9}$$

In the collocation formulation, R is forced to be zero when the boundary points are taken as the collocation points.

Finally, the system equation with matrix-form can be written as

$$Ax = b \tag{10}$$

where A is the transfer matrix, x and b are the potential vectors on epicardial surface and body surface.

2.4 The Error Indicator from the Boundary Integral Equation

In the adaptive BEM, the error estimation is the most important component, which is the factor to determine the accuracy of the approximated solutions and drives the whole discrete meshes' adaptive refinement procedure. The error estimation schemes are classified into the residual-type, the integral equation-type, the node sensitivity-type and the solution difference type [15]. In this paper, we used residual-type [16].

The approximated solution by BEM does not necessarily satisfy Eq. (5) at positions other than collocation nodes. In this work, the square of residual is used as the error indicator (see Eq. (11)). Since the collocation node is positioned at each end of the line element and the maximum discrepancy between the interpolated boundary potential and the value obtained by Eq. (5) can be expected at the points furthest from these nodes, i.e., at the centroid of that triangle element. The local error indicator at the element center is used directly as the error indicator for the entire element. In order to reduce the computational effort, the boundary element error indicator is obtained from the weighted summation of local error indicators (see Eq. (12)).

$$\hat{R}^2(p_j) = (c(p_j)\hat{\Phi}(p_j) - \sum_{m=1}^{M} \int_{S_m} (u^* \hat{q} - \hat{\Phi} q^*) \cdot d\Gamma)^2 \tag{11}$$

$$\hat{R}^2_{\Gamma_m} = \sum_j \omega_j \cdot \hat{R}^2(p_j) \quad \text{and} \quad \hat{R}_\Gamma = \sum_m \hat{R}_{\Gamma_m} \Big/ m \tag{12}$$

where ω_j is the weight and is used to compute the element error indicator, $\hat{R}_{\Gamma_m}$ is the error indicator of the element Γ_m and $\hat{R}_\Gamma$ is the mean error indicator of the whole element. The selection of ω_j and p_j is the same as that in B chtold's [16].

2.5 h-Adaptive BE Mesh Generation

The flowchart of adaptive mesh generation is shown in Fig. 1. The calculation of electric potential starts from an initial triangular mesh and the triangular mesh is partially divided into small triangles by a refinement procedure and new node is

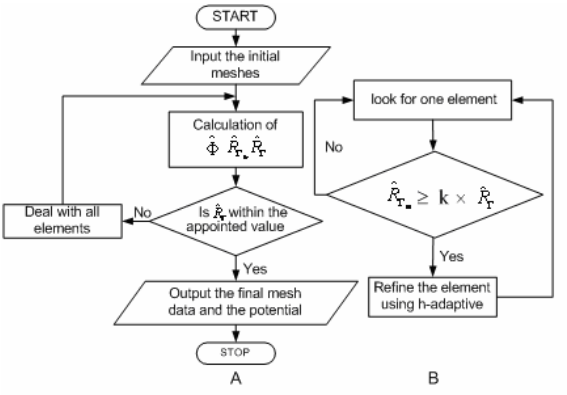

Fig. 1. A. The flowchart of the adaptive triangular mesh generator. B. The process of refinement for a specific element.

added on the center point of the refined element. Then the triangles are rearranged using the joint quality factors of triangular pair [19]. The criterion for the mesh refinement is an error indicator expressed in Eq. (13). In this equation, the parameter k is a constant which controls the degree of refinement in each iterative procedure. The iteration is stopped when the error estimation $\hat{R}_\Gamma$ is less than a predetermined value (See Fig.1 (A)).

$$\hat{R}_{\Gamma_m} \geq k \times \hat{R}_\Gamma \tag{13}$$

3 The Parametric Fourier Representation of Realistic Torso Model

In the h-adaptive BEM described above, new nodes need to be added to the initial mesh. For the regular geometry model such as sphere, it is very easy to find the parameter function. However, additional efforts have to be taken to determine the nodes in the realistic torso model and we use PFR for this problem [18]. In general, there are very sparse nodes in an initial torso model; with PFR approach [18], dense nodes can be obtained not only in in-slices but also within inter-slices. Here, the approximation quality can be easily controlled by the alternation of number of harmonics.

At first, the PFR for each closed polygon is determined. In the next step, a new set of equiangular points is generated by PFR for each closed polygon. For the realistic torso model, two PFR sets are used. The first set is for the transversal slice and it can generate more nodes in one slice. After the nodes in each transversal slice are determined, a closed curve in the sagittal direction is then formed. The second set of PFR is for the closed curve in the sagittal direction. The dense nodes can be gotten determined from the second set. Fig.2 shows the meshing results for a human torso using the above described PFR method. In this case, the number of harmonics is 10, and the nodes of the torso boundary are 412(A), 1322(B) and 5402(C), respectively.

4 The Inverse Calculation of the ECG Problem

The geometry model generated by the proposed h-adaptive BEM is used for the ECG inverse calculation. The ECG inverse problem is ill-posed and it requires the regularized numerical procedure [1, 2]. In the paper, the zero-order Tikhonov regularization and the GCV are applied [20, 21]. With respect to assumed 'exact' solution from forward simulation, the inverse solution is evaluated using relative error (RE) and correlation coefficient (CC).

5 Results

Two simulation protocols with increased complexity are used to validate the proposed h-adaptive BEM for ECG problem. The first one is the concentric sphere heart-torso model which is often used in ECG simulation, with known analytical BSP distribution induced by a limited number of dipoles placed within the inner sphere. In this model, the radii of the two spheres are 4 and 10 centimeter, respectively. The number of nodes and elements of 'heart' sphere are 122 and 240, and the 'torso' sphere is 38 and 72. The second one is the realistic heart and torso geometry models based on CT images with less nodes on the torso compared with previous application [22]. The initial numbers of nodes and elements are 165 and 315 for the heart, and 210 and 416 for the torso, respectively.

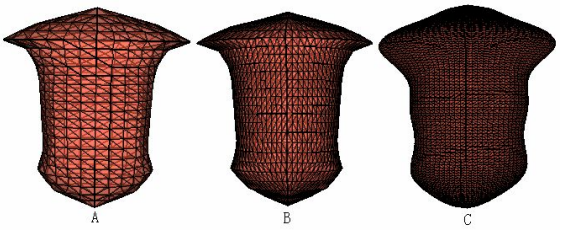

Fig. 2. The BE model of a realistic torso. A, the initial torso model (412 nodes); B, the torso model generated with PFR for transversal slices (1322 nodes); C, the torso model using PFR for both the transversal slices and sagittal direction (5402 nodes).

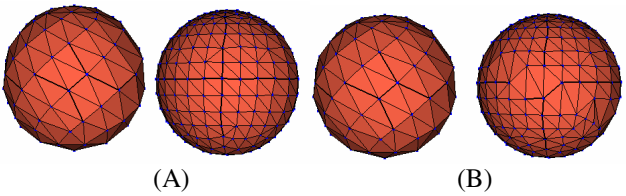

Fig. 3. The refined results of sphere mesh for torso. (A) Model I, dipole orientation: zero degree. (B) Model II, dipole orientation: 30 degrees.

In this study, we only refine the torso meshes and keep BE meshes of the heart model unchanged. For the sphere model, two different dipole orientations are used for the forward ECG calculations, i.e., the single dipole is located at the center of the sphere with a zero degree of azimuth angle in the first simulation (Model I), and with a 30 degree of azimuth angle in the second one (Model II). In the realistic torso-heart model based simulation, a single dipole is located inside the heart model and its orientagtion: both altitude and azimuth angles are 100 degree.

For the concentric sphere model, the BE meshes are generated with two-iteration refinement. Fig.3 shows the mesh profile and Fig.3 (A) is for the Model I and Fig.3 (B) is for Model II. It is noted that for the first-iteration refinement, the mesh results of these two models are quite similar to each other, while for the second-iteration the forward calculation of BSPs modify the mesh profiles. The RE and CC of those forward calculated BSPs using different meshes are summarized in Table 1. From this table, it can be seen that the RE of forward calculation is decreased while the CC is increased after mesh refinement.

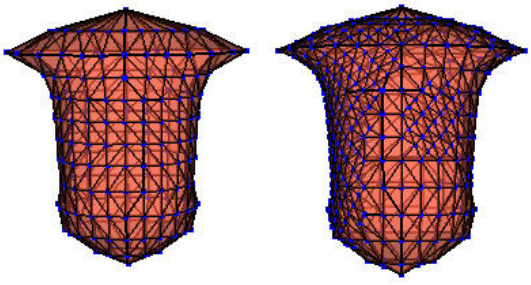

Fig. 4. The refinement of the realistic torso model. A. The initial mesh; B. The refined mesh.

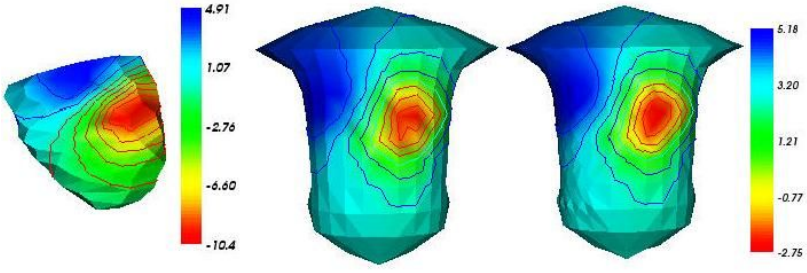

Fig. 5. Epicardial and body surface potential (BSP) distributions. A. Eepicardial potential distribution; B. BSP distribution simulated using initial BE meshes; C. BSP distribution simuated using refined BE meshes.

Fig.4 shows the results for the realistic heart-torso BEM model and Fig.4 (A) is the initial mesh model and (B) is the refined mesh model. For the realistic torso model, single-iteration refinement is enough and the parameter k is 0.3 (see Eq.15). The

corresponding BSP distributions in the realistic-model based simulation are shown in Fig.5. From this figure, it can be seen that the potential distribution is much smoother using the refined meshes.

For all these three models with various meshes, the EPs are inversely calculated. Fig.6 shows the EP distribution and Fig.6 (A) is the 'exact' solution obtained from forward modeling, Fig.6(B) and (C) are the inverse solutions using initial and refined torso meshes. RE and CC of the inverse calculations are summarized in Table.1. From this table, it can be seen that the RE and CC values in Model I and Model II are not constant, the RE in Model I increases and CC in Model I decreases, and the RE in Model II decreases and CC increases. These variations in the inverse solutions implied that the dense mesh structure might not provide the improved solution for ECG problem. In the realistic torso-heart model, the RE decreases almost 10% and the CC increases as well, this demonstrates that the h-adaptive BEM provide high-quality BE meshes and leads to better solution. This is clearer in Fig.6, in which the inversely recovered EP distribution using the refined torso meshes is more similar to the 'exact' profile, especially in the back part of the heart model. Therefore, the application of the h-adaptive BEM can improve the ECG inverse solution.

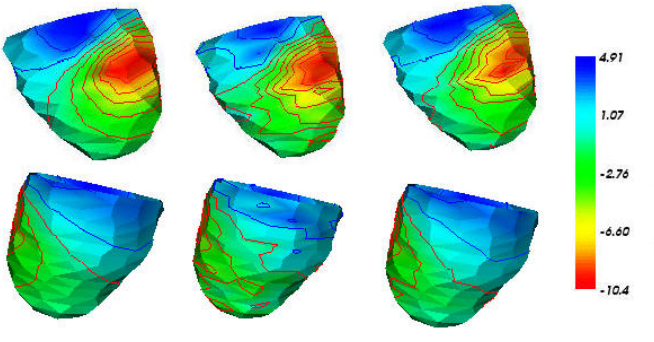

Fig. 6. The 'exact' (forward solution) and the inversely calculated EPs using the initial and refined torso mesh models. Left panel: 'exact' solution; Middle panel: inverse solution using initial mesh; Right panel: inverse solution using refined mesh model.

Table 1. CC and RE results of the application of h-adaptive BEM in three simulations

	Iteration	node	mesh	CC forward	RE forward	CC inverse	RE inverse
Model I	0	38	72	0.9998	0.1872	0.9994	0.0345
	1	110	216	1.0000	0.0776	/	/
	2	326	648	1.0000	0.0471	0.9988	0.0501
Model II	0	38	72	0.9968	0.1670	0.9995	0.0316
	1	110	216	0.9971	0.0874	/	/
	2	304	604	0.9974	0.0743	1.0000	0.0026
Realistic model	0	210	416	/	/	0.9769	0.2001
	1	421	838	/	/	0.9901	0.1296

6 Discussion and Conclusion

This study describes an adaptive BEM implementation and an approach for creating a more detailed realistic BEM models from the initial coarse torso meshes. The proposed algorithm is tested with a concentric sphere model and realistic human data model with a dipole source inside the heart model. Compared to the standard BEM, the accuracy of the forward and inverse solution for this specific ECG problem is improved by using the new adaptive BEM. For example, for the concentric sphere model, the RE of the forward solution is decreased by near 10%; for the realistic human torso model, the RE of the inverse solution is also decreased by 10%. Interestingly, the results show that denser mesh structure does not always lead to better numerical solution. From the sphere model simulation, it is found that the dipole orientation influences the accuracy of the adaptive BEM solution. Therefore, to obtain robust and accurate inverse solution, more work need be done for the realistic model, in which the dipole orientations can be varied constantly during the activation course.

In conclusion, the application of adaptive BEM in the ECG problem can avoid complicated mesh construction procedure and thus save a lot of computational time. Using this adaptive technique, for patient-specific ECG/EEG studies, it is feasible to build BEM models with automatic mesh generation.

Acknowledgments. This project is supported by the 973 National Key Basic Research & Development Program (2003CB716106), the 863 High-tech Research & Development Program (2006AA02Z307), the National Natural Science Foundation of China (30570484) and the Program for New Century Excellent Talents in University (NCET-04-0550).

References

1. Gulrajani, R.M.: The Forward and Inverse problems of Electrocardiography. IEEE. Eng. Med. Bio. 17(122), 84–101 (1998)
2. Dössel, O.: Inverse Problem of Electro- and Magnetocardiography: Review and Recent Progress. Int. J. Bioelectromagnetism 2(2) (2000)
3. Michel, C.M., Murray, M.M., Lantza, G., Gonzaleza, S., Spinellib, L., Peralta, R.G.: EEG source imaging. Clin. Nerophysiol. 115, 2195–2222 (2004)
4. Seger, M., Fischer, G., Modre, R., Messnarz, B., Hanser, F., Tilg, B.: Lead field computation for the electrocardiographic inverse problem-finite elements versus boundary elements. Comp. Meth. Prog. Biomed. 77(3), 241–252 (2005)
5. Johnson, C.R.: Computational and numerical methods for bioelectric field problems. Crit. Rev. Biomed. Eng. 25(1), 1–81 (1997)
6. Johnson, C.R.: Adaptive Finite Element and Local Regularization Methods for the Inverse ECG Problem. In: Inverse Problems in Electrocardiology, Advances in Computational Biomedicine, Edited by Peter Johnston, WIT Press vol. 5, pp. 51–88
7. Nixon, J.B., Rasser, P.E., Teubner, M.D., Clark, C.R., Bottema, M.J.: Numerical model of electrical potential within the human head. Int. J. Numer. Methods Eng. 56, 2353–2366 (2003)

8. Harrild, D.M., Henriquez, C.S.: A finite volume model of cardiac propagation. Ann. Biomed. Eng. 25(2), 315–334 (1997)
9. Ghosh, S., Rudy, Y.: Accuracy of quadratic versus linear interpolation in noninvasive electrocardiographic imaging (ECGI). Ann. Biomed. Eng. 33, 1187–1201 (2005)
10. Akalm-Acar, Z., Gençer, N.G.: An advanced boundary element method (BEM) implementation for the forward problem of electromagnetic source imaging. Phys. Med. Biol. 49, 5011–5028 (2004)
11. Fischer, G., Tilg, B., Wach, P., Modre, R., Leder, U., Nowak, H.: Application of high-order boundary elements to the electrocardiographic inverse problem. Comput. Meth. Pro. Biomed. 58, 119–131 (1999)
12. Buist, M., Pullan, A.: Torso Coupling Techniques for the Forward Problem of Electrocardiography. Ann. Biomed. Eng. 30, 1187–1201 (2002)
13. Ferguson, A.S., Stroink, G.: Factors affecting the accuracy of the boundary element method in the forward problem - I: Calculating surface potentials. IEEE Trans. Biomed. Eng. 44, 1139–1155 (1997)
14. Fuchs, M., Jörn, K., Wagner, M., Hawes, S., Ebersole, S., Ebersole, J.S.: A standardized boundary element method volume conductor model. Clin. Nerophysiol. 113, 702–712 (2002)
15. Kita, E., Kamiya, N.: Error estimation and adaptive mesh refinement in boundary element method, an overview. Eng. Anal Bound Elem. 25, 479–495 (2001)
16. Bächtold, M., Emmenegger, M., Korvink, J.G., Baltes, H.: An error indicator and automatic adaptive meshing for electrostatic boundary element simulations. IEEE Trans.Computer-Aided Design. 16, 1439–1446 (1997)
17. Hren, R., Stroink, G.: Application of the surface harmonic expansions for modeling the human torso. IEEE Trans. Biomed. Eng. 42, 521–524 (1995)
18. Zilkowski, M., Brauer, H.: Methods of mesh generation for biomagnetic problems. IEEE Trans. Magn. 32, 1345–13487 (1996)
19. Lindholm, D.A.: Automatic triangular Mesh Generation Surfaces of Polyhedra. IEEE Trans. Mag. 6, 2539–2542 (1983)
20. Hansen, P.C.: Rank-Deficient and Discrete Ill-Posed Problems: Numerical Aspects of Linear Inversion. SIAM, Philadelphia, 199
21. Shou, G.F., Jiang, M.F., Xia, L., Wei, Q., Liu, F., Crozier, S.: A comparision of different choices for the regularization parameter in inverse electrocardiography problem. IEEE Eng. Med. Biol. Soc. 28th Ann. Int. Conf. 28, 3903–3906 (2006)
22. Xia, L., Huo, M., Wei, Q., Liu, F., Crozier, S.: Electrodynamic Heart Model Construction and ECG Simulation. Methods Inf. Med. 45, 564–573 (2006)

Contributions of the 12 Segments of Left Ventricular Myocardium to the Body Surface Potentials

Juho Väisänen[1], Jesús Requena-Carrión[2], Felipe Alonso-Atienza[2], Jari Hyttinen[1], José Luis Rojo-Álvarez[2], and Jaakko Malmivuo[1]

[1] Ragnar Granit Institute, Tampere University of Technology, Tampere, Finland
juho.vaisanen@tut.fi
[2] Teoría de la Señal y Comunicaciones, Universidad Carlos III, Leganés, Spain

Abstract. Experimental and inverse approaches have been applied in studying the contributions of different parts of the myocardium to the ECG measurements. Also optimal electrode locations for different clinical purposes have been studied by applying body surface maps. It is valuable to know where the measured ECG is actually generated. Thus the measurements can be designed to be most optimal to measure certain myocardial sources. Here we assess the contributions of 12 left ventricular segments to the potentials of 117 surface leads. The study is based on the numerical lead field analysis combined with the cardiac activation modeling. We analyzed the contributions of the signals generated by different segments to the total signal generated by the left ventricle. It was found that anterior segments have high contributions to the leads on the lower left thorax and inferior segments on the leads on the lower left back. These results were expected based on the previous clinical studies.

1 Introduction

Today various electrode systems are applied in measuring the electrical activity of myocardium. The properties and benefits of these electrocardiography (ECG) lead systems, such as multielectrode systems with 24 to 190 electrodes or standard 12-lead ECG have been studied widely. All the studies have tried to answer, one way or another the questions; How many leads are needed for different measurement purposes and where they should be located. Trägårdh and colleagues [1] have recently published a good review of these clinical studies. In the present paper we study the contributions of 12 left ventricular segments to the body surface potentials measured in 117 leads, i.e. which source locations within the left ventricular myocardium are actually measured by each lead. The analysis is based on the sensitivity distributions of surface electrodes and simulated cardiac activation.

The past body surface potential map (BSPMs) studies have suggested optimal electrode locations for different clinical cases such as detection of infarctions and ischemia [2-4]. Many of these studies suggest electrode locations which are specific to measure and indicate changes in the activation of different parts of myocardium such as anterior segments of left ventricle. The studies of optimal measurement leads

F.B. Sachse and G. Seemann (Eds.): FIMH 2007, LNCS 4466, pp. 300–309, 2007.

to detect different cardiac abnormalities have been mainly conducted by statistical data analysis of measured BSMPs [5-7]. The statistical methods and BSPMs are very applicable when surface measurements are studied and evaluated. Despite of their efficiency these methods might be impractical or even unuseful when designing and optimizing new measurements and devices such as implantable ECG monitors.

The true origins of the electrophysiological phenomena measured are of interest in many cases. Inverse problems and experimental setups have been applied in studying the effects of spatial and temporal characteristics of cardiac activation on the body surface potentials [8-12]. For example MacLeod and colleagues found in [8] that some locations of infarcts are more visible in some body surface potentials than in others and there exist so called silent changes in cardiac activation which are not projected to the body surface. These studies suggest that there are electrode locations which are sensitive to activation arisen in certain areas of myocardium.

When designing novel measurement devices and setups it would be beneficial to know where to locate the electrodes to measure the target signals and monitor their source regions as efficiently as possible. One might also desire to concentrate the measurement in a certain area of the cardiac muscle, like in a segment of the left ventricle. Thus the electrodes should be located in such places that the measurement is most specific to the activation arising in this region of interest. This is especially of interest when monitoring different cardiac arrhythmias or changes in activation of certain segment of myocardium after infarctions. Also designing of active cardiac devices such as implantable defibrillators and pacemakers could benefit of such approach where the measurement and stimulating lead configurations could be studied by modeling approach.

Modeling of measurements and their sensitivity distributions together with simulation of cardiac activity serves time and cost effective approach to study the properties of measurements. In the past only few methods have been applied in analyzing the sensitivity distributions of measurement setups. Thus the possibilities of sensitivity distribution analysis have not been utilized as efficiently as possible. The lead field and reciprocity approaches provide effective tools to analyze the sensitivity distributions. In this paper we apply the lately developed method which combines the lead field approach with dynamic source model of cardiac activation in studying the origins of the body surface potentials. The sensitivity distributions were calculated in a realistic model of human thorax by applying finite difference method (FDM). We simulated the dynamic source distribution in left ventricular myocardium and calculated the lead fields of 117 body surface leads. Signals in these leads can be solved by combining the lead fields and source distributions. In [13] we have presented a method to analyze the contribution of certain source volume to the measured signal by estimating the mean square difference (MSD) between signal generated by these sources and the signal generated by the whole source volume. Here we studied the contributions of 12 segments of left ventricle to the source volume which generates signal having 10 % MSD when compared to the signal generated by whole source volume. This analysis was applied to all leads and thus we can estimate which electrode location is most optimal to measure different segments of left ventricular myocardium with the applied activation model.

2 Material and Methods

2.1 Finite Difference Method

In the FDM the segmented volume data, e.g. from an MRI dataset, are divided into cubic elements forming a resistive network. In short the resistances of the elements correspond to the tissue resistivities and the dimensions of the elements correspond to the resolution of the dataset. The network can be described as a set of linear equations which present the potentials and currents in the model. The FDM is based on the Poisson's equation that can be used to describe the bioelectric quasistatic source-field problems [14]. FDM models are discrete and thus continuous Poisson's functions have to be discretized to form linear equations. A potential distribution within the model for a specific source configuration is solved with these linear equations with iterative methods [15]. The use of FDM method in modeling sensitivity distributions is validated in [16].

Realistic model of human anatomy
The FDM allows the implementation of complex anatomic geometries from the image data, and the resulting potentials and currents can be calculated within the whole volume conductor model [15]. In the present study we applied a FDM model of the 3D male thorax based on the Visible Human Man dataset (VHM) [17, 18]. The applied dataset represents data on 95 segmented slices where resolution in the slices close to the heart was 1.67 mm x 1.67 mm x 4 mm and elsewhere 1.67 mm x 1.67 mm x 8 mm. Model contains altogether 2.7 million nodes with 2.6 million elements. The model applied contains over 20 different organ and tissue types with corresponding resistivities which are listed in Table 1 [16]. Figure 1 illustrates the model with 117 electrode locations applied in the study.

Table 1. Resistivity values in the model. Blood masses include atrium, ventricles, aortic arch, ascending aorta, descending aorta, superior vena cava, inferior vena cava, carotid artery, jugular vein, pulmonary artery, pulmonary vein and other blood.

Organ/tissue	Resistivity (Ωcm)	Organ/tissue	Resistivity (Ωcm)
Air	10^{10}	Kidney	600
Skeletal muscle	400	Liver	600
Fat	2000	Heart muscle	450
Bone	2000	Heart fat	2000
Lungs	1325	Blood masses*	150
Stomach	400	Other tissues and organs on thorax	460

2.2 Lead Field and Reciprocity

The sensitivity distribution of the measurement configurations can be illustrated and analyzed with lead fields. Lead fields are thus applied to describe and study the

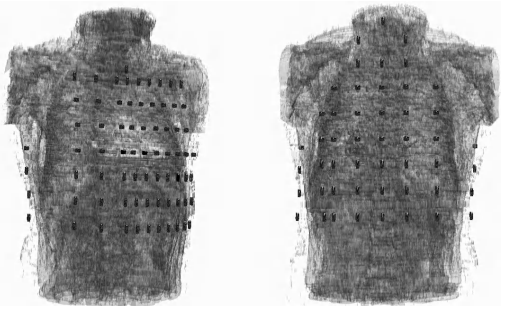

Fig. 1. 3D model of torso containing 117 electrode locations

measurement of the electric fields in the volume conductor. Lead current density vectors define the relationship between the measured potential in the lead and the current sources in the volume conductor following Equation 1. The measured lead voltage is dependent on the magnitudes of the lead and source current vectors as well as the angle between these vectors [14].

$$z[n] = \sum_{V} \frac{1}{\sigma} \frac{1}{I_r} \bar{J}_L \bullet \bar{J}^i[n] \tag{1}$$

Where $z[n]$ is the lead voltage as a function of time n, $\bar{J}_L$ is the lead current density vector [A/cm^2] , I_r is the applied reciprocal current [A], $\bar{J}^i_{[n]}$ is the current source density vector [A/cm^2] as a function of time, σ is the conductivity [1/Ωcm] of the source location in the volume conductor and V is the source volume.

The lead field in the volume conductor can be established by applying the principle of reciprocity. In [14] it is stated that the current field in the volume conductor raised by the reciprocal unit current (I_r=1 A) applied to the measurement electrodes corresponds to the lead current density and hence to the lead field. The essential benefit of this method is that the sensitivity of a measurement lead at all source locations in the volume conductor can be calculated with a single calculation.

2.3 Cardiac Activation Model

In our implementation we opted for a state machine approach defined previously in [19]. This model of cardiac electric activity reproduces electric restitution of both action potential duration (APD) and conduction velocity (CV), as well as curvature effects. Cardiac tissue is modeled as a grid of discrete elements characterized by three discrete states, namely, *Rest*, *Refractory*1 and *Refractory*2, and transitions among them. The excitation of an element, i.e. the transition from *Rest* to *Refractory*1 is interpreted as a probabilistic event, depending on the amount of excitation in its neighborhood, and the excitability of the element, that can be accessed through the restitution curve of CV. Transitions from *Refractory*1 to *Rest* through *Refractory*2 depend on the current of APD. Additionally, a membrane voltage is assigned at every

time instant. Finally, non-conservative sources at each time n and location i, $\bar{J}^i[n]$, are solved based on the voltage differences and conductivities between neighboring elements.

2.4 Mean Square Difference Estimating Contribution of the Sources to the Signal

In [13] we introduced a method to analyze the contributions of the sources to the measured signal. The contribution of certain sources to the measured signal is defined by the mean square difference (MSD) between the signal generated by these sources and signal generated by whole source volume. Let V be the total source volume and V_o be subset of the sources within the V. Based on (1), we define that the ECG signal $z[n]$ is generated by V and $z_o[n]$ is generated by the source in V_o. If we measure the similarity between $z[n]$ and $z_o[n]$ based on MSD, we obtain:

$$MSD\{V_o\} = E\left[(z[n] - z_o[n])^2 \right] \tag{2}$$

Furthermore, by normalizing MSD by the mean power of whole source volume $z[n]$, P_{zz}, we can obtain a more convenient measurement of similarity relative to the mean power of $z[n]$:

$$MSD_n\{V_o\} = \frac{MSD\{V_o\}}{P_{zz}} \tag{3}$$

2.5 Calculations

We calculated the sensitivity distributions, the lead fields, in a realistic model of the male thorax by applying the principle of reciprocity. The lead fields were calculated for standard 117 body surface electrode leads illustrated in Figure 2. The same lead arrangement has been adopted for example by Kornreich and colleagues [4, 20]. The current distribution corresponding to the lead field current density was generated into the volume conductor by applying the unit currents to the electrode pairs. The calculations were executed with bioelectric field software which applies the Incomplete Cholesky Preconditioner and Conjugate Gradient for solution [21].

Here we study the contributions of the sources of left ventricular segments to the signals measured with 117 leads. The left ventricle was divided into 12 segments based on the standard 12 segment left ventricular subdivision recommended by the Committee on Nomenclature of Myocardial Wall Segments of the International Society of Computerized Electrocardiography [22, 23] illustrated in Figure 3.

We solved source distribution $\bar{J}^i[n]$ for the activation starting on the apex and conducting through the left ventricle over one second. The source distribution was combined with the sensitivity distributions to solve the measured potentials in the surface leads as described by (1). For each lead we evaluated the source volume V_o within the left ventricle which generates signal with 10 % MSD_n compared to the signal generated by whole left ventricle. Further we observed the proportions of the 12 segments in V_o and studied which segments have the largest influence on the signals measured with surface leads.

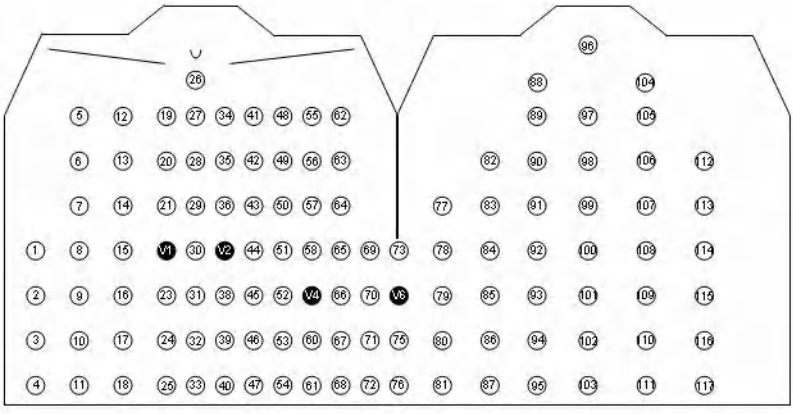

Fig. 2. 117 body surface electrode leads

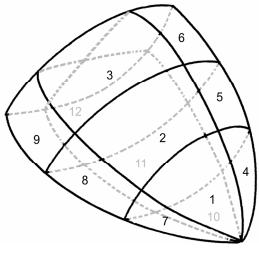

Fig. 3. The standard 12-segment left ventricular subdivision. Segments 1-3 anteroseptal, 4-6 anterosuperior, 7-9 inferior and 10-12 posterolateral.

3 Results

Figure 4 presents for 117 leads the proportions of the 12 left ventricular segments to the source volume which produces signal having 10 % MSD_n when compared to the total signal generated by the left ventricle.

From the results we may observe the segments of the left ventricle which have the highest proportions of the sources measured with surface leads. Thus these leads are most optimal to measure activation generated within the segments. As an example over 30 percent of the sources that produce the signal with 10 % MSD_n in the lead 93 are within the segment 8. Further Segments 8 and 9 have together over 60 % of the sources which produce the signal having 10 % MSD_n in the lead 93.

There are leads that are most optimal to measure different segments. For example approximately 50 % of the sources producing signal with 10 % MSD_n in leads on the mid left thorax are in segments 1, 4 and 5 and fewer than 10 % of the sources are within the segments 8, 9 and 12. Thus these leads are most optimal to measure the signal originating from anterior segments. Leads in lower left back are mainly

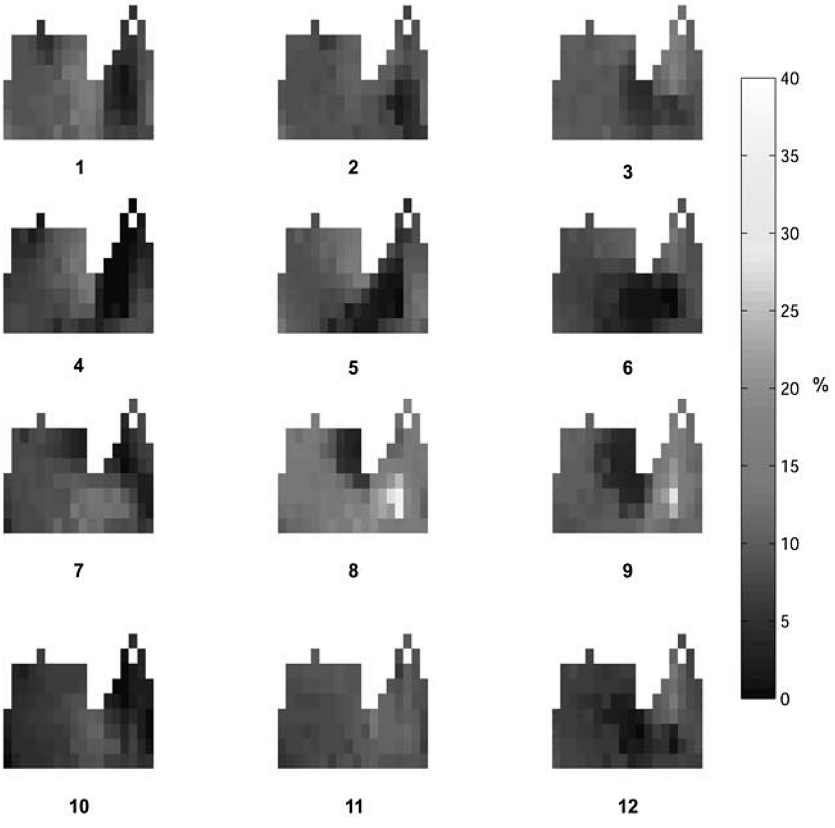

Fig. 4. For 117 leads the proportions of the 12 left ventricular segments in the volume generating signal with 10% MSD_n compare to the signal generated by whole left ventricle. The larger the proportion the higher is the contribution of the segment into the signal measured on the lead and more likely changes in measured signal are originating from the corresponding segment.

measuring the activation of segments 8 and 9 because these segments have approximately 60 % share of the sources measured with these leads.

4 Discussion

Realistic and highly accurate models of the human anatomy are needed to carry out efficient modeling and simulation of the measurements leads. The FDM enables effective use of the models and thus leads to a more accurate modeling of measurements. Nevertheless the accuracy of the results can be affected by the resolution of the model and the number of conductivities modeled. These factors can affect the potential distribution within volume conductor and further the current density vectors which correspond to the sensitivity vectors. The higher the resolution of FDM grid the lower is the numerical error produced by discretization of

conductivities and thus more accurate current density vectors are achieved. Numerical approach applied here takes into account double sided differences of potentials in calculation of sensitivities and thus decreases the numerical error produced by the discretization of conductivities.

The resolution of the FDM model defines the time needed for the calculation. A calculation of sensitivity distribution of a lead in this study took approximately 15 minutes with AMD 3000+ 64Bit, 2 GB RAM. Solving the one second of cardiac activation in left ventricle took less than 3 seconds with Intel P4 2,4GHz and 1.5 GB RAM. Models with higher resolution can be applied in studies with high computational resources without excessive computation times.

Although the model utilized possesses high anatomical accuracy, it has certain other shortcomings. In the present study we applied the finite difference model with a network of resistances featuring the tissue impedance. The human tissues also have capacitive characteristics possibly affecting the current distribution on the thorax. However, it has been recognized that the ratios between conductivities and permittivities of the human tissues on the frequency range of ECG are such that the dielectric behavior of tissues is mainly resistive [24]. Thus the model containing only resistive properties is relevant for our purposes.

Furthermore, the model applied in the present study is isotropic. Anisotropic conductivities, especially of the cardiac muscle would improve the simulations. The model was based on the anatomy of a single human subject and the segmentation of the tissues might also have some shortcomings. In the future we will apply other thorax models to study the effect of model on the results. Also the resolution and segmentation of models will be enhanced.

The MSD was found to be an efficient approach when the contributions of different segments were observed. In the present study we decided to observe the 10% difference but in future studies also other difference should be considered when the contributions of sources are observed. It would be valuable to investigate if the proportions are the same with the larger differences. Also other statistical properties of signals such as standard deviation and correlation will be included in the analysis in future studies.

Kornreich and colleagues have studied which are the most optimal leads to detect anterior and inferior myocardial infarctions. The anterior infarction volume contains segments 1-7, 10 and 11 which are supplied by left descending artery or its branches [23]. The inferior infarction volume contains segments 8 and 9 supplied by inferior descending artery or its proximate coronary [23]. Kornreich and colleagues found in [4] that the optimal leads to detect anterior infarction are located in the left thorax around leads 50 and 69. They also found that the inferior infarction is most optimally detected from the leads on the left lower back. The same conclusions can be obtained from our results because segments involved in anterior infarction have high contributions to the signals measured with leads on the mid-left thoracic region and segments involved in the inferior infarction have high contributions to the leads on lower left back.

Although the model and segmentation of left ventricle to 12-segments are quite coarse the study shows that there are locations which are more specific to measure individual segment and locations which are sensitive for number of segments. It is also shown that the modeling and the analyzing methods presented here provide excellent tools when studying the contribution of myocardial sources to the measured

body surface potentials. In the present study only one type of activation model was applied. The activation model has impact on the results and in the future we will thus apply multiple activation models to study e.g. the effect of starting point of ectopic beat on the sensitivities of the leads. In the future this method will be also applied in studying and designing of implantable ECG monitors as well as analyzing the origins of signals measured with implantable cardiac defibrillators and pacemakers.

Acknowledgements. Authors would like to thank PhD Noriyuki Takano for providing the FDM solver software and MSc Tuukka Arola for providing FDM visualization tool. The work has been supported by grants from the Finnish Cultural Foundation Pirkanmaa Region and the Ragnar Granit Foundation.

References

1. Tragardh, E., Engblom, H., Pahlm, O.: How many ECG leads do we need? Cardiology Clinics 24 (3), 317–330 (2006)
2. Horacek, B.M., Warren, J.W., Penney, C.J., MacLeod, R.S., Title, L.M., Gardner, M.J., Feldman, C.L.: Optimal electrocardiographic leads for detecting acute myocardial ischemia. J. Electrocardiol 34 Suppl, 97–111 (2001)
3. Kornreich, F.: Identification of best electrocardiographic leads for diagnosing acute myocardial ischemia. J. Electrocardiol 31 Suppl, 157–163 (1998)
4. Kornreich, F., Montague, T.J., Rautaharju, P.M., Block, P., Warren, J.W., Horacek, M.B.: Identification of best electrocardiographic leads for diagnosing anterior and inferior myocardial infarction by statistical analysis of body surface potential maps. Am. J. Cardiol. 58(10), 863–871 (1986)
5. Kornreich, F., Montague, T.J., Rautaharju, P.M.: Body surface potential mapping of ST segment changes in acute myocardial infarction. Implications for ECG enrollment criteria for thrombolytic therapy. Circulation 87(3), 773–782 (1993)
6. Finlay, D.D., Nugent, C.D., Donnelly, M.P., Lux, R.L., McCullagh, P.J., Black, N.D.: Selection of optimal recording sites for limited lead body surface potential mapping: a sequential selection based approach. BMC Med. Inform. Decis. Mak. 6, 9 (2006)
7. Aldrich, H.R., Hindman, N.B., Hinohara, T., Jones, M.G., Boswick, J., Lee, K.L., Bride, W., Califf, R.M., Wagner, G.S.: Identification of the optimal electrocardiographic leads for detecting acute epicardial injury in acute myocardial infarction. Am. J. Cardiol. 59(1), 20–23 (1987)
8. MacLeod, R.S., Lux, R.L., Taccardi, B.: A possible mechanism for electrocardiographically silent changes in cardiac repolarization. J. Electrocardiol. 30 Suppl, 114–121 (1998)
9. Burnes, J.E., Taccardi, B., MacLeod, R.S., Rudy, Y.: Noninvasive ECG imaging of electrophysiologically abnormal substrates in infarcted hearts: A model study. Circulation 101(5), 533–540 (2000)
10. He, B., Li, G., Zhang, X.: Noninvasive imaging of cardiac transmembrane potentials within three-dimensional myocardium by means of a realistic geometry anisotropic heart model. IEEE Trans Biomed Eng. 50(10), 1190–1202 (2003)
11. Fukuoka, Y., Oostendorp, T.F., Sherman, D.A., Armoundas, A.A.: Applicability of the single equivalent moving dipole model in an infinite homogeneous medium to identify cardiac electrical sources: a computer simulation study in a realistic anatomic geometry torso model. IEEE Trans Biomed Eng. 53(12 Pt 1), 2436–2444 (2006)

12. Brooks, D.H., MacLeod, R.S.: Electrical imaging of the heart. Signal Processing Magazine, IEEE 14(1), 24–42 (1997)
13. Requena Carrión, J., Väisänen, J., Rojo Álvarez, J.L., Hyttinen, J., Atienza, F.A., Malmivuo, J.: Numerical Analysis of the Resolution of Surface Electrocardiographic Lead Systems. In: proc. 4th Functional Imaging and Modeling of the Heart (2007)
14. Malmivuo, J., Plonsey, R.: Bioelectromagnetism: Principles and Applications of Bioelectric and Biomagnetic Fields. Oxford University Press, New York (1995)
15. Johnson, C.R.: Computational and numerical methods for bioelectric field problems. Crit Rev. Biomed. Eng. 25(1), 1–81 (1997)
16. Kauppinen, P., Hyttinen, J., Laarne, P., Malmivuo, J.: A software implementation for detailed volume conductor modelling in electrophysiology using finite difference method. Comput. Methods Programs Biomed. 58(2), 191–203 (1999)
17. Ackerman, M.J.: The Visible Human Project. J. Biocommun 18(2), 14 (1991)
18. Kauppinen, P., Hyttinen, J., Heinonen, T., Malmivuo, J.: Detailed model of the thorax as a volume conductor based on the visible human man data. J. Med. Eng. Technol. 22(3), 126–133 (1998)
19. Atienza, F.A., Carrion, J.R., Alberola, A.G., Alvarez, J.L.R., Munoz, J.J.S., Sanchez, J.M., Chavarri, M.V.: A probabilistic model of cardiac electrical activity based on a cellular automata system. Revista Espanola De. Cardiologia 58(1), 41–47 (2005)
20. Kornreich, F., Rautaharju, P.M., Warren, J., Montague, T.J., Horacek, B.M.: Identification of best electrocardiographic leads for diagnosing myocardial infarction by statistical analysis of body surface potential maps. Am. J. Cardiol. 56(13), 852–856 (1985)
21. Takano, N.: Reduction of ECG Leads and Equivalent Sources Using Orthogonalization and Clustering Techniques. in Ragnar Granit Institute Tampere University of Technology (2002)
22. Wagner, G.S., Cowan, M.J., Flowers, N.C., Ginzton, L.E., Ideker, R.E., Laks, M.M., Selvester, R.H., Swiryn, S.R.: Report of Committee on Nomenclature of Myocardial Wall Segments. in proc. Computerized Interpretation of Electrocardiograms VII proc. Engineering Foundation Conference (1984)
23. Startt/Selvester, R.H., Wagner, G.S., Ideker, R.E.: Myocardial Infaction. In: Macfarlane, P.W. and Lawrie, T.D.V., Editors.Comprehensive Electrocardiology: Theory and Practice in Health and Disease Pergamon Press pp. 565–629 (1989)
24. Gabriel, S., Lau, R.W., Gabriel, C.: The dielectric properties of biological tissues: II. Measurements in the frequency range 10 Hz to 20 GHz. Phys Med. Biol. 41(11), 2251–2269 (1996)

Numerical Analysis of the Resolution of Surface Electrocardiographic Lead Systems

Jesús Requena-Carrión[1], Juho Väisänen[2], José Luis Rojo-Álvarez[1], Jari Hyttinen[2], Felipe Alonso-Atienza[1], and Jaakko Malmivuo[2]

[1] Departamento de Teoría de la Señal y Comunicaciones, Universidad Rey Juan Carlos, Fuenlabrada, Spain
jesus@tsc.uc3m.es
[2] Ragnar Granit Institute, Tampere University of Technology, Tampere, Finland

Abstract. Non-invasive electrocardiographic (ECG) techniques for assessing the electrical activity of selected regions within the cardiac muscle can benefit from suitable positioning of surface electrodes. This positioning is usually guided heuristically and complemented by clinical and experimental studies, but there is a lack of general methods to characterize quantitatively the ability of a given electrode configuration to focus on selected regions of the heart. In this study we explore an approach to the characterization of the resolution of surface ECG systems based on the concept of Resolution Mass (RM). By integrating bioelectric signal modeling and numerical methods, we explore, in an application example, the location and size of the RM for a multielectrode ECG system. The concept of RM combined with bioelectric signal modeling and numerical methods constitutes a powerful tool to investigate the resolution properties of surface ECG systems.

1 Introduction

Surface electrocardiogram (ECG) is one of the most common diagnostic methods for cardiac diseases. In many diseases, such as ischemia and infarction, the diagnosis involves an estimation of the localization and extension of an abnormal region within the heart. This region is usually determined by detecting well known anomalies in the morphology of conventional 12-lead ECG signals. Diagnostic methods based on ECG techniques can be further refined by an adequate choice of the position and configuration of surface electrodes [1] [2]. From the general principles of Bioelectromagnetism, it is expected that each electrode configuration focuses on different regions of the heart. Therefore, electrode configurations show distinctive intrinsic resolution properties that can provide us with valuable insight into regional information. Usually, the positioning of surface electrodes is guided heuristically and complemented by means of studies in which extended multielectrode systems are used [3] [4] [5]. Nevertheless, a widely accepted quantitative approach to the study of the resolution properties of electrode configurations is still lacking. As a consequence, there is limited agreement on the nature of these resolution properties.

F.B. Sachse and G. Seemann (Eds.): FIMH 2007, LNCS 4466, pp. 310–319, 2007.

The aim of this study is to explore the notion of resolution of surface ECG systems using the concept of Resolution Mass (RM). The RM is defined as the myocardial mass that contributes the most in power terms to the ECG signal. Considering that the heart is the object of our investigation, and that we can only access its state indirectly through ECG signals, we form our approach from two starting points. On the one hand, in order to place the notion of resolution in a quantitative framework, we define a measurement over ECG signals, since they are the only observations. Conventional mean power is a meaningful candidate due to its clear physical meaning. On the other hand, we link ECG signals to the electrical activity of the heart, so that any statement from the previously defined measurement over ECG signals can be extended to the heart itself. This implies modeling ECG signals based on Bioelectromagnetism Theory, according to which bioelectric phenomena arise as a result of the interplay of source and conducting elements in the body [6]. In the context of lead systems, Lead Field Theory is a convenient mathematical formulation from which we can benefit both conceptually and computationally. From these starting points, we approach the notion of resolution by asking what the contribution in power terms of a certain myocardial mass within the heart is to a given ECG signal. We propose to answer it by determining the similarity in mean power between the signals generated by the myocardial mass under investigation and by the whole myocardium, respectively. The knowledge of the contributions of different myocardial masses will, in turn, allow us to decide which one of them can be established as the RM. Since this procedure is not feasible in experimental settings and classical analytical techniques fail in this scenario, numerical analysis will be crucial to this study, by constituting the basic tool to carry what has come to be widely known as experiments *in silico*.

In the following sections, we firstly introduce our implementation of the model of ECG signals in terms of the dynamics of the heart and the lead fields associated to the electrode configuration, i.e., in terms of source and conducting elements. Secondly, we provide a definition of RM, and we propose a numerical procedure to estimate it. Thirdly, we investigate, as an example, the resolution properties of an ECG system over the ventricles. Finally, we summarize our results and propose future applications of the concept of RM.

2 Bioelectric Signal Modeling

In the electric characterization of the human body, two simultaneous features are described, namely its behavior as a source volume and as a conductor volume [6]. A source volume is a tissue that can generate non-conservative electric currents, whereas a conductor volume allows source elements to induce electric potentials in other regions of the body. When such electric potentials are recorded on the skin, a surface ECG signal is obtained. Consequently, any model of ECG signals in terms of the electrical properties of the human body will consist of a description in terms of both cardiac sources and conducting properties of the body.

2.1 Modeling the Cardiac Tissue as a Bioelectric Source

In our implementation we opted for a state machine formulation for the electric activity of cardiac tissue defined previously [7]. This formulation is able to reproduce the electric restitution of both action potential duration (APD) and conduction velocity (CV), as well as curvature effects. Cardiac tissue is modeled as a grid of discrete elements characterized by three discrete states, namely, *Rest*, $Refractory1$ and $Refractory2$, and three transitions among them. The excitation of an element, i.e. the transition from *Rest* to $Refractory1$, is interpreted as a probabilistic event depending on the amount of excitation in its neighborhood and the excitability of the element, which is accessible through the current value of CV. Transitions from $Refractory1$ to *Rest* through $Refractory2$ depend on the current value of APD. Both APD and CV values are updated at every new diastolic interval (DI) based on the curves of electric restitution. Transitions among states, at every time instant n, are defined as follows:

$$\begin{aligned} Rest \rightarrow Refractory1 &: P^j_{exc} \propto CV \cdot Q^j_{exc} \\ Refractory1 \rightarrow Refractory2 &: n - n^j_{desp} \geq F \cdot APD \\ Refractory2 \rightarrow Rest &: n - n^j_{desp} \geq APD \ , \end{aligned} \tag{1}$$

where j identifies an excitable element in the grid, P^j_{exc} is the probability of excitation of j, Q^j_{exc} is the amount of excitation within a neighborhood around j, n^j_{desp} is the instant of depolarization of j, and F is a scalar representing the fraction of APD that j spends at $Refractory1$ while depolarized. Additionally, a membrane voltage is assigned at every time instant. Its value is the usual rest voltage during *Rest* state, and a standard version of an action potential temporarily scaled by the APD during $Refractory1$ and $Refractory2$. Finally, source elements are computed from the voltage differences and conductivities between neighboring elements.

2.2 Modeling the Body as a Bioelectric Conductor

Based on the conducting properties of the body, the solution of the forward problem allows us to obtain the electric potential induced by a source element at every location of the body. From the principle of superposition, given a distribution of source elements within the body, the total electric potential can be expressed as the superposition of the electric potentials generated individually by every source element. Nevertheless, when studying signals recorded by lead systems, we are only interested in the electric potentials induced at a finite number of locations in the body. Furthermore, a formulation that explicitly includes the measurement sensitivity distribution of the lead system could be conceptually more powerful. In this context, Lead Field Theory provides an adequate formulation that is equivalent to the forward solution. It has conceptual

advantages, since it includes in its definition the measurement sensitivity distribution of the lead system, and, if implemented numerically, it is computationally less demanding. According to Lead Field Theory, the signal recorded by a lead system, $z[n]$, can be expressed as a linear combination of source elements in the source volume V as follows:

$$z[n] = \sum_{V} \frac{1}{\sigma} \frac{1}{I_r} \overline{J}_L \cdot \overline{J}_i[n] \; . \tag{2}$$

In this discretized formulation, I_r is the reciprocal current, $\overline{J}_L$ is the lead current density and constitutes the measurement sensitivity distribution, $\overline{J}_i[n]$ denotes the source elements in V, and σ is the conductivity. Conceptually, this approach allows us to interpret the dynamics of $z[n]$ in terms of the dynamics of those regions of V where the sensitivity of the lead system is highest. Computationally, when simulating $z[n]$, it overcomes the need of solving the forward problem for every source element $\overline{J}_i[n]$ at every time instant n. Instead, by virtue of the Reciprocity Theorem, $\overline{J}_L$ is obtained by solving the forward problem once and for all for a reciprocal current applied to the surface electrode, and then, at every time instant n, $z[n]$ is readily calculated from (2).

3 Measuring the Resolution

Let V_o and V_c be two disjoint subsets of the source volume V such that $V = V_o \cup V_c$. From (2), we can express the ECG signal $z[n]$ generated by V as the sum of the signals $z_o[n]$ and $z_c[n]$ induced, respectively, by V_o and V_c:

$$\begin{aligned} z[n] &= \sum_{V} \frac{1}{\sigma} \frac{1}{I_r} \overline{J}_L \cdot \overline{J}_i[n] \\ &= \sum_{V_o} \frac{1}{\sigma} \frac{1}{I_r} \overline{J}_L \cdot \overline{J}_i[n] + \sum_{V_c} \frac{1}{\sigma} \frac{1}{I_r} \overline{J}_L \cdot \overline{J}_i[n] \\ &= z_o[n] + z_c[n] \; . \end{aligned} \tag{3}$$

If we measure the similarity between $z[n]$ and $z_o[n]$ based on Mean Square Difference (MSD), we obtain:

$$\begin{aligned} MSD\left\{V_o\right\} &= E\left[\left(z[n] - z_o[n]\right)^2\right] \\ &= E\left[\left(z_c[n]\right)^2\right] \\ &= P_{z_c z_c} \; , \end{aligned} \tag{4}$$

where E denotes statistical mean. Thus, $MSD\left\{V_o\right\}$ is a measurement of the error involved when approximating ECG signal $z[n]$ to $z_o[n]$. If we normalize

$MSD\{V_o\}$ by the mean power of $z[n]$, $P_{zz} = E\left[(z[n])^2\right]$, we can obtain a more convenient measurement of similarity relative to the mean power of $z[n]$:

$$MSD_n\{V_o\} = \frac{MSD\{V_o\}}{P_{zz}} = \frac{P_{z_c z_c}}{P_{zz}} . \tag{5}$$

We define the RM at level α, RM_α, of a surface ECG as the smallest region V_o within the heart that involves a MSD_n less than α when approximating at the recording site the electric potential generated by the whole heart to the electric potential generated by the RM, i.e.,

$$RM_\alpha = \arg\min_{V_o} \{Size(V_o)\}, \forall V_o / MSD_n\{V_o\} \leq \alpha . \tag{6}$$

In other words, we are measuring the resolution properties of an ECG system in terms of the power of the component z_c of the ECG signal generated in the region excluded from the RM, V_c. The RM has, thus, a clear physical meaning and it is suitable to carry out fair comparisons between electrode systems, since it is obtained from a measurement defined over the ECG signal. In this study, we investigate two properties of the RM, namely, its mass center and its size. The mass center of a RM allows us to determine the location of the RM within the whole source volume. The size is a meaningful parameter to describe the scope of the RM, since it informs us of the ability of the electrode system to focus on selected regions of a given size within the source volume.

We used numerical methods to estimate RM_α in two ways. On the one hand, we obtained the lead field based on Finite Difference Methods (FDM) featuring the Visible Human Man model (VHM), by calculating the electric potential generated by a reciprocal current applied to the surface electrodes [8]. According to the Reciprocity Theorem, generated lead current fields ($\overline{J}_L$) raised by the reciprocal current (I_r) corresponds to the lead field. On the other hand, we generated implicitly the dynamics of $\overline{J}_i[n]$ using a computer, i.e., through numerical simulations. Then, by implementing the model of cardiac tissue as defined earlier, we simulated $\overline{J}_i[n]$ and, for different choices of V_o, from (3) we generated $z_o[n]$, $z_c[n]$ and $z[n]$. Subsequently, from (4) and (5), we estimated $MSD_n\{V_o\}$ and, finally, for every α we determined RM_α according to (6).

4 Example

The characterization of the resolution properties of a surface ECG system based on the determination of RM_α is exemplified here for a 117 unipolar electrode ECG system. From this system, a total of 18 unipolar electrodes distributed around the thorax on the cross section located at the fourth intercostal space were investigated (Figure 1); among them, electrodes numbered 22 and 37 correspond respectively, to precordial leads V_1 and V_2 in conventional 12-lead ECG.

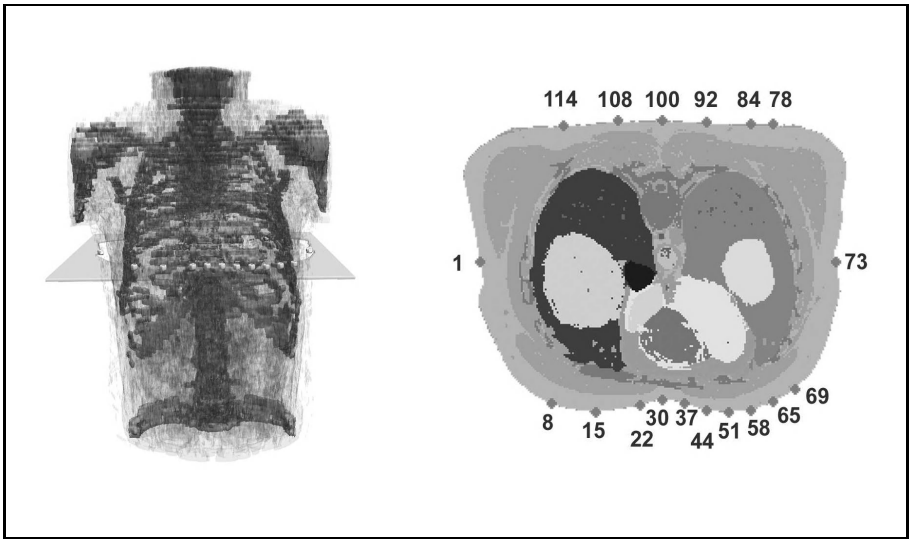

Fig. 1. Thorax model as described by the VHM dataset. Studied surface electrodes are positioned around the thorax on a cross section located at the fourth intercostal space.

We studied RM_α within the ventricles (Figure 2) as a function of α and the position of the electrodes. For this purpose, we calculated numerically $\overline{J}_L$ as described earlier. Then, we programmed the state machine of electric activity of cardiac tissue, and we simulated the stimulation of the ventricular apex at 60 beats per minute during 8 seconds. Progressively larger source volumes V_o were chosen to synthesize signals $z[n]$, $z_o[n]$ and $z_c[n]$, from which corresponding $MSD_n\{V_o\}$ were obtained. Finally, for several values of α, RM_α was determined according to (6).

Figure 3 shows estimated RM_α for electrode 37 (precordial lead V1 in 12-lead ECG) and three values of α: 0.1, 0.2 and 0.5. As it is expected, larger α values lead to a smaller size of RM_α, since α measures the MSD_n involved when approximating the signal induced by the ventricles to the signal induced by RM_α. Furthermore, we can observe that $RM_{0.1}$, $RM_{0.2}$ and $RM_{0.5}$ are geometrically close to the position of electrode 37, which agrees with the fact that the measurement sensitivity decreases with the distance to the electrode. This observation was confirmed for every electrode.

In Table 1, the sizes of $RM_{0.1}$, $RM_{0.2}$ and $RM_{0.5}$ relative to the size of the ventricles can be explored for every electrode. Apart from the decrease in size for larger values of α that was noted earlier, two qualitatively different sets of results are relevant, depending on whether electrodes are positioned on the anterior or the posterior chest. In general, RM_α for anterior electrodes is comparatively smaller than for posterior electrodes. These results can be explained by the fact that distances from the skin surface to the ventricles are greater on the posterior than on the anterior chest (see Figure 1). For example, while the size of $RM_{0.5}$

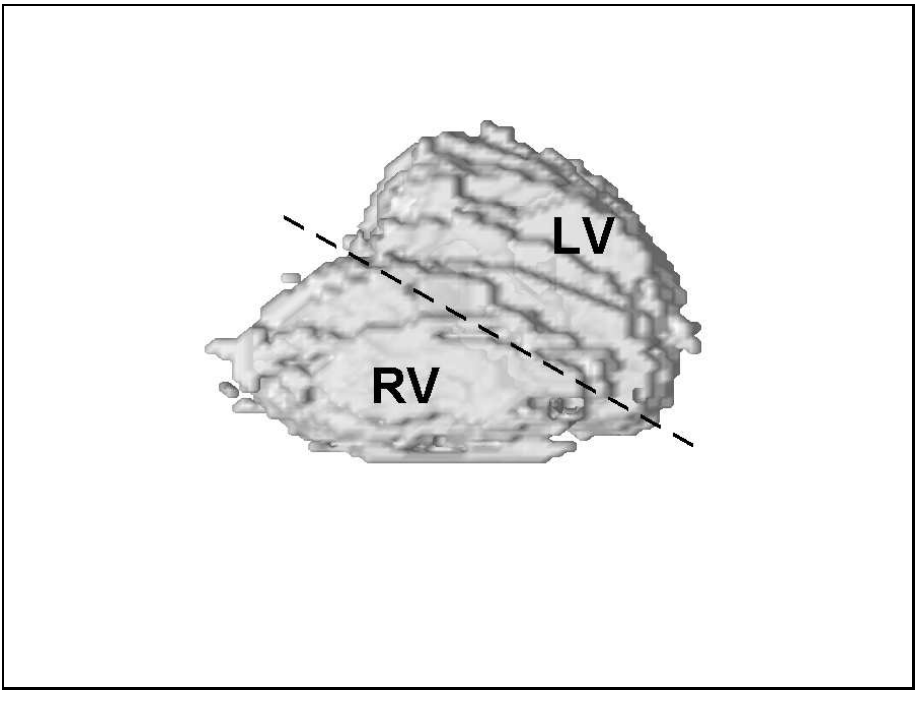

Fig. 2. Superior view of the ventricular myocardial mass as described by the VHM dataset. Right ventricle (RM) and left ventricle (LV) are, respectively, the masses below and above the dashed line.

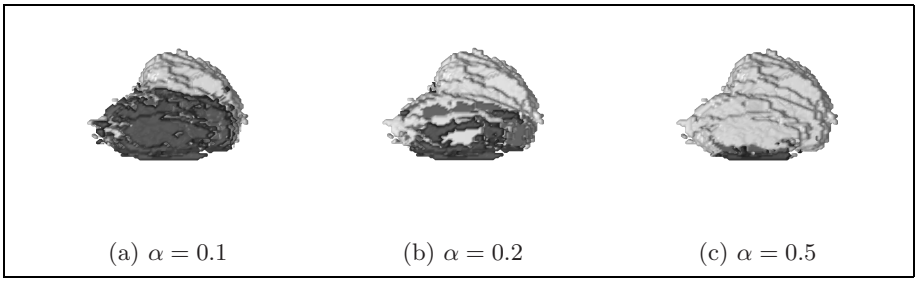

(a) $\alpha = 0.1$ (b) $\alpha = 0.2$ (c) $\alpha = 0.5$

Fig. 3. Superior view of the ventricles (*light gray*) in the VHM model and estimated RM_α (*dark gray*) of electrode 37 (precordial lead V1 in 12-lead ECG) for different values of α. We can observe that larger α values lead to smaller RM_α.

for electrode 84 is roughly 83% of the size of the ventricles, for electrode 37 it is 13%. Therefore, the ability of unipolar electrodes on the posterior chest to focus on small regions of the ventricles will be, in general, poorer than that of electrodes on the anterior chest. It is equally remarkable that the amount of

Table 1. Size of RM_α (relative to the size of the ventricles), for α: 0.1, 0.2 and 0.5

Electrode	1	8	15	22	30	37	44	51	58	65	69	73	78	84	92	100	108	114
$RM_{0.1}$ (%)	55	84	85	73	63	65	64	63	58	54	52	57	87	90	84	69	54	47
$RM_{0.2}$ (%)	25	75	73	53	32	47	44	43	40	38	37	47	85	89	79	58	43	35
$RM_{0.5}$ (%)	10	10	13	2	1	13	22	22	19	17	16	21	75	83	67	28	16	11

Table 2. Decrease of the size of RM_α (relative to the size of the ventricles)

Electrode	1	8	15	22	30	37	44	51	58	65	69	73	78	84	92	100	108	114
$RM_{0.1} - RM_{0.2}$(%)	30	9	12	20	31	18	20	20	18	16	15	10	2	1	5	9	11	47
$RM_{0.2} - RM_{0.5}$(%)	15	65	60	51	31	34	22	21	21	21	21	26	10	6	12	12	27	24

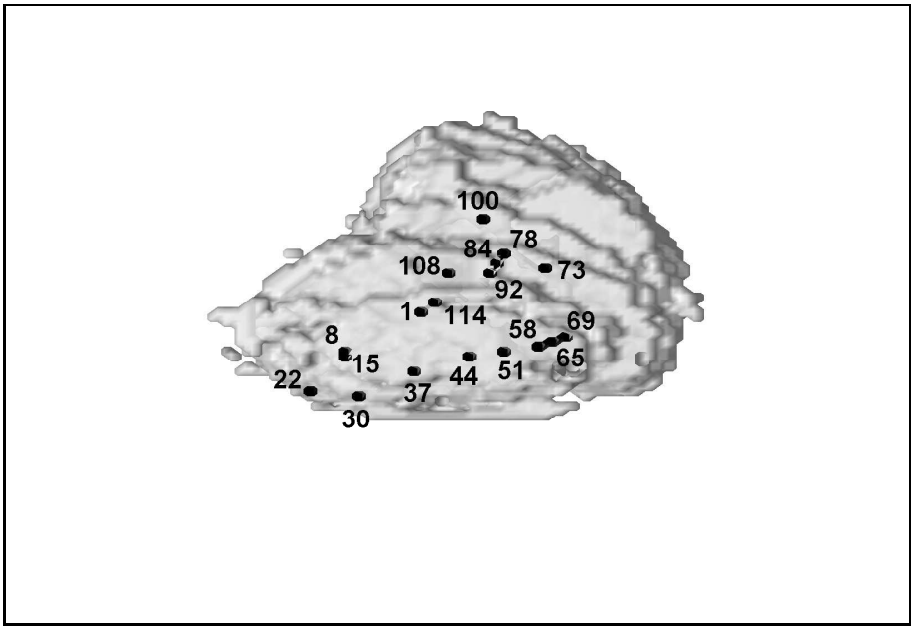

Fig. 4. Locations of the centers of $RM_{0.5}$ in the ventricles for every electrode

variation of the size of RM_α for increasing α is, in general, larger for electrodes positioned on the anterior chest, as shown in Table 2. If we compare once again electrode 84 to electrode 37, $RM_{0.1} - RM_{0.2}$ is for the former 1% whereas for the latter is 18%.

The locations of the centers of the $RM_{0.5}$ for every electrode are shown in Figure 4. Not surprisingly, they are distributed following the locations around the thorax of the corresponding electrodes. These results confirm, therefore, that

electrodes on the anterior (posterior) chest focus on anterior (posterior) walls of the ventricles. Noticeably, the centers of electrodes on the anterior chest are closer to the periphery of the ventricles. Again, this observation can be explained by the relatively smaller size of $RM_{0.5}$ due to the distance separating skin positioning from the ventricles.

5 Discussion

The elucidation of the resolution properties of surface ECG systems can provide us with valuable clinical information, since it allows us to map patterns observed in ECG signals to the regions within the heart that generate them. In this study we combined bioelectric signal modeling and numerical methods to explore the notion of resolution, as expressed in the concept of RM. We defined the RM in terms of the MSD_n resulting from approximating at the recording site, the signal induced by the whole source to the signal induced by the RM. It is, thus, a measurement that has a clear physical meaning and, since it is defined over recorded ECG signals, it is suitable to carry out fair comparisons of the resolution properties of different surface ECG systems.

Numerical methods proved to be the best choice to study the RM, as compared to experimental settings and other analytical techniques. Numerical approaches have, however, general limitations. Since an underlying model is assumed, the significance and generality of the results depend considerably on the ability of the model to describe the physical phenomena under investigation. In this study we have described the conducting properties of the body based on the VHM dataset, and the electrical activity of the heart based on a state machine model. Besides, the dynamics of the sources elements have been generated by simulating the stimulation of the apex at 60 beats per minute. In order to investigate the impact of the choice of the signal model on the scope of the results, in the future we will implement different thorax models and simulate cardiac electrical activity based on other descriptions and stimulation protocols.

In an application example, we showed that the RM in the ventricles depends on the positioning of surface electrodes. Specifically, we showed that both the location and the size of the RM depend on the proximity of the electrodes to the ventricles and on their angular coordinate around the thorax. Our results confirm that, by appropriately positioning the electrodes we can increase the amount of signal from a region of interest within the heart, although there are limits to the ability of an electrode to focus on selected regions smaller than the RM. By placing the notion of resolution in a quantitative framework, this approach complements other experimental and clinical settings intending to establish the limits of the electrocardiography [9]. The determination of the resolution properties of electrode systems can allow us to assess the convenience of standard electrode positioning and to explore new positioning for extracting the maximum amount of physiological information from the ECG. Thus, a quantitative definition of optimal electrode placement can be achieved based on the concept of RM.

In summary, the combination of bioelectric signal modeling and numerical simulations constitute a powerful method to study the resolution properties of ECG systems. Firstly, they provide the formulation needed to estimate the RM. Key features of the RM include its location and its size, from which we can establish limits to the ability of the electrode system to focus on selected regions within the heart. Secondly, it forms a framework to assess, by implementing different anatomical models, the influence on the resolution properties, of factors often regarded as sources of variability, such as the shape of the body, the proportion of tissues or the size of the heart. Thirdly, complete multielectrode systems and varied electrode configurations can be systematically studied and compared, in order to determine optimal electrode placements. Numerical approaches to the resolution can complement other experimental and clinical settings, both as a means of explanation and of future experimental design.

Acknowledgments. This work has been partially supported by a Research Grant from Guidant Spain, and from the Research Project GR/SAL/0471/2004 from Comunidad de Madrid. Jesús Requena-Carrión is supported by grant 01-836-04 from Consejería de Educación de la Comunidad de Madrid.

References

1. Lux, R., Bilbao, M., Pelter, M., Fleischmann, K., Zegre, J., Schindler, D., Drew, B.: Optimal Leads, Estimation, and Continuous Monitoring Improve Detection of Acute MI and Transient Ischemia. J. Electrocardiol. 37 Suppl, 240–243 (2004)
2. Trägård, E., Engblom, H., Pahlm, O.: How many ECG leads do we need? Cardiol. Clin. 24, 317–330 (2006)
3. Kornreich, F., Montague, T.J., Rautaharju, P.M., Block, P., Warren, J.W., Horáček, B.M.: Identification of Best Electrocardiographic Leads for Diagnosing Anterior and Inferior Myocardial Infarction by Statistical Analysis of Body Surface Potential Maps. Am. J. Cardiol. 58, 863–871 (1986)
4. Kornreich, F., Montague, T.J., Smets, P., Rautaharju, P.M., Kavadias, M.: Knowledge-Based System for Classification of Body Surface Potential Maps. In: Computers in Cardiology pp. 479–482 (1990)
5. Horáček, B.M., Warren, J.W., Penney, C.J., MacLeod, R.S., Title, L.M., Gardner, M.J., Feldman, C.L.: Optimal Electrocardiographic Leads for Detecting Acute Myocardial Ischemia. J. Electrocardiol. 34 Suppl, 97–111 (2001)
6. Malmivuo, J., Plonsey, R.: Bioelectromagnetism: Principles and applications of Bioelectric and Biomagnetic Fields. Oxford University Press, New York (1995)
7. Alonso Atienza, F., Requena Carrión, J., García Alberola, A., Rojo Álvarez, J.L., Sánchez Muñoz, J.J., Martínez Sánchez, J., Valdés Chávarri, M.: A probabilistic model of cardiac electrical activity based on a cellular automata system. Rev. Esp. Cardiol. 58(1), 41–47 (2005)
8. Kauppinen, P., Hyttinen, J., Heinonen, T., Malmivuo, J.: Detailed model of the thorax as a volume conductor based on the visible human man data. J. Med. Eng. Technol. 22(3), 126–133 (1998)
9. MacLeod, R., Kornreich, F., van Oosterom, A., Rautaharju, P., Selverster, R., Wagner, G., Zywietz, C.: Report of the first visualization of the reconstructed electrocardiographic display symposium. J. Electrocardiol. 38, 385–399 (2005)

Simultaneous High-Resolution Electrical Imaging of Endocardial, Epicardial and Torso-Tank Surfaces Under Varying Cardiac Metabolic Load and Coronary Flow

Shibaji Shome[1,2] and Rob Macleod[1,2,3]

[1] Nora Eccles Harrison Cardiovascular Research and Training Institute,
University of Utah, UT, USA
http://www.cvrti.utah.edu
[2] Department of Bioengineering,
University of Utah, UT, USA
http://www.bioen.utah.edu
[3] Scientific Computing and Imaging Institute,
University of Utah, UT, USA
macleod@cvrti.utah.edu
http://www.sci.utah.edu

Abstract. We present an experimental preparation that allows simultaneous, high resolution mapping of endocardial, epicardial and torso tank surfaces from an isolated canine heart. The preparation additionally permits control over blood flow rate through a targeted region of the cardiac tissue, the heart rate and the mechanical load on the left ventricle. Adjustment of heart rate and left-ventricular load through a fluid-filled balloon inserted into the left ventricle allow control of metabolic demand. Cardiac potential measurements occur by means of flexible sock-mounted electrode arrays applied to the epicardium and the intraventricular balloon. A preliminary study using this preparation suggests the existence of a heterogenous response of the myocardium to ischemia. Such an experimental model is a useful testbed for many studies, including validation of forward and inverse solutions.

1 Introduction

Cardiac ischemia results from a reduction in blood supply, an uncompensated increase in metabolic demand, or some combination of the two. Understanding of the electrocardiographic markers for all these conditions is necessary to achieve accurate differential diagnosis and monitoring of ischemia and infarction.

In a previous study, we showed that the electrocardiographic responses to ischemia brought about through reduction in blood supply need not have similar characteristics as that induced by uncompensated increases in demand despite assumptions to the contrary by classical ischemia theory[1]. However, our previous experimental setup induced changes in metabolic load by means of only

F.B. Sachse and G. Seemann (Eds.): FIMH 2007, LNCS 4466, pp. 320–329, 2007.

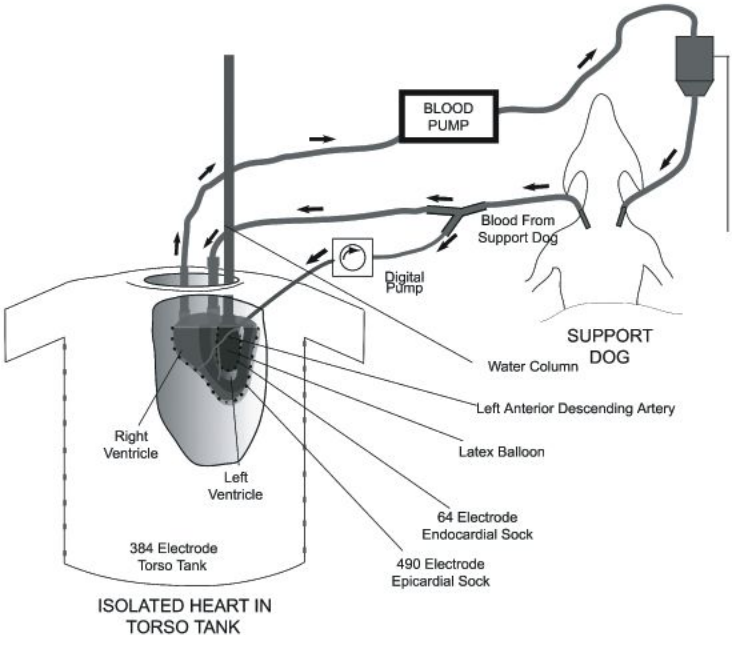

Fig. 1. Schematic of the experimental setup

changes in heart rate. It is well known that pacing rate itself influences cardiac repolarization and we therefore sought to separate the rate effect from that of metabolic load in characterizing the electrocardiographic response to demand ischemia. Moreover, this preparation employed retrograde perfusion by means of the aorta so that the left ventricle contracted around an empty chamber without preload or afterload. Therefore, we sought to retain the Langendorff perfusion method and introduce control over metabolic load by having the left ventricular chamber of the isolated heart pump against a vertical water-filled column. In this study we detail the experimental setup designed to achieve these goals and present results from an exemplary investigation. Some aspects of this study have been presented previously in preliminary form[2].

2 Methods

2.1 Experimental Setup

The experimental setup consisted of a canine heart suspended in a human torso shaped tank, the construction of which has been described previously[1,3] and shown in Fig. 1.

Briefly, the basis preparation employed Langendorff retrograde perfusion by means of cannula inserted in the aorta and the right ventricles. Perfusion was by means of blood supplied from a second, support dog, which was cannulated

to provide arterial blood to perfuse the isolated heart. The right ventricular cannula extracted venous blood that returned through the coronary sinus and the right atrium of the isolated heart and pumped it back to the support dog via a blood pump and a cannula in the jugular vein. In order to control the perfusion to a region of the myocardium, we cannulated a segment of the left anterior descending artery (LAD) and perfused it via a digital rotary pump with blood from the support dog, which allowed for precise control of the coronary flow rate. The temperature of the blood from the support dog was monitored and maintained at physiological levels by means of heated water jackets.

A latex balloon was secured to the end of a rigid tube, the other end of which was connected to a flexible tube of a larger lumen suspended vertically. A 'T' in the rigid tube allowed for the placement of a pressure transducer probe. The balloon was then inserted into a 64-electrode endocardial sock which was held in place by silk ties. This formed the endocardial balloon-sock apparatus that we inserted by means of an incision in the left atrial appendage. Altering the pressure in the balloon forced the heart to work against pressure from the fluid column and also allowed the measurement of potentials from the endocardial region.

The isolated, perfused heart was then suspended in a human torso shaped tank which was filled with an electrolyte of conductivity of 500 Ω-cm. To control the heart rate we applied a bipolar pacing clip to the right atrial appendage. To control the metabolic load we manually adjusted the height of water in the fluid column guided by the readings from the pressure transducer.

The support dog was ventilated with room air and maintained under anaesthesia by means of sodium pentobarbital infusions at regular intervals. Regular monitoring of the blood gases ensured that perfusion and ventilation were adequate so that the pH remained stable throughout the course of the experiment.

2.2 Protocol

We performed two different interventions in the experiment protocol as enumerated below:

1. Varied Load: The heart rate and the coronary flow were maintained at control levels while the metabolic load was progressively increased.
2. Varied Load under Reduced Perfusion: Coronary flow was reduced to $\approx$30 % of normal and then metabolic load increased as in intervention 1 above.

Each parameter change was maintained for 2 minutes.

2.3 Signal Acquisition, Processing and Visualization

Epicardial signals were measured from both ventricles using a 490 electrode sock[1]. The construction of the endocardial sock was similar to that of the epicardial sock in that each electrode consisted of a knot of 0.3 mm silver wire tied into a nylon stocking and the electrodes were spaced about 5 mm apart.

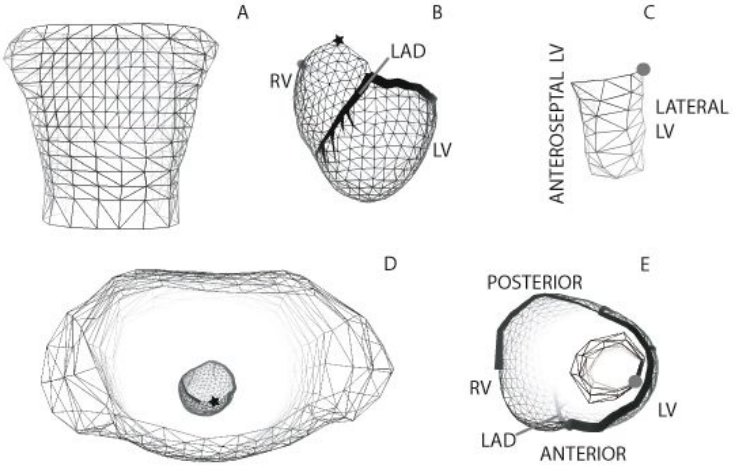

Fig. 2. Panels A, B and C depict the geometric meshes on which the data were visualized. The actual orientation of each mesh with respect to the others is shown in Panels D and E.

The nylon stocking material allowed the electrode array to flex and conform to the shape of the endocardial balloon located inside the sock.

The electrolytic torso tank contained 372 electrodes and the potential reference for all unipolar time signals was a Wilson Central Terminal constructed from separate electrodes in the tank. The signals from all 926 electrodes were acquired simultaneously at a sampling rate of 1000 Hz. Each recorded data segment was 5 s in duration out of which a representative beat was selected for further analysis. At the end of the experiment, a three-dimensional mechanical digitizer (Microscribe from Immersion Corp.) was used to locate landmarks marked on the tank and electrode array, which then provided the reference points for proper orientation of the sock geometry within the torso tank.

Signal post processing consisted of gain adjustment, windowing of representative beats, and baseline correction. In the case of inadequate signal quality of the original recording, Wave Equation Based interpolation[4] was used to reconstruct epicardial electrograms. In this study we present the data as the ST-80 potential, which is the mean potential computed over a 9-ms window centered at 80 ms beyond the J-point in each electrogram. All signal processing steps were carried out using customized software. The data was visualized using *map3d*[5] by mapping the electrograms acquired during the experiment onto the representative geometry for each electrode set. The geometric meshes for each electrode set are shown in Panels A,B and C of Fig. 2.

The orientations of the meshes in Fig. 2 are the same as those presented in the results section. However, the relative positions of each mesh with respect to the others are shown in Panels D and E in Fig. 2. The rightmost edge and the leftmost edge of the endocardial sock as seen in Panel C are aligned with the left

anterior free wall section of the epicardial sock and the left antero-septal region of the epicardial sock, respectively. Similarly, the locations of the marker (star) in Panel B and again in Panel D show that the lateral right ventricle region of the epicardial sock is closest to the anterior torso surface. Because the effects of ischemia were predominantly in the left ventricle, Panel A (and the torso results shown below) shows the posterior view of the torso mesh.

3 Results

We focus here on two results that illustrate one aspect of the interaction between coronary flow and metabolic (mechanical) load on the heart. In both cases, the load increased from control to 2.5 and then 4 times control but in the first case, coronary perfusion was at control levels while in the second case, coronary flow was less that half the level at control.

Varying Load with Normal Coronary Flow. The results for variation in left ventricular load on heart and torso potentials under normal perfusion levels are shown in Fig. 3. Panel A shows the ST-80 potentials computed on the torso, epi- and endocardial surfaces with heart rate set to 125 bpm, normal coronary flow, and load at control levels (16 mmHg). Panel B shows potentials recorded with the load set to 2.5 times the control level. We note that on the anterior epicardium, the maximal ST-elevation is at 1.52 mV in both the normal case and with load at 2.5 times the normal. Moreover, we observe that the potentials on the endocardial surface shift towards less negative values when the load is increased to 2.5 times the normal load. In Panel C, with load set to 4 times the control level, we observed a larger region of elevated ST-potentials on all 3 surfaces. The magnitude of the maximal ST-elevation on the epicardial surface is 3.11 mV. Similarly, the maximal ST-elevation on the endocardial surface was 2.08 mV and the elevated region spanned the antero-septal aspects of the left ventricular endocardium, larger than the extent during the load of 2.5 times the normal. Further, this region on the endocardium aligned with the region of ST elevation on the epicardium.

Varying Load Under Reduced Coronary Flow. The results following increases in left ventricular load under reduced coronary flow conditions with normal heart rate are shown in Fig. 4. Panel A shows the ST-80 potentials computed on the torso, epi- and endocardial surfaces with coronary flow reduced by 66% to 10 ml/min, load at the normal level, and heart rate at 125 bpm. Panel B shows potentials with load increased to 2.5 times the normal load and Panel C, with 4 times the normal load, always with the same, reduced coronary flow and normal heart rate. In contrast to the case in Fig. 3, the reduced coronary flow resulted in a much more focused region of elevated potential that had lower maximum amplitude on the torso and epicardial surfaces, as illustrated by the dense grouping of isocontour lines in the maps. Moreover, potentials bordering the region of elevation became more negative (ST-segment depression) as load increased. Endocardial potentials were all negative and became progressively less negative as load increased but without any pronounced focal areas.

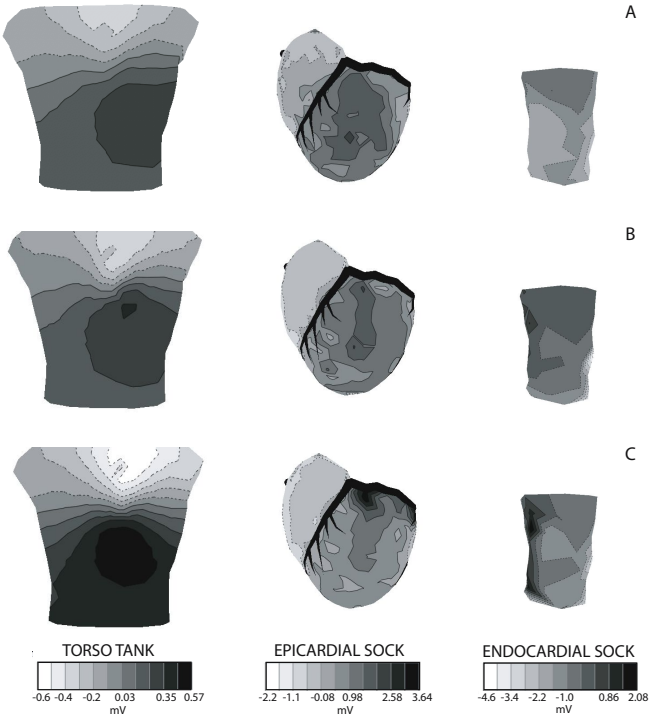

Fig. 3. Torso, epicardial and endocardial ST-80 potentials are shown under conditions of varying metabolic load with heart rate at 125 bpm and coronary flow at normal flow of 37 ml/min. The color map used to represent potentials shown for each mesh is at the bottom of the figure and is common across all 3 panels for each mesh. Panel A: Load at normal. Panel B: Load at 2.5 times normal load. Panel C: Load at 4 times normal load.

4 Discussion

In a previous study we presented an experimental and computer simulation framework developed by our group for the investigation of electrocardiographic characteristics of ischemia[6,2]. In this study, we present an experimental preparation that augments, supports, and provides new directions for these simulation studies. The simulations differed from these experiments in that they assigned reduced transmembrane potentials to predetermined ischemic regions, whereas the experiments examined the role of metabolic load and coronary flow conditions on ischemic stress in an isolated canine heart.

Previous studies have shown that variable reduction in coronary perfusion can lead to both ST-segment depression and elevation on or directly adjacent to the ischemic region, depending on the extent of the flow reduction[1,2,7]. The proposed mechanism for such variations was the variable extent of ischemia

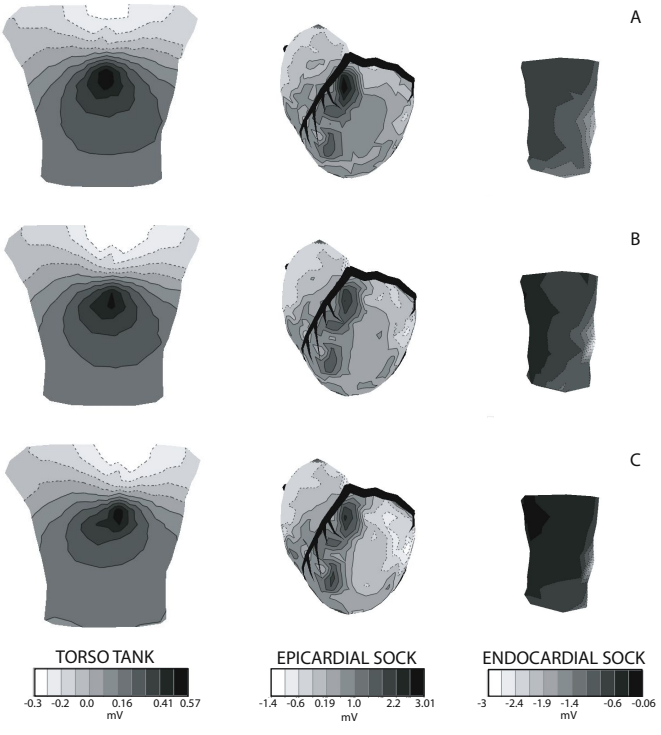

Fig. 4. Torso, epicardial and endocardial ST-80 potentials are shown under conditions of varying metabolic load with heart rate at 125 bpm and coronary flow at 1/3 rd of normal flow. The color map used to represent potentials shown for each mesh is at the bottom of the figure and is common across all 3 panels for each mesh. Panel A: Load at normal. Panel B: Load at 2.5 times normal load. Panel C: Load at 4 times normal load.

from sub-endocardial to transmural, combined with anisotropic conductance of the myocardium, an idea first clearly demonstrated by simulation studies [8]. The reason ischemia initially affects the endocardium preferentially lies in the observation that the sub-endocardial region has a higher myocardial oxygen demand than the rest of the heart [9]. Therefore, with increased wall tension and metabolic load, the myocardial oxygen demand would increase in the sub-endocardium, and lead to vasodilation of the arterioles [9].

In the first set of results presented here, perfusion through the LAD was maintained at normal levels while load was progressively increased. The resulting epicardial potentials showed an initially modest ST elevation, which then grew sharply and formed a focussed region at maximum load levels. The endocardial potentials showed a similar but slightly more diffuse pattern in the anteroseptal aspect, forming a vertical band of elevated potentials under maximum load conditions. One possible explanation for this response is that the increase in

load caused an initial reduction in endocardial/septal perfusion which became transmural in extent, either because the entire transmural myocardium segment was underperfused, or through some steal behavior that robbed the epicardium of blood in order to attempt to sustain endocardial function.

Another possible explanation for these results is that the compressive effects of the water filled balloon on the endocardium led to injury currents not directly related to ischemia. This response cannot be ruled out, however, such a response would likely result in uniform ST-elevation over the all regions of the endocardium in contact with the balloon, a result we did not observe. One might also postulate that only certain parts of the balloon were in contact with the endocardium and that these generated focal pressure points. However, we measured consistent electrogram amplitude all over the balloon, suggesting a fairly uniform contact on all aspects.

The findings in Fig. 4 differ substantially from those in Fig 3, even though the variable stressor in both cases was the same, *i.e.,* an increase in mechanical load in the left ventricle. In this case, the focal elevation visible on the epicardium only at full load during normal perfusion was apparent under normal load and reduced perfusion, with an additional slight downward shift in location. (We note parenthetically that this shift in location could well arise from movement of the recording sock over the course of the experiment and is thus unlikely to be significant.) More unexpected was the finding that the peak amplitude of the elevated ST potentials actually decreased slightly with increased mechanical load, even as the regions peripheral to the presumed perfusion bed of the cannulated artery showed a growing depression with load. The endocardial potentials showed a trend of increasingly positive potentials on the septal aspect even though the values were negative over the entire surface.

One possible mechanisms for these findings is that the subepicardial region experienced increased demand and/or reduced perfusion and hence showed ST elevation even as the endocardium remained negative. Such an imbalance is contrary to conventional ideas about the transmural differences in demand the perfusion described above. Another possible mechanism for these differences is an extension of a finding shown by Antzelevich *et al.* [10] that the response to physiological challenges by cells in the midmyocardial region of the heart is larger than that for any other part of the heart. Under this scenario, the suppression of potential would be largest in the midmyocardium, slightly smaller in the epicardium, and smallest in the endocardium, with a net extracellular current flow from the endocardium to epicardium. As in the case of load changes under full perfusion, the increase in mechanical load would exacerbate the demand on the subendocardium, thus leading to a progressive elevation of the endocardial surface and depression of the epicardial surface. This is a classic response to subendocardial ischemia [11] and is an additative component in the net electrocardiographic field that we measured.

A substantial challenge in this study was to establish the locations of all the sock electrodes, both epicardial and endocardial, with respect to the same torso-tank based coordinate system. For the epicardial sock, we digitized reference

locations marked on the sock and then used this information to align a previously measured standard geometry for this sock. The standard sock geometry was based on the mold over which the sock was applied during fabrication; consistent electrode location therefore depended both on the consistency of shape and size of the hearts in each study and our ability to place the sock in the same relative orientation on the heart. Determining the endocardial sock geometry was even more challenging. As with the epicardial sock, a mold created from a sample heart was the basis of the endocardial sock fabrication. However, placing the sock, stretched over the endocardial balloon, into consistent location and orientation in the beating heart is difficult. At the end of each experiment, we opened the left ventricular freewall, observed the placement of the sock experiment, and selected for analysis only those experiments in which the sock appeared to deploy properly. To orient the endocardial and epicardial socks in the same coordinate system, we carried out stimulations of the heart by means of electrodes on one sock and observed the resulting potential fields on the other. From these data we determined nearest neighbor relationships between the socks, then aligned based on these nearest neighbors.

The variations in torso tank potentials following ischemia are, at best, simplified versions of what one might expect to observe from clinical electrocardiography. The presence of inhomogeneous regions of the thorax will certainly alter the signals in unpredictable ways so that extending these results to the clinical setting is challenging. The point of the study was not to demonstrate clinical impact of the varied response to different forms of ischemic stress but rather to illustrate the fundamental observation that ischemia is a diverse phenomenon worthy of more detailed experiment study, especially before assuming that traditional clinical markers are the most useful metrics of acute ischemia.

The preliminary results from these experiments suggest that ST-segment potentials may not match those predicted by conventional theory alone. In order to explain the myocardial response to demand ischemia, the behavior of the mid-myocardial layers to metabolic stress under reduced flow conditions needs to be characterized. A robust computer model that contains a description of the transmural electrophysiological behavior along with accurate tissue structure and anisotropy (currently under development in our lab) could explain experimental observations of potential pattern distributions. An experimental approach that can provide the necessary information about intramural variations in the response to ischemia is multielectrode plunge needles; experiments using this approach are currently underway in our lab as is detailed magnetic imaging of the myocardium in order to construct subject specific models against which to compare measurements and explore the role of structure and the spatial organization of the ischemic zone.

Acknowledgments

This work was supported by the Richard A. and Nora Eccles Harrison endowment and the Nora Eccles Treadwell Foundation.

References

1. MacLeod, R.S., Punske, B., Shome, S., Yilmaz, B., Taccardi, B.: The role of heart rate and coronary flow during myocardial ischemia. J. Electrocardiol. pp. 43–51 (2001)
2. MacLeod, R.S., Shome, S., Stinstra, J.G., Punske, B.B., Hopenfeld, B.: Mechanisms of ischemia-induced ST-segment changes. J. Electrocardiol. 38(Suppl), 8–13 (2005)
3. MacLeod, R.S., Taccardi, B., Lux, R.L.: Electrocardiographic mapping in a realistic torso tank preparation. In: Proceedings of the IEEE Engineering in Medicine and Biology Society 17th Annual International Conference, pp. 245–246. IEEE Press, New York (1995)
4. Ni, Q., MacLeod, R.S., Lux, R.L., Taccardi, B.: A novel interpolation method for electric potential fields in the heart during excitation. Annal. Biomed. Eng. 26(4), 597–607 (1998)
5. MacLeod, R.S., Johnson, C.R.: Map3d: Interactive scientific visualization for bioengineering data. In: Proceedings of the IEEE Engineering in Medicine and Biology Society 15th Annual International Conference, pp. 30–31. IEEE Press, New York (1993)
6. Hopenfeld, B., Stinstra, J.G., MacLeod, R.S.: Mechanism for ST depression associated with contiguous subendocardial ischemia. J. Cardiovasc. Electrophysiol. 15(10), 1200–1206 (2004)
7. Li, D., Li, C.Y., Yong, A.C., Kilpatrick, D.: Source of electrocardiographic ST changes in subendocardial ischemia. Circ. Res. 82, 957–970 (1998)
8. Hopenfeld, B., Stinstra, J.G., MacLeod, R.S.: The effect of conductivity on ST segment epicardial potentials arising from subendocardial ischemia. Annal. Biomed. Eng. 33(6), 751–763 (2005)
9. Reiber, H.C.: 3-D artery view gauges bypass odds. Computers in Medicine, pp. 8–8 (1986)
10. Antzelevitch, C., Shimizu, W., Yan, G.X., Sicouri, S.: Cellular basis for QT dispersion. J. Electrocardiol. 30(Suppl), 168–175 (1998)
11. Holland, R.P., Brooks, H.: TQ-ST segment mapping: Critical review and analysis of current concepts. Am. J. Cardiol. 4, 110–129 (1977)

Characteristic Strain Pattern of Moderately Ischemic Myocardium Investigated in a Finite Element Simulation Model

Espen W. Remme and Otto A. Smiseth

Dep. of Cardiology, Rikshospitalet-Radiumhospitalet Medical center, 0027 Oslo, Norway
Espen.Remme@rr-research.no

Abstract

Background: Myocardial ischemia in the left ventricular (LV) myocardium introduces non-uniform and pathological strain patterns. Total passive segments lengthen when pressure increases during early systole and shorten when pressure drops at the end of ejection. Moderately ischemic segments typically lengthen during isovolumic contraction, start shortening during ejection and continue shortening, usually at an increased rate, after aortic valve closure.

Aim: The aim of this study was to investigate possible mechanisms for the characteristic strain patterns in moderately ischemic regions using a simulation model of the LV wall.

Methods: A thick-walled truncated ellipsoidal finite element model was used to represent the LV geometry. The model included mathematical descriptions of fiber orientation, passive elastic properties, and actively generated fiber stress. A severely ischemic region and a moderately ischemic border zone were incorporated in the model. The severely ischemic region was made stiffer and generated no active fiber stress during systole. The border zone was made slightly stiffer, active fiber stress was reduced and generated at a slower rate while the relaxation rate was slower than in the normal regions. The cardiac cycle was simulated by applying physiological pressure-volume boundary conditions.

Results: The strain pattern in the severely ischemic region resembled the pressure curve with lengthening during pressure rise and shortening during pressure decrease, while the border zone started shortening after an initial early systolic lengthening and continued shortening during isovolumic relaxation at an increased rate.

Conclusion: The characteristic moderately ischemic strain pattern may be caused by slower mechanical activation and relaxation rates.

1 Introduction

Regional myocardial ischemia impairs contractile performance of affected myofibers and introduces a non-uniform deformation pattern during the cardiac cycle. A

F.B. Sachse and G. Seemann (Eds.): FIMH 2007, LNCS 4466, pp. 330–339, 2007.

severely ischemic region typically exhibits a total passive behavior where the segments stretch when the pressure increases during early systole and shorten as pressure decreases during late systole/early diastole. Thus, their deformation pattern has a shape similar to the cavity pressure curve. The resulting pressure-segment length loops are narrow and run clockwise due to viscoelastic properties of the myocardium and the loop area reflects work performed on the passive segment by actively contracting segments. The loop follows the typical nonlinear shape of the stress-strain characteristic of passive soft elastic tissue (Fig. 1, left). The typical deformation sequence of moderately ischemic segments starts with early systolic stretching during isovolumic contraction, subsequent shortening during ejection and continued shortening after aortic valve closure, often at an increased shortening rate, followed by lengthening during diastole. Moderately ischemic segments have a counter-clockwise pressure-segment length loop as they perform some work (Fig. 1, middle), however, the loop area is smaller than for healthy segments which shorten during systole at high pressures and lengthen during diastole at low pressure and thus perform more work (Fig. 1, right). [1]

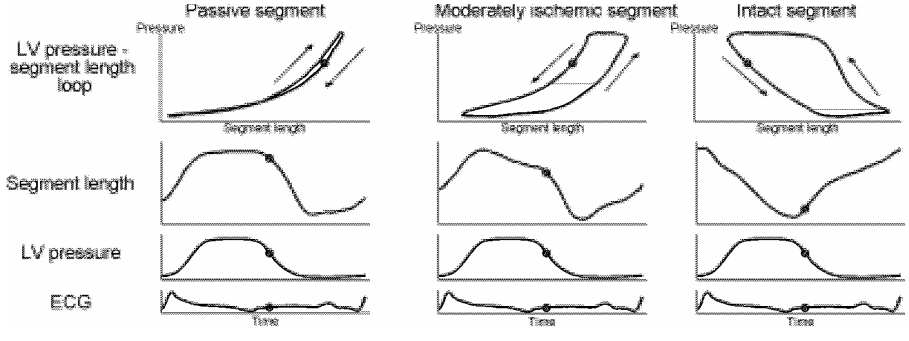

Fig. 1. The figure shows typical recordings from an infarcted dog heart (data material from Lyseggen et al. [1]). Traces from a total passive, a moderately ischemic, and an intact segment are shown on the left, in the middle, and on the right respectively. The circle indicates the time of aortic valve closure. The arrows indicate the direction of the pressure-segment length loops.

The passive behavior of infarcted and severely ischemic segments is due to the inability of myofibers to produce active force. However, the etiology of the deformation pattern of moderately ischemic segments is not clear. Some previous studies [2, 3] have investigated the deformation in ischemic LV models but have not investigated the mechanisms behind the characteristic *shape* of the deformation *trace* of moderately ischemic segments. We hypothesize that early systolic lengthening of a moderately ischemic region is caused by a reduced and slower generation of active fiber stress in this region and thus it is stretched by normal regions that start contracting earlier. We further hypothesize that pronounced post-systolic shortening of a moderately ischemic region is caused by a prolonged active contraction due to a slower relaxation rate of active fiber stress in this region compared to a more rapid decline in normal regions. During isovolumic conditions, following aortic valve

closure, the slower relaxing moderately ischemic segments will shorten as they win the 'tug of war' with the normal segments which lengthen. The aim of this study was to investigate our proposed hypothesis and other possible mechanisms using a finite element model of the left ventricular myocardium. We investigated the deformation pattern in the simulation model where the border zone between a severely ischemic region and the normal region was made moderately ischemic. The active fiber stress in the border zone was reduced throughout systole and was generated at a slower rate during early systole and relaxed at a slower rate during late systole compared to the normal region. Other simulation cases were also carried out for comparison. These included a baseline simulation with all regions given normal properties, a simulation case where there was a mixture of only severely ischemic and normal myofibers, and a simulation case with no severely ischemic region but with only a normal and a moderately ischemic region.

2 Methods

Finite Element Model

The finite element modeling principles used in this study have been described in detail by Nash and Hunter [4]. A briefer explanation follows below.

The LV myocardium was represented by a truncated elliptically shaped finite element model with 48 elements (four elements in the circumferential and longitudinal directions, and three in the transmural direction) using rectangular Cartesian coordinates and cubic Hermite basis functions. The myofiber angle with respect to the circumferential direction was set to vary linearly in the transmural direction from 90° at the endocardial nodes to -65° at the epicardial nodes.

The myocardial passive elastic properties were modeled by the pole-zero law [4] and considered incompressible. The pole-zero strain energy function W is shown in Eq. (1) where index *f* refers to the fiber-axis, *s* to the sheet-axis and *n* the sheet-normal-axis. The material parameters are shown in Table 1.

$$W = \frac{k_{ff} \cdot e_{ff}^{\,2}}{\left(a_{ff} - e_{ff}\right)^{b_{ff}}} + \frac{k_{ss} \cdot e_{ss}^{\,2}}{\left(a_{ss} - e_{ss}\right)^{b_{ss}}} + \frac{k_{nn} \cdot e_{nn}^{\,2}}{\left(a_{nn} - e_{nn}\right)^{b_{nn}}} + \frac{k_{fs} \cdot e_{fs}^{\,2}}{\left(a_{fs} - e_{fs}\right)^{b_{fs}}} + \frac{k_{fn} \cdot e_{fn}^{\,2}}{\left(a_{fn} - e_{fn}\right)^{b_{fn}}} + \frac{k_{sn} \cdot e_{sn}^{\,2}}{\left(a_{sn} - e_{sn}\right)^{b_{sn}}} \tag{1}$$

Active tension was added along the fiber direction during systole. Eq. (2) shows the steady state formula used to calculate active tension (T_a) where *actn* is a time varying mechanical activation parameter related to the intracellular Ca^{2+} concentration and λ is the myofiber stretch ratio [5].

$$T_a(\lambda, actn) = 130\,kPa\,\left(1.45(\lambda - 1)\right)\frac{actn^3}{actn^3 + 0.5^3} \tag{2}$$

Eq. (3) shows the calculation of the components of the second Piola-Kirchhoff stress tensor referred to the microstructural coordinates υ_α, where $\alpha \in (f, s, n)$; $E_{\alpha\beta}$ the components of the Cauchy-Green strain tensor; p the intramural hydrostatic pressure

field which is included to maintain incompressibility; V_α = undeformed microstructural coordinate; υ_α = deformed microstructural coordinate; and $a_{(\nu)}^{\alpha\beta}$ the contravariant metric tensor with respect to the deformed microstructural coordinates.

$$T^{\alpha\beta} = \frac{1}{2}\left(\frac{\partial W}{\partial E_{\alpha\beta}} + \frac{\partial W}{\partial E_{\beta\alpha}}\right) - pa_{(\nu)}^{\alpha\beta} + T_a \frac{\partial V_\alpha}{\partial \nu_f}\frac{\partial V_\beta}{\partial \nu_f} \tag{3}$$

Table 1. Passive material properties for the pole-zero constitutive law

Type	Axial properties		Shear properties	
Coefficients	k_{ff}	3.0 kPa	k_{fs}	3.0 kPa
	k_{ss}	3.0 kPa	k_{fn}	3.0 kPa
	k_{nn}	3.0 kPa	k_{sn}	3.0 kPa
Poles	a_{ff}	0.5	a_{fs}	0.8
	a_{ss}	0.8	a_{fn}	0.8
	a_{nn}	0.8	a_{sn}	0.8
Curvature	b_{ff}	1.5	b_{fs}	1.2
	b_{ss}	1.3	b_{fn}	1.2
	b_{nn}	1.3	b_{sn}	1.2

As described in detail below, the ventricular cycle was simulated by applying physiological pressure-volume conditions during the different phases of the cycle. This was achieved by controlling the activation parameter and the applied pressure on the endocardial surface in conjunction with the resulting cavity volume. The activation parameter was varied regionally to account for the propagation of electro-mechanical activation in the endocardium-epicardium direction and apex-base direction [6]. This was implemented by initially scaling down the activation parameter in the later activated regions compared to the earliest activated regions.

The basal nodes were fixed in the x-direction (longitudinal direction), in addition, the endocardial nodes on the z-axis were fixed in the y-direction and vice versa.

Simulating the phases of the ventricular cycle

Passive inflation

Simulations were started with a passive inflation that occurs during diastasis and atrial contraction. At the start of diastasis it is assumed that the LV wall is in its resting configuration, i.e. the stresses are approximately 0. A pressure was incrementally applied on the endocardial surface elements from 0 to 10 mmHg. The pressure-volume loop through the cardiac cycle is shown in Fig. 2 where the passive inflation phase is labeled ‘A’.

Mitral valve closure

Following passive inflation, the activation parameter was increased from 0 to produce an active fiber tension and fiber shortening. We believe an initial contraction of the wall closes the mitral valve leaflets and move them in the direction of the left atrium (LA) until they are stopped by the chordae tendinae and papillary muscles.

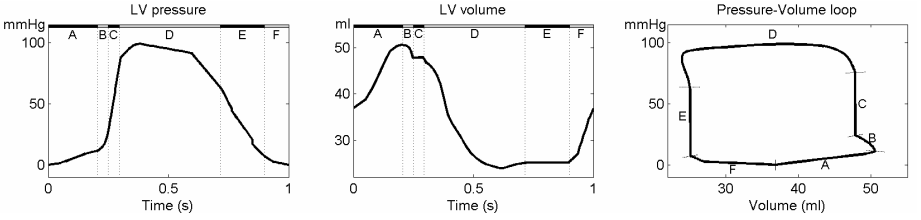

Fig. 2. Applied endocardial pressure and resulting cavity volume from the simulation of baseline conditions. The labeled phases are: A – passive inflation, B – mitral valve closure, C – isovolumic contraction, D – ejection, E – isovolumic relaxation, and F – rapid filling.

Consequently, the cavity volume encapsulated by the contracting wall is reduced as some blood moves up with the mitral valve leaflets [7]. Thus, the activation parameter was increased together with the cavity pressure so that the volume encapsulated by the wall region was reduced by 5% in an approximately linear fashion with a 14 mmHg increase of pressure. This phase is labeled 'B' in Fig. 2.

Isovolumic contraction (IVC)
After final closure of the mitral valve the volume was kept constant for each increment of the activation parameter by increasing the cavity pressure. When the pressure exceeded 75 mmHg IVC was ended. This phase is labeled 'C' in Fig. 2.

Ejection
Measurements of the LV pressure-volume relationship during ejection from 10 dogs [7] were averaged and used as an input to the model. The cavity pressure was adjusted to follow the average measured pressure trace for each load step while the activation parameter was adjusted to obtain the corresponding desired volume. This phase is labeled 'D' in Fig. 2. The small volume increase at the end of the ejection phase corresponds to the volume pushed into the ventricle by the closing aortic valve [7].

Isovolumic relaxation (IVR)
After aortic valve closure the volume was kept constant for each decrement of the activation parameter by decreasing the cavity pressure. When the pressure fell below 8 mmHg IVR was ended. This phase is labeled 'E' in Fig. 2.

Rapid filling
The rapid filling phase was split in two linear pressure-volume relationships as the pressure and activation parameter was gradually reduced to 0. During the first part, the pressure was decreased at a quicker rate with respect to the volume as opposed to the second part. The rapid filling phase is labeled with 'F' in Fig. 2.

Severely and moderately ischemic regions

Occlusion of the left anterior descending (LAD) coronary artery normally results in an infarct region in the anterio-septal apical region of the LV wall. A severely ischemic region, labeled 'X' in Fig. 3, and a moderately ischemic border zone, labeled 'B' were incorporated in the model, resembling effects that may be caused by an LAD occlusion. The remote, healthy region was labeled 'R'. Severely ischemic properties

were defined as no generation of active fiber stress (activation parameter set to 0 in Eq. (2)) and the passive elastic parameters in Eq. (1) were made stiffer by setting k_{ij} = 9 kPa (i, j ∈ (f, s, n)) as even acutely ischemic myocardium may stiffen due to cross-bridges being stuck in a rigor state. Moderately ischemic properties were defined as 50% reduction of the activation parameter during increasing active fiber stress development. This effectively caused a reduced rate of active fiber stress development in addition to a general decreased active fiber stress level. Prolonged relaxation of the moderately ischemic region was obtained by gradually changing the scaling of the activation parameter from initially 0.5 at peak (50% of that in the normal region) to 1.0 at the end of relaxation (i.e. becoming similar to the level in the normal region at the end of IVR and rapid filling). The passive elastic properties were made slightly stiffer in the moderately ischemic region by setting k_{ij} = 5.5 kPa (i, j ∈ (f, s, n)).

Simulation cases

Four different simulation cases were performed as outlined below. For the baseline simulation the ejection fraction (EF) was set to 50%, while in the other three ischemic simulation cases EF was set to 35%. Ventricular pressure was not changed during ischemia due to compensatory mechanisms that help to maintain pressure.

Baseline simulation
Initially, the cardiac cycle was simulated with normal, healthy properties in all regions of the LV model. This included normal activation parameter values and normal passive stiffness parameters.

Simulation with a severely ischemic region and a moderately ischemic border zone
The central ischemic region marked with 'X' in Fig. 3 was given severely ischemic properties. The border zone marked with 'B' was given moderately ischemic properties. The remote region was given normal properties.

Simulation with a mixture of severely ischemic and normal myofibers
The region marked with 'X' in Fig. 3 was given severely ischemic properties. In addition, 40% of the region between the two mid-ventricular circles in the figure was also given severely ischemic properties. The remaining 60% of this region was given the same properties as in the normal region. The other regions labeled 'B' were also given normal properties; hence, there were no moderately ischemic myofibers in this simulation case.

Simulation with a moderately ischemic region and a normal region
In this simulation case there was no severely ischemic region. The apical region that was previously made severely ischemic, labeled 'X' in Fig. 3, was given normal active and passive properties. The region labeled 'B' between the two mid-ventricular circles was given moderately ischemic properties. The other regions labeled 'B' were given normal properties.

Analysis of data

From each simulation case the deformation was calculated as the myocardial segment length between the 4 marked points in Fig. 3. This mimics segment lengths measured

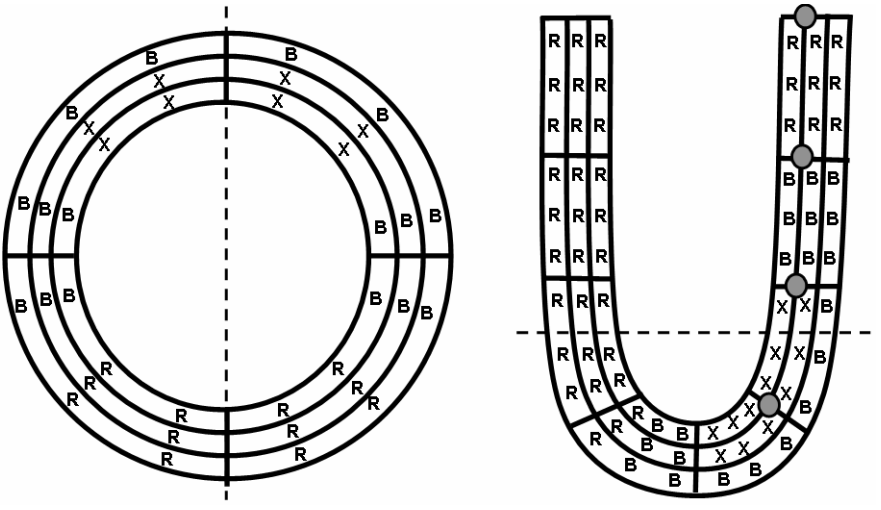

Fig. 3. Short- and long-axis schematic of the LV model. The solid lines indicate the element borders and the dashed line through the short-axis slice indicates the location of the long-axis slice and vice versa. The letters label regions that were assigned different properties for different simulation cases. For the second simulation case these were: X - severely ischemic properties, B - border zone with moderately ischemic properties, and R – remote region with normal properties. Myocardial segment lengths were extracted between the 4 circular points in the long axis slice. For the second simulation case the segment length between the two most apical circles are located in the severely ischemic region, the segment length between the two mid-ventricular circles are located in the border zone, and the segment length between the two most basal circles are in the remote, healthy region.

by sonomicrometry in experimental studies similar to the measurements shown in Fig. 1. The three extracted segment lengths were located in the apical region (which was severely ischemic in simulation case 2 and 3), in the mid-ventricular level (moderately ischemic in case 2 and 4), and in the basal, normal region, respectively. The active myofiber stress was extracted for each of these three locations, averaged over each region. A differentiation of the active myofiber stress with respect to time was performed to find the rate of mechanical activation and relaxation in these three regions.

3 Results

The baseline simulation resulted in relative uniform behavior of the three different regions with respect to segment length, active fiber stress and active fiber stress rate as shown in the top row of Fig. 4.

The second simulation case with a severely ischemic region and a moderately ischemic border zone resulted in an early systolic stretching of the mid-ventricular border zone, shortening during ejection and continued shortening after aortic valve closure at a more rapid rate. The active fiber stress in the border zone increased at a slower rate during early systole and decreased at a slower rate during relaxation

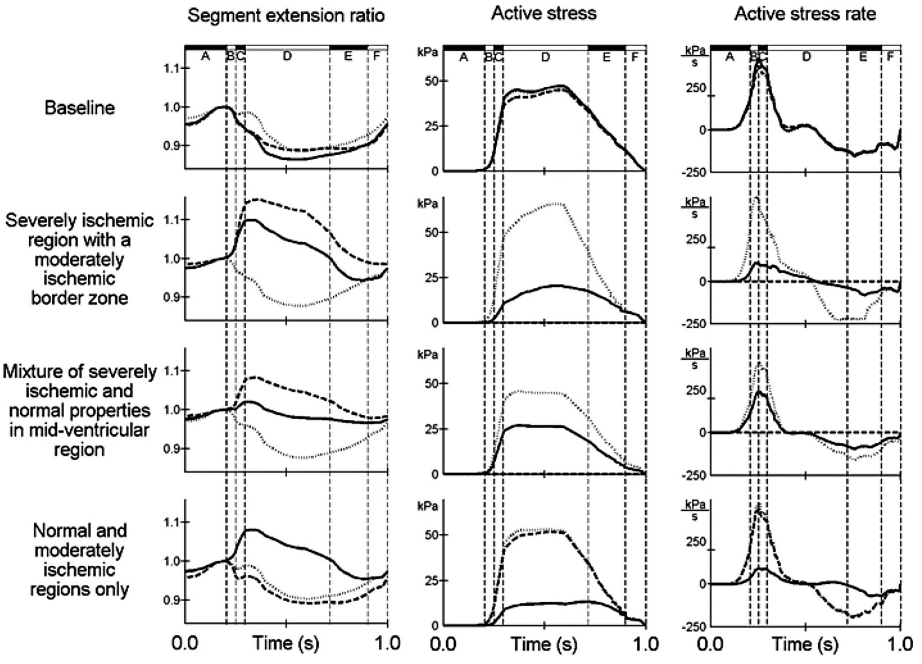

Fig. 4. Results from the four simulation cases are shown in the four rows. The three traces in each plot is from the basal region (dotted line), the mid-ventricular region (solid line), and the apical region (dashed line), see Fig. 3 for locations. The left column shows segment length extension ratios that are normalized with respect to end diastolic length. The second column shows the regionally averaged active fiber stress. The third column shows the rate of active stress changes. The labeled phases are: A – passive inflation, B – mitral valve closure, C – isovolumic contraction, D – ejection, E – isovolumic relaxation, and F – rapid filling.

compared to that in the normal region. The result from this simulation case is shown in the second row of Fig. 4.

The third simulation case with a mixture of severely ischemic and normal myofibers in the mid-ventricular region resulted in slight early systolic stretching of this region, shortening during ejection and a small post-systolic shortening. The result from this simulation case is shown in the third row of Fig. 4.

The fourth simulation case with only a moderately ischemic region at the mid-ventricular level and the rest of the wall given normal properties showed that the moderately ischemic region exhibited early systolic stretching and a rapid post-systolic shortening similar to the second simulation case. The fourth simulation case is shown in the bottom row of Fig. 4.

4 Discussion

In this study we have investigated possible mechanisms of the early systolic stretching and post-systolic shortening that is seen in moderately ischemic regions in

the ischemic left ventricle. Our simulation model reproduced this characteristic pattern in a region where active fiber stress was increased at a slower rate during early systole and was reduced at a slower rate during relaxation compared to the normal region. During beginning of systole the normal region became stronger earlier and pulled on the weaker moderately ischemic region which was stretched. The pull one region exerts on a neighboring region is the sum of passive and active forces. Stretching increases the passive forces and vice versa. Weaker regions stretch and increase the passive pull to match the active pull of stronger regions. In addition, increased sarcomere stretch increases the generation of active fiber stress (see Eq. 2). The rate of active fiber stress generation became more equal between the normal and moderately ischemic region at about 0.3-0.4 s, see second or fourth row of Fig. 4. Thus, the active fiber stress contribution to the pull increased at approximately similar rates in the two regions, causing a more matching active pull development. The moderately ischemic segment was able to shorten during ejection as the difference in active pull stopped increasing. Following aortic valve closure, the isovolumic conditions during IVR make the balance of forces between the regions evident: The global dimension must remain constant and an inhomogeneous relaxation results in regional stretching that is compensated by shortening of another region. Thus, quicker decrease of active fiber stress in the normal region and slower decrease in the moderately ischemic region caused lengthening and shortening in the two regions, respectively.

Segment length measurements over a region with a mixture of normal and severely ischemic myofibers (simulation case 3) may also exhibit early systolic stretching and shortening during IVR. However, post-systolic shortening below resting length, which is often seen in measurements and simulation cases 2 and 4, may indicate that this is an active contraction, not just a passive rebound. This implies that post-systolic contraction below resting length may be caused by a prolonged active contraction due to an impaired relaxation rate in the moderately ischemic region. A 0.5 scaling of the activation parameter would in itself reduce the relaxation rate, however to obtain the pronounced post-systolic shortening pattern we increased this scaling during relaxation, effectively maintaining (the reduced) activation longer in this region.

Limited blood supply causes a region to become ischemic. Reduced and slower generation of active fiber stress in this region is probably the result of reduced oxygen availability which in turn reduces ATP generation and impairs Ca^{2+} exchanger activities. Impaired reuptake of Ca^{2+} into the sarcoplasmic reticulum may cause prolonged contraction and a slower relaxation rate.

Limitations

The relatively simple model we applied for generation of active fiber stress in our current model, did not incorporate the details of cell metabolism and Ca^{2+} transients. The activation parameter in Eq. 2 may be viewed as a pooled effect of metabolism and Ca^{2+} transient. The model had a simplified geometry, fiber orientation, and boundary conditions. Despite these limitations, we believe the model provides qualitative insight into the deformation of the LV wall and may be used to investigate possible mechanisms of deformation and interaction between different regions in the normal and ischemic case as in our study.

Conclusion

The results supported our hypothesis that early systolic lengthening of a moderately ischemic region may be caused by a slower mechanical activation rate in this region compared to normal regions. Similarly, the post-systolic shortening of a moderately ischemic region may be caused by a slower relaxation rate of active fiber stress in this region compared to normal regions.

References

1. Lyseggen, E., Skulstad, H., Helle-Valle, T., Vartdal, T., Urheim, S., Rabben, SI., Opdahl, A., Ihlen, H., Smiseth, OA.: Myocardial Strain Analysis in Acute Coronary Occlusion - A Tool to Assess Myocardial Viability and Reperfusion. Circulation 112, 3901–3910 (2005)
2. Bovendeerd, PH., Arts, T., Delhaas, T., Huyghe, JM., van Campen, DH., Reneman, RS.: Regional wall mechanics in the ischemic left ventricle: numerical modeling and dog experiments. Am. J. Physiol. 270, H398–410 (1996)
3. Mazhari, R., Omens, JH., Covell, JW., McCulloch, AW.: Structural basis of regional dysfunction in acutely ischemic myocardium. Cardiovasc Res. 47, 284–293 (2000)
4. Nash, MP., Hunter, PJ.: Computational mechanics of the heart: from tissue structure to ventricular function. J. Elasticity. 61, 113–141 (2000)
5. Hunter, PJ., McCulloch, A., ter Keurs, HEDJ.: Modelling the mechanical properties of cardiac muscle. Prog Biophys Molec Biol. 69, 289–331 (1998)
6. Durrer, D., Dam, RT., Freud, GE., Janse, MJ., Meyler, FL., Arzbaecher, RC.: Total excitation of the isolated human heart. Circulation 41, 899–912 (1970)
7. Remme, EW., Lyseggen, E., Helle-Valle, T., Opdahl, A., Pettersen, E., Vartdal, T., Ragnarsson, A., Ihlen, H., Edvardsen, T., Smiseth, OA.: Mechanism behind pre- and post-ejection velocity spikes in normal left ventricular myocardium. In Review.

Constitutive Modeling of Cardiac Tissue Growth

Wilco Kroon[1], Tammo Delhaas[1], Theo Arts[1], and Peter Bovendeerd[2]

[1] Maastricht University, Cardiovascular Research Institute Maastricht, 6200 MB Maastricht , The Netherlands
jw.kroon@fys.unimaas.nl
[2] Eindhoven University of Technology, Department of Biomedical Engineering, 5600 MB Eindhoven, The Netherlands

Abstract. Long term responses of the heart to e.g. infarction or surgical intervention are related to response of the tissue to changes in the mechanical environment. The tissue response is likely to involve (local) change of mass. Implementation of the associated inhomogeneous change in volume for a complex geometry is cumbersome. In the present study, we propose a computational framework for finite volumetric growth. The local stimulus for growth is determined from a simulation of beat to beat cardiac mechanics, assuming the tissue to be incompressible. The related local volumetric growth is translated in a global change of cardiac shape through a simulation of long term cardiac mechanics, assuming the tissue to be compressible.

We illustrate the model by simulating growth in response to a deviation of end-diastolic sarcomeric strain from a set optimal value assumed to be preferred by the tissue. Inhomogeneity in the stimulus was reduced after inhomogeneous growth of up to 25%. The transmural redistribution of mass due to growth was found to alter an initially unphysiological linear transmural course in myofiber orientations to a more physiological course. We conclude that the model enables simulation of locally inhomogeneous growth in a realistic left ventricular geometry.

1 Introduction

Like many biological tissues, cardiac tissue is able to adapt to changes in mechanical load through growth (change in mass) and remodeling (change in tissue properties) [6,9,13,14]. Mathematical models can be used to study hypotheses on the relation between input and output of the adaptation process leading to the maintenance of cardiac tissue structure, or changes therein in response to altered mechanical load as caused by disease or intervention.

In a mathematical model proposed by Arts *et al.* (1994), left ventricular cavity volume, wall volume and internal fiber architecture were locally adapted in response to several stimuli, such as early systolic fiber stretch, fiber shortening during ejection, and contractility [1]. The model predicted a cardiac structure that was both stable and in agreement with physiological observations. Though this model indicated the physiological relevance of mechanical load induced tissue growth and remodeling, it had the drawback that it was restricted to discrete

F.B. Sachse and G. Seemann (Eds.): FIMH 2007, LNCS 4466, pp. 340–349, 2007.

radial variations in mechanics and tissue properties. Furthermore, the model was geometrically representative for the equatorial region of the left ventricle only.

Rodriguez *et al.* (1994) presented a continuum model for volumetric growth that was based on earlier work of Skalak *et al.* (1982) [9,11]. In their model, tissue expansion due to growth is described kinematically by a growth stretch tensor $\boldsymbol{U}_g$. The growth stretch tensor was chosen to be a function of a mechanical load stimulus [9,14]. In response to growth of adjacent tissue, tissue parts exhibit an extra rigid body rotation $\boldsymbol{R}_g$, such that the complete growth is described by the growth deformation gradient $\boldsymbol{F}_g = \boldsymbol{R}_g \cdot \boldsymbol{U}_g$. In general, the extra rotation $\boldsymbol{R}_g$ will partly relieve the incompatibility of the displacement field of neighboring tissue parts related to $\boldsymbol{U}_g$. Still, an extra isochoric elastic deformation $\boldsymbol{F}_e$ is needed to render the overall growth deformation compatible [9,11,12]. The stress related to $\boldsymbol{F}_e$ has generally been considered to account for the residual stresses experimentally observed in the tissue [8,12]. However, this strict coupling of incompatible volumetric growth and residual stress is under debate [6].

The above formulation of volumetric growth has been applied almost exclusively to simple geometries such as cubes or cylinders [9,11,14]. In such simple geometries, analytical methods may be used to derive expressions for $\boldsymbol{F}_e$ and $\boldsymbol{F}_g$. Finite element (FE) models allow for a more general description of both geometrical and material properties. However, determination of $\boldsymbol{F}_e$ and $\boldsymbol{F}_g$ such that growth is compatible in more complex geometries, is cumbersome.

In the present study, we propose a new model for volumetric growth that can easily be employed in a FE environment. In this model, the change in volume is prescribed by a relative volume change J_g, rather than a growth tensor $\boldsymbol{U}_g$. Volume change J_g is related to tissue loads determined from a FE simulation of beat to beat mechanics in which passive tissue is assumed incompressible and anisotropic. Cardiac change in shape due to J_g is determined from a simulation of long term cardiac mechanics, in which the tissue is assumed compressible and isotropic. In contradiction to the formulation by Rodriguez *et al.* (1994), growth induced residual stresses are neglected; residual stresses are considered to be generated via a process different from volumetric growth. The grown geometry is adopted as the new unloaded, internally un-stressed, geometry in the FE simulation of tissue mechanics during loading.

As an example, we simulated volumetric growth in an ellipsoidally shaped cardiac left ventricle. The load stimulus is taken to be the end-diastolic sarcomeric strain determined from a model of cardiac mechanics during loading developed in our group [2,7,15].

2 Method

Figure 2 shows a schematic description of the model of load induced cardiac tissue growth. Below the models are described for the simulation of mechanics of tissue loading, for the translation of tissue mechanics to growth stimulus J_g^t and for the simulation of mechanics of tissue growth.

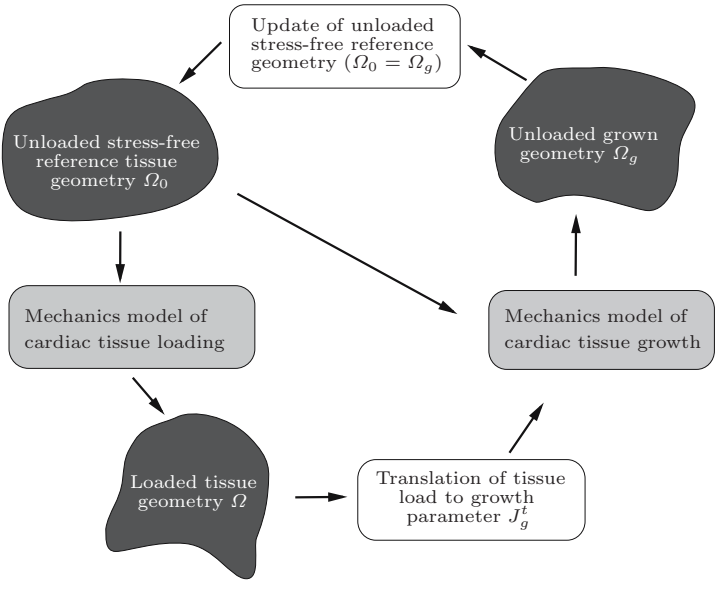

Fig. 1. Schematic view of the growth cycle. Tissue load, determined with a model of cardiac tissue mechanics during loading of the unloaded stress-free geometry Ω_0, is translated in a growth parameter J_g^t. Using this parameter in a mechanics model of growth results in grown geometry Ω_g. The grown geometry is subsequently used as the new unloaded stress-free geometry Ω_0.

2.1 Mechanics Model of Cardiac Tissue Loading

In the present study, only passive filling of the cardiac left ventricle is considered. Passive Cauchy tissue stresses $\boldsymbol{\sigma}$ are related to deformation via a strain energy density function W:

$$\boldsymbol{\sigma} = \frac{1}{J}\boldsymbol{F} \cdot \frac{\partial W}{\partial \boldsymbol{E}} \cdot \boldsymbol{F}^T \quad ; \quad J = \det(\boldsymbol{F}) \tag{1}$$

Deformation is quantified by the Green-Lagrangian strain tensor $\boldsymbol{E}$ which is related to the displacements $\vec{u}$ via the deformation gradient $\boldsymbol{F}$ according to:

$$\boldsymbol{E} = \frac{1}{2}\left(\boldsymbol{F}^T \cdot \boldsymbol{F} - \boldsymbol{I}\right) \quad ; \quad \boldsymbol{F} = \boldsymbol{I} + \left(\vec{\nabla}_0 \vec{u}\right)^T \tag{2}$$

The strain energy density W is given by [7]:

$$W = a_0\left(e^{a_1(I_E^2 + 2II_E)} - 1\right) + a_2\left(e^{a_3 E_{ff}^2} - 1\right) + a_4\left(J^2 - 1\right)^2 \tag{3}$$

where a_0 through a_4 are material parameters determining tissue behavior during loading. Furthermore:

$$I_E = \mathrm{tr}(\boldsymbol{E}) \quad ; \quad II_E = \frac{1}{2}\left(\mathrm{tr}(\boldsymbol{E}^2) - \mathrm{tr}(\boldsymbol{E})^2\right) \quad ; \quad E_{ff} = \vec{e}_f \cdot \boldsymbol{E} \cdot \vec{e}_f \tag{4}$$

where $\vec{e}_f$ is the myofiber direction vector and E_{ff} the Green-Lagrangian myofiber strain. Figure 2a shows the helix angle α_h, which is used to quantify the myofiber direction with respect to the circumferential direction $\vec{e}_\phi$ and base-to-apex direction $\vec{e}_\theta$:

$$\vec{e}_f = \cos(\alpha_h)\vec{e}_\phi + \sin(\alpha_h)\vec{e}_\theta \tag{5}$$

In (3), the value of a_4 is set such that tissue behaves virtually incompressible. With the model, myocardial wall stresses and strains due to a prescribed pressure p_{lv} in the normal direction $\vec{n}$ on endocardial surface Γ_{en} are computed from equilibrium of linear momentum. Epicardial surface Γ_{ep} is assumed to be free of traction:

$$\begin{cases} \vec{\nabla} \cdot \boldsymbol{\sigma} = \vec{0} & \text{on} \quad \Omega \\ \vec{n} \cdot \boldsymbol{\sigma} \cdot \vec{n} = -p_{lv} & \text{on} \quad \Gamma_{en} \\ \vec{n} \cdot \boldsymbol{\sigma} \cdot \vec{n} = 0 & \text{on} \quad \Gamma_{ep} \end{cases} \tag{6}$$

2.2 The Growth Stimulus

Growth is defined as a change in mass m over time. The load measure s assumed to induce growth is determined with the model of cardiac tissue loading. It is assumed that the tissue prefers the load to be equal to s_{opt}. A deviation of s from the optimal value will trigger the tissue to either increase or decrease in mass. The relation between growth and the mechanical load s is given by:

$$\frac{dm}{dt} = \beta m \left(s - s_{opt}\right) \tag{7}$$

where β represents the relative rate of growth. In this study, linear sarcomere strain at end-diastole is taken as stimulus:

$$s = \frac{l_{s,ed} - l_{s,0}}{l_{s,0}} = \sqrt{2E_{ff} + 1} - 1 \tag{8}$$

with $l_{s,0}$ and $l_{s,ed}$ the sarcomere length in the unloaded reference geometry and end-diastole geometry, respectively.

2.3 Mechanics Model of Growth

Tissue mass density ρ is considered to remain constant in time. Consequently, growth is related to the change in tissue volume V in time via:

$$\frac{dm}{dt} = \rho \frac{dV}{dt} \tag{9}$$

Theoretically, local increase in volume from a starting volume V_0 to a grown volume V_g in a time interval Δt is described with the relative volume change J_g^t:

$$J_g^t = \frac{V_g}{V_0} \approx 1 + \frac{1}{V_0}\frac{dV}{dt}\Delta t \approx 1 + \beta(s - s_{opt})\Delta t \tag{10}$$

Due to mechanical interaction of the tissue with its environment, the realized volume change J_g may deviate from the theoretical value J_g^t. The realized change J_g is determined from a growth mechanics computation, in which the tissue is described by a compressible (Neo-Hookean) constitutive model. Growth stresses $\boldsymbol{\sigma}_g$ are split into deviatoric and volumetric stresses:

$$\boldsymbol{\sigma}_g = \frac{b_0}{J_g}\tilde{\boldsymbol{B}}_g^{\ d} + b_1 J_g(J_g^2 - {J_g^t}^2)\boldsymbol{I} \tag{11}$$

where b_0 and b_1 are material parameters determining tissue behavior during growth. Change in tissue shape as a result of growth is described by the deviatoric Finger strain tensor $\tilde{\boldsymbol{B}}_g^{\ d}$:

$$\tilde{\boldsymbol{B}}_g^{\ d} = \tilde{\boldsymbol{B}}_g - \frac{1}{3}\mathrm{tr}(\tilde{\boldsymbol{B}}_g)\boldsymbol{I} \quad ; \quad \tilde{\boldsymbol{B}}_g = \boldsymbol{B}_g J_g^{-\frac{2}{3}} \quad ; \quad \boldsymbol{B}_g = \boldsymbol{F}_g \cdot {\boldsymbol{F}_g}^T \tag{12}$$

The realized volume change J_g is related to the realized growth deformation gradient $\boldsymbol{F}_g$ and the tissue displacement $\vec{u}_g$ according to.

$$\boldsymbol{F}_g = \boldsymbol{I} + \left(\vec{\nabla}_0 \vec{u}_g\right)^T \quad ; \quad J_g = \det\left(\boldsymbol{F}_g\right) \tag{13}$$

$\boldsymbol{F}_g$ is computed from solving mechanical equilibrium in the tissue, subject to zero external force along the tissue surface Γ_g and an internal force related to the stimulus J_g^t:

$$\begin{cases} \vec{\nabla} \cdot \boldsymbol{\sigma}_g = \vec{0} & \text{on} \quad \Omega_g \\ \vec{n} \cdot \boldsymbol{\sigma}_g \cdot \vec{n} = 0 & \text{on} \quad \Gamma_g \end{cases} \tag{14}$$

Finally, the position $\vec{x}_0$ of the material in the grown unloaded geometry at $t + \Delta t$ is computed from that at t according to:

$$\vec{x}_0(t + \Delta t) = \vec{x}_0(t) + \vec{u}_g \tag{15}$$

The growth induced residual stresses $\boldsymbol{\sigma}_g$ are neglected.

2.4 Simulation Parameters

Initial left ventricular geometry in the unloaded reference state is represented by a truncated ellipsoid [2,7]. The initial helix angle α_h, varied linearly from $+60^o$ at the endocardium to -60^o at the epicardium. Sarcomere length $l_{s,0}$ within the myofibers is 1.9 μm. Material parameters a_0 through a_4 in the constitutive model for cardiac tissue during loading are listed in table 1. At the end of diastole, the left ventricle was loaded by an internal cavity pressure p_{lv} of 1 kPa.

In the translation of the mechanical stimulus to growth, $\beta\Delta t$ is set to 0.25. The optimal load value s_{opt} is set to 0.12. Material parameters b_0 and b_1 in the constitutive model for cardiac tissue growth are listed in table 1. A total of 20 growth cycles were performed. After each growth cycle, sarcomere length in the new unloaded reference geometry was set to 1.9 μm.

2.5 Numerical Implementation

To solve (6) and (14), a Galerkin-type finite element method was used, as implemented in the finite element package SEPRAN. The left ventricle is divided into 252 elements with a total of 6885 degrees of freedom. In the 27-noded hexahedral elements, displacements were interpolated quadratically. A Newton-Raphson method was employed to solve the non-linear system of equations. For numerical integration a Newton-Cotes scheme was used.

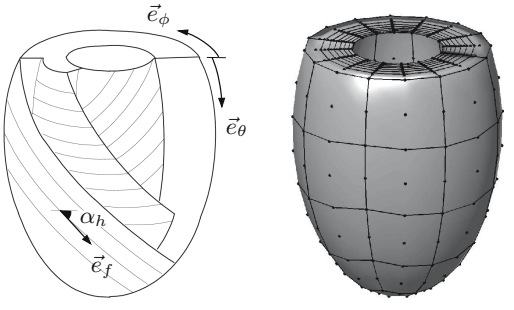

Fig. 2. a) The left ventricle is represented by a truncated ellipsoid. Myofiber orientation is quantified by helix angle α_h. b) The geometry is divided into 252, 27-noded hexahedral elements.

Table 1. Parameter settings for the constitutive model of cardiac tissue during loading and growth

Model	Parameters				
	a_0	a_1	a_2	a_3	a_4
Loading	kPa	-	kPa	-	kPa
	0.5	3.0	0.01	60.0	55.0
	b_0	b_1			
Growth	kPa	kPa			
	0.1	10			

3 Results

Passive inflation of the initial left ventricle to a cavity pressure of 1 kPa resulted in an inhomogeneous distribution of end-diastolic myofiber strain s (figure 3a).

In accordance with the transmural inhomogeneity in strain s, growth was found to be inhomogeneous as well. Figure 3c shows that, after 20 growth cycles, volumetric growth ranged from about +25% in regions with high strain (subendocardium) to -15% in regions with low strain (subepicardium). Figure 3b shows the grown geometry with the associated distribution of end-diastolic strain s. It is clear that the strain has not yet reached to optimal value of $s_{opt} = 0.12$.

Figure 4a and b show the total amount of growth and the load before and after growth in more detail at three longitudinal levels in the wall. Figure 4c shows the relative redistribution in mass within the wall, along with the resulting change in the transmural course in fiber angle α_h from linear to a more parabolic shape. In regions with positive growth, the transmural gradient in fiber angle α_h decreased, whereas a negative growth resulted in an increase in the transmural gradient in α_h.

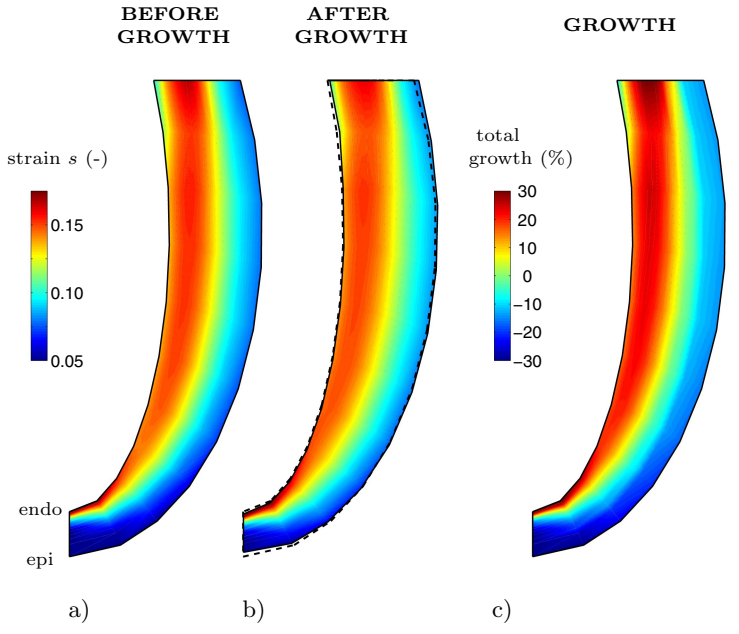

Fig. 3. End-diastolic myofiber strain s resulting from filling of the cavity to a pressure of 1 kPa using a) initial unloaded geometry and b) grown unloaded geometry after 20 growth cycles. c) Total amount volumetric growth after 20 growth cycles.

4 Discussion

In this paper, we have proposed a method to simulate load induced inhomogeneous volumetric growth in a complex tissue geometry. The stimulus for growth is determined from equilibrium of linear momentum under external load using a compressible constitutive law relating tissue stresses to tissue deformation. At maximum inflation, relative volume change J averaged over all nodes was 0.999 ± 0.005 (mean $\pm$ std), with maximum and minimum values of 1.015 and 0.975, respectively. From the tissue load a theoretical volume change J_g^t is determined. During growth we assume the tissue to be compressible. The actual change in volume J_g is calculated from the same equilibrium of linear momentum as used for the load computation, but now in absence of external loading. A strength of this approach is that within the same computational framework (such the finite element method) one can easily switch between computation of load or growth by simply changing the constitutive equation and adding/removing external load.

The growth model was initially tested in the simple case of uniaxial compression a homogeneous cube of cardiac tissue material. Strain along the fiber direction, which was parallel to the force vector, was used as stimulus for growth. After several loading and growth cycles, fiber strain reached the preferred value,

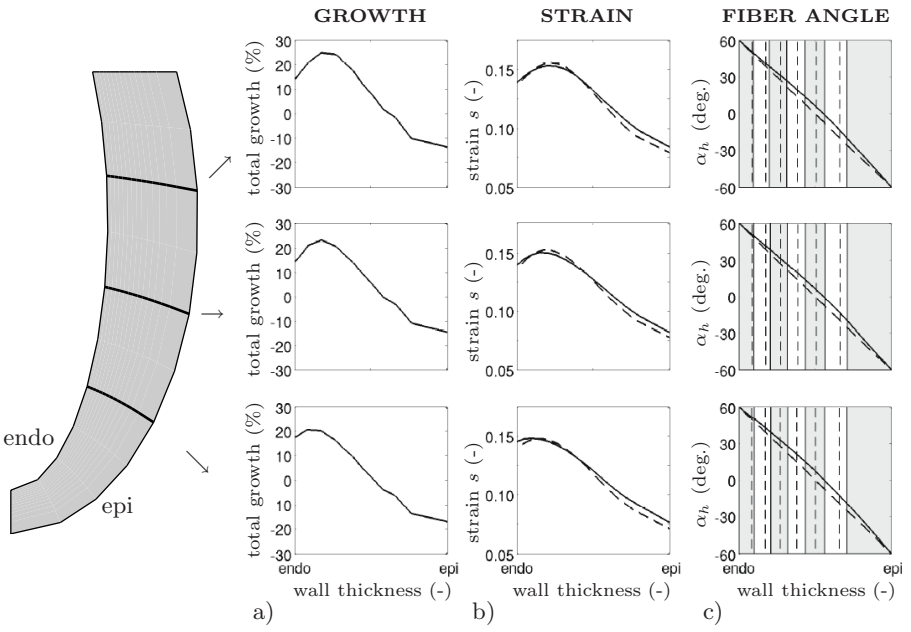

Fig. 4. Transmural variations in the left ventricular wall due to growth. a) Total amount of growth. b) Change in end-diastolic strain s c) Change in transmural course of the helix fiber angle. In b) and c) the dashed lines correspond to the initial geometry and the solid lines to the final (grown) geometry.

at cube dimensions that satisfied the analytical solution. Subsequently, volumetric growth of cardiac tissue in an ellipsoidal representation the left ventricle was chosen as a more complex test case. We were able to simulate growth to at least 25% (see figure 3). Assuming myofiber orientation was fixed to the tissue, growth caused the initially, unphysiological, linear course in fiber angle to transform in a more realistic parabolic shape. It is noted that the same effect was obtained by optimization of fiber orientation for homogeneous fiber strain at begin and during ejection [10]. Possibly, in reality, remodeling of fiber architecture and growth take place simultaneously, together altering transmural distribution of myofiber orientation. However, the focus of this study was restricted to volumetric growth. Also, within our framework the load stimulus is not restricted to strain. Other frequently used stimuli such as stress or strain rate are available within the framework and can easily be used as well. However, whether the used load measure , the optimal level of the load or the relation between load and growth are realistic, is beyond the scope of this study.

The constitutive relation used for the growth model was isotropic meaning that local deposition or resorption by the cell was assumed to be distributed equally over all directions. However, the increase in myofiber diameter in concentric hypertrophy and the increase in myofiber length in eccentric hypertrophy

suggests growth may be anisotropic. Anisotropy in growth can easily be simulated by adding anisotropy to the currently used constitutive law for growth.

Cardiovascular tissue has been shown to carry residual stresses in absence of external loading [8]. Generally, these stresses have been related to the elastic deformation $\boldsymbol{F}_e$, needed to 'mould' incompatible grown tissue parts into one continuous geometry [9,11,12,13]. If the tissue is assumed to behave elastic, i.e. no stress relaxation or creep is considered, these residual stresses will persist in the tissue after growth. However, myocardial tissue behaves viscoelastic [3]. On the time scale of a cardiac cycle, by good approximation, the viscous effects within the cardiac tissue (e.g. stress relaxation) may be neglected and the tissue may be considered elastic. However, on the much larger time scale at which growth occurs, this approximation may no longer be valid and stress relaxation is likely to occur. In addition, cardiomyocytes and the surrounding extra-cellular matrix are subject to continuous metabolic turnover. As a consequence of turnover, in time, tissue constituents bearing the growth induced residual stresses may no longer be present and stress relaxation occurs. The consequence of visco-elasticity and metabolic turnover is that residual stresses induced by growth will disappear in time. To account for the experimentally observed residual stresses within cardiovascular tissue Humphrey *et al.* (2002) and Watton *et al.* (2004) suggested that newly formed constituents may be deposited within the existing tissue under pre-stretch. This pre-stretch may be translated into the residual stress/strain when external load is absent [6,16]. The formation of new, pre-stretched, constituents occurs during continuous turnover which is not restricted to growth alone. We consider our model, in which growth induced stresses are assumed to become zero (and thus are neglected), and models in which growth induced stresses are assumed to persist as limit cases of the real physiological situation.

As a next step, the growth model will be extended with a remodeling part, to simulate changes in tissue composition and fiber orientation. Then, the complete model will be tested for its ability to simulate empirical observations of growth and remodeling, e.g. structural remodeling assessed with diffusion tensor MRI [4,5].

5 Conclusion

We presented a method capable of simulating load induced inhomogeneous volumetric growth in a complex tissue geometry. In a test case, in which volumetric growth of the cardiac left ventricle was driven by deviation of end-diastolic fiber strain from a preset optimum, we were able to simulate growth to at least 25%.

References

1. Arts, T., Prinzen, Fw., Snoeckx, Lh., Rijcken, Jm., Reneman, Rs.: Adaptation of cardiac structure by mechanical feedback in the environment of the cell: a model study. Biophys. J. 66, 953–961 (1994)
2. Bovendeerd, PHM., Arts, T., Huyghe, JM., van Campen, DH., Reneman, RS.: Dependence of local left ventricular wall mechanics on myocardial fiber orientation: a model study. J. Biomech. 25, 1129–1140 (1992)

3. Demer, LL., Yin, FC.: Passive biaxial mechanical properties of isolated canine myocardium. J. Physiol. 339, 615–630 (1983)
4. Geerts-Ossevoort, L.: Cardiac myofiber reorientation: A mechanism for adaptation? PhD thesis, Eindhoven University of Technology, Eindhoven, The Netherlands (2002)
5. Helm, PA., Younes, L., Beg, MF., Ennis, DB., Leclercq, C., Faris, OP., McVeigh, E., Kass, D., Miller, MI., Winslow, RL.: Evidence of structural remodeling in the dyssynchronous failing heart. Circ. Res. 98, 125–132 (2006)
6. Humphrey, JD., Rajagopal, KR.: A constrained mixture model for growth and remodeling of soft tissues. Math. Model. Meth. Appl. Sci. 12, 407–430 (2002)
7. Kerckhoffs, RCP., Bovendeerd, PHM., Kotte, JCS., Prinzen, FW., Smits, K., Arts, T.: Homogeneity of cardiac contraction despite physiological asynchrony of depolarization: A model study. Ann. Biomed. Eng. 31, 536–547 (2003)
8. Omens, JH., Fung, YC.: Residual strain in the rat left ventricle. Circ Res. 66, 37–45 (1990)
9. Rodriguez, Ek., Hoger, A., McCulloch, AD.: Stress-dependent finite growth in soft elastic tissues. J. Biomech. 27, 455–467 (1994)
10. Rijcken, J., Bovendeerd, AJG., Schoofs, van Campen, DH., Arts, T.: Optimization of cardiac myofiber orientation for homgeneous fiber strain during ejection. Ann. Biomed. Eng. 27, 289–297 (1999)
11. Skalak, E., Dasgupta, G., Moss, M., Otten, E., Dullemeijer, P., Vilmann, H.: Analytical description of growth. J. Theor. Biol. 94, 555–577 (1982)
12. Skalak, E., Zargaryan, S., Jain, RK., Netti, PA., Hoger, A.: Compatibility and the genesis of residual stress by volumetric growth. J. Math. Biol. 34, 889–914 (1996)
13. Taber, LA.: Biomechanics of growth, remodeling, and morphogenesis. Appl. Mech. Rev. 48, 487–545 (1995)
14. Taber, LA., Perucchio, R.: Modeling heart development. J. Elast. 61, 165–197 (2000)
15. Ubbink, SWJ., Bovendeerd, PHM., Delhaas, T., Arts, T., van de Vosse, FN.: Towards model-based analysis of cardiac MR tagging data: relation between left ventricular shear strain and myofiber orientation. Med. Image Analysis 10, 632–641 (2006)
16. Watton, PN., Hill, NA., Heil, M.: A mathematical model for the growth of abdominal aortic aneurysm. Biomechan Model Mechanobiol. 3, 98–113 (2004)

Effect of Pacing Site and Infarct Location on Regional Mechanics and Global Hemodynamics in a Model Based Study of Heart Failure

Roy C.P. Kerckhoffs[1], Andrew D. McCulloch[1], Jeffrey H. Omens[1,2], and Lawrence J. Mulligan[3]

[1] Department of Bioengineering, The Whitaker Institute for Biomedical Engineering
[2] Department of Medicine, University of California San Diego, 9500 Gilman Dr, La Jolla CA 92093-0412, USA
[3] Therapy Delivery Systems/Leads Research, Medtronic Inc., 7000 Central Ave NE, Fridley, MN 55432, USA
roy@bioeng.ucsd.edu, amcculloch@ucsd.edu, jomens@ucsd.edu, larry.mulligan@medtronic.com

Abstract. Clinical trials evaluating cardiac resynchronization therapy (CRT) have demonstrated that 30% of patients with heart failure and wide QRS do not respond to CRT (especially patients with myocardial infarcts). We have developed 3D numerical models of failing hearts, with and without chronic infarcts in different regions of the left ventricle. The hearts were coupled to a closed circulation, and the model included effects of the pericardium. The hearts were either paced at the right ventricular apex (RVA) or left ventricular free wall (LVFW). In normal and failing hearts, LV pump function was moderately better for LVFW pacing. In the normal heart model, heterogeneity of ejection strain was similar for RVA and LVFW pacing. However, in the failing heart model, LVFW pacing was associated with 44% less heterogeneity of ejection strain. This may be an important factor in the remodeling process associated with pacing.

Keywords: mechanics, hemodynamics, 3D electromechanics, ventricular pacing.

1 Introduction

Cardiac resynchronization therapy (CRT) is an increasingly popular strategy for improving pump function in heart failure patients with QRS widening. However, 30-50% of patients receiving this therapy appear to demonstrate little if any improvement. Those patients with prior myocardial infarcts appear to represent a majority of patients with a poor response [1]. There is also evidence that some patients without QRS widening may benefit from CRT. Recent work has shown that patients with mechanical dyssynchrony exhibit significant improvement in cardiac function following CRT. However, a clear understanding regarding the discrepancy between electrical and mechanical dyssynchrony is lacking. Studies in patients and animals cannot obtain complete 3D information on regional electrical activation and mechanical

F.B. Sachse and G. Seemann (Eds.): FIMH 2007, LNCS 4466, pp. 350–360, 2007.

function in the same heart. Anatomically detailed computational models of cardiac electromechanics have been shown to predict the effects of ventricular pacing on the mechanics and hemodynamics of normal and failing hearts [8, 14].

The goal of this study was to use 3D computational models of ventricular electromechanics in the dog heart to investigate the effects of single site pacing (right ventricular apex, RVA; and left ventricular free wall, LVFW) and infarct location (anterior, inferior, posterolateral, diffuse ischemia) in failing hearts on global and regional function and – in the long term – to use these findings to suggest new approaches to ventricular pacing therapy.

2 Methods

The cardiovascular model consisted of a 3D model of the canine ventricles (including passive and active mechanics) coupled to a closed circulation. The effects of the pericardium were included as pressure acting on the epicardium. The geometries used either represented a normal dog heart or a dilated heart. These hearts were either paced at the right ventricular apex (RVA), representing left bundle branch block, or left ventricular free wall (LVFW). The latter was chosen since pacing the LV alone has been shown to produce responses similar to those with bi-ventricular pacing. Active mechanical properties for a failing heart were included for the dilated hearts (lower peak active stress and longer twitch). In these failing hearts, chronic infarcts were included at several regions.

2.1 Cardiovascular Model

The 3D finite element model of the canine ventricles was coupled to a lumped-parameter systems model of the systemic and pulmonary circulations (Fig. 1A) [9]. The finite element model included left and right ventricular geometry and a 3D myofiber angle distribution. Passive stress was modeled using a strain energy function for exponential transversely isotropic material. Active stress was dependent on time, sarcomere length and intracellular calcium concentration. Active stress generated transverse to the myofiber was about 40% of active stress generated in the myofiber direction [13].

The systemic and pulmonary circulations were each modeled with two lumped windkessel compartments in series, one compartment for arterial and capillary blood and one for venous blood (Fig. 1A). The atria were represented with time-varying elastance models.

A total of eleven models were designed with different properties: three contained a normal heart and eight contained dilated failing hearts (Fig. 1C). In the three simulations with the normal heart, one represented a heart paced at the right atrium (RA), one was paced at the right ventricular apex (RVA), and one was paced at the left ventricular free wall (LVFW) (Fig. 1D). Of the failing hearts, one was free of infarct and three had infarct locations; anterior, posterolateral, and inferior (all chronic, Fig. 1E).

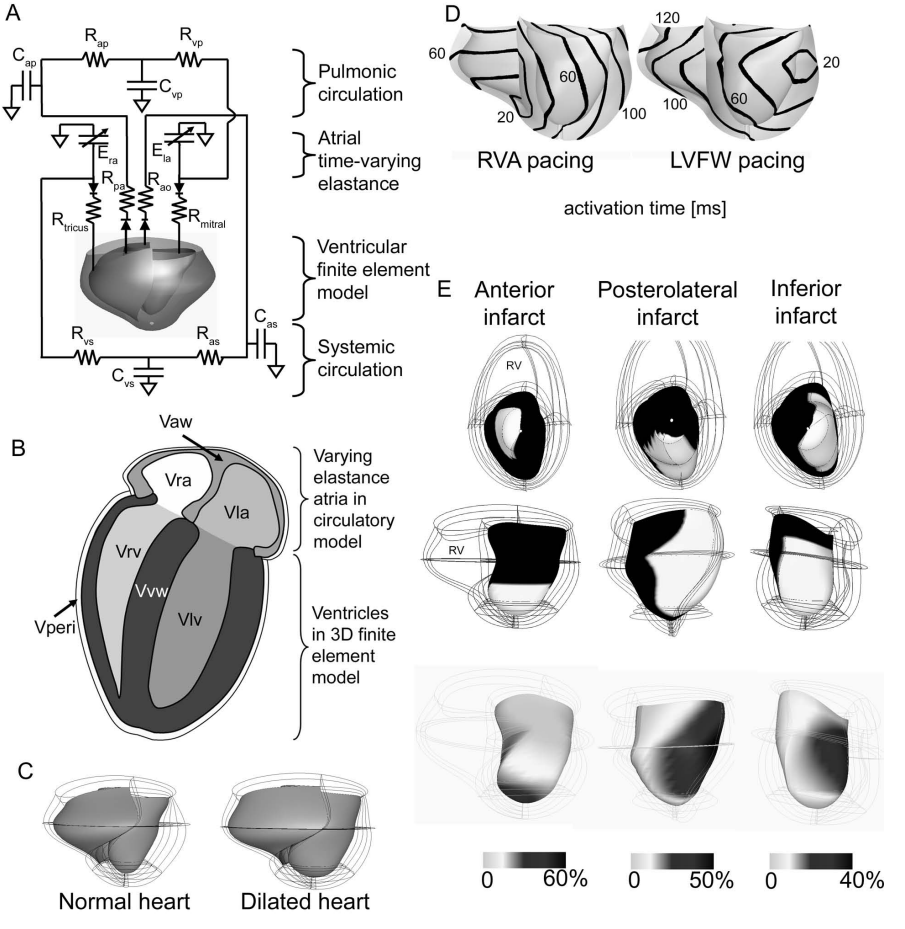

Fig. 1. Overview of the cardiovascular model. A) Electric analog schematic of the circulatory model with the ventricular finite element model embedded. C_{ap} compliance of pulmonic arteries and capillaries; C_{vp} compliance of pulmonic veins; C_{as} compliance of systemic arteries and capillaries; C_{vs} compliance of systemic veins; R_{ap} resistance of pulmonic arteries and capillaries; R_{vp} resistance of pulmonic veins; R_{as} resistance of systemic arteries and capillaries; R_{vs} resistance of systemic veins; E_{la} left atrial time-varying elastance; E_{ra} right atrial time-varying elastance; R_{mitral} mitral valve resistance; R_{tricus} tricuspid valve resistance; R_{ao} aortic valve impedance; R_{pa} pulmonic artery impedance. Note that aortic pressure is in fact mean pressure over the aorta, arteries and capillaries. The same applies for pulmonary artery pressure. B) Volumes contributing to the total volume in the pericardium model. See Table 1 for an explanation of the parameters. C) The geometries of the normal and dilated heart without an infarct. D) Electrical activation times for pacing at the right ventricular apex (RVA) and left ventricular free wall (LVFW) in the failing heart. E) Top views (top) and side views (middle) of the locations and thickness (bottom) of the three transmural infarcts, shown here at the LV endocardium. The thickness was based on measured values from literature [3] and is given as a percentage of the wall thickness in the dilated heart without an infarct.

2.2 Heart Geometry and Myofiber Orientation

Two different geometries were used in the models: the normal heart had a LV cavity to wall volume ratio of 0.27, while those of the dilated hearts ranged from 0.57 to 0.77 (Fig. 1C). The normal geometry has been used before [9], while the dilated ones were created by inflating the normal geometry to the desired cavity to wall volume ratio, and defining that state as the undeformed one. The same realistic myofiber architecture was included in both geometries, since the myofiber distribution in normal and dilated hearts is not significantly different [6]. However, because of the thinner walls in the dilated heart, the transmural fiber gradient is larger in this heart, as noted by Helm et al [6].

2.3 Mechanical Material Properties

The normal heart included canine passive and active material properties as modeled previously [9]. In the dilated hearts, passive properties of the non-infarcted tissue were the same as in the normal heart. The passive properties of the infarct were based on a 22 week old infarct as determined by Walker et al [16], being about 15 times stiffer and less anisotropic as compared to healthy tissue. The active properties of the failing non-infarcted tissue were scaled from human data [12], in which the peak force was 27% lower than in healthy tissue, and the force twitch duration was 17% longer.

2.4 Pericardium

The pericardium plays an important role in direct ventricular interaction, and as suggested by Bleasdale et al [2], direct ventricular interaction plays an important role during LV pacing of failing hearts. We therefore included a pericardium. The effect of the pericardium was modeled by pericardial pressure acting on the ventricular epicardium, and was added to the atrial cavity pressures. Pericardial pressure p_{peri} was exponentially dependent on total volume V_{tot} encompassed by the pericardium [5], normalized to a reference volume $V_{tot,0}$:

$$p_{peri} = \alpha(\exp(\beta(\frac{V_{tot}}{V_{tot,0}} - 1) - 1)) \tag{1}$$

where

$$\begin{aligned} V_{tot} &= Vvw + Vaw + Vperi + Vlv + Vrv + Vla + Vra \\ V_{tot,0} &= Vvw + Vaw + Vperi + Vlv_{rest} + Vrv_{rest} + Vla_{rest} + Vra_{rest} \end{aligned} \tag{2}$$

See Fig. 1B and Table 1 for explanation of the volume components and the effect of scaling the PV-relation. In this pericardium model, Vlv, Vrv, Vla, Vra are variables, determined from the cardiovascular model, while the other components are parameters. The difference in the pericardial PV relation between normal and dilated hearts, as determined by Freeman and Lewinter [4], was included in the analysis.

Table 1. Parameters and values of the pericardium model for the normal and failing hearts and infarct size. Parameters α and β were adopted from Freeman et al [5]. Note that these parameters are the same for both the normal and dilated hearts, since after scaling with unloaded volumes (the approach used in the model), the scaled PV relation for normal and remodeled pericardia are very similar [4].

Parameter	Description	Normal heart	Failing heart no infarct	Failing heart anterior infarct	Failing heart postlat infarct	Failing heart inferior infarct
α [mmHg]	pressure scaling factor	0.031	0.031	0.031	0.031	0.031
β [-]	exponential shape factor	6.76	6.76	6.76	6.76	6.76
Vaw [ml]	atrial wall volume	5.94	5.94	5.94	5.94	5.94
Vvw [ml]	ventricular wall volume	132	119	117	109	112
Vperi [ml]	pericardial fluid volume	10.0	15.0	15.0	15.0	15.0
Vla_{rest} [ml]	unloaded left atrial cavity volume	14.0	14.0	14.0	14.0	14.0
Vra_{rest} [ml]	unloaded right atrial cavity volume	14.0	14.0	14.0	14.0	14.0
Vlv_{rest} [ml]	unloaded left ventricular cavity volume	26.1	45.6	47.4	54.9	56.8
Vrv_{rest} [ml]	unloaded right ventricular cavity volume	22.3	30.0	30.1	30.5	25.6
Infarcted tissue [%]	Volume percentage of LV affected by infarct	0	0	11	26	34

2.5 Activation Sequences

The activation sequences for pacing at the RVA (QRS width 126 ms) and LVFW (QRS width 139 ms) (Fig. 1D) in the failing heart were calculated previously by solving modified Fitz-Hugh-Nagumo equations in a monodomain setting [14]. The QRS width for pacing at the RVA and LVFW in the normal hearts was 86 and 107 ms, respectively. The activation times served as input to the mechanics model, in which myofiber contraction was initiated with an 8 ms delay after the local electrical activation.

2.6 Simulations and Data Analysis

For every simulation, steady state values were obtained. Steady state was defined as the state in which the LV and RV stroke volume difference, normalized to LV stroke volume, was less than 2%. Hemodynamic data were obtained every 4 ms. Deformed ventricular geometries were obtained every 8 ms. LV dp/dt_{max}, dp/dt_{min}, maximum pressure, stroke volume SV, ejection fraction EF, stroke work SW, potential energy PE, and efficiency (=SW/(SW+PE)*100) were calculated for every heartbeat.

2.7 Numerical Solutions

The FE anatomic model of the canine heart was discretized into 48 tricubic Hermite elements, with 1968 degrees of freedom.

The nonlinear FE model was solved with a modified Newton iteration scheme. Integration was performed with 3x3x3 Gaussian quadrature points. Convergence was reached when both the maximal incremental displacement solution and the maximal value of the residuals were lower than 10^{-5}. The Jacobian was calculated and factorized in the first iteration of a new time step and when the solution was diverging. The system of linear equations was solved with SuperLU, a direct solver optimized for sparse matrices. The circulatory model was integrated in time with the Radau5 solver. Absolute and relative tolerances were set at 10^{-4}. The initial guess for the step size was set at 10^{-3}.

The combined multi-scale model was solved with the Continuity 6.3 package (http://www.continuity.ucsd.edu). All simulations were solved on a 105 node Dell™ Rocks Linux cluster with 3.2 GHz 64 bit Xeon® processors (11 simulations, one for each processor) and 2 GB of RAM. On average, it took 2.1 minutes to solve one time step, resulting in a simulation time of 5.5 hours per cardiac cycle. However, recently we have parallelized the code for Jacobian and residual vector assembly, which brought down the simulation time to 36 minutes per cardiac cycle on 13 processors running in parallel. Maximum total RAM needed was about 200 MB per simulation.

3 Results

3.1 Steady State Values

The normal heart (synchronous, LVFW and RVA pacing) functioned at lower diastolic pressures and volumes than the failing hearts (Table 2). The highest hemodynamic performance was seen in the synchronously stimulated normal heart. The PV loops of the failing hearts were shifted more to the right (Fig. 2). This rightward shift was larger for the LV than for the RV. Also, the larger the infarct, the higher were the end-diastolic pressures. In all simulations with the failing hearts, LV hemodynamic performance was slightly improved for LVFW pacing than RVA pacing, while RV hemodynamic performance improved when the RVA was paced. Results for the normal and failing heart without an infarct were qualitatively similar to previously published experimental results (Table 3).

The patterns of strain during pacing (shortening in early activated regions and stretching in late activated regions) were similar to those in experiments [17] (Fig. 3A). In the normal hearts, mean LV ejection strain was most negative for the RVA paced heart, while it was less negative for the LVFW paced heart (Fig. 3B). In both the RVA and LVFW paced normal hearts, LV ejection strain was respectively 66 and 69% more heterogeneous than in the synchronously stimulated heart (as determined by the standard deviation). RV ejection strain was most negative in the LVFW paced normal heart, but also most heterogeneous. In the failing hearts, LV ejection strain was less negative in all LVFW paced hearts, but less heterogeneous than in the RVA paced hearts. In the failing heart without an infarct, LVFW pacing decreased heterogeneity of LV ejection strain by 44% (vs. RVA pacing). RV ejection strain was most negative in all LVFW paced hearts, while RV ejection strain heterogeneity was similar in RVA and LVFW paced hearts.

Table 2. Left and right (L and R, resp) steady-state hemodynamic results from the simulations for the normal and failing hearts. RAp right atrial paced; RVp paced at right ventricle; LVp paced at left ventricle; dp/dt_{max} Maximum pressure increase; dp/dt_{min} Minimum pressure decrease; EF Ejection fraction; PE Potential energy; p_{max} Peak pressure; $Q_{out,max}$ Maximum ventricular outflow; SV Stroke volume; SW Stroke work.

		Normal Heart			Failing, No Infarct		Failing, Anterior Infarct		Failing, Posterolat. Infarct		Failing, Inferior Infarct	
		RAp	RVp	LVp	RVp	LVp	RVp	LVp	RVp	LVp	RVp	LVp
dp/dt_{max} [mmHg/sec]	L	1630	1440	1479	635	713	576	665	511	567	462	528
	R	463	406	314	236	217	245	231	251	252	264	251
p_{max} [mmHg]	L	101.0	97.4	100.2	88.4	89.7	83.3	84.5	65.1	65.8	69.3	70.6
	R	27.7	26.2	25.1	24.6	24.0	25.9	25.3	23.4	23.0	29.7	28.8
SV [ml]	L	19.7	18.7	19.3	18.3	18.4	17.3	17.5	14.9	15.1	13.7	13.9
	R	19.5	18.7	19.2	18.6	18.5	17.5	17.4	15.1	15.3	14.0	14.0
EF [%]	L	43.8	42.3	43.1	22.0	22.4	21.0	21.4	17.0	17.3	15.8	16.1
	R	51.5	50.4	50.7	40.4	39.9	37.6	37.1	31.9	32.1	33.2	33.0
SW [mmHg·ml]	L	1662	1523	1619	1314	1361	1133	1178	680	701	644	674
	R	370	324	325	324	308	327	307	250	235	299	275
PE [mmHg·ml]	L	501	493	503	1494	1459	1344	1308	1145	1137	1051	1037
	R	124	130	125	139	147	155	167	197	207	207	223
Efficiency [%]	L	76.8	75.5	76.3	46.8	48.3	45.7	47.4	37.3	38.1	38.0	39.4
	R	74.9	71.4	72.1	70.0	67.7	67.8	64.7	56.0	53.1	59.1	55.2

Table 3. Comparison with experimentally obtained hemodynamic data. RVp(%) represents percentage change with respect to RAp and LVp(%) represents percentage change with respect to RVp. See Table 2 for further explanation of abbreviations.

		Normal Heart			Failing, No Infarct	
	Experiment/Simulation	RAp (abs)	RVp (%)	LVp (%)	RVp (abs)	LVp (%)
dp/dt_{max} [mmHg/sec]	Liu et al [11]	1162±106.1	**-28.5**	**8.5**		
	Verbeek et al [15]	1627±644	**-17.3**			
	Leclercq et al [10]				1048±242	**24.9**
	Simulation	1630	**-11.7**	**2.7**	635	**12.3**
p_{max} [mmHg]	Liu et al [11]	94.5±4.7	**-7.9**	**12.8**		
	Verbeek et al [15]	98.8±12.0	**-6.7**			
	Leclercq et al [10]				86.6±7.7	**5.9**
	Simulation	101	**-3.6**	**2.9**	88.4	**1.5**
EF [%]	Leclercq et al [10]				23±12.7	**21.7**
	Simulation	43.8	**-1.6**	**1.9**	22	**1.8**

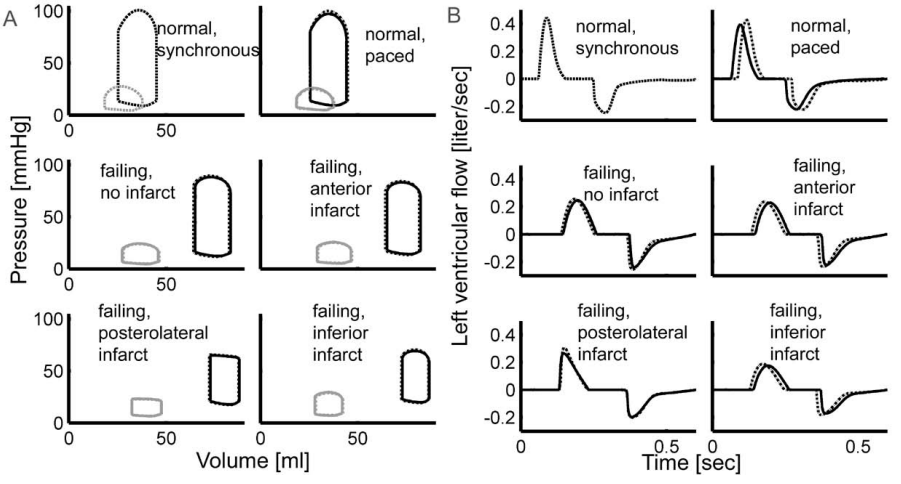

Fig. 2. A) Steady state LV (black) and RV (gray) PV-loops, and B) left ventricular flows (aortic flow is positive; mitral flow is negative). In all simulations: the normal synchronously stimulated heart, dashed lines; RVA paced, solid lines; LVFW paced, dash-dotted lines.

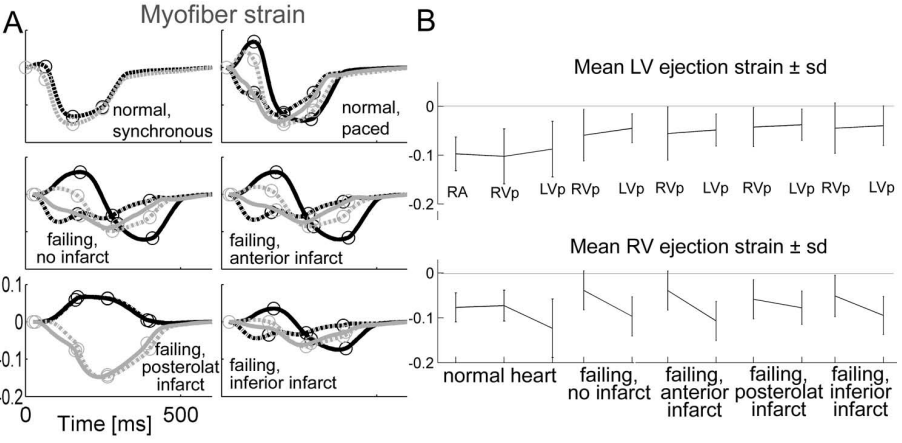

Fig. 3. A) Myofiber natural strain at a location in the equatorial midwall in the LVFW (black lines) and equatorial midwall in the septum (gray lines) for a full cardiac cycle paced synchronously (top left panel) or at RVA (solid lines) and LVFW (dash-dotted lines) in the other panels. For the posterolateral infarct simulation, the strain at the LVFW (black) was in the infarct. Circles denote phase B) mean LV and RV myofiber strain during ejection (± sd) in steady state.

4 Discussion

We have developed a number of computational models of the ventricularly paced failing heart with and without chronic infarcts, and a pericardium. Results on global function were qualitatively similar to previously published experimental results.

LVFW pacing was always associated with improvements in LV stroke work and dp/dt_{max} under all conditions (Table 2). The improvements in stroke work and dp/dt_{max} were associated with lower EDP, suggesting that LVFW improved diastolic function with small improvements in global contractile function.

However, in the failing LVFW paced heart, improvements in regional contractile function were large, compared with RVA pacing, which has also been shown experimentally [7]. Changes in regional loading have been shown to contribute to the disease process observed with abnormal conduction. Although mean LV ejection strain was slightly less negative with LVFW pacing, as compared with RVA pacing, it was less heterogeneous, especially in the failing hearts with no and anterior infarct. Interestingly, with LVFW pacing, there was no change in heterogeneity of LV ejection strain in the normal hearts, compared to RVA pacing, whereas LVFW pacing decreased heterogeneity in the failing hearts. The smallest differences in regional function, comparing LVFW with RVA pacing, were seen in the failing heart with a posterolateral infarct.

A more thorough comparison is needed between computational and experimental results, especially for the failing hearts with infarcts. This will be subject in future studies.

4.1 Limitations

Several physiological responses (baroreflex) and pathophysiologies (mitral regurgitation) affecting hemodynamics were not included in the models of heart failure. For example, a drop in aortic pressure due to decreased cardiac function will result in a baroreflex mediated increase in the resistance of the peripheral circulation by vasoconstriction. Also, mitral regurgitation has been shown to develop in patients and animals with LBBB and dyssynchrony, which might develop dilated atria. Inclusion of these mechanisms in the model would be interesting directions for future study.

The depolarization wave was not affected by the infarcted regions. In reality, depolarization travels around and/or slowly through infarcts. This might have a larger effect on the results for a pacing location close to an infarct (LVFW) than those remote (RVA). This could explain the relative small differences in global hemodynamics between the LVFW and RVA paced failing hearts with an infarct. This will also be addressed in a future study.

5 Conclusions

Computational assessment of cardiac global and regional function to understand the impact of pacing site in the normal and failing heart is feasible. In the normal heart model, heterogeneity of ejection strain was similar for RVA and LVFW pacing. However, in the failing heart model, while global function was moderately better for LVFW pacing, compared with RVA pacing, LVFW pacing was associated with 44% less heterogeneity of ejection strain. This may be an important factor in the remodeling process associated with RVA pacing.

Acknowledgments

This work was financially supported by Medtronic, Inc., the National Biomedical Computation Resource (NIH grant P41 RR08605) (to A.D.M), National Science Foundation grants BES-0096492 and BES-0506252 (to A.D.M), and NIH grant HL32583 (to J.H.O). This investigation was conducted in a facility constructed with support from Research Facilities Improvement Program Grant Number C06 RR-017588-01 from the National Center for Research Resources, National Institutes of Health. A.D.M. and J.H.O. are co-founders of Insilicomed Inc., a licensee of UCSD-owned software used in this research.

References

1. Ansalone, G., Giannantoni, P., Ricci, R., Trambaiolo, P., Fedele, F., Santini, M.: Biventricular pacing in heart failure: back to basics in the pathophysiology of left bundle branch block to reduce the number of nonresponders. Am. J. Cardiol. 91, 55–61 (2003)
2. Bleasdale, R.A., Turner, M.S., Mumford, C.E., Steendijk, P., Paul, V., Tyberg, J.V., Morris-Thurgood, J.A., Frenneaux, M.P.: Left ventricular pacing minimizes diastolic ventricular interaction, allowing improved preload-dependent systolic performance. Circulation 110, 2395–2400 (2004)
3. Fieno, D.S., Hillenbrand, H.B., Rehwald, W.G., Harris, K.R., Decker, R.S., Parker, M.A., Klocke, F.J., Kim, R.J., Judd, R.M.: Infarct resorption, compensatory hypertrophy, and differing patterns of ventricular remodeling following myocardial infarctions of varying size. J. Am. Coll. Cardiol. 43, 2124–2131 (2004)
4. Freeman, G.L., Lewinter, M.M.: Pericardial adaptations during chronic dilation in dogs. Circ. Res. 54, 294–300 (1984)
5. Freeman, G.L., Little, W.C.: Comparison of in situ and in vitro studies of pericardial pressure-volume relation in dogs. Am. J. Physiol-Heart Circ. Physiol. 251, 421–427 (1986)
6. Helm, P.A., Younes, L., Beg, M.F., Ennis, D.B., Leclercq, C., Faris, O.P., McVeigh, E.R., Kass, D.A., Miller, M.I., Winslow, R.L.: Evidence of structural remodeling in the dyssynchronous failing heart. Circ. Res. 98, 125–132 (2006)
7. Helm, R.H., Leclercq, C., Faris, O.P., Ozturk, C., McVeigh, E., Lardo, A.C., Kass, D.A.: Cardiac dyssynchrony analysis using circumferential versus longitudinal strain - Implications for assessing cardiac resynchronization. Circulation 111, 2760–2767 (2005)
8. Kerckhoffs, R.C.P., Faris, O., Bovendeerd, P.H.M., Prinzen, F.W., Smits, K., McVeigh, E.R., Arts, T.: Electromechanics of paced left ventricle simulated by straightforward mathematical model: comparison with experiments. Am. J. Physiol-Heart Circ. Physiol. 289, 1889–1897 (2005)
9. Kerckhoffs, R.C.P., Neal, M., Gu, Q., Bassingthwaighte, J.B., Omens, J.H., McCulloch, A.D.: Coupling of a 3D finite element model of cardiac ventricular mechanics to lumped systems models of the systemic and pulmonic circulation. Ann. Biomed. Eng. 35, 1–18 (2007)
10. Leclercq, C., Faris, O., Tunin, R., Johnson, J., Kato, R., Evans, F., Spinelli, J., Halperin, H., McVeigh, E., Kass, D.A.: Systolic improvement and mechanical resynchronization does not require electrical synchrony in the dilated failing heart with left bundle-branch block. Circulation 106, 1760–1763 (2002)

11. Liu, L.L., Tockman, B., Girouard, S., Pastore, J., Walcott, G., KenKnight, B., Spinelli, J.: Left ventricular resynchronization therapy in a canine model of left bundle branch block. Am. J. Physiol-Heart Circ. Physiol. 282, 2238–2244 (2002)
12. Pieske, B., Sütterlin, M., Schmidt-Schweda, S., Minami, K., Meyer, M., Olschewski, M., Holubarsch, C., Just, H., Hasenfuss, G.: Diminished post-rest potentiation of contractile force in human dilated cardiomyopathy. J. Clin. Invest. 88, 765–776 (1996)
13. Usyk, T.P., Mazhari, R., McCulloch, A.D.: Effect of laminar orthotropic myofiber architecture on regional stress and strain in the canine left ventricle. J. Elast. 61, 143–164 (2000)
14. Usyk, T.P., McCulloch, A.D.: Electromechanical model of cardiac resynchronization in the dilated failing heart with left bundle branch block. J. Electrocardiol. 36, 57–61 (2003)
15. Verbeek, X., Vernooy, K., Peschar, M., van der Nagel, T., Van Hunnik, A., Prinzen, F.W.: Quantification of interventricular asynchrony during LBBB and ventricular pacing. Am. J. Physiol-Heart Circ. Physiol. 283, 1370–1378 (2002)
16. Walker, J.C., Ratcliffe, M.B., Zhang, P., Wallace, A.W., Fata, B., Hsu, E.W., Saloner, D., Guccione, J.M.: MRI-based finite-element analysis of left ventricular aneurysm. Am. J. Physiol-Heart Circ. Physiol. 289, 692–700 (2005)
17. Wyman, B.T., Hunter, W.C., Prinzen, F.W., McVeigh, E.: Mapping propagation of mechanical activation in the paced heart with MRI tagging. Am. J. Physiol-Heart Circ. Physiol. 276, 881–891 (1999)

Effective Estimation in Cardiac Modelling

Philippe Moireau and Dominique Chapelle

INRIA, MACS team, B.P.105, 78153 Le Chesnay cedex, France

Abstract. We present a novel strategy to perform estimation for a mechanical system defined to feature the same essential characteristics as a heart model, using measurements of a type that is available in medical imaging. We adopt a sequential approach, and the joint state-parameter estimation procedure is constructed based on a robust and effective state estimator inspired from collocated feedback control. The convergence of the resulting joint estimator can be mathematically established, and we demonstrate its effectiveness by identifying localized contractility and stiffness parameters in a test problem representative of cardiac behavior and using synthetic – albeit realistic – measurements.

1 Introduction

The challenges represented by estimation in distributed mechanical systems have been recently renewed and extended – in particular – by the rapidly developing applications of biomechanics in medicine [14,2,15]. Indeed, the physical parameters considered in a biomechanical model are generally very difficult to determine *a priori* by experimentations, as living materials display very different behaviours when taken *in vivo* on the one hand, and *post-mortem* or even *in vitro* on the other hand. Moreover, for *diagnosis purposes* in medicine, estimation can be envisaged as a methodology to assess the condition of a patient's living organ, such as the heart.

In order to develop an estimation procedure of unknown quantities characteristic of the heart behavior – such as stiffness and contractility parameters for the tissue – we must rely on available imaging modalities and an accurate model. Therefore, conceptual difficulties arise from various scientific fields: image processing, modeling and estimation. In this paper we focus on *estimation*, hence we resort to synthetic measurements and simplified models, both being designed to retain the essential features – of cardiac behavior and the corresponding imaging modalities – that are of primary concern for estimation purposes. For more complex and realistic modeling approaches see in particular [8,14] and references therein. The specific objective we pursue here is to formulate an effective and robust estimation methodology inspired from filtering procedures and specifically adapted to the difficulties and essential characteristics of the cardiac framework.

2 Problem Statement

We start by introducing the fundamental challenges that must be confronted in estimation, before presenting the model and measurements considered.

F.B. Sachse and G. Seemann (Eds.): FIMH 2007, LNCS 4466, pp. 361–372, 2007.

2.1 Estimation Fundamentals and Challenges

Basic Definitions and Objectives

We consider a dynamical system written in the general formalism

$$\dot{x} = \mathcal{A}(x), \quad \text{with } x(0) = x_0 + \zeta_x, \tag{1}$$

where x is the *state vector* and $\mathcal{A}$ denotes a differential operator. The uncertainty on the state is only contained in the initial condition as represented by ζ_x. Hence, the basic objective of estimation theory consists in identifying ζ_x using the available measurements Z represented by an *observation operator* $\mathcal{H}$ with additive noise χ

$$Z = \mathcal{H}(x) + \chi, \tag{2}$$

This means that without measurements we can only perform *direct simulations* of the above system with $\zeta_x = 0$, which generates a persistent error between the real and simulated systems. Using measurements allows to reduce this error by creating a new system called the *state estimator*.

Classical Methodologies

Estimation methodologies fall into two major categories:

- *Sequential approaches* (see [1]) in which the state estimator is given by a dynamical system of the form

$$\dot{\hat{x}} = \mathcal{A}(\hat{x}) + K(Z - \mathcal{H}(\hat{x})), \quad \text{with } \hat{x}(0) = x_0, \tag{3}$$

  where K is called the *gain operator*. When $\mathcal{A}$ and $\mathcal{H}$ are linear the optimal gain is given by the well-known *Kalman filter* from [9].
- *Variational approaches* in which the state estimator is the result of a the minimization algorithm based on measurement-specific criteria. The most classical one is

$$\mathcal{J}(\zeta_x) = \int_0^T \|Z - \mathcal{H}(x)\|_\chi^2 + \|\zeta_x\|_{\zeta_x}^2, \tag{4}$$

  where the norms are chosen with respect to the characteristics of the measurement noise χ and the indetermination ζ_x.

In the case of linear operators $\mathcal{A}$ and $\mathcal{H}$, the variational approach based on the criterion (4) and the sequential Kalman approach can be shown to be equivalent [4], which – indeed – proves the optimality of the Kalman filter.

As regards complexity considerations, variational approaches typically require the computation of an adjoint state in order to compute the gradient of the criterion. This means that – at each minimization step – a double time integration must be performed (forward and backward in time for the direct and adjoint states, respectively) with a finite element problem solved at each time step for both states. This induces heavy computations, together with extensive storage because the direct state is needed at all time steps to solve for the adjoint state.

On the other hand, classical sequential approaches are intractable when dealing with distributed systems, because they necessitate the use – hence the computation, storage and various manipulations – of covariance matrices that have the size of the state vector (typically at least 10000 degrees of freedom) and have full profile. In this paper, we focus on the design of a sequential algorithm that retains the algorithmic simplicity of filtering without requiring the computation of this covariance matrix.

Parameter Estimation
In fact, as mentioned before we are primarily interested in *parameter estimation*, rather than in state estimation. Let θ denote the vector containing all the parameters that we wish to identify. We can rewrite the state dynamics as

$$\dot{x} = \mathcal{A}(x, \theta), \quad \text{with } x(0) = x_0 + \zeta_x,\ \theta = \theta_0 + \zeta_\theta, \tag{5}$$

where ζ_θ represents the unknown deviation with respect to a mean value θ_0. It is then very easy to reformulate the previous two approaches considering θ as a part of an *augmented state vector* x^e such that

$$\dot{x}^e = \mathcal{A}^e(x^e), \quad \text{with } x^e(0) = x_0^e + \zeta^e, \tag{6}$$

where

$$x^e = \begin{pmatrix} x \\ \theta \end{pmatrix}, \quad \mathcal{A}^e = \begin{pmatrix} \mathcal{A} \\ 0 \end{pmatrix}, \quad x_0^e = \begin{pmatrix} x_0 \\ \theta \end{pmatrix}, \quad \zeta^e = \begin{pmatrix} \zeta_x \\ \zeta_\theta \end{pmatrix}. \tag{7}$$

Thus we are concerned with *joint state-parameter estimation*. We emphasize that parameter estimation cannot be considered by itself and must be performed indissolubly from the state estimation, since errors in the state induce wrong inferences on the parameters.

Observability Issues
Observability and identifiability – as regards parameter estimation more specifically – are issues whose complexity lies much beyond the scope of this paper. Nevertheless, our objective in our simplified modeling is to formulate a test problem that features the same essential difficulties in this respect, without the unnecessary computational complexity associated with more "realistic" models. Namely, the parameters that we primarily want to estimate correspond to stiffness and contractility quantities – to account for the variations of such parameters due to various cardiac pathologies – and these parameters have an influence only in certain phases of the behavior, such as systole for contractility.

2.2 Physical Modeling

Our simplified mechanical model is based on a general variational formulation of the type

$$\int_\Omega \rho \ddot{\underline{y}} \cdot \delta \underline{y}\, d\Omega + \int_\Omega \underline{\underline{\Sigma}}(\underline{y}, \dot{\underline{y}}) : \delta \underline{\underline{e}}\, d\Omega = \int_\Omega \underline{f} \cdot \delta \underline{y}\, d\Omega, \quad \forall \delta \underline{y}, \tag{8}$$

where the main unknown is the displacement $\underline{y}$ between the reference position and the current position at time t. In addition, Ω represents the geometrical domain of the system, ρ the mass per unit volume, $\underline{\underline{\Sigma}}$ the second Piola-Kirchhoff stress tensor, $\delta\underline{y}$ an arbitrary test function in the displacement space with $\delta\underline{\underline{e}}$ the corresponding infinitesimal variation of the Green-Lagrange strain tensor, and $\underline{f}$ the applied loading (taken here as a 3D distributed field to fix the ideas). This equation is fundamentally a second order equation in time, but can be put into a first order form by introducing the state vector $x = (\underline{y} \quad \underline{\dot{y}})^T$. Assuming that $\underline{\underline{\Sigma}}$ is a linear function of x – which corresponds to the classical "small displacement" assumption – we thus obtain a linear form of System (1) where we decompose the operator into

$$\mathcal{A}(x) = \mathcal{A}x + \mathcal{R}, \tag{9}$$

with $\mathcal{A}$ the linear (infinite dimensional) semi-group generator and $\mathcal{R}$ the remainder corresponding to the mechanical loading. In the sequel we will consider estimation problems where either $\mathcal{A}$ or $\mathcal{R}$ depend on the parameter vector θ.

This infinite dimensional system, however, cannot be used in the practical estimation process. Hence we introduce a *discretized* version of this model. Namely, we approximate x by x_h where x_h can be represented by a finite dimensional state vector X. Note that – in the whole paper – capital letters will denote finite dimensional quantities. The resulting finite dimensional system can be written in the following formalism:

$$\dot{X} = AX + R, \quad \text{with } X(0) = X_0 + \zeta_X, \tag{10}$$

where the initial condition expresses that $x_h(0)$ is the interpolation (or projection) of $x(0)$ in the finite dimensional subspace of the state space. As for the continuous formulation, this dynamical system represents the state space form of a variational – here discrete – formulation, typically derived from (8) by using a finite element discretization. Denoting by Y the vector of degrees of freedom (dofs) corresponding to the discrete displacement field, in the linear case the variational formulation yields a matrix equation of the type

$$M\ddot{Y} + C\dot{Y} + KY = F, \tag{11}$$

where M, C and K respectively denote the mass, damping and stiffness matrices, and F the load vector. Recalling that $X = \begin{pmatrix} Y & \dot{Y} \end{pmatrix}^T$, we thus have the following expressions for A and R in (10):

$$A = \begin{pmatrix} 0 & I \\ -M^{-1}K & -M^{-1}C \end{pmatrix}, \quad R = \begin{pmatrix} 0 \\ M^{-1}F \end{pmatrix}. \tag{12}$$

As a natural norm in the state space, we will use the energy norm, $\|X\|_{\mathcal{E}}^2 = \frac{1}{2}\dot{Y}^T M\dot{Y} + \frac{1}{2}Y^T KY$.

In practice, the geometry of our simplified ventricle is depicted in Figure 1, and the characteristic dimensions of this object are – indeed – comparable to

those of a human left ventricle. The system is clamped over the planar surface at the base, and activated by a planar wave of prestress w – representing electrical activation – traveling from apex to base at wave speed $c = 0.5$ m.s^{-1}. The resulting prestress state is assumed to be isotropic and gives an external virtual work defined by

$$\delta \mathcal{W}^{PS} = \sum_{1 \le i \le 17} \int_{\Omega_i^{AHA}} \theta_i \sigma_0 w(x_3 - ct) \underline{\underline{=}} : \delta \underline{\underline{e}} \, d\Omega, \tag{13}$$

where the subdvision of the solid domain into 17 subregions is similar to the subdivision of the left ventricle advocated by the American Heart Association, see Fig. 1. In the above expression σ_0 denotes a constant contractility parameter, and θ_i a multiplicative coefficient that may take a different value in the range $[0, 1]$ within each AHA region to represent pathological contraction. Namely, setting $\theta_i < 1$ in a given region corresponds to a simplified model of infarcted tissue in that area, hence the parameters $(\theta_i)_{1 \le i \le 17}$ represent the quantities to be estimated for diagnosis purposes. In our reference simulations we take all these parameters to be 1 (healthy value) except for

$$\theta_{14} = 0.5, \tag{14}$$

Note that we can substitute $\underline{n} \otimes \underline{n}$ for $\underline{\underline{=}}$ in (13) to account for *fiber directions* associated with a vector field $\underline{n}$. Our simulations will correspond to an isotropic viscoelastic material in *linear analysis*, with material parameters

$$E_i = 12.6\, 10^3 \,\text{Pa}, \quad \nu_{\text{i}} = 0.3, \quad \eta_{\text{i}} = 0.227\,\text{s} \quad \forall \text{i} \in \{1, \ldots, 17\}, \tag{15}$$

and respectively denoting Young's modulus, the Poisson ratio and a viscoelastic coefficient associated with the Rayleigh damping $C_i = \eta_i K_i$. Also, volumic mass is set as $\rho = 10^3\,\text{kg} \cdot \text{m}^{-3}$, a standard value for biological tissues.

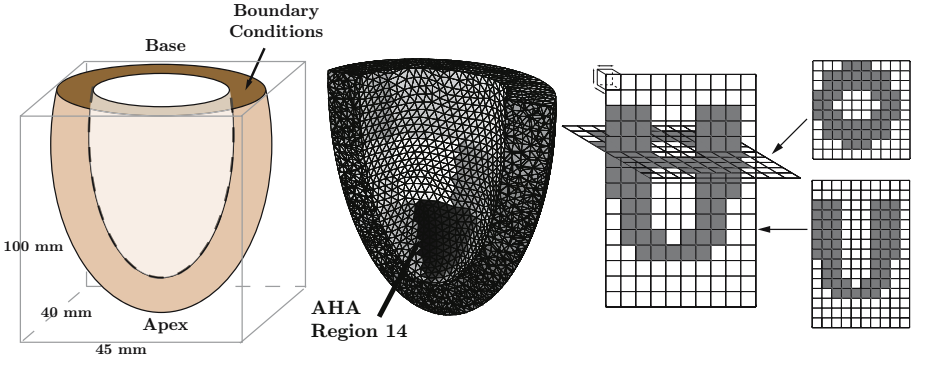

Fig. 1. Model geometry, reference mesh and measurement cells

2.3 Measurements

As regards measurements also, our objective is to retain the essential characteristics of available modalities in term of data contents and associated noise. In this paper we aim at representing the features of data such as tagged-MRI, or 3D ultrasound combined with optical flow. We point out that both modalities, after adequate processing, can provide incremental displacements between frames, a type of measurement directly related to the state variables of the above model – whether it be displacements or velocities.

In the present case, the modeled measurements are assumed to be given by

$$Z = \mathcal{H}x + \chi,$$

where $\mathcal{H}$ is here a linear operator and χ is described in more details below. More specifically, in the whole paper we will use velocities measured in a subpart Ω_m of the domain Ω and sampled by using weight functions $(s_i)_{i=1}^q$ defined on q non-overlapping "measurement cells" within Ω_m. Namely, $\mathcal{H}x = (0\ \mathcal{H}^v)(\underline{y}\ \underline{\dot{y}})^T$ consists of the q three-dimensional vectors given by

$$\int_{\Omega_m} s_i\, \underline{\dot{y}}\, d\Omega,$$

with normalized sampling functions. The additive measurement perturbation χ is taken as a white noise of diagonal covariance matrix W. Assuming a 10% error for a sampling rate of 50 ms in the data, we point out that – when rescaled according to white noise rules – this gives a 70% standard deviation for the computational time step considered.

In practice, since we do not have access to the real system, the measurements used in the estimation procedures will be provided by a "reference model" given by a rather fine finite element discretization of the above object. The corresponding mesh is displayed in Fig.1 and features nearly 40000 dofs. The observer itself will be based on a coarser discretization of nearly 6000 dofs. In all our simulations we used the energy-conserving Newmark algorithm for time discretization, with time step $\Delta t = 1\,\text{ms}$ in adequacy with the activation wave velocity. Note that – unless otherwise stated – all physical units correspond to the SI system. We also show in Fig.1 the measurement cells defined here by subdividing a (rectangular) box enclosing the geometry into $10 \times 10 \times 15$ smaller (rectangular) cells of equal sizes. The weight functions are then simply defined by scaled indicator functions of the cells. This resolution is comparable to that of standard tagged MRI images, and inferior to 3D echography.

3 State Estimation Using Collocated Damping

We now introduce the finite dimensional state estimator

$$\dot{\bar{X}} = A\bar{X} + R + K_X(Z - H\bar{X}), \quad \text{with } \bar{X}(0) = X_0 \tag{16}$$

In essence, the filter K_X that we want to use corresponds to a force proportional and opposed to the measured velocity, namely a "direct velocity feedback" (DVF) stabilization strategy, see [13,5]. In our case, the available measurements are weighted velocities within cells, hence inside each cell we apply a "filtering force" given by

$$-\gamma s_i \int_{\Omega_m} s_i \, \underline{\dot{y}} \, d\Omega.$$

We infer that K_X is simply given by

$$K_X = (0 \quad \gamma H^v M^{-1})^T.$$

Let us define the error $\check{X} = X - \bar{X}$ between (10) et (16). We have

$$\dot{\check{X}} = (A - K_X H)\check{X} - K_X(\epsilon_h + \chi), \quad \text{with } \check{X}(0) = \zeta_X. \tag{17}$$

Therefore, we are concerned with the properties – and more particularly the stability – of the dynamical system governed by $(A - K_X H)$, namely, the discretized form of a mechanical system with dissipative feedback. Note that the variational form corresponding to the filtering force is $-\gamma \int_{\Omega_m} s_i \, \underline{\dot{y}} \, d\Omega \int_{\Omega_m} s_i \, \delta\underline{y} \, d\Omega$, which ensures that we have a dissipative mechanical operator. Moreover, we can intrinsically and quantitatively justify the exponential stability of this type of system, see [10,3] and [6], respectively.

The performance of the state estimator is demonstrated in Fig.2, where we display the state convergence, both in the energy norm and using the volume indicator, and we can see that convergence is very fast, namely, excellent accuracy is obtained after about 0.1s. In [11] we also investigate the effect of changing the mesh size in the estimator, and we show that accuracy only – not stability – is changed.

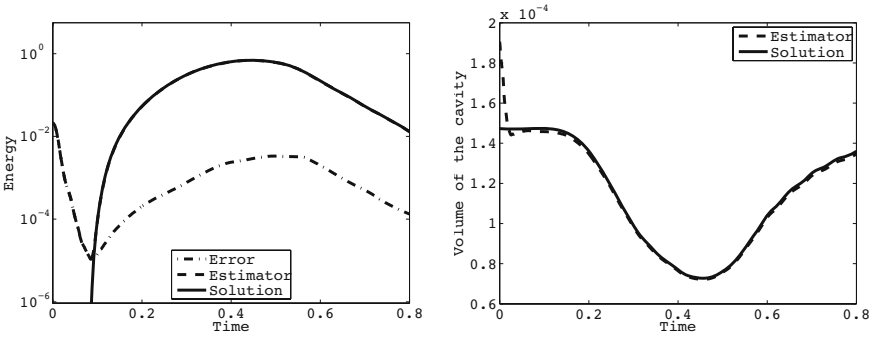

Fig. 2. State convergence in energy norm, corresponding volume estimation

4 Joint State-Parameter Estimation: The Linear Case

In this section, we consider the estimation of parameters only included in the right-hand side of the dynamical equation, and with a *linear* dependence on the parameter vector θ. Hence, we can write the following linear state-parameter system:

$$\dot{x} = \mathcal{A}x + \mathcal{B}\theta + \mathcal{R}, \quad \text{with } x(0) = x_0 + \zeta_x, \quad \theta = \theta_0 + \zeta_\theta. \tag{18}$$

4.1 Construction and Analysis of the Estimation Procedure

Since applying classical filtering techniques to perform state estimation – and *a fortiori* joint state-parameter estimation – is intractable, we propose to build a new estimator based on the above collocated observer. Namely, instead of using a standard Kalman filter on the augmented state itself, we apply the filtering procedure on the state observer $\bar{X}$ which is tracking the real state. Therefore, in this system the uncertain part to be estimated corresponds to the parameter vector only since the initial condition on $\bar{X}$ is fixed, see (16). In other words, the dynamical system considered for the (augmented) state observer $\bar{X}^e = (\bar{X} \quad \theta)^T$ is

$$\dot{\bar{X}}^e = A^e \bar{X}^e + R^e + K_X^e (Z - H^e \bar{X}^e), \quad \text{with } \bar{X}^e(0) = X_0^e + \zeta_\theta^e, \tag{19}$$

where

$$X_0^e = \begin{pmatrix} X_0 \\ \theta \end{pmatrix}, \quad \zeta_\theta^e = \begin{pmatrix} 0 \\ \zeta_\theta \end{pmatrix},$$

$$A^e = \begin{pmatrix} A & B \\ 0 & 0 \end{pmatrix}, \quad R^e = \begin{pmatrix} R \\ 0 \end{pmatrix}, \quad K_X^e = \begin{pmatrix} K_X \\ 0 \end{pmatrix}, \quad H^e = (H \quad 0).$$

Here we point out that $\bar{X}^e$ only depends on the initial condition ζ_θ. Hence we can define $\bar{X}^e(\xi)$ for an arbitrary initial condition $\theta(0) = \theta_0 + \xi$.

We then define $\hat{X}^e$ as the Kalman observer for this system. The error covariance of this observer, namely,

$$P^e = \mathbb{E}((\bar{X}^e - \hat{X}^e)(\bar{X}^e - \hat{X}^e)^T | Z), \tag{20}$$

is such that

$$P^e(0) = \begin{pmatrix} 0 & 0 \\ 0 & \mathbb{E}(\zeta_\theta \zeta_\theta^T) \end{pmatrix}. \tag{21}$$

Neglecting the modeling error introduced by the fact that Z is not the observation corresponding to $\bar{X}$ but to x, we are then in a position to apply Kalman filtering to a system with reduced rank covariance error. As shown in [12] the covariance matrix at every time remains of constant rank r, namely, the size of the parameter vector. This leads to the so-called "Singular Evolutive Extended Kalman" (SEEK) algorithm in which the evolution equation of P^e is:

$$\begin{cases} P^e = L^{eT} U^{-1} L^e \\ \dot{L}^e = (A^e - K_X^e H) L^e, \quad \text{with } L^e(0) = (0 \quad I_r)^T \\ \dot{U} = L^{eT} H^{eT} W^{-1} H^e L^e, \quad \text{with } U(0) = \left(\mathbb{E}(\zeta_\theta . \zeta_\theta^T)\right)^{-1} \end{cases} \tag{22}$$

If we decompose the equation describing L^e as $L^e = (L_X \quad L_\theta)^T$ we find that $\forall t, L_\theta = I_r$ and we finally obtain the following observer equations

$$\begin{cases} \dot{\hat{X}} = A\hat{X} + B\hat{\theta} + R + K_X(Z - H\hat{X}) + L_X\dot{\hat{\theta}}, \quad \text{with } \hat{X}(0) = X_0 \\ \dot{\hat{\theta}} = U^{-1}L_X^T H^T W^{-1}(Z - H\hat{X}), \quad \text{with } \hat{\theta}(0) = \theta_0 \\ \dot{L}_X = (A - K_X H)L_X + B, \quad \text{with } L_X(0) = 0 \\ \dot{U} = L_X^T H^T W^{-1} H L_X, \quad \text{with } U(0) = \left(\mathbb{E}(\zeta_\theta.\zeta_\theta^T)\right)^{-1} \end{cases} \tag{23}$$

and we note that we only need to manipulate a matrix of size r (namely, U), instead of a covariance matrix with the size of the extended state. Furthermore, the SEEK algorithm, as other Kalman filter, gives an optimality result in a variational context. In our case we have proven in [11] that the solution exactly corresponds to the minimum of the criterion

$$J_T(\xi) = \frac{1}{2}\xi^T U(0)\xi + \frac{1}{2}\int_0^T (Z - H^e\bar{X}^e(\xi))^T W^{-1}(Z - H^e\bar{X}^e(\xi))\, dt, \tag{24}$$

which gives a relevant solution only if the collocated estimator $\bar{X}^e(\xi)$ tracks X^e fast enough in order for $H^e\bar{X}^e(\xi)$ to closely approximate the measurement Z. As in the state estimation case, we can prove the convergence of the estimator by analyzing the dynamics of the error system. To do so, we introduce $\tilde{X} = X - \hat{X}$, $\tilde{\theta} = \theta - \hat{\theta}$ and – as in [16] – the change of variables $\eta = \tilde{X} + L_X\tilde{\theta}$. We can verify that the system governing the error $(\eta, \tilde{\theta})$ is

$$\begin{cases} \dot{\eta} = (A - K_X H)\eta - K_X(\epsilon_h + \chi), \quad \text{with } \eta(0) = \zeta_X \\ \dot{\tilde{\theta}} = -U^{-1}L_X^T H^T W^{-1}(H\eta + HL_X\tilde{\theta} + \epsilon_h + \chi), \quad \text{with } \tilde{\theta}(0) = \zeta_\theta \end{cases} \tag{25}$$

Hence the convergence of our estimator again relies on the exponential stability of the operator $(A - K_X H)$, and detailed error estimates can be obtained for the estimator, see [11].

Figure 3 shows the convergence results of parameter estimation, while state estimation provides results very similar to those shown in Fig.2. We note that the estimated parameters do not depart from their initial values until activation of the tissue occurs, which is as expected from identifiability considerations. Convergence is then accurately achieved.

5 Joint State and Parameter Bilinear Estimation

In the previous sections we have dealt with the estimation of prestress parameters, and this problem led to a linear dynamical system in the combined state and parameter variables. However, this linearity only holds when the parameters appear in the "right-hand side" of the dynamical system. When considering the estimation of other mechanical parameters – and typically that of constitutive parameters – the resulting augmented system is in general non-linear, even if the mechanical system by itself obeys linear dynamics.

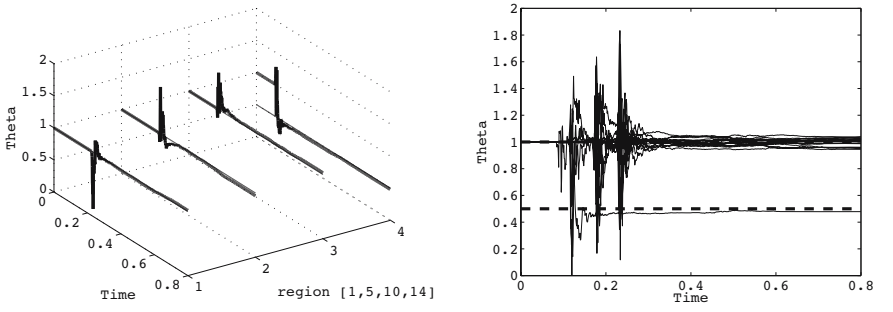

Fig. 3. Parameter convergence: in 4 individual regions (left), and globally for the 17 regions (right)

In this framework, let us consider that we want to determine unknown variations of Young's modulus with respect to a reference value. Keeping our above subdivision of Ω in 17 regions where the parameters are assumed to be constant, we can write the following bilinear augmented state-parameter system

$$\dot{X} = (A + \Delta A.\theta)X + R, \quad \text{with } X(0) = X_0 + \zeta_X, \quad \theta = \theta_0 + \zeta_\theta, \tag{26}$$

and where $\Delta\mathcal{A}$ can be decomposed into $\Delta A.\theta = \sum_{i=1}^{17} \Delta A_i \theta_i$.

Since the mechanical system by itself is linear, the above-described state estimator is applicable, and we can directly focus on extending our results on parameter estimation in the augmented system. In our case, in order to extend our estimator we note that the quantity L_X, defined in the linear framework in (23), can be interpreted as the sensitivity of the state estimator $\bar{X}$ – recall (16) – with respect to θ, i.e. $L_X = \frac{d\bar{X}}{d\theta}$. From this interpretation, introducing $\Lambda X = \partial_\theta([\Delta A X]\theta)$, we can devise an observator in the bilinear case in the form

$$\begin{cases} \dot{\hat{X}} = A\hat{X} + \Delta A.\hat{\theta}\hat{X} + R + K_X(Z - H\hat{X}) + L_X\dot{\hat{\theta}}, \quad \text{with } \hat{\mathrm{X}}(0) = \mathrm{X}_0 \\ \dot{\hat{\theta}} = U^{-1}L_X^T H^T W^{-1}(Z - H\hat{X}), \quad \text{with } \hat{\theta}(0) = \theta_0 \\ \dot{L}_X = (A + \Delta A.\hat{\theta} - K_X H)L_X + \Lambda\hat{X}, \quad \text{with } \mathrm{L_X}(0) = 0 \\ \dot{U} = L_X^T H^T W^{-1} H L_X, \quad \text{with } \mathrm{U}(0) = \left(\mathbb{E}(\zeta_\theta.\zeta_\theta^{\mathrm{T}})\right)^{-1} \end{cases} \tag{27}$$

Let us now analyse the convergence of this algorithm. We still rewrite the system satisfied by the error $(\tilde{X}, \tilde{\theta})$ using the change of variables into $(\eta, \tilde{\theta})$. A straightforward computation leads to

$$\begin{cases} \dot{\eta} = (A + \Delta A\theta - K_X H)\eta + \Delta A\tilde{\theta}L_X\tilde{\theta} + K_X(\epsilon_h + \chi), \text{ with } \eta(0) = \zeta_X \\ \dot{\tilde{\theta}} = -U^{-1}L_X^T H^T W^{-1}(H\eta + HL_X\tilde{\theta} + \epsilon_h + \chi), \text{ with } \tilde{\theta}(0) = \zeta_\theta \end{cases} \tag{28}$$

This error system is no longer linear, but the associated tangent system in $(\eta, \tilde{\theta}) = (0, 0)$ is still exactly System (25), which is stable as discussed above. From the classical theory of stability of non linear systems, we infer that there

exists a neighborhood of $(\eta, \tilde{\theta}) = (0, 0)$ – hence of $(\tilde{X}, \tilde{\theta}) = (0, 0)$ – such that System (28) remains stable. As a consequence, we expect to accurately achieve our joint estimation if the undeterminations ζ_X et ζ_θ are "small".

We have tested our observer in a configuration quite similar to the one described in the linear case, and we used the same measurement operator. In the 14th AHA region we set $\theta_{14} = 0.3$, while we let $\theta = 0$ in the other regions, which means that the infarct produces an increase of the stiffness in the region concerned. In practice, in order to improve the convergence of the joint estimator, we found that it is best to slightly delay the start of parameter estimation, to let the robust state observer achieve a sufficiently accurate pre-estimation. This modified procedure can be easily implemented, and we display the corresponding numerical results in Fig. 4. The delay parameter was set as $t_s = 0.1$ s, and the stiffness parameter covariance was taken as 0.04 in Region 14 and the adjacent parts, and very small in all other regions to represent an approximate "a priori prediction" of the infarcted area, and to enhance identifiability. In this case again, state estimation behaves as in Fig.2. Parameter convergence is not as accurate as in the linear estimation problem, albeit still adequate.

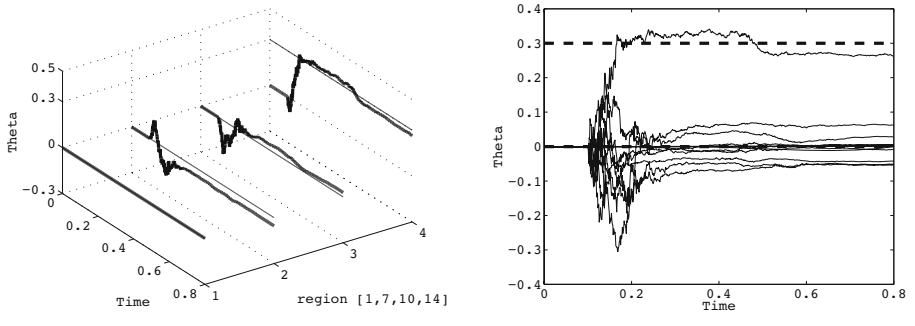

Fig. 4. Parameter convergence in the bilinear case

6 Concluding Remarks

We have proposed a joint state-parameter estimation procedure specifically adapted to the class of physical models of interest to represent cardiac behavior, and to the fundamental features of available imaging modalities. This estimator was built based on an effective and robust state estimation sequential strategy, namely, collocated feedback, which provides an estimation at the same computational cost as the simulation of the system itself.

We have demonstrated the performance of this procedure to estimate parameters of primary interest in cardiology, namely contractility and stiffness quantities. For the stiffness estimation problem we had to consider a non-linear dynamical system, which required an extension of the methodology and an adaptation of the parameter estimation dynamics with the introduction of a startup delay. This necessary adaptation confirms that parameter estimation cannot be

considered independently of state estimation, hence that a robust and effective state estimation procedure is an essential prerequisite.

Further work is being performed to evaluate the effectiveness of the proposed methodology when using *real imaging measurements* [7]. Of course, when this is achieved modeling difficulties may remain, but the estimation procedure can also be used as a tool to assess model validity, since its success would then only depend on model adequacy.

References

1. Anderson, B.D.O., Moore, J.B.: Optimal Filtering. Prentice-Hall, Englewood Cliffs (1979)
2. Augenstein, K.F., Cowan, B.R., LeGrice, I.J., Young, A.A.: Estimation of cardiac hyperelastic material properties from MRI tissue tagging and diffusion tensor imaging. In: Larsen, R., Nielsen, M., Sporring, J. (eds.) MICCAI 2006. LNCS, vol. 4190, pp. 628–635. Springer, Heidelberg (2006)
3. Bardos, C., Lebeau, G., Rauch, J.: Sharp sufficient conditions for the observation, control, and stabilization of waves from the boundary. SIAM J. Control Optim. 30(5), 1024–1065 (1992)
4. Bensoussan, A.: Filtrage optimal des systèmes linéaires. Dunod (1971)
5. Collet, M., Walter, V., Delobelle, P.: Active damping of a micro-cantilever piezocomposite beam. J. Sound Vibration 260(3), 453–476 (2003)
6. Cox, S., Zuazua, E.: The rate at which energy decays in a damped string. Comm. Partial Differential Equations 19(1-2), 213–243 (1994)
7. Duan, Q., Moireau, P., Angelini, E., Chapelle, D.: Simulation of 3D ultrasound with a realistic electro-mechanical model of the heart. In: Sachse, F.B., Seemann, G. (eds.) FIMH 2007. LNCS, vol. 4466, pp. 463–473. Springer, Berlin Heidelberg (2007)
8. Hunter, P.J., McCulloch, A.D., ter Keurs, H.E.D.: Modelling the mechanical properties of cardiac muscle. Progress in Biophysics and Molecular Biology. 69, 289–331 (1998)
9. Kalman, R.E., Bucy, R.S.: New results in linear filtering and prediction theory. ASME Trans.–Journal of Basic Engineering 83(Series D), 95–108 (1961)
10. Lions, J.-L.: Contrôlabilité exacte, perturbations et stabilisation de systèmes distribués. (Tome 1), of Recherches en Mathématiques Appliquées [Research in Applied Mathematics]. Masson, Paris, vol. 8 (1988)
11. Moireau, Ph., Chapelle, C., Le Tallec, P.: Joint state and parameter estimation for distributed mechanical systems. Submitted to CMAME.
12. Pham, D.T., Verron, J., Roubeaud, M.C.: A singular evolutive interpolated kalman filter for data assimilation in oceanography. J. Marine Systems 16, 323–341 (1997)
13. Preumont, A.: Vibration Control of Active Structures, An Introduction, 2nd edn. Kluwer Academic Publishers, Boston (2002)
14. Sainte-Marie, J., Chapelle, D., Cimrman, R., Sorine, M.: Modeling and estimation of the cardiac electromechanical activity. Comp. & Struct. 84, 1743–1759 (2006)
15. Tong, S., Shi, P.: Cardiac motion recovery: Continuous dynamics, discrete measurements, and optimal estimation. In: Larsen, R., Nielsen, M., Sporring, J. (eds.) MICCAI 2006. LNCS, vol. 4190, pp. 744–751. Springer, Heidelberg (2006)
16. Zhang, Q., Clavel, A.: Adaptive observer with exponential forgetting factor for linear time varying systems. In: Decision and Control, 2001. Proceedings of the 40th IEEE Conference on, vol. 4, pp. 3886–3891, Orlando, FL, USA (2001)

Open-Source Environment for Interactive Finite Element Modeling of Optimal ICD Electrode Placement

Matthew Jolley[1], Jeroen Stinstra[3], David Weinstein[3], Steve Pieper[2], Raul San Jose Estepar[2], Gordon Kindlmann[2], Rob MacLeod[3], Dana H. Brooks[4], and John K. Triedman[1]

[1] Department of Cardiology, Children's Hospital Boston, Boston, MA
[2] Surgical Planning Laboratory, Brigham and Women's Hospital, Boston, MA
[3] Scientific Computing Institute, University of Utah, Salt Lake City, UT
[4] Department of Electrical Engineering, Northeastern University, Boston, MA
John K. Triedman, MD, Children's Hospital Boston,
300 Longwood Ave. Boston, MA 02115
john.triedman@cardio.chboston.org

Abstract. Placement of Implantable Cardiac Defibrillator (ICD) leads in children and some adults is challenging due to anatomical factors. As a result, novel *ad hoc* non-transvenous implant techniques have been employed clinically. We describe an open-source subject-specific, image-based finite element modeling software environment whose long term goal is determining optimal electrode placement in special populations of adults and children Segmented image-based finite element models of two children and one adult were created from CT scans and appropriate tissue conductivities were assigned. The environment incorporates an interactive electrode placement system with a library of clinically-based, user-configurable electrodes. Finite element models are created from the electrode poses within the torsos and the resulting electric fields, current, and voltages computed and visualized.

1 Introduction

Implantable cardiac defibrillators (ICDs) are widely used in patients at risk of fatal cardiac arrhythmias, and indications for their use continue to expand[6], [8], [9], [22]. Although ICDs are routinely implanted in adult patients using a transvenous system, there is a growing population of pediatric and adult patients in whom transvenous ICD systems cannot or should not be implanted[19]. These include very small patients and those with intracardiac shunts or anatomical obstruction to lead placement[6], [7], [10].

In these groups, several novel, non-transvenous approaches to ICD implantation have been reported (Figure 1)[7], [10], [18], [23], [24]. Such approaches have consisted of *ad hoc* adaptations of existing ICD systems, with the goals of minimizing system invasiveness, adapting to complex anatomy, and achieving low defibrillation thresholds.[7], [12], [24]. These approaches assume efficacy by extrapolation from limited animal research, and post-implantation assessment of defibrillation thresholds (DFTs)[7]. Although defibrillation research has elucidated reasonably accurate relations between distribution of myocardial voltage gradient and both defibrillation

F.B. Sachse and G. Seemann (Eds.): FIMH 2007, LNCS 4466, pp. 373–382, 2007.

efficacy and myocardial injury, no reports currently describe the effects of interactions between variations in body size and novel ICD geometries on these fields[4], [25], [27].

Animal models of defibrillation have shown defibrillation with subcutaneous electrodes to be feasible, but little is known about ideal placement or the resulting electric fields[7], [25], [27]. In the past, insertable electrodes have been used to map the epicardium and measure electric fields transmurally in animals but these techniques are expensive, time consuming and not necessarily applicable to human anatomy. Furthermore they do not provide detailed descriptions of the electric field throughout the entire myocardium and can perturb the measured fields.

Finite element modeling (FEM) of defibrillation has been shown to correlate well with clinically observed DFTs in laboriously constructed conductivity models of the adult torso[3], [11], [14], [15], [20], [21]. These studies have shown the utility of realistic models to accurately predict threshold voltages, currents, and impedances, as well as the electric fields and voltages at known measurement locations. They also may be used to compare the relative efficacy of electrode orientations in a given torso model[3], [11].

The demands of extending these studies to highly variable electrode design and placement, not to mention body size, habitus and possible gross anatomical variability, mean that such simulation systems need to allow more automatic model creation, interactive electrode placement, a wide variety of electrodes, interactive execution of the simulations, and visualization of the results. In this study, we describe the creation of an open-source subject-specific, image-based finite element modeling software environment with the goal of enabling determination of optimal electrode placement in special populations of adults and children.

2 Methods

2.1 Image Acquisition, Segmentation

Images were constructed by segmenting normal or trivially abnormal 64-detector CT scans with 1.25mm slices obtained from a radiology trauma database with appropriate IRB approvals. Of more than 50 studies examined, three patients were selected for this study based on 1) good tissue contrast, 2) minimal cardiac motion artifact, and 3) diversity of body size and habitus: a 12 kg, 2 year old female, a 32 kg, 10 year old male, and a 75 kg, 29 year old male. Torsos were segmented into 10 tissue compartments using 3D Slicer (Table 1)[1]. Various techniques were used for segmentation including thresholding, confidence connected component analysis, and level sets. The individual label maps were hierarchically combined into one label map using the unu command line tool, part of the Teem toolkit[17]. Each combined label map was imported into SCIRun/BioPSE, to solve the bioelectric field problem.[2]

2.2 Electrode Visualization and Placement

In order to allow interactive electrode placement inside a segmented 3D volume we created new functionality in the SCIRun/BIOPSE software package. We designed

new modules which allow the user to interactively insert realistically shaped electrode wires and electrode cans into rendered images of the segmented volume. The shape model of the electrode can was generated by creating a triangular surface from the 2-D scanned images of the electrode and meshing the interior with tetrahedral elements based on the device's known thickness. The shape of the wire electrodes was determined interactively by specifying the length and diameter of the contact areas separately so the model was constrained to the desired shape of electrode. The 3 dimensional path of these "wires" was defined by a set of 5 user-movable spheres through which a cubic spline was fit and updated in real time. This interface proved to be sufficient for placing the wire electrodes into realistic clinical positions. A 3D tetrahedral model of the specified diameter and length was then created over the path defined by the spheres. The resulting shape of both electrodes could be adapted to closely resemble those used clinically and all could be moved interactively by the user in real time.

In order to support proper placement of electrodes, we expanded the visualization capabilities of SCIRun to render transparent 3D images of the separating surfaces between different tissue types and added in support to display three dimensional labels. We altered the way the user can interact with multiple simultaneous visualizations of the same the electrode placement so that one can look at the same situation from multiple view points.

2.3 Meshing and Finite Element Calculation

New modules were created in SCIRun/BioPSE to support local mesh refinement of hexahedral elements as well as finite element calculations on the resultant meshes.of varying element density.

Table 1. Comparison of conductivies used in this and prior FEM studies[3], [11], [14], [15], [21]

Tissue type	Current study (S/m)	Jorgenson (S/m)	DeJongh (S/m)	Mocanu (S/m)	Aguel (S/m)	Gabriel (S/m)
Bowel gas	0.0020	0.0020				
Connective Tissue	0.2200		0.2220			
Liver	0.1500	0.1486				0.3300
Kidney	0.0700					0.0700
Skeletal Muscle	0.2500	0.1429	0.2500	0.2500		
Fat	0.0500	0.0459		0.0500		
Bone	0.0060	0.0063		0.0100		
Lung	0.0670	0.0667	0.0780	0.0700	0.0500	
Blood	0.7000	0.6494	0.6670	0.8000	0.7700	
Myocardium	0.2500	0.2381	0.2500	0.2500	0.6000	

In order to create an electrical model of the torso, we combined the label maps and the electrode models described previously in a full hexahedral mesh. A regular mesh of hexahedral elements with a user adjustable spacing was created in the same space as the label map. Elements contained in a bounding box 1.5 times the 3D volume of

the electrode were automatically selected and each of these elements was split into 27 smaller elements to allow for a higher local mesh density around the electrodes[26]. Using a lookup table with conductivity values (Table 1), the segmented label map was transformed into a conductivity map of the torso, whose values were projected onto the computational mesh by sampling the conductivities delineated by the label map segmentation. We assumed the electrical properties of the torso to be defined by one conductivity value per element. The resulting finite element model created by the SCIRun software resulted in a set of equations similar to those used in previous defibrillation studies[3], [11], [14]. In our implementation we assumed a linear, piecewise constant and isotropic volume conductor model, with negligible capacitance and inductance. We used the Galerkin finite element formulation with tri-linear interpolation. Electrodes were assigned a constant potential over their surface. The mesh size and spacing was interactively adjusted until additional refinements did not alter the results of the defibrillation threshold parameter by more than 1 percent. We used a representative selection of electrode positions to evaluate adequate node spacing subsequently used for each model. This resulted in a basic torso mesh that was wrapped into a grid of 100 by 100 by 150 nodes in the x, y, and z-direction, with further refinement around the electrodes as noted.

2.4 Solution Calculation, Defibrillation Metrics, and Data Analysis

After the potential distribution was solved using the finite element method, the gradients of the potential field were evaluated for the full thorax assuming a tri-linear interpolation. As the electrical field scales linearly with the potential difference applied to the defibrillation electrodes, effective electrode defibrillation potentials can be computed by linear scaling. The critical mass hypothesis was used to define successful defibrillation[12], [28]. This hypothesis proposes that defibrillation depends on rendering a critical mass of the myocardium inexcitable. A shock is predicted to be successful if it produces a threshold voltage gradient over a “large” fraction portion of the myocardial mass. Empirically determined values for these thresholds vary somewhat. The criteria used in this study of a voltage gradient of 5 V/cm generated over 95% of the myocardium has been accepted in the literature as a reasonable predictor of successful defibrillation.

Calculated metrics included the voltage, voltage gradient, current, impedance, and energy threshold (E) for defibrillation (defibrillation threshold, DFT). The DFT in this study was calculated by the energy relation $E = \frac{1}{2} CV^2$, where C is the capacitance of a typical pulse generator, and V is the potential difference between electrodes required to produce a voltage gradient of 3 and 5 V/cm in 95% of the myocardium. We also calculated the percentage of myocardium above 30V/cm and 60V/cm at these thresholds, to predict possible areas of myocardial damage. We utilized a capacitance of 130uF for these estimates, based on conversations with contacts in industry. SCIRun was utilized to visualize voltage, voltage gradients, and current density. In addition the percentage of myocardium above the defibrillation threshold was calculated and visualized by projecting a color scale onto the myocardial elements.

3 Results

We utilized our newly developed functionality in SCIRun for importing segmented data, which was subsequently used in SCIRun's dataflow environment to create a computational model of the distribution of the electrical field, as shown in Figure 1(left). These dataflow networks were used for interactive placement of electrodes, remeshing of volumes around the active electrodes, calculation of FEM solutions, and presentation of data in graphs with a summary of important numerical values, as shown in figure 1(right).

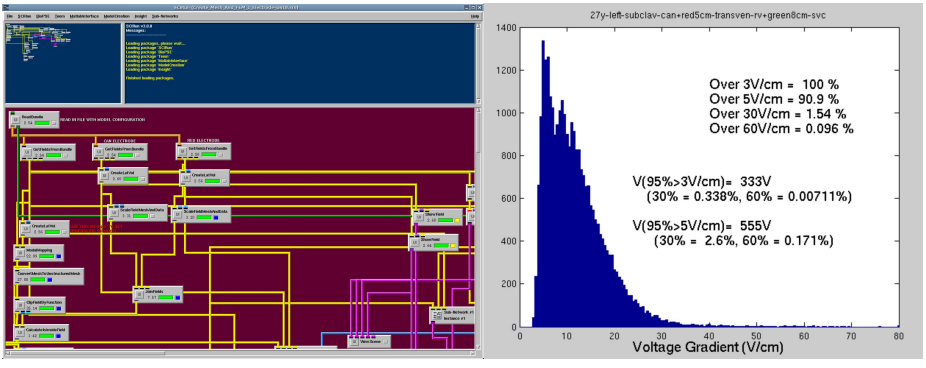

Fig. 1. SCIRUN Network: Example SCIRun Network (left) and of automatically generated numerical metrics for defibrillation (right) for a standard adult transvenous electrode configuration with a shock of 500V as well as scaled metrics

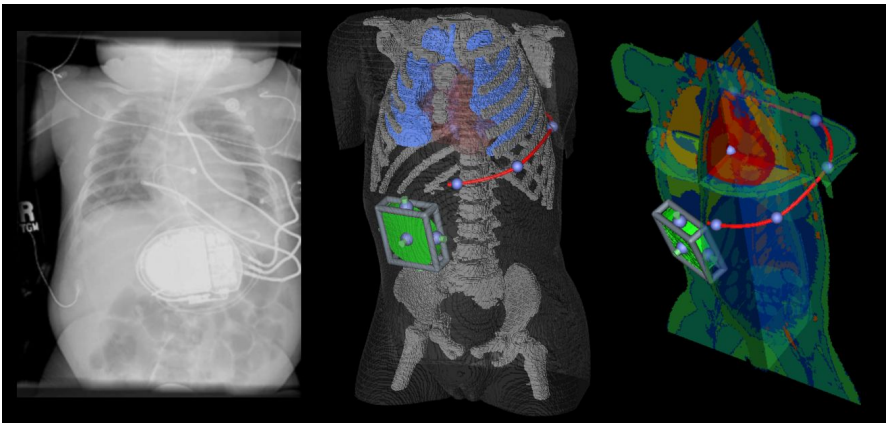

Fig. 2. Subcutaneous Electrode placement: Left: Chest x-ray of subcutaneous electrode placement in child. Middle: Example of subcutaneous electrode placement in 2-yr old model. Right: Moveable cutting planes to examine detail. Blue spheres are user moveable handles.

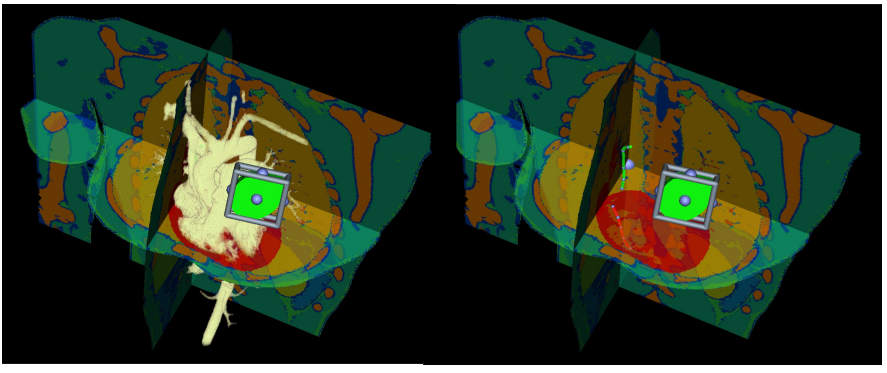

Fig. 3. Transvenous Electrode Placement: Standard adult placement with left subclavian can, 8cm coil in superior vena cava (green) and 5 cm coil in right ventricle(red) shown with (left) and without (right) rendering of blood within the 29 year old torso shown with three moveable cutting planes

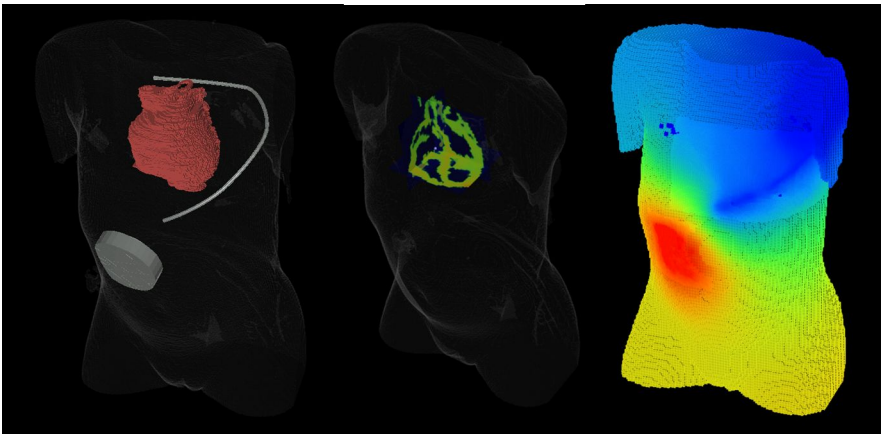

Fig. 4. Visualization of defibrillation: 2 year old child with left thoracic subcutaneous electrode and right abdominal can. Left: Electrode positions and heart within torso. Middle: Visualization of voltage gradients within the heart with three moveable cutting planes for exploration. Right: Visualization of absolute voltages on torso of model, note increased mesh density around electrodes.

Graphical representations of sample FEM solutions are shown in Figure 4 demonstrating the ability to visualize voltage gradient distribution within the myocardium as well as compute voltage and energy parameters necessary to meet the criteria of the critical mass hypothesis.

To validate our model, we compared the DFTs obtained in our 75kg adult-sized torso with standard, transvenous electrode placement to previously published adult FEM models of defibrillation[3], [11]. The calculated DFT values for our torso using standard electrode orientation are in close agreement with these models [8-12 joules, 5V/cm metric] as well as empiric clinical values.

In order to explore the clinical relevance of this newly created functionality for novel non-transvenous orientations we analyzed several exemplary situations. Clinicians have begun to use scenarios with an abdominal can and single subcutaneous 25cm electrode coil as suggested in figure 4. The best positioning of this combination and effect of small changes in electrode movement is unknown. To explore the utility of the newly created environment utilized the 2year-12kg torso and the can in the left abdomen at the level of thoracic vertebrae 12. We then extended the 25cm subcutaneous electrode to the left from the can to different locations, placing it at the level of thoracic vertebrae 6, 8, and 10 respectively. The voltage difference required to achieve 3V/cm varied from 335 volts to 654 volts, corresponding to a change in work from 7.29 joules to 27.8 joules, with the electrodes placed caudally at T6 achieving the lowest defibrillation threshold. Thus, very small changes in electrode placement in these novel configurations are predicted to have significant effect on clinical DFTs.

To compare the efficiency of the best subcutaneous orientation to a standard transvenous orientation in the 2 year old torso model we placed the can in the right and left abdomen, as well as the right and left subclavian positions, and placed a single 5cm long transvenous electrode with a diameter of 3mm in the right ventricle. The required voltage varied from 58.6 volts to 172 volts, corresponding to 0.22 and 1.92 Joules respectively, with the left subclavian can being the most efficient. In situations where it is anatomically viable and safe, standard transvenous placement of electrodes is more efficient than most subcutaneous electrode placement.

To explore the effect of body size and growth we compared the single retrocardiac electrode with an abdominal can, another orientation utilized clinically in small children, to assess the efficacy of this orientation with growth. A right abdominal can with a 5 cm electrode placed in the posterior epicardial region approximately centered in relation to the heart required 266V, 850V, and 1690V in the 2year-12kg, 10year-32kg, and 29 year-75kg torsos respectively. This corresponds to a range of approximately 3 to 185 joules expected with growth, suggesting orientations practical in one age group might fail with time.

4 Discussion

Utilization of ICD therapy in pediatric and congenital heart populations has risen, as the numbers of patients who may benefit have increased while apparent risks have decreased. Transvenous implantation often cannot be performed in children due to patient size, lack of vascular access and increased risk of embolic phenomena due to intracardiac shunts[16], [19]. Children with ICDs have high rates both of lead failure and of vascular occlusion[5], [6] and long life expectancy, resulting in the anticipated need for repeated lead extraction and reimplantation with their attendant risks. There is also growing interest in the development of extracardiac ICDs for the adult population, both to avoid lead related complications and for patients with vascular access problems or other contraindications to transvenous implant. We have utilized existing open-source tools and developed new, interactive functionality in SCIRun/BioPSE to study this problem using subject-specific FEMs and demonstrated its application.

We utilized the interactive electrode placement system to explore several clinical situations and analyze the effect of electrode placement in a given torso. A four rib change in subcutaneous electrode position is predicted to triple the DFT in Joules in a two year old torso. Transvenous electrode placement is predicted to be more efficient than subcutaneous placements, suggesting these orientation should be utilized in patients with suitable anatomy. Retrocardiac placement of a single electrode to an abdominal can is a reasonable orientation in a small child, but not in a older child or adult as the resulting DFTs are in excess of what current devices can deliver. Together these examples suggest that the rapidly adaptable environment we have created will be potentially useful in designing optimal electrode placements in children and adults with unique anatomy and other technical requirements.

Previous publications have shown that FEM can closely correlate with clinically observed results[3], [11], [13], [15]. Although this is reassuring, both the current and prior models do not incorporate many factors known to affect defibrillation. These include patient specific differences in conductivity, myocardial tissue structure, capacitive effects, the complexities of fibrillation wavefront behavior, and the effects of biphasic waveforms on membrane repolarization. Although results predicted by the critical mass hypothesis compare favorably to clinical observation, it is a gross model that largely ignores cellular level effects and does not account for variability in susceptibility of a given patient's myocardium. We expect these models to provide a platform for reasonable comparison of relative efficacies of electrode position for a given torso, and as such can serve as a useful tool for comparing novel configurations to proven electrode positions as well as general trends in comparison of different torso models. Practical application of this approach is limited at present by the availability of high resolution CT and MRI scans of children. As such scans obtained for clinical reasons will provide opportunity for further development of trends across age groups and anatomy. We plan to utilize the system to systematically explore various parameters and orientations in children and adults to better guide practitioners in situations when novel implantations are needed. We have also begun to utilize the system in a case specific manner with dedicated scans in patients with highly complicated congenital heart disease and other congenital anomalies to assess the utility of determining optimal orientations on a case by case basis.

We hope to continue to improve the tools in this open-source pipeline. Segmentation remains time intensive despite improvements in segmentation algorithms and we are actively working to create atlas based segmentation systems such that imaging can be rapidly converted to highly accurate torso models with minimal user input. The newly developed functionality in SCIRun will be improved. to be more efficient and incorporate other physically relevant parameters, and a broader library of electodes. SCIRun also has powerful visualization capabilities, and we are further exploring optimal parameters for improved perception of visual and numerical data. Once optimized the platform may be wrapped into a stand alone open source program once we are satisfied with visualization and simulation performance.

5 Conclusion

We have developed an interactive computational and visualization tool that can be used to assess the relative efficiency of non-standard ICD electrode placement in

torso models of various sizes. In patients with contraindications to standard approaches to ICD implantation, the ability to interactively assess the relative efficacy of different electrode orientations may provide insight into which orientation might be optimal in a specific patient. This image-based approach may also be of value in the design and development of extracardiac defibrillation strategies.

Acknowledgements. This work was supported by NIH P41 RR12557, NIH P41 RR12553-02 , NIH P41 RR1318, NIH U54 EB005149, NIH T32 HL07572 and a Fast Forward Grant from CIMIT.

References

1. 3D Slicer: Medical Visualization and Processing Environment for Research (2004)
2. SCIRun: A Scientific Computing Problem Solving Environment (2002)
3. Aguel, F., Eason, J.C., Trayanova, N.A. et al.: Impact of Transvenous Lead Position on Active-can ICD Defibrillation: A Computer Simulation Study. PACE, 22 p.158 (1999)
4. Alcott, G., Hunter, F., Ideker, R.: Principles of defibrillation: Cellular physiology to fields and waveforms. Clinical Cardiac Pacing and Defibrillation. 2nd edn. Saunders, Philadelphia (2000)
5. Alexander, M.E., Cecchin, F., Walsh, E.P., et al.: Implications of Implantable Cardioverter Defibrillator Therapy in Congenital Heart Disease and Pediatrics. J. Cardiovasc. Electrophysiol. 15, 72 (2004)
6. Bar-Cohen, Y., Berul, C.I., Alexander, M.E., et al.: Age, Size, and Lead Factors Alone do Not Predict Venous Obstruction in Children and Young Adults with Transvenous Lead Systems. J. Cardiovasc. Electrophysiol. 17, 754 (2006)
7. Berul, C.I., Triedman, J.K., Forbess, J., et al.: Minimally Invasive Cardioverter Defibrillator Implantation for Children: An Animal Model and Pediatric Case Report. PACE 24, 1789 (2001)
8. Bokhari, F., Newman, D., Greene, M., et al.: Long-Term Comparison of the Implantable Cardioverter Defibrillator Versus Amiodarone: Eleven-Year Follow-Up of a Subset of Patients in the Canadian Implantable Defibrillator Study (CIDS). Circulation 110, 112 (2004)
9. Buxton, A.E., Lee, K.L., Fisher, J.D., et al.: A Randomized Study of the Prevention of Sudden Death in Patients with Coronary Artery Disease. Multicenter Unsustained Tachycardia Trial Investigators. The New Eng. J. Med. 341, 1882 (1999)
10. Cannon, B.C., Friedman, R.A., Fenrich, A.L., et al.: Innovative Techniques for Placement of Implantable Cardioverter-Defibrillator Leads in Patients with Limited Venous Access to the Heart. PACE 29, 181 (2006)
11. de Jongh, A.L., Entcheva, E.G., Replogle, J.A., et al.: Defibrillation Efficacy of Different Electrode Placements in a Human Thorax Model. PACE 22, 152 (1999)
12. Frazier, D.W., Wolf, P.D., Wharton, J.M., et al.: Stimulus-Induced Critical Point. Mechanism for Electrical Initiation of Reentry in Normal Canine Myocardium. J. Clin Invest 83, 1039–1052 (1989)
13. Gold, M.R., Olsovsky, M.R., DeGroot, P.J., et al.: Optimization of Transvenous Coil Position for Active can Defibrillation Thresholds. J. Cardiovasc. Electrophysiol. 11, 25 (2000)

14. Jorgenson, D.B., Haynor, D.R., Bardy, G.H., et al.: Computational Studies of Transthoracic and Transvenous Defibrillation in a Detailed 3-D Human Thorax Model. IEEE Trans. Biol. Engin. 42, 172 (1995)
15. Jorgenson, D.B., Schimpf, P.H., Shen, I., et al.: Predicting Cardiothoracic Voltages during High Energy Shocks: Methodology and Comparison of Experimental to Finite Element Model Data. IEEE Trans. Biol. Engin. 42, 559 (1995)
16. Khairy, P., Landzberg, M.J., Gatzoulis, M.A., et al.: Transvenous Pacing Leads and Systemic Thromboemboli in Patients with Intracardiac Shunts: A Multicenter Study. Circulation 113, 2391–2397 (2006)
17. Kindlmann, G.: TEEM: Tools to Process and Visualize Scientific Data and Images (2005)
18. Kriebel, T., Ruschewski, W., Paul, T.: Implantation of an "Extracardiac" Internal Cardioverter Defibrillator in a 6-Month-Old Infant. Zeitschrift fur Kardiologie 94, 415 (2005)
19. Kugler, J.D., Erickson, C.C.: Nontransvenous Implantable Cardioverter Defibrillator Systems: Not just for Small Pediatric Patients. J. Cardiovasc. Electrophysiol. 17, 47 (2006)
20. Mocanu, D., Kettenbach, J., Sweeney, M.O. et al.: A Comparison of Biventricular and Conventional Transvenous Defibrillation: A Computational Study using Patient Derived Models. PACE 27, 586 (2004)
21. Mocanu, D., Kettenbach, J., Sweeney, M.O., et al.: Patient-Specific Computational Analysis of Transvenous Defibrillation: A Comparison to Clinical Metrics in Humans. Ann. Biomed. Engin. 32, 775 (2004)
22. Moss, A.J., Hall, W.J., Cannom, D.S., et al.: Improved Survival with an Implanted Defibrillator in Patients with Coronary Disease at High Risk for Ventricular Arrhythmia. Multicenter Automatic Defibrillator Implantation Trial Investigators. The. New. Eng. J. Med. 335, 1933 (1996)
23. Schreiber, C., Eicken, A.: Nonthoracotomy Cardioverter Defibrillator Implantation in Infants. Resuscitation 69, 350 (2006)
24. Stephenson, E.A., Batra, A.S., Knilans, T.K., et al.: A Multicenter Experience with Novel Implantable Cardioverter Defibrillator Configurations in the Pediatric and Congenital Heart Disease Population. J. Cardiovasc. Electrophysiol. 17, 41 (2006)
25. Tang, A.S., Wolf, P.D., Afework, Y., et al.: Three-Dimensional Potential Gradient Fields Generated by Intracardiac Catheter and Cutaneous Patch Electrodes. Circulation 85, 1857–1864 (1992)
26. Zhang, Y., Bajaj, C.: Adaptive and Quality quadrilateral/hexahedral Meshing from Volumetric Data. Computation Methods in Applied Mechanical Engineering 195, 942–960 (2006)
27. Zhou, X., Daubert, J.P., Wolf, P.D. et al.: Epicardial Mapping of Ventricular Defibrillation with Monophasic and Biphasic Shocks in Dogs. Circ Res. 72, 145–160 (1993)
28. Zipes, D.P., Fischer, J., King, R.M., et al.: Termination of Ventricular Fibrillation in Dogs by Depolarizing a Critical Amount of Myocardium. Am. J. Cardio. 36, 37 (1975)

Mathematical Modeling of Electromechanical Function Disturbances and Recovery in Calcium-Overloaded Cardiomyocytes

Leonid B. Katsnelson, Tatiana Sulman, Olga Solovyova, and Vladimir S. Markhasin

Institute of Immunology and Physiology, Ural Division of the Russian Academy of Sciences
Pervomayskaya str. 91, Ekaterinburg 620041, Russia
l.katsnelson@iip.uran.ru

Abstract. Rhythm disturbances and mechanical function suppression proper to the acute heart failure in the case of cardiomyocyte calcium overload are simulated in a mathematical model of cardiomyocyte electromechanical activity. Particular attention is paid to the overload caused by diminished activity of the Na^+-K^+ pump. It is shown in the framework of the model that myocardium mechanics may promote arrhythmias in these conditions. In particular, cooperative influence of the attached crossbridges on the calcium-troponin kinetics is shown to contribute to the initiation of spontaneous action potentials. Numerical experiments showed that the recovery of the normal Na^+-K^+ pump activity during the heart failure attack did not always led to the normal electromechanical function recovery in the failed cardiomyocyte. Alternative approaches were suggested in the model and compared to each other for recovery of the myocardium electrical and mechanical performance in the simulated case of the acute heart failure.

Keywords: Active myocardium mechanics – Mechano-electric feedback – Heart rhythm – Extrasystole – Arrhythmia.

1 Introduction

Rhythm disturbances are prevalent and potentially lethal complications of heart diseases. Given the complexity of intracellular mechanisms underlying arrhythmogenesis, detailed mathematical models can help to reveal causal chains of events and to identify possible targets for therapeutic interventions.

Calcium overloading of cardiomyocytes is one of the principal factors inducing rhythm disturbances on the cellular level. For example, Ca^{2+} accumulation in cardiomyocytes during heart failure is fraught with a risk of triggered activity and fibrillation, as a consequence of spontaneous Ca^{2+} releases induced by sarcoplasmic reticulum (SR) overload [1, 2]. It is well known that Na^+-K^+ pumping decrease may cause cardiomyocyte calcium overload [3]. Previous research has focused on mathematical modeling of rhythm disturbances caused by calcium overload [3-5], including the case of reduced Na^+-K^+ pump activity [3].

Nevertheless, those studies dealt with the electrical activity of cardiomyocytes, while not considering simultaneous disturbances of the mechanical function and possible role of the mechano-electric feedback (MEF) in the modelled arrhythmias.

F.B. Sachse and G. Seemann (Eds.): FIMH 2007, LNCS 4466, pp. 383–392, 2007.

We try to address the lack of such analysis with the help of our 'Ekaterinburg-Oxford' mathematical model developed earlier [6] and combining description of both the electrical and mechanical cardiomyocyte activity.

When Na^+-K^+ pump activity is reduced in the model, calcium overload developed gradually during a series of isometric contractions generated by regular pacing. We found that, if mechanics expelled from the model, only almost complete block of the Na^+-K^+ pump produced extrasystoles. This observation is fully consistent with the results of the simulation performed by Noble and Varghese [3]. However, effects of the mechanical activity of cardiomyocytes on both their Ca^{2+} handling and electrical activity proved in the 'Ekaterinburg-Oxford' model to increase significantly vulnerability for triggered activity in the case of moderately decreased Na^+-K^+ pump [7]. Now, using our mathematical model, we focus on the theoretical analysis of possible approaches to the recovery of the electromechanical function of the cardiomyocytes in these pathological conditions.

2 Cardiac MEF in the 'Ekaterinburg-Oxford' Mathematical Model

'Ekaterinburg-Oxford' mathematical model of mechano-electric interactions in ventricular cardiomyocytes has been developed earlier [6], which inherits the description of the electrical activity from the Noble'98 ventricular cell model [8] and the description of cellular Ca^{2+} kinetics and mechanical activity from the Ekaterinburg model family. Now we use the most recent version of the mechanical model described in detail elsewhere [9]. The combined model realistically simulates mechanical and electrical activity of cardiomyocytes during isometric and afterloaded contractions.

The model includes mechano-dependent cooperativity of the kinetics of Ca^{2+} - troponin C (CaTnC) binding. This is a principal link between cardiac mechanics and Ca^{2+} handling in cardiomyocytes. Three types of experimentally-established cooperativity of Ca^{2+} activation [10] are taken into account in the model [11]. Namely, the affinity of TnC for Ca^{2+} increases with the increasing of: (i) concentration of strongly-bound crossbridges (Xb) and (ii) concentration of CaTnC complexes; while, (iii) availability of actin sites for myosin heads increases due to the end-to-end interaction between tropomyosins.

These mechanisms underlie in the model a wide range of experimentally observed phenomena, such as the effects of mechanical load on muscle relaxation and mechano-Ca^{2+} coupling (e.g. length- and load-dependence of Ca^{2+} transients). In addition, mechanical modulation of Ca^{2+} transients (due to mechano-dependent CaTnC kinetics) links through to mechanical and electrical activity, via Ca^{2+}-dependent ionic currents. The model reproduces the effects of mechano-electrical coupling as an influence of muscle length on action potential (AP) duration during isometric contractions, the AP duration (APD) dependence on the muscle load during afterloaded contractions, and certain APD changes caused by passive deformations [6]. The cooperativity of the first type (Xb-CaTnC cooperativity) proves to be of

special importance in this study. It is specified in the model by an exponential function $\pi(N_A)$ in the differential equation describing CaTnC kinetics [9]:

$$\frac{dA}{dt} = a_{on} \cdot (A_{tot} - A) \cdot [Ca^{2+}]_i - a_{off} \cdot exp(-k_A \cdot A) \cdot \pi(N_A) \cdot A$$

Here A is CaTnC concentration, N_A is an average fraction of attached cross-bridges per CaTnC complex. $\pi(N_A)$ decreases with the N_A increase.

In this work Ca^{2+} overload was reached in the model via attenuation of the Na^+-K^+ pump activity (other ways of the overload were also simulated and produced similar results). The pump current i_p is described in the model as follows [8].

$$i_p = \hat{i}_p \cdot \frac{[K^+]_o}{[K^+]_o + K_{m,K}} \cdot \frac{[Na^+]_i}{[Na^+]_i + K_{m,Na}}$$

Here $[Na^+]_i$ and $[K^+]_o$ are concentrations of the intracellular sodium and extracellular potassium respectively. $K_{m,K}$ and $K_{m,Na}$ are corresponding Michaelis constants of the pump. Reduction of the pump activity was simulated with an increase in $K_{m,Na}$. The normal value of this parameter ($K_{m,Na}$ = 24.2 mM) [7] was used as a reference magnitude in our study.

3 Role of MEF in the Arrhythmias Induced by Decreased Na^+-K^+ Pump Activity

We have earlier published elsewhere [7] our model analysis of the MEF contribution to the arrhythmias in cardiomyocytes overloaded with Ca^{2+}. Here we only summarize those results briefly as a background for describing approaches to the rhythm recovery suggested in Section 4.

Essentially new aspect of that our study [7], in addition to previous works of other authors [3-5, 12] was its focus on the mechanical contribution to inducing arrhythmias in conditions where the calcium overload of cardiomyocytes was not sufficiently large to cause the rhythm disturbances by itself. In particular, Figures 1 and 2 demonstrate an extrasystolic attack followed by the force alternans in a case of such moderate calcium overload.

We showed that the following mechanical factors proved to be potentially arrhythmogenic in cardiomyocytes moderately overloaded with Ca^{2+}:

- cross-bridge kinetics during the cardiomyocyte relaxation and effects of the kinetics on the CaTnC dissociation via the Xb-CaTnC cooperativity mechanism;
- cardiomyocyte length during contraction-relaxation cycles;
- mechanical loads (as these influence both current lengths and contraction velocities);
- mechanical interaction of cardiomyocytes with different degree of Na^+-K^+ pump inhibition.

We found in the model two mechanisms of the mechanical factor contribution to the arrhythmia in cardiomyocytes moderately overloaded with Ca^{2+}. Both mechanisms are analyzed in detail elsewhere [7]. Briefly they are as follows.

First, during *any isometric/isotonic twitch* following a regular pacing, there are dynamic cooperative interactions between Xb and CaTnC kinetics. The interactions support a high rate of the CaTnC decay during the final relaxation stage of the twitch, and thus provide the cytosol with a small surplus of $[Ca^{2+}]_i$ at the end of this stage. When cardiomyocytes are moderately overloaded with Ca^{2+}, the background diastolic level of the cytosol calcium is also higher than the normal one. Therefore the surplus turns out to provide a critical increment in the diastolic $[Ca^{2+}]_i$ to *trigger* spontaneous Ca^{2+} release from the SR. The release, in its turn, activates inward depolarizing current via the forward mode of the Na^+-Ca^{2+} exchanger and the following extrasystolic AP. Thus, the described is a mechanism of the Xb-CaTnC-induced spontaneous AP generation.

Second, mechanical conditions (a decrease in the initial length and/or cardiomyocyte dynamic shortening) may intensify gradual (beat-to-beat) Ca^{2+} storage in the SR due to the length dependence of the same Xb-CaTnC-cooperativity [7]. This mechanism may additionally contribute to the cell Ca^{2+} overloading and thus promote overcoming the arrhythmogenic threshold of the SR calcium concentration.

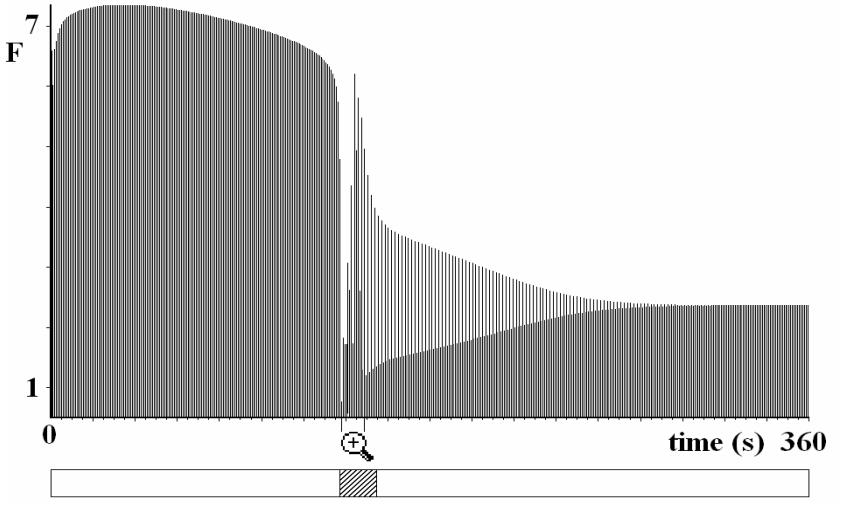

Fig. 1. Contractions of a single virtual cardiomyocyte with moderately reduced activity of the Na^+-K^+ pump (P-sample; see the text, where the sample is defined). L=0.90 L_{max} (L_{max} corresponds to the sample length where it develops a maximum active isometric tension); pacing rate: 75 stimuli/m. The panel demonstrates active tension peaks (F – arbitrary units). The magnifying lens indicates the time interval represented in detail in Fig.2. The band under the panel indicates phases of the process where P-sample distinctly responds to the recovery of the normal Na^+-K^+ pump (see Sec. 4 for details). The data shows that, unlike the stimulation rate of 60 stimuli/min, where no rhythm disturbances observed in the P-sample, a faster pacing equal to 75 stimuli/min (or higher – not shown here) at decreased Na^+-K^+ pump activity resulted in the following events. A brief increase in the force amplitudes turned into a very gradual decrease that was suddenly disrupted by the drop in force accompanied by extrasystoles (see Fig. 2 for more detail). Then a transient force alternans arose (see also Fig. 2) transferring to steady-state contractions with very low force amplitudes.

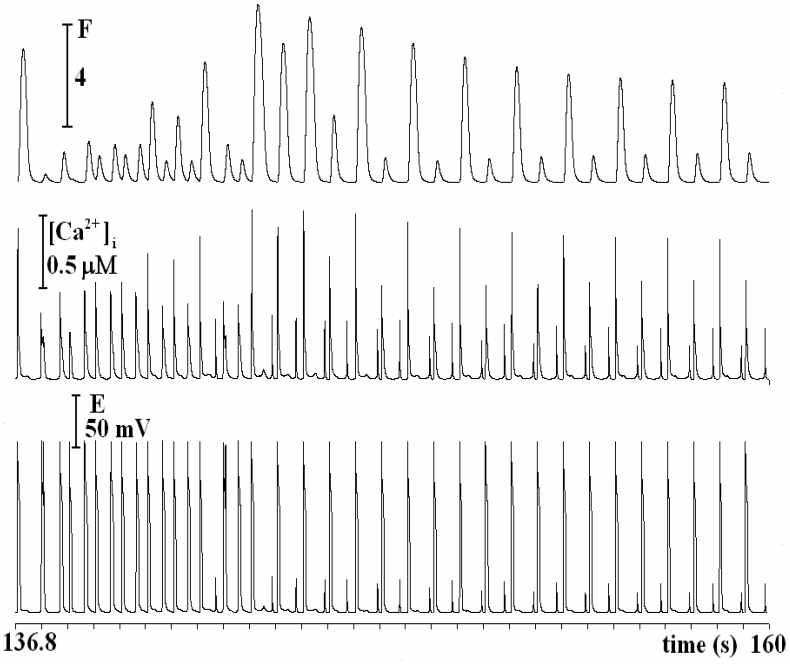

Fig. 2. Time course of the tension development (F), calcium transients ($[Ca^{2+}]_i$) and membrane potential (E) in the P-sample during 137 ÷ 160 s indicated with the magnifying lens in Fig.1. Scores under the time axis show the moments of the regular stimuli (each 0.8 s).

In general, these two mechanisms allow us to consider 3 characteristic ranges of Na^+-K^+ pump attenuation in respect with the mechanical contribution to the arrhythmogenesis. The ranges are as follows.

(1) $K_{m,Na} \geq 110$ mM (while the normal $K_{m,Na}$ is 24.2 mM) – extrasystoles arise independently of the mechanics.

(2) 40 mM $\leq K_{m,Na} <$ 110 mM - extrasystoles also arise in any mechanical conditions, but only due to the above mechanism of the Xb-CaTnC-induced spontaneous AP generation. Figures 1, 2 demonstrate an example of the rhythm disturbances revealed in the model for $K_{m,Na}=$ 40 mM (where all the other parameter values are the same as in the norm). This virtual cardiomyocyte is named in our work as P-sample (pathological sample).

The behaviour of the P-sample shown in Fig. 1 and 2 reminds sudden force fall, arrhythmia and pulsus alternans observed during the acute heart failure development. Similar disturbances arose in the P-sample not only at the length equal to $0.90\,L_{max}$ represented here, but for any lengths $\leq 0.95 L_{max}$.

(3) 37 mM $\leq K_{m,Na} <$ 40 mM - extrasystoles arise only due to the direct mechanical impacts (length or load diminution) via the mechanism of the mechanically modulated calcium overloading.

The latter range represents a border zone. When $K_{m,Na}$ lied below this zone, extrasystoles did not arise in the model in any mechanical conditions.

The first Na^+-K^+ pump inhibition range ($\boldsymbol{K_{m,Na}} \geq 110$ mM) has many things in common with findings obtained by Noble and Varghese [3], who studied effects of the almost blocked pump in the Earm-Hilgeman-Noble model of the cardiomyocyte ionic currents [13, 14]. In particular, they observed autorhythmic activity which arose in response to a single stimulus under strongly reduced Na^+-K^+ pump function. As they showed, the autorhythmic activity in that case resulted from the spontaneous Ca^{2+} release from the SR that in turn activated inward current via the Na^+-Ca^{2+} exchanger. The same processes underlie rhythm disturbances in our simulations for $\boldsymbol{K_{m,Na}} \geq 110$ mM. Reduction of Na^+-K^+ pump activity in the second ($40\,\text{mM} \leq \boldsymbol{K_{m,Na}} < 110$ mM) and the third ($37\,\text{mM} \leq \boldsymbol{K_{m,Na}} < 40\,\text{mM}$) ranges in our experiments was much more moderate than they simulated. Respectively, diastolic $[Ca^{2+}]_i$ also increased much less and thus could not cause by itself the spontaneous Ca^{2+} release from the SR without assistance of the additional MEF mechanisms we found in the model.

It is important that the predicted mechanism of the Xb-CaTnC-induced spontaneous AP generation may be verified in real experiments with a muscle sample. First, arrhythmia may be induced in the sample via a cardiac glycoside overdose. Then crossbridge attachment may be eliminated in the sample. This may be done using BDM (*2,3-butanedione 2-monoxime*) that prevents actomyosin formation [15]. The model predicts that spontaneous APs will vanish after BDM application. Moreover, the vanish is predicted to be valid for a significant range of cardiac glycoside concentrations inducing rhythm disturbances (corresponding to the found in the model range (2) of Na^+-K^+ pump attenuation: $40\,\text{mM} \leq \boldsymbol{K_{m,Na}} < 110$ mM).

4 Arrhythmia Suppression and Contractile Function Recovery

Here we use the model of the acute heart failure associated with the calcium overload to simulate suppression of the rhythm disturbances and restoration of stable contractions with amplitudes close to the normal ones. Figure 3 and Table 1 illustrate results of several "therapeutic" approaches applied to the P-sample.

First, it turned out to be quite unexpectedly that reestablishment of the normal Na^+-K^+ ATP-ase state did not always provide the recovery of the normal contractions. In this case the result substantially depended on the phases of the "acute heart failure" development, in which the reestablishment (i.e. the normal value of $\boldsymbol{K_{m,Na}}$) was done.

The band under the time axis in Fig. 1 shows such phases for the P-sample: white parts of the band indicate the phases where reestablishment of the normal $\boldsymbol{K_{m,Na}}$ resulted in the total recovery of both the normal rhythm and normal contraction pattern. However, results of the normal $\boldsymbol{K_{m,Na}}$ reestablishment was not so successful and stable during the shaded part of the band. Particularly, the reestablishment was tested (a) during the extrasystolic sub-phase indicated with the horizontal square bracket under Fig. 3; (b) after each low (odd) contraction during the transitional alternans sub-phase that succeeded extrasystolic one; (c) after each high (even) contraction during the alternans sub-phase. An example of (b) is indicated with the vertical arrow under Fig. 3A, and that of (c) – with the double-arrow. The tests showed that the normal electromechanical activity recovered totally only in the case (c) (see Fig. 3C). In the case (b) the reestablishment of the normal Na^+-K^+ pump resulted in one more transitional extrasystolic phase that passed into the steady-state alternans (Fig. 3B). The pattern similar to the latter one arose also in the case (a).

Interestingly that, unlike the above data obtained at the sample length equal 0.90 L_{max}, all the rhythm disturbances in the same P-sample at the length equal 0.95 L_{max} were suppressed as soon as the normal sodium-potassium pump activity (normal $K_{m,Na}$) was recovered, whenever the recovery was imposed during the development of the "acute heart failure".

It is important that in all the listed above cases (a), (b), (c) the normal electromechanical function totally recovered in any mechanical conditions, if the pump activity slightly overcame the control level (i.e. to the initial normal state of the pump). For instance, the additional increase of the pump activity (via the 5% decrease in $K_{m,Na}$ as compared to the reference value) turned out to be sufficient for such a total recovery of the P-sample electromechanical behaviour, whenever during the failure development the intervention was performed.

These data suggest that results of drug applications during development of the acute heart failure may depend on the mechanical conditions of heart contractions and on phases of the heart failure. Moreover, an "over-improvement" of some intracellular process may be necessary to approach a stable effect.

At present time there are practically no drugs which would specifically improve only the reduced Na^+-K^+ pump function. This significantly constricts possibilities of the normal pump reestablishment in patients. Therefore in the framework of the

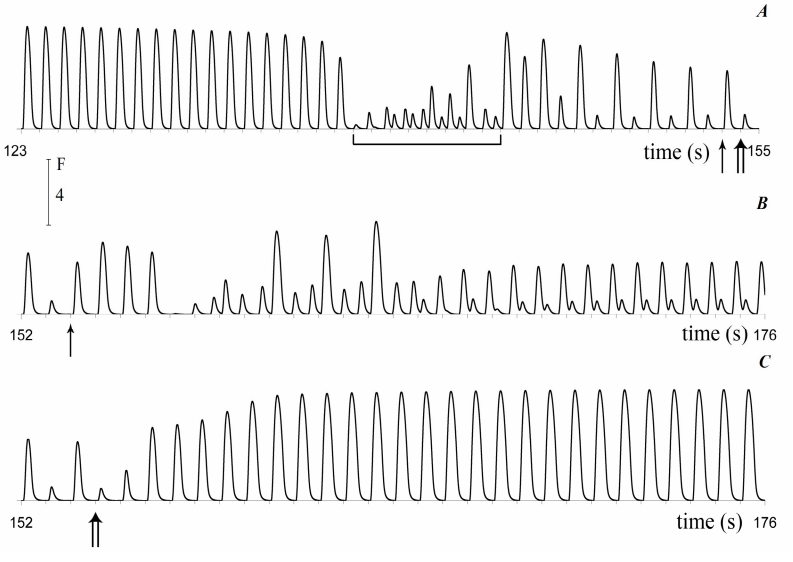

Fig. 3. Effects of recovery of the Na^+-K^+ pump activity at different instants. Panel A: enlarged fragment of Fig.1 demonstrating active force of the P-sample during the acute heart failure attack at the length 0.90L_{max} with the pacing of 75 stimuli/min. Horizontal square bracket under the panel shows a phase where extrasystoles arise spontaneously between the regular contractions. This phase is succeeded by the transitional pulsus alternans at the right-hand part of the panel where two vertical arrows (the single one and the double-arrow) indicate the instants of recovery of the control (normal) Na^+-K^+ pump state. Namely, the pump was recovered *alternatively* after either the odd or the even contraction during the force alternans. Panels B and C successively represent results of both cases of the pump recovery.

model we studied various alternative ways to modulate (amplify or attenuate) other intracellular mechanisms that may lead to some reduction of the cardiomyocyte Ca^{2+} loading and thus to the recovery of both the normal rhythm and satisfactory mechanical characteristics of the contractions without intensifying Na^+-K^+ pump activity. Particularly, such alternative interventions applied to the P-sample gave the following results.

A desired anti-arrhythmic effect resulted from a decrease in the rate of calcium uptake by the SR Ca^{2+} pump, even if the Na^+-K^+ pump function was not recovered. For example, 13% decrease in the rate of the SR calcium uptake suppressed rhythm disturbances in the P-sample at $0.95\,L_{max}$, while extrasystoles still arose for the smaller cardiomyocyte lengths. Total 'curing' of the cardiomyocyte for all the lengths ensued from 18% SR Ca^{2+} uptake rate decrease. The mechanism of the 'curing' is as follows. Redistribution between SR Ca^{2+} uptake and Ca^{2+} removal from the cytosol via the Na^+-Ca^{2+} exchange current shifted in favour of the Ca^{2+} removal from the cell due to the slowing down of the SR uptake. Thanks to this shift, the total level of Ca^{2+} in both the SR and cytosol remained lower than the arrhythmogenic thresholds.

Alternatively, the arrhythmia was suppressed with a decrease in the L-type Ca^{2+} current, $\boldsymbol{i_{CaL}}$, via respective decrease in the Ca^{2+} permeability of the L-type channels. For example, when it was decreased by 15%, extrasystoles vanished in the P-sample at $0.95\,L_{max}$, but they still arose at the smaller lengths. The total 'curing' for all the lengths was observed with the 20% decrease in $\boldsymbol{i_{CaL}}$.

Antiarrhythmic effects were also obtained at all lengths in the case of the Na^+-Ca^{2+} exchange acceleration (20% increase in its turnover rate as compared to the normal value) or of the 20% decrease in sensitivity of the SR calcium release to $[Ca^{2+}]_i$.

When the "antiarrhythmic treatment" using one of the above parameters was applied after the first extrasystole, the arrhythmia disappeared immediately. However, the time for the recovery of steady-state force amplitudes varied depending on each particular parameter change within the range of $100 \div 160$ s.

Finally, the combined effect of simultaneous SR Ca pump activity attenuation and a decrease in the L-type Ca^{2+} current was considered. It is a case of a special importance, as in a real heart both effects may result simultaneously from the same drug application (β-blockers). It turned out that 11% simultaneous decrease in both parameters suppressed the rhythm disturbances at all lengths (compared to the ~20% decrease which was necessary in the case of the individual interventions aimed at either SR pumping decrease or $\boldsymbol{i_{CaL}}$ decrease).

Table 1 demonstrates how the SR Ca^{2+} load ($[Ca^{2+}]_{SR}$) as well as 2 mechanical characteristics of contraction-relaxation (inotropic one: $\mathbf{F_m}$ – the peak active force during the steady-state contractions, and loositropic one: $\mathbf{t_{30}}$ – relaxation time to 30% of $\mathbf{F_m}$) changed in comparison with the control due to the simulated interventions at $0.90\,L_{max}$. The data for the table were obtained when the steady-state contractions set in after the respective intervention.

Summarizing the suggested "therapeutic" approaches, it may be concluded that all of them are aimed at the unloading of the cardiomyocytes overloaded with Ca^{2+}. The interventions considered either promote the beat-to-beat calcium removal from the cell or slow down calcium beat-to-beat influx into the cytosol. All these methods of calcium unloading proved to be palliatives, because Ca^{2+} level in the SR in all these cases remained essentially higher than in norm. As applied to clinical practice, this

Table 1. Results of different "treatments" of the P-sample

	SR pump rate 18%↓	*L-type Ca^{2+} current 20%↓*	*Na^+-Ca^{2+} current 20%↑*	*Ca^{2+} sensitivity of the SR Ca^{2+} release 20%↓*	*SR pump rate & L-type Ca^{2+} current 11%↓(both)*
$\mathbf{F_m}$	88.5%	95.7%	99.2%	119.7%	94.4%
$\mathbf{t_{30}}$	101.8%	104.1%	108.8%	138.2%	105.3%
$\mathbf{[Ca^{2+}]_{SR}}$	122.9%	122.7%	135.1%	134.2%	119.2%

The top row of the table indicates parameter changes as compared to the P-sample. Arrows mean an increase (↑) and a decrease (↓) in the parameter values. $\mathbf{[Ca^{2+}]_{SR}}$, $\mathbf{F_m}$ and $\mathbf{t_{30}}$ are given as a percentage of the corresponding values in the normal cardiomyocyte.

might be interpreted as follows. If the prime cause of calcium overload is unavoidable, the drug application is to be used permanently. Drugs in this situation are, in a certain sense, molecular 'prosthetic tools' aimed to support impaired native mechanisms of calcium homeostasis. Our modeling confirms that β-blockers are highly effective drugs for the correction of cardiac electromechanical function, when cardiomyocytes are overloaded with calcium.

$\mathbf{[Ca^{2+}]_{SR}}$ values in the table reveal that each particular intervention partially relieved SR of Ca^{2+} as compared with the threshold $\mathbf{[Ca^{2+}]_{SR}}$ = 142% (of the norm) in the P-sample achieved just before the beginning of the "acute heart failure" attack.

5 Conclusion

A mathematical model of the acute heart failure development has been created. The model simulates cardiomyocyte electrical and mechanical functions and deals with the heart failure associated with the Ca^{2+} overload. The model suggests that both cardiomyocyte mechanical properties (crossbridge attachment/detachment kinetics that in turn influence CaTnC kinetics) and mechanical conditions of contractions (length, load) may significantly affect a risk of the acute heart failure attack in cardiomyocytes moderately overloaded with Ca^{2+}.

We analyzed in the model a few alternative "therapeutic" approaches aimed to decrease calcium loading of cardiomyocytes, and thus to prevent from the "heart failure" development. The model predicts that simultaneous decrease in both L-type Ca^{2+} current and SR Ca^{2+} pumping seems to be the most relevant 'therapy' among the analyzed approaches. Just similar double action is typical for the effect of β-blockers.

The model shows that response of a cardiomyocyte to a prompt change of its state during alternating contractions may differ principally depending on which particular contraction (even or odd) precedes the impact. In the modelled case the impact was an instant recovery of the normal Na^+-K^+ pump activity. Meantime, there are real experimental data [16] revealing that another impact (a single extrastimulus) led to altering restitution curves depending on even or odd beat preceded the extrastimulus. It might be hypothesized that some intrinsic mechanisms underlie different cases of such altering responses. This hypothesis may be a subject of a future study.

Acknowledgments. This work is subject of a Wellcome Trust Research Development Award # 074152/Z/04/Z, President Grant for Leading Scientific Schools #4923.2006.4, The Fogarty International Center # 1 RO3 TW006250-01a1, and of a Russian Foundation for Basic Research grant # 05-04-48352.

References

1. Kihara, Y., Morgan, J.P.: Intracellular calcium and ventricular fibrillation. Studies in the aequorin-loaded isovolumic ferret heart. Circ Res. 68.5, 1378–1389 (1991)
2. Lakatta, E.G., Guarnieri, T.: Spontaneous myocardial calcium oscillations: are they linked to ventricular fibrillation? J. Cardiovasc Electrophysiol 4.4, 473–489 (1993)
3. Noble, D., Varghese, A.: Modelling of sodium-overload arrhythmias and their suppression. Can. J. Cardiol 14.1, 97–100 (1998)
4. Luo, C.H., Rudy, Y.: A dynamic model of the cardiac ventricular action potential. II. Afterdepolarizations, triggered activity, and potentiation. Circ Res. 74.6, 1097–1113 (1994)
5. Noble, D.: Modeling the heart–from genes to cells to the whole organ. Science 295.5560, 1678–1682 (2002)
6. Solovyova, O., Vikulova, N., Katsnelson, L.B., Markhasin, V.S., Noble, P.J., Garny, A.F., Kohl, P., Noble, D.: Mechanical interaction of heterogeneous cardiac muscle segments in silico: effects on Ca2+ handling and action potential. International Journal of Bifurcation and Chaos 13.12, 3757–3782 (2003)
7. Katsnelson, L.B., Solovyova, O., Sulman, T., Konovalov, P., Markhasin, V.S.: Modeling cardiomyocyte mechano-electric coupling in norm and pathology. Biophysics 51.6, 917–926 (2006)
8. Noble, D., Varghese, A., Kohl, P., Noble, P.: Improved guinea-pig ventricular cell model incorporating a diadic space, IKr and IKs, and length- and tension-dependent processes. Can. J. Cardiol 1, 123–134 (1998)
9. Katsnelson, L.B., Nikitina, L.V., Chemla, D., Solovyova, O., Coirault, C., Lecarpentier, Y., Markhasin, V.S.: Influence of viscosity on myocardium mechanical activity: a mathematical model. J. Theor Biol 230.3, 385–405 (2004)
10. Gordon, A.M., Regnier, M., Homsher, E.: Skeletal and Cardiac Muscle Contractile Activation: Tropomyosin "Rocks and Rolls". News Physiol. Sci. 16, 49–55 (2001)
11. Katsnelson, L.B., Markhasin, V.S.: Mathematical modeling of relations between the kinetics of free intracellular calcium and mechanical function of myocardium. J. Mol. Cell Cardiol 28.3, 475–486 (1996)
12. DiFrancesco, D., Noble, D.: A model of cardiac electrical activity incorporating ionic pumps and concentration changes. Philos Trans R. Soc. Lond B. Biol Sci. 307.1133, 353–398 (1985)
13. Earm, Y.E., Noble, D.: A model of the single atrial cell: relation between calcium current and calcium release. Proc R. Soc. Lond B. Biol Sci. 240.1297, 83–96 (1990)
14. Hilgemann, D.W., Noble, D.: Excitation-contraction coupling and extracellular calcium transients in rabbit atrium: reconstruction of basic cellular mechanisms. Proc R. Soc. Lond B. Biol Sci. 230.1259, 163–205 (1987)
15. Mulieri, L.A., Alpert, N.R.: Differential effects of BDM on activation and contraction. Biophys J. 45, 47a (1984)
16. Pastore, J.M., Laurita, K.R., Rosenbaum, D.S.: Importance of spatiotemporal heterogeneity of cellular restitution in mechanism of arrhythmogenic discordant alternans. Heart Rhythm 3.6, 711–719 (2006)

Locally Adapted Spatio-temporal Deformation Model for Dense Motion Estimation in Periodic Cardiac Image Sequences

Bertrand Delhay, Patrick Clarysse, and Isabelle E. Magnin

Creatis, CNRS UMR #5220, INSERM U630, INSA Bât. Blaise Pascal
F-69621 Villeurbanne Cedex, France
delhay@creatis.insa-lyon.fr

Abstract. We recently introduced a continuous state space parametric model of spatio-temporal transformations and an algorithm, based on Kalman filtering, to represent motion in an image sequence describing a periodic phenomena. One advantage of this method is to simultaneously take into account all the sequence frames to robustly estimate the parameters of a unique spatial and periodic-temporal model. However, in 3D+time, a large number of parameters is required. In this paper, we propose a criterion based on motion energy to locally adapt the trajectory model and thus the temporal complexity of the model. The influence of the model order is illustrated on true 2D+time Magnetic Resonance Images (MRI) of the heart in order to motivate the proposed adaptative criteria. Quantitative results of the proposed adapted spatio-temporal motion model are given on synthetic 2D+time MRI sequences. Preliminary experiments show a significant impact notably regarding the parameter saving while preserving the accuracy of the motion estimates.

1 Introduction

Cardiac motion estimation and modeling is particularly helpful for myocardial function analysis. The last two decades are marked by an important progress of image acquisition devices making possible to better explore the dynamics of moving organs. Magnetic Resonance Imaging (MRI) and Multiple Detector Computed Tomography (MDCT) provide meaningful information about the 3D anatomy and contractile function of the heart. 3D+time segmentation and motion estimation from cardiac images are recognized as a difficult pre-requisite tasks for quantitative analysis of cardiac function. Most of the published works does not explicitly take into account the time dimension and proceeds iteratively from one time point to the next. This results in inconsistent material point trajectories. However, it is clear, especially for cardiac motion recovery purpose, that introducing some realistic temporal constraints will greatly improve the estimated motion pattern [1]. In cardiac motion analysis, some recent works are extension of 2D/3D image registration methods to 2D+time/3D+time

F.B. Sachse and G. Seemann (Eds.): FIMH 2007, LNCS 4466, pp. 393–402, 2007.

[2,3]. Time axis is here considered as a supplementary axis which is not qualitatively different from the other spatial axes. In a similar way, in [4], the tracking of the left ventricle is performed with a 4D B-Spline model whose knots fit extracted features from Tagged MRI. In a previous paper [5], we introduced a framework based on state-space formulation and Kalman filtering by imposing a temporal consistency of the estimated motion over the whole image sequence and the whole image space. The periodicity and continuity of the motion is therefore insured but one of the main drawbacks of the method might be the number of involved parameters for motion description. This particular point makes difficult to process a full 3D+time sequence with standard computers. In this paper, we propose to locally adapt the complexity of the trajectories according to the magnitude of the underlying motion in order to focus on the description of the motion in regions which contain the meaningful information. The paper is organized as follows: in the method section, we briefly recall the model and algorithm proposed in [5] and introduce a criteria and a new method to locally adapt the complexity of the motion description. The next section illustrates the influence of the harmonic decomposition order with real 2D+time MRI and give quantitative results about parameters profit and accuracy of the motion estimation with synthetic 2D+time MRI sequences.

2 Method

Our method relies on the temporal modeling of free form deformations with a harmonic decomposition of the control point trajectories. After briefly recalling the principle, we focus on the proposal of this paper which consists in adapting the decomposition order of the model according to relevant information present in the image sequence.

2.1 Spatio-temporal Model

Let consider a periodized image sequence $\mathcal{I} = \{\mathbf{I}_j, j = 0..J\}$ (Fig. 1) where $j \in \mathbb{Z}^+$ refers to the discrete time axis and where each image $\mathbf{I}_j$ belongs to $\mathbb{R}^d$ and corresponds to the discrete time point t_j. This sequence results from the observation of cardiac motion with tomographic imaging modalities like cardiac cine-MRI or MDCT.

A Lagragian formulation of the motion consists in describing the path of each material point $\mathcal{P}$ during the motion. The time-dependent coordinates $\boldsymbol{x}(t)$ of $\mathcal{P}$ is expressed according to the reference coordinates $\boldsymbol{x}_0$ at reference time t_0. The spatio-temporal transformation $\boldsymbol{\varphi}$ is a one to one continuous mapping defined by: $\mathbb{R}^d \times \mathbb{R} \rightarrow \mathbb{R}^d$; $\boldsymbol{x}(t) = \boldsymbol{\varphi}(\boldsymbol{x}_0, t)$. In our work, the non-rigid continuous spatial transformation φ is modeled by Free Form Deformations (FFD) [6,7]. It warps an image by moving an underlying set of control points (CP) distributed over a regular grid. Instead of considering the displacement of each CP, we are looking

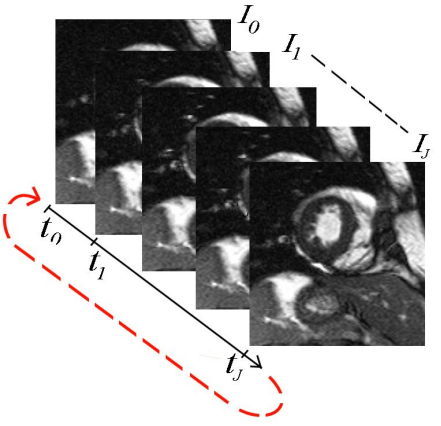

Fig. 1. Periodization of the image sequence to provide a pseudo infinite set of observations

for the whole trajectories they have to follow to fully describe the periodical spatio-temporal cardiac motion under study:

$$\begin{aligned} \boldsymbol{\varphi}(\boldsymbol{x}_0, t) &= \boldsymbol{x}_0 + \boldsymbol{u}(\boldsymbol{x}_0, t) \\ \boldsymbol{\varphi}(\boldsymbol{x}_0, t) &= \boldsymbol{x}_0 + \sum_{k \in K_{inf}(\boldsymbol{x}_0)} \boldsymbol{\xi}_k(t) \beta^k(\boldsymbol{x}_0). \end{aligned} \tag{1}$$

The displacement $\boldsymbol{u}(\boldsymbol{x}_0, t)$ of point $\mathcal{P}$ at time t is modeled by a linear combination of a tensor product of interpolating functions β^k (cubic B-Spline functions in our case) and the position $\boldsymbol{\xi}_k(t)$ at time t of the CPs. k stands for CP index and K_{inf} is the subset of the CPs which influence the motion of $\mathcal{P}$. Thus, the transformation is continuous, smooth and semi-local.

$\boldsymbol{\xi}_k(t)$ is a time dependent function representing the d-dimensional path of CP with index k. In [5], we proposed to express it as a finite sum of periodic harmonic functions (or truncated Fourier series):

$$S_{\boldsymbol{\xi}_k}(t) = \boldsymbol{a}_k^0 + \sum_{n=1}^{N} \left[\boldsymbol{a}_k^n \cos(2\pi n f t) + \boldsymbol{b}_k^n \sin(2\pi n f t) \right], \tag{2}$$

where f is the frequency of the motion to be estimated and N the decomposition order. The truncation to the first N coefficients of the decomposition is equivalent to apply a low-pass filter to the trajectory signal. Small values of N result in very smooth CP trajectories while higher values increase the complexity of the trajectories. The periodicity property of such a decomposition is very interesting for the beating heart analysis. Furthermore, velocity and acceleration can be directly derived and exploited.

2.2 Parameters Estimation

Spatio-temporal motion estimation for the whole image sequence is performed by estimating the coefficients of the Fourier series for all the CPs (size = K). All the parameters are considered as stochastic signals and stored into the state vector $\mathbf{X}$ (eq.(3)) of a state-space formulation (eq.(4)):

$$\mathbf{X}^t = \left[\boldsymbol{a}_0^0\ \boldsymbol{a}_0^1\ ...\ \boldsymbol{a}_0^N\ \boldsymbol{b}_0^1\ ...\ \boldsymbol{b}_0^N \mid ... \mid \boldsymbol{a}_{K-1}^0\ \boldsymbol{a}_{K-1}^1\ ...\ \boldsymbol{a}_{K-1}^N\ \boldsymbol{b}_{K-1}^1\ ...\ \boldsymbol{b}_{K-1}^N\right]. \quad (3)$$

$$\begin{aligned} \mathbf{X}_{j+1} &= \mathbf{A}_j\mathbf{X}_j + \Gamma\mathbf{v}_j \\ \mathbf{Z}_j &= \mathbf{C}_j\mathbf{X}_j + \mathbf{w}_j \end{aligned} \quad (4)$$

The state vector is not directly measurable but it can be recursively estimated according to a set of successive measurements $\mathbf{Z}_j$. Kalman filter [8] allows to take into account the whole sequence in a recursive way so that we only need results of a previous estimation to perform the next Kalman filter iteration. The image sequence $\mathcal{I}$ is periodized ($\mathcal{I}|\mathcal{I}|\mathcal{I}|\mathcal{I}$..., Fig.(1)) to give a pseudo infinite set of observations. At each innovation step, the new measurement $\mathbf{Z}_j$ is computed from non rigid FFD based registration between image $\boldsymbol{I}_j$ and reference image $\boldsymbol{I}_0$. The Kalman filter provides a useful prediction of the state to initialize the registration at each time point.

The registration similarity criterion must be chosen according to the expected relation between the images to be registered. In the monomodal case, we can assume that the photometric level of material points remains almost constant during motion. The sum of squared differences (SSD) measure has therefore been chosen:

$$SSD_j(\boldsymbol{I}_0, \boldsymbol{I}_j, \boldsymbol{\xi}(t_j)) = \sum_{\boldsymbol{x}\in\Omega} (\boldsymbol{I}_0(\boldsymbol{x}_0) - \boldsymbol{I}_j(\boldsymbol{\varphi}(\boldsymbol{x}_0, t_j)))^2 \quad (5)$$

with Ω the image overlapping domain. Optimization of the criterion is performed through a gradient descent algorithm. The obtained value for $\boldsymbol{\xi}(t_j)$ stands for the new measurement $\mathbf{Z}_j$ to be introduced in the Kalman filter.

The registration algorithm relies on two multi-level pyramidal representations. A first multiresolution pyramid $\mathcal{P}_1$ decomposes the successive observations within the image sequence $\mathcal{I}$, applying a low-pass Gaussian filter to each image I_k independently and then, decimating the number of pixels (or voxels). The second pyramid $\mathcal{P}_2$ allows for the multiscale decomposition of the spatio-temporal FFD transformation [9,10,3] (see [5] for more details).

2.3 Harmonic Order Adaptation

The total number of parameters increases with the number of CPs and with the order of decomposition of their trajectories. Let consider a $\mathbb{R}^d$ space, a warping

grid of size M and a harmonic decomposition order N. The transformation is thus defined by $(2N+1) \times d \times M^d$ parameters.

We observed that for meaningful areas in the image sequence, a decomposition order of $N = 4$ (*i.e.* 9 parameters to describe a CP trajectory path for $d = 2$) is largely sufficient to recover the spatio-temporal motion. The model described in section 2.1 implies that the number of parameters is the same for each CP whatever the region it influences. Indeed, the CPs outside of the heart generally experience a very short trajectory. An adaptation of the harmonic decomposition would avoid spending too much time for meaningless regions of the image and, at the same time, reduce the parameter number of the spatio-temporal model.

We propose to estimate the energy associated to the trajectory of CP with index k through the Parseval formula:

$$E_k = \left|\boldsymbol{a}_k^0\right|^2 + \frac{1}{2}\sum_{n=1}^{N}(|\boldsymbol{a}_k^n|^2 + |\boldsymbol{b}_k^n|^2) \tag{6}$$

The motion estimation starts with $N = 0$ so that $\boldsymbol{a}_k^0$ is the only parameter to be estimated for each CP. This value corresponds to the mean position of the k^{th} CP all over the spatio-temporal motion. The overall algorithm (algorithm 1) consists in alternatively increasing the transformation scale and the image resolution. The algorithm starts with the lower scale of the transformation pyramid and the lower image resolution. After convergence of the Kalman filter at this step, a higher level of the transformation is considered. The previous state vector, which contains the estimated parameters, is used to initialize the state vector corresponding to the current transformation scale. The projection operation is performed according to the following scheme:

$$\mathbf{X}^{l+1} = \left(\uparrow_2 \mathbf{X}^l\right) * \mathbf{H}, \tag{7}$$

where $\uparrow_2$ stands for the upsampling operation, l the pyramid level and where,

$$\mathbf{H} = \frac{1}{\sqrt{2}}\left[\frac{1}{8}\ \frac{1}{2}\ \frac{3}{4}\ \frac{1}{2}\ \frac{1}{8}\right], \tag{8}$$

is called the mirror filter [11] whose coefficients depend on the interpolating function β.

The harmonic adaptation step occurs just before the transformation level change. To this aim, the motion energy of each CP is computed according to Eq(6). If $E_k > \mu$ where μ is a fixed threshold, the harmonic order N_k is incremented. Until now, μ is experimentaly tuned, but some decision criteria are being investigated.

Data: $\mathcal{I}$, configuration file and input parameters
Initializations ($\mathcal{P}_1$ computation, Image Gradient, $N_k = 0$);
while *CurrentLevel* < *TotalCurrentLevel* **do**
  Initialize Kalman Filter;
  while *KalmanIteration* < *MaxKalmanIteration* **do**
    Prediction of the State at time k+1;
    Initialize registration parameters according to the prediction;
    Perform Gradient Descent Search;
    Filtering step;
    KalmanIteration = *KalmanIteration* + 1;
  end
  if *Increase transformation level* **then**
    Locally adapt the decomposition order N_k;
    Project parameters onto next transformation level;
    Increase $\mathcal{P}_2$ level;
    CurrentLevel = *CurrentLevel* + 1;
  else
    Increase $\mathcal{P}_1$ level;
    CurrentLevel = *CurrentLevel* + 1;
  end
end
Result: Spatio-temporal model parameters;

Algorithm 1: Flowchart of the estimation/prediction algorithm with local adaptation of the trajectory complexity

3 Results

For all the tests, the level number of both the image pyramid and the transformation pyramid are set to 4. The number of cycles used for Kalman convergence is fixed to 7 for each level of the pyramids (In general, 4 or 5 cycles are sufficient).

3.1 Harmonic Decomposition Order Influence with True 2D+time MRI Sequences

The ability to capture coarse motion from a reduced spatio-temporal model order will be studied on a true patient sequence. This sequence has been acquired using a cine MRI acquisition (1.5T Siemens Magnetom Vision scanner, Helsinki Medical imaging Center) and is composed of 28 time points covering the cardiac cycle (Fig 2, first row). A short axis slice was selected in the middle part of the heart, between the base and the apex. Image dimensions were 160×160, spatial resolution was $1mm \times 1mm$ and temporal resolution was $30ms$.

Figure 2 shows the values of E_k (Eq.(6)) at different transformation scales (FFD grid size 5×5, 7×7, 11×11, 19×19, respectively). Only the first term $\boldsymbol{a}_k^0$ of the Fourier series (*i.e.* model order $N = 0$) is considered for all CPs. This corresponds

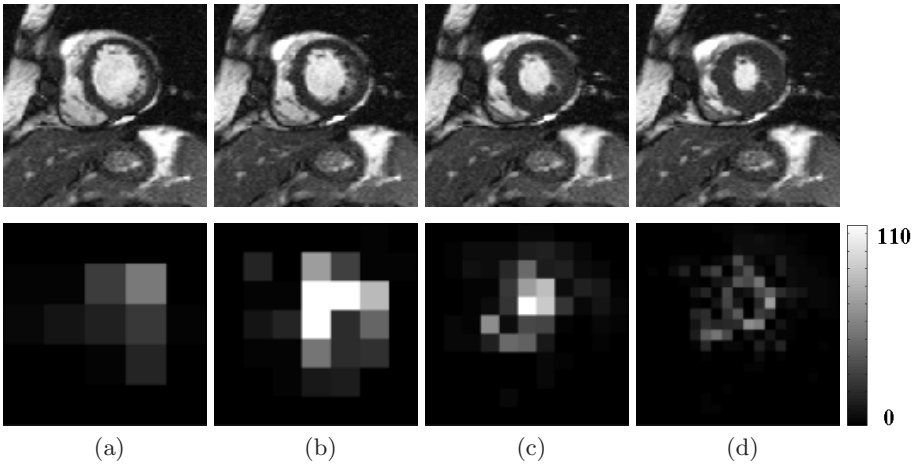

Fig. 2. The first row shows four images from the true MRI sequence during systole. The second rows illustrates the energy E_k at decomposition order $N = 0$ (mean term) for all the CPs. The intensity value in images a-b-c-d) respectively corresponds to the energy value at different scales of the transformation (one pixel per CP). The FFD grid size is 5×5, 7×7, 11×11, 19×19, respectively. The colorbar is expressed in mm^2.

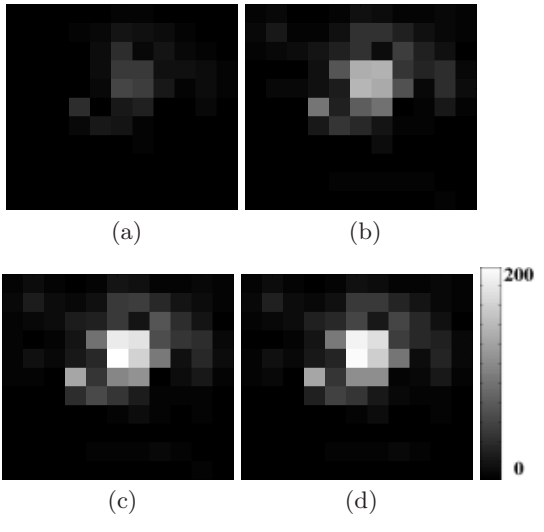

Fig. 3. Illustration of the energy E_k with model order $N = 0$ (a), $N = 1$ (b), $N = 2$ (c) and $N = 4$ (d) for all the CPs and a transformation scale 11×11

to the mean CP position over the full cycle. It is clear on this figure that interesting regions, where motion occurs, are well detected even at order $N = 0$.

Figure 3 illustrates E_k maps for a fixed transformation scale according to the decomposition order. We experimentally observed that order $N = 4$ is enough to

Table 1. MQE (in mm) and MAE (in degree) between the reference and the estimated motions fields. All the 22 time-points have been considered to compute the errors. The last column gives the number of parameters required to obtain the results.

	Quadratic error	Angular Error	Number Of Parameters
Adaptative decomposition	0.24 ± 0.28	3.7 ± 8.0	1 830
Grid Size: 19×19; $N = 4$	0.25 ± 0.29	3.8 ± 8.7	6 498
Grid Size: 19×19; $N = 2$	0.29 ± 0.29	4.1 ± 8.6	3 610

describe the most complex trajectories in the sequence. This value corresponds to 9 parameters to describe trajectories in each direction and for each CP. It is a good trade-off between the smoothness of the estimated trajectories and the number of images in the processed sequences.

3.2 Quantitative Results with Synthetic 2D+time MRI Sequences

Algorithm 1 was applied on a synthetic 2D sequence of a realistic beating heart. This sequence was generated from an actual 2D MRI short axis slice. The synthetic motion is defined from a spatio-temporal analytical model described in [12]. Dimensions of the images are 160×160 pixels and spatial resolutions are $1mm \times 1mm$. Gaussian noise (mean $= 0$, $\sigma = 5$ square intensity unit) has been independently added to each image of the generated sequence. The theoretical spatio-temporal motion field is used as a reference to assess the performance of the proposed algorithm in terms of mean quadratic (MQE) and mean angular errors (MAE) over the whole sequence. Because of the high number of involved parameters, standard computer architectures (with 1Gb of RAM) fail to converge when N is high and constant for all the CPs. In that case, there is a trade-off to find between the final FFD grid resolution (spatial resolution) and the decomposition order (temporal resolution). This problem is overcome with the proposed method. The Table 1 quantitatively compares our method,

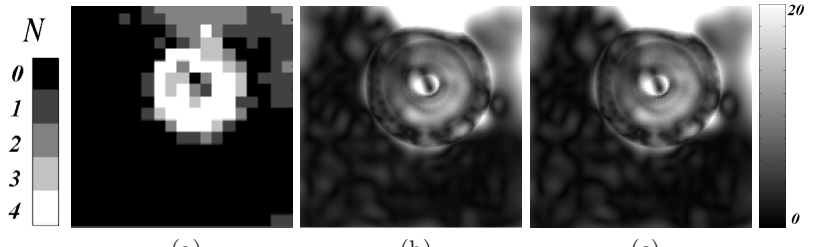

Fig. 4. Cartography of the harmonic order used for the final motion model a). Dark pixels correspond to small N values and bright pixels correspond to high values. b) and c) display the MQE map (mm) for reference and estimated motion fields, respectively. b) corresponds to the configuration where the FFD grid size is 19×19 and $N = 4$. c) corresponds to the map associated to the proposed algorithm.

the case where $N = 4$ for all CPs of a 19×19 FFD grid (computed on a SGI, 64GB RAM) and an acceptable configuration for a standard computer architecture (Grid Size $= 19 \times 19$, $N = 2$). Results show that the parameter number is significantly reduced with the proposed method. This important properties allow to reach the final transformation scale while considering a decomposition order $N = 4$ for some of the crucial points for the final spatio-temporal motion model. A cartography for N is given in Fig 4.a). The accuracy is even increased (Tab. 1), especially for meaningful areas of the processed sequence as illustrated in Fig 4.b) c). This is because parameter reduction results in a low-pass filtering of the background noise.

4 Conclusion

We presented a method to adapt the complexity of a spatio-temporal motion model to the content of the image sequence. The parameters of a continuous state space parametric model are estimated by an algorithm, based on Kalman filtering from an image sequence describing a periodic phenomena. All the sequence frames are taken into account to infer the spatio-temporal model. Reduction of the parameter number using the proposed approach allows to obtain a better accuracy. Complementary tests have to be conducted to evaluate the influence of other method's parameters. As applied to cardiac imaging, such an approach allows for the direct determination of motion parameters that can be exploited for clinical interpretation and diagnosis, helping for instance in the detection of contraction abnormalities. The parameters profit with the proposed scheme makes now possible to conduct tests with 3D image sequences.

Acknowledgments

We truly thank J. Lötjönen and the Helsinki Medical imaging Center for providing us cine-MR data of the heart, and the Research group GDR STIC-Santé of the CNRS. This work has been supported by the French research project ACI-AGIR (http://www.aci-agir.org/) and the Région Rhônes Alpes through the PP3-I3M project of cluster ISLE. It is also part of the French ANR (http://www.agence-nationale-recherche.fr/) project GWENDIA.

References

1. Montagnat, J., Delingette, H.: 4D deformable models with temporal constraints: application to 4D cardiac image segmentation. Medical Image Analysis 9(1), 87–100 (2005)
2. Perperidis, D., Mohiaddin, R., Rueckert, D.: Spatio-temporal free-form registration of cardiac MR image sequences. Medical Image Analysis 9(5), 441–456 (2005)
3. Ledesma-Carbayo, M.J., Kybic, J., Desco, M., Santos, A., Sühling, M., Hunziker, P., Unser, M.: Spatio-temporal nonrigid registration for ultrasound cardiac motion estimation. IEEE Transactions on Medical Imaging 24(9), 1113–1126 (2005)

4. Huang, J., Abendschein, D., Davila-Roman, V., Amini, A.: Spatio-temporal tracking of myocardial deformations with a 4D B-spline model from tagged MRI. IEEE Transactions on Medical Imaging 18(10), 957–972 (1999)
5. Delhay, B., Clarysse, P., Pera, C., Magnin, I.E.: A spatio-temporal deformation model for dense motion estimation in periodic cardiac image sequences. In: Larsen, R., Nielsen, M., Sporring, J. (eds.) MICCAI 2006. LNCS, vol. 4190, Springer, Heidelberg (2006)
6. Sederberg, T.W., Parry, S.R.: Free-form deformation of solid geometric models. In: SIGGRAPH '86: Proceedings of the 13th Annual Conference on Computer Graphics and Interactive Techniques, pp. 151–160. ACM Press, New York (1986)
7. Rueckert, D., Sonoda, L.I., Hayes, C., Hill, D.L.G.: Nonrigid registration using free form deformation: application to breast MR images. IEEE Transactions on Medical Imaging 11, 712–721 (1999)
8. Kalman,: A new approach to linear filtering and prediction problems. Journal of Basic Engineering 82(1), 35–45 (1960)
9. Noblet, V., Heinrich, C., Heitz, F., Armspach, J.-P.: 3D deformable image registration: a topology preservation scheme based on hierarchical deformation models and interval analysis optimization. IEEE Transactions on Image Processing 14(5), 553–565 (2005)
10. Rohlfing, T., Maurer, C.R., Bluemke, D.A., Jacobs, M.A.: Volume-preserving nonrigid registration of MR breast images using free-form deformation with an incompressibility constraint. IEEE Transactions on Medical Imaging 22, 730–741 (2003)
11. Mallat, S.: A wavelet tour of signal processing.ition, 2nd edn. Academic Press, San Diego (1998)
12. Clarysse, P., Basset, C., Khouas, L., Croisille, P., Friboulet, D., Odet, C., Magnin, I.E.: 2D spatial and temporal displacement field fitting from cardiac MR tagging. Medical Image Analysis 3, 253–268 (2000)

Visualisation of Dog Myocardial Structure from Diffusion Tensor Magnetic Resonance Imaging: The Paradox of Uniformity and Variability

Stephen H. Gilbert, Alan P. Benson, Pan Li, and Arun V. Holden

Computational Biology Laboratory, Institute of Membrane and Systems Biology & Cardiovascular Research Institute, Worsley Building, Faculty of Biological Sciences, University of Leeds, Leeds LS2 9JT, UK
{stephen,alan,pan,arun}@cbiol.leeds.ac.uk
http://www.cbiol.leeds.ac.uk

Abstract. It has been assumed that myocardial structure is uniform amongst individuals of a species, and between higher mammalian species. However, recent studies show that myolaminar structure, a critical component in myocardial function, varies markedly between dogs. Diffusion tensor magnetic resonance imaging (DT-MRI) data from 12 canine hearts is visualised and described qualitatively and quantitatively. Large confluent zones of primarily positive or negative sheet angles intersect at approximately 90°. The location of these stacks and their zones of intersection differ between dog hearts, but their overall morphology is consistent. As such there is no single model of adult canine heart structure; rather cardiac form belongs to a constrained distribution between extremes of structure. This variation must be considered in the construction of averaged anatomical atlases of myocardial architecture, where a range of maps may be required. These could be produced from DT-MRI datasets grouped by myolaminar structure.

Keywords: Cardiac structure, Diffusion tensor magnetic resonance imaging.

1 Introduction

Since researchers first set out to mechanistically understand (i.e. model) cardiac function, the importance of elucidating cardiac muscle fibre architecture has been appreciated. This architecture determines how the contraction of each individual myocyte is combined into a single functional four-chamber pump. The linking of myocytes by gap junctions and desmosomes respectively determine the spread of electrical excitation and the dynamic distribution of tension throughout the myocardium during coordinated contraction of the ventricles. The key role played in this contraction by laminae and the cleavage planes separating them has previously been demonstrated [2,3]. It is interesting to observe that, despite the established importance of myocardial structure and the significant research attention it has received, no definitive or universal schema of cardiac structure

F.B. Sachse and G. Seemann (Eds.): FIMH 2007, LNCS 4466, pp. 403–412, 2007.

exists. In fact, considerable disagreement exists between proponents of different structural models [1].

Streeter [4] synthesised evidence of the regularly coursing helical fibre orientation in the dog, monkey and human, to propose a model of the left ventricle as nested toroidal geodesics of preferentially branched myocytes. This model was extended to both ventricles, as nested pretzel geodesics, based on data from optical polarisation microscopy of the foetal human heart [5]. The three layered ventricle model was proposed by Rushmer in 1953 [6], where the ventricles are described as superficial, middle and deep layers, with the fibres coursing between these layers as a continuum (sometimes known as a functional syncytial mesh). LeGrice et al. [7] proposed a simple laminar model, were the ventricle wall consists of ordered laminae separated by extensive cleavage planes running in an approximately radial direction. Recent evidence has indicated the existence of two laminae populations at varying transmural depth [8,9,10,11,12,13], and this led to the proposition of our model of complex laminar structure [1]. The model of the ventricles as distinct muscle bundles has been largely rejected, but it is related to early descriptions of the Helical Ventricular Myocardial Band model, although this has been developed to take account of evidence of a continuum of myofibre structure [14].

A principal reason for the many models is the differing levels of structure approached by different modellers [15].

Although there is still some controversy, it is becoming increasingly evident that myolaminar architecture is organised, but highly complex [11]. With the development of improved imaging modalities, it would seem that a complete mechanistic model of mammalian myocardial contraction could soon be formulated. However, DT-MRI and histological studies indicate that, despite uniformity of net myofibre long axis orientation, there are large differences between species in local myocardial sheet structure [8,9,10,11,12,3]. Intriguingly, in addition to this, DT-MRI evidence shows that there are also large differences in local myocardial structure between individual dogs [12,13,16]. When sheet orientation was analysed from selected myocardial regions of seven mongrel dogs, a bimodal distribution of sheet angles was present throughout the hearts with dual peaks at 45.5° and 117.6° [13]. In histological sheet studies, which examined a number of dogs [8], rats [3,2] and pigs [9], similar findings were not reported. We explored the variation of cardiac structure within canines in further detail. Twelve DT-MRI datasets are individually quantitatively described, allowing the nature of the reported bimodal distribution of sheet structure to be followed within individuals and between individuals. A detailed qualitative digital dissection and visualisation of the three dimensional sheet angles for the 12 hearts was carried out. Sheet angle distributions within selected sectors are extracted and compared to the distribution of all heart sheet angles for the same anatomical sector.

2 Methods

DT-MRI data from nine canine mongrel ex-vivo whole heart scans were obtained courtesy of P. Helm and R. Winslow at the Center for Cardiovascular

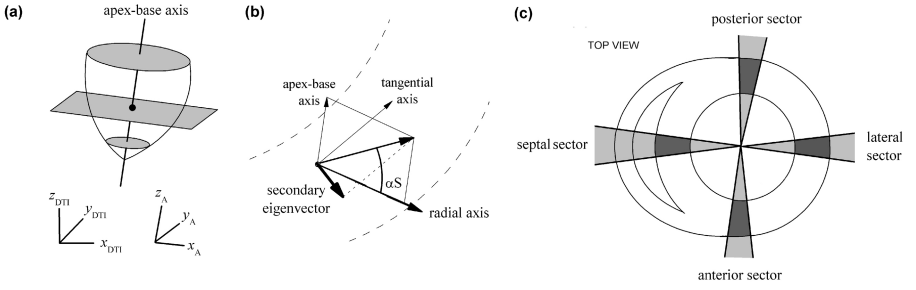

Fig. 1. (a) Diagrammatic representation of the axis fitted to the centre of the left ventricle and of the distinct axes of the material coordinate system (A subscripts) and the diffusion tensor (DTI subscripts). (b) Definition of the three axes which pass through any voxel in the left ventricular wall, and the sheet angle αS. (c) Anterior, septal, posterior and lateral sectors selected for analysis.

Bioinformatics and Modeling and E. McVeigh at the NIH, and are referred to here by numbers. These datasets were acquired and pre-processed as described in [16], and have been compiled into a comprehensive resource of cardiac DT-MRI data available online at http://www.ccbm.jhu.edu/index.php. We also visualised DT-MRI data from three mongrel dog hearts acquired from E. Hsu, then at the Center for In Vivo Microscopy, Duke University: the acquisition of these data was a whole-ventricle analogue of the technique described in detail previously [17]. Here these datasets are referred to by letters. Each DT-MRI dataset consists of three orthogonal eigenvectors with corresponding eigenvalues (the diffusion tensor) for each voxel of the corresponding MRI geometry data. The eigenvectors are ordered, with the primary eigenvector having the largest eigenvalue and the tertiary eigenvector the smallest.

In order to describe cardiac sheet structure it is necessary to establish a clear definition of the sheet angle, as the definition of the sheet angle is different between reports. In this study the sheet angle has been defined as the angle between the transverse plane and the projection of the secondary eigenvector onto the radial-longitudinal plane. Positive sheet angles rise to the heart base from endocardium to epicardium, or LV endocardium to RV endocardium in the septum (Fig. 1b).

There is no uniformly accepted system for reporting cardiac geometrical data, with some reports adopting a cylindrical coordinate system [18] and others a prolate spheroidal system [19]. These alternative coordinate systems (referred to as material coordinate systems) have been adopted in preference to the Cartesian system to take account of the anatomic form of the heart. In this study for simplicity we use the cylindrical system (Fig. 1a). A linear apex-base axis was fitted to the centre of the left ventricle of each heart. The intersection of this apex-base axis with each MR imaging slice gave the slice centroid. The radial axis for each voxel was defined as a line perpendicular to the apex-base axis connecting the centroid and the voxel (Fig. 1b). The tangential axis for each voxel was defined as the axis orthogonal to the apex base and radial axis. For any particular location

within the three-dimensional space we then defined three orthogonal reference planes: i) the transverse plane is approximately the short axis of the heart, with the apex-base axis normal to this plane; ii) the circumferential-longitudinal plane lies approximately tangential to the epicardial surface, with the radial axis normal to this plane; and iii) the radial-longitudinal plane, which is perpendicular to the transverse and circumferential-longitudinal planes and passes through the centroid and the voxel. Fibre and sheet angles were calculated with respect to these three reference planes.

We took the secondary eigenvector to indicate the orientation of the sheet plane. For any given sheet orientation, the secondary eigenvector can take one of two directions, both being perpendicular to the local fibre orientation and lying in the sheet plane but at 180° to each other. It was therefore necessary to apply a polarity to the secondary eigenvector. This was done by flipping the secondary eigenvector if the angle formed by the circumferential axis and the projection of the secondary eigenvector onto the transverse plane was less than 180°. Thus all secondary eigenvectors pointed to the side of the circumferential axis that was away from the centroid, approximately in an endocardial to epicardial orientation. Secondary eigenvectors are expected to point principally in the radial direction [7,10,21,22] and so we calculate the sheet angle as the angle between the transverse plane and the projection of the secondary eigenvector onto the radial plane. This also allows comparisons to data from histological studies [7,3,19] which were generally taken from slices made in the radial plane.

In order to demonstrate the sheet architecture in individual hearts, and the variable distribution of sheet structure between hearts, it was necessary to choose specific locations from which to extract data. This image segmentation was performed manually using anatomical features. The equatorial slice chosen was the most basal slice in which both LV papillary muscles are in full contact with the ventricular walls. We chose four 15° wide sectors for data extraction, each separated by 90° (from mid sector). The lateral and septal sectors were located on a line dividing the right and left ventricles into roughly equal halves. Anterior and posterior sectors were located on a perpendicular through this line at the centroid (Fig. 1c). The positioning of the sectors was so as to minimise inclusion of papillary muscle or right ventricular free wall fusion sites. If it was necessary to include voxels containing papillary muscle within a sector, these were later digitally removed by visual inspection.

3 Results

3.1 Sheet Angle Distribution

Sheet angle distributions are shown in Fig. 2.

Pooled Sectors. In the pooled data, anteriorly there is an approximately normal distribution of sheet angle centred at ∼0°. In the septum there is a bimodal distribution with peaks at ∼−45° and ∼0°. In the posterior sector there is a

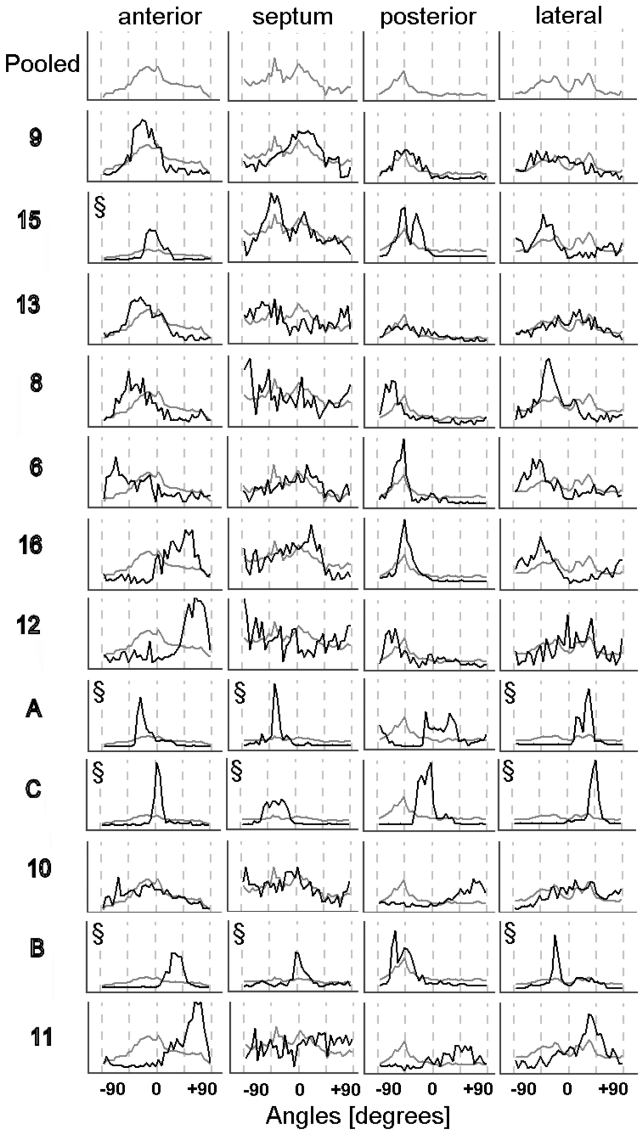

Fig. 2. Histograms of sheet angles in 12 normal canine hearts computed using the secondary eigenvector of diffusion in four anatomical locations. For each heart, sheet angle distribution in the selected anterior, septal, posterior and lateral sectors of a mid-heart slice are shown (black in plots) from left to right respectively. The distribution of the pooled data is shown for comparison (grey in plots). The hearts are ordered so as to demonstrate a distribution of changing sheet angle properties, from heart 9 (top) to heart 11 (bottom). The same normalised frequency scale is used throughout each distribution, except in cases marked by §, where tight angle distributions necessitated rescaling. Data for numbered hearts from the same group of experimenters, data from lettered hearts from a second group - see Methods.

strongly skewed distribution, peaking at ∼−45°. The lateral free wall has a bimodal sheet angle population centred at ∼−22° and ∼+22°.

Anterior Sector. The ∼0° centred, approximately normally distributed, pooled anterior sheet angle overlies a much more complex patterns sheet angle distribution in the individual hearts. Three hearts (15, C, 10) have unimodal distributions, somewhat resembling the pooled distribution, peaking at ∼0°. Five hearts (9, 13, 8, 6, A) have unimodal distributions skewed to negative sheet angle, peaking at ∼−22°. The remaining four hearts (16, 12, B, 11) have unimodal positive skewed sheet angle distribution peaking between ∼+22° and ∼+67°. Four hearts (15, A, C, B) have more narrow distributions of anterior sheet angle.

Septal Sector. Although the pooled distribution in the septal sector is bimodal, only one heart (15) clearly follows this pattern. Three hearts (9, 6, B) have unimodal ∼0° centred distributions, two (A, C) have negative skewed unimodal distributions peaking at ∼−22°. The remaining six hearts (13, 8, 16, 12, 10, 11) have irregular sheet angle distributions, with a combination of positive and negative sheet angle across the −90° to +90° range. These may represent bimodal distributions obscured by experimental noise. Three hearts (A, C, B) have more narrow distributions of septal sheet angle.

Posterior Sector. The pooled distribution in the posterior sector is unimodal with a peak at approximately ∼−45°. A similar pattern is seen in the individual angle distributions for eight hearts (9, 15, 13, 8, 6, 16, 12, B). A positive skewed unimodal distribution is followed by two hearts (10, 11) and two hearts have ∼0° centred distributions. There is a similar spread of angle values across the distributions, with no individual hearts having exceptionally narrow distributions.

Lateral Sector. The pooled distribution in the lateral sector is bimodal, but only two individual hearts follow this pattern (15, 16). Three hearts (13, 6, B) have unimodal negative distributions centred between ∼−45° and ∼−22°. Three hearts (A, C, 11) have positive unimodal distributions centred between ∼+22° and ∼+45° (A, C). Three hearts (9, 13, 12, 10) have sheet angle following a unimodal distribution centred on ∼0°. The remaining heart (12) has an irregular sheet angle distribution, with a combination of positive and negative sheet angle across the −90° to +90° range. These may represent a bimodal distribution obscured by experimental noise. Three hearts (A, C, B) have more narrow distributions of septal sheet angle.

Three hearts (A, C, B), all from the same data source, have a tighter distribution of sheet angle in all four extracted segments.

3.2 Visualisation

All hearts were visualised in three dimensions and the sheet conformation of the selected slices studied in detail. The sheet structure visualised on the cut surface of a short axis slice displays regions of confluent positive or negative sheet angulation (Fig. 3). These confluent zones of like sheet orientation often have sharp angular change at their abutments with regions of opposite sheet

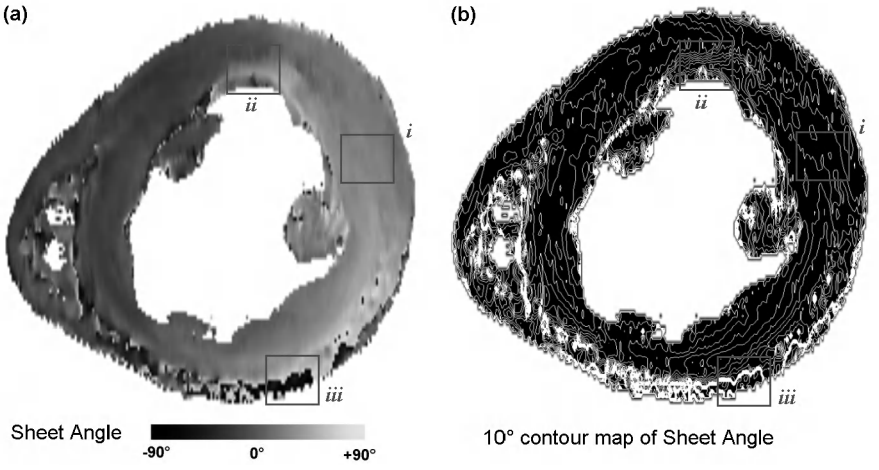

Fig. 3. Visualisation of the sheet angle in the selected equatorial slice of Heart A. (a) Sheet angle shaded with a grey monochrome angular scale, shown in the scale bar. (b) White 10° contours showing angular change with distance are applied to a black silhouette of the slice geometry. Regions of slow angular change with distance are black, and individual contours can be discerned, as in box *i*. Regions of more rapid angular change with distance show crowded contours, as in box *ii*. Regions of near instantaneous angular change with distance are white due to crowded contours, as in box *iii*.

angle (visible as white zones in Fig. 3b). The regions of opposite sheet angle often run adjacently in the circumferential direction. In other cardiac regions, sheets merge more gently into each other. As such, positive and negative sheets are not features of a regularly undulating continuum of sheet structure. These confluent regions are oriented as continuous elongated stacks of like sheet angle in three-dimensions [1].

4 Discussion

There is a striking amount of variation of sheet angle between individual hearts. The sheet angle is predominantly positive, negative or planar (close to 0°) within any sector depending on individual heart chosen. As a consequence, for the equatorial slice selected, some pairs of hearts have similar sheet orientation and other pairs have different or opposite sheet orientation. Hearts 9 and 15 have similar sheet orientation in all extracted sectors. Likewise, hearts 16 and 12 have similar sheet angle in the sectors. However, these pairs have different sheet orientation to each other in the anterior segment (9 and 15 are negative to planar, 16 and 12 are strongly positive). Visualisation of the three dimensional distribution of sheet angle conformation [1] shows that this variation in sheet pattern is not limited to the selected equatorial slices alone, but is a generalised feature. In fact sheet structure can be seen to follow an inter-individual distribution, with some

hearts having very similar structure, while other hearts have radically different structure. Overall there is a continuum of structural form, with some whole heart sheet conformation forms predominating over others.

Helm et al. [13] showed that sheet angles belong to two populations following a bimodal distribution with average peaks at 45.5° and 117.6° in all cardiac regions where eigenvector sorting was statistically valid (26 out of 30 selected regions, note that angular scale they adopted and the reported sheet angle differ from this study). We found bimodal distributions for the pooled values of the septal and lateral sectors, but not of the anterior and posterior sectors. We also found that most individual heart sheet angle distributions were unimodal, with a minority of bimodal distributions. In the anterior and posterior wall we found the sheet angle to belong to a single population for each individual heart, but that in some hearts this was a positive population, and in other hearts this was a negative population.

There are several reasons that may explain why we found less bimodal distributions. The definition of sheet angle adopted by Helm et al. [13] is not the same as used by us – their sheet angles is defined relative to the tertiary eigenvector using the prolate spheroidal material coordinate system [19]. Additionally, the selected regions were at different base-apex locations (apical and basal slices selected rather than equatorial), and different transmural locations (septal sectors were not studied; anterior, lateral and posterior transmural wall sectors were subdivided into five regions).

We found a greater proportion of sheet angles to be approximately planar ($-22° <$ Sheet Angle $< +22°$). This may be due in part to i) differences in the definition of the reported angle, and ii) inclusion of hearts A, B and C in this analysis, which have a greater proportion of planar sheet structure.

The histograms in Fig. 2 show varying smoothness (also apparent in visualisations in [1]), possibly indicating differences of tissue handling or quality of DT-MRI imaging. This varying smoothness is also observed in extractions of fibre orientation (data not shown), although the reported regular $\sim 120°$ change in fibre helix angle (defined in [1]), from endocardium to epicardium, can easily be observed in all datasets. Similarly, sheet features in the noisy datasets are less prominent but have similar morphology to those seen in the smooth datasets. As such, this variable noise in the data is not an important limitation to this study.

Until recently, research into cardiac structure demonstrated uniformity within and between mammalian species, and this uniformity has been an assumption in modelling. The results from this and cited studies suggest that cardiac structure, although highly ordered, varies significantly between individual mongrel dogs. The sheet angle orientation of selected regions within and between hearts has been shown to follow a bimodal distribution [13], but the structure underlying this phenomenon had not been described. The visualisations in Fig. 3 suggest that cardiac structure has an intricate architecture of merging sheet populations, which meet obliquely in the short-axis cardiac circumference. The precise location of these abutments varies from heart to heart, and some hearts have opposite sheet polarity to others at a selected anatomical location.

The combined quantitative and qualitative analysis of sheet angle presented here allows examination of the variation in structure between hearts. Detail of the spatial relationships between sheets in three dimensions, and their association with fibre structure, can be seen in three dimensional visualisations of DT-MRI fibre angle and sheet angle – see [1] for the canine data discussed here, [10] for mouse, [22] for rabbit and [12,13] for dog. Further understanding of these complex spatial relationships can be obtained from algorithmic fibre and sheet tracking studies, reviewed in [1].

An implication of the results is that there is no single model of the adult canine heart; rather cardiac form belongs to a constrained distribution between extremes of structure. It is hypothesised that this variation could be a factor in canine breed-specific developmental cardiac disease and, if this inter-individual variation extends to man, it could be important in human myocardial disease predisposition. Are some sheet conformations more efficient, more resistant to myocardial failure or of different electrical conduction and arrythmogenesis potential? Do inbred populations such as laboratory rats and mice have more uniform cardiac sheet structure, as suggested by the data [2]?

A further implication of the highly variable sheet structure between individual hearts is that image registration methods may produce meaningless results. An averaged sheet structure will lose the intricacy of sheet architecture and will define a regional sheet orientation opposite in polarity to some of the individual hearts on which it is based. If such methods are to be used, an analysis of cardiac sheet structure should first be performed by visualisation and quantification to select a series of hearts with broadly similar sheet architecture.

Acknowledgments. This work was supported by the European Union through the Network of Excellence BioSim, contract No. LSHB-CT-2004-005137. SHG is supported by the UK Medical Research Council, PL by the Overseas Research Students Award Scheme.

References

1. Gilbert, S.H., Benson, A.P., Li, P., Holden, A.V.: Regional localisation of left ventricular sheet structure: integration with current models of cardiac fibre, sheet and band structure. Eur. J. Cardio-thoracic Surg. to appear (2007)
2. Spotnitz, H.M., Spotnitz, W.D., Cottrell, T.S., Spiro, D., Sonnenblick, E.H.: Cellular basis for volume related wall thickness changes in the rat left ventricle. J. Mol. Cell. Cardiol. 6, 317–331 (1974)
3. Chen, J., Liu, W., Zhang, H., Lacy, L., Yang, X., Song, S.K., Wickline, S.A., Yu, X.: Regional ventricular wall thickening reflects changes in cardiac fiber and sheet structure during contraction: quantification with diffusion tensor MRI. Am. J. Physiol. 289, H1898–H1907 (2005)
4. Streeter, J.D.D.: Gross morphology and fiber geometry of the heart. Williams and Wilkins, Baltimore pp. 61–112 (1979)
5. Jouk, P.S., Usson, Y., Michalowicz, G., Grossi, L.: Three-dimensional cartography of the pattern of the myofibres in the second trimester fetal human heart. Anat. Embryol. 202, 103–118 (2000)

6. Rushmer, R.F., Crystal, D.K., Wagner, C.: The functional anatomy of ventricular contraction. Circ. Res. 1, 162–170 (1953)
7. LeGrice, I.J., Smaill, B.H., Chai, L.Z., Edgar, S.G., Gavin, J.B., Hunter, P.J.: Laminar structure of the heart: ventricular myocyte arrangement and connective tissue architecture in the dog. Am. J. Physiol. 269, H571–H582 (1995)
8. Arts, T., Costa, K.D., Covell, J.W., McCulloch, A.D.: Relating myocardial laminar architecture to shear strain and muscle fiber orientation. Am. J. Physiol. 280, H2222–H2229 (2001)
9. Dokos, S., Smaill, B.H., Young, A.A., LeGrice, I.J.: Shear properties of passive ventricular myocardium. Am. J. Physiol. 283, H2650–H2659 (2002)
10. Jiang, Y., Pandya, K., Smithies, O., Hsu, E.W.: Three-dimensional diffusion tensor microscopy of fixed mouse hearts. Magn. Reson. Med. 52, 453–460 (2004)
11. Harrington, K.B., Rodriguez, F., Cheng, A., Langer, F., Ashikaga, H., Daughters, G.T., Criscione, J.C., Ingels, N.B., Miller, D.C.: Direct measurement of transmural laminar architecture in the anterolateral wall of the ovine left ventricle: new implications for wall thickening mechanics. Am. J. Physiol. 288, H1324–H1330 (2005)
12. Helm, P., Beg, M.F., Miller, M.I., Winslow, R.L.: Measuring and mapping cardiac fiber and laminar architecture using diffusion tensor MR imaging. Ann. N. Y. Acad. Sci. 1047, 296–307 (2005)
13. Helm, P.A., Tseng, H.J., Younes, L., McVeigh, E.R., Winslow, R.L.: Ex vivo 3D diffusion tensor imaging and quantification of cardiac laminar structure. Magn. Reson. Med. 54, 850–859 (2005)
14. Kocica, M.J., Corno, A.F., Carreras-Costa, F., Ballester-Rodes, M., Moghbel, M.C., Cueva, C.N.C., Lackovic, V., Kanjuh, V.I., Torrent-Guasp, F.: The helical ventricular myocardial band: global, three-dimensional, functional architecture of the ventricular myocardium. Eur. J. Cardiothorac. Surg. 29, S21–S40 (2006)
15. Grant, R.P.: Notes on the muscular architecture of the left ventricle. Circulation 32, 301–308 (1965)
16. Helm, P.A., Younes, L., Beg, M.F., Ennis, D.B., Leclercq, C., Faris, O.P., McVeigh, E., Kass, D., Miller, M.I., Winslow, R.L.: Evidence of structural remodeling in the dyssynchronous failing heart. Circ. Res. 98, 125–132 (2006)
17. Hsu, E.W., Muzikant, A.L., Matulevicius, S.A., Penland, R.C., Henriquez, C.S.: Magnetic resonance myocardial fiber-orientation mapping with direct histological correlation. Am. J. Physiol. 274 (1998) H1627–H1634 339–348 (2001)
18. Geerts, L., Bovendeerd, P., Nicolay, K., Arts, T.: Characterization of the normal cardiac myofiber field in goat measured with MR-diffusion tensor imaging. Am. J. Physiol. 283, H139–H145 (2002)
19. LeGrice, I.J., Hunter, P.J., Smaill, B.H.: Laminar structure of the heart: a mathematical model. Am. J. Physiol. 272, H2466–H2476 (1997)
20. Tseng, W.Y., Wedeen, V.J., Reese, T.G., Smith, R.N., Halpern, E.F.: Diffusion tensor MRI of myocardial fibers and sheets: correspondence with visible cut-face texture. J. Magn. Reson. Imaging 17, 31–42 (2003)
21. Scollan, D.F., Holmes, A., Winslow, R., Forder, J.: Histological validation of myocardial microstructure obtained from diffusion tensor magnetic resonance imaging. Am. J. Physiol. 275, H2308–H2318 (1998)
22. Scollan, D.F., Holmes, A., Zhang, J., Winslow, R.L.: Reconstruction of cardiac ventricular geometry and fiber orientation using magnetic resonance imaging. Ann. Biomed. Eng. 28, 934–944 (2000)

Statistical Comparison of Cardiac Fibre Architectures

Jean-Marc Peyrat[1], Maxime Sermesant[1,2], Xavier Pennec[1], Hervé Delingette[1], Chenyang Xu[3], Elliot McVeigh[4], and Nicholas Ayache[1]

[1] INRIA - Asclepios Research Project, Sophia Antipolis, France
jean-marc.peyrat@sophia.inria.fr
[2] King's College London, Cardiac MR Research Group, Guy's Hospital, London, UK
[3] Siemens Corporate Research, Princeton, New Jersey, USA
[4] Laboratory of Cardiac Energetics, National Heart Lung and Blood Institute, National Institutes of Health, Bethesda, Maryland, USA

Abstract. In this paper, a statistical atlas of DT-MRIs based on a population of nine *ex vivo* normal canine hearts is compared with a human cardiac DT-MRI and with a synthetic model of the fibre orientation. The aim of this paper is to perform a statistical inter-species comparison of the cardiac fibre architecture and to assess the quality of a synthetic description of the fibre orientation. We present the framework to build a statistical atlas of cardiac DT-MRIs providing a mean and a covariance matrix of diffusion tensors at each voxel of an average geometry. The comparison of human and synthetic data with this atlas involves the non-rigid registration into the average atlas geometry where voxel to voxel comparison can be performed. For each eigenvector of the diffusion tensors, we compute the angular difference with the average atlas and its Mahalanobis distance to the canine population. The results show a better consistence of the fibre orientation than the laminar sheet orientation between the human and the canine heart, while the homogeneous synthetic model appears to be too simple compared to the complexity of real cardiac geometry and fibre architecture.

1 Introduction

The cardiac fibre architecture plays a key role in normal and pathological heart functions. For many years, the orientation of these fibres and their arrangement in laminar sheets have been studied with histological slices [22, 13]. Recently, the measurements of fibre structure have been eased with diffusion tensor magnetic imaging (DT-MRI) since a correlation between the myocardium fibre architecture and diffusion tensors has been shown [19, 10]. The acquisition of high resolution *in vivo* DT-MRI is a very challenging task due to cardiac motion [8]. Hence, modeling the cardiac fibre architecture [4, 12, 18] is essential for clinical applications such as the planning of patient-specific cardiac therapies [21]. This architecture has been included into an electromechanical model based on a single canine DT-MRI acquisition of an *ex vivo* heart [20] or a synthetic model [21] registered on the patient data. These electromechanical models are usually limited to the cardiac

F.B. Sachse and G. Seemann (Eds.): FIMH 2007, LNCS 4466, pp. 413–423, 2007.

fibre orientation whereas the laminar sheets have been shown to contribute to the cardiac motion [3, 7, 14, 24], especially for a better electromechanical modeling of the wall thickening and the apico-basal torsion.

We propose here to compare a statistical atlas of the complete cardiac fibre architecture of a population of nine *ex vivo* canine hearts with a human heart and a synthetic model used in [21]. The inter-species comparison of the cardiac fibre architecture is a first step to assess the relevance of a canine statistical atlas for clinical applications. A one-to-one comparison between the synthetic model and the canine hearts has already been performed [23] but the quantification of their differences was limited to the percentage of angular differences below a given threshold. We propose here to extend these studies comparing the synthetic model with a statistical atlas including an information about the variability of the population. We also study the spatial distribution of their differences to know where the synthetic model needs to be improved.

First, we present an extension of the framework for building a statistical atlas of the cardiac fibre architecture proposed in [17]. Second, we perform an inter-species comparison of the cardiac fibre architecture between a human heart and a population of canine hearts. Finally, we compare the synthetic model used for electromechanical modeling with the statistical atlas.

2 Data Acquisition

We used a DT-MRIs dataset of *ex vivo* fixed normal hearts (9 canine and 1 human) acquired [11] by the Center of Cardiovascular Bioinformatics and Modeling (CCBM) at the Johns Hopkins University and available on the internet[1]. Each heart was placed in an acrylic container filled with Fomblin, a perfluoropolyether (Ausimon, Thorofare, NJ). Fomblin has a low dielectric effect and minimal MR signal thereby increasing contrast and eliminating unwanted susceptibility artifacts near the boundaries of the heart. The long axis of the hearts were aligned with the z-axis of the scanner. Images were acquired with a 4-element knee phased array coil on a 1.5 T GE CV/i MRI Scanner (GE, Medical System, Wausheka, WI) using a gradient system (from 14 to 28 gradients) with 40 mT/m maximum gradient amplitude and a 150 $T/m/s$ slew rate. The resolution of the images are around $0.3 \times 0.3 \times 0.9$ mm^3 per voxel. The acquisition temperature was different from one heart to another in a range from 18 to 25°C.

3 Construction of the Statistical Atlas

The construction of the statistical atlas of the cardiac fibre architecture is based on a framework [17] using the Log-Euclidean metric [2]. We modified this framework providing an average cardiac geometry that includes both atria and where diffusion tensors are normalized to minimize the influence of acquisition parameters on statistics. We also relied on another reorientation strategy [1] in the diffusion tensor registration process.

[1] http://www.ccbm.jhu.edu/research/DTMRIDS.php

Pre-Processing: First, we apply a basic threshold to the DT-MRIs based on the Log-Euclidean norm [2] to segment the meaningful cardiac structures in terms of cardiac fibre architecture. While our previous work [17] was focusing on the compact myocardium of the ventricles, we extend the construction of the atlas to the atria. To avoid any influence of the dispersion of the diffusion rates that are not due to an intrinsic variability between hearts such as the temperature of acquisition, we perform a global normalization of each diffusion tensor field to equalize the average value of the histogram of the norm of diffusion tensors of each heart. The statistical analysis of the diffusion rates can still give an information about the spatial variability of diffusion rates. The resulting normalized atlas is finally scaled by the average of all these normalization factors to include realistic averaged diffusion rates.

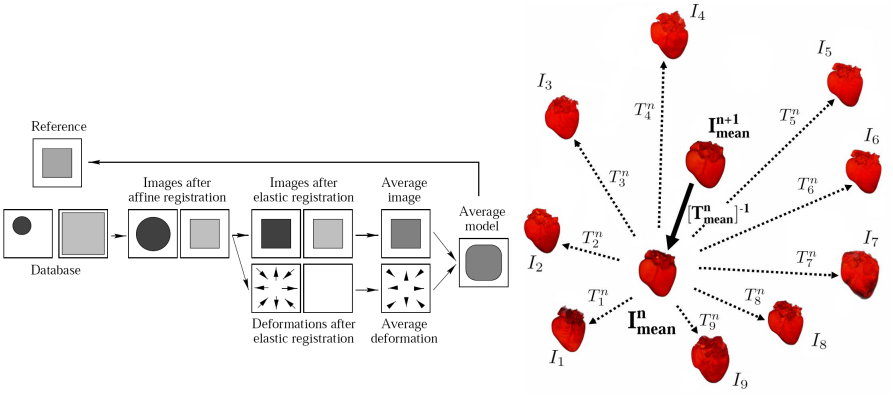

Fig. 1. [*Left*] Registration of anatomical MRIs using an iterative process averaging the intensities (light and dark grey) and the shape (circles and squares) of the dataset (from Guimond *et al.* [9]). [*Right*] The iterative registration process uses the average geometry as a reference for the next step. The deformation field T_i^n is a composition of an affine transformation S (in our case a non-uniform scaling transformation) and a non-rigid deformation.

Registration of the Anatomical MRIs: The core of the registration algorithm is exactly the same as the one we already presented [17]. First, we proceed to a global registration based on a non-uniform similarity transformation defined by three manually located landmarks: the apex and the two corner points in the valve plane. Secondly, to find the residual non-rigid deformation we use a hybrid intensity- and landmark-based registration algorithm [5]. With this algorithm we can interactively select pairs of landmarks which will constrain the non-rigid intensity-based registration. This hybrid algorithm can be used with any intensity-based registration algorithm and in this case, we combine it with a diffeomorphic registration algorithm [6] based on the mutual information.

In this framework, the geometry of the average anatomical MRI is the geometry of a chosen reference heart. We propose here to add to this framework

an iterative process that converges to an average geometry and intensities of anatomical MRIs. We based this modification on the brain averaging strategy proposed by Guimond *et al.* [9]. We iteratively build an average geometry while we register the dataset on it. We first register the dataset of images $\{I_i\}_{i=1,...N}$ on the current reference image I^n_{mean} (the initial reference image I^0_{mean} is chosen among the dataset) according to the steps described at the beginning of this section. The resulting deformation fields T^n_i registering the initial images I_i to the current reference image I^n_{mean} are averaged. The inverse of this average deformation field T^n_{mean} is applied to the current reference image I^n_{mean} which then gets closer to a barycentric geometry of the dataset (see Fig. 1). Finally, the intensities are averaged in this new average geometry. Therefore through the deformation fields T^n_i, the original geometry and intensities of each heart are taken into account in the new average heart I^{n+1}_{mean}. One iteration can be summarized in the following equation:

$$I^{n+1}_{mean}(x) = \frac{1}{N}\sum_{i=1}^{N} I_i\Big(T^n_i \circ [T^n_{mean}]^{-1}(x)\Big)$$

where:

x is the voxel position,
I_i is the anatomical MRI of the sample i where $i = 1 \cdots N$ ($N = 9$ in our case),
I^n_{mean} is the current average anatomical MRI at the step n,
T^n_i is the deformation field matching the current average image I^n_{mean} to I_i,
$T^n_{mean} = \frac{1}{N}\sum_{i=1}^{N} T^n_i$ is the average deformation field at the step n.

These steps are repeated using the new average heart I^{n+1}_{mean} as the reference geometry until it converges. In practice, a few iterations are sufficient to get a stable geometry. Finally, the outputs of this process are an average geometry and intensities of the anatomical MRIs and a dense deformation field for each heart of the dataset.

Registration of the DT-MRIs: Since the anatomical MRIs and the DT-MRIs are co-acquired, we can apply directly the deformation fields obtained in the previous section to the DT-MRIs. We use the Log-Euclidean metric to interpolate diffusion tensors, and the *Finite Strain* (FS) reorientation strategy is preferred to the *Preservation of the Principal Direction* (PPD) [1] to transform the tensors. Indeed, the FS has the property to preserve the gradient of the diffusion tensor field and thus the transmural variations of the fibre and laminar sheet orientations known to be common features between hearts. Furthermore, this reorientation strategy is consistent with the similarity-invariant Log-Euclidean metric used afterwards. The statistics computed with the Log-Euclidean metric should not depend on the reference geometry which would not be the case with the PPD where the reorientation depends on the original tensor.

Statistics: The Log-Euclidean framework [2] provides a consistent and rigorous framework to study the statistical variability of diffusion tensors. Indeed,

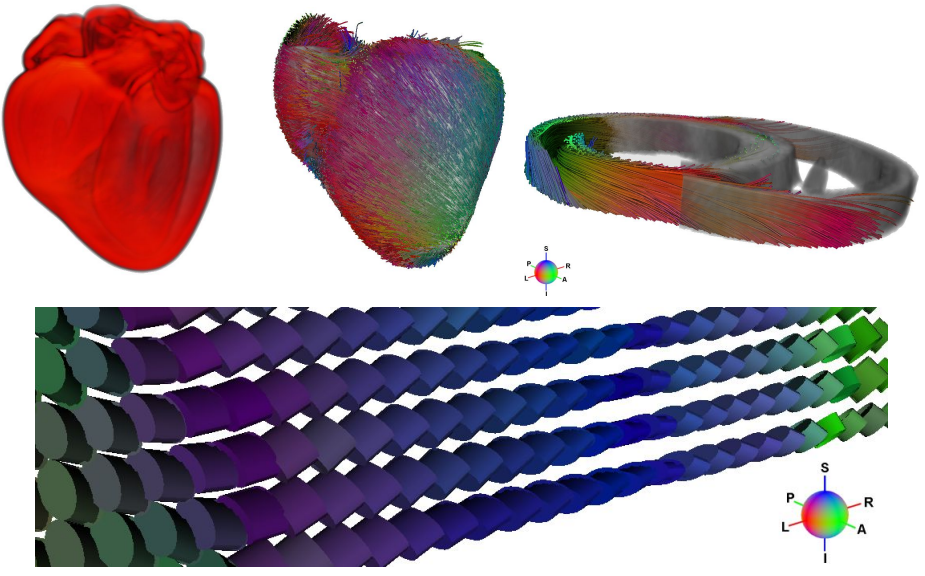

Fig. 2. [*Upper Left*] Average geometry of the canine hearts. [*Upper Middle*] Side view of fibre tracking computed on the average DT-MRI. [*Upper Right*] Fibre tracking on a few slices of the average DT-MRI to show the transmural variation of fibre orientation. [*Down*] Transmural variation of the laminar sheet orientation. Tensor visualization with cylinders. The base of the cylinder is the plane given by the primary and secondary eigenvectors. The height of the cylinder shows the laminar sheet orientation. The colors describe the orientation of the primary eigenvector according to the color sphere.

in this framework the space of diffusion tensors becomes a vector space where the statistics are consistent with the positivity constraint of the diffusion tensors. We compute the Log-Euclidean mean $\overline{D}_{log}$ of all the registered DT-MRIs $\{D_i\}_{i=1,\dots N}$ and the corresponding unbiased covariance matrix Cov of the whole diffusion tensors [15] at each voxel x of the average geometry:

$$\overline{D}_{log}(x) = \exp\left(\frac{1}{N}\sum_{i=1}^{N}\log\Big(D_i(x)\Big)\right)$$

$$Cov(x) = \frac{1}{N-1}\sum_{i=1}^{N} vec\Big(\Delta D_i(x)\Big).vec\Big(\Delta D_i(x)\Big)^t$$

where:

N is the size of the dataset,
$\Delta D_i(x) = \log\big(D_i(x)\big) - \log\big(\overline{D}_{log}(x)\big)$,
$vec(D) = (D_{11}, \sqrt{2}D_{12}, D_{22}, \sqrt{2}D_{31}, \sqrt{2}D_{32}, D_{33})^t$ is the minimal representation [15] of the diffusion tensor $D = (D_{ij})_{i,j=1,2,3}$

We project this covariance matrix of diffusion tensors along specific directions in the tangent plane at the mean diffusion tensor to extract the variances of the eigenvalues and eigenvectors orientations [16].

Resulting Statistical Atlas: We applied this framework to the dataset of 9 canine hearts presented previously in Section 2. We obtain an average geometry and a smooth cardiac DT-MRI atlas describing the whole cardiac fibre architecture: the fibre and laminar sheet orientations (see Fig. 2). The norm of the covariance matrix, homogeneous to a ratio, shows a global stability of the cardiac fibre architecture among the population of canine hearts (see Fig. 3). The average variability of the whole diffusion tensor is around 10%. A higher norm of the covariance matrix at the RV and LV endocardial apices and in the papillary muscles reveals regions where the fibre structure is probably not as much structured as the compact myocardium.

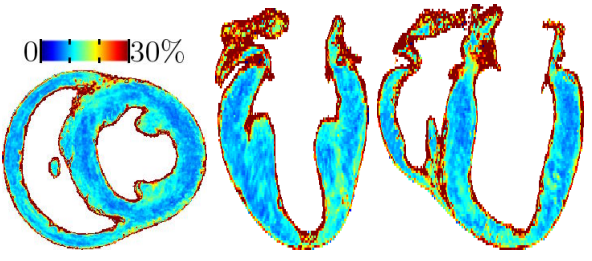

Fig. 3. Global variability $\sqrt{Tr(Cov)}$ (homogeneous to a ratio and expressed as a percentage) of the whole tensor in three different orthogonal views: a short axis and 2 long axis views

4 Comparisons of Cardiac Fibre Architectures

4.1 Comparison Measures

Any given new dataset can be registered with the atlas using the presented methodology. Then we perform the comparison using different measures:

- the normalized Mahalanobis distance $\tilde{\mu}$ to the atlas at each voxel, given by the formula [15]: $\tilde{\mu}^2(\overline{D}_{log}, D_{heart}) = \frac{1}{d} vec(\Delta D)^t . Cov^{-1} . vec(\Delta D)$ where $d = 6$ is the dimension of the diffusion tensors space.
- the spatial distribution of the angular difference of the primary eigenvector (see Fig. 5).
- the histograms of the angular difference of the eigenvectors with the atlas, for a qualitative statistical comparison (see Fig. 6, left column).
- the histograms of the Mahalanobis distance of the eigenvectors orientation to the atlas, for a quantitative statistical comparison (see Fig. 6, right column). This gives the angular differences of the eigenvectors normalized by the variance of the statistical atlas at each voxel. Thus, we measure the difference of the eigenvectors orientation according to its dispersion among the population used to build the atlas.

A synthetic view of the histogram comparison is then given by the mode of the distributions (see Table 1).

4.2 Atlas Comparisons with a Human Heart and a Synthetic Model

We proceed to a limited inter-species comparison of the fibre architecture between human and canine hearts. Indeed, the difficulty to obtain normal human hearts for research purpose (normal hearts are preferably used for transplantation) is the main obstacle to the building of a human atlas. In our case, only one human heart is available in the JHU database, and the quality of this dataset is lower than those of canine hearts. The mode of the normalized Mahalanobis distance is 1.49 whereas it is lower than 1 for canine hearts of the dataset. Most of the important differences are located in the right ventricular wall and part of the septum. In Fig. 6 and Table 1, we observe that the fibre orientation of the human heart is closer to the canine population than its laminar sheet orientation.

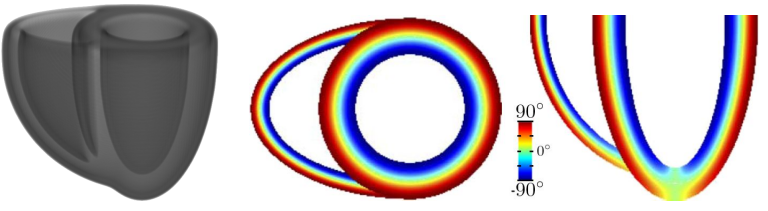

Fig. 4. [*Left*] Geometry of the synthetic model. [*Middle and Right*] Elevation angle of the synthetic fibre orientation in short axis and long axis views (from Sermesant *et al.* [21]).

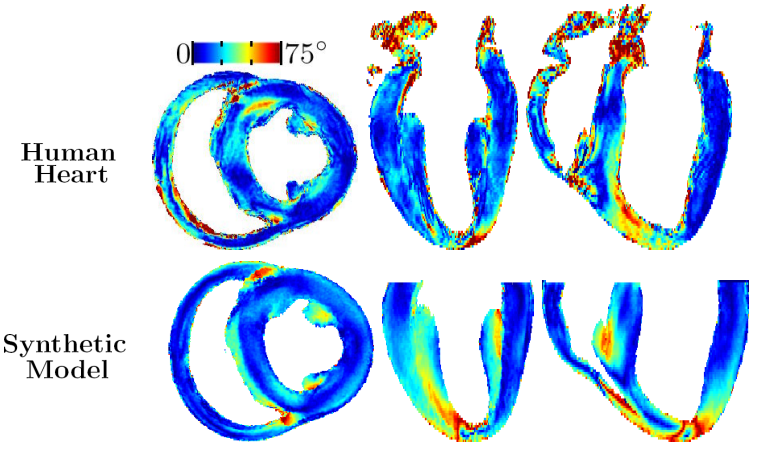

Fig. 5. [*Up*] Angle between the primary eigenvector of the atlas and the human heart. [*Down*] Angle between the primary eigenvector of the atlas and the fibre orientation of the synthetic model. (one short axis and two long axis views).

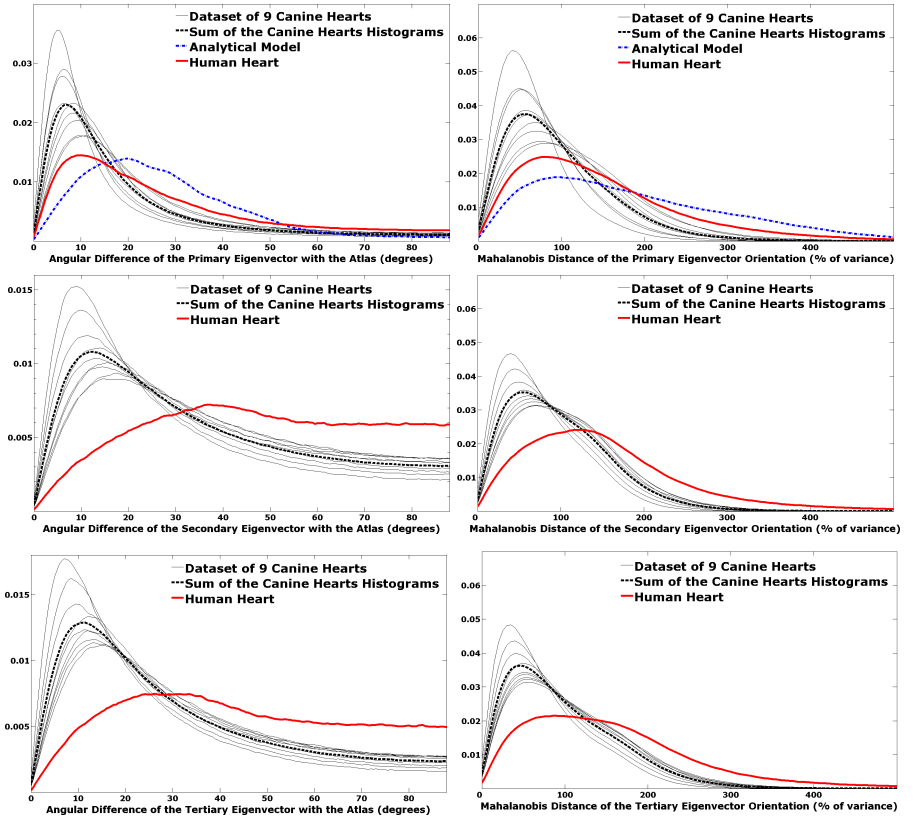

Fig. 6. [*Left Column*] Normalized histograms of the primary, secondary and tertiary eigenvectors variations around their mean. [*Right Column*] Mahalanobis distance of the primary, secondary and tertiary eigenvectors variations around their mean.

Table 1. Modes of the distributions of the angular differences of the eigenvectors and their Mahalanobis distances (respectively in degrees and % of the variance)

Eigenvector/Heart	Sum of Canine Histograms	Human Hist.	Synthetic Model Hist.
Primary	6.9° - 58%	10.1° - 81%	19.6° - 95%
Secondary	11.6° - 57%	36.2° - 115%	-
Tertiary	11.4° - 46%	29.1° - 109%	-

The synthetic model proposed in [21] describes the fibre orientation in an ellipsoidal template geometry of the ventricle(see Fig. 4). The orientation difference between the primary eigenvector of the atlas and the fibre orientation of the synthetic model has a mode of 19.6 degrees while the mode for the canine hearts is 6.9 degrees, and respectively 0.95 and 0.58 for the mode of its Mahalanobis distance (see Fig. 6 and Table 1). The synthetic model is clearly different from

the population of canine hearts. For instance, we observe in the short axis view a modeling problem at the crossing of the two ventricular walls. Indeed, the synthetic model has an important discontinuity in this region. Furthermore, the synthetic approach reaches its limits at the right ventricular and left ventricular apices (see Fig. 5) where the fibre organization modeling probably needs different analytical laws from the compact myocardium. The ellipsoidal geometry and the fibre orientation of the synthetic model are too simple to be realistic in catching all the subtle variations of the fibre orientation.

5 Conclusion and Perspectives

We presented here a framework for building a statistical atlas of cardiac fibre architecture in an average geometry. This statistical framework can be extended to perform the comparisons between specimen or species. The resulting atlas has been compared to a human heart and a synthetic model of the fibre orientation. In the case of the human heart, we observed more differences on the laminar sheet orientation than on the fibre orientation. The synthetic model seems to need some improvements for a better description of the fibre organization, especially adding an accurate description of the laminar sheet orientation. Having access to canine and human heart databases of greater size should help in improving the relevance of the statistical atlas and the inter-species comparisons. The effects of these differences on the electromechanical behavior still remain to be studied for a complete evaluation of the relevance to use such atlases in patient-specific clinical applications.

Acknowledgment

This research was funded by Siemens Corporate Research, Princeton, NJ. Acquisition of the DT-MRIs data was funded by the Intramural Research Program of the National Heart Lung and Blood Institute (E.R. McVeigh Z01-HL4004609). We thank Drs. Patrick A. Helm and Raimond L. Winslow at the Center for Cardiovascular Bioinformatics and Modeling for provision of data, P. Fillard and N. Toussaint for provision of diffusion tensors and fibre tracking computation and visualization tools[2].

References

1. Alexander, D.C., Pierpaoli, C., Basser, P.J., Gee, J.C.: Spatial Transformations of Diffusion Tensor Magnetic Resonance Images. IEEE TMI 20(11), 1131–1139 (2001)
2. Arsigny, V., Fillard, P., Pennec, X., Ayache, N.: Fast and Simple Calculus on Tensors in the Log-Euclidean Framework. In: Duncan, J.S., Gerig, G. (eds.) MICCAI 2005. LNCS, vol. 3749, pp. 115–122. Springer, Heidelberg (2005)

[2] http://www-sop.inria.fr/asclepios/software/MedINRIA/

3. Arts, T., Costa, K.D., Covell, J.W., McCulloch, A.D.: Relating Myocardial Laminar Architecture to Shear Strain and Muscle Fiber Orientation. Am. J. Physiol Heart Circ Physiol 280, H2222–H2229 (2001)
4. Ayache, N.: Computational Models for the Human Body. In: Handbook of Numerical Analysis, Elsevier, Amsterdam (2004)
5. Azar, A., Xu, C., Pennec, X., Ayache, N.: An interactive Intensity- and Feature-Based Non-Rigid Registration Framework for 3D Medical Images. In: Proc. of ISBI'06 (2006)
6. Chefd'hotel, C., Hermosillo, G., Faugeras, O.: Flows of diffeomorphisms for multimodal image registration. In: Proc. of ISBI'02 (2002)
7. Costa, K.D., Holmes, J.W., McCulloch, A.D.: Modelling cardiac mechanical properties in three dimensions. Philosophical Transactions of the Royal Society A: Mathematical, Physical and Engineering Sciences 359(1783), 1233–1250 (2001)
8. Dou, J., Reese, T.G., Tseng, W.I., Van Wedeen, J.: Cardiac diffusion MRI without motion effects. Magnetic Resonance in Medecine 48(1), 105–114 (2002)
9. Guimond, A., Meunier, J., Thirion, J.-P.: Average brain models: A convergence study. Technical Report 3731, INRIA, Sophia-Antipolis, France (July 1999)
10. Helm, P., Beg, M.F., Miller, M.I., Winslow, R.L.: Measuring and mapping cardiac fiber and laminar architecture using diffusion tensor MR imaging. Ann. N. Y. Acad Sci. 1047, 296–307 (2005)
11. Helm, P.A., Tseng, H.J., Younes, L., McVeigh, E.R., Winslow, R.L.: Ex Vivo 3D Diffusion Tensor Imaging and Quantification of Cardiac Laminar Structure. Magn. Reson. Med. 54(4), 850–859 (2005)
12. Hunter, P.J., Pullan, A.J., Smaill, B.H.: Modeling Total Heart Function. Annu Rev. Biomed Eng. 5, 147–177 (2003)
13. LeGrice, I.J., Smaill, B.H., Chai, L.Z., Edgar, S.G., Gavin, J.B., Hunter, P.J.: Laminar structure of the heart: ventricular myocyte arrangement and connective tissue architecture in the dog. Am J Physiol Heart Circ Physiol (1995)
14. LeGrice, I.J., Takayama, Y., Covell, J.W.: Transverse Shear Along Myocardial Cleavage Planes Provides a Mechanism for Normal Systolic Wall Thickening. Am. J. Physiol Heart Circ Physiol 77, 182–193 (1995)
15. Pennec, X., Fillard, P., Ayache, N.: A Riemannian Framework for Tensor Computing. International Journal of Computer Vision (2006)
16. Peyrat, J.-M., Sermesant, M., Pennec, X., Delingette, H., Xu, C., McVeigh, E., Ayache, N.: Towards a Statistical Atlas of Cardiac Fiber Architecture. Research Report 5906, INRIA (2006)
17. Peyrat, J.-M., Sermesant, M., Pennec, X., Delingette, H., Xu, C., McVeigh, E., Ayache, N.: Towards a Statistical Atlas of Cardiac Fiber Structure. In: Duncan, J.S., Gerig, G. (eds.) MICCAI 2005. LNCS, vol. 3749, pp. 115–122. Springer, Heidelberg (2005)
18. Sachse, F. (ed.): Computational Cardiology - Modeling of Anatomy, Electrophysiology, and Mechanics. LNCS. Springer, Heidelberg (2004)
19. Scollan, D.F., Holmes, A., Winslow, R.L., Forder, J.: Histological validation of myocardial microstructure obtained from diffusion tensor magnetic resonance imaging. Am. J. Physiol Heart Circ Physiol 275, H2308–H2318 (1998)
20. Sermesant, M., Delingette, H., Ayache, N.: An electromechanical model of the heart for image analysis and simulation. IEEE TMI 25(5), 612–625 (2006)

21. Sermesant, M., Rhode, K., Sanchez-Ortiz, G.I., Camara, O., Andriantsimiavona, R., Hegde, S., Rueckert, D., Lambiase, P., Bucknall, C., Rosenthal, E., Delingette, H., Hill, D.L., Ayache, N., Razavi, R.: Simulation of cardiac pathologies using an electromechanical biventricular model and XMR interventional imaging. Med. Image Anal. 5(9), 467–480 (2005)
22. Streeter, D., Ramon, C.: Muscle pathway geometry in the heart wall. J. Biomechanical Engineering 105, 367–373 (1983)
23. Sundar, H., Shen, D., Biros, G., Litt, H., Davatzikos, C.: Estimating Myocardial Fiber Orientation by Template Warping. In: Proc. of ISBI'06 (2006)
24. Usyk, T.P., Mazhari, R., McCulloch, A.D.: Effect of Laminar Orthotropic Myofiber Architecture on Regional Stress and Strain in the Canine Left Ventricle. Journal of Elasticity 61, 143–164 (2000)

Extraction of the Coronary Artery Tree in Cardiac Computer Tomographic Images Using Morphological Operators

M.A. Luengo-Oroz[1], M.J. Ledesma-Carbayo[1], J.J Gómez-Diego[2], M.A. García-Fernández[2], M. Desco[2], and A. Santos[1]

[1] Biomedical Image Technologies, ETSI Telecomunicación, Universidad Politécnica de Madrid, 28040, Madrid, Spain
[2] Hospital General Universitario Gregorio Marañón, C/Doctor Esquerdo 46, 28007, Madrid, Spain

Abstract. Quantitative measurements of the coronary artery tree substructures from Cardiac Multislice-CT data sets is an important goal to improve the diagnosis and treatment of coronary artery disease. This paper presents an algorithm based on morphological grayscale reconstruction through 2D slice images devoted to the extraction of the 3D coronary artery tree. The proposed procedure is conceived as a first step prior to the segmentation and inspection of interesting substructures in the coronaries. The correct extraction of the left coronary arteries has been validated in 9 CT-datasets with satisfactory results, particularly concerning speed and robustness.

1 Introduction

The conventional way of imaging coronary arteries is by using invasive coronary angiography, but this technique implies invasive clinical procedures and risks to the patient. Multislice CT (MSCT) imaging is a recent non-invasive imaging technique that provides high resolution data of the heart anatomy. An intravenous contrast agent is used to enhance the visibility of blood, and consequently the vessels. Areas containing the contrast agent are highlighted in the resultant output images as they have a larger Hounsfield value. Segmentation of the coronary arteries provide a valuable tool for clinicians interested in the detection and quantification of plaques, calcifications or stenosis. However, segmentation of the coronary tree is a difficult task due to low contrast conditions, the vicinity to the heart cavities, and its complex structure, including branching and curvatures. On the other hand, the clinical context demands minimal user interaction procedures, as well as fast and efficient algorithms.

In medical imaging, vessel segmentation (see a very complete review in [1]) is the core of many diagnosis systems that perfom vessel analysis and visualization, and it may also be required in therapeutic tools such as computer-guided surgery. However, vessel segmentation is still an open problem and many methods have been proposed depending on the imaging modality, the human interaction required and many other factors. Concerning segmentation of the coronary

F.B. Sachse and G. Seemann (Eds.): FIMH 2007, LNCS 4466, pp. 424–432, 2007.

tree from MSCT, in [2] the segmentation is achieved using a combination of thresholding, region-growing, and morphological operations. Although a very good visualization interface is provided, the segmentation algorithm uncorrectly selects areas that do not belong to the coronary tree. In [3], a particle-based approach to vessel segmentation is performed with interesting results, but non principal branches are missed. Regarding other segmentations methods, we find that level-sets are not suited for real-time applications as they are computationally time-consuming; parametric cylindrical models may not be suited for the non-linear vessel structures and region-growing techniques may be sensitive to local conditions. Because of these difficulties for the accurate detection of the whole coronary tree, we propose to decompose the segmentation task in two different phases; a first phase would deal with the extraction of the coronary tree and in a second phase the coronary substructures would be segmented and classified into regions such as lumen, plaque or calcium. In this paper we propose a solution to the first phase of this scheme using a fast segmentation technique based on mathematical morphology that extracts the 3D coronary tree from an initial seed point given by the human expert. In order not to bias the posterior quantitative segmentation two important requirements for the extraction method should be taken into account: not losing any coronary information and maintaining the local intensity differences. On the other hand we also make the hypothesis that the vessel is a causal structure in the sense that there is no possibility for the artery to grow backwards. It should be noted that the extraction of the coronary tree is very useful on its own as it clearly facilitates the visual inspection of the coronaries with minimal user interaction through longitudinal and transversal sections or using rendering techniques.

This article is organized as follows: firstly, we present the MACTSE (Morphological algorithm for causal tubular structures extraction) algorithm used for the coronary tree extraction giving the implementation details. Then we present and discuss the results on 9 clinical data sets in which the correct extraction of the left coronary arteries has been evaluated by an expert.

2 Morphological Algorithm for Causal Tubular Structures Extraction (MACTSE)

2.1 Theorical Framework

Mathematical morphology is a nonlinear image processing technique based on geometric analysis that allows to incorporate to the algorithms a priori knowledge of shapes, such as the narrow tubular branching structures of the coronary tree. A tutorial on the technique can be found in [4]. These techniques have been widely used in vessel extraction with successful results [5] and also in segmentation and quantification of 2D angiograms [6,7]. Morphological grayscale reconstruction methods through 2D slice images have been previously used in [8] for the segmentation of the airway tree with successful results. In the case

of the coronary artery tree, the image conditions are different as there are not as many scale changes in the coronary arteries as in bronchia and the existence of other surrounding structures may compromise the segmentation process. In order to solve this challenging problem we propose to use a 2D morphological reconstruction by dilation that is propagated through the slices. A priori information of the coronary radius and the z-axis sampling is used to define the size of the object that is being searched and the area of search in the next slice respectively.

2.2 General Architecture

The proposed procedure can be sketched in the following steps (see fig. 1):

1. The human expert selects a seed point in the first slice where the coronary artery is found.
2. The proposed segmentation method (detailed in section 2.3) is performed from the seed point in the 2D slice i.
3. A set of potential seed points is automatically generated for the morphological segmentation of the slice $i + 1$.
4. Steps 2 and 3 are repeated until there are no potential seeds for the prolongation of the tubular structure.

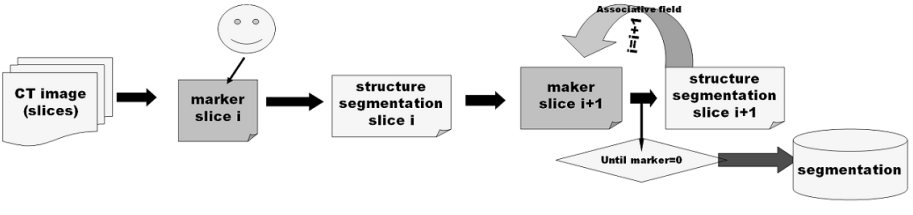

Fig. 1. Scheme of the architecture of MACTSE

2.3 Implementation Details

In order to clarify nomenclature, we introduce some basic morphological operators that can be applied to an image G. The two elementary operations are dilation $\delta_B(G)$ and erosion $\varepsilon_B(G)$ and can be composed together to yield a new set of operators given by opening $\gamma_B(G) = \delta_B[\varepsilon_B(G)]$ and closing $\varphi_B(G) = \varepsilon_B[\delta_B(G)]$. Morphological *openings* (*closings*) filter out light (dark) structures from the images according to the predefined size and shape criterion of the structuring element.

The main morphologic al operator we use is the morphological reconstruction by dilation [9] which consists in an iterative process of geodesic dilations of

the marker image inside the source image until stability. We denote by M the marker image generated from the seed points. The geodesic dilation of size k with structuring element B of the marker image M with respect to the image G is $\delta_G^k(M) = \delta_G^1 \delta_G^{k-1}(M)$, where $\delta_G^1(M) = \delta_B(M) \wedge G$; $\delta_G^1(M)$ indicates a dilation of image M by the structuring element B restricted to G. The reconstruction by dilation of image G from marker M, is denoted $R_B(M, G) = \delta_G^k(M)$ where k is chosen such that $\delta_G^k(M) = \delta_G^{k+1}(M)$ (idempotence).

Hereafter we present the MACTSE algorithm (see an example in fig. 2). Let S_i be the first slice where it is possible to find a coronary artery, M_i the seed selected by the human expert and B_r is a disc structuring element of radius r. MACTSE works as follows:

A) **Segmentation of the 2D slice S_i.** A reconstruction by dilation is performed on the original image highlighting the marked regions (M_i) (see fig. 3). Then the top-hat opening by reconstruction is used to extract only the bright sections of tubular-like structures (SG_i).
   1. $(IR_i) = R_{B_1}(M_i, S_i)$
   2. $(SG_i) = (IR_i) - R_{B_1}(\gamma_{B_{\mu_1}}(IR_i), IR_i)$

B) **Generation of potential seed points for the segmentation of slice S_{i+1}.** The new seed points for the following slice segmentation will be generated searching in an area of higher probability that is obtained from the segmentation of slice S_i. We denote this region as associative field A_i and it is created by the dilation of the binary mask of the segmentation of the slice

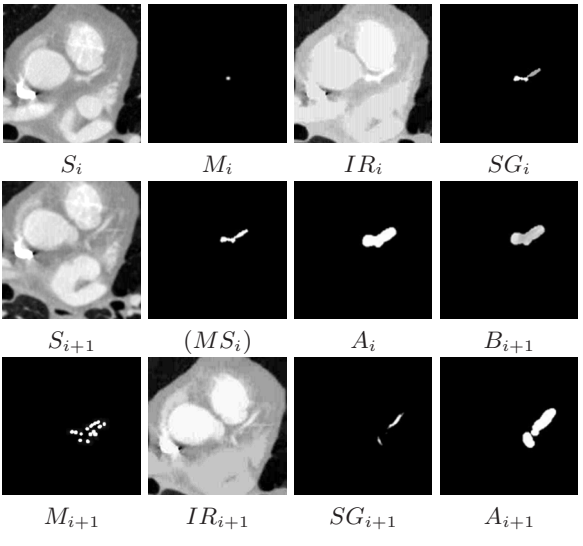

Fig. 2. MACTSE procedure example

S_i thresholding with a value λ. Then the selected seed points correspond to the regional maxima from the intersection of the associative field A_i and S_{i+1}.

3. $(MS_i) = Threshold_\lambda(SG_i)$
4. $(A_i) = \delta_{B_{\mu_2}}(MS_i)$
5. $(B_{i+1}) = (S_{i+1}) \wedge (A_i)$
6. $(M_{i+1}) = RegionalMaxima(B_{i+1})$

C) **Stopping criterion.** The process (A) and (B) are repeated until no potential seed points for the next slices are generated.

7. If $(M_{i+1}) = 0$ then $[end]$ else repeat steps 1 to 6 for $[(M_{i+1}, S_{i+1})]$

Notice that the output is not a binary segmentation, but a grey-level reconstruction of the regions with levels of intensity in each slice corresponding to the difference from the vessel to the background (the plateau around the vessel).

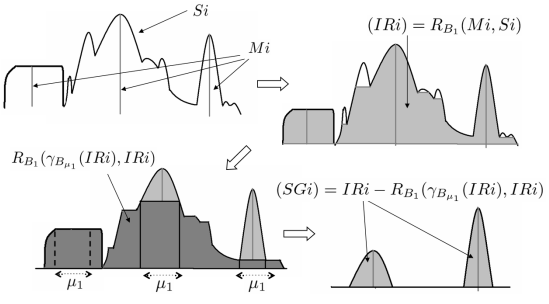

Fig. 3. Scheme of the segmentation of the vessel candidates in one slice

Prior knowledge from the image characteristics is used to adjust the algorithm parameters μ_1 and μ_2(see fig. 4). These values correspond to the radius of the structuring elements used in the steps 2 and 4. On the one hand, we define the concept of associative field as the region where there is high probability to find the continuation of the vessel. It is adjusted depending on the distance between two slices, $\mu_2 = f(\Delta Z_{slice(i),slice(i+1)})$. This parameter allows tracking the tubular structure even in undersampled z-axis images where the continuation of the tube is not so closely aligned in two consecutive slices. On the other hand, the fact that all the cross-sections of a cylinder have at least one direction of a size equal to the diameter is used to adjust the size parameter μ_1.

Generally, the segmentation results may be mathematically described as a function of the parameters regarding the property of ordering preservation of morphological operators. These order relationships allow us to construct a hierarchy of embedded segmentations with increasing segmented volume and details by modifying $\mu_1 \uparrow$, $\mu_2 \uparrow$ or $\lambda \downarrow$. Regarding the dependence on the parameters we find that if $\mu_1 \uparrow$ or $\lambda \downarrow$, smaller structures are detected: overdetections may occur and all the small branches are tracked. If $\mu_2 \uparrow$, more potential vessel candidates

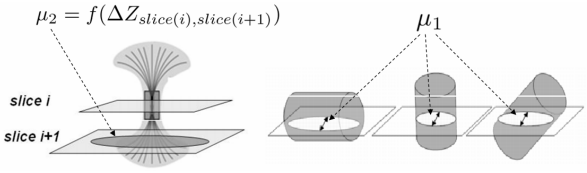

Fig. 4. μ_2 and μ_1 are the radius of the ball structuring elements used to define respectively the associative field and the tubular vessel size

are marked and consequently more details are captured. Modifying parameters in this way allows the user to tune the algorithm easily because of these order relationships and the small variability of each parameter.

3 Coronary Artery Segmentation from CT-Images

3.1 Data Analyzed

The reconstruction algorithm has been tested on 9 3D-MSCT data sets. The images were acquired with a Toshiba Aquilion 16 CT scanner with a slice resolution of $0.5mm$ and a slice spacing of $0.5mm$ (isotropic). Five of the cases present minimal or inexistent lesions. The other four cases present medium or severe problems. The original data has a size of 512x512 in the horizontal plane and between 200 and 300 slices for the z-axis. No pre-processing has been done in the images. The number and length of visible coronary artery segments differs largely in the set of patient data particularly in the pathological cases. We restricted the analysis to the left coronary arteries: the left anterior descending (LAD) coronary artery and the left circumflex (LCX) coronary artery and their branches. The coronary extraction results have been visually evaluated by an expert.

3.2 Extraction Results and Discussion

Table 1 shows the expert evaluation of the severity of the lesions and image quality of the 9 data sets analyzed, together with the assessment of the extraction results. The main branches LAD and LCX are correctly extracted in all cases but patient f. The extraction is satisfactory both for the coronaries without lesions (see fig. 5) and for pathological cases (see fig. 6). The misdetection of LAD in patient f is due to the low image quality, severe lesions and mainly to the presence of a stent that make the signal to be very fuzzy in one slice.

The algorithm parameters have been manually tuned in each case in order to achieve the best reconstruction. In all the cases the optimal choice for the three parameters corresponds to the following range: $\mu_1 \in \{8, 9, 10\}$, $\mu_2 \in \{2, 3, 4\}$, $\lambda \in \{1, 2, 3\}$. A choice of $\mu_1 = 8, \mu_2 = 3, \lambda = 3$ provides acceptable results detecting the main branches in 5 of the cases. The small range of variability of the

Table 1. Segmentation results. Legend: (i) Severity of the pathology: no calcium(1)-multiple lesions(4); (ii) Image quality: bad(1)-excellent(4); (iii) Main branches detection: Yes/No; (iv) Artifacts: No/Ventricular wall - W (in parenthesis the starting point of the artifacts expressed as a proportion of the heart length)/Vein ; (v) Small branches tracking: poor(1)-excellent(4)

Patient	Severity	Image quality	Main branches	Artifacts	Small branches
a	1	3	Yes	V	4
b	1	1	Yes	W($\frac{3}{4}$)	1
c	1	4	Yes	V	3
d	2	4	Yes	No	2
e	2	4	Yes	W($\frac{2}{3}$)	3
f	3,stent	2	NO LAD	No	1
g	4	3	Yes	No	3
h	4	3	Yes	W($\frac{1}{2}$)	3
i	4,stent	3	Yes	W($\frac{3}{4}$)	3

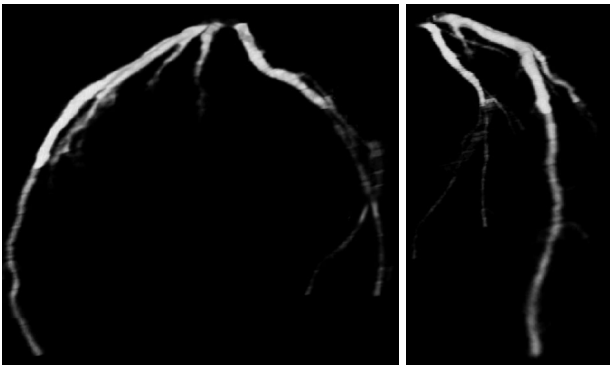

Fig. 5. Left coronary tree without lesions. Video renderings are available at www.die.upm.es/im/videos/CT/.

parameters could be interesting for the implementation of a user interaction interface in order to perform the fine tuning. The main drawback of the algorithm is the extraction in most of the cases of regions that do not correspond to the coronaries in the lowest half of the vessel tree. In cases b, e, h, i, these regions correspond to structures located in the low ventricular wall with granulated texture that is interpreted by the algorithm as potential bifurcations of the artery. In cases a, c a vein that crosses very near the arteries is selected. This overdetection could be avoided tuning the parameters, however the smaller branches wouldn't be detected.

The main advantages of the proposed approach in comparison to other methods, specially those who work with the 3D volume, is its independence from intensity variations during the acquisition procedure. Because of the local nature

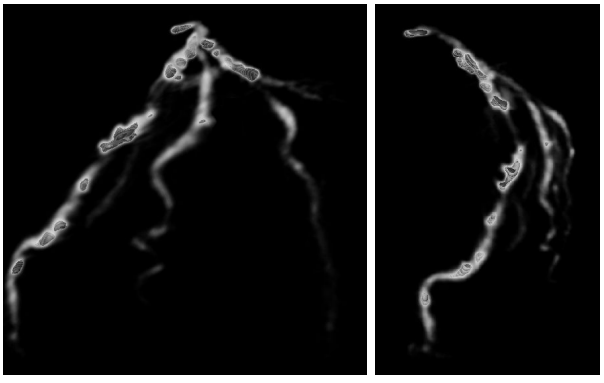

Fig. 6. Left coronary tree with severe calcifications. The isosurfaces superimposed to the rendering are at calcium-level intensity.

of the residues of the morphological reconstruction during the 2D slice analysis, the algorithm is able to follow the arteries in the presence of intensity changes between two slices (which is an important problem for the commercial stations). The algorithm also behaves in a robust way in presence of horizontal shifts between two slices because the associative field permits to track the vessel even if it is misaligned. Concerning computational efficiency, reconstructions are performed in less than 15 seconds in a PentiumIV 3.2GHz, RAM-2GB.

4 Conclusions and Perspectives

The proposed algorithm performs an efficient extraction of the coronary tree from a seed-point initialization. The algorithm is designed to minimize the loss of interesting structures, but in some cases overdetects adjacent regions in the more distal areas of the tree. It behaves in a robust way in the presence of intensity variations or displacement shifts. It works well also in z subsampled volumes, a feature that could be used either to gain speed or to reduce the radiation dose to the patient. A larger validation process including different pathologies should be done. Concerning MACTSE, the most interesting improvement would be to modify the dilation that provides the associative field by deforming the structuring element according to the direction of the vessel in previous frames. Further developments will be devoted to assist in the diagnosis of unhealthy arteries with quantitative data. Current state-of-the-art measurements in order to obtain a quantitative estimation of stenosis or aneurysms are based on crosssectional areas of vessels at different locations[10]. These measurements are strongly dependent on the estimation of the central axis which is a sensitive task specially in the presence of stenosis. As an alternative methodology, our future workplan is to develop directly a three dimensional classification in the extracted coronary tree based on the Hounsfield density values associated to each tissue and to measure volumetric parameters.

Acknowledgements

This work was supported by the grant FPI-CAM(0362/2005); projects PI041495 and PI041920, from the Spanish Health Ministry; and the CDTEAM project from the CENIT program (Spanish Ministry of Industry).

References

1. Kirbas, C., Quek, F.: A review of vessel extraction techniques and algorithms. ACM Comput. Surv. 36, 81–121 (2004)
2. Mueller, D., Maeder, A., O'Shea, P.: Improved direct volume visualization of the coronary arteries using fused segmented regions. In: DICTA05, pp. 110–118 (2005)
3. Florin, C., Paragios, N., Williams, J.: Particle filters, a quasi-monte carlo solution for segmentation of coronaries. In: Duncan, J.S., Gerig, G. (eds.) MICCAI 2005. LNCS, vol. 3749, pp. 246–253. Springer, Heidelberg (2005)
4. Serra, J.: Image analysis and mathematical morphology. Academic Press, London I,II (1982)(1988)
5. Zana, F., Klein, J.: Robust segmentation of vessels from retinal angiography. In: Int. Conf. on Digital Signal Proc. pp. 1087–1090. IEEE, New York (1997)
6. Angulo, J., Nguyen-Khoa, T., Massy, F., Drüeke, T., Serra, J.: Morphological quantification of aortic calcification from low magnification images. Image Analysis and Stereology 22, 81–89 (2003)
7. Qian, Y., Eiho, S.: Morphological method for automatic extraction of the coronary arteries. Med. Imaging 18, 231–238 (2000)
8. Kiraly, A.P., Higgins, W.E., McLennan, G., Hoffman, E.A., Reinhardt, J.M.: Three-dimensional human airway segmentation methods for clinical virtual bronchoscopy. Academic Radiology 9, 1153–1168 (2002)
9. Vincent, L.: Morphological grayscale reconstruction in image analysis: efficient algorithms and applications. IEEE Trans. Image Proc. 2, 176–201 (1993)
10. Ferencik, M., Lisauskas, J.B., Cury, R.C., Hoffmann, U., Abbara, S., Karl, W.A.S., Brady, T.J., Chan, R.C.: Improved vessel morphology measurements in mdct coronary angiography with non-linear post-processing. Eur. J. Radiology 57, 380–383 (2006)

Segmentation of Myocardial Regions in Echocardiography Using the Statistics of the Radio-Frequency Signal

Olivier Bernard, Basma Touil, Arnaud Gelas, Remy Prost, and Denis Friboulet

CREATIS, CNRS UMR 5220, U630 INSERM, INSA, Blaise Pascal, 69621 Villeurbanne, France
bernard@creatis.insa-lyon.fr

Abstract. We present an original Radial Basis Functions-based multiphase level set approach for the segmentation of cardiac structures in echocardiography. The method relies on two main contributions. We first describe a distribution allowing for the modeling of the radiofrequency signal for both blood and myocardial regions. We then formulate the problem of segmenting several cardiac regions in echocardiography using a Maximum Likelihood framework based on the proposed distribution. We minimize the resulting functional using a RBF-based multiphase level set model. Results obtained on both simulation and data acquired in vivo demonstrate the ability of our method to segment myocardial regions in echocardiography imaging.

1 Introduction

Echocardiography represents one of the most popular modalities in the field of cardiac imaging because it yields real-time analysis of the cardiac structures, while being low-cost and non-invasive. Segmentation of echocardiographic images remains an important procedure to assess the heart function. However, the segmentation of cardiac structures is particularly difficult in echocardiography mainly due to the speckle phenomenon and low contrast. As noted in a recent review [1], due to these difficulties most of the existing work has been devoted to the segmentation of the endocardium, i.e. the interface that separate blood pool and tissue border and only few studies have been proposed done for the segmentation of the whole myocardium. Moreover, most of the proposed approaches are based on the analysis of B-scan images that are constructed from the envelope of the echo signal. With the introduction of ultrasound devices, the radiofrequency (RF) signal has become more readily available. The interest of such signal resides in the fact that it potentially contains more information than the envelope echo. Despite of this interest, there is a very limited amount of work based on the exploitation of the RF signal [1].

We propose in this paper an original level set model for echocardiographic image segmentation driven by the statistics of the radiofrequency signal. Based on the assumption that the scatterers present inside the system resolution cell

F.B. Sachse and G. Seemann (Eds.): FIMH 2007, LNCS 4466, pp. 433–442, 2007.

are uniformly distributed and that their amplitude follow a K distribution, we first propose in Section 2 a distribution well adapted to characterize the statistics of the radiofrequency signal for both blood and myocardial regions. In Section 3 we propose to exploit this distribution in a Maximum Likelihood framework in order to perform tissue segmentation. In this context, we derive in Section 4 a multiphase level set formulation of the segmentation functional. The ability of the proposed method to segment cardiac structures in echocardiographic images is evaluated in Section 5 from both simulation and data acquired in vivo.

2 Ultrasound Image Information Using the Statistics of the Radiofrequency Signal

The K distribution has been initially designed for the envelope signal [2]. The interest of such distribution in echocardiographic images relies on its ability to model both fully speckle (blood pool) and partially developed speckle (tissue area) situations. We briefly recall in this section the assumptions attached to the K distribution and give the corresponding pdf for the RF signal (detailed derivation can be found in [3]). The backscattered ultrasonic signal results from the individual energy contributions of each scatterer embedded in the resolution cell. This situation can mathematically be described as a random walk in the complex plane [4]. From this random flight model, the analytic signal can be expressed as a random process depending on the number of scatterers present inside the resolution cell, their relative position and contribution. Thus, a joint density function of the envelope and phase can be obtained by expressing both statistical properties of the phase and amplitude of each scatterer. This results in a K distribution when the scatterers phase is assumed to be uniformly distributed [5] and when their amplitude is modeled as a K distribution itself [6].

2.1 Physical Model: K_{RF} Distribution

The RF signal corresponds to the real part of the analytic signal. The pdf of the RF signal thus corresponds to the marginal distribution obtained by integrating the pdf corresponding to the analytic signal with respect to its imaginary part, which yields the following expression (see [3] for details):

$$f_X(x) = \frac{\beta}{\sqrt{\pi}\Gamma(\nu)} \left(\frac{\beta |x|}{2} \right)^{\nu-0.5} K_{\nu-0.5}(\beta |x|) \tag{1}$$

where Γ is the Gamma function and $K_{\nu-0.5}$ is the modified Bessel function of the second kind of order $\nu - 0.5$. This expression is completely specified by its two parameters ν and β, such that ν controls the shape and β the scale of the pdf.

The corresponding distribution is called K_{RF}. This pdf may thus provide the basis for segmentation of echocardiographic images by separating regions corresponding to fully speckle (blood pool) and partially developed speckle

(tissue area). K_{RF} distribution however has two main drawbacks. Indeed numerical simulations show that the consistency of the K_{RF} parameters decreases rapidly as the shape parameter of the distribution increases, yielding unreliable estimates in blood regions [3]. Moreover, the expression of the distribution is complex, increasing the computational cost of a segmentation approach.

2.2 Modeling RF Signal Statistics Using Generalized Gaussian

From the observation that fully speckle situations correspond to a Gaussian pdf and non-fully speckle situations yields Laplacian-like distribution, we showed in [7] that the Generalized Gaussian distribution (G.G.) is a good candidate for approximating (1). G.G. has the following expression:

$$g_X(x) = \frac{b}{2a\Gamma(1/b)} exp\left(-\left(\frac{|x|}{a}\right)^b\right) \tag{2}$$

b and a are the two parameters of the distribution where b controls the shape and a the scale of the pdf. The G.G. pdf corresponds to a Gaussian distribution when $b = 2$ and to a Laplace distribution when $b = 1$.

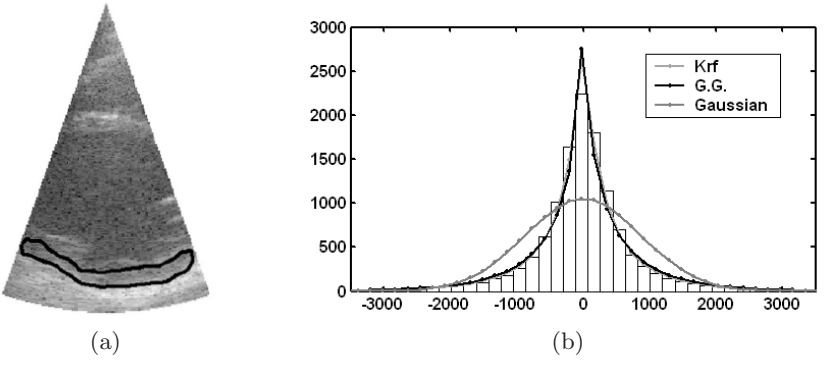

(a) (b)

Fig. 1. Fits of the proposed distributions to the RF data from a Parasternal long axis view in the myocardial tissue. The resulting KS associated to the K_{RF}, Generalized Gaussian and the Gaussian is respectively 0.0194, 0.0132 and 0.0885.

This distribution has the advantage to have a simple expression with robust parameters estimation. In Figure 1, an example of the fit obtained for a Parasternal long axis view in the myocardial tissue is given. This example illustrates qualitatively how the K_{RF} and Generalized Gaussian distributions better fits the data than the conventional Gaussian. The ability of the proposed distributions to model the RF data has also been evaluated quantitatively through the Kolmogornov-Smirnov measure (KS). The results shown in Figure 1 yields a lower KS for the K_{RF} (0.0194) and the Generalized Gaussian (0.0132) than the Gaussian (0.0885). K_{RF} and Generalized Gaussian distributions are so closed

that it is difficult to distinguish in Figure 1. The ability of the G.G. to model cardiac RF data observed on the example given in Figure 1 has been validated on a set of ultrasound cardiac images including the principal orientations used in clinical practice [7].

3 A Variational Framework for Ultrasound Image Segmentation

The framework we use for segmentation is based on the approach initially described by Zhu & Yuille [8]. Let $\Omega \subset \mathbb{R}^2$ denote the image plane and let $f : \Omega \times \mathbb{R} \rightarrow \mathbb{R}$ be a given ultrasound radiofrequency image. Under the assumption that the image is composed of a set of regions following a Generalized Gaussian distribution with different parameters values, the Maximum-Likelihood function corresponding to this image can be written as:

$$ML\left(f(\mathbf{x})\right) = \prod_{i=1}^{n} \left(\prod_{\mathbf{x} \in R_i} p\left(f(\mathbf{x})/\zeta_i\right) \right) \tag{3}$$

where n corresponds to the number of regions present in the image and $p(.)$ corresponds to the Generalized Gaussian distribution with parameters vector $\zeta_i = \{a_i, b_i\}$. Maximizing criterion (3) is equivalent to minimize its negative logarithm, which is given (up to a constant) by the following energy functional:

$$E\left(C, \{\zeta_i\}\right) = \sum_{i=1}^{n} \left(\int_{R_i} -log\left[p\left(f(\mathbf{x}/\zeta_i)\right)\right] d\mathbf{x} \right) \tag{4}$$

where C is a closed subset in Ω, made up of the regions boundaries. For brevity sake, we will note $p\left(f(\mathbf{x}/\zeta_i)\right)$ as p_i in the remainder of the paper.

4 A RBF-Based Multiphase Level Set Method

In order to minimize the functional (4), we need to specify an appropriate representation for the boundary C. In this paper, we choose an implicit RBF-based level set representation of the boundary [9]. In contrast to the conventional finite difference narrow band implementations, the RBF-based level set scheme allows an overall control of the level set (*i.e.* over the whole computational domain of the level set) with a reasonable computational cost and allows to avoid the usual reinitialization step of the level set. In this formalism, the implicit function ϕ is modeled using a RBF decomposition according to the following inner product:

$$\phi(\mathbf{x}) = \Psi(\mathbf{x}) \cdot \alpha \tag{5}$$

with

$$\begin{cases} \Psi(\mathbf{x}) = [\varphi(\|\mathbf{x} - \mathbf{x}_1\|), \cdots, \varphi(\|\mathbf{x} - \mathbf{x}_P\|)] & (6) \\ \alpha = [\mu_1, \cdots, \mu_P]^T & (7) \end{cases}$$

where φ is a RBF, $\{\mathbf{x}_j\}$ corresponds to the RBF centers and $\{\mu_j\}$ corresponds to RBF coefficients. Our implementation is build upon Wendland's C^2 compactly supported RBFs, which allows reducing the computational complexity of the algorithm [9].

Based on the work of Chan and Vese [10], we first present a two-phase level set model derived from the functional (4) with a single level set function ϕ. This model is subsequently extended to a multiphase model with a vector-valued level set function.

4.1 The Two Phase Model

In this subsection, we restrict the class of permissible segmented region to two-phase solutions. Let the boundary C in the functional (4) be represented as the zero level set of a function ϕ. Using the Heaviside step function

$$H(\phi) = \begin{cases} 1 \text{ if } \phi \geq 0, \\ 0 \text{ if } \phi < 0 \end{cases} \tag{8}$$

we can embed the Maximum-Likelihood energy (4) in the following *two-phase functional*:

$$E(\phi, \zeta_1, \zeta_2) = \int_\Omega - log(p_1)\ H(\phi)\, d\mathbf{x}\ +\ \int_\Omega - log(p_2)\ (1 - H(\phi))\, d\mathbf{x} \tag{9}$$

where p_1 (respectively p_2) corresponds to the Generalized Gaussian distribution whose parameter vector ζ_1 (respectively ζ_2) is computed inside (respectively outside) the zero level set. This functional is now simultaneously minimized with respect to the parameter vectors ζ_1 and ζ_2, and with respect to the embedding level set function ϕ. To this end, we alternate two fractional steps. The first step is computed using the Maximum-Likelihood estimator of the Generalized Gaussian parameters described in [11]. Then for fixed parameter vectors, the gradient descent on the functional (9) for the level set function ϕ allows to derive the following expression:

$$\frac{\partial \phi}{\partial \tau} = \delta_\epsilon(\phi) \left[log\left(\frac{p_1}{p_2}\right) \right] \tag{10}$$

where $\delta_\epsilon(.)$ is a regularized version of the Dirac function [12].

4.2 The General Multiphase Model

The above approach based on the evolution of one level set permits to segment only two structures in an ultrasound image. This limitation can be overcome by using multiple level set functions. We follow for this purpose the approach described by Chan & Vese in [10], who introduced a compact representation of up to n phases which needs only $m = log_2(n)$ level set functions. This approach has the main advantage to generate a partition of the image plane and therefore does not suffer from overlap or vacuum formation.

Let $\boldsymbol{\phi} = (\phi_1, \cdots, \phi_m)$ be a vector level set function, with $\phi_i : \Omega \rightarrow \mathbb{R}$. Let $H(\boldsymbol{\phi}(\mathbf{x}) = (H(\phi_1(\mathbf{x})), \cdots, H(\phi_m(\mathbf{x}))))$ be the associated vector Heaviside function. This function maps each point $\mathbf{x} \in \Omega$ to a binary vector and therefore permits to encode a set of $n = 2^m$ phases R_i defined by:

$$R = \{\mathbf{x} \in \Omega \mid H(\boldsymbol{\phi}(\mathbf{x})) = \text{ constant } \} \tag{11}$$

We thus propose to replace the functional (4) by the following multiphase functional:

$$E(\boldsymbol{\phi}, \{\zeta_i\}) = \sum_{i=1}^{n} \left(\int_{\Omega} - log(p_i)\ \chi_i(\boldsymbol{\phi})\, d\mathbf{x} \right) \tag{12}$$

where χ_i denotes the indicator function for the region R_i.

Because in ultrasound imaging there is a limited number of structures to be segmented, it seems reasonable to assume that n should be small. We thus explicitly give in this part the functional for the case of $n = 4$ phases. The corresponding expression is:

$$\begin{aligned} E(\{\zeta_i\}, \boldsymbol{\phi}) = & \int_{\Omega} - log(p_{11})\ H(\phi_1)\ H(\phi_2)\, d\mathbf{x} \\ & + \int_{\Omega} - log(p_{10})\ H(\phi_1)\ (1 - H(\phi_2))\, d\mathbf{x} \\ & + \int_{\Omega} - log(p_{01})\ (1 - H(\phi_1))\ H(\phi_2)\, d\mathbf{x} \\ & + \int_{\Omega} - log(p_{00})\ (1 - H(\phi_1))\ (1 - H(\phi_2))\, d\mathbf{x} \end{aligned} \tag{13}$$

where p_{ij} corresponds to the Generalized Gaussian distribution with parameters ζ_{ij} given by

$$\begin{cases} \zeta_{11} = \text{ML estimate of } \zeta \text{ in } \{\phi_1 \geq 0,\ \phi_2 \geq 0\} & (14) \\ \zeta_{10} = \text{ML estimate of } \zeta \text{ in } \{\phi_1 \geq 0,\ \phi_2 < 0\} & (15) \\ \zeta_{01} = \text{ML estimate of } \zeta \text{ in } \{\phi_1 < 0,\ \phi_2 \geq 0\} & (16) \\ \zeta_{00} = \text{ML estimate of } \zeta \text{ in } \{\phi_1 < 0,\ \phi_2 < 0\} & (17) \end{cases}$$

ML corresponds to the Maximum-Likelihood estimator of the Generalized Gaussian parameters described in [11].

Using Euler-Lagrange equations, the minimization of (13) with respect to $\boldsymbol{\phi}$ (for fixed parameters values $\{\zeta_{ij}\}$) yields to the following evolution equations:

$$\begin{cases} \dfrac{\partial \phi_1}{\partial \tau} = \delta_\epsilon(\phi_1) \left[log\left(\dfrac{p_{11}}{p_{01}}\right) H(\phi_2) \ + \ log\left(\dfrac{p_{10}}{p_{00}}\right) (1 - H(\phi_2)) \right] & (18) \\ \dfrac{\partial \phi_2}{\partial \tau} = \delta_\epsilon(\phi_2) \left[log\left(\dfrac{p_{11}}{p_{10}}\right) H(\phi_1) \ + \ log\left(\dfrac{p_{01}}{p_{00}}\right) (1 - H(\phi_1)) \right] & (19) \end{cases}$$

5 Experiments

5.1 Simulated Data

The proposed method has been tested on a simulated image given in figure 2. This image consists of three regions generated using a Generalized Gaussian distribution with different parameters. These parameters have been chosen from real data (in parasternal long axis orientation) and correspond to the three main tissues usually present in the cardiac image, *i.e.* pericardium (brighter region), myocardium and blood (the darker regions). The results presented on figure 2(b) and (c) show how the multiphase level set allows to properly segment these different regions based on their statistics.

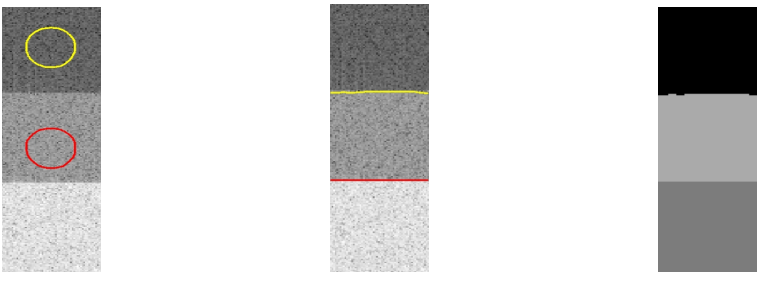

(a) (b) (c)

Fig. 2. Segmentation of a simulated image using two level set functions. (a) initialization. (b) segmentation result. (c) obtained regions.

5.2 In Vivo Data

The ability of the proposed method to segment myocardium region from RF image was tested on ultrasound cardiac images acquired in vivo. Data were acquired using Toshiba Powervision 6000 equipped with an RF interface for research purposes and a 3.75 MHz-probe. The RF sample frequency was fixed to 25 MHz.

We first illustrate on Figure 3 the segmentation obtained by using the two phase model (equation (10)) on an apical four chambers view with a narrow angle focused on the septum. This image has indeed only two regions with different statistics (blood pool and septum region). These results show that the energy functional stabilizes to a minimum value as the variation of the RBF coefficients tends to zero. This illustrates the fact that the level set globally converges to a solution.

Figure 4 shows the result obtained for a parasternal long axis view using again the two phase model. In contrast with the example used in Figure 3, this image has three statistically different regions corresponding to the blood pool, the myocardium and pericardium. Figure 4(a) shows the initialization of the level set inside myocardial and figure 4(b) and (c) show the result obtained at convergence. From this example, it can be observed that the model yields proper

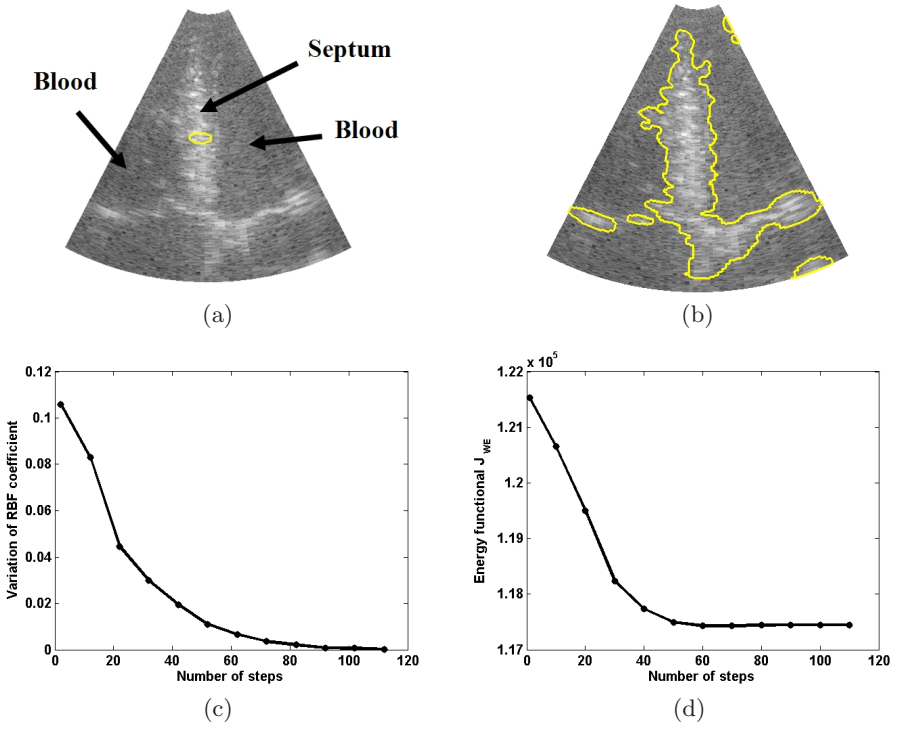

Fig. 3. Segmentation of an apical four chambers view using a single level set function. (a) initialization. (b) segmentation result. (c) variation of RBF coefficient. (d) variation of the energy functional (9).

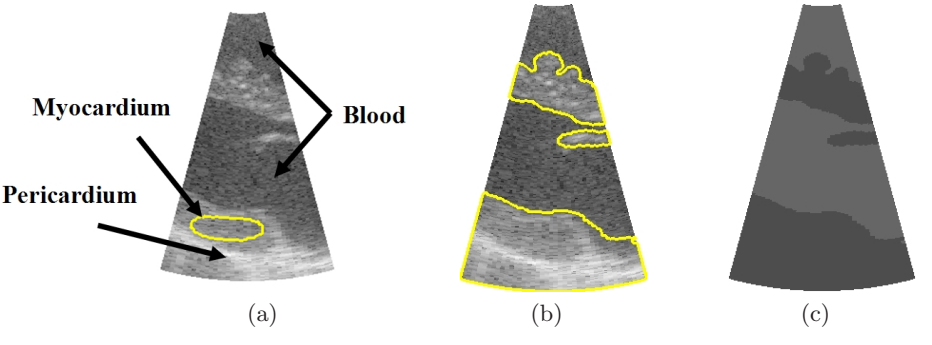

Fig. 4. Segmentation of a parasternal long axis view using a single level set function. (a) initialization. (b) segmentation result. (c) obtained regions.

segmentation of all the blood/tissue interfaces in the image. However, because there are more than 2 statistical regions present in the lower part of the image, the method can not separate the myocardium from the pericardium.

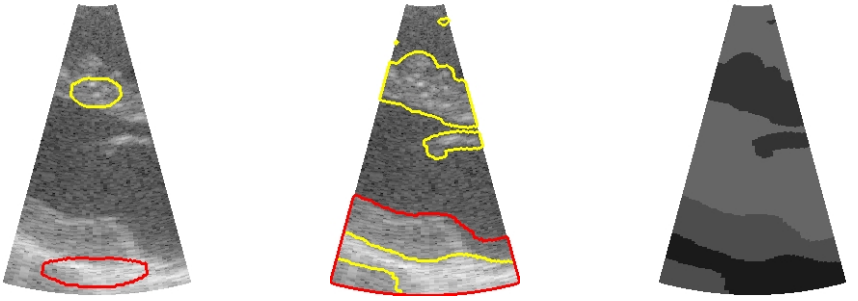

(a) (b) (c)

Fig. 5. Segmentation of a Parasternal long axis view using two level set functions. (a) initialization. (b) segmentation result. (c) obtained regions.

Figure 5 shows the result obtained for the same parasternal image using the four phase level set described in Section 4. Figure 5(a) shows the initialization of the two level sets and Figure 5(b) and (c) show the result obtained at convergence. In contrast with the previous example, the four phase model allows proper segmentation of the three different regions. In particular, the tissue regions corresponding to the myocardium and the pericardium are clearly separated.

6 Conclusions

We have presented in this paper a method for the segmentation of myocardial region in echocardiographic images using the statistics of the radiofrequency signal. The problem of segmentation is formulated in a Maximum Likelihood framework using the Generalized Gaussian distribution as an a priori model of the statistics. We minimize this functional using a RBF-based multiphase level set model. This formulation allows segmenting echocardiographic images into several homogeneous regions from a statistical point of view. Simulation results show that our model is well suited to segment several regions distributed according to a Generalized Gaussian distribution. In contrast with previously described approaches, results obtained from in vivo echocardiographic data acquired in parasternal long axis view show that the proposed method yields proper segmentation of the myocardial tissue.

References

1. Noble, J.A., Boukerroui, D.: Ultrasound image segmentation: A survey. IEEE Transactions on Medical Imaging 25(8), 987–1010 (2006)
2. Shankar, P.M.: A model for ultrasonic scattering from tissues based on the k distribution. Phys. Med. Biol. 40, 1633–1649 (1995)

3. Bernard, O., D'hooge, J., Friboulet, D.: Statistics of the radio-frequency signal based on k distribution with application to echocardiographic images. IEEE Trans. Ultrason. Ferroelect. Freq. Contr. 53(9), 1689–1694 (2006)
4. Pearson, K.: The problem of the random walk. Nature 72, 294–342 (1905)
5. Goodman, J.W.: Statistical Optics. Wiley, New York (1985)
6. Jakeman, E., Pusey, P.N.: A model for non-rayleigh sea echo. IEEE Trans. Antennas Propagat. 24(6), 806–814 (1976)
7. Bernard, O., D'hooge, J., Friboulet, D.: Statistical modeling of the radio-frequency signal in echocardiographic images using modified k-distribution and generalized gaussian distribution. In: IEEE International Ultrasonics Symposium, Vancouver, Canada, in press (2006)
8. Zhu, S., Yuille, A.: Region competition: unifying snakes, region growing, and bayes/mdlfor multiband image segmentation. IEEE Trans. Patt. Anal. Mach. Intell. 18, 884–900 (1996)
9. Gelas, A., Bernard, O., Friboulet, D., Prost, R.: Compactly supported radial basis functions based collocation method for level-set evolution in image segmentation," IEEE Transaction on Image Processing, in press (2007)
10. Vese, L., Chan, T.: A multiphase level set framework for image segmentation using the mumford and shah model. Int. J. Comput. Vis. 50, 271–293 (2002)
11. Mallat, S.G.: A theory of multiresolution signal decomposition: the wavelet representation. IEEE Trans. Patt. Anal. Mach. Intell. 11, 674–693 (1989)
12. Chan, T., Vese, L.: An active contour model without edges. In: Scale-Space Theories in Computer Vision, pp. 141–151 (1999)

A Hyperelastic Deformable Template for Cardiac Segmentation in MRI

Youssef Rouchdy[1], Jérôme Pousin[2], Joël Schaerer[3], and Patrick Clarysse[3]

[1] Projet ICARE, INRIA Sophia-Antipolis, 2004 route des lucioles - BP 93 FR-06902 Sophia Antipolis
[2] Institut C. Jordan, UMR CNRS 5028, INSA de Lyon, 69621 Villeurbanne cedex, France
[3] CREATIS CNRS UMR 5220, INSERM U630, INSA Bât. Blaise Pascal, 69621 Villeurbanne cedex, France

Abstract. This article proposes a hyperelastic 3D deformable template for the segmentation of soft structures. It relies on a template, which is a topological, geometrical and material model of the structure to segment. The template is modeled as an elastic body which is deformed by forces derived from the image. The proposed model is based on the nonlinear three-dimensional elasticity problem with a boundary condition of pure traction. In addition, the applied forces depend on the displacements. For computations, a convergent algorithm is proposed to minimize the global energy of template deformation. A discrete algorithm using the finite element method is presented and illustrated on MR images of mice.

1 Introduction

Most recent medical imaging systems can provide a great amount of data explaining the anatomy and function of a patient's organs. However, the development of efficient tools for automatic processing is mandatory to fully exploit the wealth of information obtained by medical imaging systems and to provide quantified parameters. The context of this paper is related to the extraction of the heart's anatomy and motion from temporal image sequences, more precisely Magnetic Resonance Imaging (MRI) sequences. Currently, a clinical examination results in a stack of slices covering the whole heart at successive time points over the cardiac cycle. These imaging data constitute the input of the segmentation tracking approach proposed in this paper. The methodology we follow for the segmentation is based on the deformable model principle and, as such, relies on a *a priori* model of the structure to be segmented [12]. In the great variety of deformable models, our approach uses a volumetric tetrahedral mesh of the heart with elastic properties. We call it Deformable Elastic Template (DET). The linear DET model has been previously introduced in [14], [15] for the segmentation of the heart ventricles. In this paper, we introduce the new nonlinear DET model, which is less sensible to initialization, along with several improvements towards the automatic segmentation of cardiac structures in MR images.

F.B. Sachse and G. Seemann (Eds.): FIMH 2007, LNCS 4466, pp. 443–452, 2007.

2 Related Work

Segmentation and motion estimation of the cardiac structures is one of the most popular applications in medical image analysis. Numerous segmentation techniques have been tested in this context from basic thresholding and low-level methods to more sophisticated modeling and learning approaches [6]. The used methodology and the results depend on the imaging modalities and the number of dimensions (2D, 3D, 2D+time, 3D+time). Up to now, Magnetic Resonance Imaging and Ultrasounds have been mainly addressed for both static and dynamic segmentation. However, the inherent difficulties (image artifacts, noise and motion) are such that no generic method has truly emerged yet for routine practice. It is clear that prior knowledge needs to be taken into account to better constrain the segmentation. Therefore, methods based on *a priori* models of the heart geometry, known as deformable models, have retained attention and obtained a certain success in practice. The final segmentation results from the minimization of a global energy functional which establishes the balance between an internal energy, constraining the structure's shape, and an external energy, representing the action of image data onto the model. Contour and surface models have been extensively studied for segmenting soft structures. Their extension to shape tracking through 2D or 3D image sequences has generally come to the use of the result at time point t as an initialization for the segmentation at time point $t+1$ with some temporal smoothness constraints [8]. The extraction of both endocardial and epicardial cardiac surfaces is considered either as the coupled segmentation of two surfaces [8] or through the introduction of more complex volumetric models [14]. These latter models involve a volumetric representation of the heart associated to behavioral laws, such as elasticity. Level set methods, which can be closely linked with the previous deformable models, have also been investigated in this context [13]. In this particular approach, however, the shape topology is allowed to change during the optimization process which is not always desirable. Another popular approach is based on prior learning or cardiac atlases. The prior model is a summary representation of the manual segmentation of a (great, as big as possible) number of patient data sets. One of the main difficulties is to be able to establish a unique correspondence between all the segmentations to build up the model [6,9]. This statistical model then constrains the segmentation of the new data set through active shape (shape only)[7] or active appearance models (taking into account image grey levels) [11]. Such approaches are very interesting but face the problem of representativity of the database (defined by the number of individuals). It is however clear that prior models of anatomical structures can greatly improve the segmentation. The volumetric deformable model proposed here incorporates both geometry and physics of the cardiac structures.

3 Hyperelastic Model for Soft Structure Segmentation

A geometric template represents the object's interfaces as well as its interior and the properties assigned to it. The template is first placed within the image close

to the structure to be extracted. It is then deformed iteratively by applying a force field so that its edges stick to the borders of the targeted structure. Segmentation through template deformation is achieved by the minimization of a global energy (or functional). The global energy is generally composed of two terms. The first term is computed from the image data. Its role is to guide the deformation towards the border of the targeted object. The second term introduces a regularity constraint on the desired deformations. It also ensures that the problem is expressed in a suitable functional space.

The initial Deformable Elastic Template introduced in [14] relied on linear elasticity to deform the template. In this article, the regularization term comes from nonlinear elasticity and allows for large deformations. No part of the geometrical model is maintained fixed during the deformation process, which contributes to the better robustness of the segmentation against model initialization. The equivalence between the minimization problem and local elasticity equations is ensured when the material is hyperelastic and the applied forces are conservative (i.e. derived from a potential energy) [5]. Our contribution is the introduction and the proof of the convergence of an incremental algorithm. To our knowledge, this is the first time that the incremental method is used in cardiac segmentation. In [16], Rabbit et al. propose an algorithm, based on the Taylor formula, to solve 2D registration by hyperelastic model. This algorithm was applied to cardiac image registration in [1]. The convergence result of this algorithm is not proven.

For the considered applications, Saint-Venant Kirchhoff material is considered which is hyperelastic and the simplest model among all nonlinear models. The applied forces are assumed to be conservative. Let Ω be the domain to be deformed (a bounded subset of $\mathbb{R}^3$), let ν be the unit outward normal to $\partial\Omega$ the boundary of Ω, $u : \overline{\Omega} \to \mathbb{R}^3$ be the displacement and E be the following strain tensor

$$E(u) = \frac{1}{2}\big(\nabla u^t + \nabla u + \nabla u^t \nabla u\big), \tag{1}$$

A Saint-Venant Kirchhoff material is hyperelastic and homogeneous, thus the strain energy is independent of a particular point $x \in \bar{\Omega}$ and defined by the relation

$$W(x, E) = W(E) = \tfrac{\lambda}{2}\,(\mathrm{Tr}E)^2 + \mu \mathrm{Tr}E^2 \tag{2}$$

The internal energy is defined for the reference state Ω by

$$E_{int}(u) = \int_{\Omega} W(\nabla(\mathbf{1} + u)(x))\,\mathrm{d}x \tag{3}$$

while the external energy is expressed for the deformed state as:

$$E_{ext}(u) = -\int_{\partial\Omega} \hat{G}(\mathbf{1} + u)\,d\sigma \tag{4}$$

The function $\hat{G}$ is the potential of the applied surface forces g. In the implementation only the force field g is used to deform the mesh. The function $\hat{G}$ and g are connected by the relations:

$$G(\psi) = -\int_{\partial\Omega} \hat{G}(\mathbf{1} + u(x))\,\mathrm{d}\sigma(x) \quad G'(\phi)v = \int_{\partial\Omega} g(\phi(x)) \cdot v(x)\,\mathrm{d}\sigma(x) \tag{5}$$

the applied surface forces g can be computed from the norm of the image gradient, an edge map obtained using a Canny operator [4] smoothed with a Gaussian filter, or a distance map [2], [18]. The Gradient Vector Flow algorithm (GVF) introduced in [21] generates a force field by an iterative diffusion process, which is not derived from a potential. Although it is not conservative, we observed that the force field obtained by the GVF method leads to reasonable numerical results as compared to more conventional gradient based techniques.

When the applied force field is conservative, the minimization of the global energy

$$E_{total}(u) = E_{int}(u) + E_{ext}(u) \tag{6}$$

is "formally" equivalent to solving the following Euler equations (see [5]):

$$\mathrm{div}\big((\mathbf{1} + \nabla u)\Sigma\big(E(u)\big)\big) = 0 \quad \text{in } \Omega; \tag{7a}$$

$$-(\mathbf{1} + \nabla u)\Sigma\big(E(u)\big) \cdot \nu + g(u) = 0 \quad \text{on } \partial\Omega, \tag{7b}$$

where Σ is a tensor defined by

$$\Sigma(E) = \lambda \mathrm{Tr}(E)\mathbf{1} + 2\mu E \tag{8}$$

4 Approximation of the Model Using an Incremental Method

The problem (7) can be written as

$$L(u) = f(u) \quad \text{in } \Omega \times \partial\Omega, \tag{9}$$

where

$$L(u) = \begin{pmatrix} \mathrm{div}\big((\mathbf{1} + \nabla u)\Sigma\big(E(u)\big)\big) \\ \mathbf{1} + \nabla u)\Sigma\big(E(u)\big) \cdot \nu \end{pmatrix}, \quad f(u) = \begin{pmatrix} 0 \\ g(u) \end{pmatrix}.$$

To solve problem (9), an incremental method is proposed, which consists in letting the forces vary by small increments from 0 to their calculated value and

computing corresponding approximate solutions by successive linearizations. For $\lambda \in [0, 1]$, define $u(\lambda)$ as the solution to

$$L(u(\lambda)) = \lambda f(u(\lambda)) \quad \text{in } \Omega \times \partial\Omega \tag{10}$$

After differentiating this relation with respect to λ and adding an initial condition, we obtain

$$u'(\lambda) = \left(L'(u(\lambda)) - \lambda f'(u(\lambda))\right)^{-1} f(u(\lambda)),\ 0 \leq \lambda \leq 1, \tag{11a}$$

$$u(0) = 0. \tag{11b}$$

Note that, if u is a solution of the differential equation (11), by integration of this equation, u is also solution of equation (10). Therefore, the study of the partial differential equations (10) reduces to solving the ordinary differential equation (11). In [17], sufficient conditions for the convergence of the Euler's algorithm are given for the problem (11). In next sections, this incremental method is applied to image segmentation.

5 Finite Element Discretization

For the numerical optimization of the total energy (7) with the incremental method presented in the previous section, the finite element method is used. Let M be a positive number, $\{\psi_1, \cdots, \psi_M\}$ a function basis for the approximation of the displacements. The algorithm is detailed below:

Let U_0 a vector containing displacement components.

- Initialization step: $U_0 = 0 \quad \text{and} \quad u_0 = 0$;
- Iterations
  - (i) Assemble the stiffness matrix at iteration n

$$\mathcal{K}_{ij}^n = \int_{\Omega_h} k(u_n, \psi_i, \lambda_n) : \nabla\phi_j \, \mathrm{d}x - \left\langle g'(u_n) \cdot \psi_i, \psi_j \right\rangle, \quad 1 \leq i, j \leq M;$$

  - (ii) Solve the linear system, with U_{n+1} as unknown

$$\mathcal{K}^n U_{n+1} = \mathcal{K}^n U_n + (\lambda_{n+1} - \lambda_n)\mathcal{F}(U_n);$$

  - (iii) Compute the approximate displacement at iteration $n + 1$

$$u_{n+1} = \sum_{i=1}^{i=M} U_{n+1,i}\, \psi_i;$$

  - (iv) If $\|u_{n+1} - u_n\| < \epsilon$ stop, otherwise go to (i).

Where $\mathcal{F}$ has the components:

$$\mathcal{F}_j(U_n) =< g(u_n), \psi_j >,\ 1 \leq j \leq M$$

and

$$k(u,w) = (\mathbf{1} + \nabla u)\Sigma\big(\epsilon(w) + \frac{1}{2}(\nabla u^t \nabla w + \nabla w^t \nabla u)\big) + \nabla w \Sigma\big(\mathbf{E}(u)\big).$$

The scalar product $< \cdot, \cdot >$ is defined on $\partial\Omega$ for the two functions α and β by :

$$< \alpha, \beta >= \int_{\partial\Omega} \alpha(x)\beta(x)\mathrm{d}\sigma.$$

The stiffness matrix $\mathcal{K}^n$ can be updated at each iteration, but this is quite time consuming. The convergence of the algorithm can be accelerated by updating the stiffness matrix $\mathcal{K}^n$ after several iterations instead of updating it at each iteration. Two types of iterations are thus used: internal and external iterations. With the external iterations, the stiffness matrix is updated, which permits large displacements. Internal iterations do not require the computation of the matrix. Hence, less computing time is needed for internal iterations than for external iterations. The number of external iterations should therefore be reduced as much as possible but depends on the problem. If only small displacements are required it is not necessary to update the stiffness matrix. In that case, internal iterations suffice.

6 Tests

To evaluate the method, an example with a known target object is considered. A sphere is transformed into an ellipsoid, i. e. the template is a sphere and the target border is an ellipsoid. The axes of the ellipsoid are chosen in such way that the transformation demands large displacements. A force field is computed from the image. The mesh representing the template has 15 019 tetrahedrons and 3 003 nodes and satisfies the quality conditions introduced in [3]. The segmentation result obtained with the proposed method is shown in Fig 1-(a). The result with the linear DET model id shown in Fig 1-(b). Note that the linear model is unable to correctly detect the ellipsoid.

7 Simultaneous Segmentation of the Left and Right Heart Ventricles in 3D Cine MR Images

7.1 Experimental Data

Mouse heart cine MR images were acquired with a 7 T magnetic resonance scanner with a whole body coil for RF excitation and a 15 mm surface coil for MR signal reception. An ECG-gated FLASH sequence was used to acquire short-axis cine images with 25 mm^2 FOV, 256×256 pixels, 1 mm slice thickness,

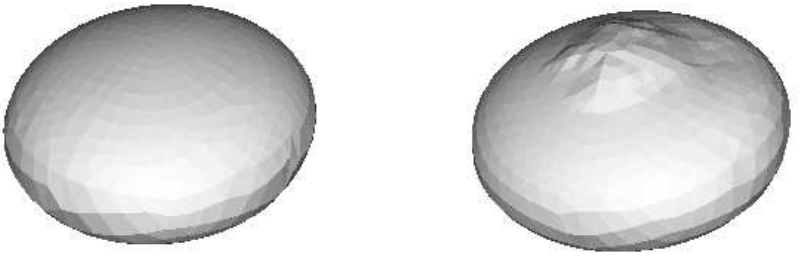

Fig. 1. Nonlinear DET demonstration for the segmentation of an ellipsoid from a spherical template (a): result obtained with nonlinear DET, (b): result obtained with linear DET

7/3.5 ms TR/TE, 64 KHz bandwidth and 20 degrees flip-angles. Cine images (16 frames over the cardiac cycle) were acquired for 7 slice levels, covering the entire left ventricle (LV). With a cardiac frequency of 450 b.p.m, the total acquisition time was 20 minutes.

7.2 Image Data Preprocessing and Initial Model Placement

High resolution MR images have a relatively low SNR. Furthermore, the abundance of small features in the images (papillary muscles, coronaries, etc.) can lead to local minima of the model energy, leading to inaccurate segmentation. Both problems need to be addressed before the image edges can be extracted. We applied morphological operators to remove small features and noise while preserving strong edges (see [19]).

The non rigid segmentation algorithm requires that the model be initialized close to the targeted object, in this case the mouse heart. Various solutions have been proposed to solve this problem. A fully automatic approach can be used, optimizing an affine transformation to match two criteria: distance to the closest edge, and appearance. In [10], the Powell optimization method is used to minimize the resulting energy. Results can be further improved by repeating the Powell optimization with several random initializations and keeping the result with the lowest energy, thus reducing the risk of falling into a local minimum.

The fully automated method was found to yield generally good results, however it is not always robust. In order to give more reproducible results, a semi-automatic approach was preferred here. In this approach, a medical expert selects several fiducial points located on the heart contours, both on the heart model and in the acquired images. This information is used to compute the best affine registration using a least squares approach. Registration can be further refined by adding a thin-plate spline registration step with the same fiducial points. More details on this process can be found in [20].

7.3 Results

Four 4D MRI sequences corresponding to 4 different mice were processed using our method. The model parameters were set to: Young modulus of 10 Pa for the

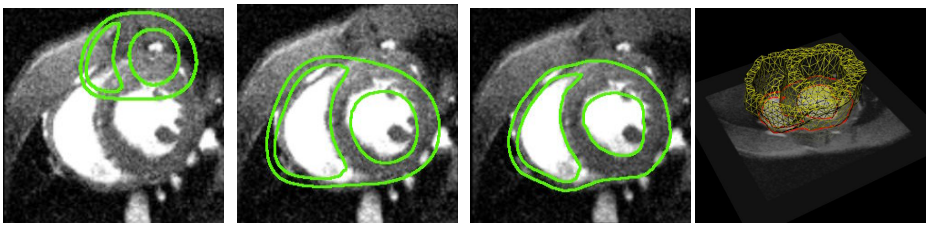

(a) (b) (c) (d)

Fig. 2. Segmentation of 3D mouse MR data : (a) Initial positioning of the DET model, (b) Result of affine positioning, (c) Segmentation result, and (d) 3D mesh obtained as a result of the segmentation process

LV and 40 Pa for the right ventricle (RV), and a Poisson coefficient of 0.485 for the whole model. Figure 2 illustrates the 3D segmentation process. Results show that although we are still experiencing a few specific problems, our method is able to correctly locate the heart borders in the images.

7.4 Segmentation over the Cardiac Cycle

Segmentation tracking of the heart is achieved by taking the segmentation result at the present time frame as the initial solution for the next time frame, and repeating the process for all the times frames in the MRI sequence. Once the 3D contours have been extracted, it is straightforward to compute the enclosed ventricle volumes. The overall volume variation pattern is coherent. However, localized problems persist during early diastole. These problems may be tackled by incorporating temporal constraints for the tracking of the heart shape over time.

8 Discussion and Conclusions

This article presents the non linear deformable elastic template model for the segmentation of soft structures in image sequences. One striking feature of this model is that convergence results for the incremental method, which is used to approximate a solution for a 3D nonlinear elastic template under successive forces, are available. This sets a convenient framework for the segmentation of soft structures in 3D and 3D+time images.

The proposed model has been experimented here for the segmentation of MR image sequences of mouse hearts.The proposed method was able to retrieve the heart contours in most cases, allowing the computation of volume variation curves. However, manual interactions and corrections of the results would still be needed to use the method routinely. Remaining problems include inaccuracies in the segmentation of the pericardium due to the presence of numerous anatomical structures close to the heart, and localized errors during the early diastolic phase due to motion artifacts.

Note that for the segmentation over a cardiac cycle, progressive segmentation (see section 7.4) was used. It would be interesting to include a temporal constraint in the model by introducing non stationary equations for the segmentation over the cardiac cycle. Larger scale experiments, including quantitative evaluation of the segmentation accuracy is also be needed to fully validate the method.

Acknowledgments. We thank Prof. M. Schatzman for interesting discussions and her constant support. We are also very grateful to B. Hiba and M. Janier for providing the MR images of the mice. The Région Rhônes-Alpes is gratefully acknowledged for its support through the project PP3-I3M of the cluster ISLE. This work is partially funded by the french ACI-AGIR project (http://www.aci-agir.org/).

References

1. Veress, AI., Gullberg, GT., Weiss, JA.: Measurement of strain in the left ventricle during diastole with cine-MRI and deformable image registration. J Biomech Eng 7(127), 207–1195 (2005)
2. Borgefors, G.: Distance transformation in digital images. Computer Vision Graphics and Image Processing 48, 344–371 (1986)
3. Borouchaki, H., George, P.L.: Triangulation de Delaunay et métrique riemannienne. Applications aux maillages éléments finis. Rev. Européenne Élém. Finis 5(3), 323–340 (1996)
4. Canny, J.F.: A computational approach to edge detection. IEEE Transactions on Pattern Analysis and Machine Intelligence 8, 679–698 (1986)
5. Ciarlet, P.G.: Mathematical elasticity. Vol. I. In: Studies in Mathematics and its Applications, vol. 20, North-Holland Publishing Co., Amsterdam (1988)
6. Frangi, A.F., Rueckert, D., Schnabel, J.A., Niessen, W.J.: Automatic construction of multiple-object three-dimensional statistical shape models. IEEE Transactions on Medical Imaging 21(9), 1151–1166 (2002)
7. Kaus, M.R., von Berg, J., Weese, J., Niessen, W., Pekar, V.: Automated segmentation of the left ventricle in cardiac MRI. Medical Image Analysis 8, 245–254 (2004)
8. Klein, G.J., Huesman, R.H.: Four-dimensional processing of deformable cardiac PET data. Medical Image Analysis 6, 29–46 (2002)
9. Lötjönen, J., Kivistö, S., Koikkalainen, J., Smutek, D., Lauerma, K.: Statistical shape model of atria, ventricles and epicardium from short- and long-axis MR images. Medical Image Analysis 8, 371–386 (2004)
10. Mäkelä, T., Pham, Q.C., Clarysse, P., Nenonen, J., Lötjönen, J., Sipilä, O., Hänninen, H., Lauerma, K., Knuuti, J., Katila, T., Magnin, I.E.: A 3-D model-based registration approach for the PET, MR and MCG cardiac data fusion. Medical Image Analysis 7, 377–389 (2003)
11. Mitchell, S.C., Bosch, J.G., Lelieveldt, B.P.F., van der Geest, R.J., Reiber, J.H.C., Sonka, M.: 3D active appearance models: segmentation of cardiac MR and ultrasound images. IEEE Transactions on Medical Imaging 21(9), 1167–1178 (2002)
12. Montagnat, J., Delingette, H.: A review of deformable surfaces: topology, geometry and deformation. Image and Vision Computing 19(14), 1023–1040 (2001)

13. Osher, S., Sethian, J.A.: Fronts propagating with curvature-dependent speed: algorithms based on hamilton-jacobi formulations. J. Comput. Phys. 79(1), 12–49 (1988)
14. Pham, Q.-C., Vincent, F., Clarysse, P., Croisille, P., Magnin, I.E.: A FEM-based deformable model for the 3D segmentation and tracking of the heart in cardiac MRI. In: 2nd International Symposium on Image and Signal Processing and Analysis (ISPA 2001), vol. 1, pp. 250–254, Pula, Croatia (2001)
15. Picq, M., Pousin, J., Rouchdy, Y.: A Linear 3D Elastic Segmentation Model for Vector Fields. Application to the Heart segmentation in MRI. To be published in Journal of Mathematical Imaging and Vision (2007)
16. Rabbitt, R., Weiss, J., Christensen, G.: Mapping of hyper-elastic deformable templates using the finite element method. In: Kučera, L. (ed.) WG 2002, LNCS vol. 2573, pp. 252–265. Springer, Heidelberg (2002)
17. Rouchdy, Y., Pousin, J., Schaerer, J., Clarysse, P.: A nonlinear elastic deformable template for soft structure segmentation. Application to the heart segmentation in MRI. Accepted in Inverse Problems (2007)
18. Saito, T., Toriwaki, T.I.: New algorithm for euclidean distance transformation of an n-dimensional digitized picture with applications. Pattern recognition 27, 1551–1565 (1994)
19. Schaerer, J., Rouchdy, Y., Clarysse, P., Hiba, B., Croisille, P., Pousin, J., Magnin, I.E.: Simultaneous segmentation of the left and right heart ventricles in 3D cine MR images of small animals. In: Proceedings of Computers in Cardiology, pp. 231–234, Lyon (2005)
20. Schaerer, J., Qian, Z., Clarysse, P., Metaxas, D., Axel, L., Magnin, I.E.: Fast and automated creation of patient-specific 3d heart models from tagged mri. In: Larsen, R., Nielsen, M., Sporring, J. (eds.) MICCAI 2006. LNCS, vol. 4190, Springer, Heidelberg (2006)
21. Xu, C., Prince, J.L.: Snakes, shapes and gradient vector flow. IEEE Trans. Image Processing 7, 359–369 (1998)

Automated Segmentation of the Left Ventricle Including Papillary Muscles in Cardiac Magnetic Resonance Images

R. El Berbari[1,2,3], I. Bloch[3], A. Redheuil[4], E.D. Angelini[3], E. Mousseaux[4], F. Frouin[1,2], and A. Herment[1,2]

[1] INSERM U678, F-75013 Paris, France
[2] Université Pierre Marie Curie, F-75013 Paris, France
[3] GET, ENST TSI Department, CNRS UMR 5141, F-75013 Paris, France
[4] APHP, HEGP Department of Cardiovascular Radiology, F-75015 Paris, France

Abstract. A novel approach to segment cardiac magnetic resonance (CMR) images is presented in order to overcome some challenges such as problems with papillary muscles and the non homogeneities of the cavity due to blood flow. It consists in filtering short axis CMR images, using connected operators (area-open and area-close filters) to homogenize the cavity, prior to the segmentation which is performed using GVF-Snake algorithm in two steps. Validation was performed on thirty-nine slices by comparing resulting segmentation to the manual contours traced by an expert. This comparison showed good results with an overall average similarity area of 90.7% and an average distance between the two contours of 0.6 pixel.

1 Introduction

Cardiac magnetic resonance imaging is one of the essential non invasive modalities for the diagnosis of cardiovascular diseases. Left ventricle performance is a primary indicator for the diagnosis and treatment of many heart diseases. It has been proven that its dysfunction after myocardial infarction is not necessarily an irreversible process. Clinically, the distinction between reversible and irreversible injury within the risk region is important in the follow-up of the patient in order to select the appropriate course of action following an ischemic event. Recent studies [1,2] have shown that CMR delayed enhancement (DE) images acquired 15 to 20 minutes after the injection of a contrast agent, such as chelate of gadolinium, allow the clinician to detect and localize nonviable areas which are characterized by hyper-enhanced signal [1]. Moreover, differentiating between the left ventricle cavity and the infarcted area in a DE image raises a major difficulty, owing to the fact that blood and the infarcted zone have almost the same gray level intensity. Different algorithms for quantifying infarcted myocardium [3] were applied using manual traced contours.

In an earlier work [4] our group explored the idea of segmenting cine images because of their high contrast between cavity and myocardium and using this segmentation to evaluate myocardial infarct transmurality on DE images. This

F.B. Sachse and G. Seemann (Eds.): FIMH 2007, LNCS 4466, pp. 453–462, 2007.

feasibility study has shown encouraging results. Here we intend to pursue this idea and improve the segmentation step making it more robust and automatic.

Numerous cardiac segmentation methods have been developed and used to estimate the myocardial boundaries. A registration based model was used in [5] and a clustering technique in [6]. However including the papillary muscles within the endocardial delineation remains a limitation. Techniques using prior knowledge learned from images models [7] force the act of including or excluding papillary muscles in the endocardial surface. So results obtained from these techniques depend on the model. Deformable models have also been used widely in segmenting cardiac images [11,12,13,14,15]. Although the active contour models have been quite successful in the segmentation of the myocardium boundaries using CMR images, they still suffer from problems associated with flow related signal loss and lack of clear delineation between the myocardium and adjacent anatomic structures such as papillary muscles besides problems due to initialization sensibility.

The aim of this study is to develop a method for accurate detection of the endocardium in CMR images. For this purpose a combination of a number of image processing techniques from the field of filtering and segmentation are used and extended to create a segmentation pipeline that would reduce the need for manual correction.

First the image undergoes a filtering step described in Section 2.3. GVF snake algorithm (Section 2.4) is then used to detect the endocardium. In Section 2.5, the two main steps of the segmentation procedure are described. Then the evaluation (Section 2.6) is performed comparing the obtained segmentation with manual contours drawn by an expert. Finally segmentation results are presented in Section 3, and discussed in Section 4.

2 Materials and Methods

2.1 Data Acquisition and Description

The CMR data were acquired at the European Hospital Georges Pompidou (HEGP), in the cardiovascular section, service of radiology. All studies were performed with the same 1.5-T MRI system (Signa LX, General Electric Medical Systems, Waukesha, WI, USA), using a thoracic phased-array surface coil for radiofrequency signal detection. After the injection of a first amount of the contrast agent (gadolinium, Gd-DTPA) using 1.5 times the conventional dose, the first pass perfusion study was acquired. Five minutes later 0.5 times the dose was injected and cine images were acquired using an electrocardiogram and respiration gated FIESTA (fast imaging employing steady state acquisition) sequence. DE images were acquired 15-20 minutes after the first injection. Cine images were acquired in short axis view at the basal, middle and apical levels of the left ventricle with the following parameters: flip angle 40°, TE 2 ms, TR 5 ms, slice thickness 8 mm, space between slices 12 mm, time resolution 60 ms.

Thirteen subjects were studied: five patients with a cine acquisition before the gadolinium injection and eight patients after the injection.

Figure 1(a) shows a cardiac image at the apical level with a non homogenous cavity inducing the presence of small gradients that present difficulties for the segmentation, image (*b*) shows a case with the papillary muscles totally included in the cavity and in image (*c*) we can see the most difficult case to segment where the papillary muscles are connected to the myocardium.

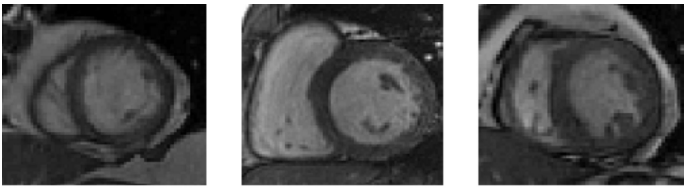

Fig. 1. CMR images, (a) non homogenous cavity, (b) papillary muscles included in the cavity, (c) papillary muscles connected to the myocardium

2.2 Method Overview

The aim of the overall approach is to propose a robust method to extract the Left Ventricle (LV) cavity including the papillary muscles from CMR images. The process is summarized in Figure 2. The first step consists in filtering the original image using alternately area-open and area-close filters (Section 2.3), in order to include the papillary muscles into the cavity and to homogenize it. Using the GVF snake algorithm (Section 2.4), an approximative contour is created from an edge map image obtained by applying the Canny edge detector on the filtered image, with one point clicked in the cavity as initialization. This first segmentation is close to the true contour, but frequently it is interior to it with a distance up to two or three pixels. This approximate contour is then refined in a second step, taking it as snake initialization. This final step allows adjusting the contour and encroaching on details of the cavity's boundary referring to the gradient information in the image to segment.

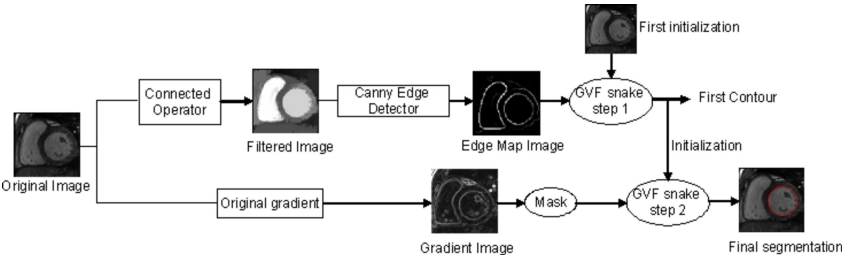

Fig. 2. Overview of the proposed segmentation approach

2.3 Connected Opening and Closing

Methods for segmenting separately the papillary muscles have been proposed in the literature [16]. Here a different approach is proposed where the papillary muscles are handled through a filtering process.

The objective is to produce an image that consists mostly of flat and large regions. A flat zone L_h at level h of a gray scale image I is defined as a connected component of the set of pixels $\{p \in I/g(p) = h\}$ where g is the gray level function. Connected operators like area opening and closing are useful in such cases. The area opening of an image I, with scale parameter λ, is defined as the image containing only connected component of I of area larger than λ. The area closing is defined by duality. In this paper an algorithm developed by Meijster and Wilkinson is used to implement these filters on CMR images.

The filtering algorithm detailed in [17] can be summarized as follows: for each flat zone in the image, an arbitrary element is chosen as root. At the beginning, each pixel p is processed as a singleton set, being its own root. Then a union procedure is called for each pixel $n \in N_p$ where N_p represents the neighborhood of p, to associate a root for sets containing both n and p. Figure 3 shows how to perform an area opening using this algorithm where S_n represents the set containing n and R_n the root of this set. The final step consists of a *resolving* scan which assigns to each root pixel a unique label, and to each non root pixel in a set the label of its root.

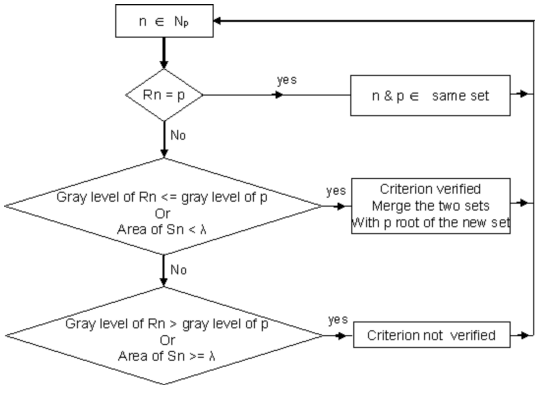

Fig. 3. Union procedure for area-open filter [17]

Figure 4 shows an original CMR image in (a) with respectively its area opening in (b) and then the area closing of the opening image in (c) with a λ value of 800 pixels. It appears that zones constituting the papillary muscles corresponding to sets of low gray level are merged completely with the blood cavity zone corresponding to a high gray level set. In the resulting image all connected components are larger than λ.

Fig. 4. (a) Original image, (b) area opening of the original image, (c) area closing of the opening ($\lambda = 800$ pixels)

2.4 GVF Snake

The original snake model proposed by Kass et al. [8] was modified by Cohen [9] to obtain more stable results and solve the shrinkage problem around strong edges. Then Xu et al. [10] have proposed a new class of external forces called Gradient Vector Flow (GVF) characterized by a non null attraction even far from contours and this to tackle both problems of initialization and poor convergence to boundary concavities. In this paper the GVF model framework is used to segment CMR images. This model is described in details in [10]. A snake is a curve $X(s) = [x(s), y(s)]$, $s \in [0, 1]$, that evolves through the spatial domain of an image in order to verify a force balance equation:

$$F_{int} + F_{ext} = 0$$

$$F_{int} = \alpha X''(s) - \beta X''''(s) \text{ and } F_{ext} = \kappa V(x, y) + \kappa_p P(x, y)$$

where α and β are weighting parameters that control respectively the elasticity of the contour and its rigidity, and $X''(s)$ and $X''''(s)$ denote the second and fourth derivatives of $X(s)$ with respect to s. The external force includes a pressure force P orthogonal to the contour and a Gradient Vector Flow force defined as: $V(x, y) = [u(x, y), v(x, y)]$ that minimizes the energy functional

$$\varepsilon = \int\int \mu_{gvf}(u_x^2 + u_y^2 + v_x^2 + v_y^2) + |\nabla f^2||V - \nabla f|^2 dxdy$$

This formulation produces the effect of keeping V nearly equal to the gradient of the edge map f when it is large, but forcing the field to be slowly-varying in homogenous regions. μ_{gvf} is a regularization parameter governing the tradeoff between the first and second terms in the integrand.

Five parameters control the snake deformations: α for elasticity, β for rigidity, μ_{gvf} for GVF regularization, κ is the external force weight and κ_b the pressure force weight.

2.5 Image Segmentation

First step: Images are cropped to a region of interest around the left ventricle and then filtered using successively area-open and area-close with λ as parameter. For each slice, a series of filtered images corresponding to a set of different

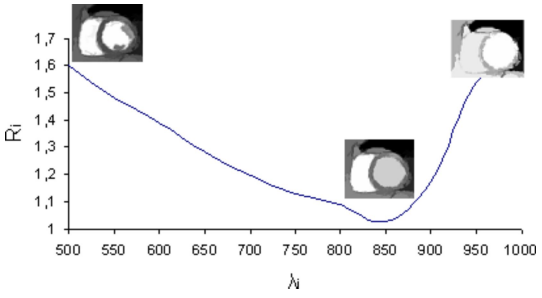

Fig. 5. Plot of the ratio R_i in function of λ

Table 1. Snake Parameters

	α	β	κ	κ_p	μ_{gvf}
first step	1	40	1.6	0.7	0.3
second step	1	1	1.6	0.1	0.1

values of λ is obtained. These values vary from 100 to 600 for apical level slices, and from 500 to 1500 for the two middle and basal slices. A high value of the rigidity parameter β in the first segmentation step (Table 1) is used to obtain a series of approximative contours segmenting the whole cavity including papillary muscles. For each value of λ, a ratio between the area limited by the resulting segmentation and λ is calculated as follow:

$$R_i = \frac{S_i}{\lambda_i} \tag{1}$$

where S represents the cavity surface. The optimal value of λ and so the optimal contour including papillary muscles is chosen so as to have R_i minimum (Figure 5). We should note that this minimum is always close to 1, which means that the segmentation result approximately corresponds to one of the flat zones of the filtered image. This constraint permits an automatic setting of λ which is adapted to the individual patient's morphology.

Second step: The final accurate segmentation is then obtained using the optimal contour as initialization with an edge map obtained by multiplying the gradient of the original image by a mask keeping only information between the first obtained contour and its dilation of three pixels. In this step, low values of β, κ_p and μ_{gvf} (Table 1) are used, allowing to refine the contour according to the original gradient information in the image to segment and to pick up small details on the cavity's boundary (Figure 6).

2.6 Segmentation Evaluation

One of the methods commonly used for assessing the validation of CMR images segmentation is to compare the area of the segmented object in the image against

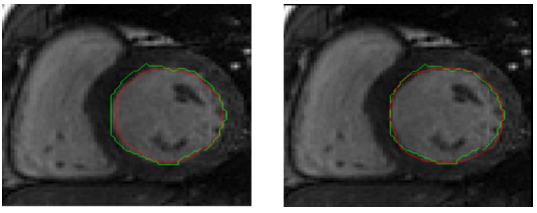

Fig. 6. Left: superposition of the first approximate contour (red) and the manual contour (green). Right: the final segmentation (red) and the manual one (green).

the reference one. Manual contours were assisted by an experienced cardiologist. The area similarity measure S_{area} [11], between the automatic segmentation S_a and the manual one S_m, is defined as the ratio between their common part over the area of the union.

$$S_{area} = \frac{|(S_a \bigcap S_m)|}{|(S_a \bigcup S_m)|} \tag{2}$$

where S_a (respectively S_m) represents the surface limited by the automatic (respectively manual) contour. $|S|$ represents the number of pixels that belong to area S. Besides the area similarity measure, mean and maximum distances (in pixels) between the two contours were calculated to evaluate the obtained segmentation.

3 Results

A total of thirty nine images taken at the end-diastolic (ED) phase of the cardiac cycle, where the images of contraction best correspond to DE images, were analyzed. The whole set of images was processed using the same values of snake parameters (Table 1). The segmentation illustrated in Figure 7 shows good visual results. Figure 8 shows for all analyzed slices the similarity area percentage between manual and automatic contours (a), as well as maximum and mean distance between the two contours (b). Almost all slices show a similarity area percentage higher than 84%, except for the slices number thirty-first and thirty-nine, with values respectively of 75% and 71%. These two slices are at the apical level, and have a very low contrast between the cavity and the myocardium. Figure 9 shows such a case.

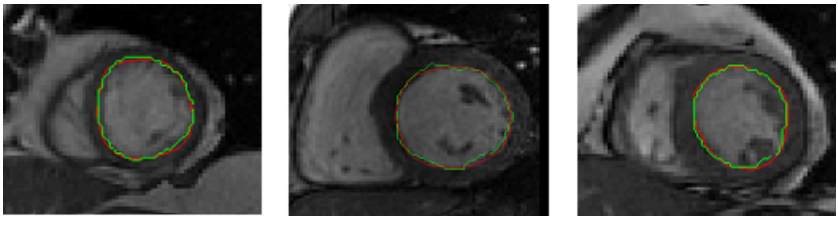

Fig. 7. Superposition of automatic segmentation (red) and manual contour (green)

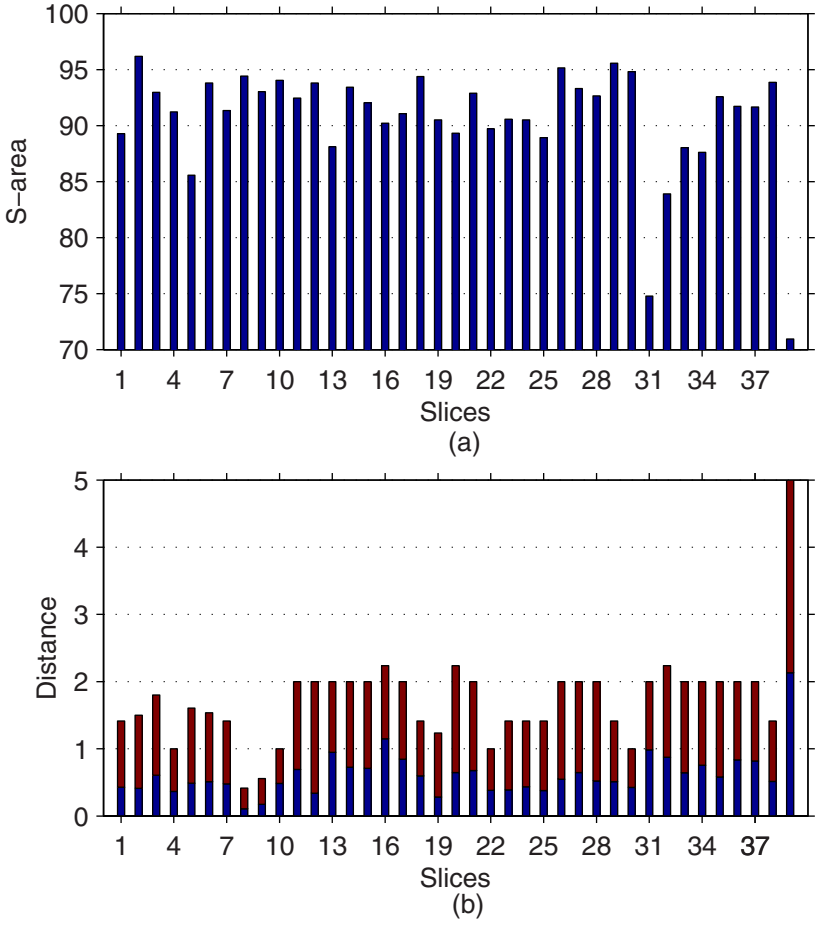

Fig. 8. For each processed image, (a) similarity area percentage, (b) maximum (red) and mean (blue) distance between the two contours

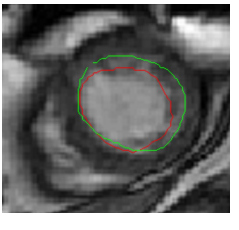

Fig. 9. The segmentation of the thirty-ninth slice with a maximum distance of 5 pixels and a similarity area value of 71%

4 Discussion and Conclusion

In this paper, a 2D segmentation approach for endocardial surface detection in CMR images, robust to papillary muscles and the non homogeneity within the cavity, was proposed. Although new imaging techniques tend toward 3D acquisitions, they still are anisotropic. The processing could be adapted to 3D data taking into account this anisotropic feature but it still encounters a major difficulty related to the gray level variation between different level slices, due to the blood flow. Therefore processing 2D multilevel data seems more appropriate.

Area opening and closing filters depending on gray level connectivity were used to merge gray level zones corresponding to papillary muscles into the cavity. Setting the morphological parameter λ was done automatically in such a way that it is adapted to the individual patient's morphology. Applying a GVF snake algorithm to filtered images provided a rough contour in the first step that was refined in the second one according to the gradient information of the original image. An accurate segmentation of the cavity including the papillary muscles is thus obtained. An important issue in the segmentation concerns the parameters setting. In this work snake parameters were optimized and fixed at the same values for all analyzed images. Setting the initialization was simply done by clicking one point in the cavity, getting through the susceptibility of snake to initialization. Therefore, applying this method to a clinical data set was convenient and not complicated.

For evaluation, similarity area measures and distances between the resulting segmentation and a manual tracing were computed (Figure 8). Segmentation results exhibit very good agreement with the manual traced contours, with an overall average value of $90.7\% \pm 5\%$ for the area similarity and 0.6 ± 0.3 pixel corresponding to 0.88 ± 0.44 mm for the mean distance between the two contours, to be compared with 1.28 ± 0.28 mm obtained by [7].

Most of the cine images acquisitions in this study were taken after the injection of the gadolinium contrast agent. This acquisition protocol aims to decrease the total time of examination but it also reduces the contrast between the myocardium and the cavity. Unfortunately this contrast is important for achieving a good segmentation method. Although the proposed method deals with this problem in some cases, the algorithm can be misled by some myocardium pixels with high gray level that were considered as pixels belonging to the cavity.

For future work, segmenting the epicardial surface will be the next step, in order to have a myocardium segmentation useful to quantify myocardial infarcted areas on DE images. Another important topic is to extend this method to segment the right ventricle, where first tests have shown encouraging results.

References

1. Gerber, BL., Garot, J., Bluemke, DA, Wu, KC., Lima, JA.: Accuracy of contrast-enhanced magnetic resonance imaging in predicting improvement of regional myocardial function in patients after acute myocardial infarction. Circulation 106, 1083–1089 (2002)

2. Beek, AM., Kuhl, HP., Bondarenko, O., Twisk, JW., Hofman, MB., van Dockum, WG., Visser, CA., van Rossum, AC.: Delayed contrast-enhanced magnetic resonance imaging for the prediction of regional functional improvement after acute myocardial infarction. J. Am. Coll Cardiol 42, 902–904 (2003)
3. Hsu, LY., Natanzon, A., Kellman, P., Hirsch, GA., Aletras, AH., Arai, AE.: Quantitative myocardial infarction on delayed enhancement MRI. Part I: Animal validation of an automated feature analysis and combined thresholding infarct sizing algorithm. J. Magn Reson Imaging 23, 298–308 (2006)
4. El Berbari, R., Kachenoura, N., Redheuil, A., Bloch, I., Mousseaux, E., Frouin, F.: Using cine MR images to evaluate myocardial infarct transmurality on delayed enhancement images. IEEE International Symposium on Biomedical Imaging: From Nano to Macro pp. 145–148 (2006)
5. Noble, NMI., Hill, DLG., Breeuwer, M., Schnabel, J., Hawkes, D., Gerritsen, FA., Razavi, R.: Myocardial delineation via registration in a polar coordinate system. In: Dohi, T., Kikinis, R. (eds.) MICCAI 2002. LNCS, vol. 2488, pp. 651–658. Springer, Heidelberg (2002)
6. Lynch, M., Ghita, O., Whelam, PF.: Automatic segmentation of the left ventricle cavity and myocardium in MRI data. Comput Biol Med. 36, 389–407 (2006)
7. Kauss, M., Berg, JV., Niessen, W., Pekar, V.: Automated segmentation of the left ventricle in cardiac MRI. In: Ellis, R.E., Peters, T.M. (eds.) MICCAI 2003. LNCS, vol. 2878, pp. 432–439. Springer, Heidelberg (2003)
8. Kass, M., Witkin, A., Terzopoulos, D.: Snakes: Active contour models. Int. J. Comput Vis. 1, 321–331 (1988)
9. Cohen, LD.: On active contours models and balloons. CVGIP Image Understanding 53, 211–221 (1991)
10. Xu, C., Prince, JL.: Snakes, Shapes, and Gradient Vector Flow. IEEE Trans Med. Imag 7, 359–369 (1998)
11. Pluempitiwiriyawej, C., Moura, JM., Fellow, Wu YJ., Ho, C.: STACS: new active contour scheme for cardiac MR image segmentation. IEEE Trans Med. Imag 24, 593–603 (2005)
12. Graves, MJ., Berry, E., Eng, AA., Westhead, M., Black, RT., Beacock, DJ., Kelly, S., Niemi, P.: A multicenter validation of an active contour-based left ventricular analysis technique. J. Magn Reson Imaging 12, 232–239 (2000)
13. de Garcia, MM.P., Malpica, N., Ledesma-Carbayo, MJ., Jiménez-Borreguero, LJ., Santos, A.: Semi automatic estimation and visualization of left ventricle volumes in cardiac MRI. Computers in Cardiology 32, 399–402 (2005)
14. Tanki, N., Murase, K., Kumashiro, M., Momoi, R., Yang, X., Tabuchi, T., Nagayama, M., Watanabe, Y.: Quantification of left ventricular volumes from cardiac cine MRI using active contour model combined with gradient vector flow. Magn Reson Med. Sci. 4, 191–196 (2005)
15. Jolly, MP.: Automatic segmentation of the left ventricle in cardiac MRI and CT images. Int. J. Comput Vis. 70, 151–163 (2006)
16. Spreeuwers, LJ., Bangma, SJ., Meerwaldt, RJHW., Vonken, EJ., Breeuwer, M.: Detection of trabeculae and papillary muscles in cardiac MR images. Computers in Cardiology 32, 415–418 (2005)
17. Meijster, A., Wilkinson, MHF.: A comparison of algorithms for connected Set Openings and Closings. IEEE Trans Patt Anal Mach Intell 24, 484–494 (2002)

Simulation of 3D Ultrasound with a Realistic Electro-mechanical Model of the Heart

Q. Duan[1], P. Moireau[2], E.D. Angelini[3], D. Chapelle[2], and A.F. Laine[1]

[1] Dpt. of Biomedical Eng., Columbia University, NY, USA
[2] Project MACS, INRIA-Rocquencourt, France
[3] Dpt. TSI, GET-Ecole Nationale Supérieure des Télécommunications, LTCI CNRS-UMR 5141, France

Abstract. This paper presents a first set of experiments to integrate a realistic electro-mechanical model of a beating heart into simulated real-time three-dimensional (RT3D) ultrasound data. A novel ultrasound simulation framework is presented, extended from the model of Meunier [12]. True three-dimensional transducer modeling was performed, using RT3D acquisition design. Myocardium and blood scattering parameters were defined in three dimensions. Ultrasound data sets were generated for a normal case and a pathological case, simulating left bundle branch block. Accuracy of an optical flow tracking method was evaluated on the simulated data to measure displacements on the myocardial surfaces and inside the myocardium over a cardiac cycle. The proposed simulation framework has important motivations in a cardiac modeling context as part of this project is focused on the design of effective parameter estimation methods, based on cardiac imaging.

1 Introduction

Ultrasound is the cardiac screening modality with the highest temporal resolution, but is still limited to two-dimensions in most hospitals and clinical centers. Development of 3D echocardiography started in the 1990s [23], with real-time 3D (RT3D) ultrasound based on matrix phased arrays. A new generation of RT3D transducers was introduced by Duke University and more recently by Philips Medical Systems (Best, The Netherlands) with the SONOS 7500 transducer followed by the IE33 model that acquires a fully sampled cardiac volume within four cardiac cycles. This technical advance increased the spatial resolution and image quality, which makes 3D ultrasound techniques increasingly attractive for quantitative cardiac diagnosis on patients [2,1]. Since RT3D ultrasound acquires volumetric ultrasound sequences with fairly high temporal resolution using a fixed-positioned transducer, it can capture complex 3D cardiac motion very well. Cardiac motion analysis from clinical image sequences has been an active research area over the past decade. Previous efforts using ultrasound data for motion analysis include intensity-based speckle tracking and optical flow (OF), or dedicated imaging set ups such as strain-imaging, and elastography. In [16] for example, a shape tracking approach was used to track endocardial surface

F.B. Sachse and G. Seemann (Eds.): FIMH 2007, LNCS 4466, pp. 463–473, 2007.

patches in 3D echocardiography for motion analysis. In a previous study [8,7] we developed a framework to derive several dynamic cardiac measures based on four-dimensional optical flow using RT3D ultrasound sequences. This framework was applied to a clinical data set from a heart transplant patient and the dynamic measurements, computed with this method, agreed with findings in other cardiac biomechanics studies.

In this paper, in order to quantitatively evaluate our tracking method, we present a framework to generate 3D simulated ultrasound data using a realistic electro-mechanical model of a human heart, namely, a model that generates displacement and deformation patterns – as well as global physiological indicators such as pressures and flows – representative of clinical observations. A numerical cardiac phantom was used to mimic realistic anatomy, along with acoustic impedance of cardiac tissue and blood, as well as motion field of the myocardium during a cardiac cycle. Based on this phantom, simulated linear three-dimensional ultrasound data sets were generated, using similar transducer parameters as in the RT3D ultrasound machine from Volumetrics (Durham, NC). Details of the 3D ultrasound simulation framework as well as performance of our optical flow based method in tracking myocardial tissues were explored by simulating consecutive RT3D ultrasound frames of the beating heart under known motion fields, including translation, rotation, and thickening deformations. Our approach also has important motivations in a cardiac modeling context. Indeed, part of this project is focused on the design of effective parameter estimation methods – relevant for diagnosis assistance – based on clinical measures and simulations from a mathematical model of the beating heart [17,21]. Difficulties encountered in such estimation fall into two main categories:

- Modeling difficulties, namely, the mathematical model must accurately represent actual phenomena observed in clinical measurements and reflect pathologies of interest targeted in a diagnosis assistance setup; and
- Estimation difficulties, namely, the parameter estimation procedure *per se* must be carefully designed in order to be effective when the model is adequate, taking into account the presence of measurement errors.

Therefore, when focusing on the design of a parameter estimation strategy for a given class of models, one crucial step consists in generating synthetic measurements from the model for a specific choice of parameters. Indeed, by doing so we can circumvent modeling difficulties. The parameter estimation procedure is then assessed by processing these synthetic measurements, combined with well-chosen measurement noise components, and extracting modeling parameters to be compared with the initial values. Of course, for this assessment to be meaningful, the generation of synthetic measurements must be carefully designed, close to physiological conditions, while the processing of these measurements must take into account the constraints and uncertainties associated with a given modality of observation (e.g. cardiac imaging). In this context, this paper presents a first series of experimentation integrating our cardiac model into 3D echocardiographic data sets.

2 Electro-mechanical Model of the Heart

2.1 Heart Anatomy

We use the "Generic Anatomical Heart Model" presented in [21], which approximates the ventricles by truncated ellipsoids This generic model could be adapted to specific patient anatomies by fitting the model geometry to medical image segmentation results – in particular when pursuing the above-mentioned estimation and diagnosis goal – but this was not needed for the present study.

2.2 Bio-physical Properties of the Model

The electro-mechanical model employed to generate realistic deformation patterns of the heart during a complete cycle was fully described in [17]. The underlying contraction law is based on physiological considerations and satisfies essential thermo-mechanical requirements. This law incorporates contractility parameters that can be varied to simulate cardiac pathologies such as infarcts. Electrical activation is modeled based on the bidomain equations [15], with action potential propagation initiated near the apex on the endocardial surface. Blood inside each ventricle is modeled as a simplified lumped pressure / volume system, and cardiac cycle phases are distinguished through coupling conditions between the internal fluid and the different compartments of the cardiovascular system – in particular systemic and pulmonary circulations, both represented with Windkessel models. Numerical methods – including finite element procedures – used to obtain simulations of this global heart model were also described in [17]. Simulation results are illustrated in Fig.1, where we compared simulation of a normal heart (our reference) with results corresponding to a left bundle branch block (LBBB) modeled via initiation of the electrical activation in the right ventricle only.

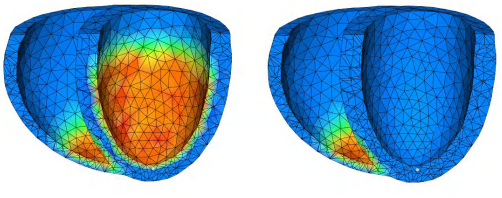

Fig. 1. Electrical activation at early stage: Reference (left) and LBBB (right)

2.3 Motion Field Generation and Format

We used several numerical simulation results with the model described above to generate rasterized 3D images of the cardiac tissue over a complete cycle, with a spatial sampling of 1 mm^3 and a temporal sampling of 5 ms, comparable to 3D echography sampling capabilities. We recall that the rasterization of an

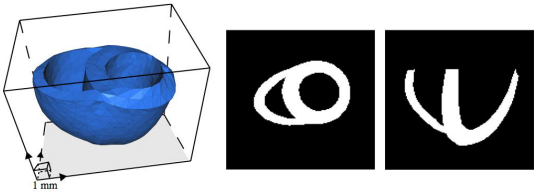

Fig. 2. Myocardial mesh and corresponding rasterization during systole

object consists in computing the set of voxels enclosed within the object boundaries. The algorithm used is described in [20], see also [4]. In Fig. 2, we show cross-section views of these images during systole. The 3D ultrasound simulation procedure takes these images as an input, and optical flow tracking results can then be assessed using the reference values of the displacements between two subsequent images, whose exact values can be obtained for each voxel by simple post-processing of the model simulations.

The physics of ultrasound imaging being rather well-known, accurate simulations of the measurements can be obtained, including for 3D echography [9]. Hence, the remaining key point in the assessment of estimation procedures concerns the processing step leading to data used as an input in the estimation, such as the optical flow that provides displacements or velocities, for which the corresponding errors must be accurately determined.

3 3D Ultrasound Simulation

3.1 Review of Existing Methods

Simulating ultrasonic B-scanning images can be dated back to 1980 [3]. In their paper, Bamber et al. modeled the ultrasonic image formation process in the far–field as a convolution of the point spread function from the transducer and the scattered distribution of underlining tissues defined by local density and compressibility.

Several studies have been performed since then, with more or less elaborate models. In [14], Narayanan et al. used a very simple simulation framework for transmitted pulses and received echo signals to study the influence of the scattering cross-section and the number of scatterers per cells on the envelope signal statistics. Their model was derived from the extensive review of first and second order statistics of complex random signals from Wagner et al. [27]. Proposing to model the scattering cross-section as a Gamma random variable, and setting the number of scatterers to 7, 13 and 38 they showed strong deviation from a Rayleigh distribution as randomness of the cross sections increased and number of scatterers decreased.

In the field of specific cardiac applications, a study of reference in [5] demonstrated that the K-distribution is generally more appropriate than the Rayleigh distribution to simulate backscatters from myocardial tissue in the frequency

range of 5-15 MHz. The K-distribution is generated by a sparse density of Poisson scatterers (average number of scatterers per resolution cell ρ between 9 and 12), whereas the Rayleigh distribution is generated by a dense distribution of Poisson scatterers (ρ above 12) [25,5].

In a seminal paper [12], Meunier and Bertrand proposed a three-dimensional inhomogeneous continuum model to mimic myocardial tissue as a collection of acoustic cells with individual impedance. Their work was motivated by the need to understand mean gray level changes occurring with different tissue motions. An important assumption was made in their work, assuming small and dense scatterers per resolution cells, leading to Rayleigh distributed amplitudes of the envelope signals. In [13], the same authors looked at the problem of decorrelation between tissue and speckle patterns under linear transformations (2D rotation, translation and deformation). They identified threshold values of deformation amplitudes to guarantee visual correlation of backscattered patterns between two consecutive ultrasound frames.

Jensen [9] developed an extensive ultrasound simulation software called FIELD in 1996 based on Tupholme-Stepanishen's method, which simulates acoustic fields generated from arbitrarily designed transducers. Modeling is based on the numerical computation of a transmit excitation function (e.g. sine wave with Gaussian envelope) with the spatial impulse response of the transducer, which is the sum of small individual array elements, organized according to a pre-defined geometry.

A 3D extension of the model,generating 3D ultrasound image volume can also be simulated, as shown in [11] and [30] most recently.

Regarding the three-dimensional aspect of the ultrasound simulation problem, a first approach was proposed by [18] to simulate acoustic fields generated by phased array transducers, with waves propagating in a uniformly lossy media. Their approach was based on a double integral of the Huygens-Fresnel equations to describe the spatial behavior of the wave front pressure in the acoustic field, generated from a matrix of transducers. Later, with the introduction of the Volumetrics RT3D transducer from Smith and Von Ramm, several papers [22,29,28] were published, performing similar simulations for different geometrical designs of the transducer matrix.

3.2 Proposed Simulation Framework

In this section, we propose a 3D ultrasound simulation framework, based on the extension of Meunier et al. approach [12] in 3D. This model assumes that the point spread function (PSF) $H(x, y, z)$ of the transducer is linear and position-independent, leading to formation of the radio-frequency (RF) signal $RF(x, y, z)$ via convolution of the system PSF with the impulse response $T(x, y, z)$ of the tissue:

$$RF(x, y, z) = H(x, y, z) * T(x, y, z) \tag{1}$$

3.3 Image Formation Model

The far–field PSF was approximated by a cosine function combined with a 3-D Gaussian envelope:

$$H(x,y,z) = exp\left(-\frac{1}{2}\left(\frac{x^2}{s_x^2}+\frac{y^2}{s_y^2}+\frac{z^2}{s_z^2}\right)\right) cos\,(2\pi f z) \tag{2}$$

where (s_x^2, s_y^2, s_z^2) define the size of the PSF in lateral, elevation and axial directions, respectively, and f defines the transducer spatial frequency. This model assumes that time gain compensation was applied to correct for depth-dependent attenuation of the echos. It is also important to note that this model neglects several points: multiple scattering, multiple simultaneous interrogating directions, dispersion and attenuation phenomena and velocity variations.

3.4 Scattering Modeling of the Tissues

The tissue function $T(x,y,z)$ represents the scattering structure of the medium and can be related to the continuum tissue structure via the Laplacian operator applied to the compressibility distribution $B(x,y,z)$: $T(x,y,z) = \Delta\,(B(x,y,z))$. Bamber and Dickinson in [3] proposed the following function $T(x,y,z)$ describing tissue echogeneity of a weakly inhomogeneous continuum in the far–field of an ultrasound beam, formed by plane-waves propagating in the z-direction:

$$T(x,y,z) = \frac{1}{4}\frac{\partial^2}{z^2}\left(\frac{\rho(x,y,z)}{\rho_0} - \frac{\beta(x,y,z)}{\beta_0}\right) \tag{3}$$

where ρ and β are the density and compressibility functions, with reference values ρ_0 and β_0. Seggie suggested in [19] to modify this model and replace the *compressibility* distribution with an *impedance* distribution $Z_{3D}(x,y,z)$, arguing that for weak scattering, backscattering are mainly due to fluctuation in impedance. Pursuing this approach, Meunier et al. [12] proposed to model the impedance function with a common kernel function $C(x,y,z)$ and a "echogeneity" parameter a_n, which is proportional to the number of scatterers in a pixel:

$$T(x,y,z) = \frac{\partial^2}{z^2} Z_{3D}(x,y,z), \quad Z_{3D}(x,y,z) = \sum_n Z_n(x,y,z),$$
$$Z_n(x,y,z) = a_n\; C_{3D}(x-x_n, y-y_n, z-z_n)$$
$$C_{3D}(x,y,z) = \exp\left(\frac{-1}{2}\left(\frac{x^2}{\sigma_x^2}+\frac{y^2}{\sigma_y^2}+\frac{z^2}{\sigma_z^2}\right)\right)$$

The parameters $(\sigma_x, \sigma_y, \sigma_z)$ model the tissue cell dimensions and control the modeling of tissue anisotropy while a_n controls the modeling of scatterer density within scanned pixels, which depends on both the transducer and the tissue. Because of important undersampling in the receiving mode of RT3D ultrasound

transducers, assumption of large scatterers density (above 5 per pixel) can certainly be made in our simulation framework, leading to typical Rayleigh distributed RF signals as discussed in [12].

3.5 Model Simplification

In a 2D simulation framework, assuming that the diffraction angle in the elevation direction y (i.e. the slice thickness) is very small, Meunier et al. in [12] further separated the transducer PSF in separated components $H(x, y, z) = H(x, z) \times H(y)$. Combined with the approximation of the tissue function as the 2D derivative, in the axial direction, of a 3D tissue function, they obtained a 2D RF image formation model in the image plane (x, z). In this work, we did not use typical 2D transducer parameters to set our acquisition parameters for a RT3D transducer, as done in previous studies. Instead, we used available parameters from the commercial Volumetrics machine from Duke University [26] and estimated unknown parameters from sample RT3D ultrasound data. To approximate the actual image resolution of commercial RT3D ultrasound transducers, we set the PSF parameters to $(1, 2, 0.5)mm$ for Full Width Half Maximum (FWHM) dimensions in axial, lateral, and transverse directions. The corresponding PSF parameters (s_x^2, s_y^2, s_z^2) can be derived using the relationship $FWHM = 2.35 \times standard\ deviation$ as used in [12]. The transducer frequency was set to 3MHz (2.5-3.5 MHz can be used with the Volumetrics transducer). The velocity of the acoustic wave in the human body was set to the standard $1540m/s$ average value.

In medical ultrasound systems, $H(x, y, z)$ is a narrowband signal. In this context, the second order derivative operator in Eq.3 can be discarded since the second derivative of a narrow-band is almost identical to the shape to the sign-reversed signal itself. This assumption is also used to simplify the model in other studies, explicitly in [10] or implicitly in [12,30].

3.6 Myocardium and Blood Cell Kernels Parameters Setting

We chose a 3D Gaussian to model the impedance inhomogeneities as in [12]. Thus, the general cell kernel function was expressed as a Gaussian function with $(\sigma_x, \sigma_y, \sigma_z) = (10, 10, 35)\ \mu m$ given the fact that myocardial cells are elongated with dimensions around $(20, 20, 70)\ \mu m$. Since myocardial cells are tightly connected and the myocardial fibers are parallel to each other at a scale of 100 or 1000 μm, a (1:1:3.5) ratio can be observed at the image pixel scale. Recent studies on 2D or 3D ultrasound simulations only included modeling of the myocardium tissue. Since in actual clinical RT3D echocardiography, both myocardium and blood are imaged, we also built a tissue model for the blood. The average size of the blood cells is about $(10, 10, 2)\ \mu m$. However, since blood cells are not tightly connected to each others and pixel volumes are much larger than individual blood cell volumes, the echogeneity within each blood pixel is mainly determined by the number of cells within each pixel, a random variable with Poisson distribution. We used $a_n = 10\ or\ 30$ to generate two volumes with different contrast between blood and myocardium, as illustrated in Fig. 3. The simulation with the highest density gave more satisfactory visual ultrasound data appearance.

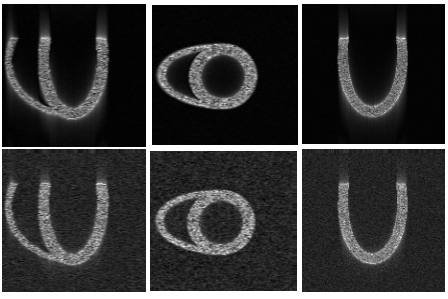

Fig. 3. Orthogonal views of a 3D ultrasound simulated volume of data: (top) low density of scatterers in blood pool, (bottom) high density

4 Results and Discussion

We generated two sets of simulations for the normal and pathological (LBBB) cases, varying the echogeneity parameters of the blood. These simulations provided very realistic volumes of images as illustrated in Fig. 3. We ran our OF tracking algorithm on the simulated dataset with the highest blood density, to compute the displacement vector field $\boldsymbol{u}$ on the endocardial and epicardial surfaces, initialized by the geometry of the first frame of the cardiac model. For computational efficiency, challenged by the very high spatial resolution of the simulated ultrasound data, we downsampled the point density on the myocardial surfaces by $50^{(1/3)}$ in each dimension, tracking about 500 points. Maximum displacement values, from the model, between two consecutive frames was 13 mm and rms angular displacements between consecutive frames between 10 and 75 deg. Accuracy of the motion field on the endocardial surface was computed via magnitude and angular errors over the whole cardiac cycle, as illustrated in Fig. 4. Epicardial tracking errors were very similar.

We also computed displacement maps from the true and estimated motion fields between the first frame (initiation of the depolarization) and end–systole (ES), after projection of the displacement vector field $\boldsymbol{u}$ in a cylindrical coordinate system (r, θ, z), with the z axis oriented along the long axis of the ventricle. In this coordinate system, and using the AHA 16-sectors partition of the LV, we illustrate in Fig. 4 the circumferential component u_θ, the radial component u_r and the twisting $\partial u_\theta / \partial z$ of the displacement vector field $\boldsymbol{u}$ of the myocardium. Computation of these maps required tracking of the endocardial and epicardial surfaces, spatial interpolation of the motion field with radial-basis functions as described in [6] and correction for global translation of the myocardium between the first frame and ES. Note that the twist values, being computed as derivatives, need to be rescaled with respect to the sectorial height for physical values, which averages 20mm. End–diastole corresponded to frame 4 or 5. We observed that maximum error measurements occurred at end-systole (i.e. frame 10). We also observed that specific displacement maps were very similar between the model and the OF estimations on our simulated data. Motion patterns between the

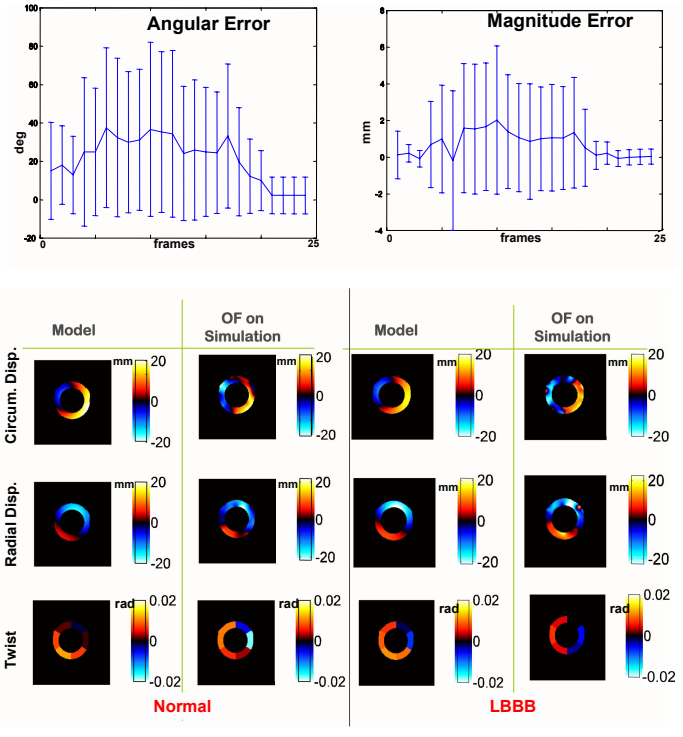

Fig. 4. Evaluation of displacements computed from optical flow (OF) on simulated RT3D ultrasound data: (top) Angular and magnitude error measurements on the endocardial surface. (bottom) Dense myocardial displacement fields from OF tracking of the myocardial surfaces.

normal and disease case were quite similar, as expected, since LBBB only incurs delayed contractions of the LV.

Regarding motion estimation errors, in a recent study, [24], the authors evaluated their OF method on simulated 2D ultrasound B-mode images, with Rayleigh distributions, computed as the modulus of complex RF signals. Motion was simulated on a short-axis like slices, with area-preserving radial displacements and a global translation. The overall velocity was set to a maximum of 2 pixels (versus 13 pixels for us). Results showed accuracy of angular estimates between 2.5° and 5°, depending on the image SNR, and magnitude accuracy between 7% and 10%. We are below such accuracy but we remain within an average error of 2 ± 4 pixels, despite very large displacements between consecutive frames.

5 Conclusions

Additional experiments will be performed to evaluate the accuracy of OF on simulated data and evaluate the precision of OF displacement estimation in additional disease cases, such as LAD, incurring local abnormal contractions.

Regarding data assimilation perspectives, we emphasize that, once the procedure has been validated using synthetic measurements such as described in this paper the remaining difficulties in processing real data will focus on modeling aspects not parameter estimation nor image processing issues.

Acknowledgments. The authors would like to thank M. Alba (INRIA) for his contribution in generating the model simulation outputs.

References

1. Angelini, E., Homma, S., Pearson, G., Holmes, J., Laine, A.: Segmentation of real-time three-dimensional ultrasound for quantification of ventricular function: a clinical study on right and left ventricles. Ultrasound in Medicine and Biology 31(9), 1143–1158 (2005)
2. Angelini, E., Laine, A., Takuma, S., Holmes, J., Homma, S.: LV volume quantification via spatio-temporal analysis of real-time 3D echocardiography. IEEE Transactions on Medical Imaging 20(6), 457–469 (2001)
3. Bamber, J.C., Dickinson, R.J.: Ultrasonic b-scanning: a computer simulation. Physics in Medicne and Biology 25, 463–479 (1980)
4. Bresenham, V.: Algorithm for computer control of a digital plotter. IBM Systems Journal 4(1), 25–30 (1965)
5. Clifford, L., Fitzgerald, P., James, D.: Non-rayleigh first-order statistics of ultrasonic backscatter from normal myocardium. Ultrasound in Medicine and Biology 19(6), 487–495 (1993)
6. Duan, Q., Angelini, E., Gerard, O., Homma, S., Laine, A.: Comparing optical-flow based methods for quantification of myocardial deformations on rt3d ultrasound. In: IEEE International Symposium on Biomedical Imaging, Arlington, VA, USA, pp. 173–176 (2006)
7. Duan, Q., Angelini, E.D., Herz, S.L., Ingrassia, C.M., Gerard, O., Costa, K.D., Holmes, J.W., Laine, A.F.: Dynamic cardiac information from optical flow using four dimensional ultrasound. In: International Conference of the IEEE Engineering in Medicine and Biology Society (EMBS), pp. 4465–4468 (2005)
8. Duan, Q., Angelini, E.D., Herz, S.L., Ingrassia, C.M., Gerard, O., Costa, K.D., Holmes, J.W., Laine, A.F.: Evaluation of optical flow algorithms for tracking endocardial surfaces on three-dimensional ultrasound data. In: SPIE International Symposium, Medical Imaging San Diego, CA, USA (2005)
9. Jensen, J.A.: Field: A program for simulating ultrasound systems. Medical & Biological Engineering & Computing 34(1.1), 351–353 (1996)
10. Kallel, F., Bertrand, M., Meunier, J.: Speckle motion artifact under tissue rotation. IEEE Transactions on Ultrasonics, Ferroelectrics and Frequency Controls 41, 105–122 (1994)
11. Meunier, J.: Tissue motion assessment from 3d echographic speckle tracking. Physics in Medicine and Biology 43, 1241–1254 (1998)
12. Meunier, J., Bertrand, M.: Echographic image mean gray level changes with tissue dynamics: A system-based model study. IEEE Transactions on Biomedical Engineering 42(4), 403–410 (1995)
13. Meunier, J., Bertrand, M.: Ultrasonic texture motion analysis: theory and simulation. IEEE Transactions on Medical Imaging 14(2), 293–300 (1995)

14. Narayanan, V.M., Shankar, P.M., Reid, J.M.: Non-rayleigh statistics of ultrasonic backscattered signals. IEEE Transactions on Ultrasonics, Ferroelectrics and Frequency Control 41(6), 845–852 (1994)
15. Neu, J.C., Krassowska, W.: Homogenization of syncytial tissues. Crit. Rev. Biomed. Eng. 21, 137–199 (1993)
16. Papademetris, X., Sinusas, A.J., Dione, D.P., Duncan, J.S.: Estimation of 3D left ventricular deformation from echocardiography. Medical Image Analysis 8, 285–294 (2004)
17. Sainte-Marie, J., Chapelle, D., Cimrman, R., Sorine, M.: Modeling and estimation of the cardiac electromechanical activity. Computers and Structures 84, 1743–1759 (2006)
18. Sarti, A., Bassi, P., Lamberti, C.: 3D modeling of phased array generated ultrasounds in lossy media. Computerized Medical Imaging and Graphics 17(4–5), 339–343 (1994)
19. Seggie, D.A., Leeman, S., Burge, R.E.: Realistic simulation of b-scan images. In: IEEE Ultrasonics Symposium, pp. 714–717 (1983)
20. Sermesant, M., Forest, C., Pennec, X., Delingette, H., Ayache, N.: Deformable biomechanical models: Application to 4d cardiac image analysis. Medical Image Analysis 7(4), 475–488 (2003)
21. Sermesant, M., Moireau, P., Camara, O., Sainte-Marie, J., Andriantsimiavona, R., Cimrman, R., Hill, D.L., Chapelle, D., Razavi, R.: Cardiac function estimation from mri using a heart model and data assimilation: Advances and difficulties. Medical Image Analysis 10(4), 642–656 (2006)
22. Smith, S.W., Pavy, H.G., Von Ramm, O.T.: High speed ultrasound volumetric imaging system-part I: Transducer design and beam steering. IEEE Transactions on Ultrasonics, Ferroelectrics and Frequency Control 38(2), 100–108 (1991)
23. Smith, S.W., Ramm, O.T.V.: Real time volumetric ultrasound imaging system. Journal of Digital Imaging 3, 261–266 (1990)
24. Suhling, M., Arigovindan, M., Jansen, C., Hunziker, P., Unser, M.: Myocardial motion analysis from b-mode echocardiograms. IEEE Transactions on Image Processing 14, 525–553 (2005)
25. Tuthill, T.A., Sperry, R.H., Parker, K.J.: Deviations from rayleigh statistics in ultrasonic speckle. Ultrasonic Imaging 10(2), 81–89 (1988)
26. Von Ramm, O., Smith, S., Pavy, H.G.: High-speed ultrasound volumetric imaging system part II: parallel processing and image display. IEEE Transactions on Ultrasonics, Ferroelectrics and Frequency Control 38(2), 109–115 (1991)
27. Wagner, R.F., Insana, M.F., Brown, D.G.: Statistical properties of radiofrequency and envelope-detected signals with applications to medical ultrasound. Journal of the Optical Society of America 4, 910–922 (1987)
28. Yen, J.T., Smith, S.W.: Real-time rectilinear volumetric imaging. IEEE Transactions on Ultrasonics, Ferroelectrics and Frequency Control 49(1), 114–124 (2006)
29. Yen, J.T., Steinberg, J.P., Smith, S.W.: Sparse 2D array design for real-time rectilinear volumetric imaging. IEEE Transactions on Ultrasonics, Ferroelectrics and Frequency Control 47(1), 93–110 (2000)
30. Yu, W., Yan, P., Sinusas, A.J., Thiele, K., Duncan, J.S.: Towards pointwise motion tracking in echocardiographic image sequences: Comparing the reliability of different features for speckle tracking. Medical Image Analysis 10, 495–508 (2006)

Automated, Accurate and Fast Segmentation of 4D Cardiac MR Images

Jean Cousty[1], Laurent Najman[1], Michel Couprie[1],
Stéphanie Clément-Guinaudeau[2], Thomas Goissen[2], and Jerôme Garot[2]

[1] Institut Gaspard-Monge, Laboratoire A2SI, Groupe ESIEE, France
{j.cousty,l.najman,m.couprie}@esiee.fr
[2] CHU Henri Mondor, Créteil, France

Abstract. We propose a new automated and fast procedure to segment the left ventricular myocardium in 4D (3D+t) cine-MRI sequences based on discrete mathematical morphology. Thanks to the comparison with manual segmentation performed by two cardiologists, we demonstrate the accuracy of the proposed method. The precision of the ejection fraction and myocardium mass measured from segmentations is also assessed. Furthermore, we show that the proposed 4D procedure maintains the temporal coherency between successive 3D segmentations.

1 Introduction

In cardiology, obtaining precise information on the size and function of the left ventricle (LV) is essential both in clinical applications –diagnosis, prognostic, therapeutic decisions– and in the research fields.

Thanks to 3D images acquired at different times of the heart cycle, Magnetic Resonance (MR) permits a complete morphological LV characterization. The precision on the measures extracted from MR images has been demonstrated to be excellent [1] and MR imagery is a "gold standard" for LV analysis as a result.

However, due to considerable amount of data, the analysis and, in particular, the segmentation of such images is fastidious, time consuming and error-prone for human operators. Automated segmentation of cardiac images has been shown to be a challenging task.

Since the 90's, many approaches for solving this problem have been proposed, notably in the framework of deformable models [2, 3, 4]. From a time series of 3D images of the LV, most existing methods iteratively segment each 3D image independently [5, 6, 7]. Despite a constant improvement in the accuracy of the produced segmentations, the temporal consistency of the resulting segmentations –a desired feature in the case of a time series of 3D images– is not taken into account by these approaches. Only a few methods consider the time series as a whole 4D image. Although it uses a 4-dimensional atlas, the method in [8] independently assigns each pixel to one of the objects and does not take into account global properties (*e.g.* connectedness or presence of holes) relative to the temporal consistency of the produced segmentations. In [9], the authors propose a 4D deformable model with temporal constraints. Despite promising results

F.B. Sachse and G. Seemann (Eds.): FIMH 2007, LNCS 4466, pp. 474–483, 2007.

on synthetic SPECT images, the resulting segmentation scheme was not fully assessed on real cardiac images.

In order to take into account the time continuity in 4D cine-MRI, we investigate a new LV segmentation scheme based on discrete mathematical morphology. This theory [10] consists of analyzing geometrical objects through their interaction with predefined geometrical shapes. The notions of neighborhood and connectivity are the basis of this framework. In particular, operators dedicated to image segmentation are extended to 4-dimensional spaces by defining elementary 4-dimensional neighborhoods.

The main features of the LV segmentation method proposed in this paper are: (*i*), accuracy assessed against manual segmentations performed by two cardiologists; (*ii*), resulting segmentations taking into account temporal consistency; (*iii*), automated and fast; and (*iv*) few parameters whose setting relies on physical and anatomical facts. In this paper, the general idea of the method is described; more details will be provided in a forthcoming extended version.

2 Segmentation Method

Segmentation schemes in mathematical morphology [11] comprise three main steps: recognition, delineation and smoothing. Recognition is the process of determining roughly the whereabouts of the object. Delineation consists in the precise spatial localization of the object borders. Smoothing can be defined as the process of matching the smoothness properties of the segmented object with the *a priori* smoothness properties of the ground truth.

The recognition process consists in finding markers (landmarks) for each object to be segmented. At this step, prior information can be taken into into account in the segmentation process. This prior knowledge derives from the modeling of the objects which are to be segmented. The delineation process, which is generally performed by watershed algorithms, looks for divides, localized on the "most contrasted areas" of the image, that separate the selected markers. Finally, the smoothing step filters the objects obtained after the delineation process by removing their non-significant parts, with respect to prior knowledge about the shape of the objects. The left ventricular myocardium (LVM) is delimited by two surfaces: the epicardial border (EpB) and the endocardial border (EnB). We consider (Fig. 1a): (*i*), the left ventricular chamber (named LVC) delimited by EnB and surrounded by LVM; and (*ii*), an object called $LVCM$, made by the union of the LVC and LVM, delimited by EpB and surrounded by LVB, the Left Ventricular Background that is the complementary set of $LVCM$.

The LVC is a connected set whose intensity is very high and which is surrounded by a significantly darker zone (see Fig. 1b). It is known, from anatomical description, that the EnB is an irregular surface.

The left ventricular myocardium surrounds the LVC and its intensity is darker than the one of LVC. The thickness of the LVM is not known in advance. It can change from one patient to another and it is neither constant everywhere around the chamber of a same patient. Nevertheless, the thickness of the LVM

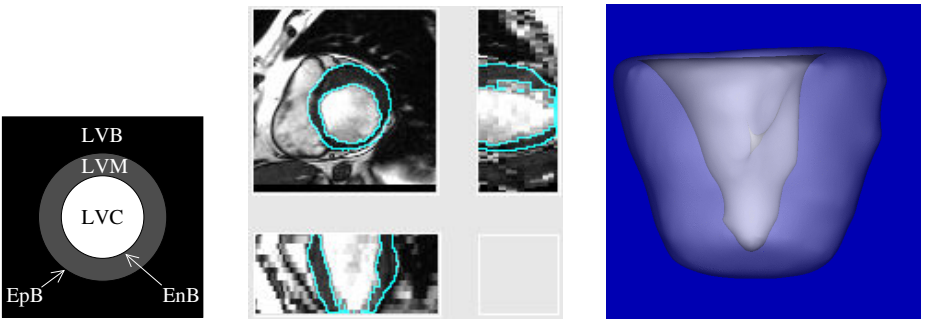

(*a*) (*b*) (*c*)

Fig. 1. (*a*), Objects of interest in LV images; (*b*), example of Left Ventricular Myocardium segmentation and (*c*), a surface rendering

is bounded, and since we only consider live patients, it cannot be null. Contrary to the EnB, the EpB is a smooth surface.

Last, the LVB is composed of several tissues including among other the liver, the stomach, the right ventricle and the lungs. Some of them, such as the right ventricle or the lungs, have characteristic intensities and can be used as landmarks for the LVB.

The proposed segmentation method is composed of two consecutive steps which consist of LVC segmentation, followed by $LVCM$ segmentation. Then, LVM is simply the set difference between them. Since endo- and epicardial borders differ both in terms of contrast and shape, we segment them by different strategies.

2.1 Endocardial Border Segmentation

The segmentation of the EnB is performed independently on each volume of the sequence. The idea is, first, to find a marker for the LVC (*i.e.*, a subset of the LVC made of points which belong to the LVC with certainty). Then, this marker is dilated conditionally to a second set made of points which possibly belong to the LVC.

The LVC is made of a very light core object surrounded by a "ring" of lower intensity (see Fig. 1). The core object C_t can be segmented, separately in each volume, by selecting the appropriate *connected component* of an upper-threshold $I_t[s_1]$ of the input image I_t at level s_1, *i.e.*, $I_t[s_1] = \{x \in V_t \mid I_t(x) \geq s_1\}$, where V_t is the set of voxels of the t-th 3D-image. In our experiments, the images are cropped such that, in each 3D volume, the center belongs to the core of LVC. To this aim, the user selects a single point roughly located at the center of the LVC in one of the 3D images of the sequence. Then, in each 3D image, a box whose center is the specified point is automatically cropped. This step, which is the only user interaction of the whole method, could be automated but the physicians who made the evaluation prefer to keep this control point.

Thus, in the 3D graph (induced by the classical 6-adjacency relation) corresponding to the image under consideration, C_t is the connected component of $I_t[s_1]$ which contains the center of the volume.

This core object is surrounded by a "ring" of lower intensity, still higher than the intensity of the LVM, which is a partial volume effect due the presence of both blood and muscle within the space of a single voxel. In order to get this ring segmented, we perform a second upper threshold $I_t[s_2]$ of I_t at level $s_2 < s_1$; $I_t[s_2]$ and C_t are combined together thanks to *a geodesic dilation of size* r_1 *of* C_t *in* $I_t[s_2]$ (see [10], chapter 6.1). In other words, LVC_t, the segmentation of the LVC in the t-th volume of the 4D sequence, is the set of all points *linked* to C_t by a *path in* $I_t[s_2]$ of *length* less than a predefined value $r_1 \in \mathbb{N}$.

2.2 Epicardial Border Segmentation

In this section, we describe $LVCM$ segmentation. This segmentation is performed after the one of the LVC. It must preserve some anatomical constraints. Since we consider live patients, the left ventricular myocardium does not have any hole. This leads to the constraint $EpB \cap EnB = \emptyset$. In the graph framework assumed in this paper, it means that, in each 3D graph of the 4D-sequence, the spatial neighborhood of LVC_t should be included in $LVCM_t$, the segmentation of the $LVCM$ in the t-th image: LVM must be at least one pixel thick.

The segmentation of $LVCM$ is performed thanks to a watershed-based procedure. Marker selection plays a primary role in the result of the watershed. In our application, it allows, in particular, to take into account the prior knowledge of the heart by imposing constraints on the markers. Since we want to get the separation between $LVCM$ and LVB, we need to select two markers, one for each of these objects. In the following, $mLVCM$ and $mLVB$ denote these two markers whereas $wLVCM$ and $wLVB$ denote the corresponding objects in the segmentation obtained through the watershed. The recognition process, described below, is performed independently on each volume of the 4D-sequence. On the other hand, the watershed is applied on the 4D-graph associated to the 4D-sequence starting from the union of all the markers extracted in 3D.

***mLVCM*: Recognition of the *LVCM*.** We first tackle the problem of computing $mLVCM_t$, for any given t. The watershed transform extends the markers as much as possible. Thus, by definition, each marker taken as an input of the watershed transform is included in the corresponding object obtained after the watershed. Hence, in order to fulfill the pre-cited inclusion constraint, we need to impose the inclusion of the spatial neighborhood of LVC_t in $mLVCM_t$.

In order to compute this marker, the basic idea is to dilate the already known left ventricular chamber as much as possible while ensuring that the marker lies in the "true" $LVCM_t$. Since we are dealing with infarcted ventricles, it is not reasonable to use the same dilation parameter everywhere around the chamber and for every different dataset. Thus, the dilations must be constrained in order to fit each particular anatomy. To this aim, we introduce a definition

of a *constrained dilation*, which, due to space restriction, is not provided in this paper but will be given in a forthcoming extended version.

In our application, the goal is to find a constraining set which is able to capture some of the features which are particular to the shape of the heart under consideration. Therefore, this set is extracted from the images. Some bright and dark regions (corresponding, for instance, to the right ventricle, the vascular network or the lungs) surrounds the LVM. These regions can be classified as non-myocardium objects and, thus, used as our constraining set. Some robust markers of these zones can be easily extracted by upper and lower threshold of the image: $\mathcal{T}_t = \{x \in V_t \setminus N_t(LVC_t) \mid I_t(x) < s_3 \text{ or } I_t(x) > s_4\}$, where $N_t(LVC_t)$ denotes the dilation of size 1 of LVC_t, $s_3 \in \mathbb{N}$ and $s_4 \in \mathbb{N}$. Then, $mLVCM_t$,the marker of the $LVCM$ in the t-th 3D image is defined as the dilation of size r_2 of $N_t(LVC_t)$ constrained by $\mathcal{T}_t$. The constrained dilation is designed to take into account that we deal with markers of an object rather than with its precise segmentation. Thus, the set $\mathcal{T}_t$ does not need to be a precise segmentation; it is used as a landmark for the right ventricle, the vascular network, etc...

***mLVB*: Recognition of the *LVB*.** We now explain how to compute, in each 3D image of the sequence, the marker for the left ventricular background ($mLVB_t$). We consider the following facts: (a), the thickness of a left ventricular myocardium cannot exceed a given threshold, denoted by r_3; (b) the set $\mathcal{T}_t$ is made of points which are in the background of the left ventricular chamber and myocardium. We deduce from fact (a) that the points farther from LVC_t than a distance of r_3 have to belong to LVB_t. This set is denoted by $LVB_t^{r_3}$. From fact (b), we also want $\mathcal{T}_t$ to be included in $mLVB_t$. In order to satisfy these two requirements, the easiest way is to consider $mLVB_t$ as the union of $LVB_t^{r_3}$ and $\mathcal{T}_t$. We observe that this set is not necessarily connected. Using it as a watershed marker can induce some unwanted configurations of $wLVCM_t$, obtained after the watershed process. In particular, $wLVCM_t$ can have some cavities.

In order to overcome this problem, the idea is to derive $mLVB_t$ by a topology-preserving transformation. It is straightforward that the left ventricular background contains a unique cavity made of the left ventricular chamber and myocardium. We remark that $mLVCM_t$ is, by construction, connected and that it must be surrounded by LVB_t. The complementary set of $mLVCM_t$ thus contains a unique cavity, and obviously, surrounds $mLVCM_t$. Therefore, we choose to derive $mLVB_t$ from the complementary set of $mLVCM_t$. The idea is to reduce this set while both preserving its topology and respecting facts (a) and (b).

To this aim, we use a *constrained ultimate homotopic skeleton* [12]. Roughly speaking, an ultimate homotopic skeleton of a set X constrained by a set C, has the same topology as X, contains C, and cannot be reduced (by point removal) while keeping these two invariants. Thus, we compute $mLVB_t$, the marker of the left ventricular background, as the skeleton of $\overline{mLVCM_t}$ (*i.e.*, the *complementary set* of $mLVCM_t$) constrained by $\mathcal{T}_t \cup LVB_t^{r_3}$. We finally obtain a set $mLVB_t$ which has the desired topology and which respects facts (a) and (b).

Delineation. The watershed transformation [11] is used as a fundamental step in many powerful segmentation procedures. It is a graph-based method that allows, from a gradient image, to find a "thin" separation between the components of a given set of points called marker. In this application, we use the watershed approach that we have developed since it has good robustness properties [13, 14]. We consider the 4D graph corresponding to the 3D+t sequence. The neighborhood of each voxel corresponds to its 6 neighbors in 3D and the voxels just "before" and "after" in the time sequence. In this graph, the watershed of the 4D gradient magnitude image is computed, starting from the two markers made by the union of all $mLVCM_t$ and $mLVB_t$. As a result, we obtain, a first segmentation of $LVCM$, denoted $wLVCM$ lying on a background object $wLVB$.

Smoothing. In order to obtain the final segmentation of $LVCM$, we use shape filters coming from mathematical morphology. An *alternating sequential filter (ASF) with parameters* r *and* r' is a sequence of intermixed *openings* and *closings* by balls of increasing size, where r and r' specify the radius of respectively the smallest and largest ball (see [10], chapter 8.3). An opening of a set X by a ball of radius r is the union of all balls of radius r which are included in X. On the other hand, the closing of X is the complementary of the opening of $\overline{X}$. Thus, an ASF smoothes the object and its complementary in a balanced way while preserving the "most significant balls" of both object and background.

The endocardial border can be modeled as the surface of a cone. Each section (perpendicular to the height axis) of a cone is a disc. Then, we consider 2-dimensional ASF, with parameters r_4 and r_5, for smoothing each 2D section of the 3D $wLVCM_t$.

3 Experiments

3.1 Image Acquisition

In our experiment, for each patient, the cine MRI dataset consisted of a succession of contiguous (no gap) LV short-axis 2D planes that were successively imaged over time (2D+t). The most basal slices included in the analysis were located just above mitral valve within LVC. To be included, the basal myocardium had to be visible in the entire circumference at end-systole. The most apical slice was chosen as the one with the smallest visible LVC at end-systole. The sequences were registered to the heart-cycle, and could therefore be stacked in order to construct 3D sequences. The number of 3D volumes during the entire cardiac cycle ranged from 22 to 37, depending on heart rate (49-91). Typically, the spatial resolution of each volume is $1,7 \times 1,7 \times 6\ mm^3$. Before applying the segmentation procedure, the images were over-sampled in order to get isotropic voxels. When a misalignment of the different sections of a same volume was observed, a translation-only registration procedure was possibly applied as a preprocessing step.

3.2 Parameters

Our method comprises two kinds of parameters. A first series is related with the shape of a left ventricle and can be expressed by distance measures. In our experiment, r_1, r_2, r_3, r_4 and r_5 were set up to respectively 9, 5, 25, 7 and 12 mm. These parameters are neither patient-specific nor device-specific. On the other hand, our method comprises a series of parameters relative to the intensity of the images. In our experiment, s_1, s_2, s_3, s_4 were set up to respectively 170, 105, 20, 170. These parameters are not patient-specific but they are device-dependent which means that they must be re-estimated for each device.

The proposed method relies on a succession of operators. The results of each of these operators are well specified with respect to anatomical constraint. Thus, each of them can be tuned separately: the operators –and, thus, the parameters– are independent. One of the two cardiologists estimated these parameters by independently tuning each operator thanks to qualitative assessment. This choice is the less time-consuming one since it does not require manual segmentation and minimizes the number of tests to be performed. For instance, s_1 is estimated by interactively thresholding the image: the highest threshold such that all points (above this threshold) connected to the center of the 3D volume belong to the LVC with certainty is kept. We emphasize that only 3 training datasets were enough to set up these parameters. Their complete tuning took four hours of work for the practician. We recall that if one wish to use the proposed method on a different device, only the parameters relative to image intensity need to be re-calibrated. This would require less than one hour.

Furthermore, during the setting of the parameters, we noticed their robustness with respect to small variations of typically, $\pm$ 5% for the parameters relative to the intensity of the images and $\pm$ 10% for the shape parameters. In a forthcoming extended version, we intend to make a systematic study of the impact of these small variations on the resulting segmentations.

3.3 Results

Four-dimensional cardiac cine-MR images were acquired in 18 consecutive patients which were not specifically chosen for this application. Images were processed automatically by the proposed 4D method. In Fig. 1, we show (b) the internal border (on 3 orthogonal sections of a 3D volume) of the segmented LVM, obtained by the 4D-method, superimposed to the corresponding sections of the original image and (c) a surface rendering of the segmentation. For comparison, the dataset was also manually segmented by 2 independent experts (cardiologists), called e_1 and e_2 in the sequel. For each 2D section, they manually overlaid EnB and EpB at both end-diastolic and end-systolic time.

Accuracy: Point-to-Surface Measurement. Given two surfaces ∂X and ∂Y represented by two sets of polygons, the *point-to-surface measurement* (P2S) between ∂X and ∂Y estimates the mean distance between the vertices of ∂X and ∂Y. A symmetrical measure is obtained by taking the maximum from the P2S between ∂X and ∂Y and the P2S between ∂Y and ∂X.

The P2S achieved by other groups for segmenting the endocardial and epicardial border on their datasets are presented in Table 1a.

On our dataset, the surfaces (EnB and EpB) were extracted from the segmentations by a marching cube algorithm. The P2S was computed from the segmentations obtained by the automated method and the two experts. In order to evaluate the inter-observer variability the P2S between the two experts is also provided. Table 1b presents the mean and standard deviation of these measures at end-diastolic time and end-systolic time. We note that, in all cases of Table 1b, the P2S is less than 1 pixel. We achieved a mean P2S of 1.51mm $\pm$ 0.38 for the endocardial border and a mean P2S of 1.81mm $\pm$ 0.43 for the epicardial border. These results compare favorably with those obtained by other groups on their own datasets (see Table 1b). Furthermore, the P2S between automatic and manual segmentations is in the same range as the inter-observer P2S. This is a strong indication that the automated method produces as satisfying a segmentation as either manual one.

Table 1. (a), Point to surface measurements from the results of different cardiac segmentation methods. (b), More details on the segmentations obtained by our method, (mean point to surface in mm $\pm$ standard deviation).

(a)

	EnB	EpB
[6]	2.01 $\pm$ 0.31	2.77 $\pm$ 0.49
[4]	2.75 $\pm$ 0.86	2.63 $\pm$ 0.76
[5]	2.28 $\pm$ 0.93	2.62 $\pm$ 0.75
[8]	1.88 $\pm$ 2.00	2.75 $\pm$ 2.62
[7]	1.97 $\pm$ 0.54	2.23 $\pm$ 0.46
ours	1.51 $\pm$ 0.38	1.81 $\pm$ 0.43

(b)

	soft. vs. e_1	soft. vs. e_2	e_1 vs. e_2
End-diastolic time			
EnB	1.52 $\pm$ 0.35	1.67 $\pm$ 0.43	1.37 $\pm$ 0.47
EpB	2.04 $\pm$ 0.35	1.68 $\pm$ 0.39	1.23 $\pm$ 0.41
End-systolic time			
EnB	1.50 $\pm$ 0.41	1.35 $\pm$ 0.34	1.15 $\pm$ 0.41
EpB	1.90 $\pm$ 0.56	1.61 $\pm$ 0.41	1.31 $\pm$ 0.83

Assessment of Critical Parameters. Left ventricular ejection fraction (EF) and left ventricular myocardium mass (MM) are critical parameters for cardiac diagnosis and remodeling prevention. Their estimation is routinely used by cardiologists. The EF is the amount of blood ejected during a heart cycle expressed as a fraction of the tele-diastolic volume. In our dataset the EF (resp. MM) range was 20-75% (resp. 94-197 g).

From the segmented images, the EF can be simply computed by $(|LVC_{\max}| - |LVC_{\min}|)/|LVC_{\max}|$, where $|LVC_{\max}|$ (resp. $|LVC_{\min}|$) is the maximal (resp. minimal) volume of the left ventricular chamber along the heart cycle. Let X_p^o denote the measure of the parameter X performed by operator o for patient p, where $X \in \{EF, MM\}$, $o \in \{e_1, e_2, s\}$, and $p \in [1, 18]$. We take $refX_p = (X_p^{e_1} + X_p^{e_2})/2$ as a reference value for the parameter X on patient p and we evaluate the deviation $\Delta X_p^o = |X_p^o - refX_p|/refX_p$. Notice that $\Delta X_p^{e_1} = \Delta X_p^{e_2}$. Over all 18 patients, the automated method achieved a mean deviation on the EF (resp. MM) of 0.032 (resp. 0.050) whereas the experts achieved 0.055 (resp. 0.052). Furthermore, we observe that ΔEF_p^s (resp. ΔMM_p^s) is less than $\Delta EF_p^{e_1}$ (resp. $\Delta MM_p^{e_1}$) in 8 (resp. 9) of the 18 patients. In other words, the deviation on the EF (resp. MM) achieved by the automated method is less than the deviation

achieved by the experts in 8 (resp. 9) of the 18 patients. We conclude that the automated tool produces reliable assessment of left ventricular functional parameters comparable to the experts'.

Further experimental analysis, including, in particular, a qualitative assessment of the method, will be provided in an extended version of this paper.

Temporal Consistency. The proposed segmentation scheme has been tested using the 4D watershed-based procedure described above and also with a variant using only 3D watersheds (one per volume V_t). It is visible on the computer screen that, contrary to the 3D variant, the 4D algorithm helps keeping the temporal coherency between successive segmentations along the heart cycle. In order to precisely evaluate this temporal coherency, we compute, for both methods, the P2S between successive EpBs along the cardiac cycle. The means of these measurements among all patients are plotted along the cardiac cycle in Fig. 2. We observe that both curves have the same shape but that there is a nearly constant difference between them. Thus, this confirms the fact that segmentations obtained by the 4D method are more regular.

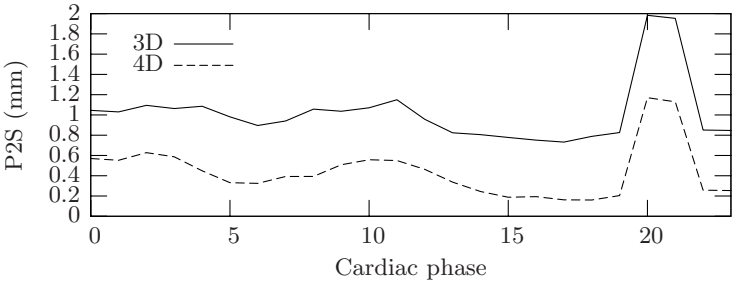

Fig. 2. The point to surface measurements between the successive EpBs along the cardiac cycle

The segmentation of endocardial borders is performed independently on each 3D volume of the sequence. Nevertheless, we have not noticed any regularity problem in the EnBs produced by the automated software. This explains why we have not developed a 4D procedure to segment the LVC.

4 Conclusion and Perspectives

In this paper, we propose a fast (worst computation time among the 18 datasets is 4'3" on a conventional personal computer) and automated procedure to segment the left ventricular myocardium in 4D cine-MRI sequences, taking into account temporal consistency. This procedure can be used in clinical routine. Thanks to the comparison with manual segmentations performed by two cardiologists, we demonstrated the accuracy of the proposed method and the precision of the ejection fraction and myocardium mass derived from the automated segmentations.

References

1. Buser, P.T., Auffermann, W., Holt, W.W., Wagner, S., Kircher, B., Wolfe, C., Higgins, C.B.: Noninvasive evaluation of global left ventricular function with use of cine nuclear magnetic resonance. Journal of the American College of Cardiology 2(13), 1294–1300 (1989)
2. McInerney, T., Terzopoulos, D.: A dynamic finite element surface model for segmentation and tracking in multidimensional medical images with application to cardiac 4D image analysis. Computerized Medical Imaging and Graphics 19(1), 69–83 (1995)
3. van der Geest, R.J., Buller, V.G.M., Jansen, E., Lamb, H.J., Baur, L.H.B., van der Wall, E.E., de Roos, A., Reiber, J.H.C.: Comparison between manual and semiautomated analysis of left ventricular parameters from short-axis MR images. Journal of Computer Assisted Tomography 21, 756–765 (1997)
4. Mitchell, S.C., Lelieveldt, B.P.F., van der Geest, R.J., Bosch, H.G., Reiber, J.H.C., Sonka, M.: Multistage hybrid active appearance model matching: Segmentation of left and right ventricles in cardiac mr images. IEEE Trans. on Medical Imaging 20(5), 415–423 (2001)
5. Kaus, M.R., von Berg, J., Weese, J., Niessen, W., Pekar, V.: Automated segmentation of the left ventricle in cardiac MRI. Medical Image Analysis 8, 245–254 (2004)
6. Lötjönen, J., Kivistö, S., Koikkalainen, J., Smutek, D., Lauerma, K.: Statistical shape model of atria, ventricles and epicardium from short- and long-axis MR images. Medical Image Analysis 8, 371–386 (2004)
7. van Assen, H., Danilouchkine, M.G., Frangi, A.F., Ordàs, S., Westenberg, J.J.M., Reiber, J.H.C., Lelieveldt, B.P.F.: SPASM: A 3D-ASM for segmentation of sparse and arbitrarily oriented cardiac MRI data. Medical Image Analysis 10, 286–303 (2006)
8. Lorenzo-Valdés, M., Sanchez-Ortiz, G.I., Elington, A.G., Mohiaddin, R.H., Rueckert, D.: Segmentation of 4D cardiac MR images using a probabilistic atlas and the EM algorithm. Medical Image Analysis 10, 286–303 (2006)
9. Montagnat, J., Delingette, H.: 4D deformable models with temporal constraints: application to 4D cardiac image segmentation. Medical Image Analysis 9, 87–100 (2005)
10. Soille, P.: Morphological Image Analysis. Springer, Heidelberg (1999)
11. Beucher, S., Meyer, F.: The morphological approach to segmentation: the watershed transformation. In: Dougherty, E. (ed.) Mathematical Morphology in Image Processing, Marcel Decker, pp. 443–481 (1993)
12. Couprie, M., Coeurjolly, D., Zrour, R.: Discrete bisector function and Euclidean skeleton in 2D and 3D. Image and Vision Computing (to appear) (2006)
13. Najman, L., Couprie, M., Bertrand, G.: Watersheds, mosaics and the emergence paradigm. Discrete Applied Mathematics 147(2-3), 301–324 (2005)
14. Couprie, M., Najman, L., Bertrand, G.: Quasi-linear algorithms for the topological watershed. Journal of Mathematical Imaging and Vision 22(2-3), 231–249 (2005)

Author Index